AD-A266 394

ANNUAL REPORT

University Research Initiative

Contract No.: N00014-92-J-1808
March 1992 - April 1993

DTIC
ELECTE
JUN 21 1993
S A D

The Processing and Mechanical Properties of High Temperature/ High Performance Composites

by

A.G. Evans & F. Leckie
University of California,
Santa Barbara

University of Pennsylvania
Harvard University
Washington State University
Carnegie Mellon University
University of Virginia

This document has been approved for public release and sale; its distribution is unlimited.

93-13750

93 6 17 035

Book 1 of 5:

CONSTITUENT PROPERTIES OF COMPOSITES

REPORT DOCUMENTATION PAGE

Form Approved
OMB No. 0705-0188

1. AGENCY USE ONLY (Leave blank)	2. REPORT DATE	3. REPORT TYPE AND DATES COVERED
	930228	ANNUAL REPORT 920301 TO 930228

4. TITLE AND SUBTITLE

The Processing and Mechanical Properties of High Temperature/ Performance Composites

5. FUNDING NUMBERS

N00014-92-J-1808

6. AUTHOR(S)

Evans, Anthony G.
Leckie, Frederick A.

7. PERFORMING ORGANIZATION NAME(S) AND ADDRESS(ES)

MATERIALS DEPARTMENT
COLLEGE OF ENGINEERING
UNIVERSITY OF CALIFORNIA
SANTA BARBARA, CA 93106-5050

8. PERFORMING ORGANIZATION REPORT NUMBER

9. SPONSORING/MONITORING AGENCY NAME(S) AND ADDRESS(ES)

OFFICE OF NAVAL RESEARCH
MATERIALS DIVISION
800 NORTH QUINCY STREET
ARLINGTON, VA 22217-5000

DEF. ADV. RESEARCH PROJ. AGENCY
1400 WILSON BLVD..
ARLINGTON, VA 22209

10. SPONSORING/MONITORING AGENCY REPORT NUMBER

11. SUPPLEMENTARY NOTES

12A. DISTRIBUTION/AVAILABILITY STATEMENT

See Distribution List

12B. DISTRIBUTION CODE

13. ABSTRACT (Maximum 200 words)

The annual report of the University Research Initiative project at UCSB on High Temperature, High Performance Composites consists of five books. The books are entitled as follows: 1-Constituent Properties of Composites, 2-Constituent Properties and Macroscopic Performance: CMCs, 3-Constituent Properties and Macroscopic Performance: MMCs, 4-Constitutive Laws and Design 5-Processing and Miscellaneous Properties

14. SUBJECT TERM

Design, Interfaces, Coatings, Toughening, Processing, Computation, Mechanisms, Composites, Ceramics, Intermetallics

15. NUMBER OF PAGES

2430

16. PRICE CODE

17. SECURITY CLASSIFICATION OF REPORT	18. SECURITY CLASSIFICATION OF THIS PAGE	19. SECURITY CLASSIFICATION OF ABSTRACT	20. LIMITATION OF ABSTRACT
UNCLASSIFIED	UNCLASSIFIED	UNCLASSIFIED	

SUMMARY

OF

TABLE OF CONTENTS

Accession For
NTIS GRA&I
DTIC TAB
Unannounced
Justification
By
Distribution/
Availability Codes
Dist Special
A-1
AD-A216146

BOOK 1

CONSTITUENT PROPERTIES OF COMPOSITES

11.	The Directionality of Interfacial Cracking in Bimaterials	J.S. Wang G. Beltz
12.	Crack Direction Effects Along Copper/Sapphire Interfaces	G. Beltz J.S. Wang
13.	Steady State Matrix Cracking of Ceramics Reinforced by Aligned Fibers and Transforming Particles	Y.L. Cui B. Budiansky
14.	A High-Toughness γ-Titanium Aluminide	H.E. Dève A.G. Evans D.S. Shih
15.	On the Mechanics of Stress-Induced Phase Transformation in Zirconia	B. Budiansky L. Truskinovsky
16.	Deformation of Nanoscale Cermets	A.G. Evans J.P. Hirth

BOOK 2

CONSTITUENT PROPERTIES AND MACROSCOPIC PERFORMANCE: CMCs

26.	On the Flexural Properties of Brittle Multilayer Materials	C.A. Folsom F.W. Zok F.F. Lange
27.	The Creep Behavior of CAS/Nicalon Continuous-Fiber Composites	C.H. Weber J.P.A. Löfvander A.G. Evans
28.	Stress Corrosion and Fatigue Cracking in a Unidirectional Ceramic-Matrix Composite	S.M. Spearing F.W. Zok A.G. Evans
29.	Tensile and Flexural Ultimate Strength of Fiber-Reinforced Ceramic-Matrix Composites	F. Hild J.-M. Domergue F.A. Leckie A.G. Evans
30.	Fracture Resistance Characteristics of a Metal-Toughened Ceramic	B.D. Flinn C.S. Lo F.W. Zok A.G. Evans
31.	On the Strength of Ductile Particle Reinforced Brittle Matrix Composites	G. Bao F.W. Zok
32.	SiC/CAS: A Notch Insensitive Ceramic Matrix Composite	C. Cady T.J. Mackin A.G. Evans
33.	Notch Sensitivity and Stress Redistribution in CMCs	T.J. Mackin T.E. Purcell M.Y. He A.G. Evans

BOOK 3

CONSTITUENT PROPERTIES AND MACROSCOPIC PERFORMANCE: MMCs

43.	The Mechanics of Crack Growth in Layered Materials	M.Y. He F.E. Heredia D.J. Wissuchek M.C. Shaw A.G. Evans
44.	Small Scale Yielding at a Crack Normal to the Interface Between an Elastic and a Yielding Material	M.Y. He R.M. McMeeking Zhang
45.	Cracking and Stress Redistribution in Ceramic Layered Composites	K.S. Chan M.Y. He J.W. Hutchinson
46.	The Effect of Interface Diffusion and Slip on the Creep Resistance of Particulate Composite Materials	P. Sofronis R.M. McMeeking
47.	*Power Law Creep of a Composite Material* Containing Discontinuous Rigid Aligned Fibers	R.M. McMeeking
48.	Effects of Misfit Strain and Reverse Loading on the Flow Strength of Particulate-Reinforced Al Matrix Composites	S.M. Pickard S. Schmauder D.B. Zahl A.G. Evans
49.	Continuum Models for Deformation: Discontinuous Reinforcements	J.W. Hutchinson R.M. McMeeking

BOOK 4

CONSTITUTIVE LAWS AND DESIGN

60.	A Direct Method for the Shakedown Analysis of Structures Under Sustained and Cyclic Loads	W. Jiang F.A. Leckie
61.	Creep of Fiber Reinforced Metal-Matrix Composites: Constitutive Equations and Computational Issues	N. Aravas C. Cheng
62.	On Neutral Holes in Tailored, Layered Sheets	B. Budiansky J.W. Hutchinson A.G. Evans
63.	The In-Plane Shear Properties of 2-D Ceramic Matrix Composites	P.A. Brøndsted F.E. Heredia A.G. Evans
64.	Transverse Cracking in Fiber-Reinforced Brittle Matrix, Cross-Ply Laminates	Z.C. Xia R.R. Carr J.W. Hutchinson
65.	Plane Strain Delamination Growth in Composite Panels	P-L. Larsson F.A. Leckie
66.	Mixed Mode Delamination Cracking in Brittle Matrix Composites	G. Bao B. Fan A.G. Evans
67.	Mixed Mode Cracking in Layered Materials	J.W. Hutchinson B.-X. Wu
68.	Crazing of Laminates	J. Lemaitre F.A. Leckie D. Sherman

BOOK 5

PROCESSING AND MISCELLANEOUS PROPERTIES

69.	Computer Aided Manufacturing Through Selective Material Deposition	F.B. Prinz L.E. Weiss M. Terk
70.	Environmentally Compatible Double Coating Concepts for Sapphire Fiber-Reinforced γ-TiAl	T.J. Mackin J. Yang C.G. Levi A.G. Evans
71.	Modeling the Fracture of Fibers During Metal Matrix Composite Consolidation	D.M. Elzey H.N.G. Wadley
72.	The Effect of Processing on the Interface Structure/Property Relationship in a Ti 24Al 11Nb (at%) Composite	Cantonwine thesis (part of Wadley contribution)
73.	The Evolution of Metastable B$_f$ Borides in a Ti-Al-B Alloy	M. De Graef J.P.A. Löfvander McCullough C.G. Levi
74.	Measurement of Residual Stresses in Sapphire Fiber Composites Using Optical Fluorescence	Q. Ma D.R. Clarke
75.	Compressive Failure of Fiber Composites	B. Budiansky N.A. Fleck
76.	Compressive Failure of Fiber Composites: The Roles of Multi-Axial Loading and Creep	W.S. Slaughter N.A. Fleck B. Budiansky
77.	Prediction of Kink Width in Fiber Composites	N.A. Fleck L. Deng B. Budiansky
78.	Mechanical Properties of Partially Dense Alumina Produced from Powder Compacts	D.C.C. Lam F.F. Lange A.G. Evans

79.	Cracking Due to Localized Hot Shock	V. Tvergaard Z.C. Xia J.W. Hutchinson
80.	The Physics and Mechanics of Brittle Matrix Composites	A.G. Evans F.W. Zok
81.	*In Situ* Growth of SiC in $MoSi_2$ by Melt Processing	D.J. Tilly J.P.A. Löfvander C.G. Levi

EXECUTIVE SUMMARY

1. GENERAL STRATEGY

The overall program embraces property profiles, manufacturing, design and sensor development (Fig. 1) consistent with a concurrent engineering philosophy. For this purpose, the program has created networks with the other composites activities. *Manufacturing* research on MMCs is strongly coupled with the 3M Model Factory and with the DARPA consolidation team. Major links with Corning and SEP are being established for CMC manufacturing. *Design Team* activities are coordinated by exchange visits, in February/March, to Pratt and Whitney, General Electric, McDonnell Douglas and Corning. Other visits and exchanges are being discussed. These visits serve both as a critique of the research plan and as a means of disseminating the knowledge acquired in 1992.

The program strategy concerned with design attempts to provide a balance of effort between *properties* and *design* by having studies of mechanisms and property profiles, which intersect with a focused activity devoted to design problems (Fig. 2). The latter includes two foci, one on MMCs and one on CMCs. Each focus reflects differences in the property emphases required for design. The intersections with the mechanism studies ensure that commonalties in behavior continue to be identified, and also facilitate the efficient transfer of models between MMCs and CMCs.

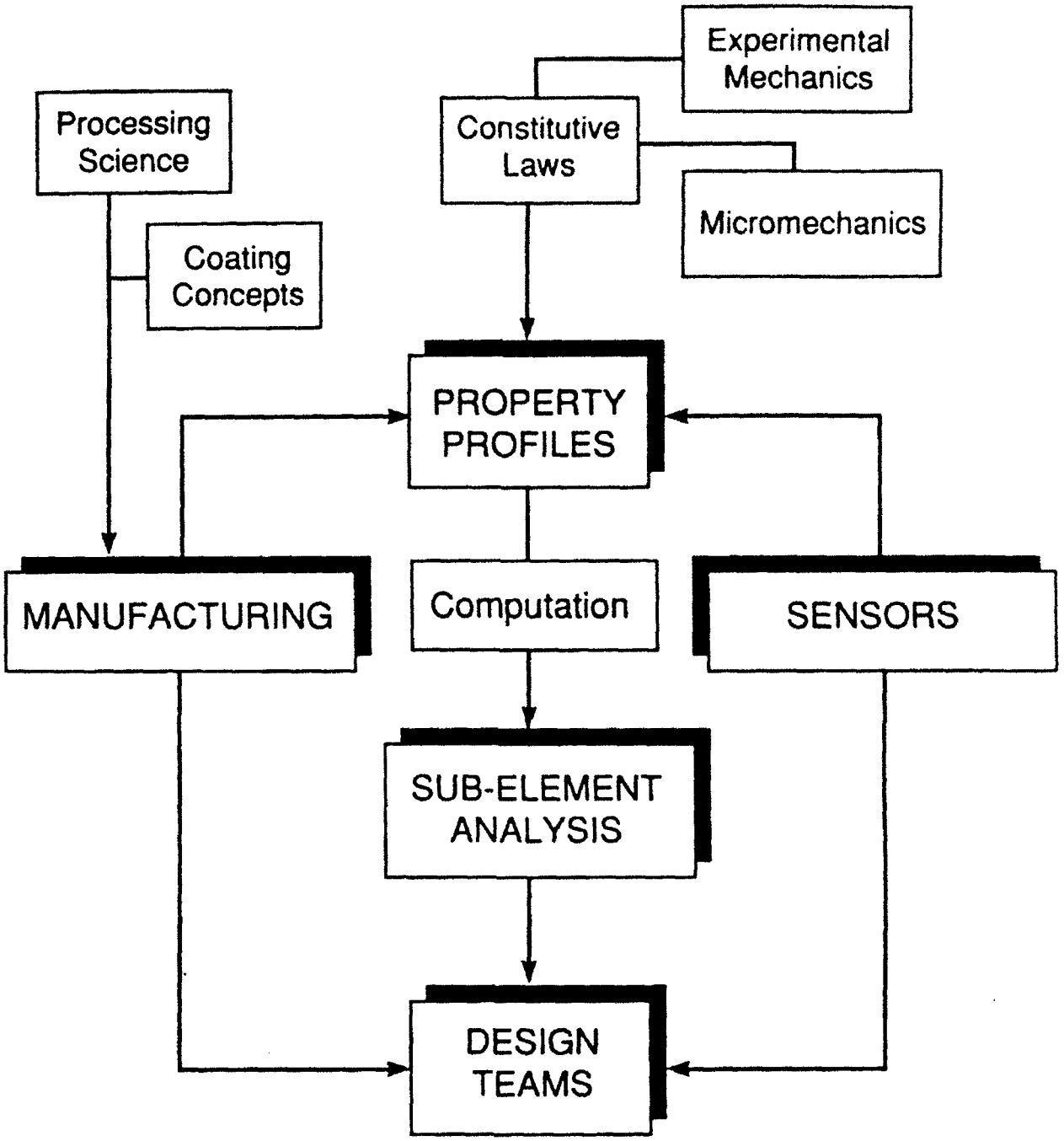

Fig. 1 The Concurrent Engineering Approach

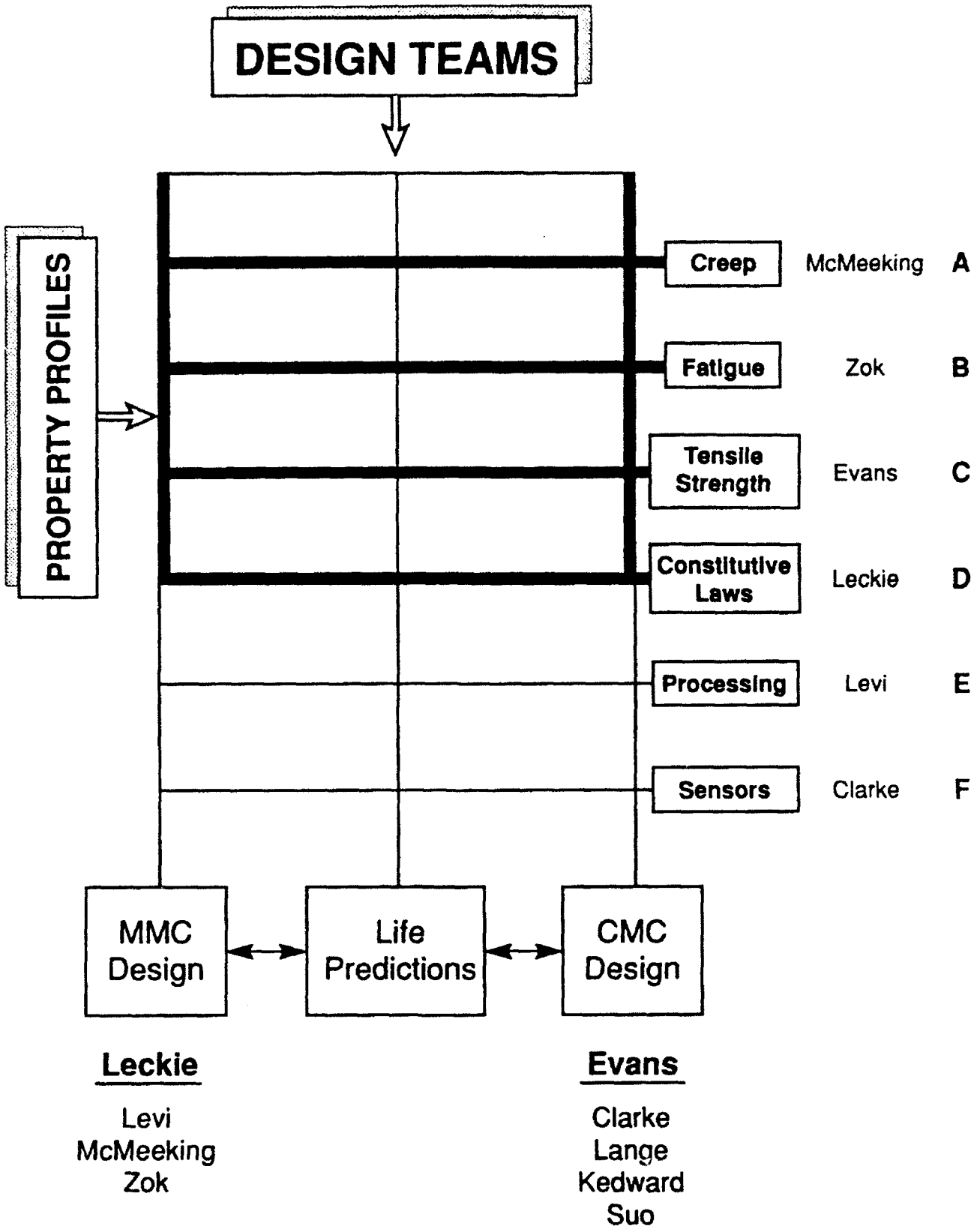

Fig. 2
Matrix Structure of Program

2. PROPERTY PROFILES

Each research activity concerned with properties begins with experiments that identify the principal property-controlling phenomena. Models are then developed that relate the physical response to constituent properties. These models, when validated, provide the constitutive laws required for calculating stress redistribution, failure and damage progression. They also provide a solid physics and mechanics understanding, which can be used to judge the effectiveness of the simplified procedures needed for design purposes.

2.1 Fatigue

Studies of the propagation of dominant mode I fatigue cracks from notches in MMCs, including the role of fiber bridging and fiber failure, have been comprehensively addressed (Zok, McMeeking). Software programs that include these effects have been developed. These are being transferred to Pratt and Whitney and KAMAN Sciences. The effects of thermal cycling on crack growth in MMCs have also been modelled (McMeeking). The results highlight the opposing effects of cycling on matrix crack growth and fiber failure (the fatigue threshold), when thermal cycles are superposed onto load cycles. Notably, matrix crack growth is enhanced by out-of-phase thermomechanical cycling, but fiber failure is suppressed (and vice versa for in-phase cycling). Experimental studies that examine these predictions are planned (Zok).

Studies have also been conducted on systems that exhibit *multiple* matrix cracking (Zok). The tensile stress-strain behavior of composites containing such cracks is analogous to the behavior of unidirectional CMCs

under monotonic tensile loading. As a result, models developed to describe the tensile response of the CMCs have found utility in describing the MMCs. However, two important differences in the two classes of composite have been identified and are presently being addressed. The first deals with the nature of the crack patterns. In the CMCs, the cracks are more or less uniformly spaced and generally span across the entire composite section. In contrast, the MMCs exhibit a broader distribution of crack sizes, many of which are short compared with the specimen dimensions. Methodologies for measurement and interpretation of crack densities in MMCs are being developed. The second problem deals with degradation in the interfacial sliding properties with cyclic sliding in the MMCs. Such degradation is presently being studied using fiber push-out tests in fatigued specimens.

Thermal fatigue studies on MMCs subject to transverse loading have been performed and have established the conditions that allow shakedown (Leckie). The shakedown range is found to be strongly influenced by the extent of matrix creep, which defines a temperature limitation on the use of the material. The eventual outcome of this activity would be the specification of parameters that ensure shakedown and avoid ratcheting.

The next challenge for MMCs concern the quantification of transitions in fatigue behavior, especially those found at higher temperatures. These include multiple matrix cracking and shear band formation. Experimental studies are in progress which will be used to establish a mechanism map. The map, when developed, would explicitly identify the transitions (Zok). The analogous behavior found in CMCs will facilitate this development. Other high temperature phenomena to be explored include changes in the interfacial sliding behavior due to both relaxations in the thermal residual stresses and the growth of reaction products near the fiber-matrix interface.

Fatigue damage studies on 2-D CMCs will focus on interface and fiber degradation phenomena, especially at elevated temperatures (Evans, Zok). Cyclic loading into the stress range at which matrix cracks exist is known to modify the interface sliding stress and may weaken the fibers. These degradation effects can be distinguished, because they change the hysteresis loop and reduce the UTS, respectively. Experiments that probe these material responses are planned. In addition, models that include the influence of cyclic fiber failure and pull-out on fatigue damage will be developed (Suo).

2.2 Matrix Cracking

Models of the plastic strain and modulus changes caused by various modes of matrix cracking have been developed. These solutions have provided a rationale for experimental studies on the tensile and shear behavior of CMCs and on the fatigue of MMCs (Hutchinson, Zok, Evans, Suo, Budiansky, McMeeking). The information has been used in two distinct ways. (i) Test methodologies have been devised that relate stress/displacement measurements to constituent properties (Table I). (ii) Stress/strain curves and matrix crack evolution have been simulated for specific combinations of constituent properties.

The development of the procedures and their implementation are still in progress. Independent solutions have been established for matrix cracks in 0° plies and 90° plies upon tensile loading. The former has been experimentally validated on 1-D materials (SiC/SiC and SiC/CAS). Measurements of plastic strain, hysteresis loops and crack densities have been checked against the models for consistency.

TABLE I

Relevant Constituent Properties and Measurement Methods

CONSTITUENT PROPERTY	MEASUREMENT
Sliding Stress, τ	• Pull-Out Length, $\bar{h}$ • Saturation Crack Spacing, $\bar{l}_s$ • Hysteresis Loop, $\delta\varepsilon_{1/2}$ • Unloading Modulus, $\bar{E}_L$
Characteristic Strength, S_c, m	• Fracture Mirrors • Ultimate Strength, S
Misfit Strain, Ω (q)	• Bilayer Distortion • Permanent Strain, ε_p • Residual Crack Opening
Matrix Fracture Energy, Γ_m	• Monolithic Material • Saturation Crack Spacing, $\bar{l}_s$ • Matrix Cracking Stress, $\bar{\sigma}_{mc}$
Debond Energy, Γ_i	• Permanent Strain, ε_p • Residual Crack Opening

The next challenge is to couple the models together in order to simulate the evolution of matrix cracks in 2-D materials, subject to tensile loading (Hutchinson, Budiansky). Related effects on the ultimate tensile strength caused by stress concentrations in the fibers in the presence of matrix cracks, would also be evaluated. Experimental measurements of stress/strain behavior in 2-D CMCs, with concurrent observations of matrix crack evolution, would be used to guide and validate such models (Evans, Kedward).

2.3 Constitutive Equations

Constitutive equations provide the link between material behavior at the meso-scale and the performance of engineering components. The equations can be established from the results of uniaxial and transverse tensile tests together with in-plane shear loading. For a complete formulation, which describes accurately the growth of failure mechanisms and the conditions of failure at the meso-scale, it is also necessary to perform calculations which are valid at the micro-scale.

These procedures have been completed for metal-matrix composites (Jansson, Leckie), and the resulting constitutive equations are operational in the ABAQUS finite element code. The behavior of simple panels penetrated by circular holes have been studied and the results await comparison with experiments which are planned for the coming year. The constitutive equations are formulated in terms of state variables which include the hardening tensors and damage state variables which describe debonding at the interface and void growth in the matrix. The format is sufficiently general to allow the inclusion of failure mechanisms such as environmental attack as the appropriate understanding is available. For

example, the effect of matrix and fiber creep mechanisms (Aravas) have also been introduced into ABAQUS, and it is proposed to extend the creep conditions t· ·nclude the effects of variable loading and temperature.

A similar approach has been taken towards the modulus of CMCs. In this case, efforts have been made to include the influence of matrix cracking, in-plane shearing and fiber breakage. The latter consideration is based on the global load sharing model (Hayhurst). The equations are also available in ABAQUS. At present, matrix cracking is introduced by assuming a matrix stress accompanied by an increase of strain. However, based on the more recent understanding of the growth of matrix cracks (above) it is intended to introduce these mechanisms into the constitutive equations for CMCs.

2.4 Creep

The emphases of the creep investigations have been on the anisotropic characteristics of unidirectional layers in which the fibers are elastic, but the matrix creeps. Experiments and models of the longitudinal creep properties of such materials have been initiated (McMeeking, Leckie, Evans, Zok, Aravas). The critical issues in this orientation concern the incidence of fiber failure and the subsequent sliding response of the interface. A modelling effort has established an approach that allows the stochastic evolution of fiber failure to occur as stress is transferred onto the fibers by matrix creep (McMeeking). This approach leads to creep rates with a large power law exponent. Various attempts are underway to incorporate the interface sliding initiated by fiber breaks and to introduce sliding into the creep rate formulation. Experiments being performed on unidirectional Ti matrix materials are examining the incidence of fiber failures on the creep

deformation (Evans, Leckie, Zok). These results will guide the modelling effort concerned with interface sliding effects. Insight will also be gained about fiber failure stochastics during creep, especially differences from room temperature behavior.

The transverse creep properties are expected to have direct analogies with composite deformation for a power law hardening matrix (Section 2.3). In particular, the same effects of debonding and matrix damages arise and can be incorporated in an equivalent manner (Leckie, Aravas). Testing is being performed on Ti MMCs and on SiC/CAS to validate the models.

Experiments on Ti-matrix 0°/90° cross-ply composites are planned. Creep models appropriate to cross-ply materials will be developed by combining those corresponding to the unidirectional materials in the longitudinal and transverse orientations, using a rule-of-mixtures approach. Such an approach is expected to be adequate for loadings in which the principal stresses coincide with the fiber axes. Alternate approaches will be sought to describe the material response in other orientations.

Some CMCs contain fibers that creep more extensively than the matrix. This creep deformation has been found to elevate the stress in the matrix and cause time dependent evolution of matrix cracks. This coupled process results in continuous creep deformation with relatively low creep ductility. Experiments on such materials are continuing (Evans, Leckie) and a modelling effort will be initiated (Suo). The models would include load transfer into the matrix by creeping fibers, with sliding interfaces, leading to enhanced matrix cracking.

2.5 Tensile Strength

The ultimate strength (UTS) of both CMCs and MMCs (as well as fatigue and creep thresholds) is dominated by fiber failure. With the global load sharing (GLS) concept of fiber failure now well established, the recent emphasis has been on defining the constituent properties needed to ensure GLS. The approach has been to perform local load sharing calculations and then compare experimental UTS data with the GLS predictions (Curtin, Evans, Leckie). The situation is unresolved. However, initial calculations on CMCs (Curtin) and MMCs (Evans) have provided some insight. Two key remaining issues concern the magnitude of the stress concentration in intact fibers caused by matrix cracks and the role of fiber pull-out in alleviating those stresses. Calculations of these effects are planned (Budiansky, Suo).

Degradation of the fiber strength upon either high temperature (creep) testing, atmospheric exposure, or fatigue are other topics of interest. Rupture testing performed under these conditions will be assessed in terms of degradation in fiber properties.

3. DESIGN TEAMS

3.1 The Approach

The overall philosophy of the design effort is to eventually combine *material models*, with a *materials selector*, and a *data base*, within a unified software package (Prinz). One example of a composites data base is that developed for MMCs by KAMAN Sciences, which forms the basis for a potential collaboration. The materials selector has already been developed

for monolithic materials (Ashby) and is available for purchase. This selector requires expansion to incorporate phenomena that have special significance for high temperature composites, including creep and thermal fatigue. These new features will be developed and included in the advanced selector software (Ashby).

The modelling approach is illustrated in Table II. Failure mechanisms and their effect on material behavior have been introduced into constitutive equations. The stress, strain and damage fields which develop in components during the cycles of loading and temperature can then be computed. Experiments shall be performed on simple components such as holes in plates, and comparison made with the computational predictions. Since constitutive equations are modeled using the results of coupon tests, it is likely that additional failure modes shall come to light during component testing. These mechanisms shall be studied and the appropriate mechanics developed so that their influence is correctly factored into the constitutive equations. In this way, increased confidence in the reliability of the constitutive equations can be established in a systematic way.

In practice, it is most probable that the constitutive equations are too complex for application at the creative level of the design process. It is then that simple but reliable procedures are of greater use. Some success has been achieved in this regard for MMCs subjected to cyclic mechanical and thermal loading (Jansson, Ponter, Leckie), as well as for strength calculations of CMC panels penetrated by holes (Suo) and the fatigue of MMCs (Zok, McMeeking). In all cases simplifications are introduced after a complete and reliable analysis has been completed which provides a standard against which the effects of simplification can be assessed.

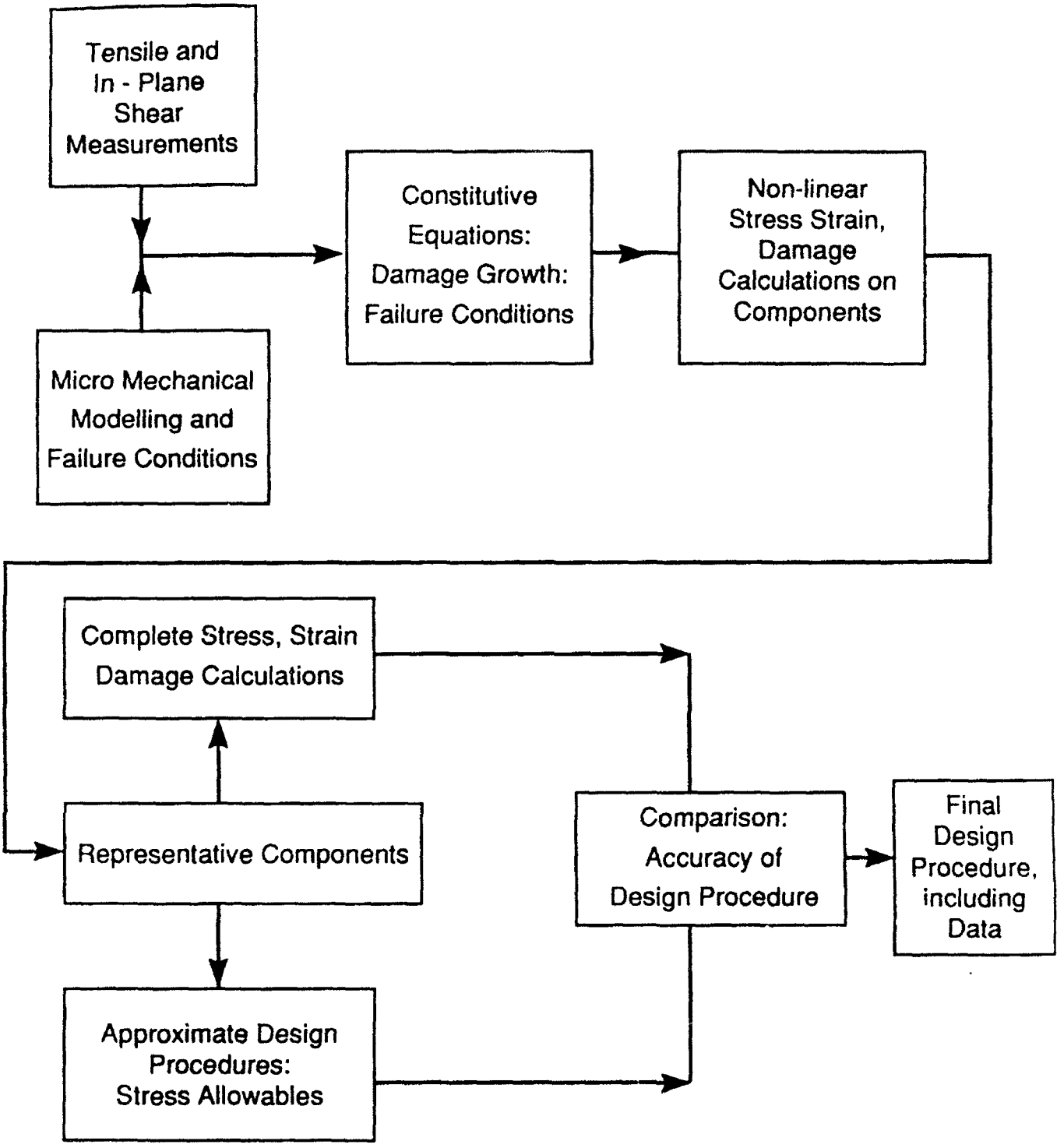

Table II

The Modelling Approach

3.2 Ceramic Matrix Composite Design

The design effort on CMCs will have its major focus on pin-loaded holes used for attachments (Fig. 3). A smaller activity, expected to expand in 1994, will address delamination cracking. The hole design includes several related topics. Each topic is concerned with aspects of constitutive law development (Table III), highlighted during the study group. Combined experimental and modelling efforts on the *tensile properties* of CMCs have established that the plastic strains are dominated by matrix cracks in the 0° plies. The matrix cracking models developed in the program demonstrate that these strains are governed by four independent constituent properties [(Table I) τ, Γ_i, Ω and Γ_m] which combine and interrelate through five non-dimensional parameters (Table IV). This modelling background suggests a concept for using model-based knowledge to develop constitutive laws. The following steps are involved (Table III). (i) A model-based methodology for inferring the constituent properties of unidirectional CMCs from macroscopic stress/strain behavior has been devised and is being experimentally tested on a range of materials (Evans). (ii) Upon validation, the models would allow stress/strain curves to be simulated (Hutchinson). This capability would facilitate a sensitivity study to be performed, in order to determine the minimum number of independent parameters that adequately represent the constitutive law. A strictly empirical law would require 3 parameters (yield strength, hardening rate and unloading modulus). Consequently, the objective might be to seek 3 combinations of the 4 constituent properties. (iii) Experiments would be performed and models developed that establish the matrix cracking sequence in 2-D materials (Hutchinson, Evans, Kedward). These would be conducted on

DESIGN PROBLEM IN CMC's

Design of Holes in Nozzles / Combustors

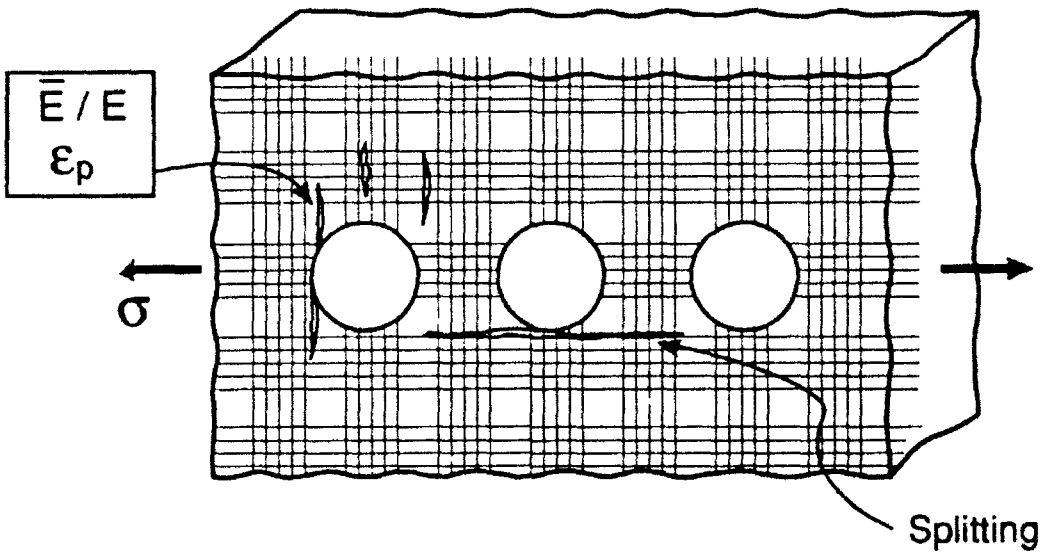

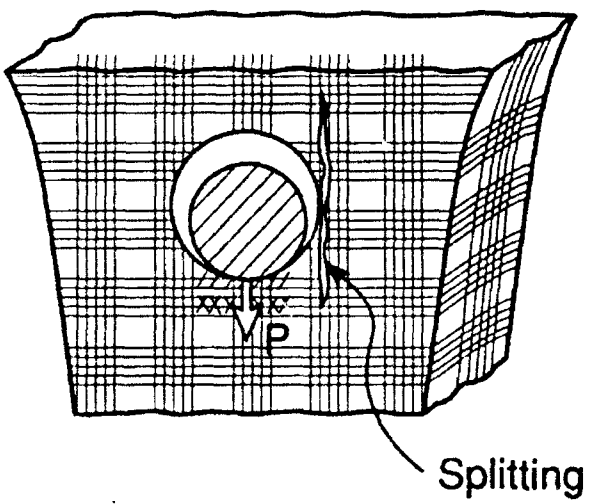

Issues

Tensile Rupture
Crushing
Splitting

Design Variables

Hole Size
Hole Spacing
Fiber Architecture
Material Choice
New Concepts

Fig. 3

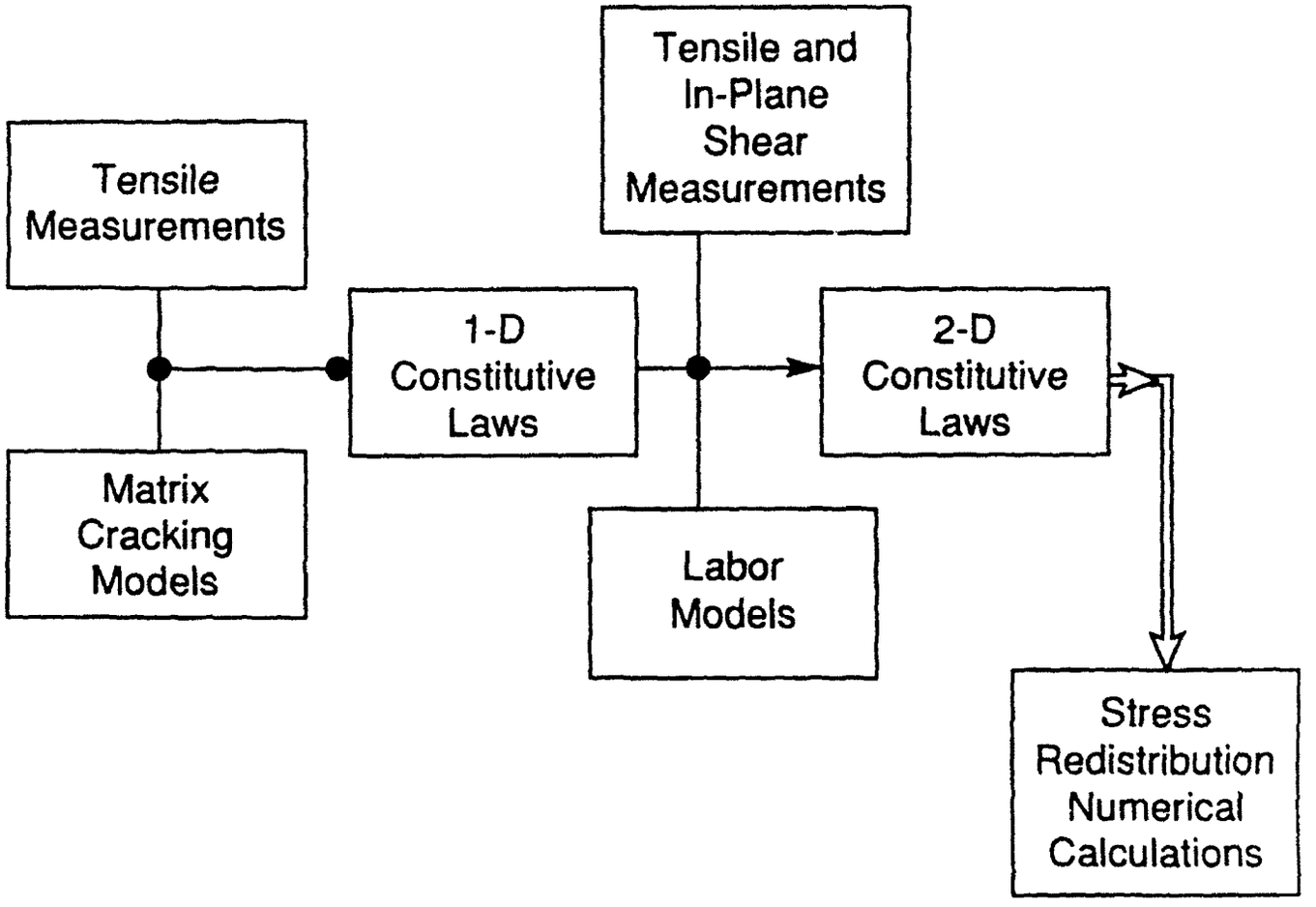

Table III

Design Strategy for CMCs

TABLE IV

Summary of Non-Dimensional Coefficients

$\mathcal{A}_b = [f/(1-f)]^2 \left(E_f E_L / E_m^2\right)(a_o \tau / R S_u)$, Flaw Index for Bridging

$\mathcal{A}_p = \left(a_o / \bar{h}\right)\left(S_p / E_L\right)$, Flaw Index for Pull-Out

$\mathcal{D} = \Gamma_m (1-f)^2 E_f E_m / f \tau^2 E_L R$, Crack Spacing Index

$\mathcal{H} = b_2 (1-a_1 f)^2 R \bar{\sigma}_p^2 / 4 \bar{d} \tau E_m f^2$, Hysteresis Index

$I = \bar{\sigma}_p / E_m \Omega$, Misfit Index

$\mathcal{M} = 6 \tau \Gamma_m f^2 E_f / (1-f) E_m^2 R E_L$, Matrix Cracking Index

$Q = E_p f \Omega / E_L (1-\nu)$, Residual Stress Index

$\Delta_i = (1/c_1 \Omega)\sqrt{\Gamma_i / E_m R}$, Debond Index

CMCs with a range of different constituent properties and fiber architectures. The plastic strains would be related to constituent properties by adapting the 1-D models.

The in-plane shear behavior will be characterized by performing experiments and developing models of matrix cracking that govern the plastic *shear strain* in 2-D CMC (Evans, Hutchinson, Bao). The information will be used to establish the constitutive laws for in-plane shear, as well as interlaminar shear. For continuity of interpolation between tension and shear, the shear models will include the same constituent properties as those used to represent the tensile behavior.

The model-based constitutive laws, based on matrix damage, will be built into a CDM (continuum damage mechanics) formulation, compatible with finite element codes (Hayhurst). Computations will be performed to explore *stress redistribution* around holes and other strain concentration sites. The calculations will establish visualizations of stress evolution that can be compared with experimental measurements performed using the SPATE method, as well as by Moiré interferometry (Mackin, Evans). These experiments will be on specimens with notches and holes, loaded in tension. The comparisons between the measured and calculated stress patterns will represent the ultimate validation of the constitutive law. The composite codes, when validated, will be made available to industry.

Some preliminary experimental work will be performed on pin-loaded holes. Damage patterns will be monitored and stress redistribution effects assessed using SPATE (Kedward, Evans, Mackin). These experiments will be conducted on SiC/CAS and SiC/C. The results will provide the focus for future CDM computations, based on the constitutive law for the material.

Smaller scale activities will involve basic aspects of stress redistribution around holes caused by fatigue and creep *damage*, using the experience gained from the matrix cracking studies. Some experimental measurements of these effects will be performed using SPATE (Zok, Evans).

Some delamination crack growth measurements and calculations are also envisaged (Ashby, Kedward, Hutchinson). Cantilever beam and C-specimens will be used for this purpose (Fig. 4). During such tests, crack growth, multiple cracking and stiffness changes will be addressed. Models of bridging by inclined fibers will be developed (Ashby) and used for interpretation.

3.3 Metal Matrix Composite Design

The 3D constitutive equations for MMCs are now available for use in the ABAQUS finite element code, and the immediate task is to use these equations to predict the behavior of representative components (Leckie). One such system is a ring-type structure which is being studied together with Pratt and Whitney. Clearly no experimental verification is possible with a component of this scale, but the experience of Pratt and Whitney shall provide invaluable input on the effectiveness of the calculations. A component sufficiently simple to be tested is the panel penetrated by holes. The holes shall be both unloaded and loaded (Jansson), and it is expected to include the effects of cyclic mechanical and thermal loading.

It is proposed to develop simplified procedures which are based on shakedown procedures (Jansson, Leckie). Demonstrations have already been made of the effectiveness of the Gohfeld method (which uses only simple calculations) in representing the behavior of MMCs subjected to cyclic thermal loading.

TRANSVERSE CRACKING OF CMC

CONVENTIONAL COUPON TESTS

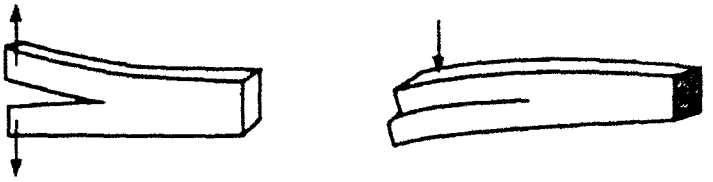

- Fiber Bridging Problem ($\mathcal{G} >> \Gamma_T$)

IMPROVED TESTS

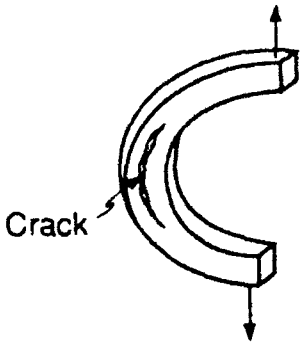

da/dN vs. $\mathcal{G}$

SUB - ELEMENT TEST

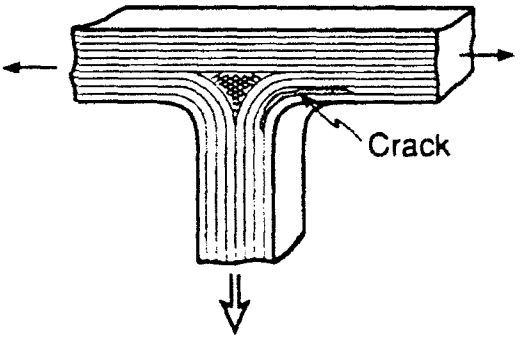

DESIGN PROBLEM

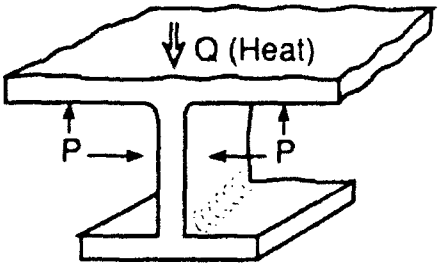

- Thermal Conductivity
- Fiber Architecture
- Matrix Toughness

Fig. 4

During the complex histories of stress and temperature, it is known that the matrix-fiber interface properties change. Fatigue loading (Zok) is know to decrease the interface sliding stress. Transverse creep appears to cause matrix-fiber debonding (Jansson), which might result in loss of the ability to transfer stress between matrix and fiber. It is intended to study this effect of transverse creep on the integrity of the longitudinal strength of the material by performing tests on panels which shall allow rotation of the stress fields. A good understanding now exists of the fatigue properties of MMCs (Zok). It is intended to extend the ideas developed from earlier theoretical studies (McMeeking, Evans) to include cyclic thermal effects and experimental programs on holes in plates.

4. MANUFACTURING

The activities in processing and manufacturing have had the following foci:

- Matrix development to address specific requirements identified by the design problems, particularly first matrix cracking in CMCs (Lange) and creep strengthening in MMC/IMCs (Levi, Lucas).
- Hybrid architectures which offer possible solutions to environmental degradation and thermal shock problems (Evans, Lange, Leckie, Levi, Yang, Zok).
- Software development that predicts and controls fiber damage and interface properties during densification (Wadley).
- Processing techniques to generate model MMC sub-elements (Leckie, Levi, Yang).

4.1 Metal Matrix Composites

Work on MMC matrix development has focused on dispersion strengthening approaches to increase the *transverse* tensile and creep strength of 1-D and 2-D fiber architectures. The initial work has emphasized a model system, Cu/Al_2O_3, wherein dispersoids are produced by internal oxidation of a dilute Cu-Al alloy deposited by PVD onto sapphire fibers. These are subsequently consolidated by HIP'ing. Specimens with fiber volume fractions of $0.3 \leq f \leq 0.5$ and 2-3% γ-Al_2O_3 dispersoids (~ 20 nm in size) have been produced in this manner and will be tested to assess their transverse creep behavior. The new emphasis will be on higher temperature matrices based on TiB dispersoids in Ti-(Cr/Mo)-B alloys (Levi). Initial solidification studies have demonstrated the potential of these materials as *in-situ* composites. Efforts are underway to develop sputtering capabilities to implement this concept.

Fiber damage during densification of composite prepregs generated by plasma-spray (GE) and PVD (3M) have also been emphasized (Wadley). Interdiffusion studies coupled with push-out tests have been used to study the evolution of reaction layers in Ti/SiC composites and their effect on the relevant interfacial properties as a function of process parameters. Additional efforts under other programs have focused on developing predictive models for fiber breakage during densification. The interdiffusion and breakage models are being incorporated into software that predicts pressure-temperature paths, which simultaneously minimize fiber damage and control the interface properties.

The feasibility of producing MMC sub-elements consisting of fiber reinforced rings (1-D) and tubes (2-D) has been demonstrated by using

liquid metal infiltration of Al alloy matrices (Levi). These are presently undergoing testing in combined tension/torsion modes. Future efforts will be directed toward extending the technique to other shapes (e.g., plates with reinforced holes), as well as devising methods to modify the (currently strong) interfaces. The identification of methods that provide the appropriate interfacial debonding/sliding characteristics should enable the use of these composites as *model systems* for higher temperature MMCs, such as Ti.

4.2 Intermetallic Matrix Composites

The focus of the IMC processing activities has been on the synthesis of $MoSi_2/\beta$-SiC_p composites by solidification processing. These materials are of interest as potential matrices for fiber composites. Significant progress was made in the elucidation of the relevant Mo-Si-C phase equilibria, the growth mechanisms of SiC from the melt and their impact on reinforcement morphology, as well as the orientation relationships between matrix and reinforcements, and the interfacial structure. An amorphous C layer, $\leq$5 nm thick, was found at the $MoSi_2$/SiC interface in the as cast condition, and persisted after 12 h heat treatments at 1500°C. This interfacial layer has been reproduced in α-$SiC_p/(MoSi_2 + C)$ composites produced by powder metallurgy techniques and was found to exhibit promising debonding and pull-out behavior during fracture (Levi). Future efforts are aimed at implementing this *in-situ coating* concept in α-SiC fiber composites.

4.3 Ceramic Matrix Composites

The processing issues for creating CMCs with high *matrix strength* continue to be explored (Lange, Evans). The basic concept is to create a strong ceramic matrix framework within a fiber preform, by means of slurry

infiltration followed by heat treatment. This strong framework would then be infiltrated by a polymer precursor and pyrolyzed to further densify the matrix. It has been demonstrated that strong matrices of Si_3N_4 can be produced using this approach (Lange). Further work will address relationships between matrix strength and microstructure (Lange, Evans).

4.4 Hybrids

These activities cover materials consisting of thin monolithic ceramic layers alternating with layers containing high strength fibers bonded by a glass or metallic binder. The primary motivation behind this concept is the potential for manufacturing shapes that have a high resistance to environmental degradation and also have good thermal shock resistance. The concept has been demonstrated using alumina plates and graphite reinforced polymer prepregs (Lange). The availability of glass-ceramic bonded SiC_f prepregs and tape-cast SiC plates has facilitated the extension of this technique to high temperature systems (Lange). Future assessment will address new crack control concepts. These concepts would prevent damage from propagating into the fiber reinforced layers, especially upon thermal loading (Zok, Lange). If successful, this concept would allow the development of hybrid CMCs which impart resistance to environmental degradation, as well as high thermal strain tolerance.

Preliminary work has been performed on laminates consisting of alumina plates and sapphire-fiber reinforced Cu monotapes (Levi). The latter are produced by deposition of Cu on individual fibers which are subsequently aligned and bonded by hot pressing between two Cu foils. After suitable surface preparation, the alumina/monotape assemblies are

bonded by hot pressing. Future work is aimed at implementing the concept with Ni based alloys.

5. SENSORS

The principal challenge being addressed is the non-destructive and non-evasive measurement of stresses in composites (Clarke, Wadley). The motivation is to make detailed measurements of stresses in components for incorporation into evolving design models, as well as validation of the stress distributions computed by finite element methods. A major emphasis has been placed on measuring the residual stresses in sapphire fibers in various matrices, using the recently developed technique of optical fluorescence spectroscopy. These measurements have provided data on the distribution of residual thermal stresses in the fiber reinforcement, as a function of depth below the surface. This approach will be extended, in conjunction with finite element modelling (Hutchinson), to measure the stresses during the process of fiber pull-out from a variety of metal and ceramic matrices. Initial experiments indicate that such in-situ measurements are feasible.

The technique will also be applied to the measurement of the stresses in sapphire fibers located in the vicinity of pin-loaded holes in order to understand the manner in which the stresses redistribute during loading. It is anticipated that this measurement will provide information about the detailed fiber loadings and also about the stresses that cause debonding of the fibers from the matrix. Moreover, in support of the activities on thermal ratcheting, the redistribution of stresses with thermal cycling will be established. This will be accomplished by using the fluorescence technique as well as Moiré interferometry, based on lithographically defined features.

MATERIALS

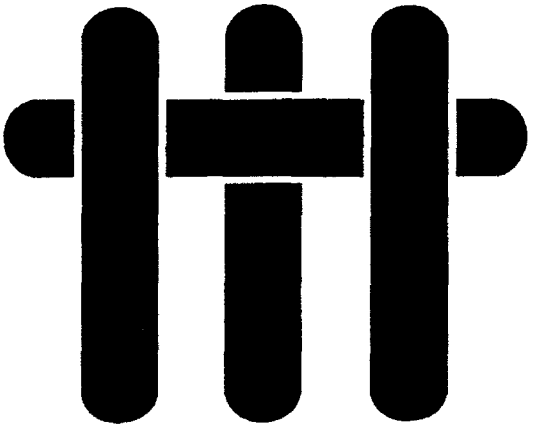

A MICROCOMPOSITE TEST PROCEDURE FOR EVALUATING THE CONSTITUENT PROPERTIES OF CERAMIC MATRIX COMPOSITES

by

J. Lamon, F. Rebillat

Laboratoire des Composites Thermostructuraux
UMR 47 CNRS-SEP-UB1
Domaine Universitaire
3 Allée de la Boëtie
33600 Pessac (France)

and

A.G. Evans

Materials Department
College of Engineering
University of California
Santa Barbara, California 93106–5050

KJS 3/15/93

ABSTRACT

A microcomposite test procedure for evaluating the constituent properties of CMCs produced by chemical vapor infiltration is described. The analysis and experimental results demonstrate that the interface sliding resistance τ_o can be obtained from the unload/reload hysteresis, after one (or more) matrix crack has been induced. The non-linear strain can also be used to provide an independent determination of τ_o, as well as give values for the misfit strain and the interface debond energy. Results obtained on SiC/C/SiC and SiC/BN/SiC materials are evaluated.

1. INTRODUCTION

The critical importance of interface properties for the thermostructural performance of ceramic matrix composites (CMC)[1-6] dictates the need for straightforward and convenient *test methods*. Tests that involve the tensile deformation of a single fiber within a specified matrix are preferred,[7,8] since the interpretation of results is direct and unequivocal.[9] For composites reinforced with relatively large diameter fibers (100–150 μm), this has been achieved both in tension (pull-out)[7,8] and by push-in.[10-14] The former is preferable since it duplicates all of the features that occur upon tensile loading of an actual composite. The single fiber tension experiments on materials with large diameter fibers have been performed by using careful sectioning and etching procedures. These procedures leave one intact fiber within the test configuration.[8] However, for the much smaller diameter fibers (10–20 μm) typically used with CMCs, an equivalent test methodology has been lacking. Various push-through[13,14] and push-in[15] procedures have been devised and have provided useful information. The limitation of these procedures concerns (i) either the need to have a matrix that can be preferentially dissolved[15] or (ii) the use of a sharp indentor which penetrates the fiber.[13,14] Consequently, it is difficult to obtain unequivocal interface information on CMCs having either chemically durable matrices (such as SiC) or relatively high debond/sliding resistance. A test procedure that addresses these limitations is proposed. The procedure is particularly appropriate for CMCs produced by chemical vapor infiltration (CVI)[16]. The test configuration is referred to as a 'microcomposite.'[17] It consists of a concentric cylinder element containing a single fiber, with a coating, plus a matrix annulus. It is representative of the constituents in the actual composite, fabricated by using identical vapor deposition conditions. The applicability of this procedure is analyzed in this article. This is achieved by conducting

several critical experiments and by using analytical solutions for interface debonding and sliding[7,9] to interpret the results.

2. METHODOLOGY AND ANALYSIS

2.1 Background

Composite cylinders produced by chemical vapor deposition (Fig. 1) are tested in tension, using conventional single fiber test procedures. The loads and the axial strain in the gauge sections are monitored. An acoustic emission transducer attached to the system is used to detect the incidence of matrix cracks. By testing in situ, in the scanning electron microscope (SEM), it is also possible to measure the opening displacement of matrix cracks, once formed. Following the formation of one (or more) matrix cracks, an unload/reload cycle is performed. Repetitive cycling is used when the fatigue behavior of the interface requires characterization. A schematic of a typical experimental result (Fig. 2) indicates the experimental quantities that can be measured and used to evaluate the constituent properties of the composites. These include: (i) the non-linear displacement following matrix cracking, Δ_i, (ii) the width of the hysteresis loop, $\delta\Delta$, and (iii) the permanent displacement, Δ_p. These parameters provide information about the interface debond energy, Γ_i, the frictional sliding resistance along the debonded interface, τ_o, and the residual stress. Interpretation of the results can be performed, provided that values for the Young's Moduli, E_f and E_m, (subscripts f for fiber and m for matrix) and Poisson's ratio, ν_f and ν_m, are known. The analysis is restricted to materials wherein the debonding energy is small enough that the reverse slip zone does not reach the end of the debond zone upon full unloading.[7,9] The corresponding solution when Γ_i is large is described elsewhere.[18]

The test method recognizes the following factors. Upon unloading and reloading, only interface sliding occurs (no debonding).[7] Consequently, when Γ_i is small, the

hysteresis $\delta\Delta$ may be used to evaluate τ_o, without the need for independent information about either the debond energy, Γ_i, or the misfit strain ε_T. The loading non-linearity Δ_i and the permanent deformation Δ_p both contain combined information about τ_o, Γ_i and ε_T.[9] However, it will be shown that, it is still possible to evaluate τ_o, ε_T and Γ_i from both Δ_i and Δ_p. In practice, there may be problems with measurement precision and it is preferable to evaluate the residual strain, independently. Then, Γ_i can be obtained from Δ_i and Δ_p.

2.2 Analytical Relationships

Consistent with previous approaches for characterizing the interface,[9] it is assumed that debonding precedes frictional sliding. Furthermore, when the interface is in *residual compression*, debonding is considered to be a strictly mode II phenomenon. It occurs with a debond energy Γ_i. Following debonding, frictional sliding occurs subject to a shear resistance τ given by:

$$\tau = \tau_o - \mu\sigma_{rr} \qquad (1)$$

where σ_{rr} is the radial stress at the interface, μ is a Coulomb friction coefficient and τ_o is a 'constant' shear resistance attributed to fiber roughness. Most experimental results indicate that τ is dominated by τ_o, because of the inherent roughness of most commercial fibers.[8-11] For simplicity, it will also be assumed here that the τ_o term is dominant. Then, if the experimental results identify discrepancies, solutions available for the additional Coulomb term can be included.[9]

When the interface is in *residual tension*, debonding occurs subject to mixed mode I/II displacements.[19] Nevertheless, a small frictional resistance can still arise, because of fiber roughness, as exemplified by the SiC/LAS system.[20,21] In such cases, the results

are analyzed in the same manner as composites with interfaces subject to residual compression.

2.1.1 The Hysteresis Loop

The opening displacement of the crack, u, upon unloading is given by[7]

$$u_u = u_p - \left[\frac{(b_2 + b_3)(1 - a_1 f)^2 R}{4\tau_o E_m f^2}\right](\bar{\sigma}_p - \bar{\sigma}_u)^2 \qquad (2)$$

where R is the fiber radius, f is the area fraction of the element occupied by the fiber, $\bar{\sigma}$ is the stress on the composite element, the subscript p refers to the peak stress reached before unloading, while the subscript u refers to the actual value during the *unloading* phase: the constants a_i, b_i are the same as those originally defined by Hutchinson and Jensen[9] (as summarized in Table I). A convenient non-dimensional form of Eqn. (2) is

$$U_u = U_p - U'(1 - S_u)^2 \qquad (3)$$

where

$$U = u/R$$
$$S_u = \bar{\sigma}_u/\bar{\sigma}_p$$
$$U' = \left[(b_2 + b_3)(1 - a_1 f)^2 \bar{\sigma}_p^2/4\tau_o E_m f^2\right].$$

The corresponding result for reloading is[7]

$$U_R = U_o + U' S_R^2 \qquad (4)$$

where

$$S_R = \bar{\sigma}_R/\bar{\sigma}_p$$

$\bar{\sigma}_R$ is the stress reached on unloading and

$$U_o = u_o/R$$

with u_o being the residual crack opening at zero load. Note that, when the results are expressed in terms of *measured* values of u_p, u_o and $\bar{\sigma}_p$, there is no influence of the *residual stress* on the hysteresis formulae. Consequently, experimental data for $\bar{\sigma}(u)$ can be matched directly with Eqns. (3) and (4) to evaluate τ_o. If the experimental results do not match, a Coulomb friction term must be included.[9]

Determination of τ_o may be conveniently made by measuring the hysteresis loop width, δu (Fig. 2a). The non-dimensional form is

$$\delta U = U_p - U_o - U'\left(1 - 2S + 2S^2\right) \tag{5}$$

This loop has a maximum width (at $S = 1/2$), given by

$$\delta U_{1/2} = U_p - U_o - U'/2. \tag{6}$$

Re-expressing Eqn. (6) in full form gives

$$\tau_o = \left(b_2 + b_3\right)\left(1 - a_1 f\right)^2 \bar{\sigma}_p^2 R/8E_m f^2\left[u_p - u_o - \delta u_{1/2}\right] \tag{7}$$

where

$$\delta u_{\frac{1}{2}} = \left|u_u - u_P\right|_{\frac{1}{2}}$$

as illustrated on Fig. 2a.

When the crack opening displacements cannot be measured, the preceding results can be re-expressed in terms of alternative displacement quantities. The tensile displacement w along a gauge section (length L_o) when only one matrix crack exists in that section consists of two terms,

$$w = w_o + \Delta \tag{8}$$

One term , w_o, is associated with the elastic stretching of the fiber and matrix. The other term, Δ, represents the *extra* displacement caused by the existence of the crack (which has induced debonding and sliding). The latter is related to the crack opening displacement by[9]

$$\Delta = \left[\frac{b_2}{b_2 + b_3}\right] u \tag{9}$$

At the same stress, w_o (being an elastic term) has the same magnitude upon unloading and reloading. Consequently, *differences* in the measured displacement are entirely equivalent to *differences* in Δ. Re-expressing the above results in terms of displacement differences at the same stress, gives:

$$\delta\Delta = \Delta_p - \Delta_o - \left[\frac{b_2(1 - a_1 f)^2 \overline{\sigma}_p^2 R}{4\tau_o E_m f^2}\right]\left[1 - 2\overline{\sigma}/\overline{\sigma}_p + 2\left(\overline{\sigma}/\overline{\sigma}_p\right)^2\right] \tag{10a}$$

or

$$\delta\Delta = \left[\frac{b_2(1-a_1 f)^2 \bar{\sigma}_p^2 R}{2\tau_o E_m f^2}\right]\left(\bar{\sigma}/\bar{\sigma}_p\right)\left[1-\bar{\sigma}/\bar{\sigma}_p\right] \qquad (10b)$$

where $\delta\Delta$ is defined in Fig. 2b.

The effect of matrix cracks on the elastic stiffness is needed before using tensile displacements to evaluate τ. Calculations,[22] summarized in Fig. 3, indicate that, for one crack, the stiffness only changes significantly when the ratio of the gauge length to fiber radius is low (< 10). Consequently, for a typical microcomposite, the elastic stiffness when one crack exists should be the same as that determined upon initial loading. The relevant magnitude of the displacement difference is thus obtained in the manner indicated on Fig. 2b.

Larger displacements arise when *multiple cracks* have been induced upon loading. In addition, stiffness changes occur when the crack spacing is small (Fig. 3). When the latter can be neglected and when N matrix cracks have formed, Eqn. (10) may be re-expressed in terms of τ_o as:

$$\begin{aligned}\tau_o &= \frac{b_2 N(1-a_1 f)^2 \bar{\sigma}_p^2 R\left(\bar{\sigma}/\bar{\sigma}_p\right)\left[1-\bar{\sigma}/\bar{\sigma}_p\right]}{2E_m f^2 \delta\Delta} \\ &\equiv 2\mathcal{H}\left(\bar{\sigma}/\bar{\sigma}_p\right)\left[1-\bar{\sigma}/\bar{\sigma}_p\right]\end{aligned} \qquad (11)$$

2.1.2 *The Loading Non-Linearity*

During loading, matrix crack 'pop-in' occurs (Fig. 2) at a stress dictated by the flaws present in the matrix material. The ensuing displacements are non-linear and reflect the debonding and sliding processes occurring at the interface, as the matrix

crack opens. In this case, both debonding and sliding must be included, as well as the effect of the residual stress. For the constant friction case, with a single matrix crack, the crack opening displacement is given by,[9]

$$\frac{u}{(b_2+b_3)}\left[\frac{fE}{(1-f)E_m}\right]^2 = \frac{\sqrt{\Gamma_i/RE_m}\,(\bar{\sigma}_p - \bar{\sigma}_i)}{c_1\tau_o} + \frac{(\bar{\sigma}_p - \bar{\sigma}_i)^2}{2E_m\tau_o} \qquad (12)$$

where

$$\bar{\sigma}_i = \frac{E_m}{c_1}\left[\sqrt{\Gamma_i/RE_m} - c_2\varepsilon_T\right]$$

with ε_T being the mismatch strain between the coated fiber and matrix annulus. The extra displacement Δ (Fig. 2b) is related to the crack opening, u, by Eqn. (9). The corresponding solution for the debond length, l, is[9]

$$1/R = (1-f)(\bar{\sigma}_p - \bar{\sigma}_i)E_m/2f\tau_o E \qquad (13)$$

Equation (12) has three unknowns, τ_o, Γ_i and ε_T. Nevertheless it is possible to separate τ_o, Γ_i and ε_T from the shape of the $\Delta(\bar{\sigma})$ curve. Re-expressing Eqn. (12) in the following form suggests a procedure :

$$\Delta/R = \left(\frac{b_2E_m}{\tau_0}\right)\left(\frac{[1-f]E_m}{fE}\right)^2 \left\{\left(\frac{\bar{\sigma}_p/E_m}{2}\right)^2 + \left(\frac{c_2}{c_1}\right)\left(\frac{\bar{\sigma}_p}{E_m}\right)\varepsilon_T + \left(\frac{c_2}{c_1}\right)^2\frac{\varepsilon_T^2}{2} - \frac{\gamma^2}{2c_1^2}\right\} \qquad (14a)$$

or,

$$\Delta/R = A\bar{\sigma}_p^2 + B\bar{\sigma}_p + C \qquad (14b)$$

where

$$\gamma = \sqrt{\Gamma_i/RE_m}$$

When multiple cracks have been created, Δ in Eqn. (14) becomes the displacement *per crack*. Note that the coefficient A depends only on one unknown (τ_o), the coefficient B depends on two unknowns (τ_o and ε_T) whereas C depends on all three unknowns (τ_o, ε_T and Γ_i). Consequently, by using a parabolic curve fitting routine to separately evaluate A, B and C from the experimental data, the following interpretation may be made. The sliding stress τ_o is obtained from A and compared with that determined from the hysteresis. Then, with τ_o established, the misfit strain ε_T is determined from B. This value may be compared with the independently measured magnitude in order to check consistency. Finally, with τ_o and ε_T known, the debond energy may be evaluated from C.

3. ANALYSIS OF EXPERIMENTAL RESULTS

Experimental results have been obtained on various microcomposite test specimens consisting of Nicalon fibers, with either C or BN coatings and an annular SiC matrix. These specimens include a range in coating thickness and a variety of deposition conditions. The procedures used for producing and testing these specimens have been described elsewhere[17]. The deformation behaviors found for BN coatings, having a range of thicknesses, are summarized in Fig. 4. One result for a C coating, shown in Fig. 5, illustrates the use of acoustic emission to obtain the number of cracks. The

spectra of hysteresis curves are exemplified by results obtained for one BN coating (Fig. 6a) and one C coating (Fig. 6b). Graphical representations of the analysis of these curves are summarized in Figs. 7 and 8, with the number of cracks indicated on Table II.

For interpretation of the hysteresis loops, the quantity, $\delta\Delta/\bar{\sigma}_p^2$, is plotted as a function of $\bar{\sigma}/\bar{\sigma}_p\,(1-\sigma/\bar{\sigma}_p)$ (Fig. 7), as suggested by Eqn. (11) and upon recalling that $\delta\Delta$ is the loop width *per crack*. It is apparent from the linearity of the results (Fig. 7) that τ_o is both *cycle and stress invariant*, within experimental scatter. The standard deviation is ~ 20%. Such behavior is found for *all* of the materials investigated in this study. The average values of τ_o, determined from the hysterisis loops, are summarized in Table II.

Analysis of the non-linear displacements by fitting the $\Delta(\bar{\sigma}_p)$ data to Eqn. (14) (Fig. 8), is also found to provide consistent information. However, there is a propagation of errors in the consecutive determination of τ_o, ε_T and Γ_i. A fit that gives the best correlation coefficient over the complete data range is used (Fig. 8). The values obtained in this manner are summarized in Table II.

An internal consistency comparison of the constituent properties presented in Table II provides a preliminary assessment of the merit of the microcomposite test procedure. Both approaches for evaluating τ_o (hysteresis and displacement) give comparable values for each system, within the 20% standard deviation that seemingly applies to these procedures (Fig. 7). Consequently, the range in τ_o between samples reflects actual differences in coating thickness and in deposition conditions.[23] There is one exception: SiC/BN/SiC sample 2. The problems with this sample are not clear. However, it generated an unusually large number of cracks, N. It is likely that an error was made in the measurement of N.[23]

Independent measurements of the thermal expansion coefficients of Nicalon fibers and CVD SiC[2,16,17] indicate a mismatch strain, $\varepsilon_T \approx -1.6 \times 10^{-3}$. This value lies within the range found from the present displacement measurements [$\varepsilon_T = (-0.6$ to $-3.8)\ 10^{-3}$]. Again, there is one anomalous result: SiC/C/SiC, sample 4. The significance

of changes in ε_T between coatings and the errors associated with this evaluation are not apparent at this juncture, because there have not yet been independent determinations. Actual sample-to-sample variation is expected as the coating thickness varies and the deposition temperature is changed.[17,23] Further study of this issue is in progress. The errors in τ_o and, especially ε_T, propagate into determination of Γ_i. At this stage, the values given in Table II are not assigned a high level of confidence. However, it is expected that *independent* measurement of ε_T would allow Γ_i determination with the confidence needed to address differences between coatings, which can then be related to coating microstructure, etc.

Among the problems with the microcomposite test are the difficulties in exact measurement of the number of cracks, N, evaluation of the area fraction of matrix, and the occasional incidence of longitudinal cracks, which modify the measured displacement, Δ, and reduce the misfit strain, ε_T. A detailed assessment of these issues is described elsewhere.[23]

4. CONCLUDING REMARKS

A test methodology for obtaining the constituent properties of CMCs, by using microcomposite test specimens, has been described. The method allows the sliding resistance, τ_o, to be obtained from hysteresis loop measurements. Moreover, an independent check on the magnitude of τ_o can be obtained from measurements of the non-linear displacements, Δ, upon implementation of a parabolic curve fitting routine. The Δ measurements may also be used, in principle, to evaluate both the misfit strain, ε_T, and the debond energy, Γ_i. However, errors incurred in τ_o determination propagate through the analysis. It is thus considered preferable to independently measure, ε_T, in order to obtain Γ_i with reasonable confidence. Further study is needed to establish the magnitude of measurement errors and their principal origins, in order to specify levels

of confidence that can be achieved in τ_o, ε_T and Γ_i determination using the microcomposite test methodology.[23]

ACKNOWLEDGEMENTS

This work was supported by SEP and CNRS through a grant given to F. Rebillat, as well as DARPA, under the University Research Initiative Grant at UCSB.

TABLE I

Summary of Constants For Composite Element
(Type I Boundary Conditions)
Isotropic Fiber (With $\nu_f = \nu_m = \nu^*$)*

$$a_1 = E_f/E$$

$$b_2 = \frac{(1+\nu)E_m\left[E_f + (1-2\nu)E\right]}{E_f\left[(1+\nu)E_f + (1-\nu)E\right]}$$

$$b_3 = \frac{f(1+\nu)\left[E_f\,(1-2\nu)E\right]}{(1-f)\left[(1+\nu)E_f + (1-\nu)E\right]}$$

$$c_1^2 = \frac{(1+\nu)(1-f)E_m^2\left[E_f + (1-2\nu)E\right]}{4f^2EE_f\left[(1+\nu)E_f + (1-\nu)E\right]}$$

$$c_2^2 = \frac{(1-f)E_f\left[(1+\nu)E_f + (1-\nu)E\right]}{4(1+\nu)E\left[(1-2\nu)E + E_f\right]}\left[1 + \frac{2\nu E}{\left[(1+\nu)E_f + (1-\nu)E\right]}\right]$$

* Analogous results for anisotropic fibers are given in Hutchinson and Jensen.[9]

TABLE II

Constituent Properties

Material	Sample	Number of Cracks	τ_o (MPa)		ε_T (10^{-3})	Γ_i (Jm^{-2})	ℓ (μm)
			Hysteresis	Displacement			
SiC/BN/SiC	1	9	11	8	−2.4	1	440
	2	55	24	10	−1.8	0	170
	3	9	10	7	−0.7	7	490
	4	14	5	4	−1.2	3	600
	5	21		6	−1.2	1	170
	6	5	4	3	−1.0	4	1200
	7	20	5	3	−0.6	2	600
SiC/C/SiC	1	4		21	−1.6	5	200
	2	6		21	−3.8	4	200
	3	9		7	−1.5	2	390
	4	4	3	4	−0.1	0	890
	5	2	1	1	−0.6	1	3600

REFERENCES

[1] R.J. Kerans, R.S. Hay, N.J. Pagano, T.A. Parathasarthy, *Am. Ceram. Soc. Bull.*, **68** (1989) 429.

[2] R. Naslain, Fiber-Matrix Interphases and Interfaces in Ceramic Matrix Composites Processed by CVI. Proc. 4th Int. Conf. on Composite Interfaces (ICCI-IV), May 1992, Cleveland, in press.

[3] A.G. Evans, J.B. Davis and F.W. Zok, *Composite Science and Technology*, **42** (1991) 3.

[4] W.A. Curtin, *J. Am. Ceram. Soc.*, **74** (1991) 2837.

[5] D.B. Marshall, B.N. Cox and A.G. Evans, *Acta Metall.*, **33** (1985) 2013.

[6] R.J. Kotil, J.W. Holmes and M. Cominou, *J. Am. Ceram. Soc.*, **73** (1990) 1879.

[7] D.B. Marshall, *Acta Metall. Mater.*, **40** (1992) 427.

[8] D.B. Marshall, M.C. Shaw and W.L. Morris, *Acta Metall. Mater.*, **40** (1992) 443.

[9] J.W. Hutchinson and H. Jensen, *Mech. of Mtls.*, **9** (1990) 139.

[10] P.D. Jero and R.J. Kerans *Scripta Metall. Mater.*, **24** (1990) 2315.

[11] T.J. Mackin, P.D. Warren and A.G. Evans, *Acta Metall. Mater.*, **40** (1992) 1251.

[12] W.C. Carter, E.P. Butler and E.R. Fuller, *Scripta Metall. Mater.*, **25** (1991) 579.

[13] T.P. Weihs and W.D. Nix, *Scripta Metall.*, **22** (1988) 271.

[14] D.B. Marshall and W. Oliver, *J. Am. Ceram. Soc.*, **70** (1987) 542.

[15] T.J. Mackin and F.W. Zok, *J. Am. Ceram. Soc.*, **75** (1992) 3169–71.

[16] R. Naslain and F. Langlais, "CVD processing of ceramic-ceramic composite materials," Tailoring Multiphase and Composite Ceramics, Edited by R.E. Tressler, *Mat. Sci. Research*, **20**, Plenum Press, New York, 1986, 145–64.

[17] J. Lamon, C. Rechiniac, N. Lissart and P. Corne, "Determination of Interfacial Properties in Ceramic Matrix Composites using Microcomposite Specimens." Proc. 5th European Conference on Composite Materials, Bunsell et al. eds. EACM-CEC, Bordeaux, France (1992) 585.

[18] E. Vagaggini, J.M. Domergue and A.G. Evans, *J. Am. Ceram. Soc.*, in press.

[19] P.G. Charalambides and A.G. Evans, *J. Am. Ceram. Soc.*, **72** (1989) 746.

[20] K.M. Prewo and J.J. Brennan, *J. Mater. Sci.*, **17** (1982) 1201.

[21] D.B. Marshall and A.G. Evans, *J. Am. Ceram. Soc.*, **68** (1985) 225.

[22] M.Y. He, X. Wu, A.G. Evans and J.W. Hutchinson, *Mech. of Mtls.*, to be published.

[23] F. Rebillat, J. Lamon, A.G. Evans : to be published.

FIGURE CAPTIONS

Fig. 1. A typical microcomposite specimen produced by CVD.

Fig. 2. Schematic of the non-linear behavior expected in a microcomposite with a small debond energy.

Fig. 3. The change in elastic compliance caused by matrix cracks.[22]

Fig. 4. Deformation data obtained on seven different SiC/BN/SiC microcomposite specimens with a range of BN coatings (0.3 to 0.7 μm thick). The stress refers to that acting on the fiber at the location of matrix cracks.

Fig. 5. Deformation data obtained on a SiC/C/SiC microcomposite having a 1 μm thick interphase. Also shown are the acoustic emission signals used to assess the number of matrix cracks.

Fig. 6. Example of hysterisis loops obtained on microcomposite test specimens
a) Multiple loops on a SiC/BN/SiC sample
b) A single loop on a SiC/C/SiC sample

Fig. 7. A plot of the loop width parameter, $\Delta\delta/\bar{\sigma}_p^2$, as a function of relative stress, $\bar{\sigma}/\bar{\sigma}_p\left[1-\bar{\sigma}/\bar{\sigma}_p\right]$, obtained from a range of hysteresis loops, measured on a SiC/BN/SiC material. In this case, $\tau_o = 5 \pm 1$ MPa.

Fig. 8. A fit to Eqn. (14) of the non-linear displacements per crack measured on a SiC/BN/SiC material. In this case, $\tau_o = 4$ MPa, $\varepsilon_T = -1.2 \times 10^{-3}$ and $\Gamma_i \approx 3\ \mathrm{Jm}^{-2}$.

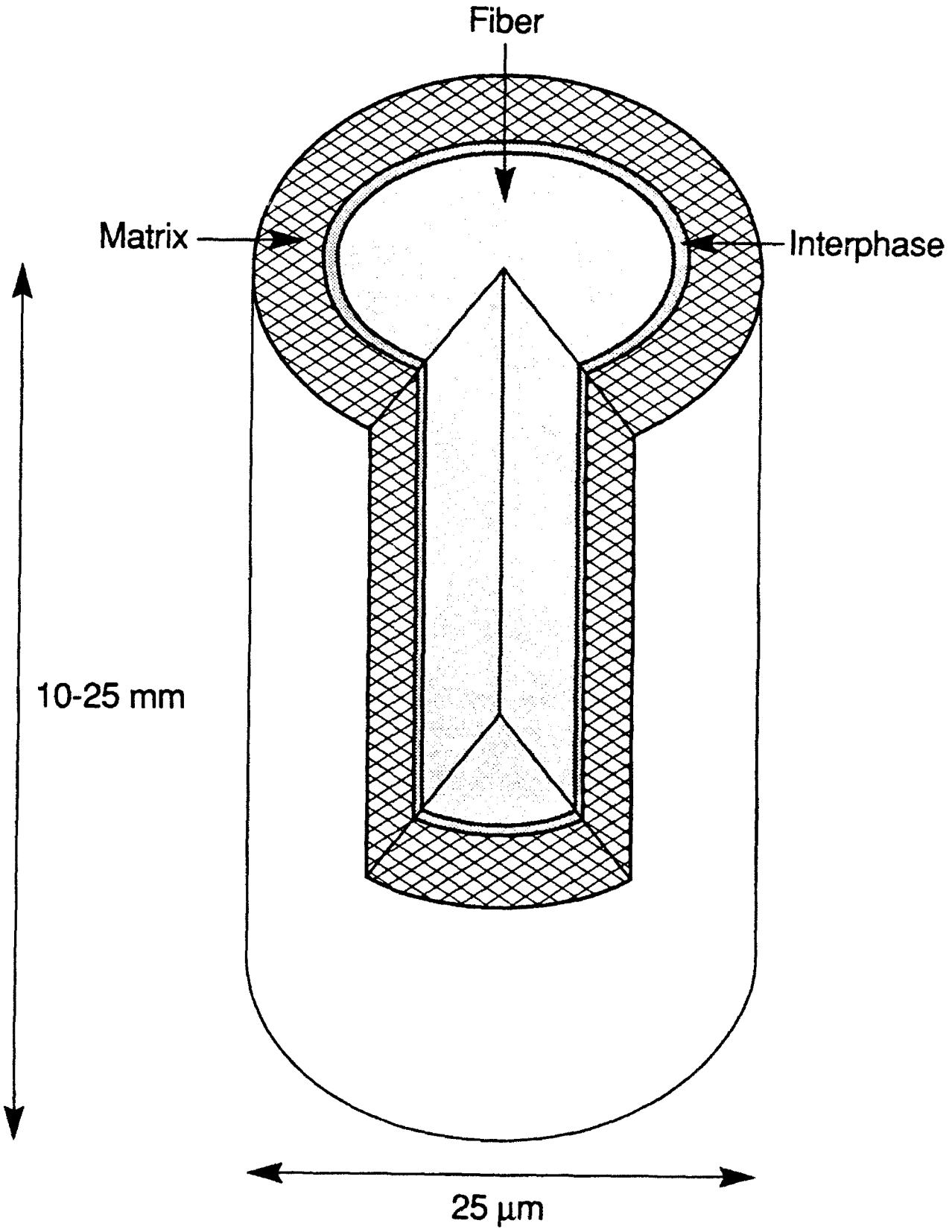

Evans.URI ft-3/93-amk-042#1042-1

Figure 1

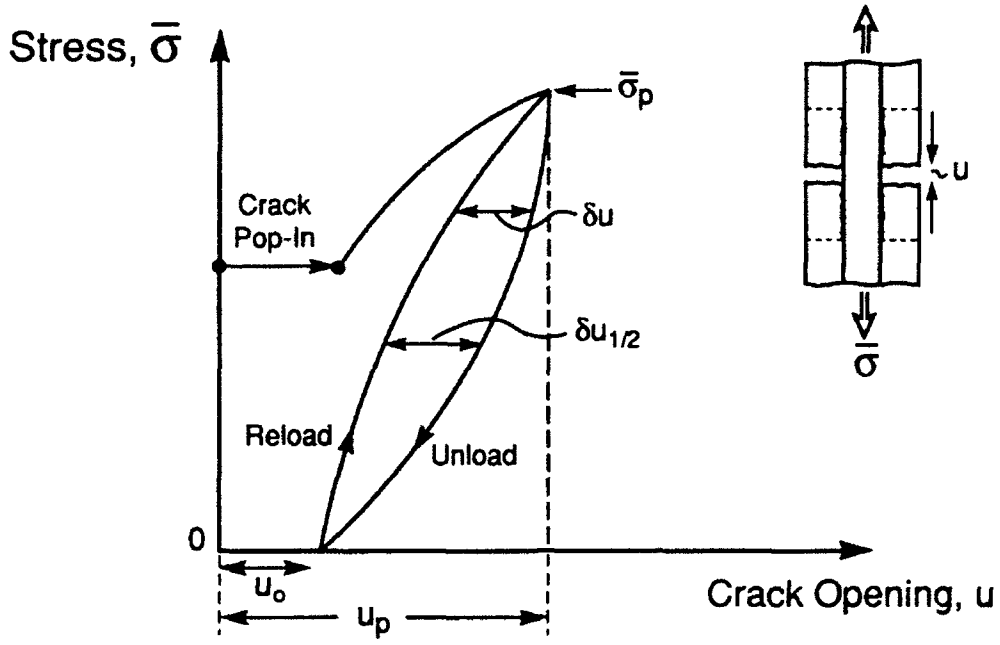

a) Crack Opening Displacements

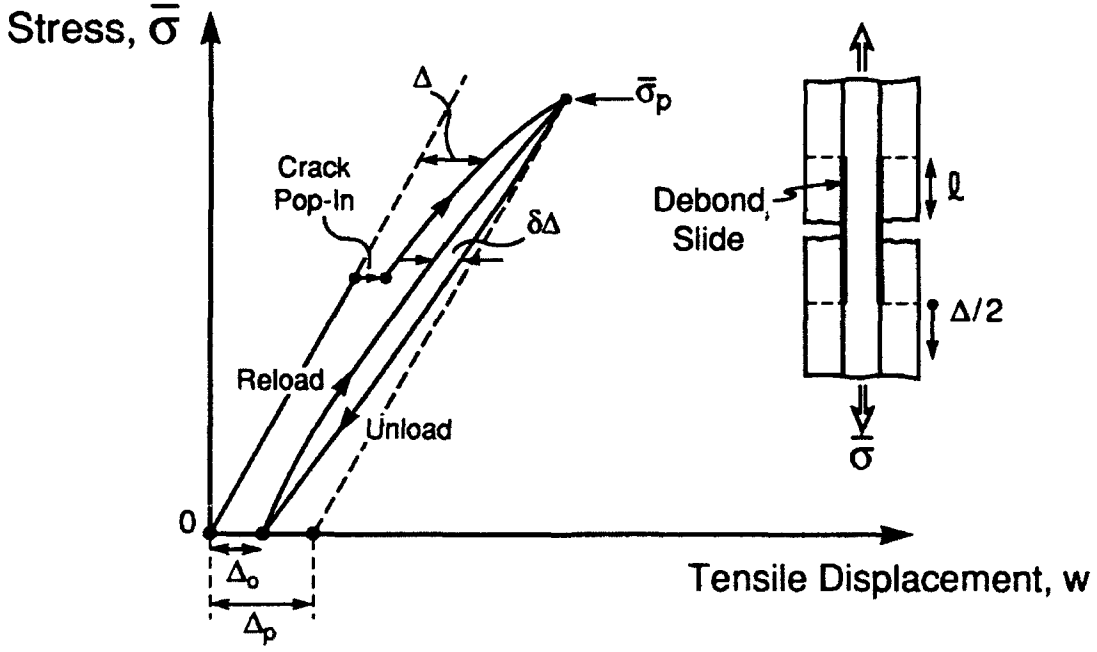

b) Tensile Displacements

Figure 2

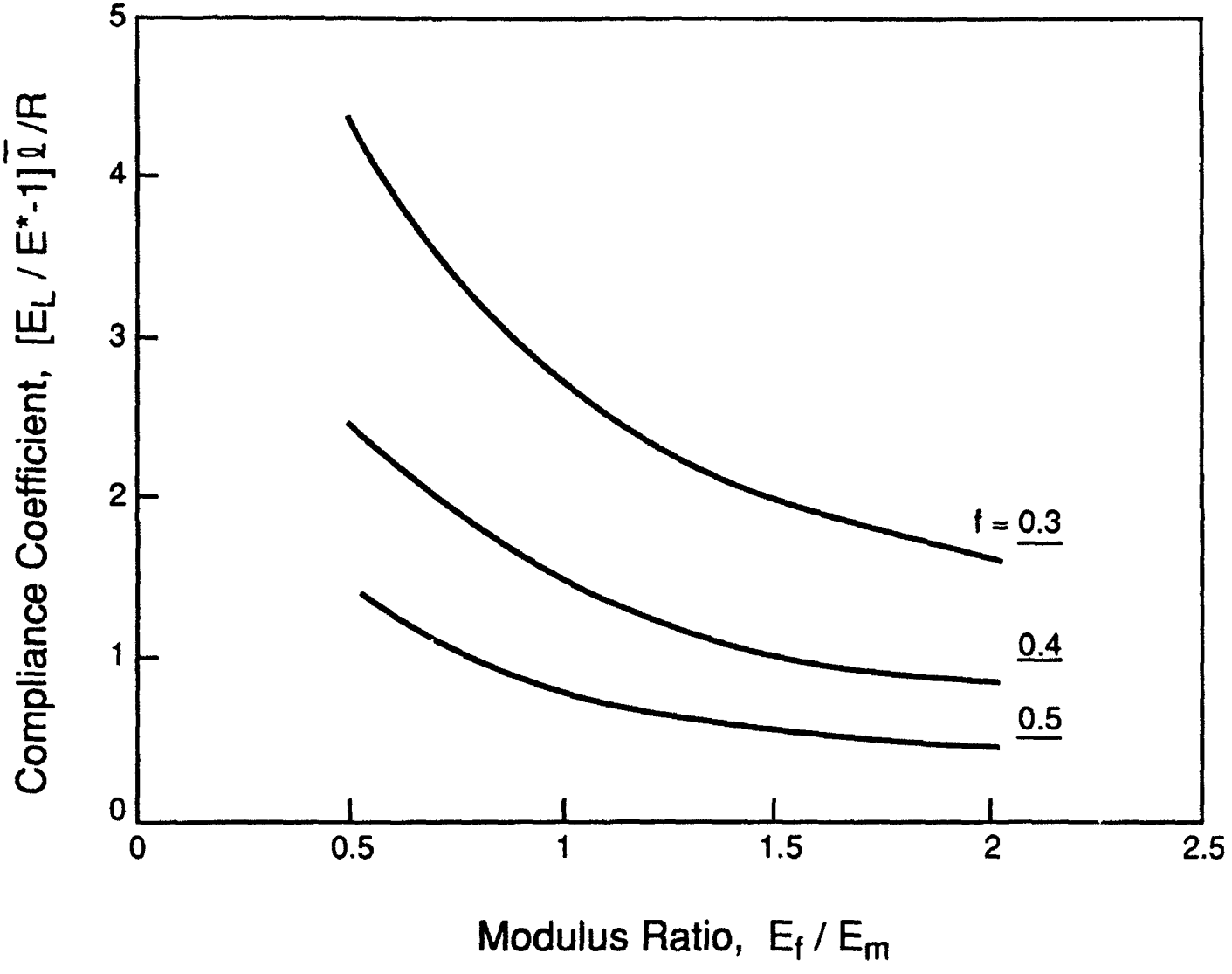
Compliance Coefficient, $[E_L / E^* - 1]\bar{\ell}/R$
Modulus Ratio, E_f / E_m
0
1
2
3
4
5
0
0.5
1
1.5
2
2.5
f = 0.3
0.4
0.5

Figure 3

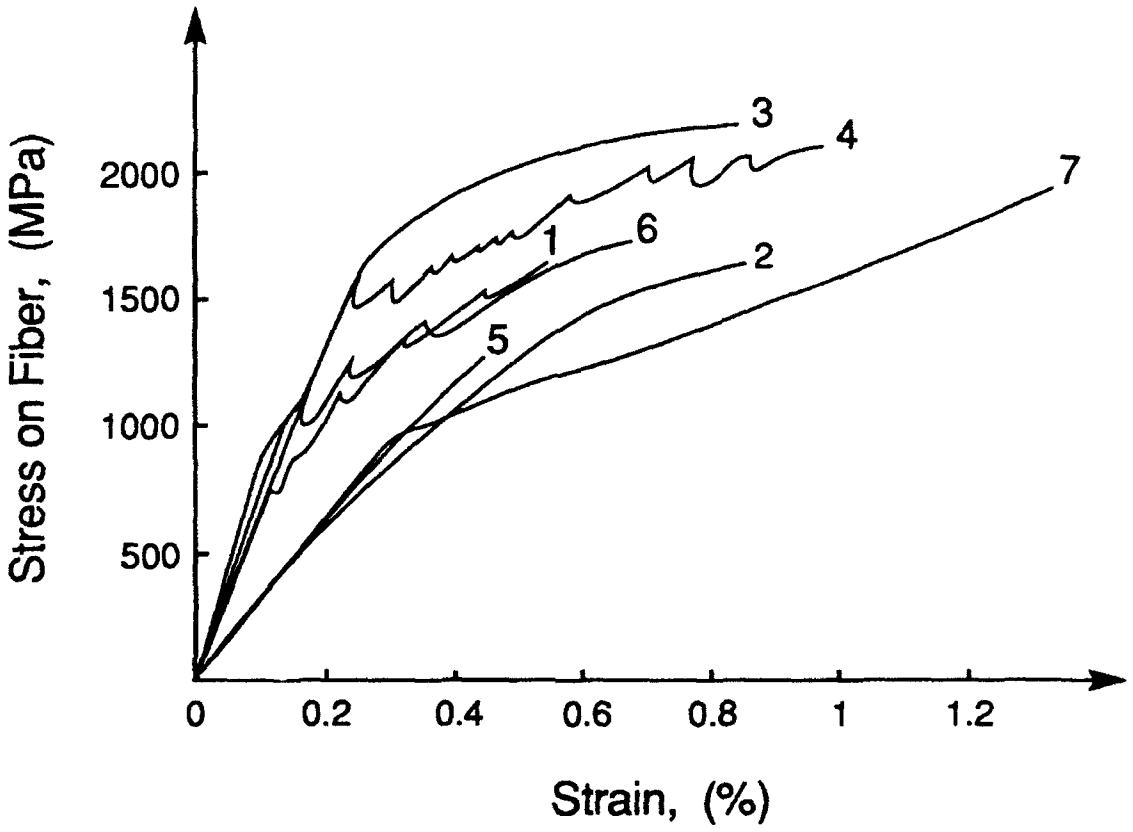
Stress on Fiber, (MPa)
2000
1500
1000
500
0
0.2
0.4
0.6
0.8
1
1.2
Strain, (%)
1
2
3
4
5
6
7

Figure 4

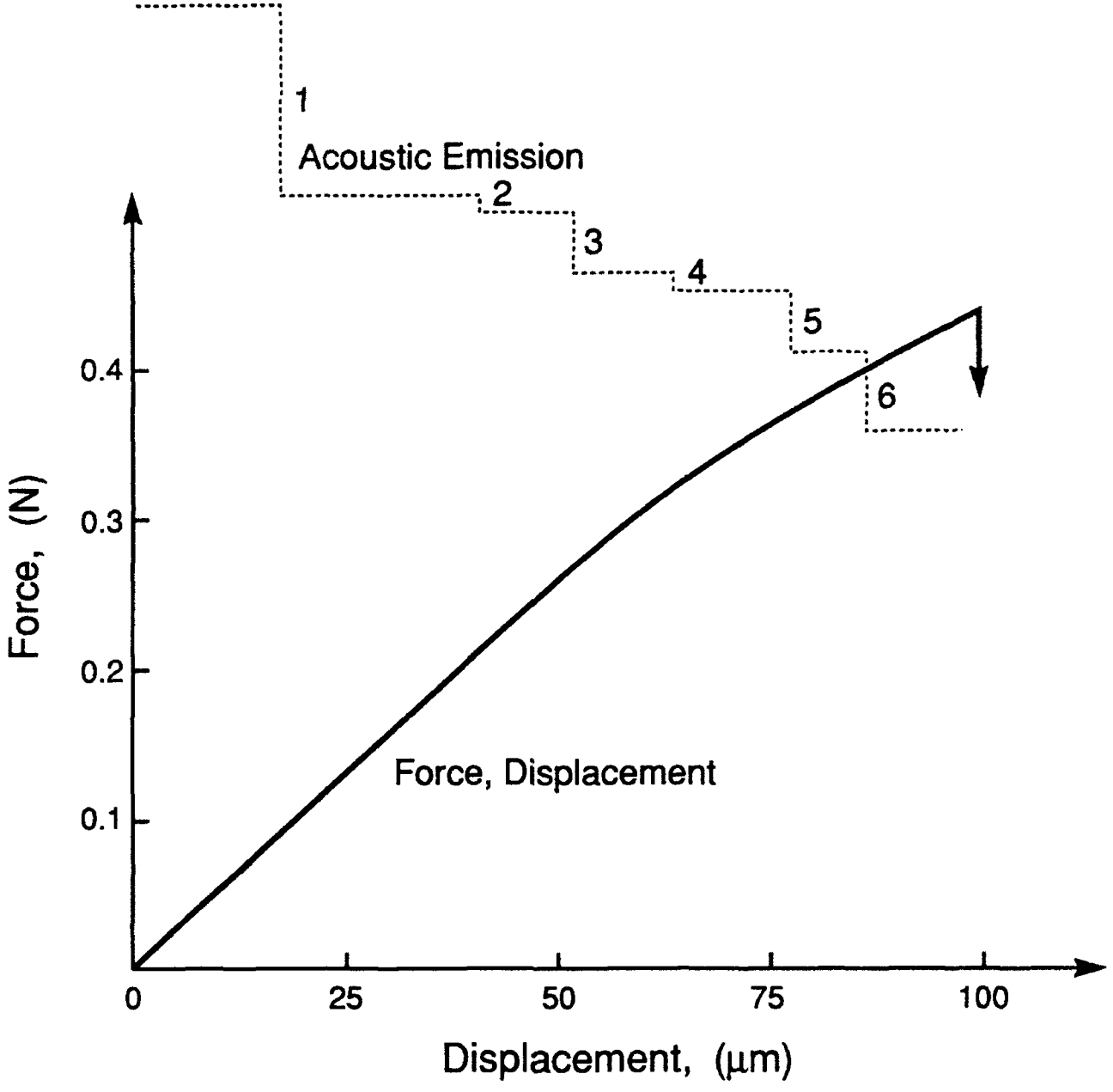
1
Acoustic Emission
2
3
4
5
6
0.4
0.3
0.2
0.1
Force, (N)
Force, Displacement
0
25
50
75
100
Displacement, (μm)

Figure 5

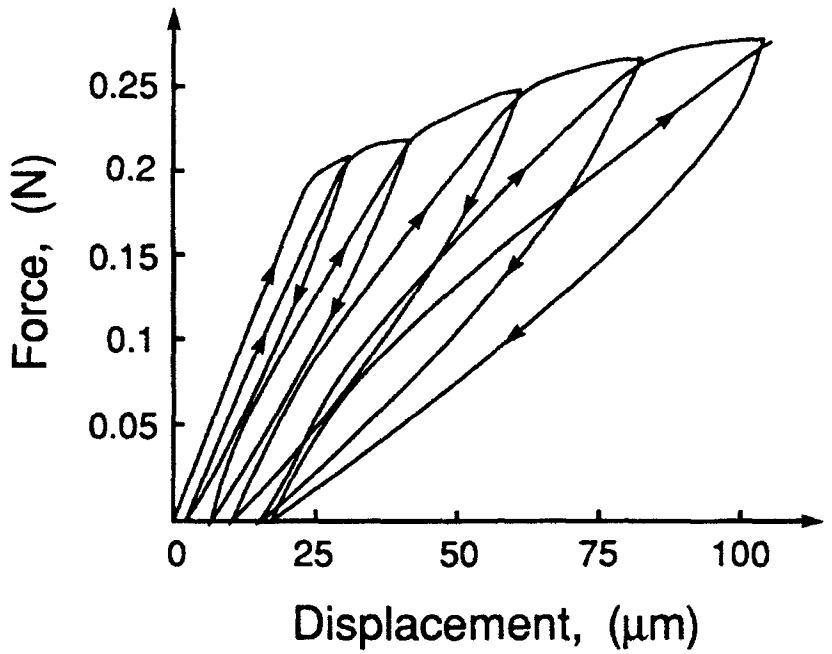

a) SiC / BN / SiC

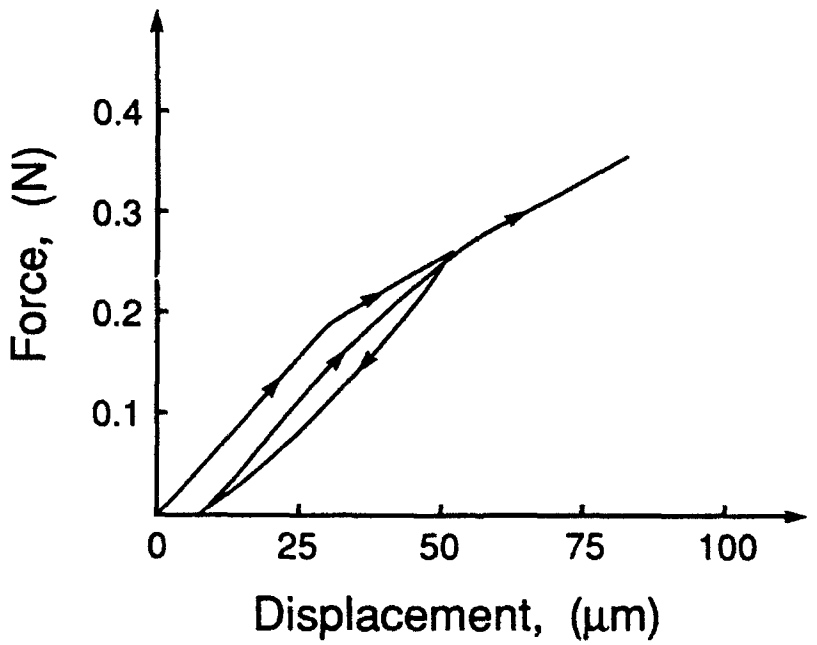

b) SiC / C / SiC

Figure 6

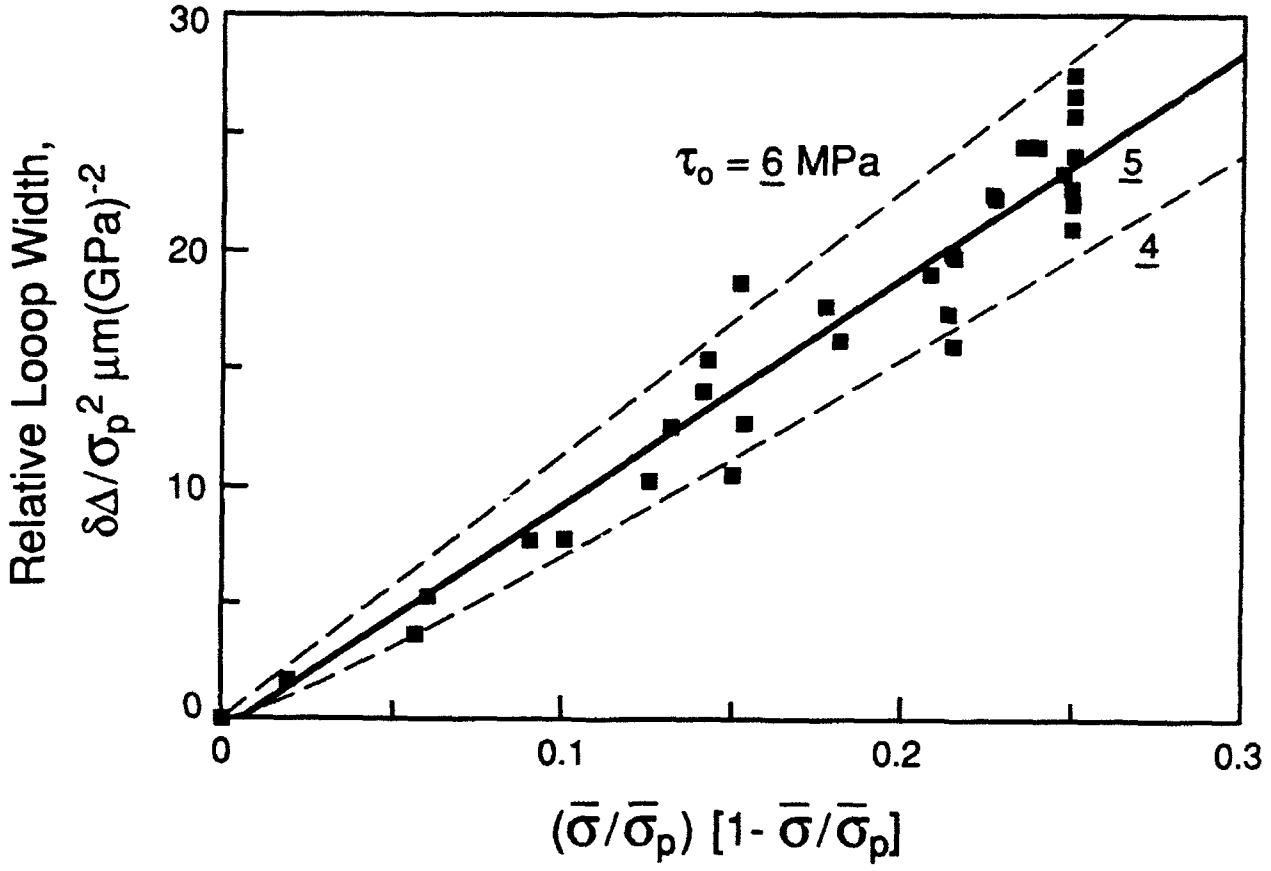
Relative Looop Width,
$\delta\Delta/\sigma_p^2$ μm(GPa)$^{-2}$
30
20
10
0
0
0.1
0.2
0.3
τ_o = 6 MPa
5
4
$(\bar{\sigma}/\bar{\sigma}_p)$ [1- $\bar{\sigma}/\bar{\sigma}_p$]

Figure 7

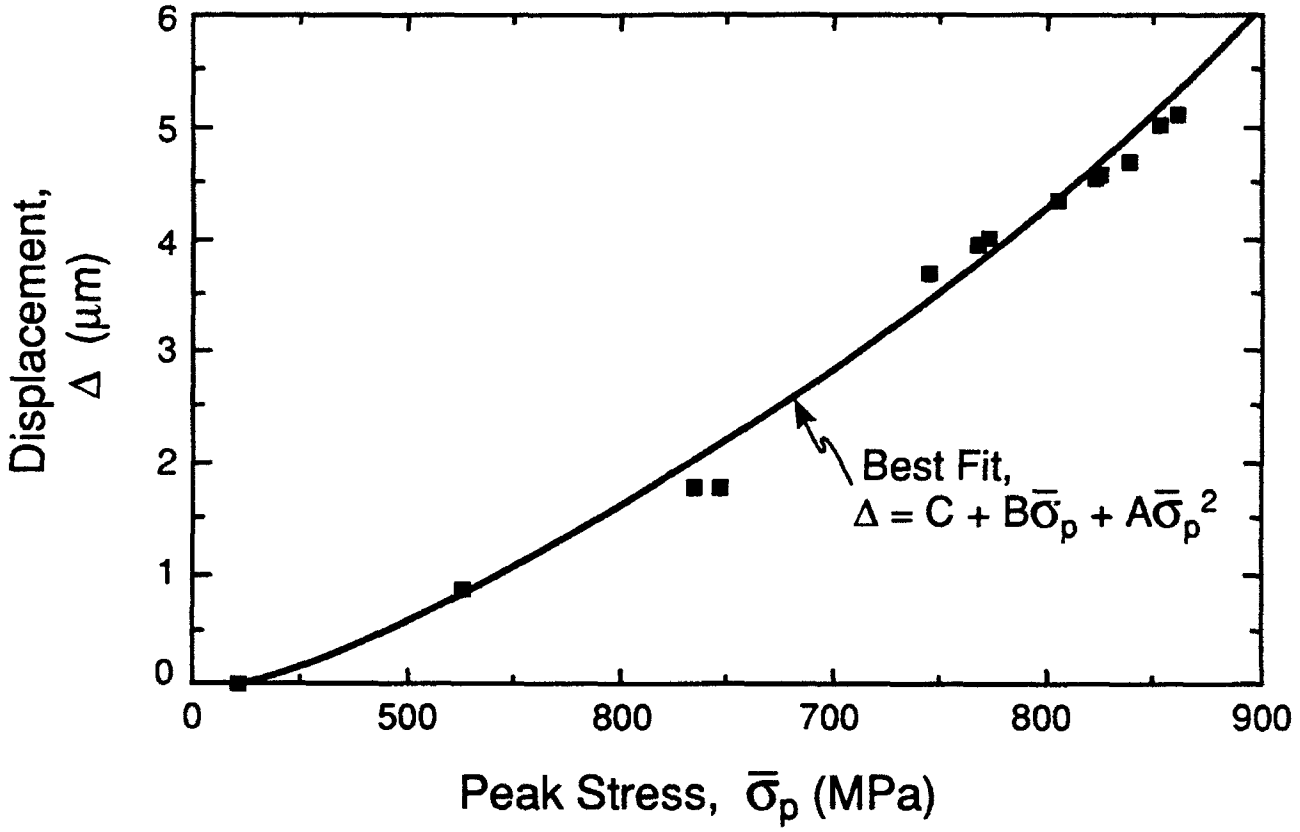
Displacement,
Δ (μm)
6
5
4
3
2
1
0
0
500
800
700
800
900
Peak Stress, $\bar{\sigma}_p$ (MPa)
Best Fit,
$\Delta = C + B\bar{\sigma}_p + A\bar{\sigma}_p^2$

Figure 8

Acta metall. mater. Vol. 40, No. 6, pp. 1243–1249, 1992
Printed in Great Britain.

0956-7151/92 $5.00 + 0.00
Pergamon Press Ltd

DESIGN, ANALYSIS AND APPLICATION OF AN IMPROVED PUSH-THROUGH TEST FOR THE MEASUREMENT OF INTERFACE PROPERTIES IN COMPOSITES

P. D. WARREN, T. J. MACKIN and A. G. EVANS

Materials Department, College of Engineering, University of California, Santa Barbara, CA 93106-5050, U.S.A.

(Received 7 October 1991)

Abstract—An improved fiber push-through test has been designed and used to obtain new information about interfaces in composites consisting of matrices of a Ti alloy and a borosilicate glass, both reinforced with SiC fibers. Interpretation of these results is accomplished through an analysis of coupled debonding and push-through, followed by push-back. The sliding stress is found to vary with push-out distance and to be substantially reduced in the vicinity of a fatigue crack in the Ti matrix composite. These effects are attributed to asperity wear, matrix plasticity and fragmentation of the fiber coating around the debonded interface. Reseating effects on push-back have been demonstrated, but have been found to diminish as the relative fiber–matrix displacement increases. Fiber roughness has been identified as an important aspect of interface sliding.

Résumé—Un essai amélioré d'enfoncement des fibres est proposé et utilisé pour obtenir de nouvelles informations sur les interfaces dans des composites formés de matrices en alliage de titane et en verre au borosilicate, toutes deux renforcées par de fibres de SiC. L'interprétation de ces résultats est effectuée par une analyse de la séparation et de l'enfoncement couplés, suivi d'une poussée en sens inverse. On trouve que la contrainte de glissement varie avec la distance d'enfoncement et qu'elle est réduite considérablement au voisinage d'une fissure de fatigue dans le composite à matrice de titane. Ces effets sont attribués à l'usure des aspérités, à la plasticité de la matrice et à la fragmentation du revêtement des fibres autour de la surface de séparation. Des effets de remise en place lors de la poussée en sens inverse sont observés, mais ils diminuent lorsque le déplacement relatif fibre/matrice augmente. On montre que la rugosité de la fibre est un aspect important du glissement interfacial.

Zusammenfassung—Ein verbesserter Faser-Durchstoß-Test wird entworfen und angewandt, um neue Informationen über Grenzflächen in Verbundwerkstoffen zu erhalten, deren Matrix entweder aus einer Ti-Legierung oder einem Borsilikat-Glas, beide verstärkt mit SiC-Fasern, besteht. Mit einer Analyse der gekoppelten Prozesse Ablösen und Durchstoßen, gefolgt von Zurückschieben, werden diese Ergebnisse interpretiert. Die Gleitungsspannung ändert sich mit der Ausziehlänge und ist in der Nähe eines Ermüdungsrisses in dem Werkstoff mit Ti-Matrix beträchtlich verringert. Diese Einflüsse werden dem Abrieb, der Plastizität in der Matrix und dem Bruch des Faserüberzugs im abgelösten Grenzflächenbereich zugeschrieben. Effekte der Wiedereinlagerung beim Zurückschieben werden gefunden, sie verschwinden aber mit steigender relativer Verschiebung zwischen Faser und Matrix. Es wird gezeigt, daß die Faserrauhigkeit ein wichtiger Aspekt der Grenzflächengleitung ist.

1. INTRODUCTION

Fiber push-through tests have been widely exploited as an approach for measuring the sliding properties of fiber–matrix interfaces in composite materials [1–5]. The advantages of this method include relative simplicity in testing and a capability for conducting experiments at elevated temperatures [6]. The disadvantages are concerned with interpretation of the measurements, because of relatively complex deformations that occur during the loading and sliding processes. The first intent of the present study is to provide a further development of the push-through test, in conjunction with an analysis that allows determination of the interface sliding stress, τ. The second objective is to apply the technique to interfaces between SiC (SCS-6) fibers and a β-Ti (15-3-3) alloy matrix, before and after fatigue crack growth [7], as well as interfaces between SiC (SCS-6) fibers and a borosilicate–glass matrix.

Previous studies on the push-through test have relied primarily on the peak load for initial push-through as a measure of "debonding." Push-back has been used to provide a measure of the sliding stress, τ, along the debonded interface. The magnitude of τ has been calculated from the force, P, and displacement, d, from the expression

$$\tau = P/2\pi R(h - d) \qquad (1)$$

where R is the fiber radius and h is the section thickness. More comprehensive analysis of coupled debonding and sliding [8, 9] during push-through allows substantial additional information to be gained from push-through and push-back tests when appropriately modified and instrumented. Solutions for pull-out [8] and push-through [9] for coupled debonding and sliding have been characterized by a debond energy, Γ_i, a sliding stress, τ, and a thermal expansion misfit strain, ϵ_T. Some of the salient results are summarized, as needed to relate the push-through force, P, to the displacement, d, in terms of τ and ϵ_T. The basic solutions are described in terms of a friction law

$$\tau = \tau_0 - \mu\sigma_r \tag{2}$$

where μ is the friction coefficient and σ_r is the compressive stress normal to the interface. During initial push-through, stable debonding proceeds with frictional sliding occurring behind the debond tip. This is followed by a load drop and push-out resisted by friction. Results are presented for the following conditions: (i) the Poisson's ratio of the fiber and matrix are the same, (ii) the misfit strain in the axial and radial directions are the same and, (iii) the radial stress is zero at the outer boundary (Type I conditions) [8, 9].

The load–displacement behavior during debonding is sensitive to the *initial* debond length which, in turn, is affected by the sectioning process and the misfit strain. However, after the debond has propagated completely along the interface, since there is no contribution from debonding, the load, P, becomes

$$\frac{P}{\pi R^2} = \frac{\hat{\sigma}_0[\exp(2\mu Bt/R) - 1]}{1 + \left[\frac{f}{(1-f)}\frac{E_f}{E_m}\right]\exp\left(\frac{2\mu Bt}{R}\right)} \tag{3}$$

where

$$\hat{\sigma}_0 = \frac{E_f\epsilon_T}{\nu} + \frac{\tau_0}{\mu}\frac{E/E_m}{B(1-f)}$$

$$B = \nu E/[(1+\nu)E_f + (1-\nu)E]$$

with E being Young's modulus, ν Poisson's ratio and $t = h - d$,† with the subscripts m and f referring to matrix and fiber, respectively. For the special case, $\mu = 0$, equation (4) reduces to equation (1) with $\tau = \tau_0$, whereupon P decreases linearly with d. However, when $\mu \neq 0$, P is slightly non-linear. This general solution has been implemented in a companion paper [10] to predict the effect of fiber roughness and of misfit on the push-out force. The results will be invoked in this article to interpret some of the experimental measurements.

†It should be noted that f in these formulae is not the fiber volume fraction, but rather the ratio

$$f = \frac{\text{area of fiber}}{\text{total area of composite}}$$

This implies that f is always small (typically 10^{-4}).

2. PUSH-THROUGH TEST

2.1. Design

For fibers having either a relatively large diameter or large values of Γ and or τ, substantial forces are needed to displace the fibers. In such cases, the indenter design and the loading arrangement needed to obtain useful information are particularly important. Many previous studies have used sharp indentors that penetrate the fiber. Two problems arise. (i) at high loads, cracks are introduced into the fibers that can influence the measurements; (ii) at moderate displacements, the indentor comes into contact with the matrix, curtailing further measurements. To obviate these problems, cylindrical indentors are preferred and used in conjunction with the apparatus schematically illustrated in Fig. 1. The test is performed by preparing a thin section of the composite. This section is located on an Al alloy base containing a 220 μm diameter hole, with the fiber of interest placed over the hole. A small SiC cylinder, 100 μm diameter, is emplaced on the fiber *ex situ* in an optical microscope. A small rod located within the hole is maintained in intimate contact with the fiber and connected to a cantilever beam with an attached strain gauge. This device measures the displacement at the bottom of the fiber during push-through. Loads are applied to the indentor through a flat Al_2O_3 plate connected to a load cell, which monitors the force, P. This system can be located within a furnace for high-temperature measurements. Two additional features of this design are noted. The use of a relatively small diameter hole minimizes bending stresses. However, loads are limited to ~40N, because at larger loads, either cone cracks form in the SiC fibers or the SiC indentor fractures.

2.2. Materials and specimens

Tests were conducted on composites consisting of (SCS-6, CVD) SiC fibers in either a Ti alloy (Ti–15V–3 Al) or a borosilicate glass (Corning 7741) matrices. The elastic and thermal properties of the specimens are listed in Table 1. In both cases, specimens were ground and polished with a final 1 μm diamond finish. Two different specimen thicknesses

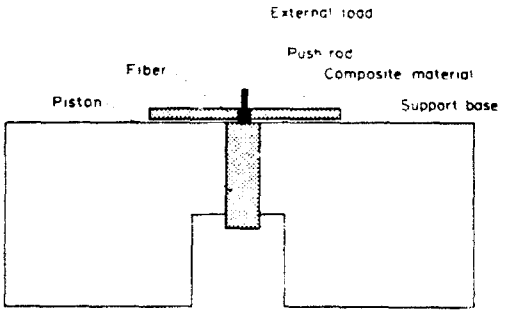

Fig. 1. Schematic diagram of the fiber push-through apparatus

Table 1. Properties of the two matrices

	Ti-15-3/SiC	Glass SiC
Modulus, E_m	115 GPa	70 GPa
Composite modulus, E	196 GPa	70 GPa
Poisson's ratio, ν_m	0.33	0.20
Thermal expansion coefficient, α_m	$7.6 \times 10^{-6}\,C^{-1}$	$3.25 \times 10^{-6}\,C^{-1}$
Thermal mismatch strain, ϵ_T	4.5×10^{-3}	7.0×10^{-4}
Radial thermal mismatch stress, σ_R	−300 MPa	−60 MPa
Volume fraction of fibers, ρ	0.35	6.8×10^{-4}
Area of fiber/area of specimen, f	4.5×10^{-4}	6.8×10^{-4}
Fiber properties		
Modulus E_f	360 GPa	
Poisson's ratio, ν_f	0.17	
Thermal expansion coefficient, α_f	$2.6 \times 10^{-6}\,C^{-1}$	

were used for each composite: 210 and 410 μm for the Ti alloy, 1.5 and 2.1 mm for the glass. Fibers were pushed out to a range of displacements up to 80 μm and then pushed back. The loads and deflections were continuously monitored. Some tests were conducted on the Ti alloy matrix composite which had been subjected to fatigue cracking at a stress amplitude $\Delta\sigma = 300$ MPa and an R ratio = 0.1 [7]. This fatigue schedule lead to matrix crack-growth without fiber failure. A push-through specimen was prepared from a 450 μm thick section of material parallel to the matrix fatigue crack (Fig. 2). Tests were conducted on fibers at different locations relative to the fatigue crack front.

3. RESULTS

3.1. Pristine materials

A variety of experimental results have been obtained. Typical results obtained on pristine material are presented in Figs 3 and 4. An increase in load occurs associated with elastic bending and stable debonding. A load drop, ΔP, often accompanies debond pop-through. The magnitude of ΔP increases as the section thickness increases (Table 2). This load drop may be used to estimate the intefacial debond energy (see Appendix). Frequently, an initial rise in load is found following pop-through, for the first 2–3 μm of fiber displacement. This is followed by a load that usually diminishes as the push-through displacement increases. Upon push-back, the load at which fiber displacements resume, P_s (Fig. 4), is usually somewhat smaller than the termination load upon push-through, P_j. Thereafter, the load remains essentially constant until the fiber reaches the original location. At that location, there is a small load drop, ΔP_d, associated with the fiber reseating into its initial position, as observed in previous studies [3, 4]. The relative load drop, $\Delta P_d/P$, usually decreases as the initial push-through distance increases (Table 2).

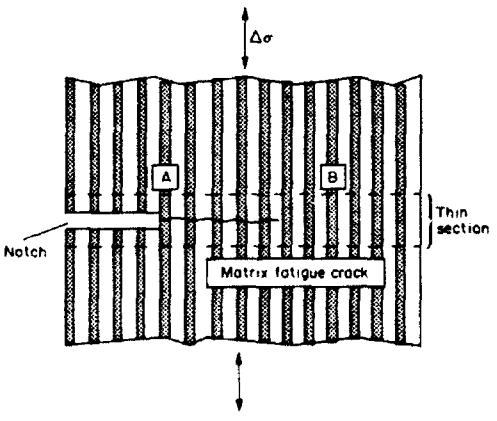

Fig. 2. Schematic of the fatigue specimen showing the notch root and fatigue crack growing from the root. The fibers are perpendicular to the fatigue crack, with a center–center spacing ≈250 μm.

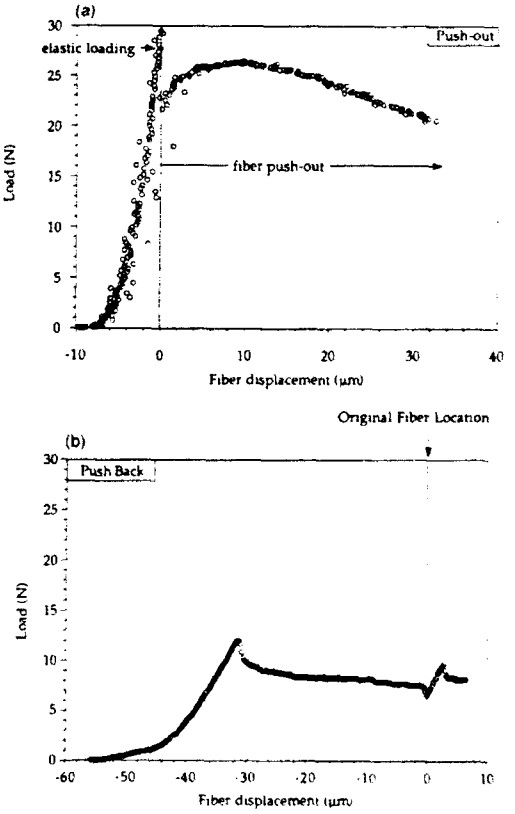

Fig. 3. Two examples of force–displacement results for push-through and push-back on the Ti-15-3/SiC material (specimen thickness 410 μm).

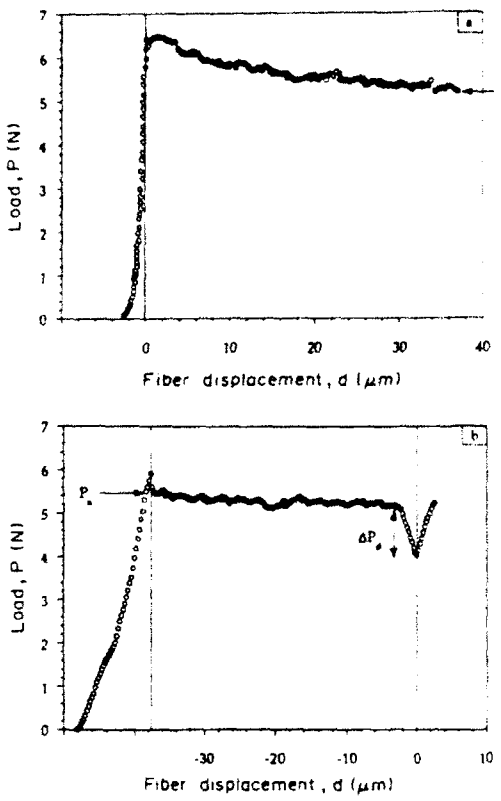

Fig. 4. Force–displacement results for push-through and push-back of the glass/SiC material (specimen thickness 1.5 mm).

A comparison of the results for the two different matrices reveal important differences. The Ti matrix composite exhibits, (i) consistently larger value of the push-out force, (ii) a substantially larger push-through load drop, ΔP, and (iii) greater differences in the relative push-back force, P_s/P_i. Also, the relative load decrease that occurs as the push-out process proceeds is larger for the Ti matrix composite. Conversely, the relative reseating load drop, $\Delta P_d/P$, is larger for the glass matrix system.

Observations of fibers following initial push-through using scanning electron microscopy (SEM) indicated that sliding in the Ti matrix system occurs at the interface between the fiber coating and the reaction product which forms at the interface [Fig. 5(a)], whereas in the borosilicate matrix system, debonding and sliding proceeds at the fiber-coating matrix interface [Fig. 5(b)].

Table 2. (a) Reseating load drop

Push-out distance (μm)	Relative load drop, ΔP_d (N)
	Ti matrix
5	0.55
10	0.36
20	0.13

(b) Push-through load drop

Section thickness (μm)	Load-drop, ΔP (N)
	Ti matrix
410	7.3
210	5.1

3.2 *Fatigued material*

The specimens prepared following fatigue crack propagation exhibited different push-out characteristics. At fiber locations ahead of the fatigue crack-tip (B in Fig. 2), the push-through characteristics are essentially the same as these on pristine specimens. However, adjacent to the notch (A in Fig. 2), the push-through force–displacement curves have the form depicted in Fig. 6. Subsequent to elastic deflection and a small load drop, push-out commences at a relatively low load but the push-through load *increases* for push-through displacements of the order of 30 μm. Thereafter, the load decreases with increasing displacement.

Push-back tests have the same features exhibited by pristine specimens: an essentially constant load, similar in magnitude to that reached upon termination of

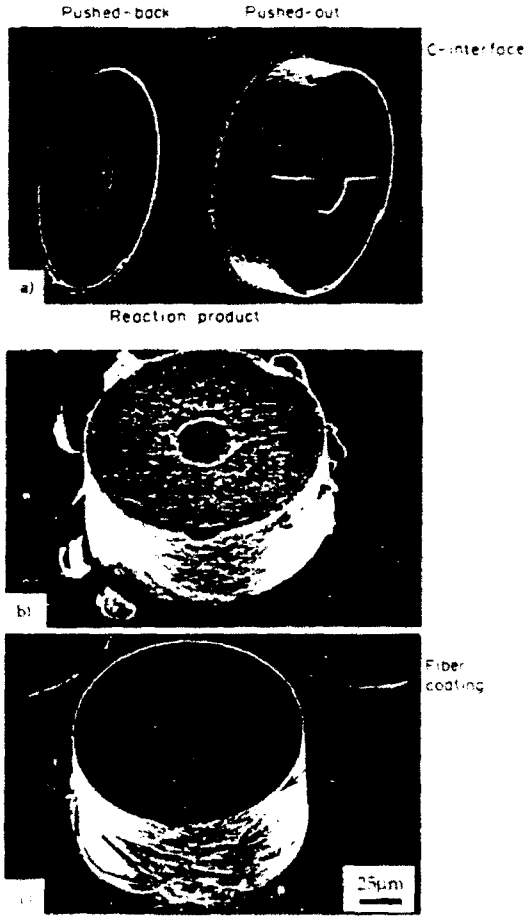

Fig. 5. SEM micrographs of fibers after push-through, (a) the Ti 15-3/SiC composite, (b) the glass/SiC composite—note the glass fragments adhering to the fiber, (c) fatigued Ti matrix sample—note the extensive damage to the coating.

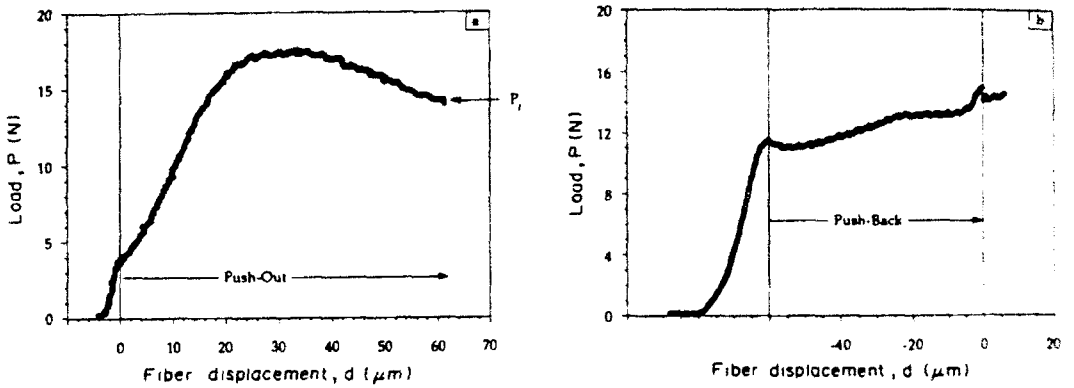

Fig. 6. Force–displacement results for push-through and push-back in the fatigued Ti–15–3 SiC material.

push-through. However, there was no load drop associated with reseating. Observations of the sliding interface indicate extensive fragmentation of the fiber coating [Fig. 5(c)].

4. ANALYSIS

Preliminary representation of the sliding behavior is made using equation (1), as plotted on Fig. 7. The Ti matrix system has a sliding stress about an order of magnitude larger than that for the glass matrix material. Also, the decrease in τ with sliding displacement is much larger for the Ti system. Attempts to fit the load–displacement results to equation (3) with consistent τ_0 and μ have yielded unacceptable correlations. The problem is illustrated *for the glass matrix system* in Fig. 8. First, by using the misfit ϵ_T and the elastic properties for this composite (from Table 1).

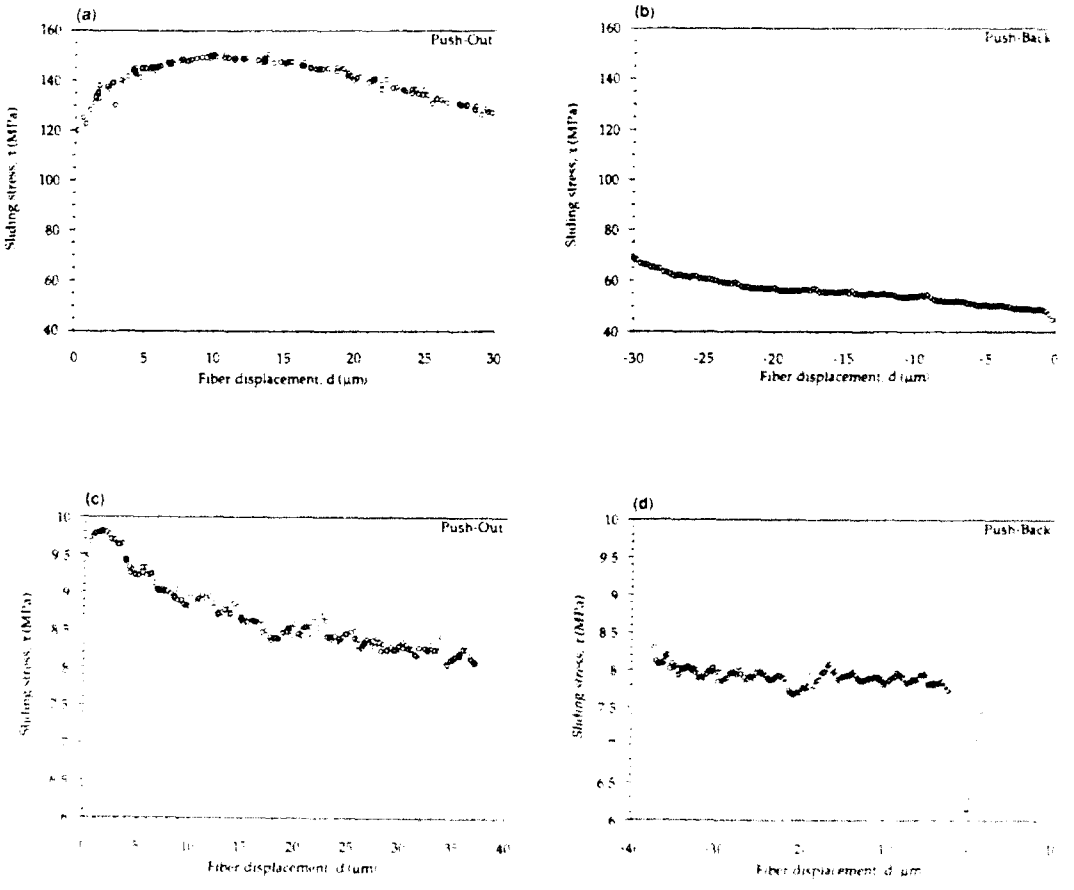

Fig. 7(a–d). *Caption overleaf*

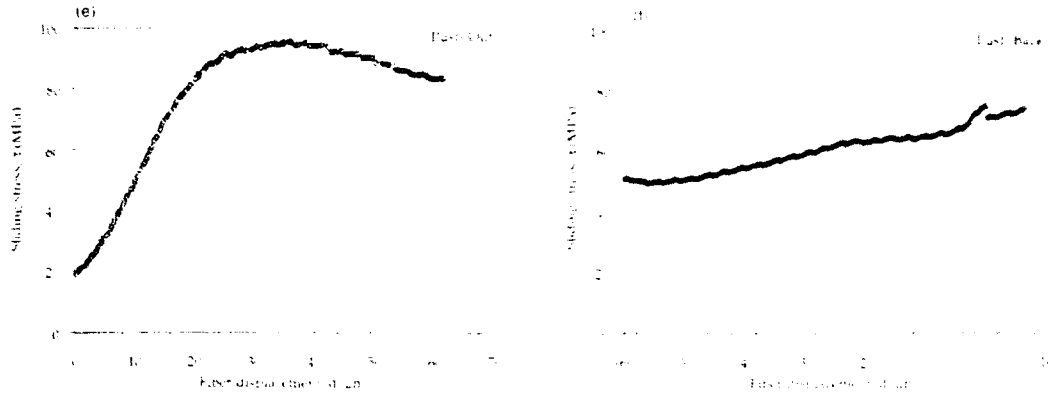

Fig. 7(e,f)

Fig. 7. Values of the sliding stress τ as a function on push-through and push-back (a,b) Ti matrix composite, (c,d) glass matrix composite, (e,f) Ti matrix after fatigue

a fit of equation (3) to the initial push-through force indicates that $\mu \approx 0.2$ and $\tau_0 \approx 2$ MPa. Then, by maintaining μ and τ_0 at these levels, equation (3) predicts a substantially smaller load reduction upon push-out than indicated by the experiments. This situation differs from that found when initial push-through measurements are made as a function of embedded lengths (Fig. 9), wherein all measurements involve small displacements ($< 2\,\mu$m). The inference is that either μ or τ_0 or both are diminishing as push-out proceeds. An assessment of the degradation is made (Fig. 10) by either regarding μ as constant and evaluating the reduction in τ_0 or vice versa. Based on an analysis elaborated in a companion paper [10], the preferred interpretation is that τ_0 decreases. This analysis relates τ_0 to fiber *roughness*. It explains various unexpected phenomena, such as the frequently found rise in initial push-out stress (Fig. 3) in terms of a geometric decorrelation. It also demonstrates that τ_0 decreases as the amplitude of the roughness decreases. The implication regarding the results presented for the glass matrix system in Fig. 10 is that wear of the interface asperities occurs as the interface slides during push-out, causing τ_0 to diminish. Direct measurements of asperity amplitudes would be needed to verify this interpretation.

The much larger reduction in τ in the Ti matrix system cannot be explained by the same asperity wear mechanism, because the extent of asperity wear that would be needed to correlate with the experiments is unacceptably large [10]. The interpretation most consistent with the measurements [Fig. 7(a)], is a reduction in misfit strain with push-out, probably caused by plastic expansion of the matrix around the fiber, as asperities slide over each other.

The large reduction in initial push-out stress induced upon fatigue crack growth (Fig. 6) has also been related to a diminished misfit strain [10]. In this case, fragmentation and removal of the fiber coating [Fig. 5(c)] is regarded as the major source of the reduced misfit. The subsequent increase in push-out load is qualitatively consistent with this interpretation, but the magnitude is larger than this mechanism could predict. Further study is needed to understand these details.

The reseating effect on push-back has been noted and explained [3, 4] in terms of asperities on the debonded interface. One notable addition provided

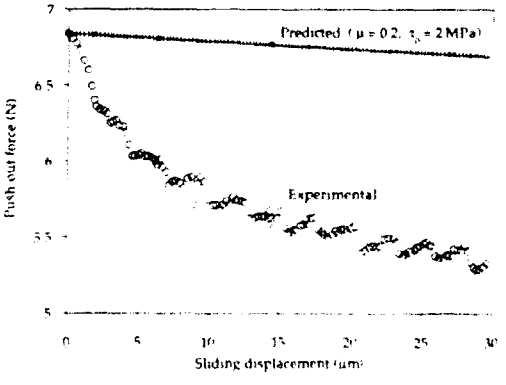

Fig. 8. A comparison of push-through measurements for the glass matrix system with prediction based on equation (4) with μ and τ_0 held constant

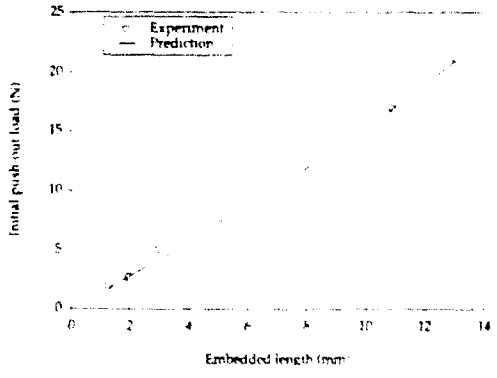

Fig. 9. A comparison of push-out data as a function of embedded length with the prediction of equation (3) [5] ($\tau_0 = 0$, $\mu = 0.2$)

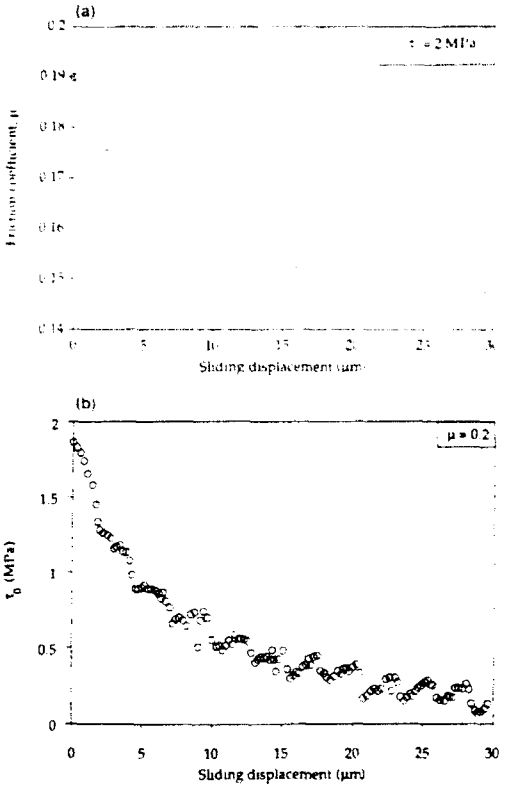

Fig. 10. Change in sliding parameters with push-out for a glass matrix system: (a) fixed, τ_0, (b) fixed μ.

by the present study concerns the reduction in the associated load drop with increase in the push-through displacement in the Ti–15–3 matrix material (Table 2). This observation is consistent with the above speculations that the matrix in this material is being plastically deformed during push-through.

5. CONCLUDING REMARKS

Based on the development of an improved push-through test, some important sliding characteristics of interfaces in metal and glass matrix composites have been identified. In particular, changes in sliding behavior caused by monotonic and cyclic sliding displacements have been revealed. Qualitative comparison with a sliding model based on fiber roughness and friction [10] have provided some insight about the origin of these effects. Changes in monotonic sliding resistance τ are larger for metal (MMC) than glass (GMC) matrix composites, suggesting that release of misfit by matrix plasticity is important for MMCs whereas asperity wear dominates for GMCs. The effects of fatigue seem to involve fragmentation of the fiber coating that also reduces the thermal expansion misfit and reduces τ.

Some of the changes are substantial and have important implications for matrix cracking in composites, subject to either monotonic or cyclic loading processes that have high sensitivity to τ. The details that govern the sliding induced changes in τ have not been elucidated and require further study.

Acknowledgement—Funding for this work was supplied by the Defense Advanced Research Projects Agency through the University Research Initiative Program of UCSB under the Coatings contract No. MDA972-90-K-0001.

REFERENCES

1. D. B. Marshall, *J. Am. Ceram. Soc.* **67**, 259 (1984).
2. D. B. Marshall and W. C. Oliver, *J. Am. Ceram. Soc.* **70**, 542 (1987).
3. P. D. Jero and R. J. Kerans, *Scripta metall. mater.* In press.
4. W. C. Carter, E. P. Butler and E. R. Fuller, *Scripta metall. mater.* **25**, 579 (1991).
5. J. D. Bright, S. Danchaivijit and D. K. Shetty, *J. Am. Ceram. Soc.* **74**, 115 (1991).
6. G. Morscher, P. Pirouz and A. H. Heuer, *J. Am. Ceram. Soc.* **73**, 713 (1990).
7. D. Walls, G. Bao and F. Zok, *Scripta metall. mater.* **25**, 911 (1991).
8. J. W. Hutchinson and H. M. Jensen, *Mech. mater.* **9**, 139 (1990).
9. C. Liang and J. W. Hutchinson, To be published.
10. T. J. Mackin, P. D. Warren and A. G. Evans, To be published.

APPENDIX

Estimating the Interface Debond Energy, Γ_i

Liang and Hutchinson [9] have shown that a load drop, ΔP, occurs after the debond has propagated completely along the interface (for $\tau_0 = 0$).

$$\frac{\Delta P}{\pi R^2} = \left[A_1 \epsilon_T + A_2 \sqrt{\frac{E_m \Gamma_i}{R}} \right] \exp\left(\frac{2\mu B h}{R}\right) \qquad \text{(A1)}$$

where

$$A_1 = \frac{E_f + E}{(1+\nu) + (1-\nu)E\ E_f}$$

$$A_2^2 = \frac{4EE_f[(1+\nu)E_f + (1-\nu)E]}{(1-f)(1+\nu)E_m^2[E_f + (1-2\nu)E]}$$

In (A1), the first term in parentheses reflects the release of residual stress when the debond propagates completely along the interface while the second term reflects the contribution to the load induced by the bond.

Measurements of ΔP enable Γ_i to be estimated provided that ϵ_T is independently known. As a first approximation, we assume that the axial mismatch strain is entirely relieved when the thin composite sections are sliced, $\epsilon_T = 0$. Values of Γ_i are then estimated for the Ti matrix composite in which debonding occurs within the fiber coating. For this case [Fig. 7(a)], $\tau = 90$ MPa and the mismatch stress $\sigma_0 = 300$ MPa (Table 1) giving $\mu = 0.3$. With this value for μ, the measured push-through load drops (Table 2) give Γ_i in the range 4–7 Jm^{-2}. A more complete analysis awaits a numerical solution that includes the influence of sectioning presently under development [9].

MATERIALS

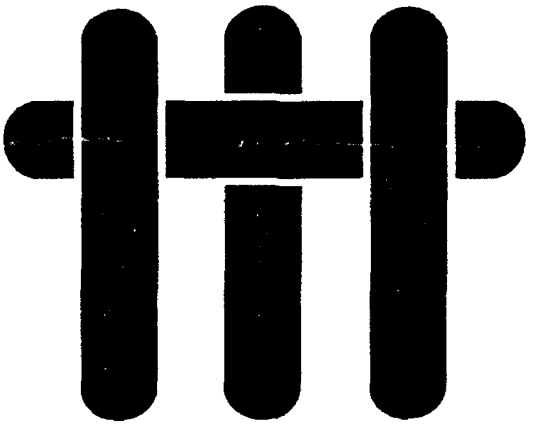

FIBER BUNDLE PUSH-OUT: A TECHNIQUE FOR THE MEASUREMENT OF INTERFACIAL SLIDING PROPERTIES

by

T.J. Mackin and F.W. Zok

Materials Department
College of Engineering
University of California
Santa Barbara, California 93106–5050

Submitted to Communications of the American Ceramic Society, June 1992
(Revised version 8/92)

7E:MS23(August 19, 1992)2:27 PM/mef

ABSTRACT

An experimental technique for the measurement of interfacial sliding properties in fiber-reinforced materials is presented. The technique involves pushing a *bundle* of fibers simultaneously through a thin section of the composite. Using this technique, sample averages are immediately available, eliminating the need for repeated single fiber tests. The technique is particularly useful for composites that contain small diameter fibers. Salient features of the technique are demonstrated through tests on a CAS/SiC composite.

1. INTRODUCTION

It has been well established that the mechanical performance of fiber-reinforced composites is strongly influenced by the debonding and sliding properties of the fiber/matrix interface (or coating).[1] Consequently, a number of experimental techniques have been developed to measure such properties, including the single fiber pull-out test,[2] the single fiber push-out test,[3-5] and the slice compression test.[6] The pull-out test provides the best simulation of the loading conditions that the interface experiences during matrix cracking, but requires meticulous sample preparation, alignment and fixturing. As a result, fiber push-out tests are more widely used and have essentially supplanted the pull-out technique.

The push-out technique most widely used involves nanoindentation.[3] This technique is limited to low loads (several grams) and is thus restricted to materials with small diameter fibers and relatively weak interfaces, and test specimens which are very thin. An alternative push-out technique was recently developed for use on materials with large diameter fibers and relatively strong interfaces.[7-11] The technique utilizes a cylindrical ceramic push-rod with a diameter slightly less than that of the fibers. The push-rod diameter is typically ~ 100 μm, and the fiber diameter ~ 140 μm. The technique is not, however, amenable to testing composites with small diameter fibers (~ 10 to 20 μm), since suitable indentors are not available. Furthermore, it would be exceedingly difficult to position such an indentor onto an individual fiber. The present article describes a modification to the existing technique which allows *bundles* of small diameter fibers to be pushed out of a thin composite section. The modified technique provides average values of the interface sliding stress over a relatively large number of fibers (~ 10 to 20) with each push-out test. The results obtained here are compared with values inferred from other micromechanical measurements.

2. EXPERIMENTAL METHODS

The fiber bundle push-out technique employs the apparatus shown in Fig. 1. The apparatus consists of a flat support base, a strain-gauged cantilever beam, and a cylindrical ceramic push-rod. A 220 μm diameter hole in the middle of the support base is fitted with a 200 μm diameter displacement piston. The piston measures fiber displacements by pushing on the end of the cantilever beam. The remainder of this paper describes the technique as explicitly applied to fiber bundle push-out: additional details of the apparatus can be found elsewhere.[7]

The material used in this study was a calcium aluminosilicate (CAS) glass ceramic reinforced with unidirectional Nicalon (SiC) fibers. The fiber diameter was ~ 15 μm and the fiber volume fraction ~ 33%. Thin sections, ~ 800 μm, were cut from the composite perpendicular to the fiber direction. The sections were then polished to a 1 μm diamond finish using an automated polishing machine. Approximately 75 μm of material was removed from each side of the specimens, essentially eliminating any damage introduced during cutting. After polishing, a small portion of the glass matrix was etched from one of the polished surfaces using a 49% HF acid solution. Matrix etching proceeded in a controlled manner by gently swabbing in 30-second intervals. Following each interval, the sample was rinsed in water and the etch depth measured using an optical microscope. The procedure was continued until ~ 10 to 15 μm of matrix was removed from the specimen, leaving protruding fibers with an aspect ratio (height to diameter) of one (Fig. 2).

A small amount of vacuum grease was applied to the chosen bundle of fibers using a tailor's pin, and a 300 μm tall cylindrical push-rod then placed on top of the bundle. The push-rods were machined from σ-SiC fibers (100 μm in diameter), provided by British Petroleum. The purpose of the vacuum grease was to hold the

push-rod in place during specimen alignment. Using an optical microscope, the specimen was placed onto the support base such that the push-rod was centered directly above the displacement piston. After alignment, the entire apparatus was placed into an Instron loading frame, equipped with an 890 N load cell with a precision of ± 0.01 N. An alumina hemisphere was then fitted into an adapter attached to the load cell. The hemisphere was used to align the load cell with the top plane of the specimen. Load was applied to the fibers by pushing the flat portion of the hemisphere against the top of the push-rod. The number of fibers pushed in a particular test was subsequently counted from either optical or SEM observations of the bottom side of the specimen.

3. MEASUREMENTS AND OBSERVATIONS

A typical load-displacement trace during fiber bundle push-out is shown in Fig. 3. The corresponding trend in the average interface shear stress, τ, with displacement is shown in Fig. 4. The average shear stress is taken to be

$$\tau = P/2\pi R(h-u)N \qquad (1)$$

where P is the applied load, R is the average fiber radius, h is the specimen thickness, u is the fiber displacement (taking into account the elastic displacement of the specimen), and N is the number of pushed fibers. In all cases, there was an initial elastic portion, followed by a small load drop (typically, ~ 10% of the peak value). The load drop is believed to occur when the fibers debond completely from the matrix. Once the fibers had debonded, further sliding occurred subject to a constant sliding stress: $\tau = 16 \pm 2$ MPa (see Table I for a summary of the results).

The values of the interface sliding stress obtained from the push-out tests have been compared with values inferred from other micromechanical measurements made on the same material[12] (Table II). The present results are in good agreement with values inferred from the matrix cracking stress and the fiber pull-out distribution following tensile fracture (τ = 10 to 15 MPa). This consistency provides confidence in the utility of both the fiber bundle push-out technique, as well as the micromechanical models that describe damage and fracture in this class of composite. The value of sliding stress obtained from the saturation crack spacing measurements (τ = 25 to 28 MPa) is somewhat higher; the source of the discrepancy is presently not understood.

SEM examination of the bottom and top sides of the tested specimens revealed several features. Notably, the bottom side "footprint" of a pushed-out bundle did not correspond exactly with the "footprint" of the push-rod, i.e., the shape of the bundles was not circular. Figure 5 shows an example of one such bundle. This effect is probably due to fiber misalignment through the thickness of the specimen. Examinations of the top sides of the specimens also revealed occasional fractured fibers around the perimeter of the pushed bundle, wherein only a portion of the fiber was loaded by the push-rod (Fig. 6). Typically, there were 1 to 2 fractured fibers in each pushed bundle. The relative uniformity of the fiber sliding distances measured on the bottom side of the specimens suggests that fiber fracture occurs early in the loading cycle (prior to the load drop) and thus does not influence the computed sliding stress.

4. CONCLUSIONS

The fiber bundle push-out test provides a simple means for measuring the interface sliding stress, provided the matrix can be preferentially etched, leaving the

fibers protruding uniformly above the matrix surface. The test is particularly useful for composites containing small diameter fibers which, heretofore, could only be tested using nanoindentation. Furthermore, the bundle tests provide instant *average* values for the sliding stress. Results of the bundle tests were shown to be in broad agreement with values inferred from other micromechanical measurements.

ACKNOWLEDGMENTS

This work was supported by the Defense Advanced Research Projects Agency through the University Research Initiative under Office of Naval Research contract No. N-00014-86-K-0753.

TABLE I

Summary of Measurements on the CAS/SiC Composite

Test Number	Number of fibers	Average sliding stress (MPa)
1	13	14
2	11	17
3	19	19
4	16	14
5	21	18

TABLE II

Comparison of Sliding Stresses Obtained from Various Micromechanical Measurements on CAS/SiC

Method	Interface Sliding Stress, τ (MPa)
Fiber bundle push-out test	14–19
Matrix cracking stress[8]	10–15
Fiber pull-out distribution following tensile fracture[8]	10–15
Saturation crack spacing[8]	25–28

REFERENCES

[1] A.G. Evans, F.W. Zok and J. Davis, "The Role of Interfaces in Fiber-Reinforced Brittle Matrix Composites," *Composite Sci. Tech.* **42** (1991), 3–24.

[2] D.B. Marshall, M.C. Shaw and W.L. Morris, "Measurement of Interfacial Sliding Resistance In Fiber Reinforced Intermetallics," *Acta Metall. Mater.*, **40** (1992), 443–54.

[3] D.B. Marshall, "An Indentation Method for Measuring Matrix-Fiber Frictional Stresses in Ceramic Composites," *J. Amer. Ceram. Soc.*, **67** (1984), 259-60.

[4] J.D. Bright, S. Danchaijivit, and D.K. Shetty, "Interfacial Sliding Friction in Silicon Carbide-Borosilicate Glass Composites: A Comparison of Pullout and Pushout Tests," *J. Am. Ceram. Soc.*, **74** (1991), 115–22.

[5] T.P. Weihs and W.D. Nix, "The Frictional Resistance to Sliding of a SiC Fiber in a Brittle Matrix," *J. Am. Ceram. Soc.*, **74** (1991), 524–34.

[6] E.P. Butler, E.R. Fuller, Jr., D.G. Brandon and R.A. Londen, "Multiple Measurements of Fiber-Matrix Interfacial Properties via the Slice Compression Test," presented at Annual Meeting, American Ceramic Society, Cincinnati, OH, April 1991.

[7] P.D. Warren, T.J. Mackin and A.G. Evans, "Design, Analysis and Application of an Improved Push-Through Test for the Measurement of Interface Properties in Composites," *Acta Metall. Mater.*, in press (1992).

[8] J.D. Bright, S. Danchaivijit and D.K. Shetty, "Interfacial Sliding Friction in Silicon Carbide-Borosilicate Glass Composites: A Comparison of Pullout and Pushout Tests," *J. Am. Ceram. Soc.*, **74** [1] 115-22, 1992.

[9] D.B. Marshall, "An Indentation Method for Measuring Matrix-Fiber Frictional Stresses in Ceramic Composites," *J. Am. Ceram. Soc.*, **67**, C, 259-260, 1984.

[10] P.D. Jero and R.J. Kerans, "The Contribution of Interfacial Roughness to Sliding Friction of Ceramic Fibers in a Glass Matrix," *Scripta Met. et. Mat.*, in press.

[11] W.C. Carter, E.P. Butler and E.R. Fuller, "Micro-Mechanical Aspects of Asperity-Controlled Friction in Fiber-Toughened Ceramic Composites, "*Scripta Met. et Mat.*, Vol. **25**, pp. 579-584, 1991.

[12] D.S. Beyerle, S.M. Spearing, F.W. Zok and A.G. Evans, "Damage and Failure in Unidirectional Ceramic Matrix Composites," *J. Am. Ceram. Soc.*, in press (1992).

FIGURE CAPTIONS

Fig. 1. Schematic representation of the apparatus used during fiber bundle push-out.

Fig. 2. Micrograph showing the protruding portion of the fibers following matrix dissolution.

Fig. 3. A typical load-displacement trace for a fiber bundle push-out test.

Fig. 4. Variation in the interface sliding stress with sliding distance. (The sliding distance is the difference between the total measured displacement and the elastic displacement, with the elastic component being calculated from the slope of the initial (elastic) portion of the loading curve.)

Fig. 5. SEM view of pushed out fibers.

Fig. 6. SEM view of the top side of a tested specimen showing fractured fibers (arrowed) at the periphery of the pushed bundle.

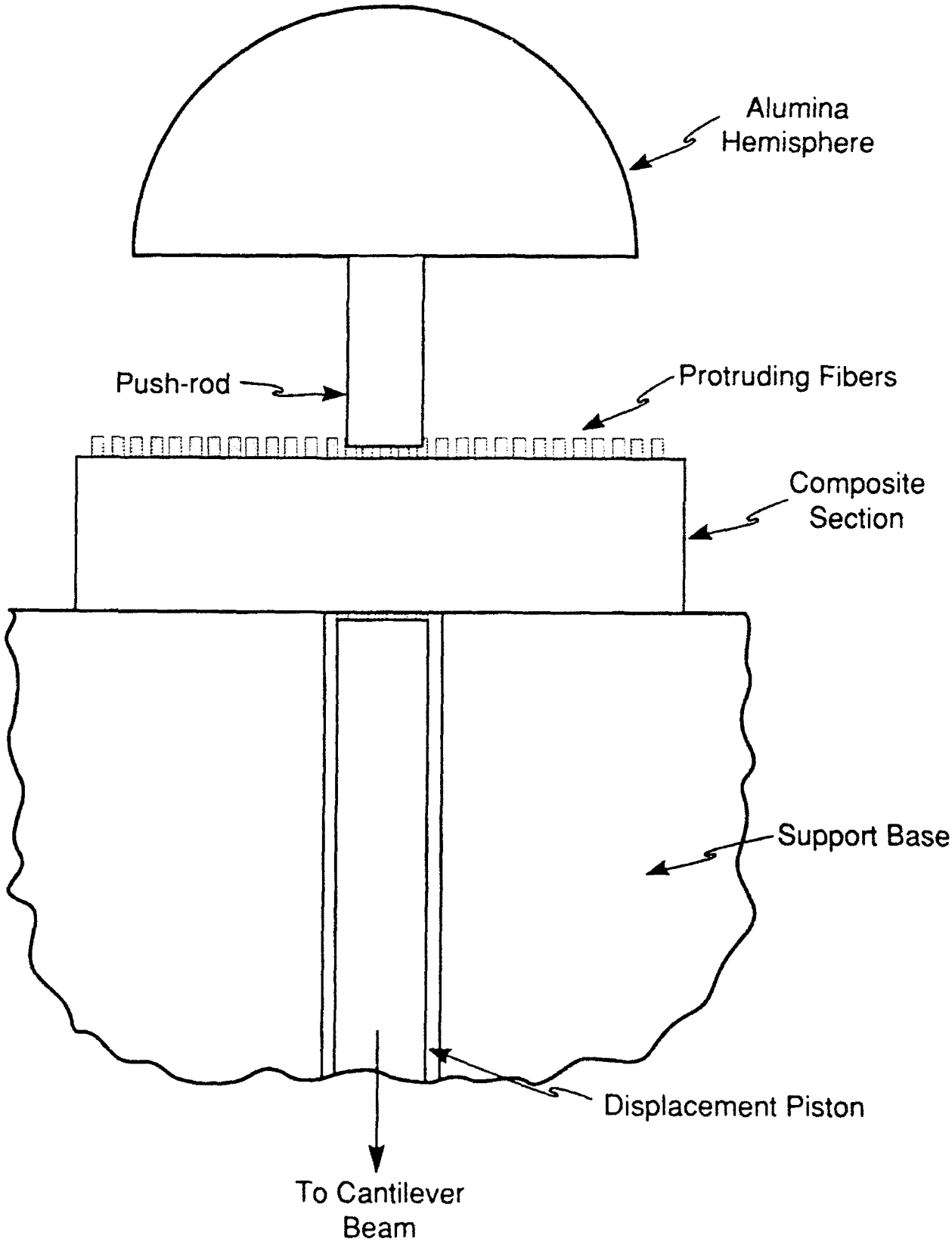

Zok.UR-5892-amx-094842-1

Fig. 1

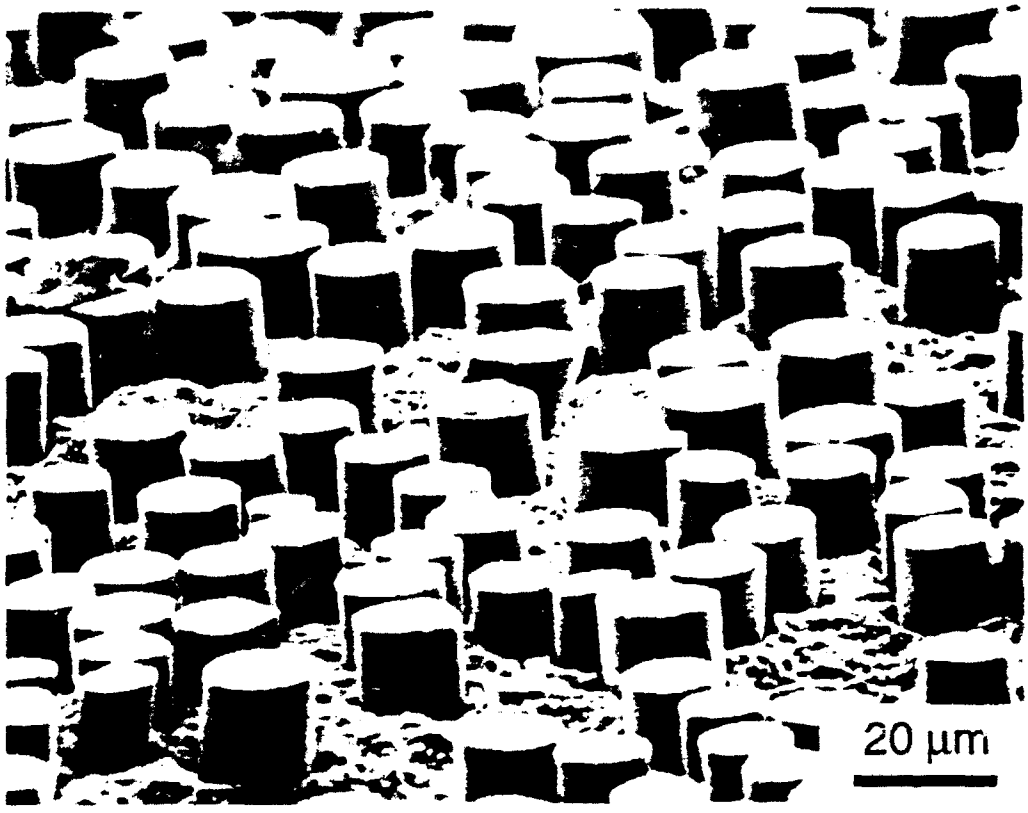

Fig. 2

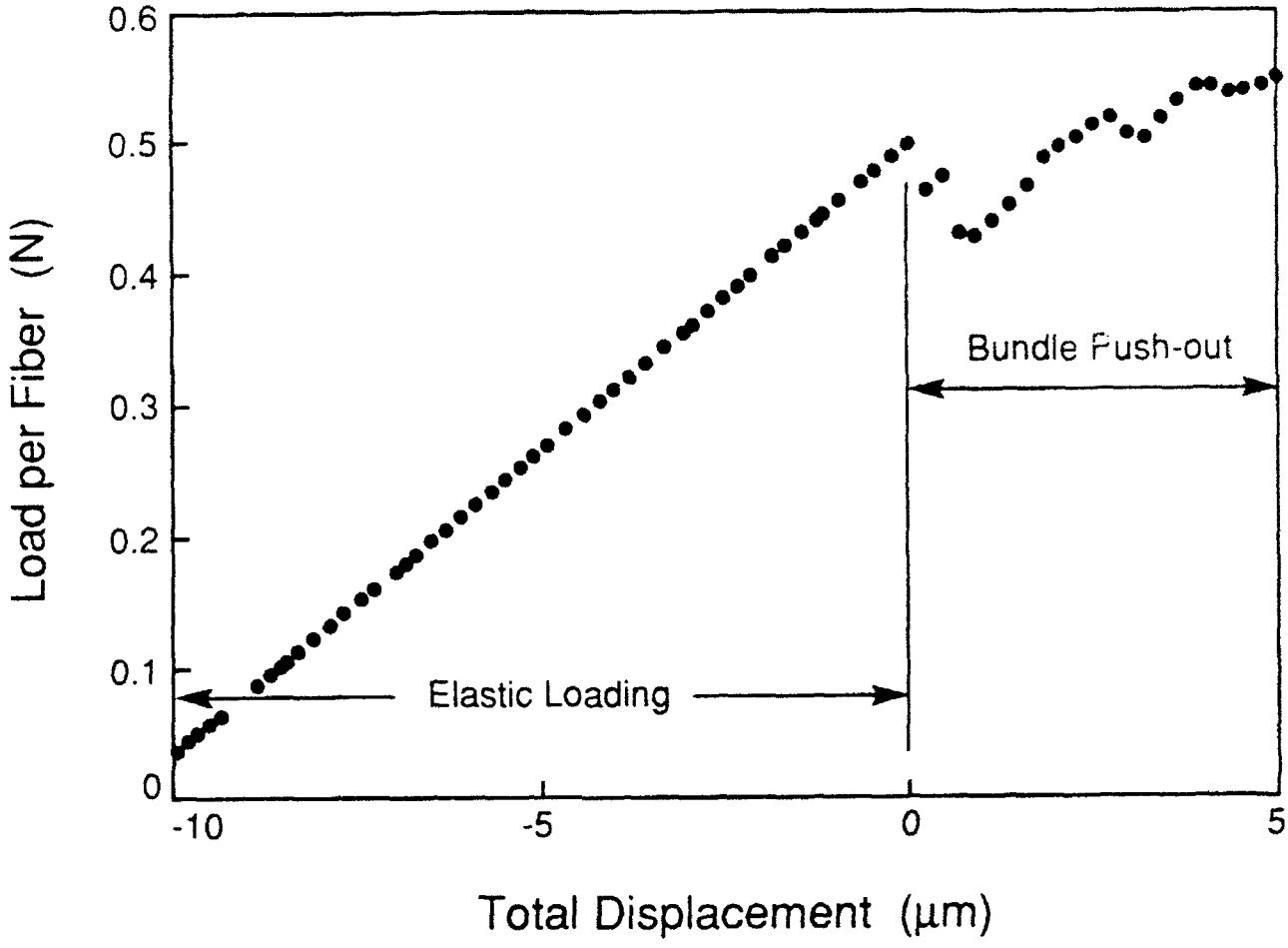
0.6
0.5
0.4
0.3
0.2
0.1
0
Load per Fiber (N)
Bundle Push-out
Elastic Loading
-10
-5
0
5
Total Displacement (μm)

Fig. 3

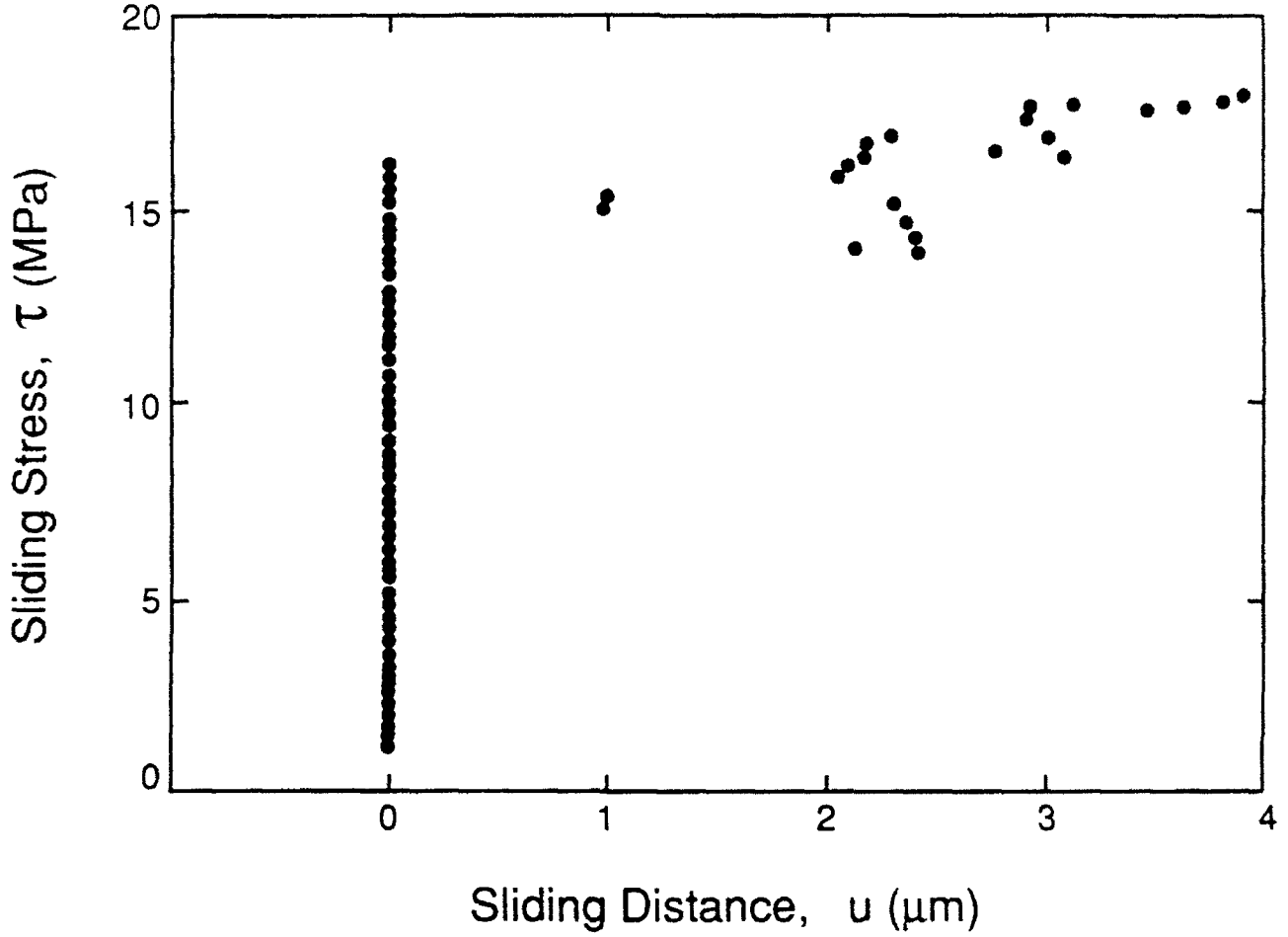

Fig. 4

Zok,Evans L R=6-92-amk-D88749-4

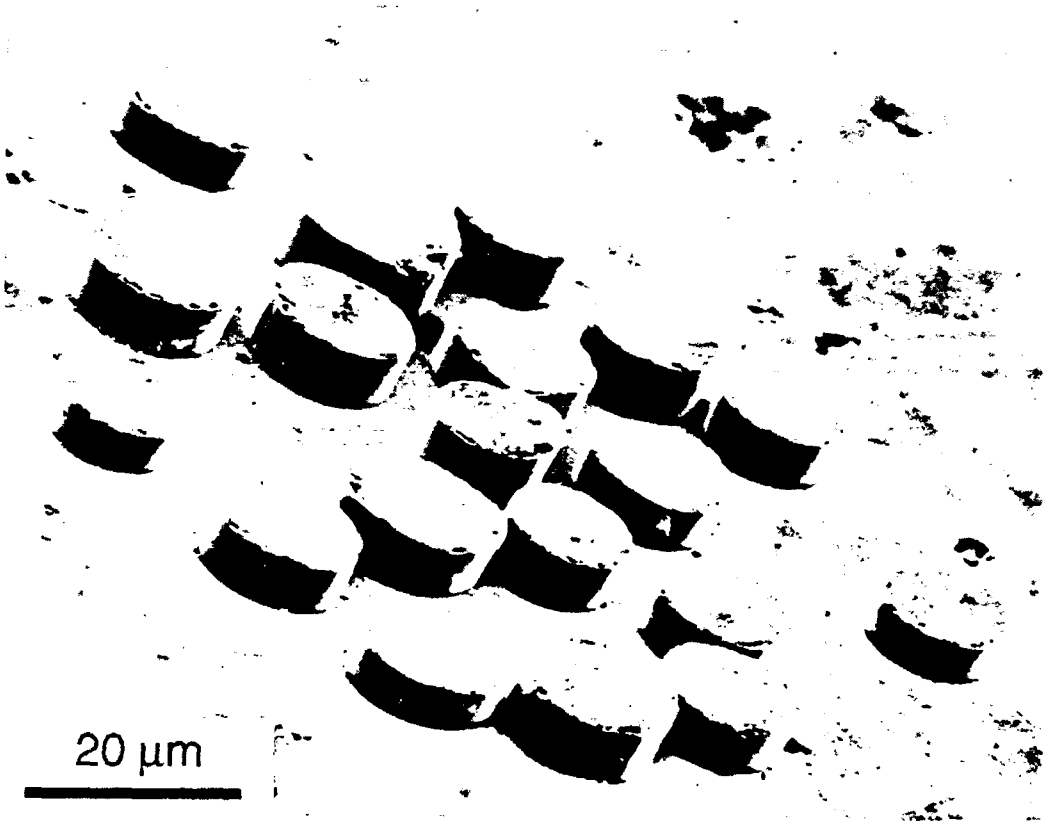

Fig. 5

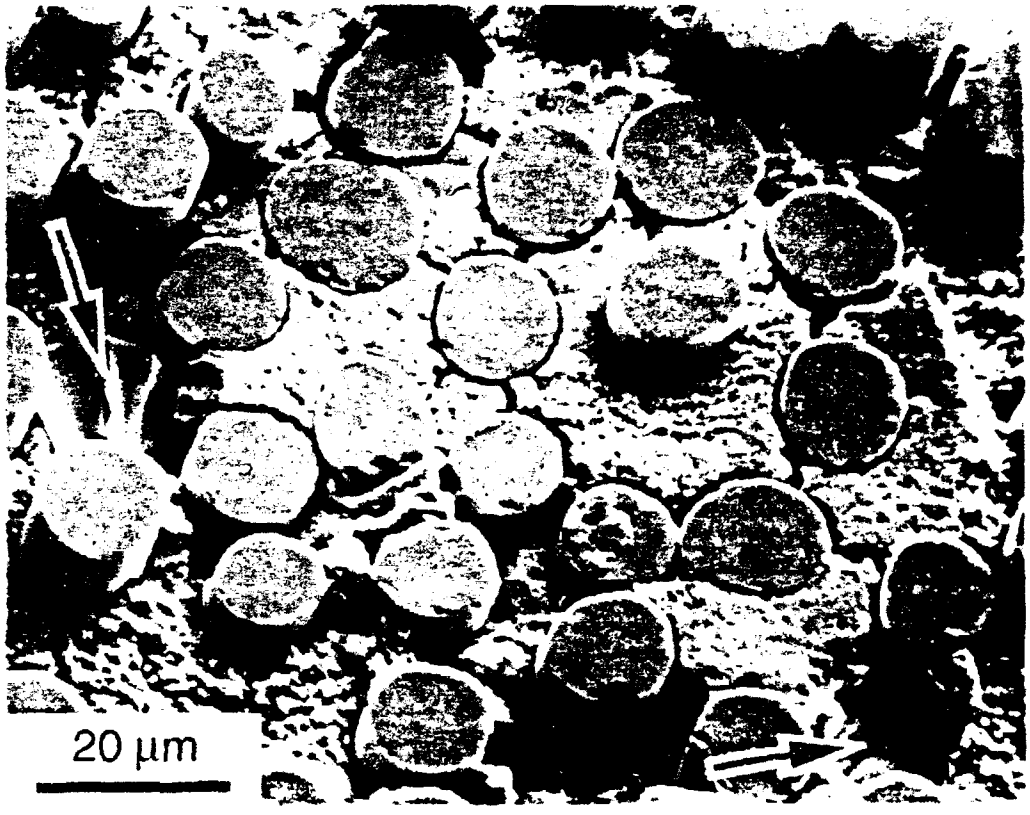

Fig. 6

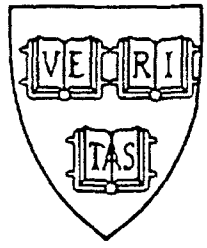

MECH-189

MECHANICS OF THE FIBER PUSHOUT TEST

C. Liang and J. W. Hutchinson

Division of Applied Sciences
HARVARD UNIVERSITY
Cambridge, Massachusetts 02138

February 1992

MECHANICS OF THE FIBER PUSHOUT TEST

C. Liang and J.W. Hutchinson
Division of Applied Sciences, Harvard University
Cambridge, MA 01238

Abstract

Model equations governing the debonding and the pushout phases of the fiber pushout test are presented and are then evaluated for accuracy by comparing them with detailed numerical analyses of some specific examples. It is assumed that a residual compressive stress acts across the fiber/matrix interface and residual axial stress in the fiber is taken into account. The interface is characterized by a mode 2 debond toughness Γ and is assumed to develop a frictional stress upon sliding according to $\tau=\tau_0-\mu\sigma_r$, corresponding to a constant stress contribution and a Coulomb term. The model applies either to pushout of a single fiber embedded in a homogeneous matrix or to a fiber selected for pushout from a specimen sliced from a fiber reinforced composite. The effect of redistribution of residual stress due to slicing the composite in preparation of the specimen is addressed in the numerical examples. The detailed numerical work establishes that the debond crack advancing down the fiber becomes unstable and breaks through to the bottom of the specimen when the debond tip reaches a distance about one and one half fiber radii from the bottom. The model equations provide a reasonably accurate description of the dependence of the pushout test on its many parameters.

Notation

R_f	fiber radius
R_0	specimen radius
R_b	inner radius of support base
ρ	fiber area fraction for a specimen cut from a composite
ℓ	length of mode 2 debond crack
t	specimen thickness
E_f, E	Young's moduli of fiber and outer region
E_I	Modulus quantity for interface crack (Eq. 2.10)
ν_f, ν	Poisson's ratios of fiber and outer region
n_R	residual compressive stress acting across fiber / matrix interface
p	compressive pushout stress applied to fiber end
p_i	pushout stress to initiate debonding
p_R	residual compressive axial stress in fibers
G	energy release rate of debond crack
$\Gamma \equiv G_c$	mode 2 debond toughness of interface
K	mode 2 stress intensity factor for debond crack
$K_c \equiv \sqrt{E_I \Gamma}$	mode 2 debonding intensity toughness of interface
U	load point displacement conjugate to p
u	displacement of fiber end relative to specimen surface

1. Introduction

Fiber pushout tests are now commonly carried out with the purpose of measuring the fiber/matrix interface debonding and frictional sliding characteristics for a wide variety of fiber reinforced composite systems (see Kearns and Parthasarathy (1991) and Marshall (1992) for a listing of references). To infer these interface characteristics it is necessary to make certain assumptions about the nature of the laws governing debonding and friction and to then carry out a mechanics analysis of the specimen subject to these assumptions. In this way, theoretical predictions for the specimen can be fit to measured records of pushout load versus displacement using the desired interface properties as fitting parameters. The number of geometric parameters characterizing the specimen and material parameters characterizing the composite is quite large (see the Notation list), and it is essential that the mechanics solution for the specimen be in closed form, rather than numerically generated for each set of parameters, if it is to be broadly useful. At the same time, it is essential that the analytical solution, which is of necessity of an approximate

nature, be assessed for its accuracy. The approach taken in this paper is to present a closed form analytical solution in Section 2, which contains all the parametric dependencies and which is valid for a reasonably general friction law, and then in Sections 3 and 4 provide a full finite element analysis of the specimen for some specific cases to assess the accuracy of the analytical model results. The analytical model results coincide in almost all respects to solutions presented recently by Kearns and Parthasarathy (1991) and Marshall (1992) for the special case of Coulomb friction acting on the fiber/matrix interface.

The slicing process used to produce specimens from a composite is illustrated in Fig. 1, and the geometry of the specimens also detailed in this figure. It is assumed that there are residual compressive stresses p_R and n_R in the axial and radial directions, respectively, in the fibers in the composite **prior to slicing**. The slicing process redistributes these residual stresses in the vicinity of the fiber ends, and one of our objectives will be to assess the effect of this redistribution on the pushout test with the aid of the numerical calculations. In many specimens, the thickness t is chosen to be not more than, typically, 6 to 12 times the fiber radius R_f so that unduly large pushout forces can be avoided. For such 'thin' specimens it is essential that the inner support radius of the base, R_b, be small enough such that significant effects due to bending do not arise (Kallas, et al, 1991). If R_b is taken to be less than, say, $2R_f$, then bending effects are negligible and, moreover, R_b itself will have little influence on the pushout results. Similarly, the outer radius of the specimen R_0 plays essentially no role as long as it is more than several times t. The numerical results reported below also indicate that the details of the support conditions at the base (e.g. zero friction versus clamped) have relatively little influence, and clamped conditions will be used in most of the numerical calculations. Assumptions about the details of the fiber/matrix interface will be detailed below. The interface is assumed to be characterized by a mode 2 debond toughness (work of fracture) Γ or, equivalently, by a critical mode 2 interface intensity toughness K_c. A generalized friction law which combines the Coloumb law with a constant friction stress is used to describe the tractions exerted across the debonded interface behind the advancing mode 2 debond crack tip.

2. Approximate model governing pushout

The results in this section are derived from the paper by Hutchinson and Jensen (1990) wherein models for fiber pullout have been developed. The formulas below are converted to be applicable to the present pushout specimen with due regard for certain sign changes. Moreover, the separate results in that paper for cases of constant friction and Coulomb friction have been combined here according to the law

$$\tau = \tau_0 - \mu\sigma_r \tag{2.1}$$

where τ_0 is the constant friction contribution, μ is the Coulomb friction coefficient, and $-\sigma_r$ is the compressive stress acting across the sliding fiber/matrix interface. This relation has been suggested by Mackin, Warren and Evans (1992) as a phenomenological characterization which incorporates both a Coulomb component and a component independent of the compression across the interface which is thought to arise from significant asperity interaction of the kind documented in their paper and in earlier work by Jero and Kerans (1990).

2.1 Some basic equations

In specializing the results from Hutchinson and Jensen (hereafter referenced as H-J), it will be assumed that $(R_f/R_0)^2 << 1$ so that, in effect, the specimen in Fig. 1.1 has an infinite outer radius R_0, leading to a simplification of some formulas in the earlier reference. In addition, two cases will be considered: Case (i), an isotropic fiber surrounded by an isotropic outer region, and Case (ii), a transversely isotropic fiber surrounded by a transversely isotropic outer region, where the outer region can be assigned the effective elastic properties of the composite from which the specimen is sliced. The model of H-J, like that of Gao, Mai and Cotterell (1988), uses the Lame′ solution to characterize the radial dependence of the stress distribution in the fiber and the matrix at each position z through the specimen. The approach is not accurate when the mode 2 debond crack tip is within about one fiber radius from the top or bottom faces of the specimen, as will be clear in the next section where comparisons with accurate numerical solutions will be made. However, the approach is quite accurate when the crack tip is in the interior of the specimen, and it can be used to analyze the most important aspects of pushout behavior.

There are two combinations of the elastic properties, B_1 and B_2, which reappear throughout the paper. These arise in the following relations from the Lame′ solution (cf. H-J, Eq.(22))

$$(\sigma_r^- - \sigma_r^+) = B_1(\sigma_f^- - \sigma_f^+) \tag{2.1}$$

and

$$(\varepsilon_f^- - \varepsilon_f^+) = B_2(\sigma_f^- - \sigma_f^+)/E_f \tag{2.2}$$

where σ_f and ε_f are the average axial stress and strain in the fiber, σ_r is the radial stress acting across the interface, and the '+' denotes values well below the debond crack tip while the '-' labels values above the tip. These relations follow from the supposition that the changes in stress distribution from one section along the fiber to another are characterized by the Lame′ solution,

together with imposition of continuity of normal displacement and normal traction across the interface as discussed more fully in H-J. The formulas for B_1 and B_2 for the two cases are given as follows.

Case (i): Isotropic fiber and isotropic outer region.

Let E_f and ν_f denote the Young's modulus and Poisson's ratio of the fiber and let E and ν denote the corresponding quantities for the outer region. Then,

$$B_1 = \frac{\nu_f E}{(1-\nu_f)E + (1+\nu)E_f} \tag{2.3}$$

and

$$B_2 = 1 - 2\nu_f B_1 = \frac{(1+\nu_f)(1-2\nu_f)E + (1+\nu)E_f}{(1-\nu_f)E + (1+\nu)E_f} \tag{2.4}$$

(In this paper B_1 is the new notation for b_1 in H-J, while B_2 replaces b_2E_f/E, in each case for the limit with R_f/R_0 approaching zero. See the end of the Appendix for errata for the H&J paper.)

Case (ii): Transversely isotropic fiber and transversely isotropic outer region.

Let the 1-direction be aligned with the fiber axis. The relevant components of stress and strain for an elastic material with transverse isotropy with respect to the 1-axis are related by

$$\varepsilon_1 = \frac{1}{E}\sigma_1 - \frac{\nu}{E}(\sigma_2 + \sigma_3) \tag{2.5a}$$

$$\varepsilon_2 = -\frac{\nu}{E}\sigma_1 + \frac{1}{E^r}\sigma_2 - \frac{\nu^r}{E^r}\sigma_3 \tag{2.5b}$$

$$\varepsilon_3 = -\frac{\nu}{E}\sigma_1 - \frac{\nu^r}{E^r}\sigma_2 + \frac{1}{E^r}\sigma_3 \tag{2.5c}$$

With a subscript f denoting quantities associated with the fiber and unsubscripted quantities for the outer region, the expressions for B_1 and B_2 generalize to

$$B_1 = \frac{\nu_f E^r}{(1-\nu_f^r)(E_1/E_f^r)E^r + (1+\nu^r)E_f} \tag{2.6}$$

$$B_2 = 1 - 2\nu_f B_1 \tag{2.7}$$

Of the two coefficients, B_2 is generally about unity, while B_1 brings in the 'Poisson effect' and is a much stronger function of the elastic properties than B_2. For example for Case (i) with $\nu_f = \nu = 1/3$, $B_1=0.167$ and $B_2=0.889$ when $E_f/E=1$, and $B_1=0.0714$ and $B_2=0.952$ when $E_f/E=3$. To see how Case (ii) differs from Case (i), consider an isotropic fiber surrounded by a composite comprising the same fibers with area fraction $\rho=0.3$. Suppose the matrix of the composite is isotropic such that $\nu_m=\nu_f=1/3$ and $E_f/E_m=3$. A self-consistent theory determination of the

transversely isotropic elastic properties of the composite needed to evaluate B_1 and B_2 in (2.6) and (2.7) gives $E_f/E^r=2.215$ and $\nu^r=0.351$ leading to $B_1=0.0911$ and $B_2=0.939$. These values can be compared with the second set of values quoted above for Case (i), and it is seen that B_1 is the more sensitive of the two coefficients to the way in which the outer region is represented.

The central equations of the model are (2.1) and (2.2) along with the equation for axial equilibrium of the fiber and the equation for the energy release rate of the debond crack. The axial equilibrium equation for the fiber is

$$\frac{d\sigma_f}{dz} = -\frac{2\tau}{R_f} \tag{2.8}$$

where z is the axial coordinate parallel to the fiber pointing upward, and the energy release rate at the mode 2 crack tip is

$$G = \frac{1}{4}(B_2 R_f / E_f)(\sigma_f^- - \sigma_f^+)^2 \tag{2.9}$$

This equation for G is an exact steady-state result for a free-sliding fiber ($\tau = 0$) in the interior of an infinitely thick, homogeneous isotropic matrix. For a general elastic mismatch between the fiber and the matrix in Case (i), the relation between the mode 2 interface stress intensity factor K and the energy release rate is

$$G = \frac{1}{2}\left(1-\beta^2\right)\left(\frac{1-\nu_f^2}{E_f}+\frac{1-\nu^2}{E}\right)K^2 \equiv \frac{1}{E_1}K^2 \tag{2.10}$$

where β is the second plane strain Dundurs parameter and E_1 is an interface cracking modulus conveniently representing the collection of moduli quantities shown. (See, for example, Hutchinson and Suo (1991) for a background to the above equation and for the expression for β. For most systems of interest in the present context, β^2 is seldom larger than a few percent.)

2.2 Debonding phase

Let Γ denote the mode 2 toughness of the fiber/matrix interface, and let p_R be the compressive axial stress in the fiber prior to any debonding. (Expressions for p_R and n_R in terms of the thermal mismatch strains and the elastic properties of the composite are given by H-J.) Then imposition of the debonding criterion, $G = \Gamma$, with $\sigma_f^+ = -p_R$ and $\sigma_f^- = -p_i$ gives the compressive pushout stress in the fiber needed to start the debond moving down the interface before any appreciable frictional resistance develops,

$$p_i = p_R + 2\sqrt{\frac{\Gamma E_f}{B_2 R_f}} \tag{2.11}$$

In writing this equation it has been assumed that an initial debond region of length on the order of

R_f pre-exists, otherwise a larger initiation pushout stress p_i would be required, as will be made clearer in Section 4.

Once debonding has started, the debond length ℓ increases with pushout stress p according to

$$\frac{\ell}{R_f} = \frac{1}{2\mu B_1} \ln\left[\frac{\tau_0 + \mu n_R + \mu B_1 (p - p_R)}{\tau_0 + \mu n_R + \mu B_1 (p_i - p_R)}\right] \tag{2.12}$$

where n_R is the compressive stress acting across the interface prior to any debonding. Alternative, equivalent expressions to (2.12) are

$$p = p_R + 2\sqrt{\frac{\Gamma E_f}{B_2 R_f}} e^{\zeta} + \frac{\tau_0 + \mu n_R}{\mu B_1}\left[e^{\zeta} - 1\right] = p_i + \left\{2\sqrt{\frac{\Gamma E_f}{B_2 R_f}} + \frac{\tau_0 + \mu n_R}{\mu B_1}\right\}\left[e^{\zeta} - 1\right] \tag{2.13}$$

where $\zeta = 2\mu B_1 \ell / R_f$. The limit to (2.12) and (2.13) for $\tau_0 = 0$ corresponding to Coulomb friction coincides with the results given by Kearns and Parthasarathy (1991) and Marshall (1992) for Case (i), although the form is somewhat different. In particular, the role of the residual axial compression in the fiber p_R is transparent in the first of the formulas in (2.13)--it simply adds to the pushout stress. The second expression in (2.13) emphasizes how the debond toughness and the friction combine to give the increment of pushout stress required over and above initiation. The limit for constant friction ($\mu = 0$) is the elementary result $\ell / R_f = (p - p_i)/(2\tau_0)$. Note that the above results hold for Case (ii) as well when (2.6) and (2.7) are used for B_1 and B_2.

Kearns and Parthasarathy and also Marshall introduce a reference tensile stress quantity, σ_f^0, which is the stress in the debonded portion of the fiber required to reduce the radial component of the interface traction, σ_r, to zero. By (2.1), this quantity is related to the residual stress quantities by $n_R = B_1(\sigma_f^0 + p_R)$. If n_R is eliminated from (2.13) in favor of σ_f^0, then for the Coulomb friction limit one obtains the form which these authors give, i.e.

$$p = -\sigma_f^0 + \left\{2\sqrt{\frac{\Gamma E_f}{B_2 R_f}} + p_R + \sigma_f^0\right\} e^{\zeta} \tag{2.13a}$$

The sliding displacement of the top of the fiber relative to the matrix (see Fig. 1) is given by

$$\frac{u}{R_f} = B_2\left[\frac{p - p_i}{2\mu B_1 E_f} - \frac{(\tau_0 + \mu n_R)}{\mu B_1 E_f}\frac{\ell}{R_f}\right] \tag{2.14}$$

where $p - p_i$ may be expressed in terms of ℓ / R_f using (2.11) and (2.13). Within the frame work of the model, the displacement U through which p works can be approximated by u plus a contribution due to the deformation of the specimen under p in the absence of debonding. Thus,

$$\frac{U}{R_f} = \frac{u}{R_f} + C\frac{p}{E_f} \tag{2.15}$$

The constant C has been evaluated using the numerical procedures of the next section. For Case (i) with $\nu_f = \nu_m = 1/3$ and E_f/E in the range 1 to 5, C is well approximated by $1.46(E_f/E)^{1/2}$. The limit of (2.14) for constant friction (μ=0) is

$$\frac{u}{R_f} = \frac{2B_2\ell}{R_f}\sqrt{\frac{\Gamma}{B_2R_fE_f}} + \frac{B_2\tau_0}{E_f}\left(\frac{\ell}{R_f}\right)^2 \tag{2.16}$$

In the next section, where a full numerical analysis of the specimen under constant friction conditions will be given, it will be seen that the debond crack advances stably until the crack tip reaches a distance of about $1.5R_f$ from the bottom of the specimen where it becomes unstable and breaks through to the bottom surface by dynamic advance. Let p^* and U^* denote the load and displacement associated with the point where the debond crack loses stability. A good approximation to these instability values can be obtained from the above equations by taking ℓ to be $t-1.5R_f$, i.e.

$$p^* = p_R + 2\sqrt{\frac{\Gamma E_f}{B_2R_f}}e^{\zeta^*} + \frac{\tau_0+\mu n_R}{\mu B_1}\left[e^{\zeta^*}-1\right] \tag{2.17}$$

$$\frac{U^*}{R_f} = C\frac{p^*}{E_f} + B_2\left[\frac{p^*-p_i}{2\mu B_1E_f} - \frac{(\tau_0+\mu n_R)}{\mu B_1E_f}\frac{t}{R_f}\right] \tag{2.18}$$

Here $\zeta^*=2\mu B_1(t-1.5R_f)/R_f$. These two equations contain the many parameters in the pushout problem. Moreover, the three contributions to the pushout stress at break-through are clearly exposed in (2.17), respectively due to residual stress, debonding toughness and friction.

2.3 Pushout phase

After the debond tip has broken through to the bottom of the specimen the pushout force is opposed only by friction. However, the axial stress in the fiber at the bottom is now relieved with a redistribution of the compressive stress acting across the fiber/matrix interface. At the bottom after break-through, this compressive stress becomes n_R-B_1p_R; which is assumed to be positive in what follows. With d as the remaining length of the fiber in the matrix (d=t-u), the pushout stress is

$$p = \left[\frac{\tau_0+\mu(n_R-B_1p_R)}{\mu B_1}\right]\left(e^{\zeta_d}-1\right) \tag{2.19}$$

where $\zeta_d=2B_1\mu d/R_f$. In the limit $\mu\to 0$, this reduces to the elementary result $p=2\tau_0 d/R_f$ implying a

linear drop-off of pushout load with displacement. The limit of Coloumb friction ($\tau_0 = 0$) gives a nonlinear relation between the pushout force and displacement, i.e.

$$p = \frac{n_R - B_1 p_R}{B_1}\left(e^{\zeta d} - 1\right) \tag{2.20}$$

with the force dropping more rapidly in the beginning (d≅t) than at the end (d≅0). With (n_R-B_1p_R) identified as the redistributed compressive stress normal to the fiber/matrix interface at the bottom of the specimen, this formula agrees with that of Shetty (1988), who adapted the earlier pullout results of Takaku and Arridge (1973). It also agrees with equivalent formulas of Kearns and Parthasarathy (1991) and Marshall (1992), noting that the coefficient in (2.20) is just σ_f^0. Recent detailed elasticity calculations of Meda, Hoysan and Steif (1992) have demonstrated the accuracy of this formula.

The drop in the pushout stress Δp which occurs when the debond breaks through to the bottom of the specimen is given by (2.17) minus (2.19) with d≅t.

3. Numerical analysis of the specimen with constant friction τ_0 (Case (i))

Attention will be restricted to pushout histories which are monotonic in the sense that the average downward displacement of the end of the fiber U is increased monotonically. The debond crack length also increases monotonically under these circumstances. An important consequence of this monotonicity for the purpose of analyzing and presenting results for the specimen is that, for a given debond crack length, the quantities K, U and u are linear functions of p, τ_0 and p_R. (The residual compression across the fiber/matrix interface n_R plays no direct role in the constant friction solution.) Specifically, this means it is possible to write

$$K / \sqrt{R_f} = pf_1(\xi) - p_R f_2(\xi) - \tau_0 f_3(\xi) \tag{3.1}$$

$$UE_f / R_f = pg_1(\xi) - p_R g_2(\xi) - \tau_0 g_3(\xi) \tag{3.2}$$

$$uE_f / R_f = ph_1(\xi) - p_R h_2(\xi) - \tau_0 h_3(\xi) \tag{3.3}$$

The nine quantities f_i, g_i and h_i are functions of the normalized interface crack length, $\xi = \ell / R_f$, as well as the other dimensionless geometric and material property parameters: t/R_f, E_f/E, ν_f and ν. In addition, as discussed in the Introduction, these functions also depend very weakly on R_0/R_f, R_b/R_f and on the precise manner in which the specimen is supported on its base. The functions of ξ are plotted in Figs 2-4 for selected values of the nondimensional parameters. The fiber and outer region are each isotropic (Case (i)) $\nu_f = \nu = 1/3$, and $E_f/E = 1$ or 3. To provide a relatively severe test for the model equations, a thin specimen has been chosen with $t/R_f = 6$ but results for a thicker specimen with $t/R_f = 12$ have also been obtained and will be discussed. The results are calculated

with completely clamped conditions along the base of the specimen and with $R_0/R_f=5$ and $R_b/R_f=1.5$. Each of the three contributions will be discussed in turn, and the effects of varying certain of the parameters will also be discussed. Some of the details of the finite element procedures used to solve for these functions are discussed in the Appendix. Each contribution is analyzed as a mode 2 crack problem with crack faces which slide relative to one another but whose normal opening displacement is zero. Thus, when the individual contributions are summed, the net result applies to a mode 2 problem.

The corresponding results from the model will be compared with the full numerical calculations. The model results can be obtained in a straight forward way from the basic equations of Section 2.1. They are

$$K/\sqrt{R_f} = \sqrt{\frac{B_2 E_I}{E_f}}\left[\frac{1}{2}(p-p_R) - \tau_0\frac{\ell}{R_f}\right] \tag{3.4}$$

$$uE_f/R_f = B_2\left[(p-p_R)\frac{\ell}{R_f} - \tau_0\left(\frac{\ell}{R_f}\right)^2\right] \tag{3.5}$$

with $U=u+CpR_f/E_f$.

3.1 Contribution due to pushout stress p

The contributions to K, U and u from the pushout stress p as calculated using the finite element program are shown in Figs 2. As just discussed, the crack is modelled as a mode 2 crack in these calculations with closed, frictionless crack faces, as is consistent with the representation in in (3.1)-(3.3). Included in each of these figures are the predictions from the simple model, (3.4) and (3.5). The contribution of p to K in Fig. 2a increases sharply with crack length, reaching the 'steady-state' plateau at $\xi\cong 1$. This plateau regime persists until the crack approaches a distance of about one and one half fiber radius from the bottom of the specimen, at which point the nondimensional stress intensity factor increases dramatically as the crack breaks through to the bottom of the specimen. These features are even clearer in Fig. 5 which compares results for two specimen thicknesses, $t=6R_f$ and $t=12R_f$. The contribution to K for the shortest cracks and for cracks within the broad mid-region of the specimen are independent of specimen thickness. Similarly, for crack tips within about $1.5R_f$ from the bottom, the contribution to K from p is otherwise independent of specimen thickness. The result from the model obtained from (3.4) clearly applies to the plateau regime.

The contributions to U and u due to p are shown in Figs. 2b and 2c where the model predictions are also included. The constant C appearing in the model equations has been obtained

from the numerical results of this section. As the crack length increases, the relative difference between U and u diminishes. The agreement with the model equations improves for thicker specimens as discussed below.

3.2 Contribution due to axial residual compression p_R in the fiber, including the effect of stress redistribution due to specimen preparation

There is a significant redistribution of residual stress near the fiber ends when the specimen is sliced from the composite. Or, if a single fiber specimen is prepared with a homogeneous outer matrix without slicing such that residual stresses develop in the fiber, then the stresses near the fiber ends will also be different from what they are in the interior. Here attention will be focussed on specimens sliced from a composite with fiber area fraction ρ. As discussed the Introduction, p_R is the residual axial stress in the fibers of the composite *prior to slicing* , and the functions f_2, g_2, and h_2 in (3.1)-(3.3) reflect the redistribution resulting from the slicing process. Finite element results for the contributions due to p_R to normalized K, U and u are shown in Figs. 3. The insert in Fig. 3a shows the tractions applied to determine the contribution due p_R. The residual stress distribution in the unsliced composite 'cell' is modeled as having a compressive stress p_R in the fiber and a tensile stress $\rho p_R/(1-\rho)$ which acts over an area weighted to correspond to the the appropriate area fraction of the matrix relative to the fiber such that the total force on each of the potential top and bottom faces is zero. The slicing process then is equivalent to applying equal and opposite tractions to remove these stresses, as indicated in the insert. Plots of the *changes* in the normal and shear stresses acting on the fiber/matrix interface as calculated by this procedure are shown in Fig. 6 for the set of parameters indicated in the figure caption. The changes constitute a significant fraction of p_R but they are confined to a region a few fiber radii from the ends of the fiber.

The simplest way to compute K, U and u due to p_R is by applying the tractions shown in the insert of Fig. 3a to the specimen for each length of mode 2 crack. This is equivalent to cancelling the shear tractions acting across the interface due to introduction of the mode 2 crack. In presenting the contribution to U, $g_2(\xi)$, the very small displacement associated with $\xi=0$ is subtracted off such that $g_2(0)=0$.

Included in Figs. 3 are the predictions from the model from (3.5) which are seen to provide a reasonable approximation in the mid-region of the specimen. The redistribution due to slicing gives rise to a peak contribution to K due to p_R which exceeds the mid-region levels and which occurs at a crack length of just over one half a fiber radius. Since the contribution due to p_R is a negative (see eq.(3.1)), the effect of the redistribution is to require a larger pushout stress to start

the debond crack moving down from the top surface of the specimen than would otherwise be predicted. The contribution to K falls to zero as the crack approaches the bottom surface of the specimen since the axial residual stress is then largely relieved.

3.3 Contribution due to the constant friction stress τ_0

The contributions in (3.1)-(3.3) due to τ_0 are shown in Fig. 4, where the predictions from the model are also included. The model results for K in Fig. 4a underestimate somewhat the actual contribution, but the slope of the the relation in the interior portion of the specimen is captured by the model. This same tendency was observed in the comparative study of pullout in Fig. 7 of H-J, where it is also seen that the accuracy of the model improves as the debond length grows (assuming it is still well away from break-through). Thus, the discrepancies between the detailed numerical results and the model seen in Fig. 4 diminish significantly in the interior of the specimen for specimens thicker than the one considered in this example, as will now be discussed.

3.4 Dependence on other parameters and support conditions

The numerical results for the choice $t/R_f = 6$ shown above provide a fairly severe test for the model equations since end effects extend into the specimen a distance of between one to two fiber radii, typically, from the free surfaces. The model equations do not incorporate end effects, yet nevertheless the model captures the quantitative trends when the debond is in the interior of the specimen. Fig. 5 illustrates the applicability of the model equations to the portion of the specimen away from the ends. Generally speaking, the model predictions for K are the more accurate than those for U, which in turn are more accurate than those for u. The calculations for $t/R_f=12$ show a systematic improvement in accuracy of the model equations for all three quantities over those for $t/R_f=6$. For example with $E_f=E$, the error in the model predictions at $\ell=t/2$ drops from 3.6 to 1.8% for K, from 9.0 to 6.7% for U, and from 27 to 17% for u. For $E_f/E=3$, the error improvements for a specimen with $t/R_f=12$ rather than 6 are 14.7 to 4.0% for K, 22 to 13% for U, and 55 to 26% for u.

Some of the calculations displayed above were repeated using free sliding boundary conditions (rather than completely clamped) along the bottom surface of the specimen. This alteration had virtually no effect on the numerical results for the functions in Figs. 2-4. Similarly, reducing R_0/R_f from 5 to 3 had virtually no effect.

4. Fracture analysis of the specimen with constant friction (Case (i))

The equations (3.1) and (3.2) of the previous section will now be used to generate pushout load-displacement relations during the debonding phase and, consequently, to identify the point where the debond crack becomes unstable and dynamically breaks through to the bottom of the specimen. Impose the condition $K=K_c\equiv(E_I\Gamma)^{1/2}$ on equation (3.1) to obtain the following relation between p and the normalized debond length ξ :

$$\frac{p}{\sqrt{E_I\Gamma/R_f}}=\frac{1}{f_1(\xi)}\left[1+\frac{p_R}{\sqrt{E_I\Gamma/R_f}}f_2(\xi)+\frac{\tau_0}{\sqrt{E_I\Gamma/R_f}}f_3(\xi)\right] \tag{4.1}$$

Equation (3.2) with (4.1) supplies U as a function of ξ according to

$$\frac{UE_f}{\sqrt{E_I\Gamma R_f}}=\frac{p}{\sqrt{E_I\Gamma/R_f}}g_1(\xi)-\frac{p_R}{\sqrt{E_I\Gamma/R_f}}g_2(\xi)-\frac{\tau_0}{\sqrt{E_I\Gamma/R_f}}g_3(\xi) \tag{4.2}$$

Examples are shown in Fig. 7 where the f's and g's are those plotted in Figs. 2-4 for the case with $E_f=E$, $\nu_f=\nu=1/3$, and $t/R_f=6$. Fig. 7 isolates the effect of friction showing results for several values of the nondimensional friction parameter, in every case with $p_R=0$. Plots a and b of this figure display the dependence of p and U, respectively, on ξ, while ξ has been eliminated in plot c with p cross-plotted against U. The curves in these plots apply when the debond condition, $K=K_c$, is met. The straight lines emanating from the origin have been added to indicate behavior prior to any debond crack advance, as will be discussed below. Included in each of the three plots of Fig. 7 are predictions of the model for precisely the same case. The model predictions are given by (2.13) and (2.15) for the limit $\mu=0$. Equivalently, they can be obtained from (3.4) and (3.5) after $K=K_c$ is imposed.

Suppose for the purpose of discussion that the displacement U (rather than the load) is prescribed by the pushout devise. Any loading devise compliance could be taken into account in the following discussion, but a stiff devise is well modeled by prescribing U. The straight line emanating from the origin in Fig. 7c is the load-displacement response of the system prior to attaining the debonding condition $K=K_c$. If a debond crack of length greater than about one fiber radius pre-exists, then the dashed line segment will intersect the the debonding curve at a point such as A, and debonding will then progress smoothly as U is increased. If, however, the initial debond flaw is shorter than about one fiber radius, debonding will start at a point such as B and will advance dynamically arresting when the load drops to the lower value at B' associated with the prescribed U. Subsequently debonding will progress smoothly with increasing U until the limit point with respect to U is reached. Values at the limit point are denoted by (p^*,U^*), corresponding to the point where the debond crack becomes unstable and breaks through to the bottom of the specimen. The limit point is attained when the debond crack tip reaches a distance of about $1.5R_f$

from the bottom. (The values given by the model at which $\ell = t - 1.5R_f$ is indicated by a solid dot in Fig. 7c.) From Figs. 2a and 5, it can be seen that the instability point corresponds to the strong up-turn in the dependence of K on p. Note further that the two cases shown with nonzero τ_0 are stable under *prescribed load* almost to the same point as under prescribed U. In other words, friction stabilizes the debonding process until the point where the debond approaches the bottom of the specimen such that there is very little dependence of the break-through values, p^* and U^*, on the compliance of the loading device.

Plots of p and U as functions of ξ and p versus U are shown in Fig. 8 for examples where residual axial compression p_R in the fiber is present as well as constant friction. In this case the normalized value of $p-p_R$ has been used as the ordinate to bring to out the fact that the main effect of residual axial compression is to simply require an extra push roughly equal to p_R. The model tends to underestimate p and overestimate U, but the errors in p^* and U^* are not more than about ten percent. The range of the nondimensional residual stress parameter chosen in Fig. 8, from 0 to 2, covers the feasible range of this parameter. Using (3.4), one can readily show that the fiber will debond by residual stress alone (i.e. poke out of the matrix) if

$$\frac{p_R}{\sqrt{E_I \Gamma / R_f}} > 2\sqrt{\frac{E_f}{E_I B_2}} \tag{4.3}$$

The collection of terms on the right side of this inequality is usually fairly close to 2.

5. Closing Remarks

The detailed numerical analysis of some specific examples in Sections 3 and 4 indicate that the model equations provide a reasonably accurate characterization even for a specimen as thin as $t/R_f = 6$, with errors of about 10% being typical. The accuracy of the model predictions in the vicinity of the instability point is seen in Figs. 7 and 8 to be somewhat better than in the beginning stages of the debond process. As discussed in Section 3.4, the accuracy will be even better for thicker specimens. The detailed analysis indicates that the instability point in the debonding phase occurs when the debond reaches a distance of about $1.5R_f$ from the bottom of the specimen, and the model equations (2.17) and (2.18) can be used to predict this point. Moreover, as long as there is some friction, this instability point is not a strong function of the compliance of the pushout device. The instability is primarily associated with the strong upturn in the relation of K versus debond length seen in Figs. 2a and 5 as the debond crack approaches the bottom of the specimen.

A few remarks are in order in connection with use of the model equations of Section 2 to infer interface properties such as Γ and frictional characteristics from experimental pushout

records. Firstly, one should be cognizant of the approximate nature of the model equations in making efforts to fit the model equations to experimental pushout data. The level of error reflected by the examples in Figs. 7c and 8c is typical for relatively thin specimens. Secondly, one must be aware that it may not be possible to distinguish between a constant friction characterization and a Coulomb friction characterization if the specimen is relatively thin. To see this, consider the frictional contribution to the pushout stress in (2.13). If ζ never exceeds 1/3, say, then $e^{\zeta}-1$ can be approximated by ζ and

$$\frac{\tau_0+\mu n_R}{\mu B_1}\left[e^{\zeta}-1\right] \cong 2(\tau_0+\mu n_R)\frac{\ell}{R_f} \tag{5.1}$$

The combination $(\tau_0+\mu n_R)$ is equivalent to an effective constant friction. In other words, if $\zeta<$ 1/3, there is negligible 'Poisson effect' and the Coulomb friction contribution remains essentially unchanged at μn_R during the debonding phase. These remarks also apply to the pushout phase governed by (2.19), although note that the term $-\mu B_1 p_R$ does affect the Coulomb contribution relative to the debonding phase (5.1) in a way which does distinguish it from constant friction. Since the debond length is at most t, the condition that ζ never exceed 1/3 is simply $t/R_f<1/(6\mu B_1)$, which, depending on specific values of the parameters of the system, could be as large as 10 or more.

Equation (2.13) can be used to assess the relative importance of debonding toughness, residual axial stress, and friction to the pushout stress during the debond phase. As emphasized earlier, according to the model the residual compression in the fiber p_R simply adds to the required pushout stress. The terms

$$2\sqrt{\frac{\Gamma E_f}{B_2 R_f}} \quad \text{and} \quad \frac{\tau_0+\mu n_R}{\mu B_1}$$

each have dimensions of stress and, respectively, govern the debonding and frictional contributions. The nondimensional frictional parameter and residual stress parameter introduced in Section 4 used the first of the above quantities in their normalization. Thus, the relative importance of the contributions can be assessed from the relative magnitudes of these terms.

Finally, we wish to call attention to the fact that the relative slip u of fiber to matrix at the top of the specimen is only a tiny fraction of the fiber radius at break-through in many systems. This statement follows from inserting values for typical systems in (2.16) and from experimental records of pushout tests published in the literature. Thus, for example, a thin specimen with a fiber of radius 50 microns may undergo debonding with relative sliding u never exceeding a small fraction of a micron. If the asperity roughness has a wavelength which is long compared u (which

is the case for some fibers), then debonding does not involve the asperities sliding past one another. In fact, under these conditions, debonding will occur prior to the unseating, or unkeying, of the fiber asperity pattern from the matrix which surrounds it. The role of surface morphology during debonding under these conditions is not well understood, and it is not at all clear that a phenomenological friction law such as (2.1), whether for constant or Coloumb friction or some combination, should apply both to the debonding phase *and* the pushout phase after sliding distances on the order of the asperity wavelength have occurred. By the same token, frictional characteristics inferred from pushout tests where 'large' amounts of sliding occur may not be relevant for debonding and sliding under pullout conditions experienced in cracking applications for brittle matrix composites which involve small amounts of sliding.

Acknowledgement

The authors would like to thank A.G. Evans and D.B. Marshall for helpful discussions during the course of this work. The work was supported in part by the DARPA University Research Initiative (Sub-Agreement P. O. #VB38639-0 with the University of California, Santa Barbara, ONR Prime Contract N00014-86-K0753, the Materials Research Laboratory (Grant NSF-DMR-89-20490) and the Division of Applied Sciences, Harvard University.

References

Gao, Y-C., Y-W. Mai and B Cotterell (1988), Fracture of fiber reinforced materials, J. Appl. Math. and Phys. (ZAMP) 39, 550-572.

Hutchinson, J.W. and H.M. Jensen (1990), Models of fiber debonding and pullout in brittle composites with friction, Mech. of Materials 9, 139-163.

Hutchinson, J.W. and Z. Suo (1991), Mixed mode cracking of layered materials, Adv. Appl. Mech. 29, (ed. by J.W. Hutchinson and T.Y. Wu) Academic Press, 63-191.

Jero, P.D. and R.J. Kearns (1990), The contribution of interfacial roughness to sliding friction of ceramic fibers in a glass matrix, Scripta. Met. 24, 2315-2318.

Kallas, M.N., D.A. Koss, H.T. Hahn and J.R. Hellmann (1991), On the interfacial stress state present in a "thin-slice" fiber push-out test, to be published in J. Materials Sci.

Kearns, R.J. and T.A. Parthasarathy (1991), Theoretical analysis of the fiber pull-out and push-out tests, J. Am. Ceram. Soc. 74, 1585.

Mackin, T.J., P.D. Warren and A.G. Evans (1992) Effects of fiber roughness on interface sliding in composites, Materials Department Report, University of California, Santa Barbara, to be published.

Marshall, D.B. (1992), Analysis of fiber debonding and sliding experiments in brittle matrix composites, to be published in Acta Metall. Mater.

Meda, G., S.F. Hoysan and P.S. Steif (1991), The effect of fiber Poisson expansion in micro-indentation tests, to be published.

Shetty, D.K. (1988), Shear-lag analysis of fiber pushout (indentation) test for estimating interfacial friction stress in ceramic-matrix composites, J. Am. Ceram. Soc. 71, C-107 -C-109.

Takaku, A. and R.G.C. Arridge (1973), The effect of interfacial radial and shear stresses on fiber pull-out in composite materials, J. Phys. D: Appl. Phys., 6, 2038-2047.

Appendix

The numerical results have been obtained using a finite element code ABAQUS (Hibbitt, Karlsson & Sorensen, Inc., Providence, Rhode Island, USA) with eight-noded quadrilateral axisymmetric elements. The finite-element mesh consists of 1169 to 1305 elements. Mode 2 cracks of length ℓ are assumed to exist along the interface. Since there is a square root singularity in the strain and stress fields at the crack tip, quarter-point elements are employed in the region nearest to the tip. The radial length of the smallest and largest elements are $3.07 \times 10^{-4}\ R_f$ and $1.35 \times 10^{-4}\ R_f$, respectively. For each pre-selected ℓ, the energy release rate, G, is calculated using a J-integral option in ABAQUS. The contour selected to calculate G lies within the immediate vicinity of the tip, where the plane strain conditions are asymptotically approached. The calculation is performed for debond ratios ranging from $1 < \ell/R_f < 6$, with between twelve to twenty ratios used for a given specimen. The stress intensity factor K and the average downward displacement of the end of the fiber U are also calculated. The displacement U is obtained by averaging the nodal axial displacement of the fiber end over the intersection area of the fiber, while the relative displacement u is obtained by subtracting the average axial displacement of matrix from U. Since the linear elastic behavior is assumed, the contributions to K and U from the applied compression p, the residual axial stress p_R and constant friction τ_0 along the interface could be calculated separately as discussed in Section 3. The contribution due to axial residual compression p_R in the fiber is modeled by applying a uniform tension p_R to the fiber ends, and a compressive stress $\rho p_R/(1-\rho)$ acting over an annular region whose radius extends from R_f to $R_f/\sqrt{\rho}$ on both the top

and bottom faces of the specimen. The finite-element results for the constant friction case are obtained by applying an appropriate concentrated shear force to each nodal point along the crack faces such that an equivalent uniform shear stress τ_0 is achieved.

Errata for Hutchinson and Jensen (1990)

Eq. (24): $c_2 = \frac{1}{2} a_2 (b_2 + b_3)^{1/2}$

Eq. (47): k_1 should be replaced by $k_1/(1+k_1)$

Eq. (59): e^{ζ_i} in the numerator should be replaced by $e^{-\zeta_i}$

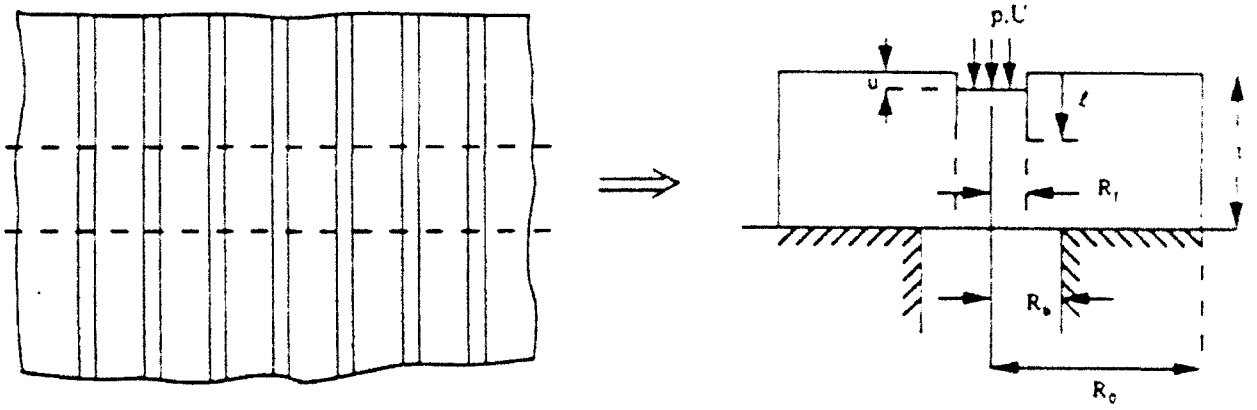

residual axial compression in fiber in composite=p_R

residual compression across fiber/matrix interface=n_R

Fig. 1 Residual stresses in composite and slicing to make a specimen. Definition of length quantities for specimen.

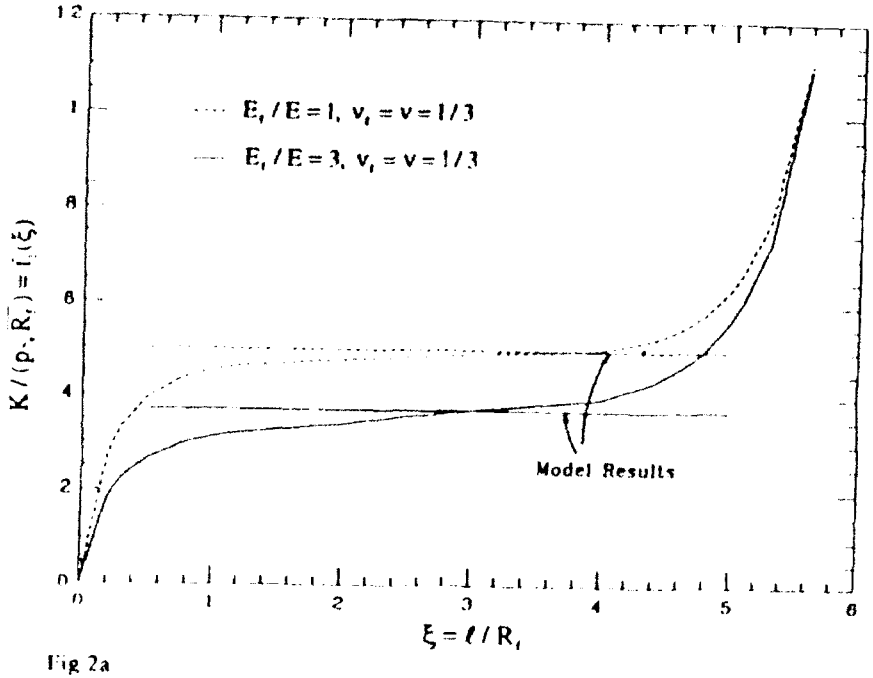

Fig 2a

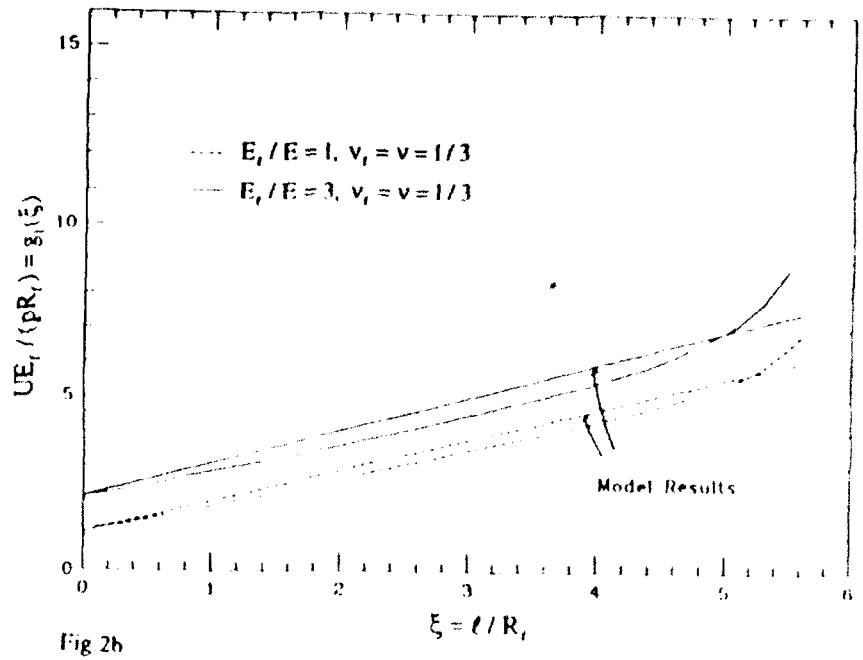

Fig 2b

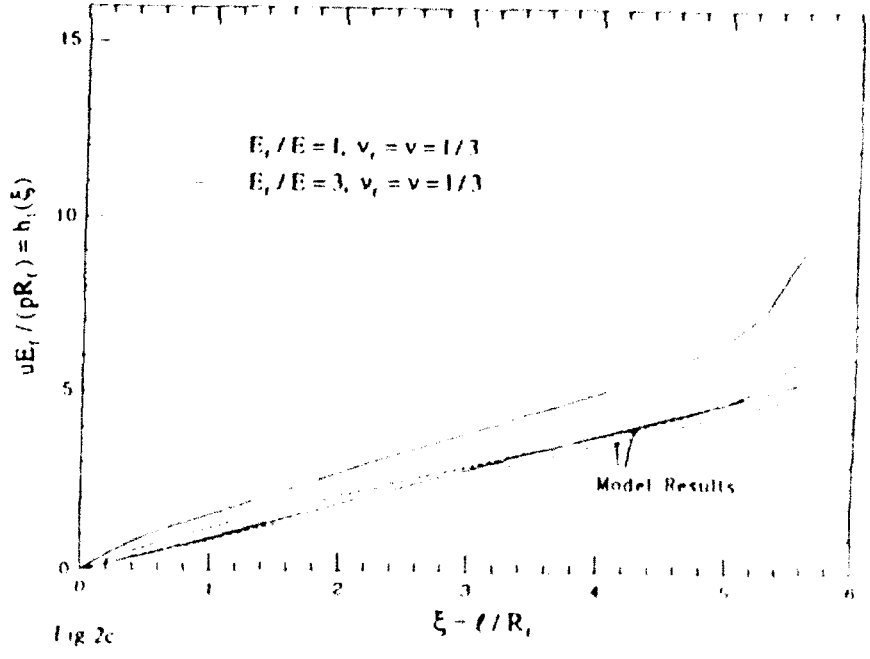

Fig 2c

Fig. 2 Contributions due to p in Equations (3.1)-(3.3). The parameters of the specimen are defined in the text.

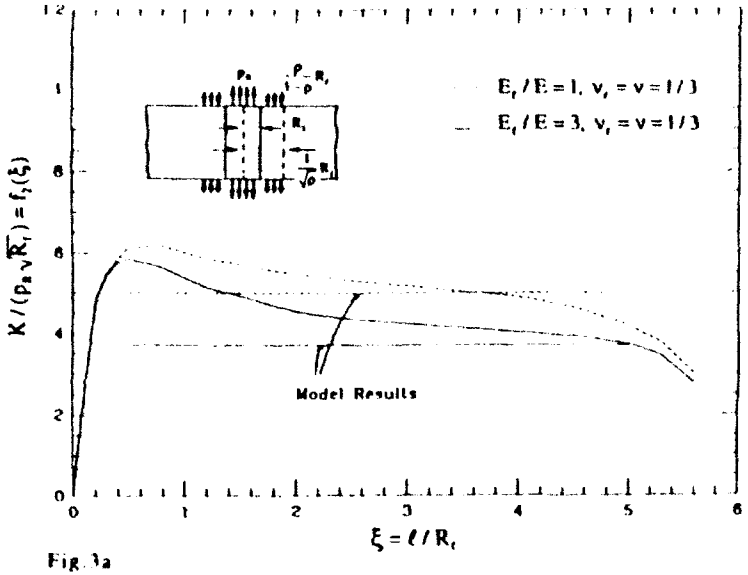

Fig. 3a

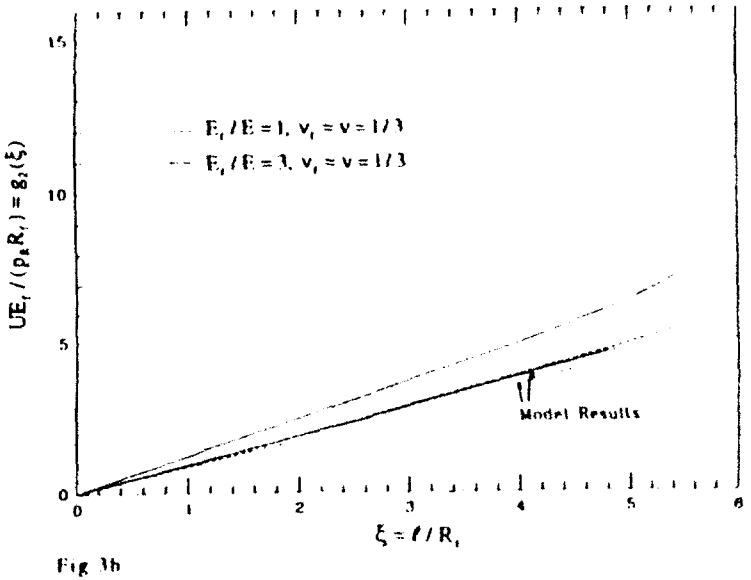

Fig. 3b

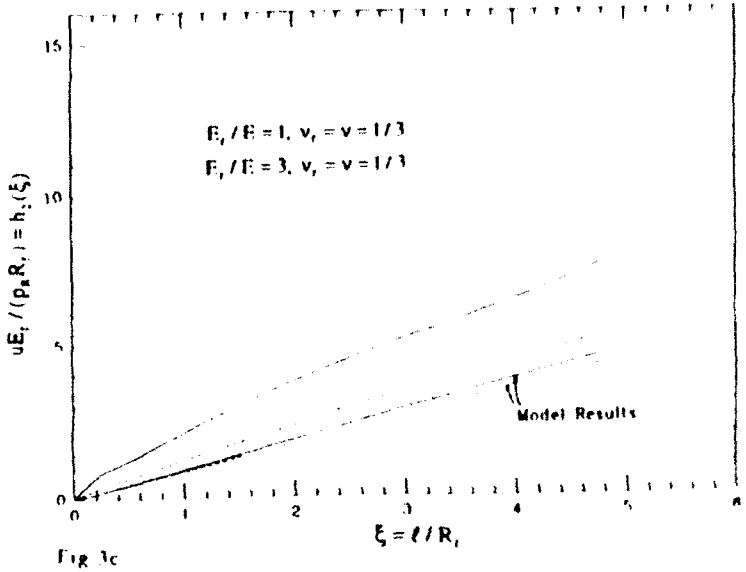

Fig. 3c

Fig. 3 Contributions due to p_R in Equations (3.1)-(3.3). The insert in a) shows the tractions applied to the specimen to generate the contribution. The parameters of the specimen are defined in the text and ρ=4/9.

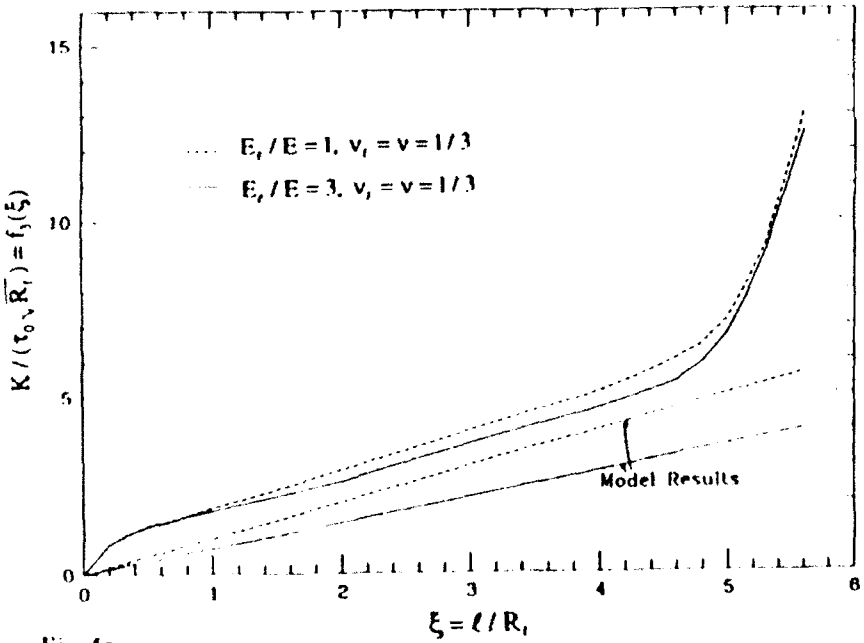

Fig. 4a

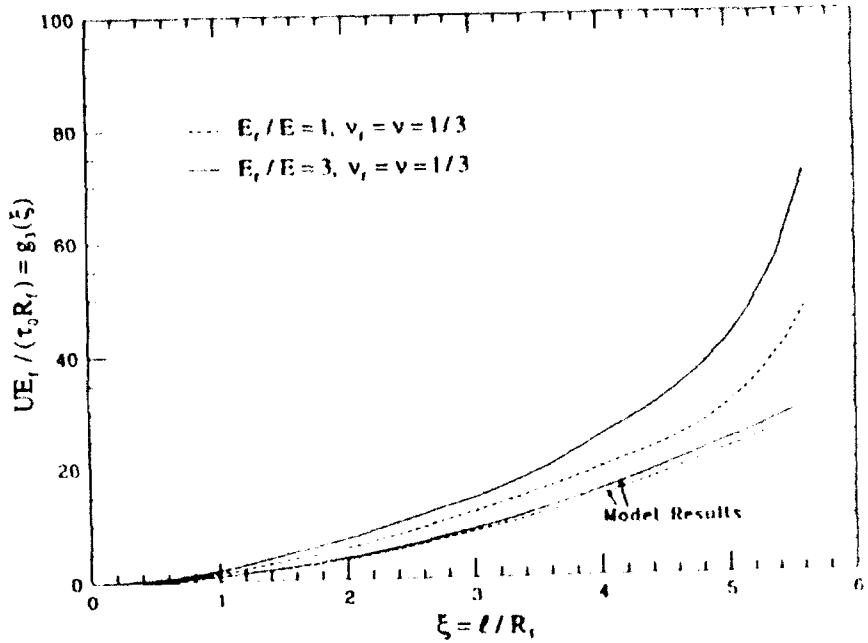

Fig. 4b

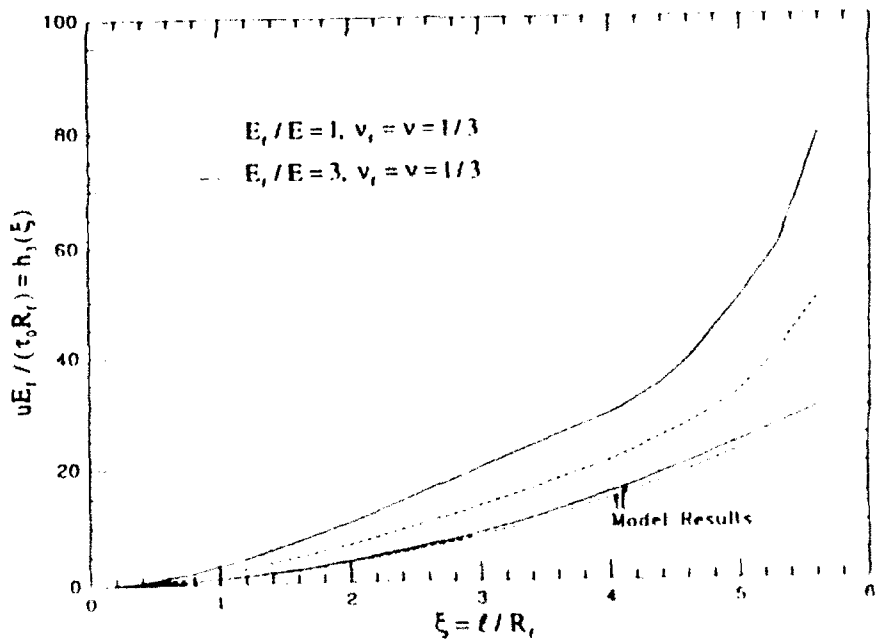

Fig. 4c

Fig. 4 Contributions due to τ_0 in Equations (3.1)-(3.3). The parameters of the specimen are defined in the text.

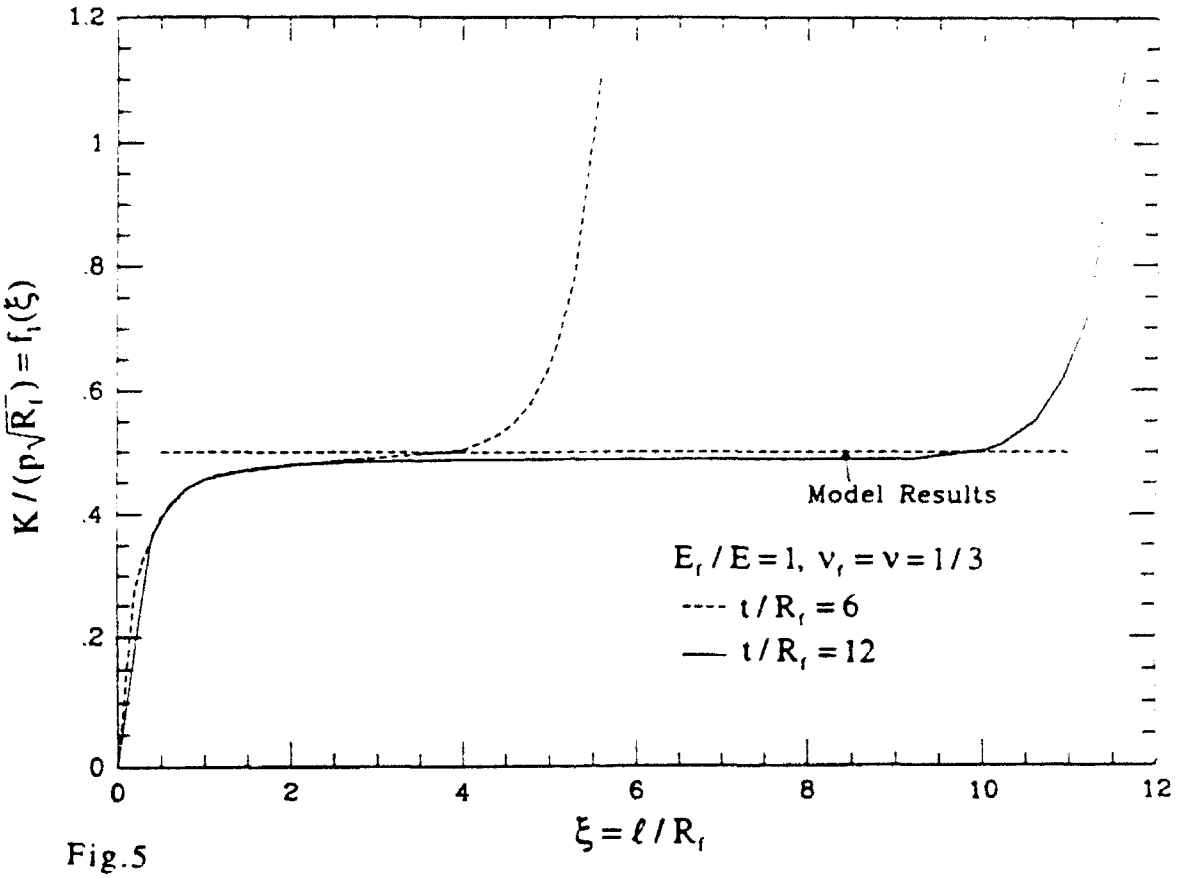

Fig.5

Fig. 5 Contributions to K in (3.1) due to p for two thicknesses of specimen. The parameters of the specimen are otherwise the same as those in Fig. 2a.

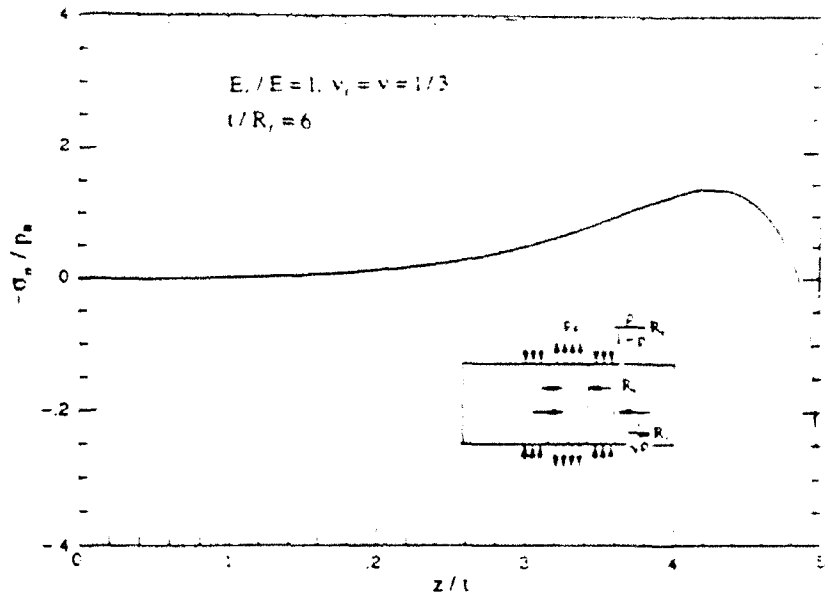

Fig 6a

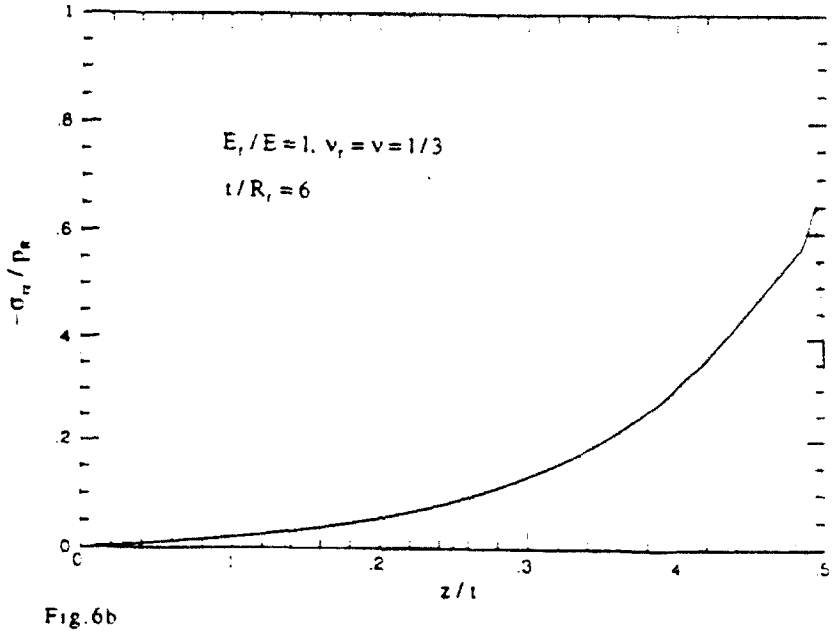

Fig.6b

Fig. 6 Changes in normal and shear stress on the fiber/matrix interface due to slicing a specimen from a composite with an axial residual compressive stress p_R in the fiber. The insert displays the tractions applied to the specimen to model the stress changes caused by slicing. The parameters of the specimen are the same as those in Figs 2-4 with $\rho=4/9$, $E_f=E$ and $\nu_f=\nu=1/3$.

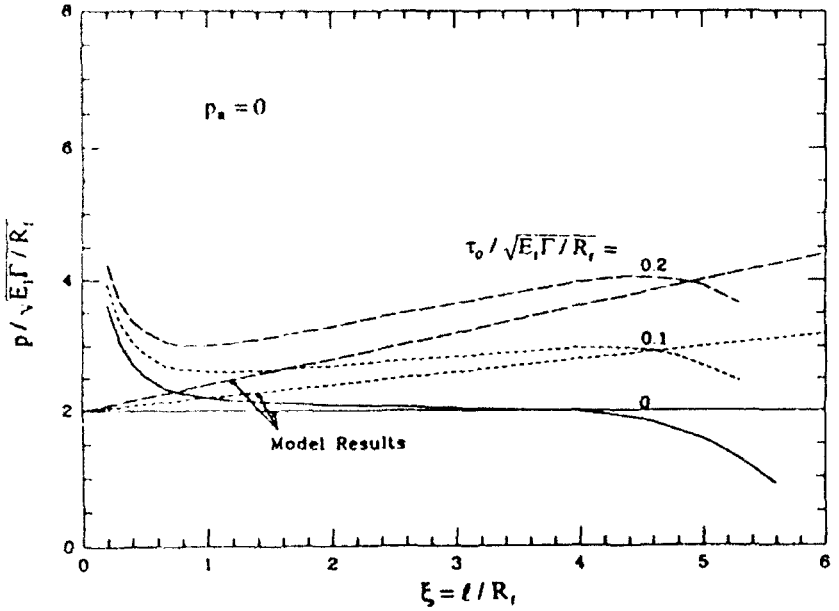

Fig.7a

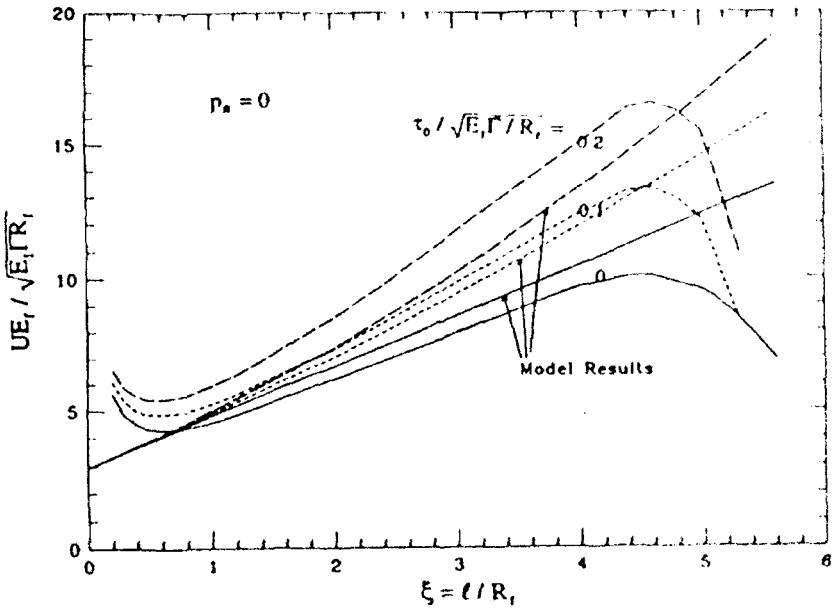

Fig.7b

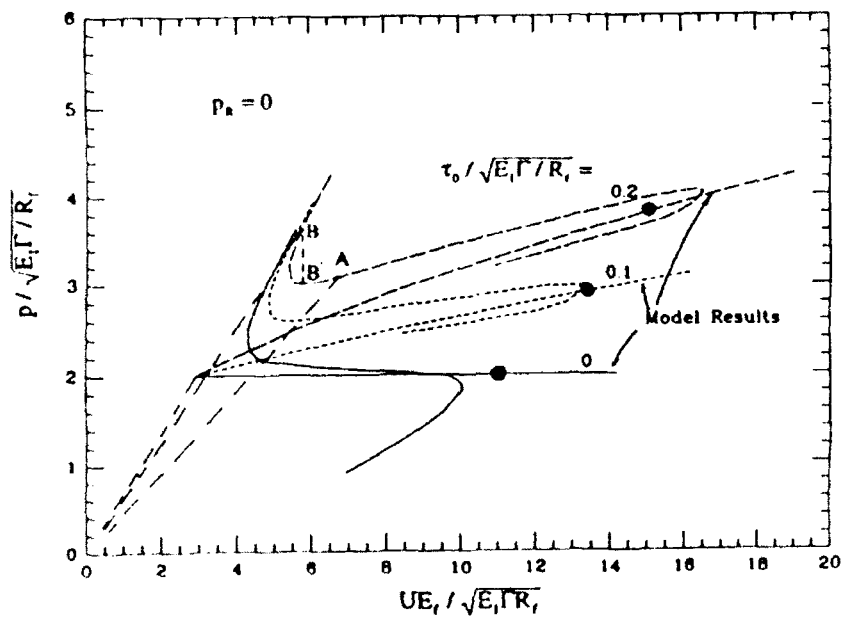

Fig.7c

Fig. 7 Pushout behavior during the debonding phase for $p_R=0$ with several levels of constant friction. Comparison of the full numerical results from (4.1) and (4.2) with the model predictions. In part c) the point where $\ell = t - 1.5R_f$ is indicated by a dot for the model predictions. The straight line segments emanating from the origin in c) correspond to the behavior prior to the onset of debonding as discussed in the text. The parameters of the specimen are the same as those of Figs. 2-4 with $t/R_f=6$, $E_f=E$ and $\nu_f=\nu=1/3$.

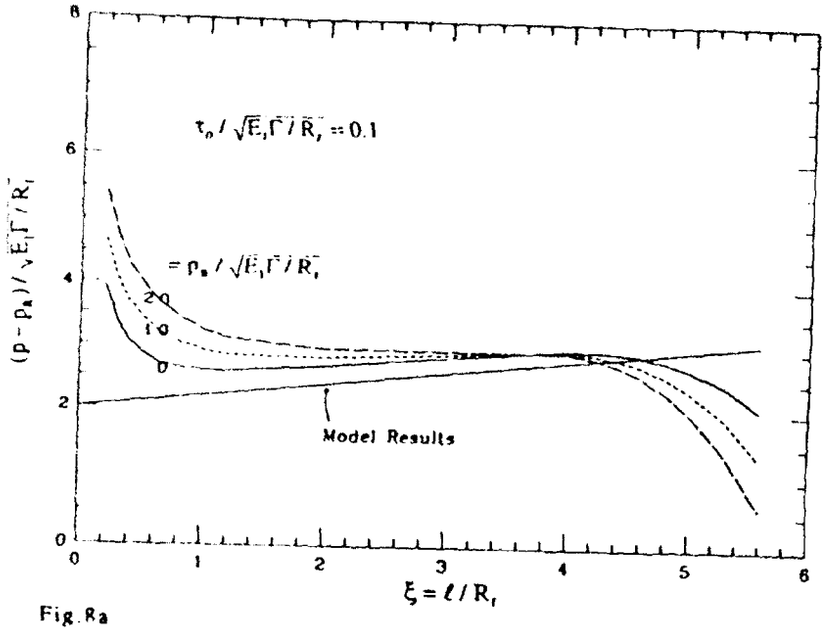

Fig. 8a

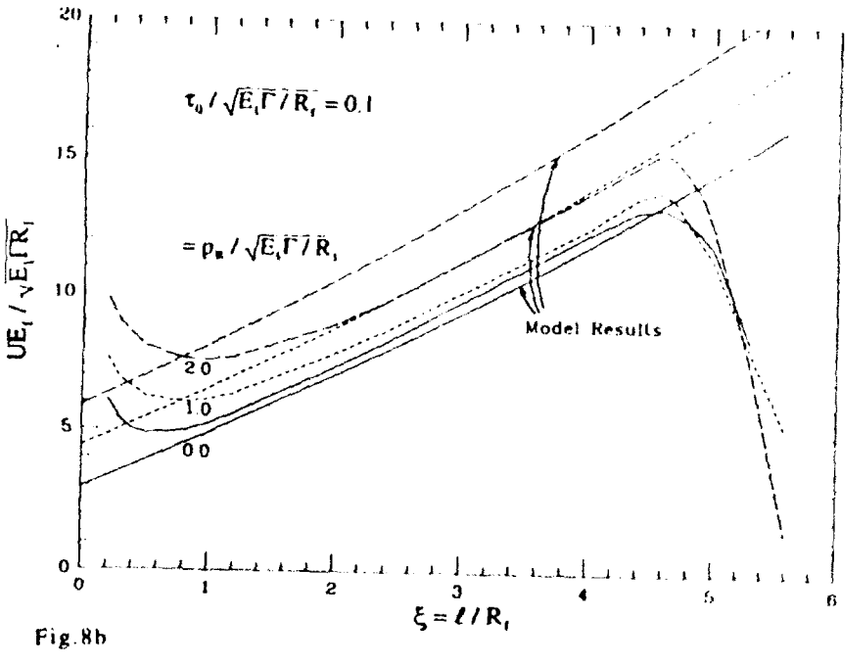

Fig. 8b

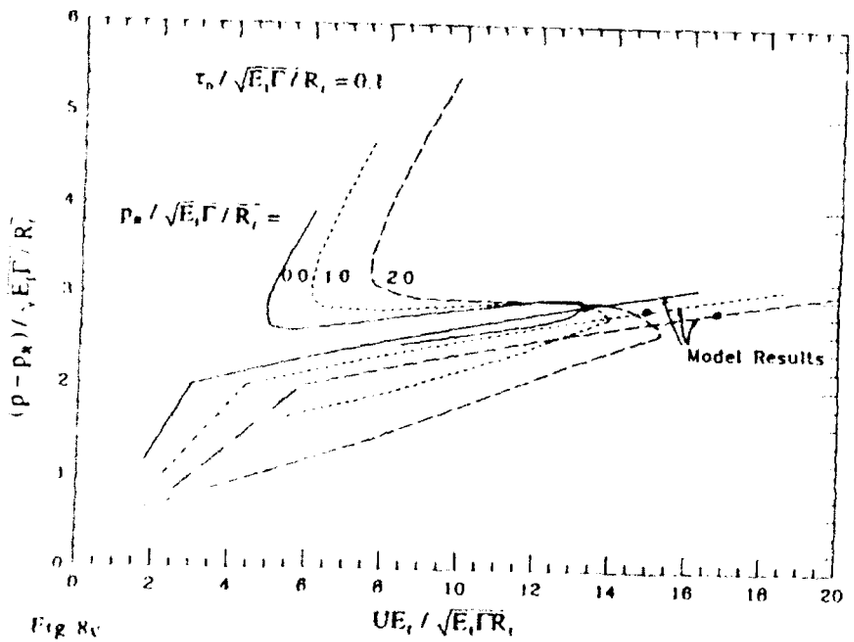

Fig. 8c

Fig. 8 Pushout behavior during the debonding phase for $\tau_0/(E_1\Gamma/R_f)^{1/2}=0.1$ with several levels of residual axial compression p_R. Comparison of the full numerical results from (4.1) and (4.2) with the model predictions. In part c) the point where $\ell=t-1.5R_f$ is indicated by a dot for the model predictions. The parameters of the system are the same as those of Figs. 2-4 with $t/R_f=6$, $E_f=E$ and $\nu_f=\nu=1/3$.

Acta metall. mater. Vol. 40, No. 6, pp. 1251–1257, 1992
Printed in Great Britain. All rights reserved

0956-7151/92 $5.00 + 0.00
Copyright © 1992 Pergamon Press Ltd

EFFECTS OF FIBER ROUGHNESS ON INTERFACE SLIDING IN COMPOSITES

T. J. MACKIN, P. D. WARREN and A. G. EVANS

Materials Department, College of Engineering, University of California, Santa Barbara, CA 93106, U.S.A.

(Received 7 October 1991)

Abstract—The presence of asperities at the fiber-matrix interface is noted experimentally as a load rise during the initial stages of push-out and as a reseating load drop during push-back. These effects are modelled by considering the elastic deformation of asperities at the interface. During fiber sliding, the decorrelation of initially matching fiber and matrix geometries results in an asperity pressure at the interface. Fractal models of interface roughness are incorporated into an equation of fiber sliding that is found to accurately reproduce experimental observations. Additionally, an asperity wear mechanism must be introduced to explain the effects of fatigue, the variation of fiber reseating with sliding distance, and the rapid decay in sliding stress during pristine fiber push-out.

Résumé—La présence d'aspérités à l'interface fibre matrice est constatée expérimentalement comme une élévation de charge pendant les stades initiaux de la poussée et comme une chute de charge pendant la poussée inverse. Ces effets sont modélisés en considérant la déformation élastique des aspérités à l'interface. Pendant le glissement des fibres, la décorrélation des géométries initialement assorties des fibres de la matrice conduisent à une pression d'aspérité à l'interface. Des modèles fractaux de la rugosité de l'interface sont incorporés dans l'équation du glissement des fibres qui reproduit avec précision les observations expérimentales. De plus, un mécanisme d'usure des aspérités doit être introduit pour expliquer les effets de la fatigue, la variation de remise en place de la fibre avec la distance de glissement, et la rapide décroissance de la contrainte de glissement pendant la première poussée sur la fibre.

Zusammenfassung—Rauhigkeiten an der Grenzfläche zwischen Faser und Matrix machen sich im Experiment als Anstieg der Last während der Anfangsphase des Ausziehens und als Lastabfall durch Wiedereinrasten während des Zurückschiebens bemerkbar. Diese Effekte werden modellhaft beschrieben, indem die elastische Verformung der Rauhigkeiten an der Grenzfläche beschrieben werden. Während des Gleitens der Faser führt das "Ausrasten" der ursprünglich passenden Faser- und Matrixgeometrien zu einem Druck durch die Rauhigkeiten an der Grenzfläche. Fraktale Modelle der Grenzflächenrauhigkeit werden in eine Gleichung der Fasergleitung eingebaut: es ergibt sich, daß diese die experimentellen Beobachtungen genau wiedergibt. Zusätzlich muß ein Rauhigkeits-Abriebmechanismus eingeführt werden, um die Effekte der Ermüdung, der Variation des Einrastens der Faser mit dem Gleitweg und den raschen Abfall in der Gleitspannung während des vorausgegangenen Ausziehens der Faser erklären zu können.

1. INTRODUCTION

Fiber-reinforced composites gain much of their toughening from the frictional sliding of fibers [1–4]. Most descriptions of sliding have employed a sliding stress, τ, that does not incorporate the microscopic roughness of the sliding surfaces [5–7]. Recent experimental evidence, however, has elevated the role of interface roughness. In particular, certain features of fiber push-out and pull-out cannot be explained by the frictional sliding of smooth fibers. For example, after a fiber has been pushed through [Fig. 1(a)] or pulled out and returned to its original location, it experiences a reseating load drop [Fig. 1(b)] [8–11]. This load drop arises from the geometric memory of the fiber–matrix debond surface: the fiber and matrix geometries re-correlate in their original orientation. Furthermore, fiber push-out is often accompanied by an increasing load during the early stages of sliding [Fig. 1(a)] [7, 11]: a phenomenon which is also attributed to geometric decorrelation during fiber displacement. Additional evidence for roughness arises from effects associated with cyclic sliding during fatigue (Fig. 2) [11]. This article develops a simple model of fiber sliding that incorporates fiber roughness, which may be used to simulate and interpret fiber push-out and pull-out measurements. The model shows that the decorrelation of initially matching fiber and matrix geometries is seemingly responsible for many of the observed phenomena.

Jero *et al.* [8, 9] first noted the importance of fiber roughness and modelled its effect as an addition to the interfacial clamping pressure. They assumed that the fiber and matrix geometries, once removed from their original position, would create a uniform asperity pressure that simply adds to any existing clamping pressure. A more detailed analysis of asperity interactions was presented by Carter *et al.* [10] wherein asperity roughness is modelled as Hertzian contacts,

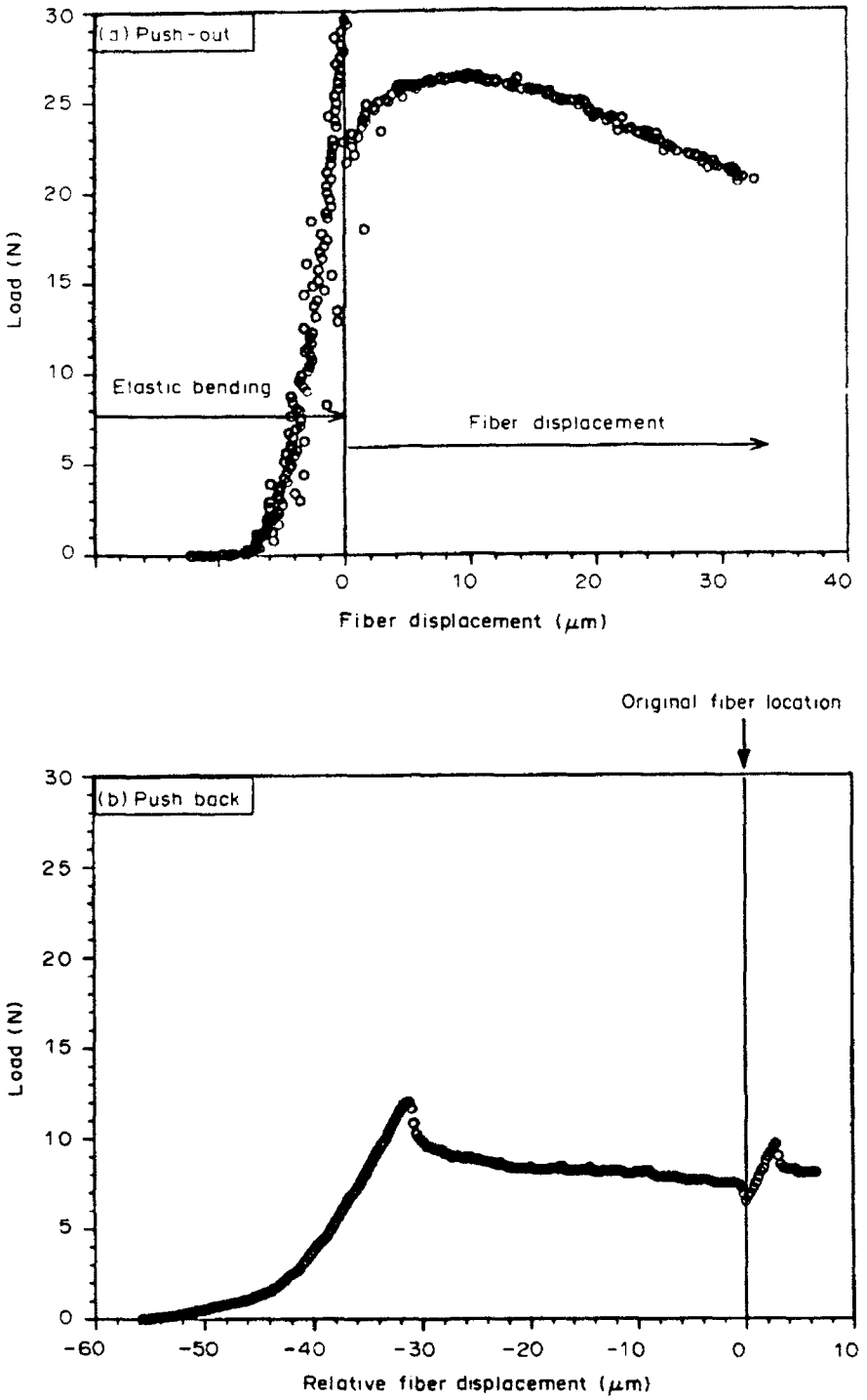

Fig. 1 Fiber push-out (a) and push-back (b) in a Ti(15-3)–SCS-6 composite. During fiber push-out, there is a notable increase in the sliding stress associated with the first few microns of fiber sliding. Note the reseating load drop associated with fiber push-back ($h = 410\ \mu m$).

leading to a sinusoidal modulation of the sliding stress. Kerans and Parthasarathy [12] include asperity pressure in a detailed treatment of fiber debonding and sliding during both push-out and pull-out experiments. They note that asperity pressure, due to roughness, plays an important role in fiber sliding. Additionally, Kerans and Parthasarathy [12] introduce discussion of abrasion during fiber sliding that would have implications during the sliding of fatigued fibers.

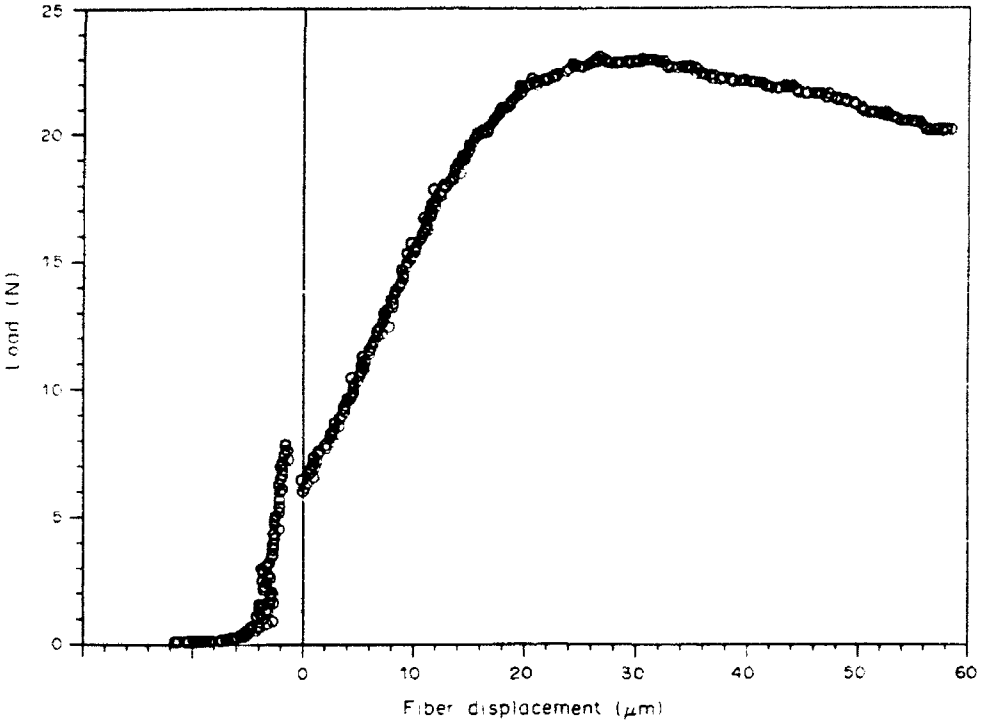

Fig. 2. Push-out for fatigued fibers ($h = 450\ \mu m$).

The present model considers an elastic asperity mismatch akin to that of Jero *et al.* [8, 9] but includes a full spectrum of fiber roughness, represented using fractal geometry. As such, computer simulations using this model illustrate all of the fundamental aspects of sliding along a rough, debonded interface, and directly demonstrate asperity effects during the sliding of both pristine and fatigued fibers.

2. SLIDING MECHANICS

Fiber sliding, in the absence of roughness, has been analyzed using a generalized sliding law [5, 13]

$$\tau = \tau_0 - \mu\sigma_r \tag{1}$$

where τ is the sliding stress, μ is a friction coefficient, σ_r is the compressive stress normal to the interface, and τ_0 is a constant sliding stress. When τ_0 and ϵ_T, the mismatch strain between fiber and matrix, are independent of location along the fiber, σ_a, the push-out stress on the fiber, σ_a, is [5, 13]

$$\sigma_a = \frac{\sigma_0[\exp(2\mu Bt\ R) - 1](1 - f)}{[f(E_f\ E_m)\exp(2\mu Bt\ R) + 1 - f]} \tag{2}$$

where f is the fiber area fraction, E is Young's modulus, R the fiber radius, and t is the embedded length of the fiber (Fig. 3), with the subscripts f and m referring to fiber and matrix, respectively, and

$$B = vE[E_f(1 + v) + E(1 - v)]^{-1}$$

$$\sigma_0 = \frac{E_f\epsilon_T}{v} + \left(\frac{\tau_0}{\mu}\right)\frac{E}{BE_m(1 - f)}$$

$$t = h - d$$

with v being Poisson's ratio (assumed to be the same for fiber and matrix). E is the composite modulus, h is the specimen thickness and d is the sliding distance of the fiber.

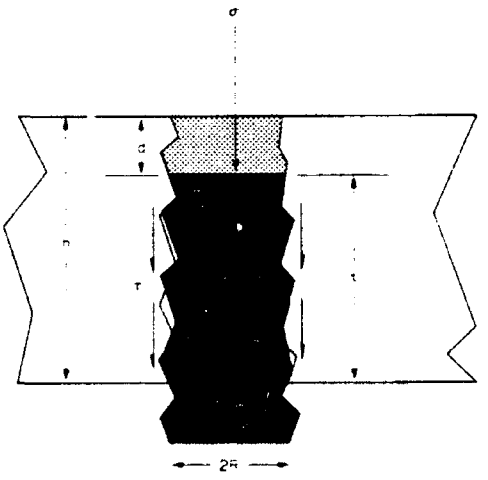

Fig. 3. Schematic of fiber sliding and the associated geometry.

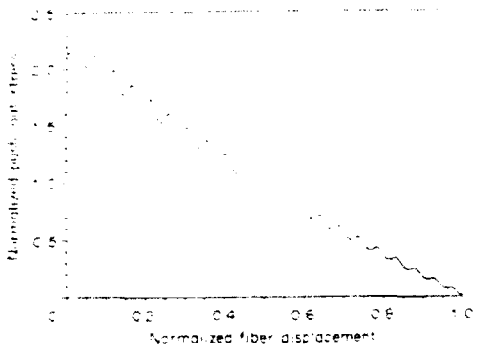

Fig. 4. A sinusoidal interface surface results in a similar modulation of the sliding stress

When the misfit is *dependent* upon z, because of roughness along the debonded interface, the push-out stress is modified. For this purpose, ϵ_T is re-expressed as

$$\epsilon_T = \epsilon_z - \delta(z)\, R \tag{3}$$

where ϵ_z is the thermal expansion misfit and $\delta(z)$ is the asperity mismatch between fiber and matrix along the embedded length of the fiber (Fig. 3). If the asperities are axisymmetric, the roughness leads to a local misfit strain, $\delta(z)\, R$, at locations where asperities in the fiber and matrix slide past each other. In essence, the asperity induces an additional pressure, p, that determines τ_0: mechanistically arising from the geometric decorrelation of fiber and matrix during fiber sliding. As such, the interfacial shear stress presented in equation (1) is entirely Coulombic

$$\tau = \mu(\sigma_r + p) \tag{4}$$

with, $\tau_0 = -\mu p$. (Note that, because p is compressive, τ_0 is positive.)

For simplicity of presentation, roughness effects are demonstrated for the case of single fiber push-out with $v_f = v_m$ and small f, such that equation (2) reduces to

$$\sigma_z = \sigma_0 \exp(2\mu Bt/R - 1). \tag{5}$$

The integral of the asperity mismatch over the embedded length of the fiber provides the asperity pressure. Hence, the push-out stress given by equation (5) becomes

$$\sigma_0(d) = \frac{E\epsilon_z}{2B}\left[\exp(2\mu Bt/R(1 - d/t)) - 1\right] + (2E\mu/R^2)\exp(-2\mu Bd/R) \times \int_d^h [\exp(2\mu Bz/R)]\delta(z)\, dz \tag{6}$$

where d is the push-out distance (Fig. 3). Consequently, by specifying an interface roughness, $\delta(z)$, the push-out stress can be computed from equation (6).

3. SIMULATIONS

Fiber push-out simulations are conducted that address the push-out force *after the debonding load drop*. The roughness of the debonded interface is modelled using fractal algorithms with identical fractal profiles assigned to both sides of the debond. Once assigned, the profiles are compared at each sliding distance to determine a diametral mismatch, $\delta(z)$, at increments along the fiber length. Using equation (6), the resulting push-out stress is determined. The simulation methodology was tested by computing the push-out behavior of a fiber that has a single wavelength, axisymmetric, sinusoidal profile. For such roughness, a sinusoidal form is demonstrated in a push-out simulation (Fig. 4). More realistic fiber profiles were simulated using a fractal geometric technique known as fractional Brownian motion (*fBm*) [14–17], a technique that has found widespread use in the simulation of natural geometries. Evidence for the utility of *fBm* modeling is presented in Fig. 5, which compares the profile of an (SCS-6)SiC fiber, taken using a profilometer [Fig. 5(a)] with a fractal representation [Fig. 5(b)]. The use of fractal modelling enables controlled simulation of fiber "roughness," and, consequently, demonstrates the role of roughness in fiber sliding.

The following simulations relate to push-out curves measured on Ti alloy (SCS-6)SiC fiber metal–matrix composite. These simulations, using known values of elastic moduli and roughness, are compared directly with experimental results [11]. The elastic constant, B in equation (6) was computed from the formulae of Hutchinson and Jensen [5]. Fiber roughness simulations were based upon a fractal analysis of SCS-6 fiber profiles, providing a profile fractal dimension of $D = 1.12$. The fiber and matrix surfaces were modelled as axisymmetric surfaces of revolution, resulting in a fiber surface dimension of 2.12. Profilometry of (SCS-6)SiC fibers indicated a roughness with a maximum amplitude of tenths of microns [Fig. 5(a)] and the fractal representations were scaled accordingly.

At the onset of fiber sliding, the fiber and matrix geometries are in perfect registry. Consequently, the roughness term vanishes from equation (6), resulting in an equation for smooth fiber push-out. Thus, a coefficient of friction was determined by matching theory and experiment at the point of initial sliding. This matching for the results on Ti SiC (SCS-6) indicated that $\mu = 0.26$.

A typical set of simulations is illustrated in Fig. 6. Various behaviors are apparent, dependent on the roughness amplitude distribution sampled within the specimen section thickness. Most relevant is the frequent appearance of rising load portions of the push-out curve. This feature is observed experimentally (Fig. 1) and is at variance with the behavior expected for smooth fibers. Furthermore, the extent of the rise is consistent with that found by experiment, as illustrated in Fig. 7. After rising to a

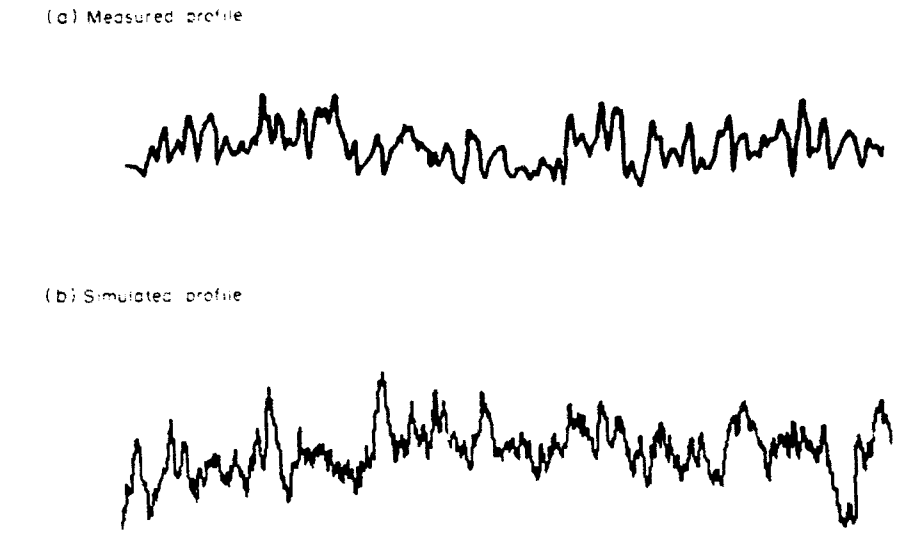

Fig. 5 Comparison of actual (a) and simulated (b) SCS-6 fiber profiles.

maximum, experimental push-outs experience a rapid decrease in the applied load. As shown in Fig. 7, simulated push-outs are found to consistently remain higher than experimental results. Such a rapid decrease in push-out load cannot be modelled without the introduction of interface wear, a process that will be discussed in connection with fiber resetting and fatigue. As expected, fibers having an interface roughness amplitude greater than that for SCS-6 fibers exhibit push-out curves with larger oscillations (Fig. 8).

Consistent with previous studies of push-out and pull-out, the push-out force is found to be strongly influenced by the friction coefficient over the full

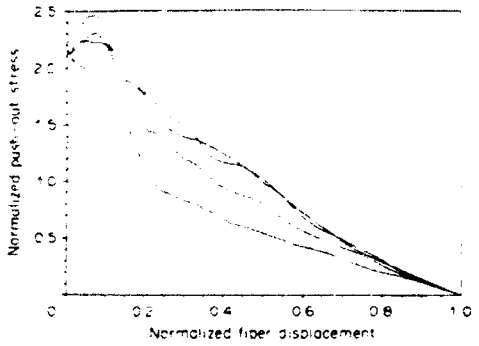

Fig. 6 Push-out simulations exhibit the same qualitative behavior as experimental push-outs. Each curve represents a random sampling from the roughness distribution.

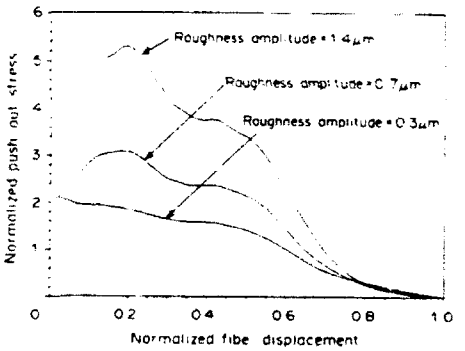

Fig. 8 An increase in roughness amplitude has a pronounced effect on fiber sliding.

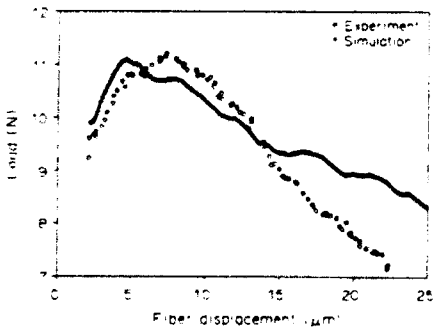

Fig. 7 Rough fiber push-out simulations resemble experimental results ($h = 210\ \mu$m).

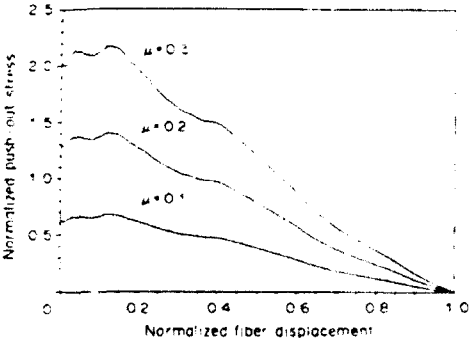

Fig. 9. An increase in the coefficient of friction, μ, increases fiber sliding stress.

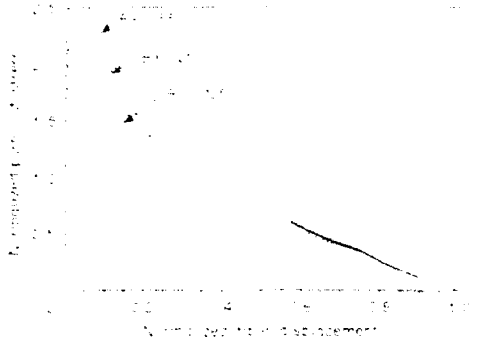

Fig. 10. An increase in the Poisson's ratio increases fiber sliding stress. B is a composite Poisson's ratio [equation (2)]

push-out distance (Fig. 9), but only moderately dependent on Poisson's ratio at initial push-through (Fig. 10). The effects of thermal expansion misfit are of particular interest (Fig. 11). As expected, the push-out force is reduced when the misfit is reduced, but is still finite when the misfit is reduced to zero. For zero misfit, the push-out curve is dependent *entirely on the roughness distribution*. Consequently, the shape of the curve changes when different segments of the roughness distribution are included in the specimen section (Fig. 11). The behavior, in essence, governs τ_i in equation (1).

4. INTERFACE FATIGUE

Experiments on interfaces subject to cyclic sliding in fatigue have revealed push-out behavior that departs significantly from that of their pristine counterparts [11] (Figs. 1 and 2). The initial sliding stress of pre-fatigued fibers was much lower and, during subsequent push-out, was followed by substantial load increase, even though the embedded fiber length is decreasing as push-out proceeds. The low initial sliding stress is attributed to interface degradation during fatigue, while the subsequent increase in fiber stress arises from an asperity mismatch pressure. Thus, in addition to roughness, the simulation of fatigued fiber sliding requires interface wear.

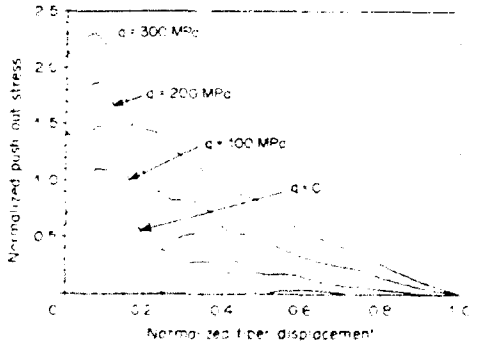

Fig. 11. A change in the thermal misfit at identical roughness changes both the character and magnitude of the sliding stress. q is the thermal expansion misfit stress, $q = E\varepsilon_t$.

Fatigue degradation of the fiber matrix interface was modelled in two ways: smoothing and fragmentation. The first simulation technique employs a low pass filter to eliminate chosen scales of roughness, akin to asperity wear. Profile filtering is performed on the Fourier spectrum of the profile, wherein a low pass cut-off frequency is chosen and the profile is reconstructed using only those wavelengths below the cut-off. In these simulations, only the fiber profile is smoothed, indicative of preferential wear at the fiber side of the interface. Consequently, the fiber and matrix no longer afford a perfect match, and small gaps form between the fiber and matrix. Asperity filtering, however, did not simulate the fatigued fiber push-out features found by experiment.

The second approach entails removing a thin shell of interface material from around the fiber, somewhat equivalent to relaxing the residual thermal stress, but permitting small gaps at the interface. The fragments formed by cyclic sliding are assumed to be removed from the interface and become relocated between the matrix crack surfaces. The results of these simulations (Fig. 12) exhibit correspondence with the experimental curves (Fig. 2). A reduction in interface sliding stress upon cyclic sliding caused by coating fragmentation thus appears to be the more plausible degradation mechanism.

5. FIBER RESEATING

Perhaps the most telling evidence of fiber geometry is that of fiber reseating [8–11]. This occurs when a fiber has been displaced within the matrix and then returned to its original location. As the fiber moves back into position, the reseating is accompanied by a considerable load drop. This phenomenon has been witnessed in at least two matrices containing (SCS-6)SiC fibers: Ti(15-3) and glass. The present simulation procedure is inherently reversible and *always* produces fiber reseating. Yet, experimental evidence suggests that the fiber is worn during sliding and that subsequent reseating is affected by the extent of sliding [11]. This effect can be simulated by introducing a wear mechanism that relaxes the clamping

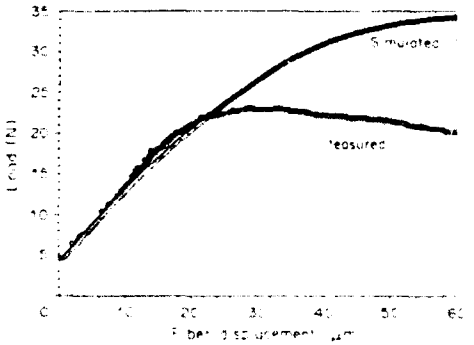

Fig. 12. Fatigue simulated by relaxing the misfit resembles experimental results

Fig. 13. Push-back resisting load drop is modified by implementing a wear process during fiber sliding.

pressure on the fiber surface. For simplicity, the wear mechanism was modelled as a linear function, reducing the asperity pressure in direct proportion to the fiber sliding distance. Simulated push-back curves for two push-out distances (Fig. 13) exhibit the same features found in the experiments [11].

6. SUMMARY

A model of fiber sliding that incorporates the effect of interface roughness has been presented. The effect is analogous to an elastic shrink-fit due to geometric decorrelation of initially matching surfaces as asperities slide past each other. The subsequent asperity pressure contributes perturbations to the clamping pressure at the interface and generates sliding phenomena in general accordance with experimental observations. One important phenomenon is the increase in initial sliding stress, after debonding, often encountered in the presence of interface roughness. This increase is influenced by the amplitude of the roughness and its fractal characteristics. Such behavior could have a substantial effect on the incidence and location of fiber failure and hence, on the frictional contribution to the fracture resistance.

Another significant finding is the change in interface properties caused by cyclic sliding in fatigue. The push-out simulations are found to have the same form as the experimental measurements when the fiber coating is assumed to fragment and relax the thermal expansion misfit between fiber and matrix. Such fragmentation has been observed experimentally. This reduction in sliding stress would have the detrimental effect of accelerating fatigue crack growth [18].

REFERENCES

1. B. Budiansky, J. C. Amazigo and A. G. Evans, *J. Mech. Phys. Solids* **36**, 167 (1988).
2. J. R. Rice, *J. Mech. Phys. Solids* **35**, 333 (1987).
3. A. G. Evans and R. M. McMeeking, *Acta metall.* **34**, 2435 (1986).
4. D. B. Marshall and A. G. Evans, *J. Am. Ceram. Soc.* **68**, 225 (1985).
5. J. W. Hutchinson and H. M. Jensen, *Mech. Mater.* **9**, 139 (1990).
6. Y.-C. Gao, Y.-W. Mai and B. Cotterell, *J. appl. Math. Phys. (ZAMP)* **39**, 550 (1988).
7. J. D. Bright, S. Danchaivijit and D. K. Shetty, *J. Am. Ceram. Soc.* **74**, 115 (1991).
8. P. D. Jero and R. J. Kerans, *Scripta metall. mater.* In press.
9. P. D. Jero, R. J. Kerans and T. A. Parthasarathy, *J. Am. Ceram. Soc.* In press.
10. W. C. Carter, E. P. Butler and E. R. Fuller, *Scripta metall. mater.* **25**, 579 (1991).
11. P. D. Warren, T. J. Mackin and A. G. Evans, *Acta metall. mater.* **40**, 1243 (1992).
12. R. J. Kerans and T. A. Parthasarathy, *J. Am. Ceram. Soc.* **74**, 1585 (1991).
13. J. W. Hutchinson, private communication.
14. B. B. Mandelbrot, *The Fractal Geometry of Nature*. W. H. Freeman, San Francisco, Calif. (1983).
15. *The Science of Fractal Images* (edited by H.-O. Peitgen and D. Saupe). Springer, Berlin (1988).
16. M. Barnsley, *Fractals Everywhere*. Academic Press, New York (1988).
17. J. Feder, *Fractals*. Plenum Press, New York (1988).
18. D. Walls, G. Bao and F. Zok, *Scripta metall. mater.* **25**, 911 (1991).

MATERIALS

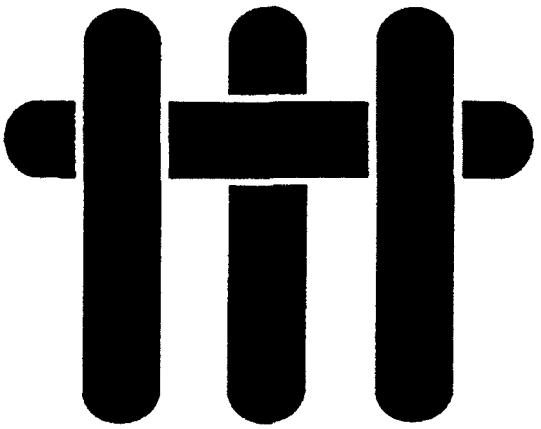

FIBER COATING CONCEPTS FOR BRITTLE MATRIX COMPOSITES*

by

J. B. Davis, J. P. A. Löfvander and A. G. Evans
Materials Department
College of Engineering
University of California
Santa Barbara, California 93106–5050

E. Bischoff
Max-Planck-Institut für Metallforschung
Seestraße 92, D–7000 Stuttgart 1, Germany

M.L. Emiliani
Pratt and Whitney, Materials Engineering
P.O. Box 109600
West Palm Beach, Florida 33410

*Supported by the Defense Advanced Research Projects Agency
under Contract No. MDA 972-90-K-001

KJS-Evans-18•F-Fl•TA-Fbr Ctng 91/03/21•10:26 AM•5/7/92

ABSTRACT

The current interest in tough, high-temperature materials has motivated fiber coating development for brittle matrix composites with brittle reinforcements. The system investigated in this study was sapphire fiber-reinforced alumina. This system is thermochemically stable for severe use conditions, exhibits little thermal expansion mismatch and utilizes the excellent strength and creep resistance of sapphire reinforcements. Porous oxide and refractory metal coatings which satisfy requirements for toughness improvement in these composites were identified by employing a variety of newly-developed mechanical testing techniques for determining the interfacial fracture energies and sliding resistances.

1. INTRODUCTION

The mechanical requirements for fiber coatings in brittle matrix composites are reflected in two properties[1-3]: debonding and sliding. These properties are manifest as an interface debond energy, Γ_i, and a sliding stress along the debonded interface, τ. A prerequisite for good composite strength and toughness is that a debond criterion be satisfied, wherein the debond energy relative to the fiber fracture energy, Γ_f, satisfy $\Gamma_i/\Gamma_f < 1/4$.[4] Control of sliding is needed to ensure a notch-resistant material, such that $\tau \lesssim 100$ MPa. Coatings of C and BN provide these properties, but both are susceptible to oxidation. Consequently, when SiC fibers are used, and when matrix cracks are present, oxidation embrittlement is encountered because the fiber oxidizes to form a silicate layer that violates debonding requirements.[5] Other coatings are thus desirable for high temperature applications. The present study examines some alternative fiber coating concepts, with emphasis on coatings for oxide fibers, such as sapphire.

Debonding of sapphire fibers* requires coatings with a debond energy, $\Gamma_i \lesssim 5$ Jm^{-2}. Few high-temperature materials have *intrinsic fracture energies* small enough to satisfy such a requirement. Potential options are oriented micas,[7] ‡ some amorphous oxides,[8] and fugitive coatings which are removed after composite consolidation.[9] However, the amorphous coatings have limitations governed by viscous flow at elevated temperatures, plus reaction with Al_2O_3. Two alternative concepts are explored in this article: i) porous oxide coatings and ii) coatings that form 'weak' interfaces with Al_2O_3. The first concept recognizes that *porosity* generally decreases the fracture energy of brittle materials, such as oxides.[10] Consequently, certain porous oxide coatings may be able to satisfy debonding requirements for sapphire fibers, by allowing debonding *within the coating* itself. The second concept is based on the expectation that certain non-

---

* $\Gamma_f \approx$ 12–20 Jm^{-2}, depending on the fracture plane.[6]
‡ This concept is being explored at Corning, by K. Chyung.

oxide coatings may allow *interface debonding*.[11] While most such interfaces have relatively high fracture energies ($\Gamma_i > 10$ Jm^{-2}),[11-13] larger than that required for the debonding of sapphire fibers, preliminary evidence has suggested that certain refractory metals provide suitably low values.[11]

An effective coating should have the attribute that it does not degrade the strength of the fibers. Consequently, coatings that either react with or dissolve the fibers are usually unacceptable. This thermochemical requirement further limits the potential set of coating materials. Various refractory materials that exhibit known thermochemical compatibility with Al_2O_3 at 1500°C have been evaluated (Table I), plus C, Y_2O_3 and the refractory metals, Mo, W, Cr and Zr.

2. APPROACH

The overall approach used to identify viable fiber coating concepts is illustrated in Fig. 1. Planar geometries readily amenable to processing and testing are used to screen candidate coating materials. The associated test procedures include a Hertzian indentation technique[14] and a mixed-mode flexure test[15] (Figs. 1a, 1b). For coatings that exhibit debonding, the fracture energy, Γ_i, may also be determined from these tests. The subset of coating materials that satisfy fiber debonding requirements is then used to address composite performance. For this purpose, sapphire fibers are coated and incorporated into a brittle matrix. Beam specimens are cut from the consolidated plate (Fig. 1c), with the fibers oriented along the beam axis. Tensile and/or flexural tests are then used to assess the interaction of a crack with the coated fibers and to obtain information about the sliding stress, τ. The magnitude of τ is ascertained from a measurement of the crack opening displacement as a function of the applied load.[16] Such tests also permit measurement of the fiber pull-out length, h, and the fiber fracture mirror radii.[17-19] The latter yield a direct estimate of the *in situ* strengths of fibers, S.[19]

The magnitudes of S and h, in turn, give another estimate of τ, and thus provide a useful consistency check. In addition, τ can be obtained from fiber push-through tests (Fig. 1d).[20-22] In the present study, a combination of the above tests is used to assess coating concepts for sapphire fibers in polycrystalline Al_2O_3.

3. EXPERIMENTAL PROCEDURES

3.1 Processing

The coatings were deposited either by evaporation, sputtering, chemical vapor deposition or by sol gel methods. For the *planar geometry*, coatings were deposited on two surfaces, each representing either the fiber or matrix component of the composite. Bonding was then conducted by hot pressing at homologous temperatures (for the coating material) in the range $0.4 < T/T_m < 0.7$. Consequently, the system experienced a thermal cycle analogous to that expected for composite processing. *Specimens containing fibers* were produced by sputter or evaporation coating sapphire fibers and incorporating them into matrices by powder processing, using either hot pressing or HIPing to achieve consolidation.

3.1.1 Coating Deposition

Oxide "sol gel" coatings were produced from liquid precursor materials. A spin coating apparatus was used to deposit the coatings onto the planar substrates used for diffusion bonding. The coated substrates were then heat treated in air to temperatures suitable for pyrolysis of the precursor, typically below 1000° C. During pyrolysis, the film is converted to an oxide. Subsequent iterations were used to increase the thickness of the coating.

Sputtered coatings were deposited onto sapphire *discs* and *fibers* in an R.F. diode sputtering unit. The sputtering targets used in most cases were high purity (≥ 99.9%):

only the W target had a lower purity (~ 99.5%). Oxide coatings were deposited by reactive sputtering using a 50%-50% mixture of research grade argon and oxygen at a total working gas pressure of 6 millitorr. The intermetallic compounds were produced from dual opposed targets of the pure elements. Both the refractory metal and intermetallic coatings were deposited in an atmosphere comprised of research grade argon at 6 millitorr working gas pressure. The top and bottom target voltages were maintained at 3kV and 0.5kV, respectively. Fibers were rotated during coating at ~ 1 rpm.

Submicron thick Mo coatings were deposited onto sapphire fibers using an electron beam evaporator and a high purity target. A glow discharge cleaning procedure was used prior to coating the fibers. Deposition was carried out at relatively high vacuum (< 10^{-6} torr), with the fibers rotated at ~ 10 rpm.

The carbon coatings were produced by a low pressure chemical vapor deposition technique in which methane was mixed with research grade argon carrier gas in a tube furnace. Flow rates of 10 cc/min, for the methane, and 100 cc/min, for the argon, were used. Throughout deposition, the furnace temperature was maintained at 1200°C to 1300°C.

3.1.2 Bonding and Consolidation

For experiments to be conducted with planar configurations, three different Al_2O_3 materials were used: i) (0001) sapphire; ii) a high purity (99.5%) polycrystalline material; and iii) a low purity (96%) material.* The test specimens were produced by diffusion bonding, using a procedure described elsewhere.[14] Bonding at $T/T_m \approx 0.5$ allowed coatings to be produced with relative density levels in the range 0.65 to 1.

---

* Coors AD-995 and Coors AD-96 Substrates.

Tests on coated sapphire fibers were conducted after incorporating into a high-purity (99.9%) polycrystalline Al_2O_3 matrix. For this purpose, submicron Al_2O_3 powder[**] was isostatically cold pressed into two thin discs ~ 5 cm in diameter. These discs were then sintered in air at 1500° C for two hours. A row of coated fibers and loose powder were placed between the discs, the assembly inserted between dies and vacuum hot pressed at 1500°C for 2hr subject to an axial pressure of ~ 2 MPa. These consolidation conditions resulted in an essentially fully dense matrix.

3.2 Testing and Analysis

3.2.1 *Mechanical Behavior*

The Hertzian indentation and mixed-mode flexure testing procedures used with planar specimens have been described elsewhere.[14-15] The flexural tests required precracking. This step was conducted in three-point flexure, using a row of Knoop indentations along the tensile surface to control the crack pop-in load and hence, the extent of the precrack along the interface.

The tests used with the specimens containing fibers have been performed using a combination of fiber push-out and pull-out techniques. The fiber push-out technique has been described previously.[20] The fiber pull-out tests required that chevron notches were machined into beams containing single fibers (Fig. 1). This notch geometry ensured stable crack growth through the beam upon flexural loading. The crack was grown until the crack front passed below the fiber. This occurred with a small crack opening, which induced some fiber debonding and sliding. After precracking, the beam was supported and the remaining matrix ligament mechanically removed. This procedure created a specimen consisting of two blocks of matrix material bridged by a single fiber, amenable to tensile testing. Tests were conducted *in situ* in a Hitachi 2100

[**] AKP-50 with a particle size ~ 0.5 μm obtained from Sumitomo Chemical.

scanning electron microscope (SEM) to permit measurement of the crack opening displacement and the corresponding tensile loads. These measurements may be used to evaluate the sliding resistance, τ.[16]

3.3 *Analytical Techniques*

Specimens for scanning electron microscopy were prepared using standard metallographic techniques. Carbon-coated samples were examined in a JEOL SM 848 SEM in secondary mode. The microscope was equipped with a Tracor Northern TN 5500 system. Samples for transmission electron microscopy (TEM) were prepared by grinding wafers to a final thickness of approximately 100 μm before cutting 3 mm specimens. These were subsequently dimple-ground and ion milled to electron transparency with Ar at 5kV and lmA at 14° incidence angle. The samples were examined at 200kV in a JEOL 2000FX TEM equipped with a LINK eXL high take-off angle energy dispersive spectroscopy system. Computer simulations and indexing of selected area diffraction (SAD) patterns were facilitated by the Diffract software package (Microdev Software, Hillsboro, Oregon 97124).

4. COATING CHARACTERIZATION

4.1 Oxides

For the oxide coatings, a range of porosities was generated, as illustrated in Fig. 2. At the equivalent bonding cycle, the thinner, sol gel coatings had lower *intracoating* porosity than the sputtered coatings, whereas the porosity at the interface was similar for both. In all cases, the grain size was about equal to the coating thickness. The most notable features found by TEM were bend contours in the sapphire caused by residual strains[23] (Fig. 3). For unstabilized ZrO_2 coatings, extensive straining in the sapphire was apparent, as well as microcracks within the coating (Fig. 3a). This effect diminished with

decreasing coating thickness (Fig. 3b). Selected area diffraction indicated that the ZrO_2 was monoclinic and the strains are attributed to the tetragonal to monoclinic phase transformation. For ZrO_2 coatings partially stabilized with 3 mol % Y_2O_3, the tetragonal phase was retained and the intensity of the strain contours diminished (Fig. 3c). However, some residual strain persisted, attributed to the thermal expansion mismatch between ZrO_2 and Al_2O_3. Such strains appear to be an inherent problem with oxide coatings, potentially leading to fiber strength degradation (Appendix).

4.2 Refractory Metals

For the refractory metal coatings, thin foil cross sections for TEM were difficult to produce, because of debonding. However, for Mo, results have been obtained in two cases: a) a thin (0.7 μm) *evaporated* coating with the high purity Al_2O_3 matrix and b) a thicker (> 3 μm) *sputtered* coating with the lower purity Al_2O_3 matrix. For the former, the coating appeared to have some discontinuity (Fig. 4a), but otherwise survived the consolidation. These discontinuities, which are induced by diffusion, are typical for thin, polycrystalline films.[24] EDS analysis was unable to detect either Mo in the Al_2O_3 or Al in the Mo. For the latter, a relatively thick (~ 300 nm) dense polycrystalline MoO_2 phase found at the sapphire interface (Fig. 4b). In addition, an amorphous silicate phase was observed at the MoO_2/Mo interface that presumably resulted from viscous flow of the silicate from the polycrystalline Al_2O_3 into porosity at this interface.

The Mo coatings were also investigated by SEM, *after debonding*. For *sputtered* coatings, oxide particles (identified as MoO_2) were found to be attached to the sapphire in regions where debonding occurred between the Mo and sapphire. X-ray diffraction of the debond surface confirmed the presence of MoO_2 on the sapphire. Shallow ridges were also apparent on the sapphire side of the debond surface, having spacings comparable to the grain size in the metal (Fig. 5a). These ridges are believed to form at

grain boundaries, by diffusion, during the bonding process, as equilibrium dihedral angles are established. Small impressions were evident on the Mo side of the debonded surface between Mo and the *higher purity* Al_2O_3 (Fig. 6), having dimensions which coincide with the Al_2O_3 grain size. These are believed to have formed by deformation of the Mo during diffusion bonding.

The *sputtered* Cr coatings exhibited similar features. A thin polycrystalline Cr oxide (~ 200 nm thick) was attached to the sapphire (Fig. 7), with the remainder of the coating being Cr. Analysis by EDS indicated no Cr in the Al_2O_3 and only trace amounts of Al in the Cr oxide. Selected area diffraction patterns established that the Cr oxide was Cr_2O_3, and significant porosity existed at the metal/oxide interface. Debonding was evident, occurring between the metal and its oxide layer.

The *sputtered* W coatings on sapphire exhibited pronounced ridges on the sapphire side of the debond surface (Fig. 5b). These have been associated with Fe and Cr rich grain boundary impurity phases, originating in the sputtering target. The resulting degradation of the sapphire, evident in Fig. 5b, illustrates the importance of selecting chemically stable coatings. Similar features were observed at C/Al_2O_3 interfaces diffusion bonded at high temperatures (> 1400°C) in high vacuum (> 10^{-6} torr). For this system the ridges are attributed to the formation of an Al_4C_3 reaction product.

Studies of the *as-sputtered* Mo and Cr films, using WDS and X-ray diffraction, revealed an oxide surface layer. In addition, there was an oxide layer adjacent to the sapphire, identified by peeling the coating from the substrate. These findings indicate that the oxide phase is initially deposited on the sapphire substrate during sputtering and that a surface oxide forms subsequent to deposition, prior to diffusion bonding.

5. MECHANICAL MEASUREMENTS

5.1 Debonding

Preliminary experiments conducted on planar specimens with a spherical indenter provided information about the incidence of debonding at a 30° crack inclination to the interface. From such experiments, it was established that most diffusion bonded coatings formed high fracture energy interfaces. Only the coatings consisting of Mo, W, Cr, Zr and C debonded consistently. Coatings of ZrO_2 and $Y_3Al_5O_{12}$* were found to exhibit variable debonding tendencies. Coatings of Nb, γ-TiAl and NiAl did not debond. Furthermore, from the list of promising coating materials, several were observed to chemically react with the sapphire during diffusion bonding. The only coating materials from this set which were found to be *chemically stable* with sapphire above 1300°C and to *reliably debond* were: Mo, Cr, porous ZrO_2 and porous Al_2O_3. Further studies were confined to these materials.

The debonding propensity of the *refractory metal* coatings was observed to vary with the purity of the Al_2O_3. When either sapphire or sapphire plus *high purity* polycrystalline Al_2O_3 were used, debonding occurred consistently, with $\Gamma_i \approx 4\ Jm^{-2}$ for Mo and 2–3 Jm^{-2} for Cr. Furthermore, as already noted, the debonding occurred at the interfaces between either Mo/Al_2O_3 or Mo/MoO_2 and Cr/Cr_2O_3. Conversely, when the *impure* Al_2O_3 was used, debonding was not observed in the Hertzian indentation test, implying a *lower bound* for Γ_i of ~ 16 Jm^{-2}.‡ This behavior is attributed to the silicate phase found at the Mo/MoO_2 interface, which seemingly forms a strong bond[25,26] and increases Γ_i for that interface. In addition, as already noted, MoO_2 appears to bond well with sapphire.

---

* Formed by chemical reaction during bonding with Y_2O_3 coatings.

‡ This lower bound is, $\Gamma_i = 0.8\,\Gamma_f$, corresponding to a crack/interface inclination of 30°, with $\Gamma_f \approx 20\ Jm^{-2}$.

The results for the *oxide coatings* were found to be sensitive to the coating porosity. The *dense* coatings, which have a relatively high interfacial fracture energy, debond along the *interface*. But debonding only occurred when the crack approached the interface at a shallow inclination. Conversely, the coatings having the *lowest relative density* ($\rho \approx 0.65$), exhibited a relatively low interfacial fracture energy, $\Gamma_i \approx 5\ Jm^{-2}$, and debonded *within the coating, at all crack inclinations*. Such debonds exhibit fracture surface features typical of those for porous ceramics.[10] These debonding tendencies are rationalized by using the coating density, ρ, as a plotting variable against the ratio of the interfacial fracture energy to sapphire fracture energy Γ_i / Γ_f, (Fig. 8a).

The debonding results obtained *for all of the above coatings* can be displayed on a debond diagram, relevant to sapphire fiber-reinforced brittle matrix composites (Fig. 8b).

5.2 Sliding Resistance

For *porous oxide coatings* on sapphire fibers in a polycrystalline Al_2O_3 matrix, single fiber tests revealed small fiber pull-out (Fig. 9). Debonding resulted in a monolayer of the oxide particles attached to the fiber that remained throughout the sliding process (Fig. 9). These particles are believed to act as asperities that resist sliding, resulting in a relatively large sliding stress, τ. This stress was estimated from the pull-out length and the fracture[16-18] mirror radius to be ~ 140 MPa (Table II). A similar value was obtained from fiber push-out measurements. This value of τ is larger than that required for optimum composite strength and toughness.

The refractory metal coatings debond readily during single fiber pull-out tests, but the coating is plastically deformed. This deformation occurs because the coating conforms to both the matrix and fiber during consolidation and results in prohibitively high sliding resistances, such that little fiber pull-out occurs (Fig. 10). Similar behavior is

found during push-out tests (Fig. 11a), which also indicate a high sliding resistance, $\tau \approx 120$ MPa (Fig. 13).

A reduction in the sliding resistance for Mo coated fibers has been achieved by *removing the coating*, after composite consolidation, to leave a gap between the fiber and matrix. This has been accomplished by heating the composite in air* (1000°C for 2 hours). The surface roughness of the fiber and the matrix then provide the sliding resistance. For coatings somewhat thicker than the asperity amplitude on the fiber (~ 1 μm), the sliding resistance obtained from crack opening displacement measurements in single fiber pull-out tests is found to be small ($\tau < 1$ MPa), with large associated pull-out lengths (Fig. 12). This sliding resistance is too low for the requisite combination of strength and toughness in the composite. For thinner (~ 0.7 μm) coatings, push-out tests indicate a sliding resistance within the requisite range, $\tau \approx 20$ MPa (Fig. 13), with no evidence of wear mechanisms on the fiber surface (Fig. 11b).

6. CONCLUDING REMARKS

The debonding and sliding properties of various coating materials on sapphire fibers have been evaluated. In general, most materials bonded well to sapphire. The notable exceptions were certain *refractory metals* (such as Mo, Cr, and W) which formed low fracture energy interfaces with sapphire. Several factors may be responsible for the low debond energies: porosity at the interfaces, oxygen dissolved in the metal (that suppresses plastic dissipation)[13] and the formation of a metal oxide (MoO_2 or Cr_2O_3).[27,28] A systematic study would be needed to identify the critical factor(s).

---

* Because Mo forms volatile oxides.

Oxide coatings, which form strong interfaces with sapphire, can also be useful debond coatings, provided that they contain a significant amount of porosity subsequent to composite consolidation. The porosity in these coatings provides a low fracture energy path causing debonding within the coating.

The sliding characteristics of the various interfaces were also investigated. The sliding resistances obtained on interfaces produced with refractory metal coatings is apparently too high for significant fiber pull-out, because the coating deforms during sliding. However, for coatings such as Mo, which form volatile oxides, the interfacial sliding resistance can be significantly reduced through coating removal by heat treatment in air. Fugitive carbon coatings also have this attribute,[9] but were not used in this study because the carbon reacted with the sapphire in the diffusion bonding experiments. It is recognized, however, that altering the processing conditions could eliminate this problem. Once the coating has been removed, the fiber surface and matrix roughness provide the sliding resistance needed for load transfer. The resultant system is also oxidatively stable. The coating thickness relative to the fiber and matrix roughness amplitude is now a key parameter.[22] An optimization study is in progress.

The *sliding resistances* of oxide coatings examined in this study were also unacceptably high, because of the undulating debond trajectory. It is believed that τ can be reduced if the grain size and porosity of the coating are carefully controlled. Further studies of the effect of debond surface irregularities on the sliding behavior are needed to address this issue.

Fiber strength degradation is another concern for oxide coatings. When reaction products with the fiber coating are avoided, potential sources of fiber strength degradation persist, including residual strain (Fig. 3) and undulations produced on the fiber surface by diffusion (Fig. 5). Some basic characteristics are amenable to analysis (Appendix). The predictions (Fig. 14) indicate that m-ZrO_2 coatings are unacceptable because, for typical coating thicknesses ($h \approx 0.1 - 1\ \mu m$), the large mismatch stresses

caused by the transformation lead to fiber strengths below the acceptable limit for high performance applications ($S < 1$ GPa). Furthermore, coatings such as YAG with a mismatch governed by thermal expansion are also predicted to cause an unacceptably low fiber strength ($S < 2$ GPa), unless the coatings are thin ($h < 3$ μm). A general implication is that oxide coatings, which typically bond well to sapphire, are a possible source of fiber strength degradation. The extent of degradation is diminished by thin coatings and small thermal expansion mismatch. Also, porosity in the coating tends to alleviate the degradation problem.

TABLE I

Some Materials Thermochemically Stable with Al_2O_3 at 1500°C

Material	References	Remarks
γ-TiAl	29	Al_2O_3 dissolves
Nb	30	Al_2O_3 dissolves
NiAl	31	
ZrO_2	32	

TABLE II

Sliding Stress with Porous Alumina Interface

Fracture Mirror Radius, a_m (μm)	*In Situ* Fiber Strength, S* (GPa)	Pullout Length, h (μm)	Sliding stress, τ # (MPa)
27	1.68	193	142

*$S = 3.5\left(\frac{K_c}{\sqrt{a_m}}\right)$, where K_c is the fiber toughness (~ 2.5 MPa)[17]

#$\tau = S\left(\frac{r}{2h}\right)$, where r is the fiber sapphire radius[17]

APPENDIX

FIBER DEGRADATION

When the coating is in residual tension caused by thermal expansion misfit, the coating cracks prior to fiber failure and may cause a degradation in fiber strength. When this crack penetrates into the fiber, the stress intensity factor, for a crack of depth, a, associated with the residual field from the coating is[33]

$$\begin{aligned} K_R &= 1.1E_c\varepsilon_T h/\sqrt{\pi a}\,(1-\nu) \\ &\equiv 1.1\sigma_o h/\sqrt{\pi a} \end{aligned} \tag{A1}$$

where ε_T is the misfit strain, h the coating thickness, E_c its Young's modulus and σ_o the misfit stress. The applied stress σ also induces a stress intensity[33]

$$K = 1.1\sigma\sqrt{\pi a} \tag{A2}$$

By adding the K's and equating to the fracture resistance of the fiber, the stress/crack length relation becomes

$$\sigma = 0.9\sqrt{\frac{E_f\Gamma_f}{\pi a}} - \frac{\sigma_o h}{\pi a} \tag{A3}$$

Differentiating Eqn. (A3) and setting $d\sigma/da = 0$ for the maximum, σ_{max}, gives a fiber strength,

$$S \equiv \sigma_{max} = 0.2\left(E_f\Gamma_f/\sigma_o h\right) \tag{A4}$$

This result applies when S is smaller than the strength S_0 of the uncoated fibers. Fiber strengths as a function of coating thickness for a range of dense and porous oxide coatings are plotted on Fig. 14.

ACKNOWLEDGEMENTS

The authors wish to acknowledge Dr. M. De Graef for helpful discussions and the TEM micrograph shown in Figure 4a.

REFERENCES

[1] J. Aveston, G.A. Cooper and A. Kelly, "Properties of Fibre Composites," *IPC Science and Technology Press*, London, (1971).

[2] D.B. Marshall and A.G. Evans, Overview No. 85, "The Mechanical Behavior of Ceramic Matrix Composites," *Acta Metall. Mater.*, **37 [10]** 2567–2583 (1989).

[3] D.B. Marshall, B.N. Cox and A.G. Evans, "The Mechanics of Matrix Cracking in Brittle-Matrix Fiber Composites," *Acta Metall. Mater.*, **33 [11]** 2013–2021 (1985).

[4] M.Y. He and J.W. Hutchinson, "A Crack Kinking Out of an Interface," *Jnl. Appl. Mech.*, **56**, 270–278 (1989).

[5] H.C. Cao, E. Bischoff, O. Sbaizero, M. Rühle, A.G. Evans, D.B. Marshall and J.J. Brennan, "Effect of Interfaces on the Properties of Fiber-Reinforced Ceramics," *J. Am. Ceram. Soc.*, **73**, 1691 (1990).

[6] S.M. Weiderhorn, "Fracture of Sapphire," *J. Am. Ceram. Soc.*, **52**, 485 (1969).

[7] D.H. Roach, S. Lathabai and B.R. Lawn, "Interfacial Layers in Brittle Cracks," *J. Am. Ceram. Soc.*, **71 [2]** 97–105 (1988).

[8] S.M. Weiderhorn, *Fracture Mechanics of Ceramics*, (Ed., R.C. Bradt *et al.*) Plenum, NY (1974) Vol. 2, p. 20.

[9] T. Mah, K. Keller, T.A. Parthasarathy and J. Guth, "Fugitive Interface Coating in Oxide-Oxide Composites: A Viability Study," *Ceram. Eng. Sci. Proc.*, **12 [9–10]** pp. 1802–15 (1991).

[10] R.W. Rice, "Effects of Inhomogeneous Porosity on Elastic Properties of Ceramics," *J. Am. Ceram. Soc.*, **58 [9–10]** 458–59 (1975).

[11] A.G. Evans, F.W. Zok and J.B. Davis, "The Role of Interfaces in Fiber-Reinforced Brittle Matrix Composites," *Composites Science and Technology* **42**, 3–24 (1991).

[12] M. Rühle and A.G. Evans, "Structure and Chemistry of Metal/Ceramic Interfaces," *Mat. Res. Soc. Symp. Proc. Vol. 120*, (1988) MRS

[13] A.G. Evans and B.J. Dalgleish, *Acta Metall. Mater.*, to be published.

[14] J.B. Davis, H.C. Cao, G. Bao and A.G. Evans, "The Fracture Energy of Interfaces: An Elastic Indentation Technique," *Acta Metall. Mater.*, **39 [5]** 1019–1024, (1991).

[15] P.G. Charalambides, H.C. Cao, J. Lund and A.G. Evans, "Development of a Test Method for Measuring the Mixed Mode Fracture Resistance of Bimaterial Interfaces," *Mech. Mater.*, **8**, 269–283 (1990).

[16] D.B. Marshall, M.C. Shaw and W.L. Morris, "Measurement of Interfacial Debonding and Sliding Resistance in Fiber Reinforced Intermetallics," *submitted to Acta Metall. Mater.*

[17] M.D. Thouless, O. Sbaizero, L.S. Sigl and A.G. Evans, "Effect of Interface Mechanical Properties on Pullout in a SiC-Fiber-Reinforced Lithium Aluminum Silicate Glass Ceramic," *J. Am. Ceram. Soc.*, **72 [4]** 525–532 (1989).

[18] F.E. Heredia, S.M. Spearing, A.G. Evans, P. Mosher and W. Curtin, *J. Am. Ceram. Soc.*, in press.

[19] W.A. Curtin, "Theory of Mechanical Properties of Ceramic-Matrix Composites," *J. Am. Ceram. Soc.*, **74 [11]** 2837–45 (1991).

[20] D.B. Marshall and W.C. Oliver, "Measurement of Interfacial Mechanical Properties in Fiber-Reinforced Ceramic Composites," *J. Am. Ceram. Soc.*, **70 [8]** 542–48 (1987).

[21] P.D. Jero and R.J. Kerans, "The Contribution of Interfacial Roughness to Sliding Friction of Ceramic Fibers in a Glass Matrix," *Scripta Metall. et Mater.*, **24**, 2315-2318 (1990).

[22] T.J. Mackin and P.D. Warren, 'The Influence of Fiber Roughness on the Sliding Behavior of Sapphire Fibers in TiAl and Glass Matrices," *Acta Metall. Mater.*, to be published.

[23] J.B. Davis, E. Bischoff and A.G. Evans, "Zirconia Coatings for Sapphire Fiber-Reinforced Composites," in Advanced Composite Materials, ed. M.D. Sacks, 631-638 (1991).

[24] K.T. Miller, F.F. Lange and D.B. Marshall, "The Instability of Polycrystalline Thin Films: Experiment and Theory," *Mat. Res. Soc. Proc. Sym. on Ultrastr. Proc.*, **121 [3]** 823–30 (1988) and *J. Mater. Res.*, **1 [5]** 151–60 (1990).

[25] S.S. Cole, Jr. and G. Sommer, "Glass-Migration Mechanism of Ceramic-to-Metal Seal Adherence"' *J. Am. Cer. Soc.*, **44[6]** 265-271 (1961).

[26] E. Samuel and P. Hrma, "MoO_2 Diffusion in Aluminosilicate Glass," *J. Am. Ceram. Soc.*, **72 [6]** 1091-92 (1989).

[27] The Metal Molybdenum, Proceedings of a Symposium sponsored by Office of Naval Research., ed. by Julius Harwood (1958) American Society for Metals.

[28] Ductile Chromium and its Alloys, Proceedings of a Conference sponsored by Office of Ordnance Research, (1957) American Society for Metals.

[29] H.E. Dève, A.G. Evans, G.R. Odette, R. Mehrabian, M.L. Emiliani and R.J. Hecht, "Ductile Reinforcement Toughening of γ-TiAl: Effect of Debonding and Ductility," *Acta Metall. Mater.*, **37**, 853-890 (1989).

[30] M. Rühle, K. Burger, W. Mader and A.G. Evans, "Some Aspects of Structures and Mechanical Properties of Metal/Ceramic Bonded Systems," in Fundamentals of Diffusion Bonding, ed. by Y. Ishida, pp. 43–70, (1987) Elsevier, New York.

[31] K.P. Trumble and M. Rühle, "The Thermodynamics of Spinel Interphase Formation of Diffusion-Bonded Ni/Al_2O_3 Interfaces," *Acta Metall. Mater.*, 39 [8] 1915–24 (1991)

[32] M. Rühle, A. Strecker, D. Waidelich and B. Kraus, "*In Situ* Observations of Stress-Induced Phase Transformations in ZrO_2-Containing Ceramics," *Advances in Ceramics*, Vol. 12, ed. by N. Claussen, M. Rühle and A.H. Heuer, pp. 256–74 (1984) American Ceramic Society, Inc.

[33] H. Tada, P.C. Paris and C.R. Irwin, *The Stress Analysis of Cracks Handbook*, Del Research Corp., Pennsylvania (1973).

FIGURE CAPTIONS

Fig. 1. The approach adopted to identify viable fiber coating concepts for brittle matrix composites consisted of developing testing procedures to evaluate the debonding and sliding propensities of various coatings on sapphire.

Fig. 2. ZrO_2 coating/sapphire interfaces produced by the following diffusion bonding schedules:

a) Sol gel coating diffusion bonded at 1300°C for 12 hours with an applied load ~ 1 MPa

b) Sputtered coating diffusion bonded at 1300°C for 12 hours with an applied load ~ 1 MPa

c) Sputtered coating diffusion bonded at 1300°C for 48 hours with an applied load ~ 3 MPa

Fig. 3. a) Extensive bend contours in the sapphire when unstabilized ZrO_2 sputtered coatings were used. It is believed that the contours result from strain in the fiber due to the $t \rightarrow m$ ZrO_2 phase transformation.

b) The bend contours in the sapphire decrease with coating thickness for the unstabilized sol gel ZrO_2 coating.

c) The extent of bend contours was further reduced when thin stabilized sol gel ZrO_2 coatings were used. The remaining stresses are believed to result from CTE mismatch across the well-bonded interface.

Fig. 4. a) A TEM micrograph shows the discontinuous submicron Mo coating on a sapphire fiber in the high purity Al_2O_3 matrix.

b) TEM micrographs of a diffusion bonded Mo/sapphire interface with the lower purity Al_2O_3. A continuous MoO_2 phase occurs adjacent to the sapphire and an amorphous silicate phase exists within the interfacial pores between Mo and the MoO_2 phase.

Fig. 5. a) Shallow ridges were observed on the sapphire surface of a Mo/Sapphire diffusion couple upon debonding.

b) Pronounced ridges on the debonded sapphire surface when an impure W coating was used. The grain boundary impurity phase is composed of Fe and Cr.

Fig. 6. The Mo coating conforms to the surface features of a high-purity polycrystalline Al_2O_3 substrate during diffusion bonding.

Fig. 7. The Cr/sapphire diffusion bond was found to contain a Cr_2O_3 phase adjacent to the interface.

Fig. 8. a) The relative density of oxide coatings plotted as a function of Γ_i/Γ_f clarifies the role of coating porosity in the debonding process.

b) A summary of the interfacial fracture energy measurements for various coatings on sapphire is presented on a "debond map." Coatings which fall within the fiber debonding regime of the map have some potential for sapphire fibers. However, coatings denoted by (*) were found to chemically react with sapphire, these were precluded from further consideration.

Fig. 9. A porous oxide interface led to fiber pull-out of a few fiber diameters. Oxide particles were observed to sinter to the sapphire fiber and remained attached during pull-out. The fracture mirror on the fiber is also visible.

Fig. 10. Short fiber pull-out lengths were observed when Mo coatings were used.

Fig. 11. The surface morphology of the pushed-out sapphire fibers was found to change when the Mo coating was removed by oxidation: a) as-hot pressed condition b) heat treated condition.

Fig. 12. Long fiber pull-out can result when thick (~ 6 μm) Mo coatings are removed by oxidation.

Fig. 13. Fiber push-out curves reveal that the interfacial sliding resistance was decreased to an acceptable level by removing the submicron thick (0.7 μm) Mo coating from the interface.

Fig. 14. The predicted influence of oxide coatings on the strength of sapphire fiber: ρ is the coating density. It is assumed that the uncoated fibers have a strength, S_o = 2.5 GPa.

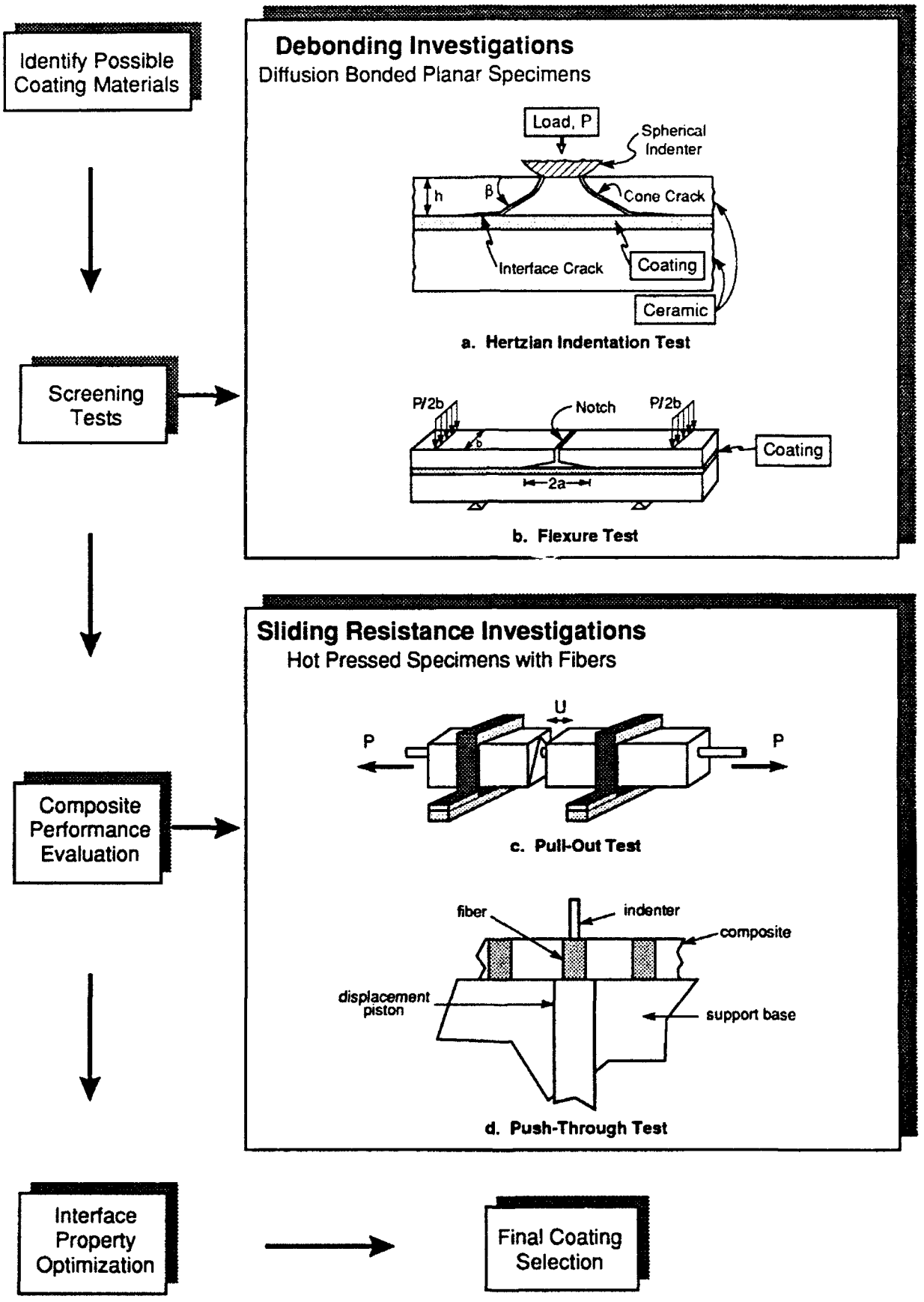
Identify Possible Coating Materials
Debonding Investigations
Diffusion Bonded Planar Specimens
Load, P
Spherical Indenter
h
β
Cone Crack
Interface Crack
Coating
Ceramic
a. Hertzian Indentation Test
Screening Tests
P/2b
Notch
P/2b
b
Coating
2a
b. Flexure Test
Sliding Resistance Investigations
Hot Pressed Specimens with Fibers
U
P
P
c. Pull-Out Test
Composite Performance Evaluation
fiber
indenter
composite
displacement piston
support base
d. Push-Through Test
Interface Property Optimization
Final Coating Selection

Figure 1

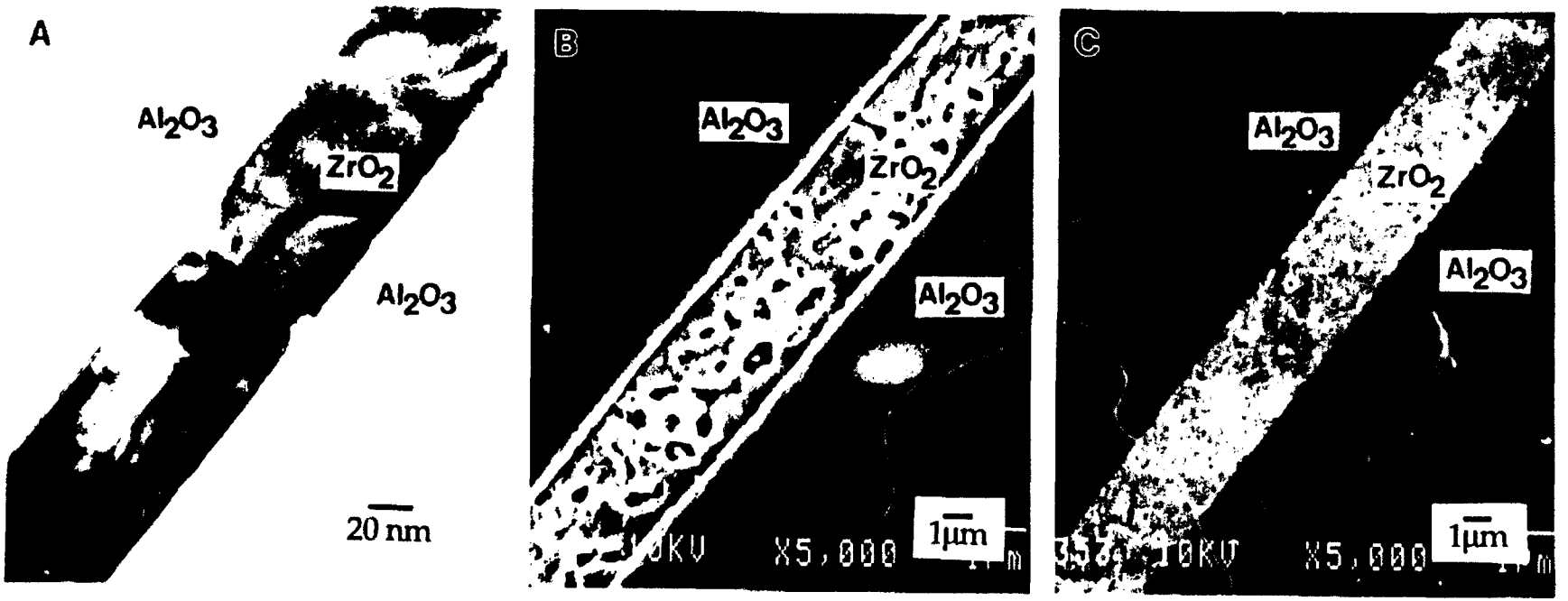
A
Al_2O_3
ZrO_2
Al_2O_3
20 nm
B
Al_2O_3
ZrO_2
Al_2O_3
X5,000
1μm
C
Al_2O_3
ZrO_2
Al_2O_3
X5,000
1μm

Figure 2

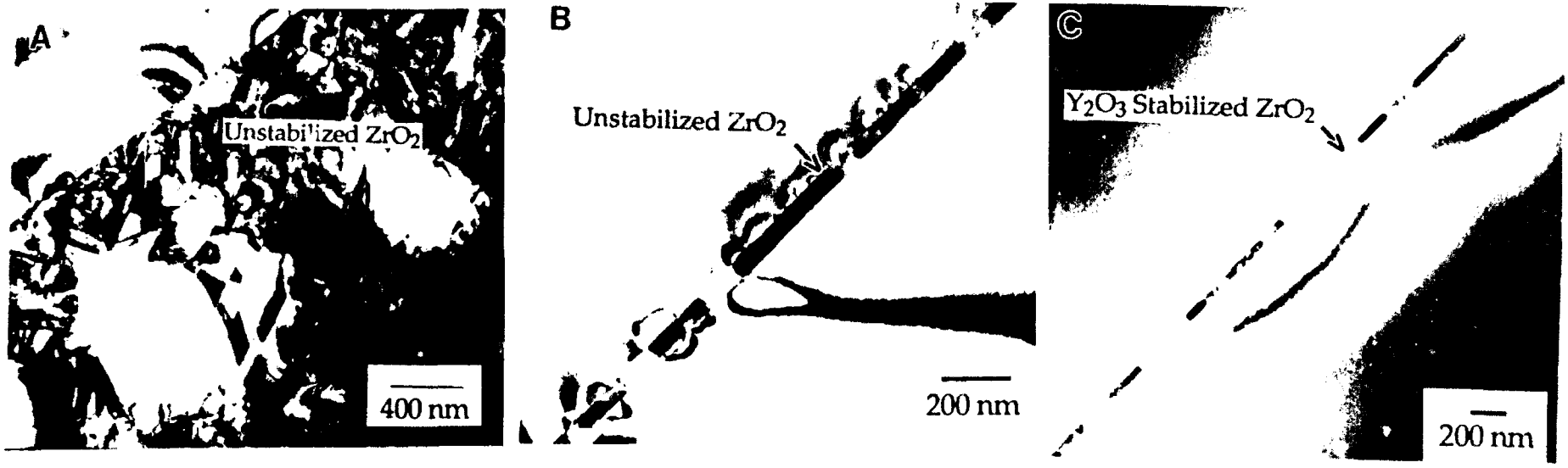
A
Unstabilized ZrO_2
400 nm
B
Unstabilized ZrO_2
200 nm
C
Y_2O_3 Stabilized ZrO_2
200 nm

Figure 3

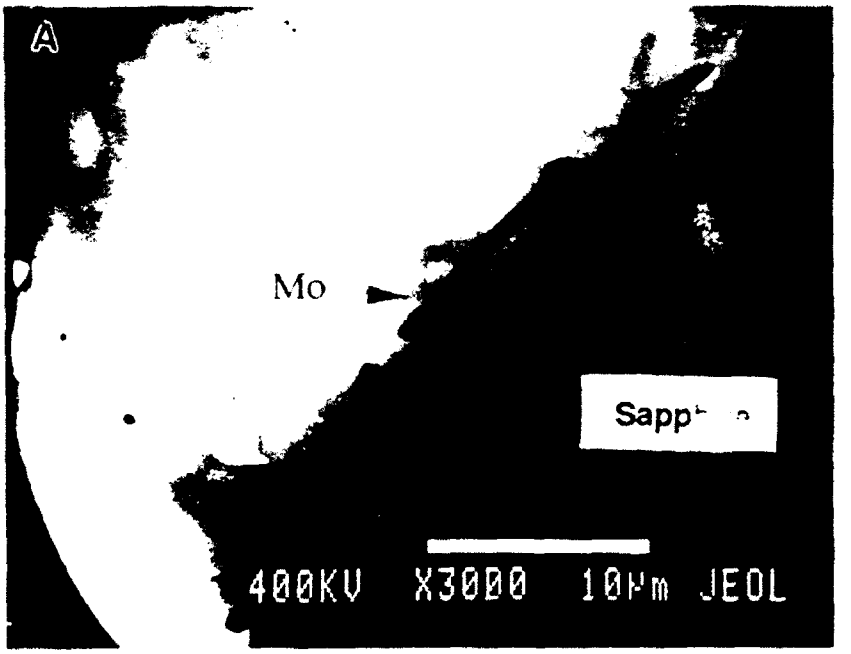

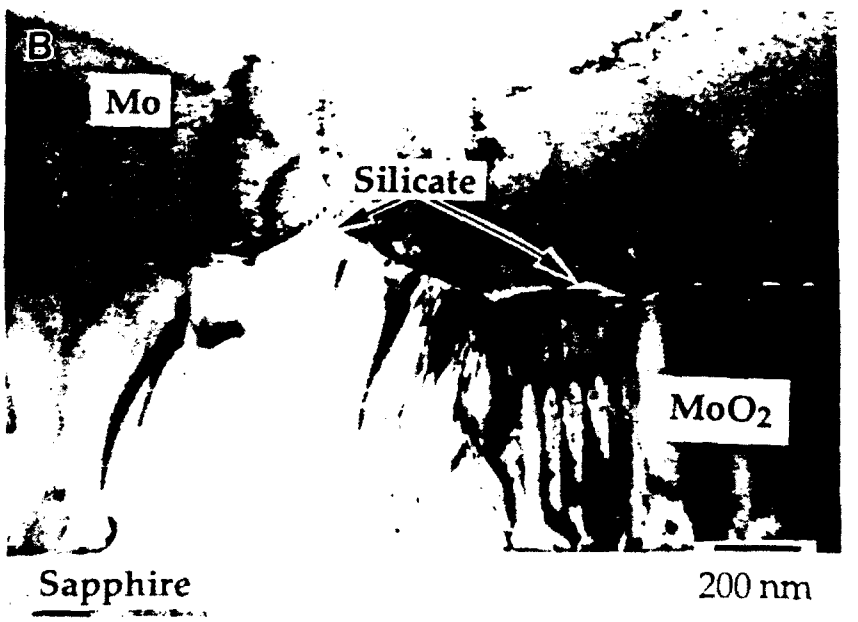

Figure 4

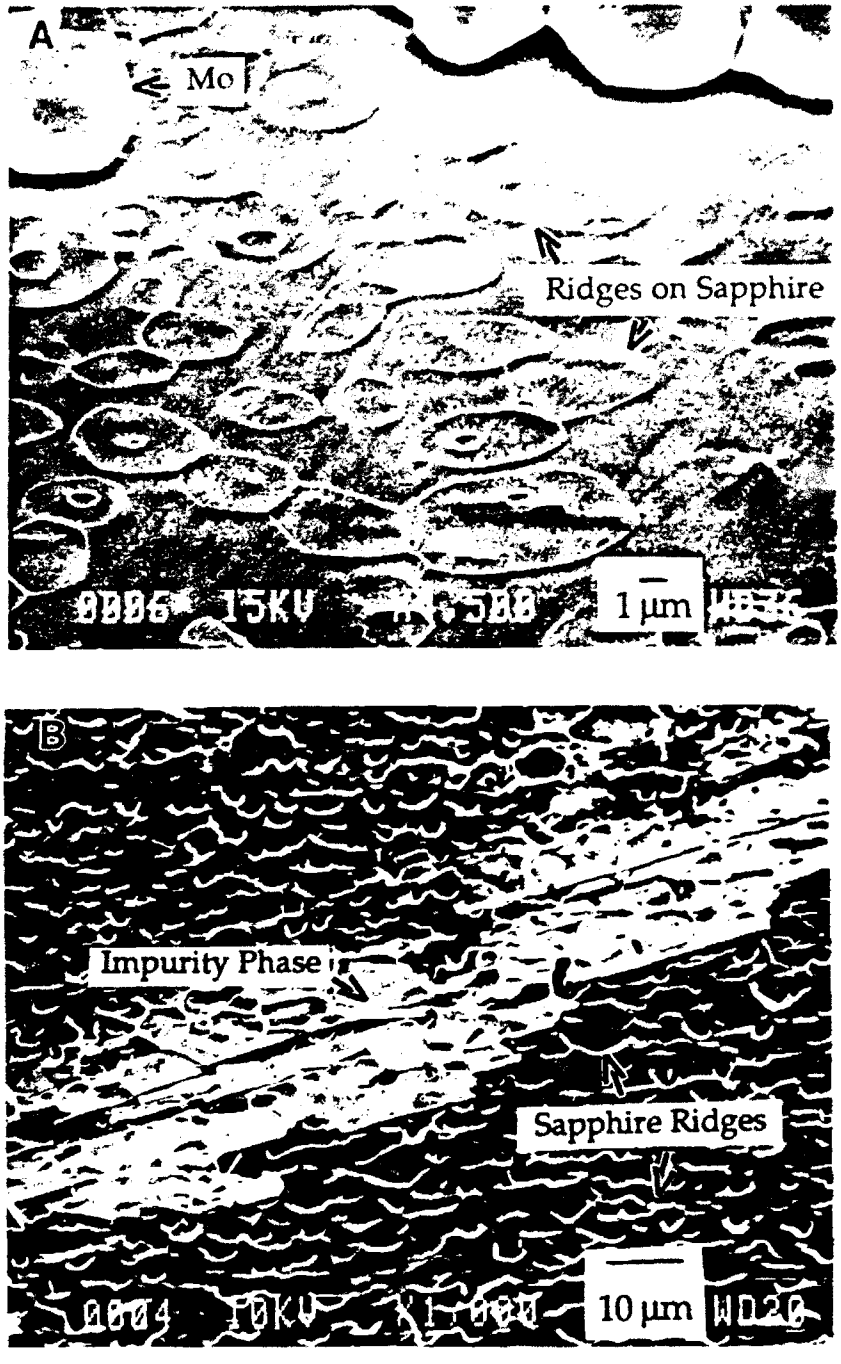
A
Mo
Ridges on Sapphire
1 µm
B
Impurity Phase
Sapphire Ridges
10 µm

Figure 5

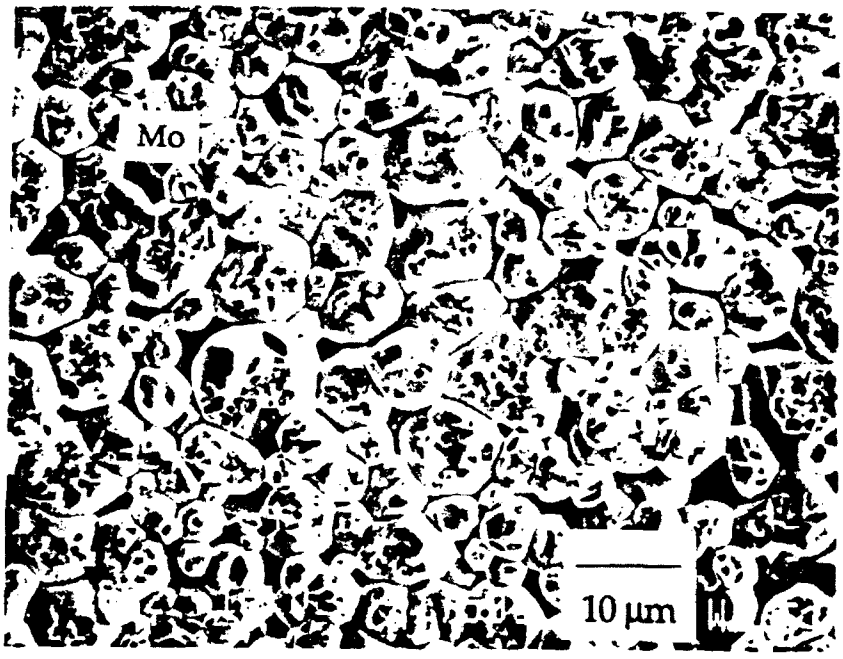

Figure 6

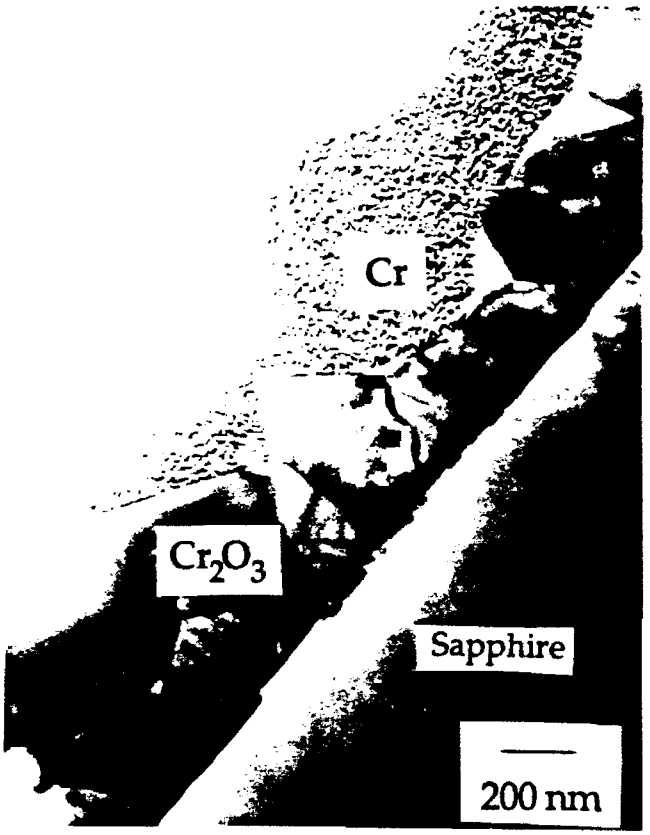

Figure 7

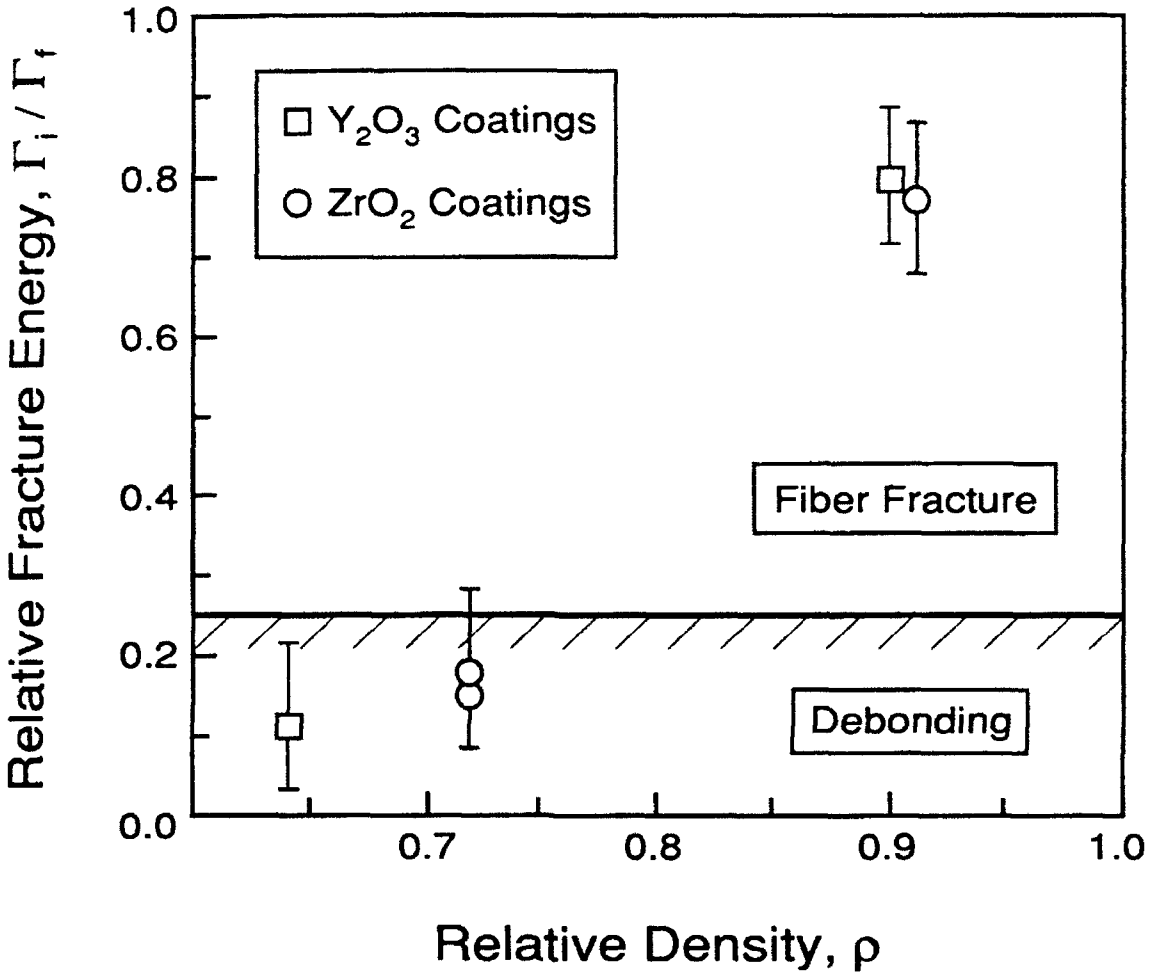
1.0
0.8
0.6
0.4
0.2
0.0
0.7
0.8
0.9
1.0
Relative Fracture Energy, Γ_i / Γ_f
Relative Density, ρ
Y_2O_3 Coatings
ZrO_2 Coatings
Fiber Fracture
Debonding

Figure 8a

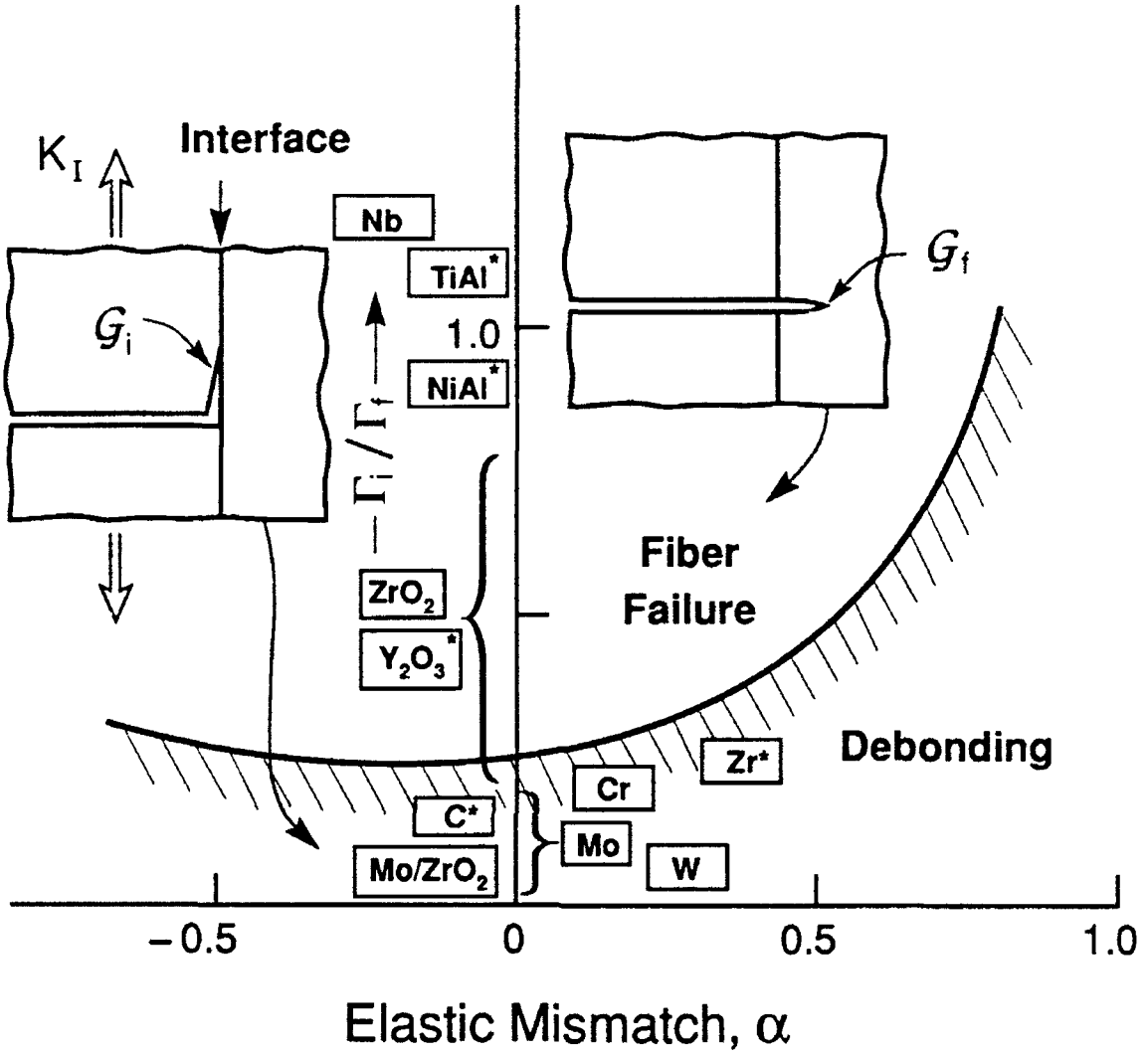
K_I
Interface
Nb
TiAl*
1.0
NiAl*
G_i
G_f
Γ_i / Γ_f
ZrO_2
Y_2O_3*
Fiber
Failure
Debonding
Zr*
Cr
C*
Mo
W
Mo/ZrO_2
−0.5
0
0.5
1.0
Elastic Mismatch, α

Figure 8b

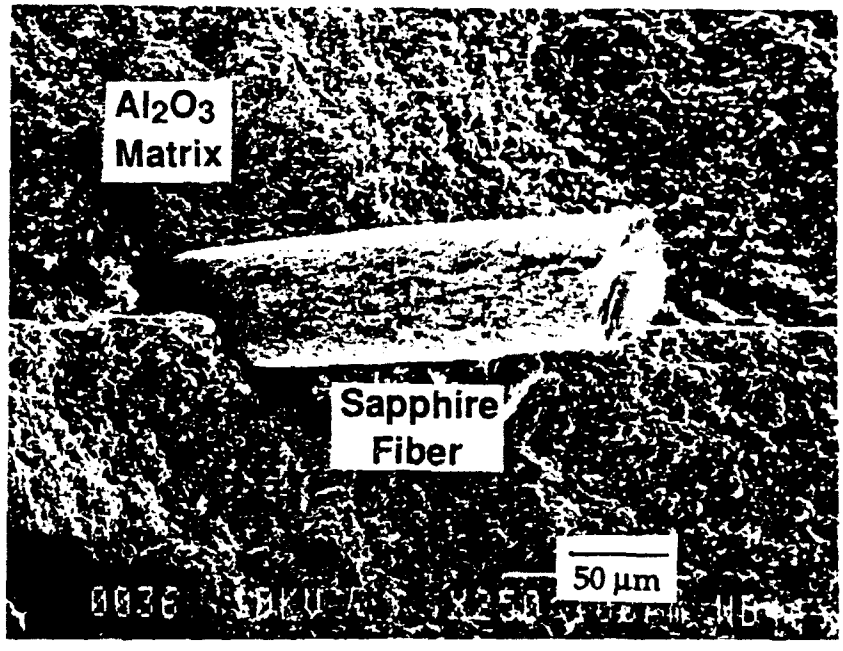

Figure 9

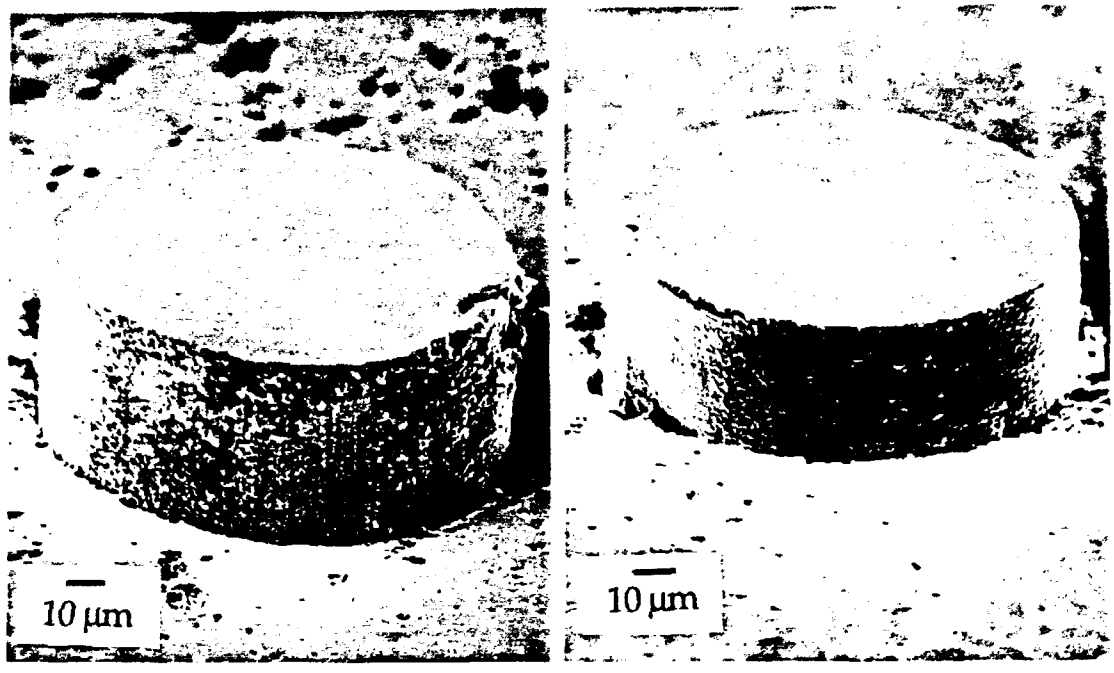

Figure 10

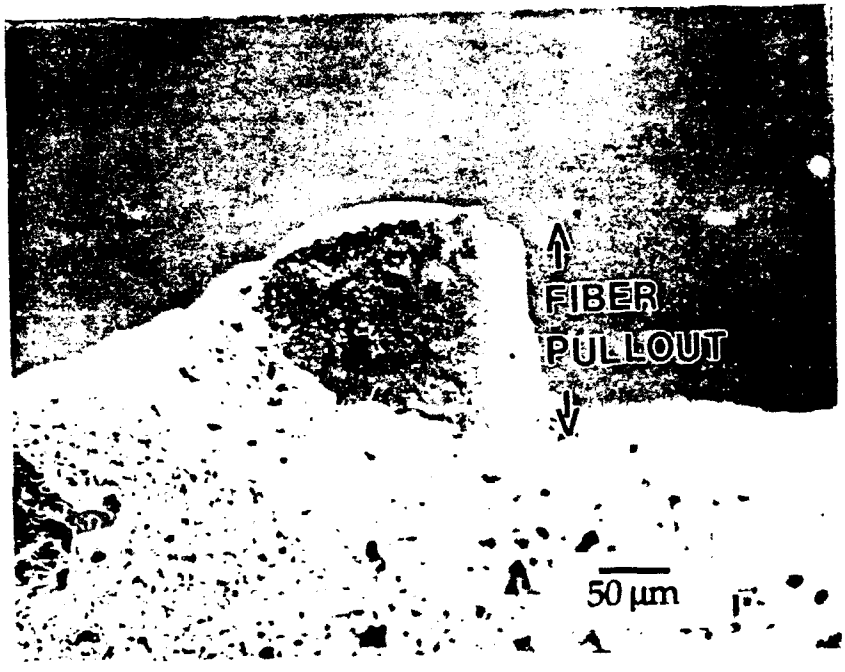

Figure 11

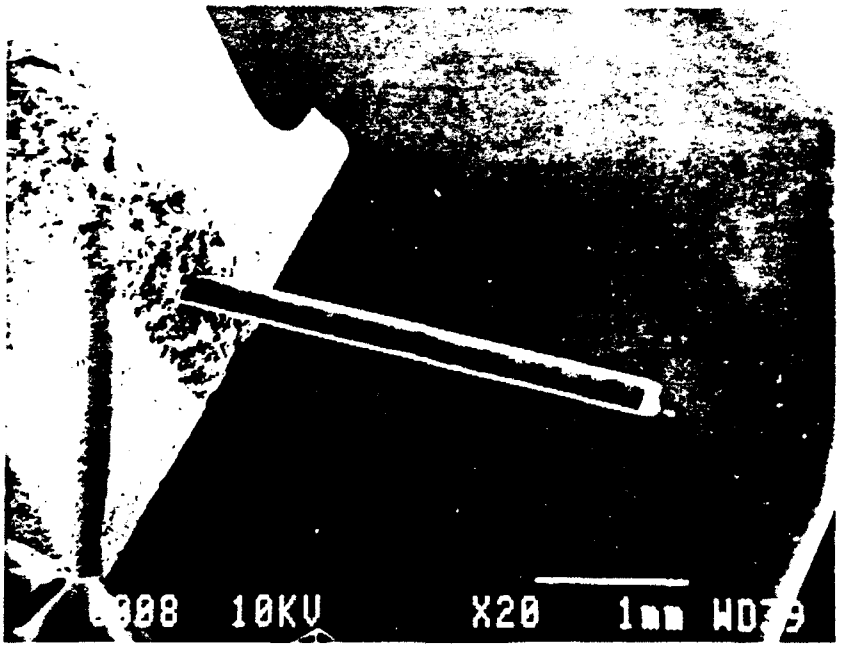

Figure 12

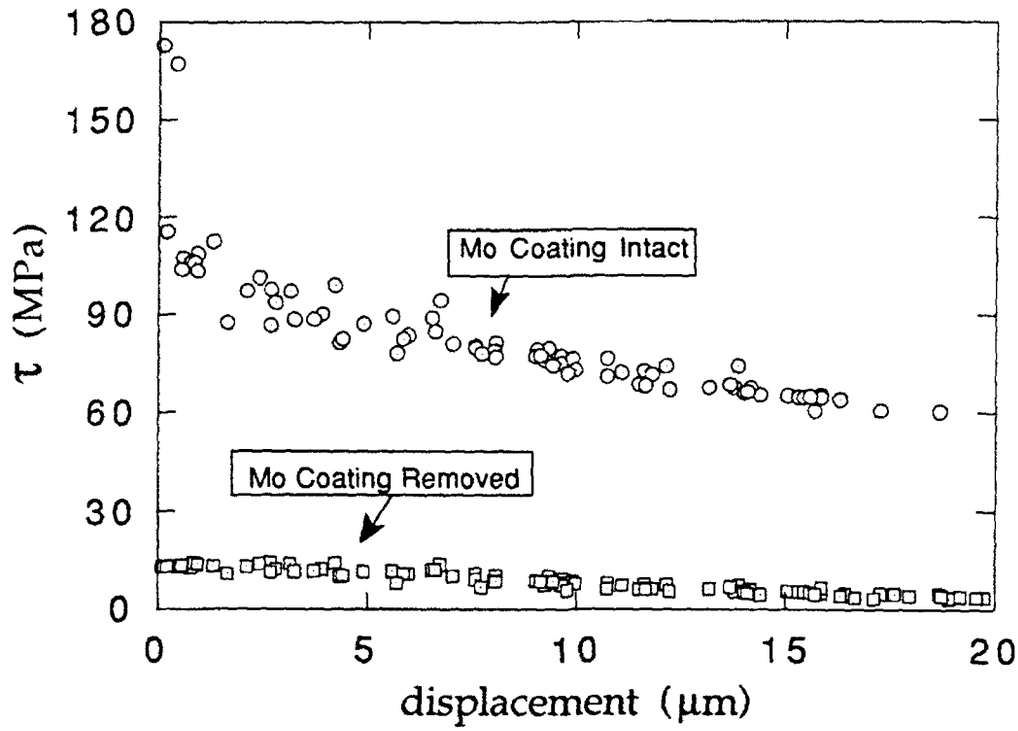
180
150
120
90
60
30
0
τ (MPa)
Mo Coating Intact
Mo Coating Removed
0
5
10
15
20
displacement (μm)

Figure 13

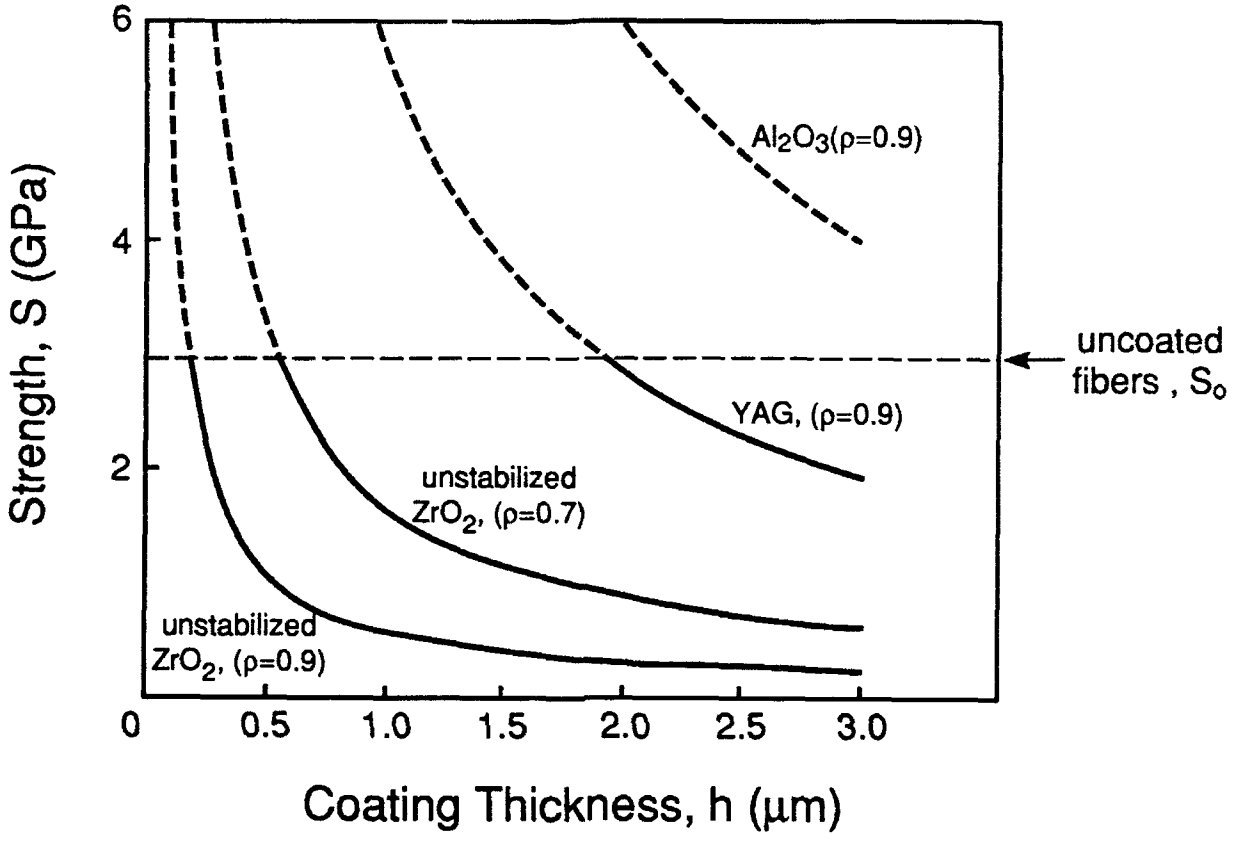
6
4
2
0
0.5
1.0
1.5
2.0
2.5
3.0
Strength, S (GPa)
Coating Thickness, h (μm)
Al2O3(ρ=0.9)
YAG, (ρ=0.9)
unstabilized ZrO2, (ρ=0.7)
unstabilized ZrO2, (ρ=0.9)
uncoated fibers , So

Figure 14

M A T E R I A L S

PRELIMINARY ASSESSMENT OF MICA AS HIGH-TEMPERATURE FIBER COATING FOR SIC COMPOSITES

by

Ana M. Segadães*, Paul D. Warren and Anthony G. Evans
Materials Department
College of Engineering
University of California
Santa Barbara, California 93106-5050

---

* Departamento de Engenharia Cerâmica e do Vidro, Universidade de Aveiro
3800 AVEIRO — PORTUGAL

ABSTRACT

The potential of mica as a fiber coating for SiC fibers in a ceramic matrix composite has been explored. It has been shown that thermochemical effects are involved that degrade a thin layer of the coating upon consolidation. However, beyond the reaction layer, the debonding properties of the mica are retained.

1. INTRODUCTION

The mechanical properties of continuous fiber-reinforced ceramic matrix composites are now known to depend on the interface or coating between the fiber and the matrix [1-7]. The key characteristics of the coating that impart notch tolerance are the fracture energy, Γ_i, compared with that for the fiber, Γ_f, and the sliding resistance, τ, along the debonded faces [4,6,7]. Notably, it is required that $\Gamma_i/\Gamma_f \leq 1/4$ and that the sliding stress be in the approximate range $0 \leq \tau \leq 100$ MPa. This coating characteristics have commonly been achieved using either C or BN coatings [7-10]. Both coatings have problems at high temperature, especially when SiC fibers (*e.g.*, Nicalon) are used, leading to oxidation and embrittlement [1,11]. Various alternatives that might obviate the problem have been proposed for oxide fibers [2], based on the use of i) double coatings of oxides with either certain refractory metals (Mo,W,Cr) or with C; and ii) porous or layered oxides. For non-oxide fibers, such as SiC or Si_3N_4, the problem is more challenging because the fiber is susceptible to oxidation, resulting in SiO_2 layer formation, with an associated volume expansion [11]. One proposal has been to use layered micaceous materials [12]. The intent of this study is to provide a preliminary assessment of the viability of this concept for a SiC/SiC composite.

The study has two specific objectives. The first is to examine the thermochemical compatibility between SiC and a common mica: phlogopite. The second is to measure the fracture energy of a mica layer, diffusion bonded to SiC, subjected to a mode mixity equivalent to that associated with debonding at a crack front [2,4], characterized by a phase angle of $\Psi \approx 50°$.

2. MATERIALS

A "high heat" grade phlogopite* [13] was used and cleaved into sheets of various thicknesses (~65-100μm). X-ray diffraction gave a c-spacing of 10.033 Å, consistent with the $KMg_3(Si_3AlO_{10})(OH)_2$ phlogopite, 1M monoclinic polymorph. The chemical composition, obtained by X-ray fluorescence**, is summarized in Table I. The thermal expansion coefficient was found to be non-linear, with an average of $9.8 \times 10^{-6}/°C$, between 138 and 810°C. The in-plane Young's modulus was determined as 154 GPa, obtained from load-strain measurements in four-point flexure with precision strain gauges bonded to the faces of the specimen. This value compares with 167 GPa calculated for the basal plane using the single crystal elastic constants measured by Simmons *et al* [14] by assuming a hexagonal structure.

Argon sintered α-SiC was used as the other material***. The thermal expansion coefficient was determined to be approximately linear and equal to $4.5 \times 10^{-6}/°C$, between room temperature and ~1100°C. X-ray diffraction indicated a predominantly Moissanite-6H hexagonal polytype.

---

* from UNIMICA Corp., NY.

** Na and K by flame photometry.

*** Hexoloy from Carborundum co., containing some B and C.

Planar SiC/mica interfaces were prepared by sandwiching a thin mica sheet between two lapped silicon carbide plates, followed by heat treatment subjected to uniaxial compression. The heat treatments were conducted in air, at 1100°C for 12 h (6°C/min heating rate, 3°C/min cooling rate), subjected to a stress of ~130 kPa.

3. FRACTURE ENERGIES

Measurements of the fracture energy, Γ_i, have been made using three test geometries (Fig. 1) having the approximate phase angles [15,16] -40, 0 and 45°. The tests performed by wedge loading require independent measurements of crack length [15]. A systematic error is inherent in these measurements, because of the small crack opening displacements. Tests performed with the flexural specimen do not require crack length measurements [16] and are, consequently, more precise. The results are summarized in Fig. 2. Also shown are results obtained in mode I on muscovite [17,18]. The present measurements for phlogopite indicate significantly larger Γ_i than for muscovite.

4. CHARACTERIZATION

Micrographs of the cross-sectioned interface obtained by scanning electron microscopy (Fig. 3) indicated that reaction between the SiC and the mica is limited to a layer < 10 μm thick; otherwise, that the original mica structure is preserved. Super-imposed EDS line scans for Mg, Al and K (Fig. 4) establish that these distinctive mica elements did not diffuse into the SiC. Furthermore, semi-quantitative EDS analysis carried out on interface fracture surfaces (Fig.5) revealed a composition similar to the original mica prior to bonding (Table I). Ultrasonic removal of the mica on either side of the fracture plane provided further details of

the reaction layer (Fig. 6). A convoluted morphology several microns thick suggests that a liquid phase has formed. Semi-Quantitative EDS analysis carried out inside the depressions indicates a SiC spectrum (Fig. 6), whereas, on the plateau, a mica-type spectrum is obtained, but with much decreased Mg content. At higher magnifications, bright white globular crystals are found on the contours of the original mica flakes (Fig. 7): EDS analysis reveals a composition close to olivine, $(Mg,Fe)_2SiO_4$. This is one of the secondary phases expected from phlogopite breakdown, presumably caused by Mg migration from the adjacent depleted layer (the Mg does not diffuse into the SiC, Fig. 4). The reaction seemingly disrupts the mica structure, locally, such that components interact as independent oxides. The major oxide constituents are MgO, Al_2O_3 and SiO_2 (Table I), and for this particular composition, a liquid phase would develop at 1365°C [19], the two solid phases remaining being enstatite ($MgO.SiO_2$) and forsterite ($2MgO.SiO_2$). The presence of the other mica constituents (especially iron oxide and K_2O) reduces the initial melting temperature below the theoretical value of 1365°C.

5. IMPLICATIONS AND CONCLUSIONS

The thermochemical issues associated with the use of mica fiber coatings in SiC/SiC composites, established by the present study, are as follows. A reaction occurs at 1100°C that results in a liquid phase which, in turn, facilitates diffusion bonding. While the associated details have not been addressed, it is apparent that Mg diffusion is involved, as well as dissociation of the mica into its constituent oxides. The reaction layer is several microns thick. However, the integrity of the mica structure appears to be retained beyond this reaction zone. Furthermore, at lower processing temperatures, the reaction layer would undoubtedly be smaller. It is thus concluded that mica coatings are viable, but that thermochemical compatibility

dictates a *minimum coating thickness* in order to retain a discrete mica layer for debonding purposes.

The occurrence of debonding is examined by means of a debond diagram [4] (Fig. 8). This diagram indicates that mica coatings in a SiC composite would allow debonding, *even if they had an isotropic fracture energy*. The anisotropy in Γ_i would further motivate debonding. However, the specifics cannot be addressed without knowledge of the fracture energy *normal to the basal plane.*

In summary, mica appears to have potential as a debond coating in SiC/SiC composites. Some reactions occur that lead to minimum requirements on coating thickness. There are also potential concerns about fiber degradation caused by the reactions. However, the key processing challenge is to orient the basal plane in the mica coatings parallel to the fiber surfaces.

ACKNOWLEDGEMENTS

The present work was supported by US DARPA No.8-482490-25601-3, and by INVOTAN and Calouste Gulbenkian Foundation, Portugal, in the form of post-doctoral scholarships.

References

[1] A. G. Evans and D. B. Marshall, *Acta Metall.* **37** (1989) 2567.

[2] A. G. Evans, F. W. Zok and J. B. Davis, *Composites Science and Technology*, **42** (1991) 3.

[3] R. W. Rice, J. R. Spann, D. Lewis and W. Coblenz, *Ceramic Eng. Sci. Proc.*, **5** (1984) 614.

[4] M.-Y. He and J. W. Hutchinson, *Intl. Jnl. Solid Structures*, **25** (1989) 1053.

[5] H. C. Cao, E. Bischoff, O. Sbaizero, M. Rühle, A. G. Evans, D. B. Marshall and J. J. Brennan, *J. Am. Ceram. Soc.*, **73** (1990) 1691.

[6] J. W. Hutchinson and H. Jensen, *Mech. of Mtls.*, **9** (1990) 139.

[7] R. W. Rice, U. S. Patent No.4642271, Feb. 10 (1987).

[8] D. C. Cranmer, *Am. Ceram. Soc. Bull.*, **68** (1989) 415.

[9] B. A. Bender, D. Lewis, W. Coblenz and R. W. Rice, *Ceramic Eng. Sci. Proc.*, **5** (1984) 1513.

[10] K. M. Prewo and J. J. Brennan, *J. Mater. Sci.*, **15** (1980) 463.

[11] E. Bischoff, M. Rühle, O. Sbaizero and A. G. Evans, *J. Am. Ceram. Soc.*, **72** (1989) 741.

[12] K. Chyung, Corning Research, private communication.

[13] W. A. Deer, R.A. Howie and J. Zussman, "Rock-Forming Minerals", Vol 3: Sheet Silicates, John Wiley & Sons, Inc., New York, 1965.

[14] G. Simmons & H. Wang, "Single Crystal Elastic Constants and Calculated Aggregate Properties", 2nd ed., p.139, MIT Press, Cambridge, MA, 1971.

[15] H. C. Cao and A. G. Evans, *Mech. of Mtls.*, **7** (1989) 295.

[16] P. G. Charalambides, J. Lund, R. M. McMeeking and A. G. Evans, *J. Appl. Mech.*, **14** (1989) 77.

[17] D. H. Roach, S. Lathabai and B. R. Lawn, *J. Am. Ceram. Soc.*, **71** (1988) 97.

[18] K. T. Wan, N. Aimard, S. Lathabai, G. H. Horn and B. R. Lawn, *J. Mater. Res.*, 5 (1990) 172.

[19] E. M. Levin, C. R. Robbins and H. F. McMurdie, "Phase Diagrams for Ceramists", Vol.1, ed. M. K. Reser, The American Ceramic Soc., Columbus, Ohio, 1974.

FIGURE CAPTIONS

Figure 1. Test specimens used to measure the fracture energies at three different phase angles.

Figure 2. Fracture energies of phlogopite as a function of phase angle. Also shown is a literature result for muscovite [17,18].

Figure 3. SEM cross-section view of the SiC/mica/SiC sandwich, showing mica's structural features still present in the mica layer.

Figure 4. EDS line scans for Mg, Al and K on SEM cross-section of the SiC/mica/SiC sandwich.

Figure 5. EDS spectra of (A) phlogopite flakes, on open sandwich, (B) secondary crystals grown on the edges of mica flakes at the interface, and (C) sintered SiC, as seen through holes in the interface.

Figure 6. Reacted mica sheet on the SiC plate, from the mica side: (A) mica flake over the reacted mica sheet; (B) detail of the reacted mica sheet, showing the SiC through the holes in the film.

Figure 7. Reacted mica sheet on the SiC plate: (A) secondary phase crystals grown on the edges of mica flakes; (B) same as A (EDS analysis reveals a composition close to olivine, $(Mg,Fe)_2SiO_4$); (C) same as B, cross-section view.

Figure 8. A debond diagram showing the location of the mica /SiC interface within the debond regime: in this diagram, α is an elastic mismatch parameter [4].

Table I. Chemical compositions (weight %)

A: natural phlogopite, as cleaved (determined by X-ray fluorescence)**

B: phlogopite from open SiC/mica/SiC sandwich, after heat treatment (semi-quantitative EDS)

C SiC from open SiC/mica/SiC sandwich, after heat treatment (semi-quantitative EDS)

D: secondary crystals grown on the edges of mica flakes at the SiC/mica interface, after heat treatment (semi-quantitative EDS)

	MgO	Al_2O_3	SiO_2	CaO	TiO_2	Fe_2O_3*	MnO	Na_2O	K_2O	BaO	Loss on Igni.
A	25.73	15.24	40.57	0.06	1.06	6.44	0.17	0.20	9.06	-	1.17
B	24.49	16.02	44.76	-	-	6.15	-	-	6.84	1.74	-
C	-	-	99.94	-	-	0.05	-	-	0.01	-	-
D	52.60	0.22	46.18	-	-	0.90	-	-	0.08	0.03	-

*total iron

**trace elements: Rb, Ba, Nb

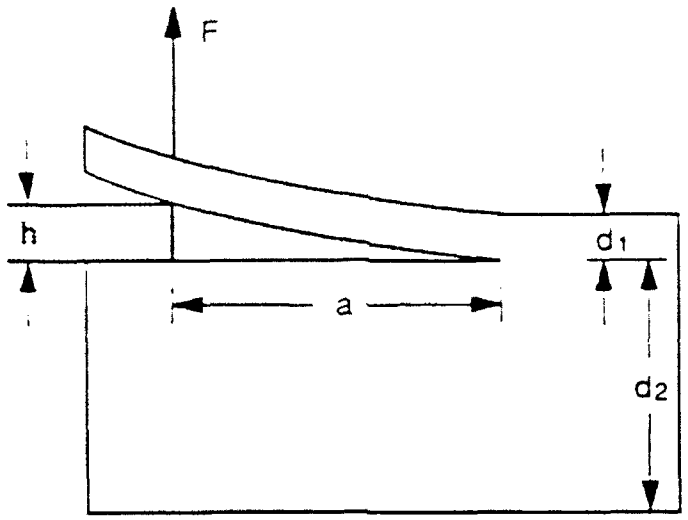

a) Assymetric Beam ($\Psi \approx -40°$ for $d_2/d_1 \approx 10$)

$$G = 3E_{11}h^2d_0^3/4a^4$$

$$(2/d_0^3 = 1/d_1^3 + 1/d_2^3)$$

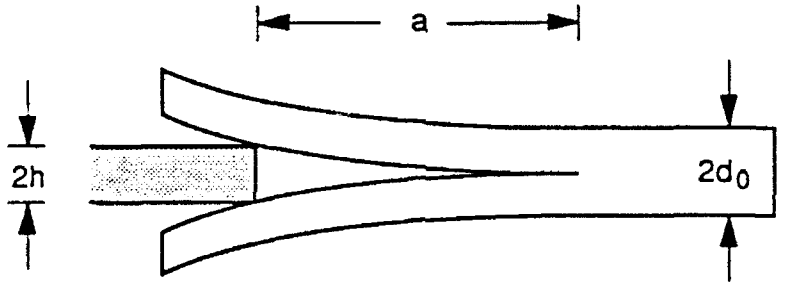

b) Symetric Beam ($\Psi = 0°$)

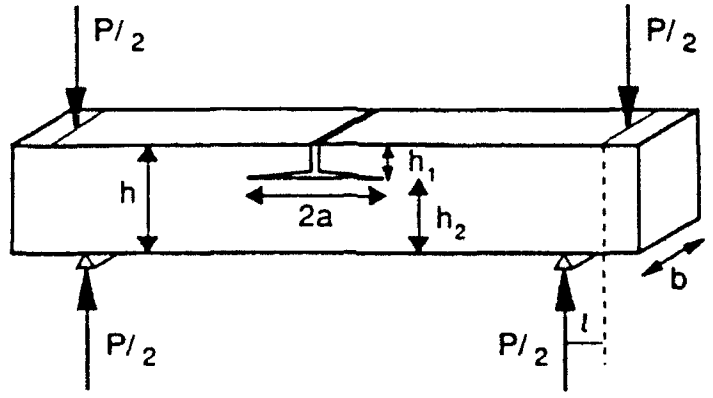

c) Flexure ($\Psi \approx 45°$)

$$G = (3P^2l^2/2b^2E_{11})\,[1/h_2^3 - 1/[h_1^3+h_2^3+3h_1h_2(h_1+h_2)]]$$

Fig. 1

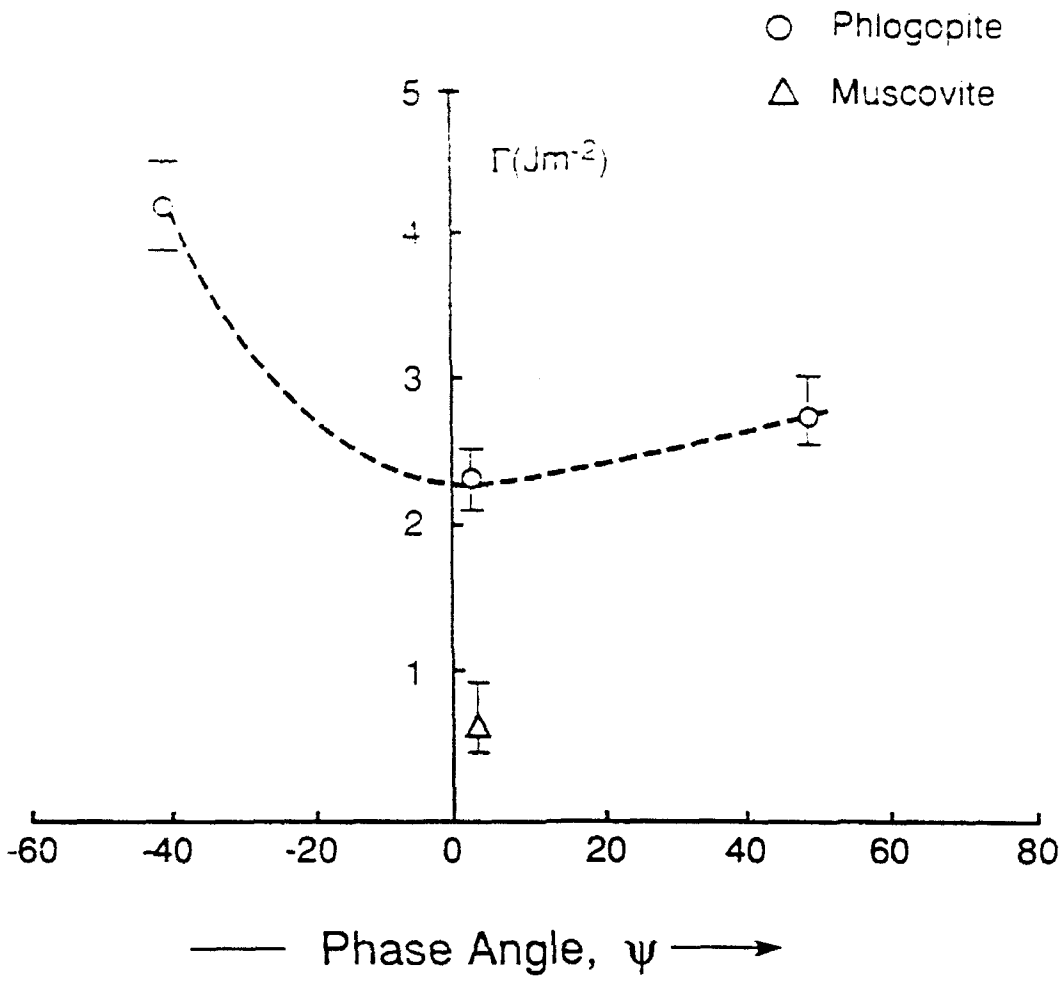
Phlogopite
Muscovite
5
4
3
2
1
Γ(Jm⁻²)
-60
-40
-20
0
20
40
60
80
Phase Angle, ψ

Fig. 2

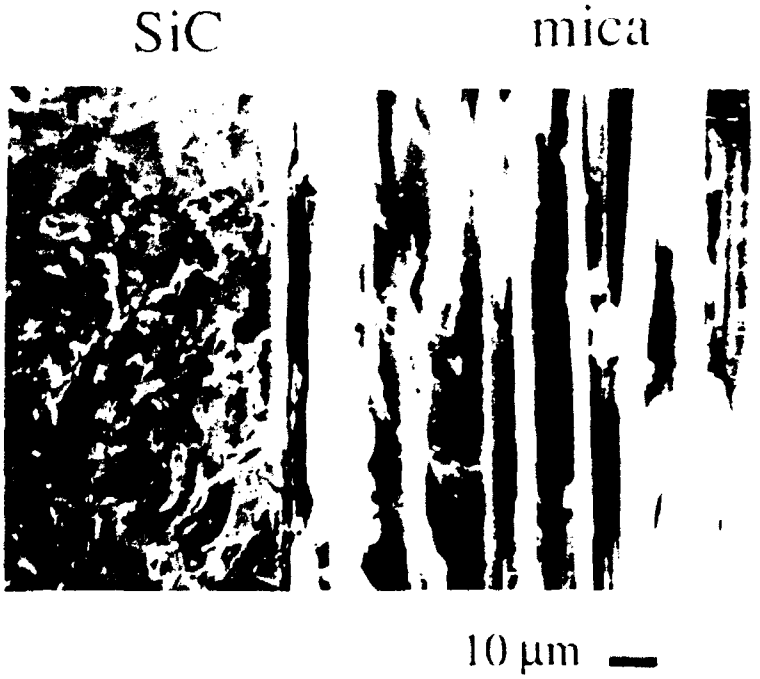

Fig. 3

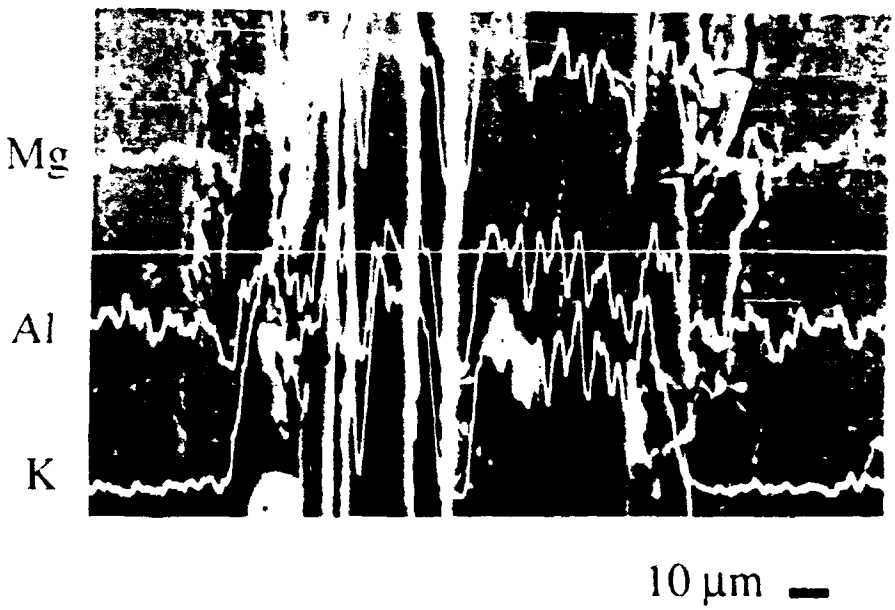

Fig. 4

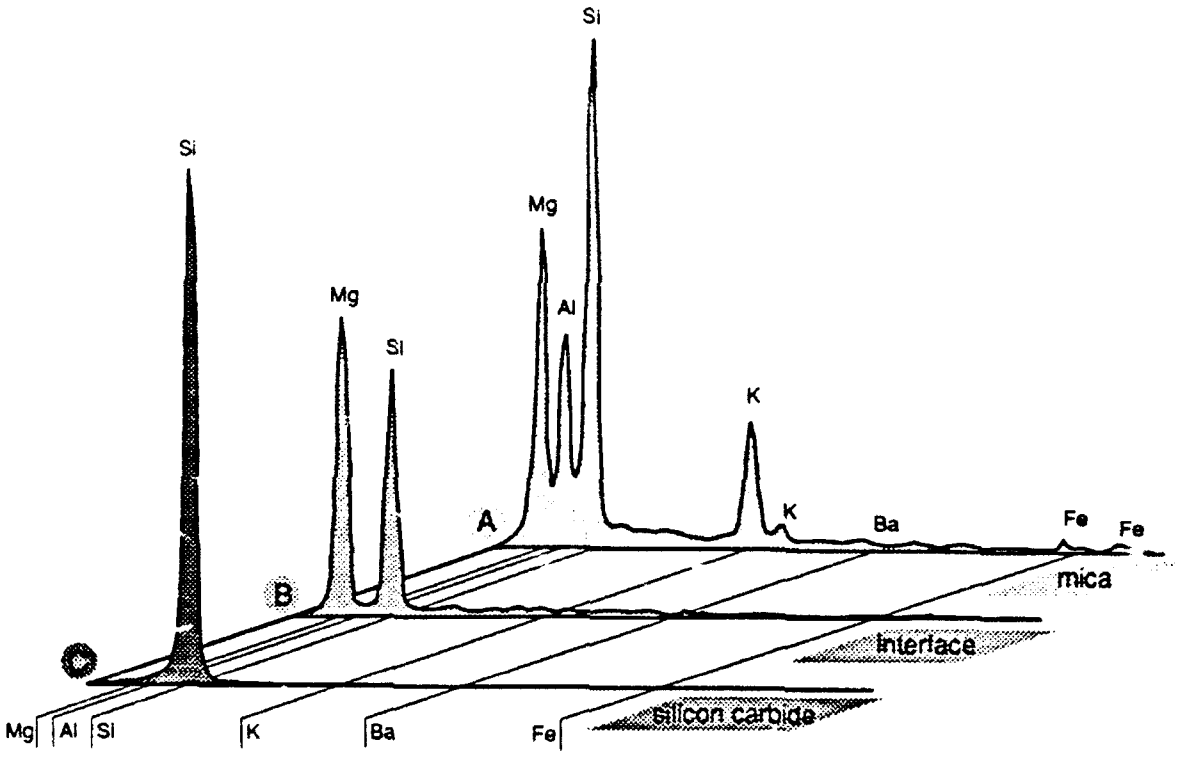
Si
Mg
Si
Si
Mg
Al
K
K
Ba
Fe
Fe
A
B
C
mica
interface
silicon carbide
Mg
Al
Si
K
Ba
Fe

Fig. 5

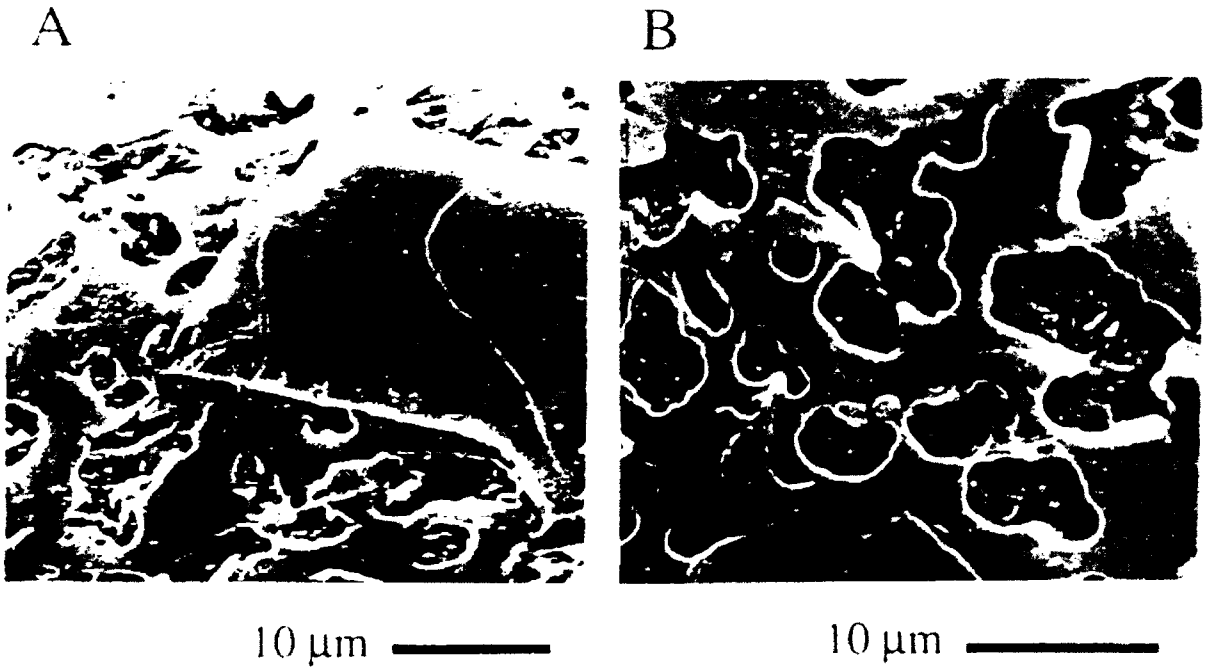

Fig. 6

Fig. 7

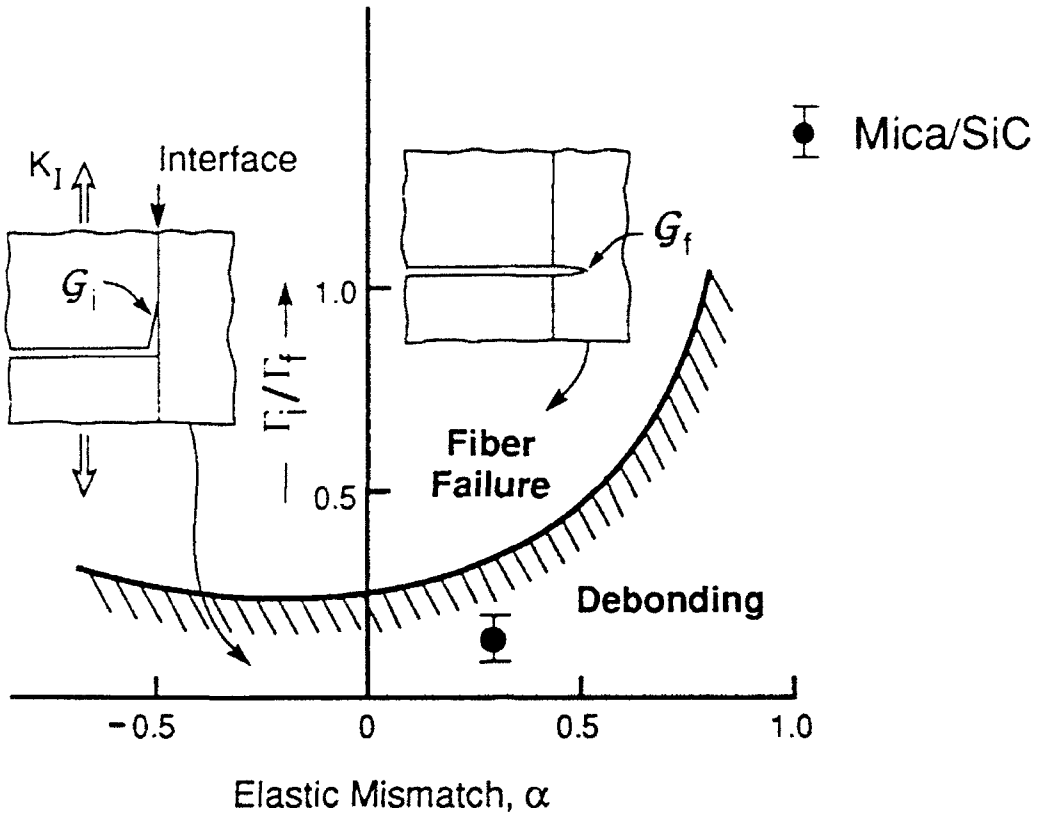
Mica/SiC
K_I
Interface
G_i
G_f
1.0
Γ_i/Γ_f
0.5
Fiber
Failure
Debonding
-0.5
0
0.5
1.0
Elastic Mismatch, α

Fig. 8

MODELS FOR METAL/CERAMIC INTERFACE FRACTURE

Z. Suo

Department of Mechanical and Environmental Engineering
University of California
Santa Barbara, CA 93106

C. F. Shih

Division of Engineering
Brown University
Providence, RI 02912

August 1992

To appear as Chapter 12 in Metal-Matrix Composites
edited by S. Suresh, A. Mortensen and A. Needleman
Butterworth-Heinemann, Stoneham, MA

12.1 INTRODUCTION

Metal-matrix composites are excellent candidate materials for advanced engineering systems. However, one major shortcoming has limited the widespread use of these composites — a tendency to fracture easily. In many systems the low ductility or brittleness is caused by microfailure processes that invariably begin at the interfaces so that the mechanical behavior and the overall performance are not limited by the bulk properties and bulk phases, but by interface properties and toughness. Theories on interface fracture are reviewed in this chapter. With a few exceptions, attention is limited to continuum mechanics considerations. Readers are referred to Rice *et al.* (1989, 1990, 1992) and references therein for atomistic and thermodynamic aspects of the subject. This article is concerned with recent advancess within the confines of small scale inelasticity and loading conditions such that a major portion of the crack faces remains open. We review works on relatively brittle interfaces where the inelastic zone is small compared to the overall component. Large-scale bridging is reviewed by Bao and Suo (1992). Large scale contact has been treated by Hutchinson and Jensen (1990) within the context of fiber pullout against frictional sliding. The focus of this article is on theories. For a broader coverage of topics, the reader is referred to Proceedings of symposia on interfacial fracture. These include those edited by Suresh and Needleman (1989), Rühle *et al.* (1990) and Ashby *et al.* (1992). Experimental aspects of interface fracture and fatigue are reviewed by Evans *et al.* (1990), Kim (1991) and Cannon *et al.* (1992). Several aspects of fatigue are also discussed in a recent article (Woeltjen *et al.*; 1992).

Mechanics of interface fracture has its root in the earlier works of Griffith (1921) and Irwin (1960) on the general theory of fracture, of Williams (1959) on the elastic stress distribution around an interface crack, of England (1963), Erdogan (1963), Rice and Sih (1963) on explicit solutions for interface cracks, and of many practicing engineers on ingenious methods to measure adhesive strength of bonds. However, the subject did not take off until the 1980's. Advanced composites for high temperature engines and layered materials for microelectronic and optical devices have been the main technical driving force for the new theoretical development. Rapid advancement in high resolution microscopes, high speed computers, and the general theory of fracture provide tools for solving these challenging technical problems.

The classical fracture mechanics, as advanced by Irwin (1960), Rice (1968) and Hutchinson (1979), and summarized in the textbook by Kanninen and Popelar (1985), is largely phenomenological. It enables us to predict, without a detailed description of the crack tip processes, crack growth in a structure by utilizing the observed crack growth behavior in a fracture specimen. The approach relies on the existence of stress intensity factor, and on fracture resistance measured by mechanical testing. Both the advantage and the deficiency of this black-box approach originate from the same fact: the approach requires little, nor does

it generate much knowledge of the physical process of fracture.

Mechanism-based fracture mechanics attempts to link the fracture resistance to the microstructural variables, providing guideline for processing better, newer materials. This approach is as old, if not as fully developed, as the phenomenological approach. Indeed, in his original paper, Griffith prescribed both a phenomenological fracture criterion, and a physical mechanism of fracture resistance: rearranging atoms in a bulk into surfaces requires energy. It was eminently clear to Irwin that any form of heat dissipation that accompanies fracture, such as plastic flow in metals, contribute to fracture resistance. But just how the two elements, atomic separation and irreversible atomic movements, are interconnected remains an open question even today. Partial theories, each valid for a particular mechanism at a particular length scale, have been devised, largely in the earlier works by Cottrell (1963) and Rice and Johnson (1970) on hole growth, by Ritchie, Knott and Rice (1973) on cleavage of alloys, and by Aveston *et al.* (1971) on fiber reinforced components. An example of the success of the approach is the thorough understanding of advanced ceramics toughened by ductile particles, or transforming particles, or strong fibers that has been achieved (Evans, 1990). As a by-product of the mechanism-based approach, short cracks, small components and other nagging questions in the framework of classical fracture mechanics can be addressed with a unified, conceptually simple viewpoint (Stump and Budiansky, 1989, Bao and Suo, 1992). The dual approach, phenomenological and mechanism-based, is kept in mind in writing this review article.

The chapter is organized as follows. We review in Section 12.2 the energy consideration for a traction-free interface crack under small-scale inelasticity conditions, leading to the concepts of debond driving force, $\mathcal{G}$, and debond resistance, Γ. Supplemented by elasticity solutions of $\mathcal{G}$ for given components and loading conditions, and experimentally measured Γ for given materials, this energy consideration is sufficient for most engineering applications. Section 12.3 reviews Williams solution for an interface crack between two elastic half spaces. The near-tip stress field lends itself to a precise definition of mode mixity; the near-tip opening sets the condition for small-scale contact. Calibration of fracture specimen is also discussed. Crack-tip plasticity is reviewed in Section 12.4. The relevant mode mixity is the ratio of shear over tension on the interface immediately outside of the plastic zone. The plastic zone size is shown to depend on the mode mixity, so is the opening of the blunted crack tip. An analysis of a metal foil sandwiched between two ceramic plates is included, demonstrating the effect of constrained plastic flow on the fracture resistance. Section 12.5 reviews results on growing cracks and the concepts leading to a fundamental understanding of fracture resistance. Included are growing crack in elastic-plastic materials, crack bridging with or without background plasticity, and cleavage in the presence of plastic flow.

12.2 ENERGY BALANCE

The following energy arguments are essentially the same as those of Griffith (1921) and Irwin (1960). Cracks often run when a test-piece is still predominantly elastic, inelastic deformation being localized in thin layers beneath the crack surfaces. Taking advantage of this fact, one can partition the total energy supplied by the applied work into 1) elastic energy stored in the test-piece and, 2) the heat dissipated by plastic flow and residual energy stored in the thin layers. From the first part comes a definition of debond driving force, $\mathcal{G}$, and from the second debond resistance, Γ. Obviously, this partition becomes meaningless when the inelastic deformation spreads over a large part of the test-piece, either because the test-piece is small, or because the material is very ductile. These have been reviewed elsewhere (Stump and Budiansky, 1989; Bao and Suo, 1992).

12.2.1 Debond Driving Force

Consider an interface crack extending over an area A (Fig. 1). Material near the crack front undergoes inelastic deformation; the interface is usually ill-defined, containing misfit dislocations, interdiffusion zone or reaction compounds. But these zones are typically small compared to the overall dimension of the test-piece, so that the crack front can be treated as a mathematical line, and the interface a mathematical plane. In computing the elastic energy stored in the test-piece, the two solids are taken to be (possibly nonlinearly) elastic. That is, each solid can be described by a strain energy density function $w(\epsilon_{11}, \epsilon_{12}, ...)$, such that stresses σ_{ij} are derived from

$$dw = \sigma_{ij} d\epsilon_{ij}. \tag{2.1}$$

Coupled with equilibrium and compatibility equations, these considerations define an elasticity problem. In particular, stress and strain are computed everywhere in the test-piece, down to the crack front and the interface; likewise the energy density w is computed everywhere. The elastic energy stored in the test-piece is an integral extended over the entire test-piece, i.e.

$$U = \int_V w dV. \tag{2.2}$$

The test-piece in Fig. 1 is loaded by displacement D, with work-conjugating force F. The elastic energy U depends on applied displacement and the crack size, i.e.

$$U = U(D, A). \tag{2.3}$$

Note that U also depends on the geometry of the test-piece and elastic moduli, but they remain constant during testing.

Upon loading, U varies as

$$dU = F dD - \mathcal{G} dA. \tag{2.4}$$

With crack size held fixed, i.e. $dA = 0$, the above equation simply states that the energy increment equals the work applied. Since all the other quantities are defined, (2.4) defines the quantity $\mathcal{G}$ when $dA \neq 0$. Just as F is the driving force for D, $\mathcal{G}$ is the driving force for crack size A. Explicitly, $\mathcal{G}$ is the decrease of elastic energy associated with a unit increment of crack area:

$$\mathcal{G} = -\frac{\partial U(D, A)}{\partial A}. \tag{2.5}$$

Note that $\mathcal{G}$ has dimension energy/area.

The above concepts can be explained graphically. Figure 2a shows a load-displacement curve of the test-piece measured with fixed crack size ($dA = 0$). The curve should be straight for linear elastic materials. From (2.4), U is the area under the load-displacement curve. Figure 2b shows two such load-displacement curves, measured in two independent tests with slightly different crack sizes, A and $A + dA$. The test-piece with the larger crack is more compliant; the shaded area is the energy decrease, dU, associated with dA. In early days, this graphical interpretation was employed to experimentally determine $\mathcal{G}$ (e.g. Rivlin and Thomas,1953).

Standard thermodynamics manipulations apply to the present discussions. For load controlled tests, for example, it is more convenient to work with the potential energy

$$\Pi = U - FD, \tag{2.6}$$

which is indicated in Fig. 2a. The independent variables are now F and A. Upon loading, (2.4) becomes

$$d\Pi = -DdF - \mathcal{G}dA. \tag{2.7}$$

An alternative definition of $\mathcal{G}$ is therefore

$$\mathcal{G} = -\frac{\partial \Pi(F, A)}{\partial A}. \tag{2.8}$$

The definitions (2.5) and (2.8) are of course equivalent.

For an interface along the x_1-axis, and with displacement and traction continuous across the interface, Rice's $J-$integral (1968)

$$J = \int (wn_1 - n_i \sigma_{ij} u_{j,1}) ds \tag{2.9}$$

vanishes over contours not enclosing any singularity. For a traction-free crack on the interface, $\mathcal{G}$ equals the $J-$integral over any path that begins at a point on the lower crack face, and ends at another point on the upper crack face. This provides a tool for calculating $\mathcal{G}$ in finite element analysis (e.g. Moran and Shih, 1987).

In general, $\mathcal{G}$ can be computed with an elasticity analysis of a given test-piece. Several illustrations requiring only elementary mechanics are given. Solutions to a wide range of geometries can be found in Hutchinson and Suo (1992) and the references therein.

Consider a fiber being pulled out of a matrix (Fig. 3). The energy stored in the fiber can be estimated by regarding the fiber as a tensile bar, clamped at the debond front. The pullout displacement is $D = L\sigma/E$, so that $U = (\sigma^2/2E)(\pi R^2 L)$. The potential energy is

$$\Pi(\sigma, L) = -\frac{\sigma^2}{2E}\pi R^2 L. \tag{2.10}$$

Since the debond area is $A = 2\pi RL$, the carrying out the differentiation in (2.8) gives

$$\mathcal{G} = R\sigma^2/4E. \tag{2.11}$$

The estimate, which ignores the compliance of the fiber-matrix junction, is accurate when the debond length is large compared to the fiber diameter. Observe that $\mathcal{G}$ does not depend on the debond length L. Once debond starts, it will run to the other end of the fiber without any increase in load.

Thin film cracking of many patterns has inspired a new problem area, e.g. Evans *et al.* (1988) and Hutchinson and Suo (1992). Figure 4 illustrates a circular interface crack emanating from the edge of a hole in a thin film, driven by a residual tensile stress in the film. The stress in the debonded film is partially relieved, leading to a reduction in the elastic strain energy. The debonded film may be treated as a ring in plane stress, clamed at the debond front. The energy release rate is found to be (Farris and Bauer, 1988)

$$\mathcal{G} = \frac{2hE\epsilon_0^2}{1-\nu^2}\left[1 + \frac{1-\nu}{1+\nu}\left(\frac{a}{a_0}\right)^2\right]^{-2}, \tag{2.12}$$

where ϵ_0 is the mismatch strain between the film and the substrate caused by thermal or epitaxial mismatch, a_0 is the hole radius, a is the debond radius, and E and ν are the elastic constants of the film. Observe that $\mathcal{G}$ decreases rapidly as a increases, so that the debond is stable. Also note that $\mathcal{G}$ scales linearly with film thickness h: the thinner the film, the smaller the decohesion area. Debond can be practically suppressed if the film is sufficiently thin.

12.2.2 Debond Resistance

The essential idea of Griffith and Irwin is illustrated in Fig. 5. Inelastic processes, such as atomic separation, twinning, phase transformation and dislocation motion, require sufficiently high stress to activate, so they are confined to a region close to the crack tip where the stress is intensified. As the crack front extends, thin layers beneath the crack surface are left in the wake in which the atoms have undergone irreversible movements. The processes near the tip

are complex and the quantification requires detailed knowledge of deformation mechanisms. Nonetheless, an effectivelyuniform deformation state along the x_1-axis is attained in the wake. Consider two cylinders of unit cross-sectional area normal to the interface, one far ahead of the crack front (A), and the other far behind (B). Let Γ be the energy spent to transform cylinder A to cylinder B. Obviously Γ depends on the deformation history that cylinder B underwent, including surface energy, heat dissipation and elastic energy trapped in the wake.

The total energy variation, elastic as well as inelastic, is given by

$$FdD - \mathcal{G}dA + \Gamma dA. \tag{2.13}$$

When D is held fixed, no work is externally applied to the test-piece; the total energy remains unchanged, so that

$$\mathcal{G} = \Gamma. \tag{2.14}$$

The driving force $\mathcal{G}$ depends on the test-piece and can be evaluated by an elastic stress analysis. Fracture resistance Γ depends on the inelastic mechanisms. Equation (2.14) provides a connection between the macroscopic loading condition of a test-piece and the microscopic inelastic process associated with debonding.

Debond resistance can be measured phenomenologically. For example, this can be carried out using fiber pullout experiment shown in Fig. 3. The stress required to drive debond is measured, which can be translated to Γ using (2.11) and noting (2.14). This approach is purely phenomenological—no detailed knowledge of physical pro ses is required, nor is such knowledge generated. Nevertheless, the key quantity, debond resistance Γ, is measured and this can be used in device design. Debond resistance has been measured for a range of bimaterials for applications to thin films and fiber/matrix composites (Evans *et al.*, 1990; Cannon *et al.*, 1992).

In principle, test-pieces of any geometry can be used to measure debond resistance. Several convenient geometries are sketched in Fig. 6. It has been observed experimentally that debond resistance depends on the geometry of the test-piece. Specifically, debond resistance depends on the ratio of the sliding to normal loading parameterized by ψ:

$$\Gamma = \Gamma(\psi). \tag{2.15}$$

Mode mixity ψ will be elaborated upon later. The trend of the curve is shown in Fig. 6. The double cantilever beam is predominantly opening mode ($\psi \approx 0°$) and the measured debond resistance is low. The fiber pullout is shear dominant ($\psi \approx 70°$), giving a high debond resistance. The other two, four-point bend and micro-indentation, produce nearly equal amount of opening and shear ($\psi \approx 45°$), representative of the conditions in thin film

delamination and fiber/matrix debonding. Micro-indentation is particularly convenient for small samples (Davis *et al.* 1991). Other geometries have also been used to measure debond resistance (Argon *et al.*, 1989; Kim, 1991; Liechti and Chai, 1992; O'Dowd *et al.*, 1992a; Thouless 1990; Wang and Suo, 1990).

The dependence of Γ on loading phase can be understood on the basis of inelastic mechanisms. For example, the fiber pullout experiment is dominated by shearing and the friction adds to the debond resistance. This mechanism has been examined quantitatively by Hutchinson and Evans (1989). In metal/ceramic interfaces, shear dominated loading produce larger plastic zones which increase debond resistance (O'Dowd *et al.*, 1992b).

12.3 WILLIAMS SINGULARITY

This section collects mathematical details that refine the concept of mode mixity. The two solids are linearly elastic and isotropic; corresponding results for anisotropic elasticity have been reviewed elsewhere (Suo, 1990). The inelastic region is taken to be small compared to all other relevant dimensions of the crack geometry, so that the crack front is a mathematical line, the interface a mathematical plane, and the crack semi-infinite. The crack faces are traction-free. This eigenvalue problem was solved by Williams (1959). The essential features of the solution, stress oscillation and crack face contact, are described below. The following interpretation is largely due to Rice (1988).

12.3.1 Slow Oscillation in Stress Field

The tractions at a distance r ahead of the crack tip, on the interface, are found to be

$$\sigma_{yy} + i\sigma_{yx} = \frac{Kr^{i\varepsilon}}{\sqrt{2\pi r}}. \tag{3.1}$$

In the above, x and y are Cartesian coordinates centered at the tip and $i = \sqrt{-1}$. The bimaterial constant ε is defined by

$$\varepsilon = \frac{1}{2\pi}\ln\left[\frac{(3-4\nu_1)/\mu_1 + 1/\mu_2}{(3-4\nu_2)/\mu_2 + 1/\mu_1}\right]. \tag{3.2}$$

Here ν is Poisson's ratio, μ the shear modulus, and subscripts 1 and 2 refer to material 1 and 2, respectively; the constant ε is bounded, $|\varepsilon| < (1/2\pi)\ln 3 \approx 0.175$.

The complex-valued stress intensity factor, K, cannot be determined by the eigenvalue problem, but can be determined by solving the full boundary-value problem for a given testpiece. The magnitude of K scales with the applied stress, and the phase angle of K represents the relative amount of shear to tension. It can be seen from (3.1) that K has dimensions

$$K = [\text{stress}]\,[\text{lengh}]^{1/2-i\varepsilon}. \tag{3.3}$$

Let $\hat{L}$ be an *arbitrary* length, and define $\hat{\psi}$ by

$$K = |K|\hat{L}^{i\varepsilon}\exp(i\hat{\psi}). \tag{3.4}$$

The magnitude, $|K|$, has the dimension stress $\times$ length$^{1/2}$, which is independent of the choice of $\hat{L}$, because $|\hat{L}^{i\varepsilon}| = 1$. Indeed, $|K|$ is related to $\mathcal{G}$ by (Malyshev and Salganik, 1965)

$$\mathcal{G} = \frac{1}{4}\left(\frac{1-\nu_1}{\mu_1} + \frac{1-\nu_2}{\mu_2}\right)\frac{|K|^2}{\cosh^2\pi\varepsilon}. \tag{3.5}$$

Consequently, $|K|$ and $\mathcal{G}$ are equivalent quantities characterizing the magnitude of the applied load.

Next examine the significance of $\hat{\psi}$. Combining (3.1) and (3.4) yields

$$\sigma_{yy} + i\sigma_{yx} = \frac{|K|}{\sqrt{2\pi r}}\exp[\hat{\psi} + \varepsilon\ln(r/\hat{L})]. \tag{3.6}$$

The identity, $(r/\hat{L})^{i\varepsilon} \equiv \exp[i\varepsilon\ln(r/\hat{L})]$, is used in the above. From (3.6) the ratio of shear stress to tensile stress at a distance r ahead of the crack tip is given by

$$\sigma_{xy}/\sigma_{yy} = \tan[\hat{\psi} + \varepsilon\ln(r/\hat{L})]. \tag{3.7}$$

Observe that the traction ratio varies with position r, and $\tan\hat{\psi}$ equals the ratio of the shear stress to the tensile stress at $r = \hat{L}$. This feature of interface cracks, caused by elastic mismatch, does not exist in mixed mode fracture in homogeneous materials. The result in (3.7) is commonly referred to as the oscillatory singularity, and ε the oscillation index. Contrary to a popular misconception, this oscillation is *not* rapid, since ε is small, and logarithm a slowly varying function. Thus, in specifying mode mixity, $\hat{L}$ need not be precisely defined, so long as it is broadly representative of the length scale of interest.

Up to this point, $\hat{L}$ has not been given any physical identity. Since Williams elastic solution describes the stress state outside of the inelastic zone, it is sensible to specify $\hat{L}$ to be on the order of the inelastic zone size. For example, in discussing dislocation emission from an atomistically sharp crack tip, a natural choice of $\hat{L}$ is atomic spacing, so that $\hat{\psi}$ describe the stress state over several atomic spacing (Rice *et al.*, 1990). For a metal/ceramic interface, where dislocation motion prevails over distances many times of the lattice constants, $\hat{L}$ should be chosen as the plastic zone size. Given two choices L and $\hat{L}$, the corresponding loading phases, ψ and $\hat{\psi}$, shift by

$$\psi - \hat{\psi} = \varepsilon\ln(L/\hat{L}). \tag{3.8}$$

Debond resistance Γ should depend on stress state surrounding the inelastic zone, which in turn is characterized by the local phase angle $\hat{\psi}$. Consequently, (2.15) can be rewritten in a more rigorous form:

$$\Gamma = \Gamma(\hat{\psi}). \tag{3.9}$$

Since the size of the inelastic zone is dependent on fracture mechanisms, ranging from nanometers to centimeters, it is meaningless to employ a single $\hat{L}$ for all bimaterials. For interfaces with debond resistance sensitive to mode mixity, the value of $\hat{\psi}$, together with $\hat{L}$, must be reported together with the value of Γ. Moreover, a common $\hat{L}$ must be used in the definition of $\hat{\psi}$ when comparing toughness values at different mode mixities.

12.3.2. Small-Scale Contact

In a homogeneous material, crack faces come into contact under compression. By contrast, interface crack faces may come into contact regardless of loading condition. The size of the contact zone depends on the mode mixity. In composites, the fiber and the matrix may remain in contact due to the residual compression or asperities, sliding against friction during pullout. This provides an example of large-scale contact (Hutchinson and Jensen, 1990). In many other technical problems, such as thin film decohesion, contact zone is small compared to the overall dimension. This section provides a criterion for small-scale contact.

Williams elastic solution shows that the displacement jump at a distance r behind the crack tip is

$$\delta_y + i\delta_x = \left(\frac{1-\nu_1}{\mu_1} + \frac{1-\nu_2}{\mu_2}\right) \frac{K r^{i\varepsilon}}{(1+2i\varepsilon)\cosh\pi\varepsilon} \sqrt{\frac{2r}{\pi}}. \tag{3.10}$$

From the above, the crack opening is

$$\delta_y = \delta\cos[\hat{\psi} + \varepsilon\ln(\hat{L}/r) - \tan^{-1}(2\varepsilon)], \tag{3.11}$$

where $\delta = (\delta_x^2 + \delta_y^2)^{1/2}$ is the magnitude of the displacement jump. If $\hat{L}$ is interpreted as the process zone size, and if the crack is required to remain open, i.e. $\delta_y > 0$, within $\hat{L} < r < 100\hat{L}$, the mode mixity must be confined within

$$\begin{aligned} -\pi/2 + 2\varepsilon < \hat{\psi} < \pi/2 + 2.6\varepsilon \qquad & \text{for} \quad \varepsilon > 0, \\ -\pi/2 - 2.6\varepsilon < \hat{\psi} < \pi/2 + 2\varepsilon \qquad & \text{for} \quad \varepsilon < 0. \end{aligned} \tag{3.12}$$

The number 100 is arbitrary, but the condition (3.12) is not sensitive to this number. When $\varepsilon = 0$, the condition in (3.12) simply states that contact will not occur under tension, which is known for homogeneous materials.

12.3.3 Specimen Calibrations

For a given test-piece, the complex stress intensity factor K can be solved by an elastic stress analysis. It has the generic form

$$K = Y\, T\, \sqrt{L}\, L^{-i\varepsilon} \exp(i\psi), \tag{3.13}$$

where T is a representative stress magnitude, L a characteristic crack dimension; Y and ψ are dimensionless real numbers which depend on elastic constants, geometric parameters and loading. Note that ψ is by definition the phase of $KL^{i\varepsilon}$. Solutions have been compiled by Hutchinson and Suo (1992).

As an example, consider a Griffith crack of length L on the interface between two materials (Fig. 7). The complex stress intensity factor is

$$K = (1 + 2i\varepsilon)\sqrt{\pi L/2}L^{-i\varepsilon}T\exp(i\omega). \tag{3.14}$$

where ω is the remote loading angle. Driving force $\mathcal{G}$ is obtained by substituting (3.14) in (3.5); the loading angle consistent with (3.13) is $\psi = \omega + \tan^{-1}(2\varepsilon)$. The mode mixity at $r = \hat{L}$ is given by

$$\hat{\psi} = \omega + \tan^{-1}(2\varepsilon) + \varepsilon\ln(\hat{L}/L). \tag{3.15}$$

For a numerical illustration consider an alumina/glass interface ($\varepsilon = -0.05$). The crack size $L = 1$ mm, and the process zone size is of the order $\hat{L} = 1$ nm. Under remote tension, $\omega = 0°$, one finds $\hat{\psi} = 34°$, that is, a large shear component exists near the crack tip. Now change the crack size to $L = 1$ cm, and everything else being the same, the new phase angle becomes $\hat{\psi} = 40°$.

12.4 CRACK TIP PLASTICITY

Plastic flow around the tip of an interface crack has been analyzed by Shih and Asaro (1988), Shih *et al.* (1991), and Zywicz and Parks (1989, 1992). Plasticity aspects of interface cracks are reviewed by Shih (1991). Consider a stationary interface crack between two materials, at least one of which is plastically deformable (Fig. 7). Small-scale yielding conditions prevail—that is, the plastic zone size r_p is much smaller than the characteristic specimen dimension, e.g. crack size L for a finite crack in an infinite body. Stress distribution over distances $r \gg r_p$ is approximately determined by elasticity, as if near-tip plasticity were non-existent. In particular, the stress field in the annulus, $r_p \ll r \ll L$, is given by Williams singular solution discussed in Section 12.3. The boundary value problem therefore consists of two semi-infinite materials bonded over $x_1 > 0$, but unbonded over $x_1 < 0$; Williams stress distribution is applied as boundary conditions as $r \to \infty$, with complex stress intensity factor

$$K = |K|L^{-i\varepsilon}\exp(i\psi). \tag{4.1}$$

Here L is the crack size, and ψ the load angle in the elasticity problem of finite crack. The elastic-plastic response is characterized by J_2 flow theory.

12.4.1 Plastic zone size

The problem contains two length scales, L and $(|K|/\sigma_Y)^2$, σ_Y being the lower yield stress of the two materials. Elementary considerations suggest that r_p scales with $(|K|/\sigma_Y)^2$, which provides a natural length to define mode mixity. Define a dimensionless number

$$\xi = \epsilon + \varepsilon \ln\left(\frac{|K|^2}{\sigma_Y^2 L}\right). \tag{4.2}$$

According to the interpretation in Section 12.3.1, $\tan\xi$ broadly represents the traction ratio σ_{xy}/σ_{yy} near $r = (|K|/\sigma_Y)^2$, or just outside of the plastic zone.

The plastic zone size is given by

$$r_p = \mathcal{R}\ (|K|/\sigma_Y)^2. \tag{4.3}$$

The dimensionless factor $\mathcal{R}$ depends weakly on material constants, but is sensitive to mode mixity, ranging from 0.15 to about 0.65 as $|\xi|$ increases from 0 to $\pi/2$. Furthermore, the shape of the plastic zone depends on the sign of ξ, which may lead to different debond resistance for loading with opposite shear directions. The above results are rigorously correct for deformation plasticity; numerical calculations have shown that they are quite accurate for flow theory.

12.4.2. Stress Distribution around a Blunted Crack Tip

Next consider the stress distribution *within* the plastic zone. The region of interest is bounded by the plastic zone size r_p, and the crack tip opening displacement δ_t. The latter is given by

$$\delta_t = \mathcal{D}J/\sigma_Y. \tag{4.4}$$

The pre-factor, $\mathcal{D}$, ranges from 0.5 to 0.7 for $|\xi| \leq \pi/6$ when the metal has low strain hardening ($N \leq 0.1$). The two lengths, r_p and δ_t, differ by a factor comparable to the yield strain.

The traction ratio, σ_{xy}/σ_{yy}, ahead of the blunted crack tip, within $\delta_t < r < r_p$, is shown in Fig. 8. Note that $\tan\xi \approx \sigma_{xy}/\sigma_{yy}$ near $r = (|K|/\sigma_Y)^2$. For the opening mode $\xi \approx 0$, the traction ratio remains small over the range of distances shown. Under mixed mode loading $\xi \neq 0$, moderate variation in the traction ratio is observed. The trends displayed in Fig. 8 are representative of metal/ceramic interfaces. Figure 9 shows the distribution of the hoop stress ahead of the crack tip. Focus on the curve for $\xi = 0$. The blunted crack tip relieves the constraint, leading to a low stress within $r < J/\sigma_Y$. The hoop stress reaches a maximum at distance $r \approx J/\sigma_Y$. The stiffer substrate provide additional constraint to plastic flow so that the stress for $\xi = 0$ is about 10% higher than the level for the corresponding homogeneous material (Shih *et al.*, 1991). The constraint is partially relieved when the loading contains a large shear component.

In recent experiments with niobium diffusion bonded to alumina, O'Dowd *et al.* (1992b) found that debond resistance varies significantly with mode mixity: for example, $\Gamma(40°)/\Gamma(0°) \approx 10$. An attempt was made to correlate mixed mode debond resistance on the basis of a cleavage stress at a characteristic distance (e.g. distance between triple point junctions in Al_2O_3), as an extension of the early work of Ritchie *et al.* (1973) on Mode I fracture in mild steels.

The evolution of cyclic near-tip fields ahead of a stationary interface crack has been investigated by Woeltjen *et al.* (1992). Under monotonic loading to peak tensile load an essentially Mode I near-tip field is observed over the major portion of the plastic zone, similar to the result in Fig. 8 for $\xi = 0$. However, a mixed-mode field is generated near the tip upon removal of the tensile load. The development of strong shear tractions ahead of the interface crack tip has important implications for fatigue fracture mechanisms and fatigue life.

12.4.3. Constrained Plasticity

Reimanis *et al.* (1991) have carried out fracture experiments with gold foils diffusion bonded between sapphire plates. The foil thickness, h, is much smaller than the overall dimension of the specimen. The plastic zone is comparable to or even larger than h, but the total inelastic zone size is small compared to specimen dimensions so that the remote load can be prescribed by a stress intensity factor. Upon loading, partial debond develops at a distance several times the foil thickness ahead of the crack tip. These micro-debonds do not connect with the crack tip. With furthur loading new debonds nucleate at a even larger distance ahead of the crack tip (see Fig. 11d). The intact metal ligaments bridge the crack, leading to a rapidly rising resistance curve ($R-$curve). Here we focus on the initiation of the micro-debond, the precursor to bridging.

The above phenomenon is an extreme form of large-scale yielding (relative to the foil thickness h) in which the metal foil is highly constrained by the sapphire plates. A finite element analysis by Varias *et al.* (1991, 1992) reveals that the hydrostatic stress in the metal foil increases steadily as the applied load increases; this is in contrast to the stress distribution ahead of an interface crack between two substrates which cannot elevate above three to four times the yield stress. The behavior of the mean stress in the metal foil is shown in Fig. 10. Near the tip ($r/h \ll 1$), the stress distribution is not affected by the constraint of the foil thickness, so the mean stress is about three times the yield stress, similar to the distribution in Fig. 9. At a distance several times of the foil thickness, the mean stress reaches the maximum, which increases with applied load; the location of the maxima shifts ahead as the load increases. These elevated stress maxima are responsible for micro-debonds.

12.5 GROWING CRACKS AND DEBOND RESISTANCE

Debond rearranges atoms that form the interface into two free surfaces, consuming the Griffith energy

$$\Gamma_G = \gamma_1 + \gamma_2 - \gamma_{int}. \tag{5.1}$$

Here γ_1 and γ_2 are the surface energies of material 1 and 2, respectively, and γ_{int} is the interface energy. The Griffith energy is small, since only a few layers of atoms participate in irreversible movements. To increase debond resistance, more atoms must be brought into the inelastic process, through mechanisms activated by stress lower than that required for atomic separation. For example, $\Gamma < 10$ J/m^2 for Al_2O_3, but even single crystal Al_2O_3 has fracture resistance exceeding 30 J/m^2. Some heat-dissipating, atomic-scale snapping processes might exist, involving atoms off the crack plane (K.-S. Kim, private communication). The fracture resistance of polycrystalline Al_2O_3 is further increased by grain-scale dissipating mechanisms such as pullout against friction (Vekinis *et al.*, 1990).

Studies on crack growth resistance in metals was initiated by McClintock and Irwin (1965) who used small scale yielding solutions for growing cracks in mode III, together with a growth criterion based on the attainment of a critical strain at a characteristic distance ahead of the tip. Later developments along this line has been given by Drugan, Rice and Sham (1982). This approach has been extended by Drugan (1991), and Ponte Castañeda and Mataga (1992) to cracks growing along bimaterial interfaces. Mechanism-based models to relate debond resistance to micromechanisms have been developed recently, which provide a focus for the subsequent presentation. We will limit our attention to predominantly opening mode of fracture.

12.5.1 Crack-Bridging

A solid will fall apart unless something holds it together. A far reaching, unifying idea, sufficiently rigorous for our purpose, is to represent the "binding" by a relation between attractive stress, σ, and separation, δ. Such a relation is sketched in Fig. 5, and is written as

$$\sigma/\sigma_B = \chi(\delta/\delta_B) \tag{5.2}$$

The dimensionless function χ describes the shape of the relation; the scale is set by σ_B and δ_B. The energy required to separate unit area of surfaces so bridged is

$$\Gamma_B = \sigma_B \delta_B \int_0^\infty \chi(\kappa) d\kappa. \tag{5.3}$$

The dimensionless integral is of order unity. In practice, the shape function χ is difficult to determine precisely, but the qunatities σ_B and δ_B are readily related to microstructural variables (Evans, 1990). One can therefore estimate fracture resistance by

$$\Gamma_B \approx \sigma_B \delta_B. \tag{5.4}$$

TABLE 1

	σ_B (N/m^2)	δ_B (m)	$\Gamma_B \approx \sigma_B \delta_B$ (J/m^2)
atomic bond	10^{10}	10^{-10}	1
ductile ligament	10^8	10^{-5}	10^3
hole growth	10^9	10^{-4}	10^5
metal foil	10^7	10^{-5}	10^2

Sketched in Fig. 11 are several bridging mechanisms; Table 1 lists the representative values of σ_B, δ_B and Γ_B for these mechanisms. Atomic bond has high strength but small debond separation, resulting in a small fracture resistance. Ductile, crack-bridging ligaments give rise to a substantially higher fracture resistance; these ligaments are believed to operate in polycrystalline steels at lower shelf (Hoagland *et al.* 1972), and in a ceramic matrix containing metallic particles. In the latter, δ_B scales with the diameter of the particles. It remains unclear for polycrystalline steels whether δ_B is set by grain size or some other microstructural lengths. Holes can nucleate in ductile alloys around hard inclusions, or on metal/ceramic interface around pores or triple point junctions. Hole growth usually dissipates large amounts of energy. Thin metallic foils sandwiched between two ceramic substrates may debond along alternating interfaces, due to either periodic weak spots fabricated during bonding (Oh *et al.* 1988), or constrained plastic flow (Reimanis *et al.*, 1991, Varias *et al.*, 1991, 1992). More detailed review on crack-bridging concepts can be found elsewhere (Bao and Suo, 1992; Suo *et al.*, 1992).

12.5.2 Crack-Bridging and Background Plasticity

It is assumed in the previous section that inleastic deformation can be fully represented by a bridging law while the background material is elastic. In practice several inelastic mechanisms can operate simultaneously. An interesting example involves a ceramic matrix containing both ductile and transforming particles. The ductile particles form bridges, while the transforming particles contribute to background dissipation. Bridging increases the height of the wake, transforming more particles and thereby dissipating more energy; transformation shields the bridging zone. Thus the synergism (Amazigo and Budiansky, 1988).

Consider the deformation history that a material distance y off the interface, experiences as the crack tip passes by. The energy density variation for the entire process is

$$W(y) = \int_0^{\boldsymbol{\varepsilon}} \sigma_{ij} d\epsilon_{ij}. \tag{5.5}$$

The integral is carried over the entire history, including both heat dissipation when the particle is in the active plastic zone, and the residual stress energy when the particle is in the wake.

Denote H_1 and H_2 as the depths of the inelastic layers in the two materials. The total energy expended in the background for the steady-state crack to move unit distance is

$$\Gamma_P = \int_{-H_2}^{H_1} W(y)dy. \tag{5.6}$$

The total fracture resistance, which includes Griffith energy, bridging energy and stress work in the background, is given by

$$\Gamma = \Gamma_G + \Gamma_B + \Gamma_P. \tag{5.7}$$

Since typically Γ_P and Γ_B are much larger than Γ_G, it is sometimes assumed that Γ_G is an irrelevant parameter for fracture involving substantial plasticity. However, several authors have pointed out that if cleavage is the basic fracture mechanism, Γ_P or Γ_B must in some way depend on Γ_G — that is, the small quantity Γ_G serves as a "valve" for large dissipation Γ_B and Γ_P (e.g. Jokl *et al.*, 1980). For example, in transformation-toughened ceramics, the matrix toughness sets the extent of the transformation zone and thereby Γ_P (McMeeking and Evans, 1982; Budiansky *et al.*, 1983).

A more familiar example is ductile fracture of alloys, where the near-tip mechanism of hole growth and coalescence serves as the valve for larger scale plastic dissipation. This process has been analyzed by Needleman (1987, 1990), Varias *et al.* (1990), and Tvergaard and Hutchinson (1992). Consider a pre-cut loaded remotely by a monotonically increasing $\mathcal{G}$. When $\mathcal{G} < \Gamma_B$, the bridging develops ahead of the crack tip, so does the plastic zone; the crack remains stationary. The crack begins to grow or, rather, the bridges start to break when $\mathcal{G} = \Gamma_B$. In this sense, background plasticity does *not* provide any shielding prior to crack growth. This can be readily understood by the $J-$integral, and the fact that plastic flow is proportional prior to crack growth. A reference length is defined by

$$R_B = \frac{1}{3\pi}\frac{\Gamma_B}{\sigma_Y \epsilon_Y}. \tag{5.8}$$

This reference length scales with the extent of the plastic zone size when $\mathcal{G} = \Gamma_B$.

As the crack grows, the bridging zone translates in the material: old bridges are broken in the wake, and new bridges are formed in the front. The background material also experiences elastic unloading and possibly reverse plastic loading. The complicated deformation shields the crack. The shielding ratio, $\mathcal{G}/\Gamma_B$, increases with the crack increment Δa, as shown in Fig. 12. It is evident that the steady-state is established when the crack growth is greater than several times R_B. The steady-state fracture resistance, Γ_{SS}, depends on σ_B/σ_Y. The trend can be better seen in Fig. 13. For a non-hardening material ($N = 0$), no contribution is derived from the background plasticity if $\sigma_B/\sigma_Y < 2$; on the other hand, the crack is "lock

up", or has infinite fracture resistance when $\sigma_B/\sigma_Y \geq 3$. Similar trends are observed for strain-hardening materials.

12.5.3 Brittle Debonding in the Presence of Plastic Flow

It is known that a sharp, cleaving crack can propagate, slowly or dynamically, surrounded by substantial dislocation motion. For example, a sharp crack can grow slowly by cleavage along a gold/sapphire interface even though the gold deforms plastically; the measured fracture energy is much larger than Γ_G (Reimanis *et al.*, 1991). Similar behavior is observed in copper/glass (Oh *et al.*, 1987) , copper/sapphire (Beltz and Wang, 1992), niobium/alumina (O'Dowd *et al.*, 1992b), and copper bicrystals contaminated by bismuth (Wang and Anderson, 1991). This phenomenon cannot be explained by the models discussed in the previous sections. Atomic cohesive strength, σ_B, is known to be orders of magnitude higher than macroscopic yield strength, σ_Y. When σ_B/σ_Y exceeds about 4, crack-bridging models within the framework of continuum plasticity predict that the crack blunts, limiting the near-tip stress to several times σ_Y (Fig. 9). Consequently, cleavage cannot proceed from the crack tip. Instead, one has to appeal to other fracture mechanisms, such as hole growth (Rice and Johnson, 1970) and cleavage from a remote defect (Ritchie *et al.*, 1973), both leading to rough fracture surfaces not observed in experiments cited in the previous paragraph.

Figure 14 conveys the essentials of a theory proposed by Suo *et al.* (1992). The fundamental process for plastic flow is discrete, consisting of at least two length scales: the Burgers vector $b \sim 10^{-10}$m, and dislocation spacing $D \sim 10^{-6}$m. On one scale, atoms exhibit individuality ultimately governed by Quantum Mechanics. On the other scale, dislocations interact through Continuum Elasticity. Continuum Plasticity applies when stress variation over a multiple of D is small compared to the macroscopic yield strength. The discreteness becomes important for events occuring between lengths b and D.

The theory is based on a single premise: the crack front does not emit dislocations. This happens, for example, for cleavable materials such as steel and silicon below the ductile-brittle transition temperature, or contaminated grain boundaries, or interfaces subjected to environmental degradation, or interfaces with a few atomic layers of brittle reaction compounds. As illustrated in Fig. 14, so long as dislocation spacing D is much larger than the lattice constant, the probability for a pre-existing dislocation to blunt a major portion of the crack front should be extremely small. Consequently, a crack which does not emit dislocation will remain nanoscopically-sharp, advancing by atomic decohesion. Within the cell essentially free of dislocations which surrounds the crack front, the crystal is linearly elastic down to a nanometer. Near the crack tip, nonlinearity arises from partial atomic separation and nanoscopic shear bands. The size of the elastic cell, represented by D, is several orders of magnitude larger than the nonlinear zone size. Consequently, information regarding the

nanoscopic nonlinearity is transmitted—to an observer outside the elastic cell—through a single quantity: the Griffith energy Γ_G. The elastic cell provides a medium through which the stress decays rapidly, matching the high atomic debond stress on one side, and the low macroscopic yield stress on the other. For example, with $b = 10^{-10}$m and $D = 10^{-6}$m, the stress decays approximately by a factor $\sqrt{D/b} = 100$ over a distance of 1 μm. The dislocation motion at the characteristic distance D away from the crack tip dissipates plastic energy, Γ_P, which is typically much larger than Γ_G. In summary, atoms around a crack front can be divided into three regions: nanoscopic decohesion zone, microscopic elastic cell, and macroscopic dislocation dissipative background.

The elastic cell is a Nanomechanics concept with imprecise, if any, continuum description. The concept can be approximately understood in terms of spatially varying yield strengths. Sketched in Fig. 15 is yield strength varying with the distance from a representative atom at the crack tip. The theoretical shear strength is approached near the crack tip; the strength decays to the macroscopic yield strength in the background. The shape of the decay function has not been investigated; dislocation cell models may provide some insight (Lubarda *et al.*, 1992; Kubin *et al.*, 1992). Nevertheless, the decay function *must* have a characteristic length comparable to the dislocation spacing D.

Consider a cleavable, rate-independent material with Griffith energy Γ_G, yield strength σ_Y and yield strain $\epsilon_Y = \sigma_Y/E$, E being Young's Modulus. The crack tip energy release rate, $\mathcal{G}_{\text{tip}}$, is shielded by background dislocation motion from the remotely applied energy release rate, $\mathcal{G}$. Dimensional analysis dictates that

$$\mathcal{G}/\mathcal{G}_{\text{tip}} = g(D\epsilon_Y\sigma_Y/\mathcal{G}_{\text{tip}}). \tag{5.9}$$

The shielding ratio g also depends on crack increment and material constants such as ϵ_Y, Poisson's ratio ν and in particular, the shape of the decay function in Fig. 15. For properties representative of metals (e.g. $D \sim 1$ μm, $\epsilon_Y \sim 10^{-3}$, $\sigma_Y \sim 10^8$ N/m^2, $\Gamma_G \sim 1$ J/m^2), the parameter $D\epsilon_Y\sigma_Y/\Gamma_G$ ranges from 10^{-2} to 10. The parameter can be understood in several ways; e.g. all else being fixed, an increase in elastic cell size D reduces the total energy dissipation. Under steady-state growth, $\mathcal{G}_{\text{tip}} = \Gamma_G$ and $\mathcal{G}$ equals the measured fracture energy Γ. The plastic dissipation Γ_P is given by $\Gamma = \Gamma_P + \Gamma_G$.

In the present theory, it is assumed that no low strength, long range bridges, such as tearing caused by cleavage plane reorientation between neighbouring grains, operate in the crack wake. These bridges are responsible for the large "cleavage energy" reported for polycrystalline steels. When operating, the bridges may serve as a bigger valve than atomic decohesion. If this is the case, a bridging law may be used in the present model. Indeed, when $\sigma_B/\sigma_Y < 4$, the present model should reduce to regular bridging model without an elastic cell.

Further simplifications are needed to make quantitative predictions (Fig. 16). The decohesion zone is small compared to D so that the square root singular elasticity solution prevails in $b \ll r \ll D$. Detailed atomistic description of decohesion is unnecessary except for a prescription of a cleavage energy Γ_G. The shape of the elastic cell is unimportant since the plastic zone height is typically much larger than D; we use a strip to represent the elastic cell. A disc translating with the crack tip can be another convenient choice, but the difference is expected to be minor in so far as $\mathcal{G}/\mathcal{G}_{\rm tip}$ is concerned. The background dislocation motion is represented by continuum plasticity. A refinement, if needed, may include individual dislocations or a dislocation network in the transition region between the elastic cell and the continuum plastic flow.

The crack starts to grow when $\mathcal{G} \geq \Gamma_G$; more load is required to maintain the growth, leading to a resistance curve. The plastic zone also increases as the crack grows, attaining a steady-state height H. The energy release rate reaches a steady-state value $\Gamma_{\rm SS}$. The model geometry is analyzed in the steady-state using finite elements. Figure 17 shows that the shielding ratio increases rapidly as D or σ_Y decrease. The influence of strain hardening exponent, N, can also be seen. For non-hardening metals, the plastic dissipation completely shields the crack tip at a finite $D\epsilon_Y\sigma_Y/\mathcal{G}_{\rm tip}$. In practice, D may be used as a fitting parameter to correlate experimental data. For example, a metal with $\sigma_Y = 10^8$ N/m^2, $\epsilon_Y = 10^{-3}$ and $\Gamma_G = 1$ J/m^2 gives $\Gamma_G/\sigma_Y\epsilon_Y = 10$ μm. If the measured fracture energy $\Gamma_{\rm SS} = 10$ J/m^2, one finds from Fig. 17 that $D \approx 0.5$ μm.

In an experiment with a single crystal of copper diffusion bonded to a sapphire disc (Beltz and Wang, 1992), interface debonding was driven in two crystallographic directions at slightly different energy release rates. The phenomenon was interpreted according to the Rice-Thomson model (1974): dislocations emit from the crack tip in one direction but not from the other. An alternative interpretation appears to be possible on the basis of the present theory: both crack tips do not emit dislocations; the different debond energies result from the different extent of background dislocation motion. Indeed, the micrographs show much denser slip lines in one case than the other. Experiments at higher magnifications are needed to ascertain which of the two interpretations is appropriate for the copper/sapphire system. Calculations within the framework of the present theory, taking into account of single crystal plasticity, are in progress to facilitate a direct comparison with such experiments.

Obviously, the competition between atomic decohesion and dislocation emission (Rice *et al.*, 1992) cannot be addressed by the present theory; instead, the consequences of the premise that dislocations do not emit from the crack front can be explored. Included in Suo *et al.* (1992) are slow cleavage cracking, stress-assisted corrosion, fast-running crack, fatigue cracking, constraint effects, and mixed mode fracture along metal/ceramic interfaces.

ACKNOWLEDGEMENTS

The work of Z. Suo was supported by NSF Young Investigator Award, by DARPA/URI Contract N00014-86-K-0753, and by a Visiting Associate Professor appointment at Brown University funded by NRC/ONR Grant N00014-90-J1380. The work of C.F. Shih was supported by NRC/ONR Grant N00014-90-J1380O, and by the Materials Research Group funded by NSF through Grant DMR-9002994.

REFERENCES

Amazigo J. C. and Budiansky, B., (1988) J. Mech. Phys. Solids **36**, 581-595.

Aveston, J., Cooper, G. A. and Kelly, A., (1971) in The Properties of Fiber Composites, pp. 15-24, Conference Proceedings, National Physical Laboratory (Guildford UK), IPC Science and Technology Press, Ltd., teddington, UK.

Argon, A. S., Gupta, V., Landis, H. S. and Cornie, J. A., (1989) J. Mater. Sci. **24**, 1406-1412.

Ashby, M. F., Rühle, M., Eds., (1992) Proceedings of International Symposium on Metal/Ceramic Interfaces. To be published in Acta Metall. Mater.

Bao, G. and Suo, Z., (1992), "Remarks on Crack Bridging Concepts," Applied Mechanics Review. In Press.

Beltz, G. E. and Wang, J.-S., (1992) Acta Metall. Mater **40**, 1675-1683..

Budiansky, B., Hutchinson, J. W. and Lambropoulos, J. C., (1983) Int. J. Solids Struct. **19**, 337-355.

Cannon, R. M. Dalgleish, B. J., Dauskardt, R. H., Fisher, R. M., Oh, T. S. and Ritchie, R. O., (1992) in Fatigue of Advanced Materials (Eds. R. O. Ritchie, R. H. Dauskardt, and B. N. Cox) MCEP Publishing Ltd., Edgbaston, U.K.

Cao, H. C. and Evans, A. G., (1989) Mech. Mater. **7**, 295-305.

Cottrell, A. H., (1963) in Tewksbury Symposium on Fracture, pp. 1-27. University of Melbourne.

Davis, J. B., Cao, H. C., Bao, G., and Evans, A. G., (1991) Acta Metall. Mater, **39**, 1019-1024.

Drugan, W. J., Rice, J. R. and Sham, T.-L., (1982) J. Mech. Phys. Solids **30**, 447-473.

Drugan, W. J., (1991) J. appl. Mech. **58**, 111-119.

England, A. H., (1965) J. appl. Mech. **32**, 400-402.

Erdogan, F., (1965) J. appl. Mech. **32**, 403-410.

Evans, A. G., (1990) J. Am. Ceram. Soc. **73**, 187-206.

Evans, A. G., Drory, M. D. and Hu, M. S., (1988) J. Mater. Res. **3**, 1043-1049.

Evans, A. G. and Hutchinson, J. W., (1989) Acta Metall. Mater. **37**, 909-916.

Evans, A. G., Rühle, M., Dalgleish, B. J. and Charalambides, P. G., (1990) Mater. Sci. Engng., **A126**, 53-64.

Farris, R. J. and Bauer, C. L., (1988) J. Adhesion, **26**, 293-300.

Griffith A. A., (1921) Phil. Trans. Roy. Soc. Lond. **A221**, 163-197.

Hoagland, R. G., Rosenfield, A. R. and Hahn, G. T., (1972) Metall. Trans. **3**, 123-136.

Hutchinson, J. W., (1979) Nonlinear Fracture Mechanics. Department of Solid Mechanics, Technical University of Denmark.

Hutchinson, J. W. and Jensen H. M., (1990) Mech. Mater. **9**, 139-163.

Hutchinson, J. W. and Suo, Z., (1992) Adv. appl. Mech. **29**, 63-191.

Irwin, G. R., (1960) in Structural Mechanics (Eds., J. N. Goodier and N. J. Hoff) Pergamon, Oxford, pp. 557-591.

Jokl, M. L., Vitek V. and McMahon, C. J., Jr., (1980) Acta Metall. **28**, 1479-1488.

Kanninen, M. F. and Popelar, C. H., (1985) Advanced Fracture Mechanics, Oxford University Press, Oxford.

Kim, K.-S., (1991) in Materials Research Society Symposium Proc. Vol. 203, pp. 3-14.

Kubin, L. P., Canova, G., Condat, M., Devincre, B., Pontikis V. and Bréchet Y. (1992) in Non-linear Phenomena in Materials Science II (Eds. G. Martin and L. P. Kubin). In press.

Liechti, K. M. and Chai, Y.-S., (1992) J. appl. Mech. **59**, 295-304.

Lubarda, V. A., Blume J. A. and Needleman, A., (1992) Acta Metall. Mater. In press.

Malyshev, B. M. and Salganik, R. L. (1965) Int. J. Fract. Mech. **5**, 114-128.

McClintock, F. A. and Irwin, G. R. (1965), ASTM-STP 381, pp. 84-113, ASTM, Philadelphia.

McMeeking R. M. and Evans, A. G. (1982) J. Am. Ceram. Soc. **65**, 242-246.

Moran, B. and Shih, C. F. (1987) Engng. Fract. Mech. **27**, 615-642.

Needleman, A., (1987) J. appl. Mech. **54**, 525-531.

Needleman, A., (1990) J. Mech. Phys. Solids **38**, 289-324.

O'Dowd, N. P., Shih, C. F. and Stout M. G., (1992a) Int. J. Solids Struct. **29**, 571-589.

O'Dowd, N. P., Stout M. G., and Shih, C. F., (1992b) Phil. Mag. (1992). In press.

Oh, T. S., Cannon, R. M. and Ritchie, R. O., (1987) J. Am. Ceram. Soc. **70**, C352-C355.

Oh, T. S., Cannon, R. M. and Ritchie, R. O., (1988) Acta Metall. **36**, 2083-2093.

Ponte Castañeda, P. and Mataga, P. A., (1992). Submitted for publication.

Reimanis, I. E., Dalgleish, B. J. and Evans, A. G., (1991) Acta Metall. Mater. **39**, 3133-3141.

Rice, J. R., (1968) J. appl. Mech. **35**, 379-386.

Rice, J. R., (1988) J. appl. Mech. **55**, 98-103.

Rice, J. R., Beltz G. E. and Sun, Y., (1992) in Topics in Fracture and Fatigue, pp. 1-58 (Ed. A. S. Argon) Springer-Verlag.

Rice J. R. and Johnson, M. A., (1970) in Inelastic Behavior of Solids (Eds. M.F. Kanninen, W. F. Adler, A. R. Rosenfield and R. I. Jaffee) McGraw-Hill, New York, pp. 641-672.

Rice, J. R. and Sih, G. C., (1965) J. appl. Mech. **32**, 418-423.

Rice, J. R., Suo, Z. and Wang, J. S., (1990) in Metal-Ceramic Interfaces, Acta-Scripta Metallurgica Proc. Ser. (Eds. M. Rühle, A. G. Evans, M. F. Ashby and J. P. Hirth) Vol. 4, pp. 269-294, Pergamon Press, Oxford.

Rice, J. R. and Thomson, R. M., (1974) Phil. Mag. **29**, 73-97.

Rice, J. R. and Wang, J. S. (1989) Mater. Sci. Engng. **A107**, 23-40.

Ritchie, R. O., Knott, J. F. and Rice, J. R., (1973) J. Mech. Phys. Solids **21**, 395-410.

Rivlin, R. S. and Thomas, A. G. (1953) J. Polym. Sci. **10**, 291-318.

Rühle, M., Evans A. G., Ashby, M. F. and Hirth, J. P., Eds., (1990) Metal-Ceramic Interfaces, Acta-Scripta Metallurgica Proceedings Series Volume 4, Pergamon Press, Oxford.

Shih, C. F. and Asaro, R. J., (1988) J. appl. Mech. **55**, 299-316.

Shih, C. F., Asaro, R. J. and O'Dowd, N. P., (1991) J. appl. Mech. **58**, 450-463.

Shih, C. F., (1991) Mater. Sci. Engng. **A143**, 77-90.

Stump, D. M. and Budiansky, B., (1989) Acta Metall. Mater. **37**, 3297-3304.

Suresh, S. and Needleman, A., Eds., (1989) Interfacial Phenomena in Composites: Processing, Characterization and Mechanical Properties, Elsevier Applied Science, London.

Suo, Z., (1990) Proc. R. Soc. Lond. **A427**, 331-358.

Suo, Z., Shih, C. F. and Varias, A. G. (1992). "A Theory for Cleavage Cracking in the Presence of Plastic Flow." Submitted for publication.

Thouless, M. D., (1990) Acta Metall. **38** 1135-1140.

Tvergaard, V. and Hutchinson, J. W., (1992) *J. Mech. Phys. Solids. In press.*

Varias, A. G., O'Dowd, N. P., Asaro, R. J. and Shih, C. F., (1990) Mater. Sci. Engng. **A126**, 65-93.

Varias, A. G., Suo, Z. and Shih, C. F., (1991) J. Mech. Phys. Solids, **39**, 963-986.

Varias, A. G., Suo, Z. and Shih, C. F., (1992) J. Mech. Phys. Solids, **40**, 485-509.

Vekinis, G., Ashby, M. F. and Beaumont, P. W. R., (1990) Acta Metall. Mater. **38**, 1151-1162.

Wang, J. S. and Anderson, P. M., (1991) Acta Metall. Mater. **39**, 779-792.

Wang, J. S. and Suo, Z., (1990) Acta. Metall. Mater. **38**, 1279-1290.

Williams, M. L., (1959) Bull. Seismol. Soc. Am. **49**, 199-204.

Woeltjen, C., Shih, C. F. and Suresh, S. (1992) "Near-Tip Fields for Fatigue Cracks along Metal–Metal and Metal-Ceramic Interfaces." Submitted for publication.

Zywicz, E. and Parks, D. M., (1989) J. appl. Mech. **56**, 577-584.

Zywicz, E. and Parks, D. M., (1992) J. Mech. Phys. Solids **40**, 511-536.

FIGURE CAPTIONS

Figure 1. A partially debonded interface is subjected to applied load.

Figure 2. Graphical interpretation of U, Π and $\mathcal{G}$.

Figure 3. A fiber is being pulled out from a matrix.

Figure 4. Thin film decohesion emanating from a circular hole.

Figure 5. Inelastic processes accompanying debond.

Figure 6. Convenient geometries to measure debond resistance.

Figure 7. (a) A finite interface crack subjected to a remote tension T at angle ω; the plastic zone size is assumed to be small compared to the crack size. (b) A small-scaled yielding problem is posed.

Figure 8. The ratio of shear over tension ahead of the crack tip, on the interface, in the range $\delta_t \leq r \leq r_p$. Metal/ceramic bimaterial; metal properties are $N = 0.1$, $\epsilon_Y = 0.003$, and $\nu = 0.3$.

Figure 9. Tensile stress ahead of the crack tip, on the interface. Note that $\delta_t \sim J/\sigma_Y$. Metal/ceramic bimaterial; metal properties are $N = 0.1$, $\epsilon_Y = 0.003$, and $\nu = 0.3$.

Figure 10. Inset: a metal foil bonded between two ceramic substrates, subjected to a remote Mode I stress intensity factor. The mean stress distribution ahead of the crack tip is plotted for several loading levels.

Figure 11. Crack-bridging mechanisms: a) *atomic adhesion*, b) *ductile ligaments* c) *hole* growth, d) alternating debonding.

Figure 12. Fracture resistance curve resulting from background plasticity shielding (from Tvergaard and Hutchinson, 1992).

Figure 13. Steady-state shielding ratio as a function of bridging strength relative to yield strength (from Tvergaard and Hutchinson, 1992).

Figure 14. A decohesion front in a network of pre-existing dislocations. The diameter of the decohesion core is about 1 nm; the average dislocation spacing is more than 100 nm.

Figure 15. Yield strength as a function of the distance from an atom at the center of an *elastic* cell.

Figure 16. A model system with a step-function decay in yield strength

Figure 17. A fracture resistance curve: the fracture energy increases as the crack grows. Computed shielding ratio as a function of various parameters: N — hardening exponent, D — elastic cell size.

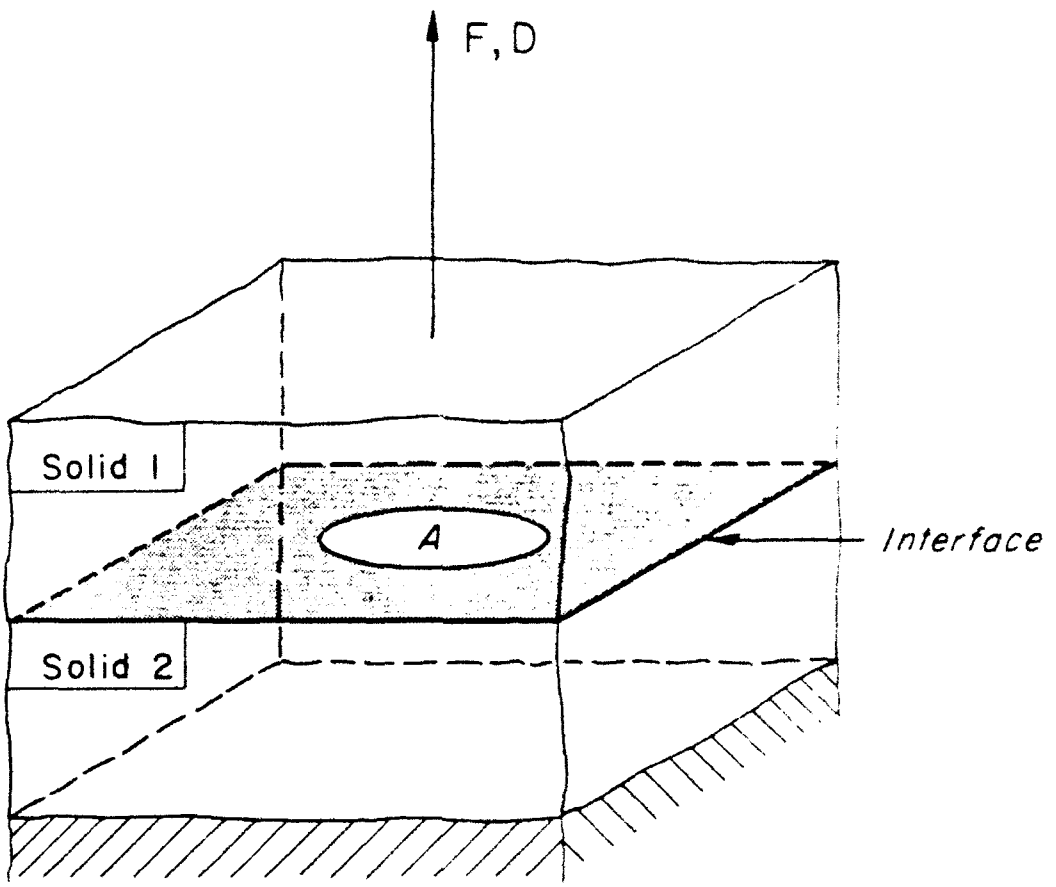

Fig. 1

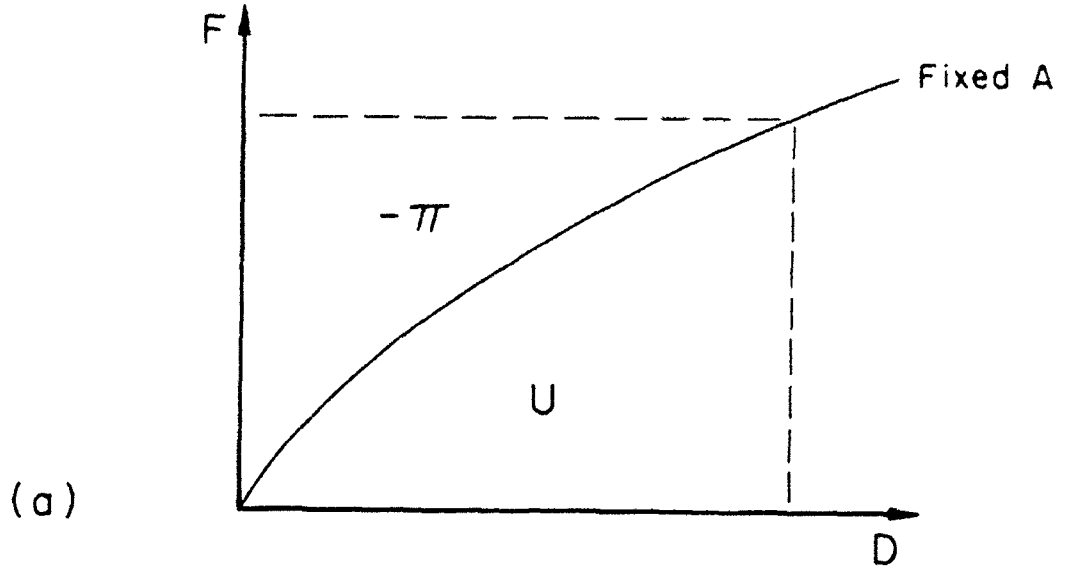

(a)

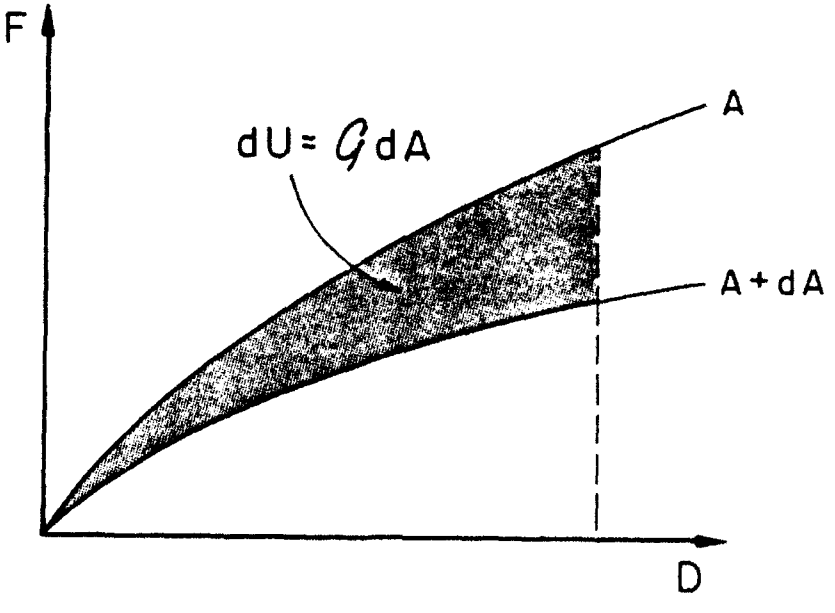

(b)

Fig. 2

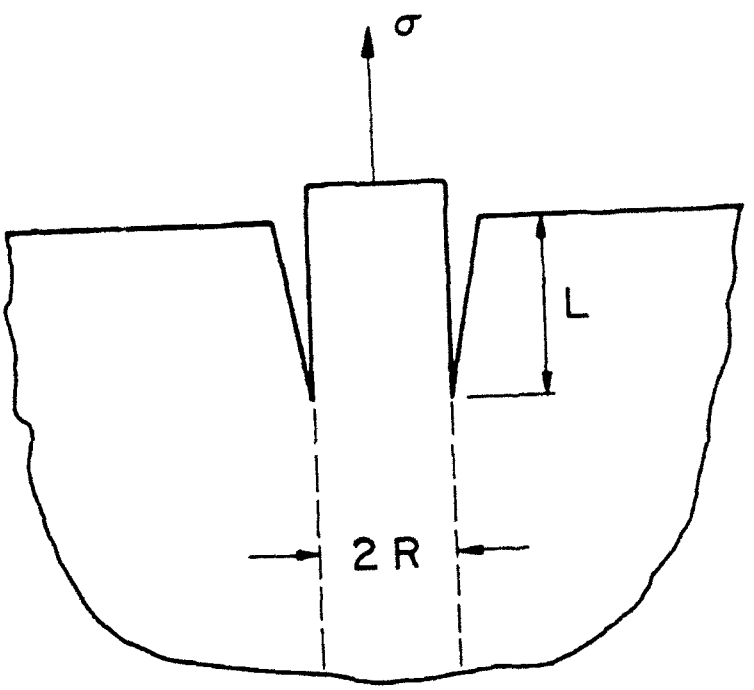

Fig. 3

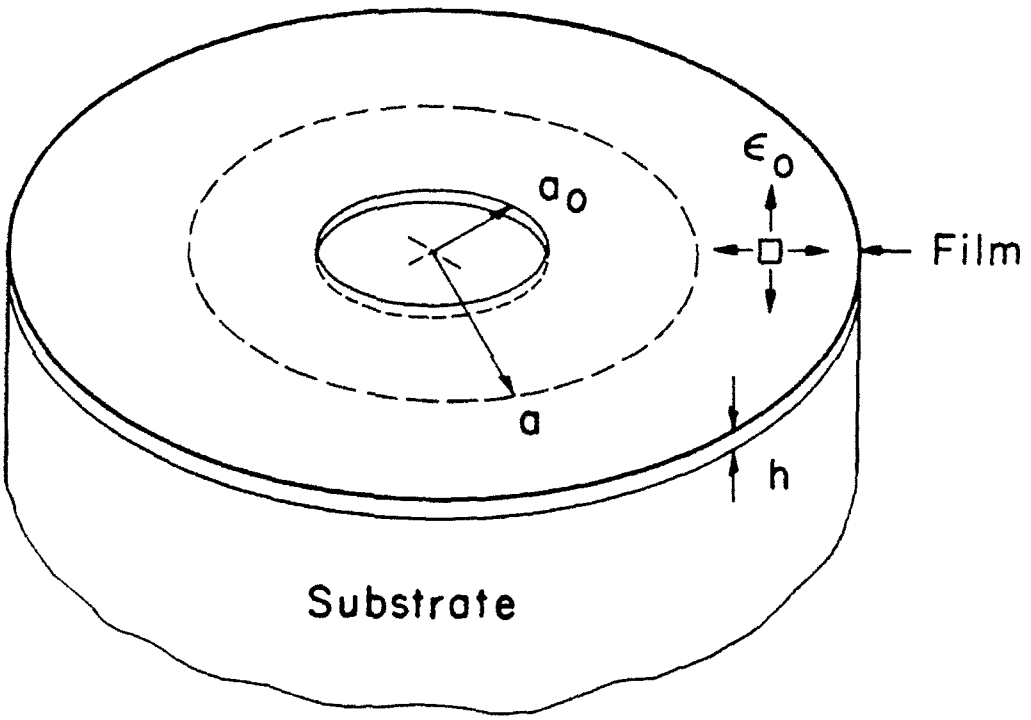

Fig. 4

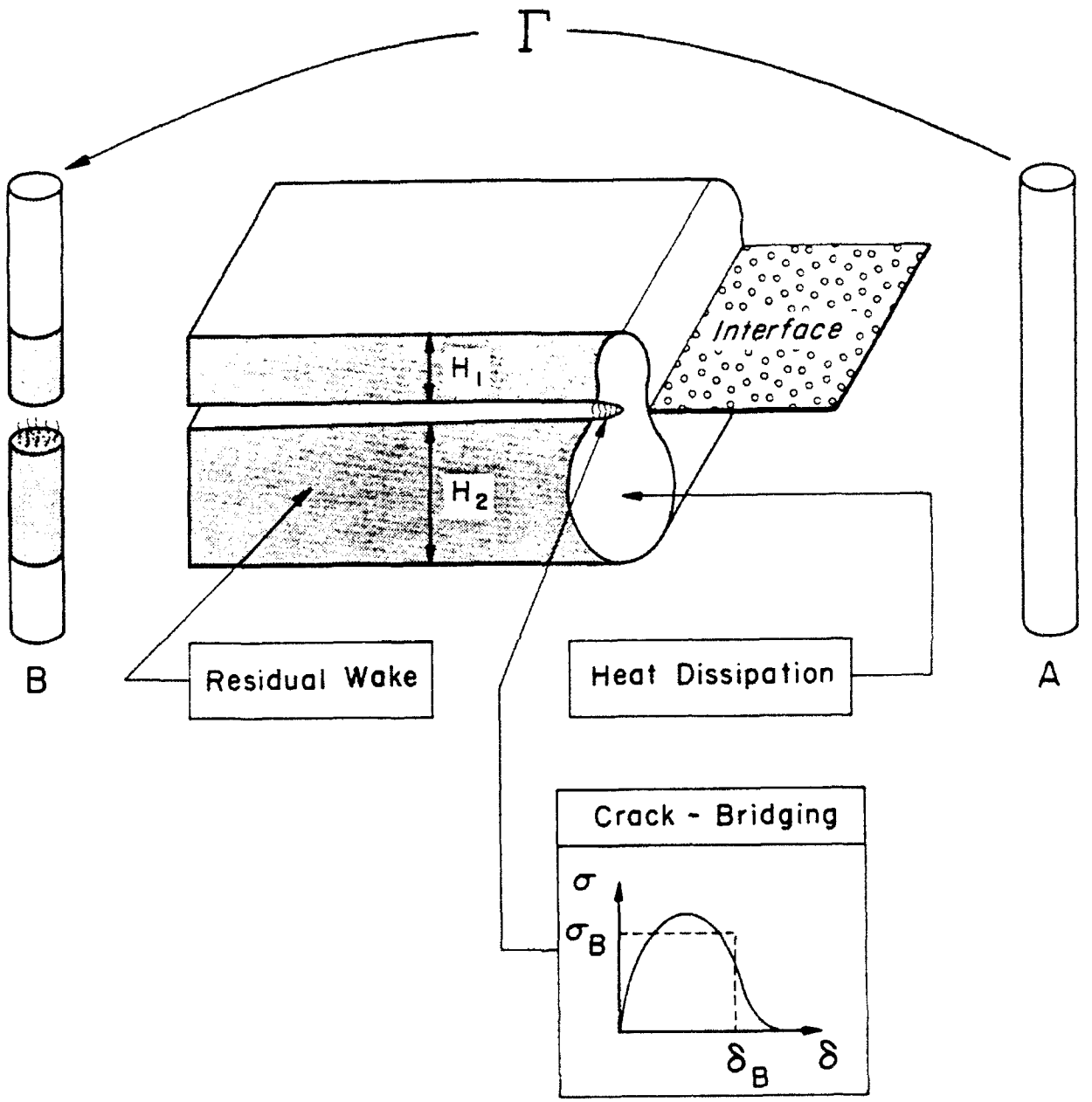
Γ
Interface
H1
H2
B
A
Residual Wake
Heat Dissipation
Crack - Bridging
σ
σB
δB
δ

Fig. 5

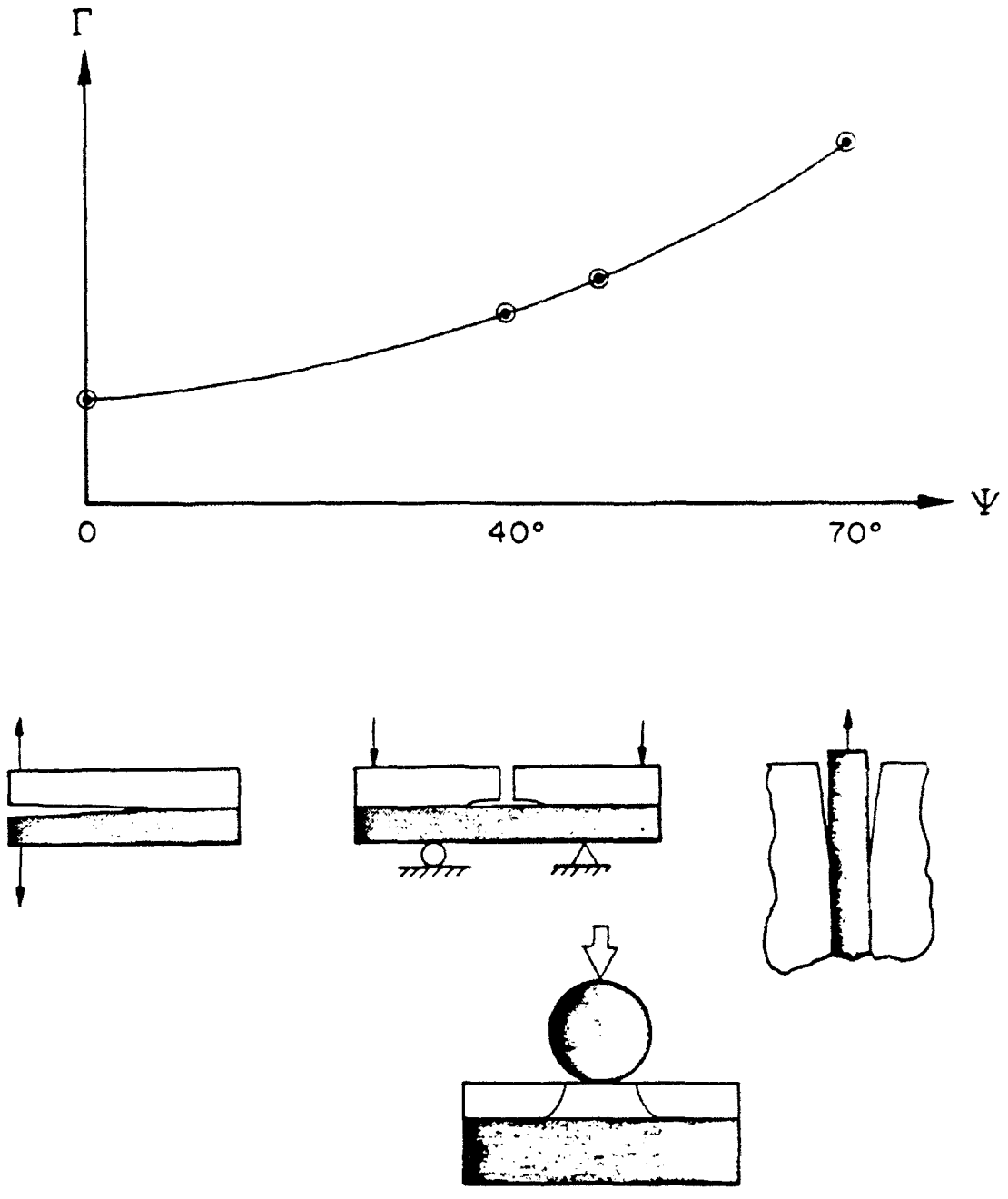

Fig. 6

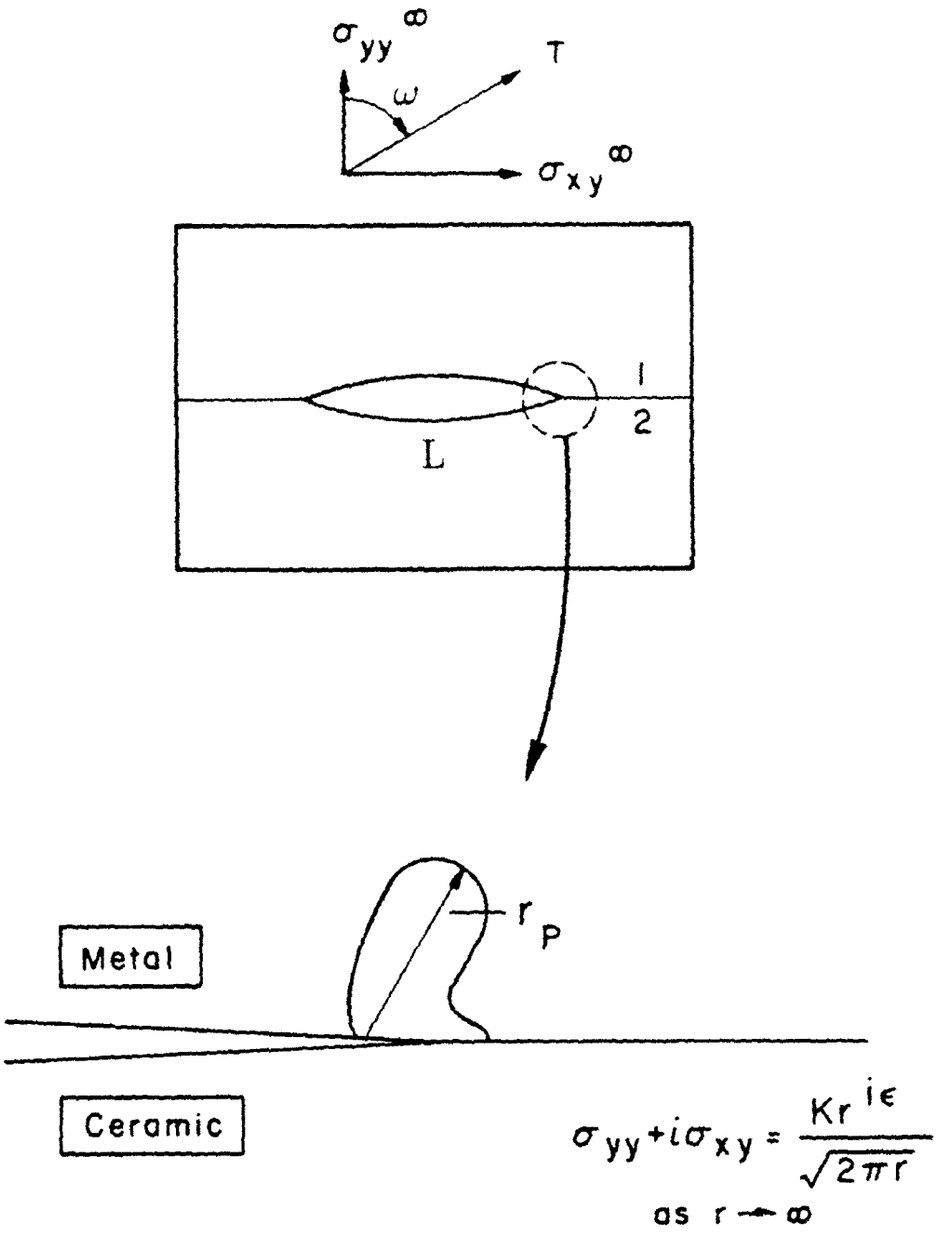
σ_{yy}^{∞}
T
ω
σ_{xy}^{∞}
1
2
L
r_p
Metal
Ceramic
$\sigma_{yy}+i\sigma_{xy} = \frac{Kr^{i\epsilon}}{\sqrt{2\pi r}}$
as $r \to \infty$

Fig. 7

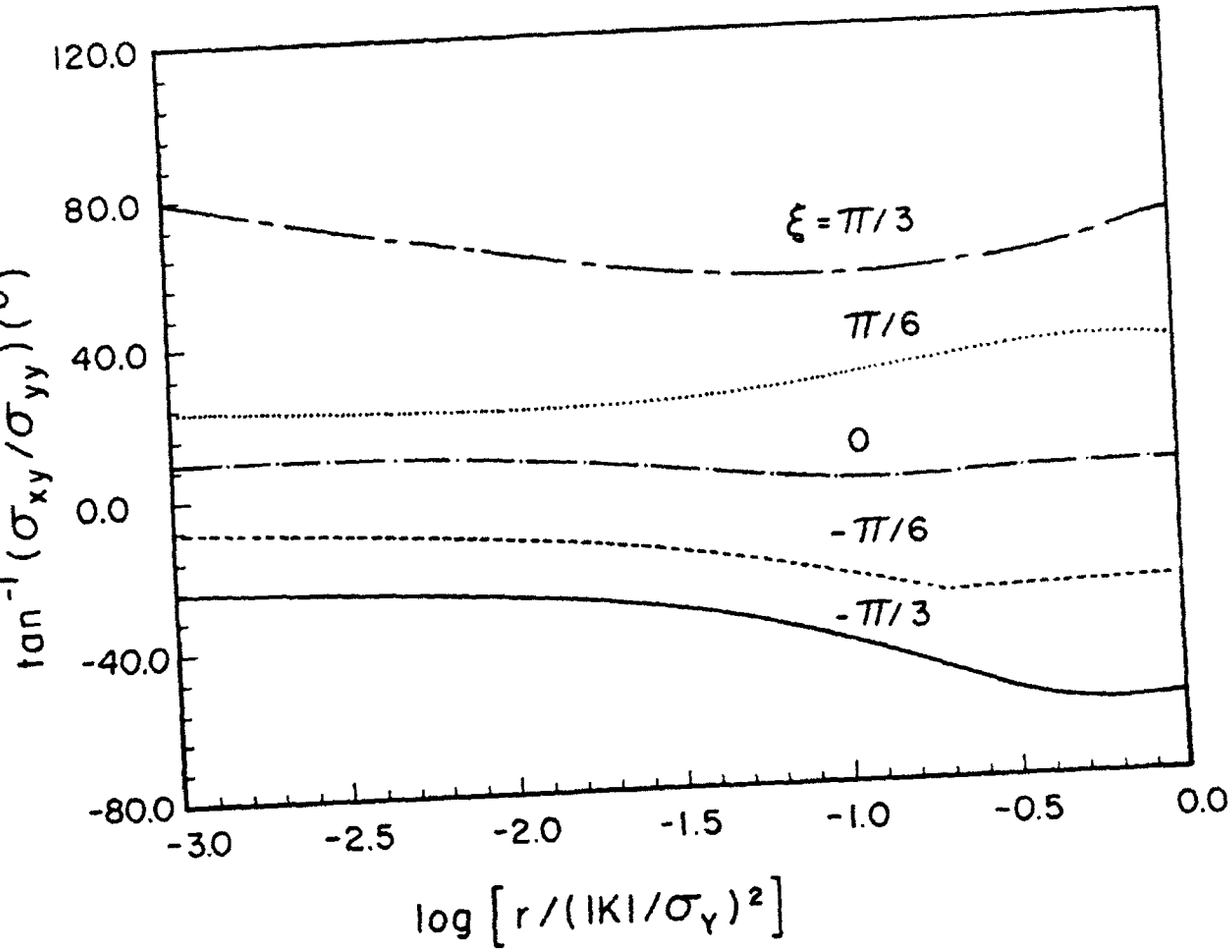
120.0
80.0
40.0
0.0
-40.0
-80.0
-3.0
-2.5
-2.0
-1.5
-1.0
-0.5
0.0
ξ = π/3
π/6
0
-π/6
-π/3
tan⁻¹ (σxy/σyy) (°)
log [r/(|K|/σY)²]

Fig. 8

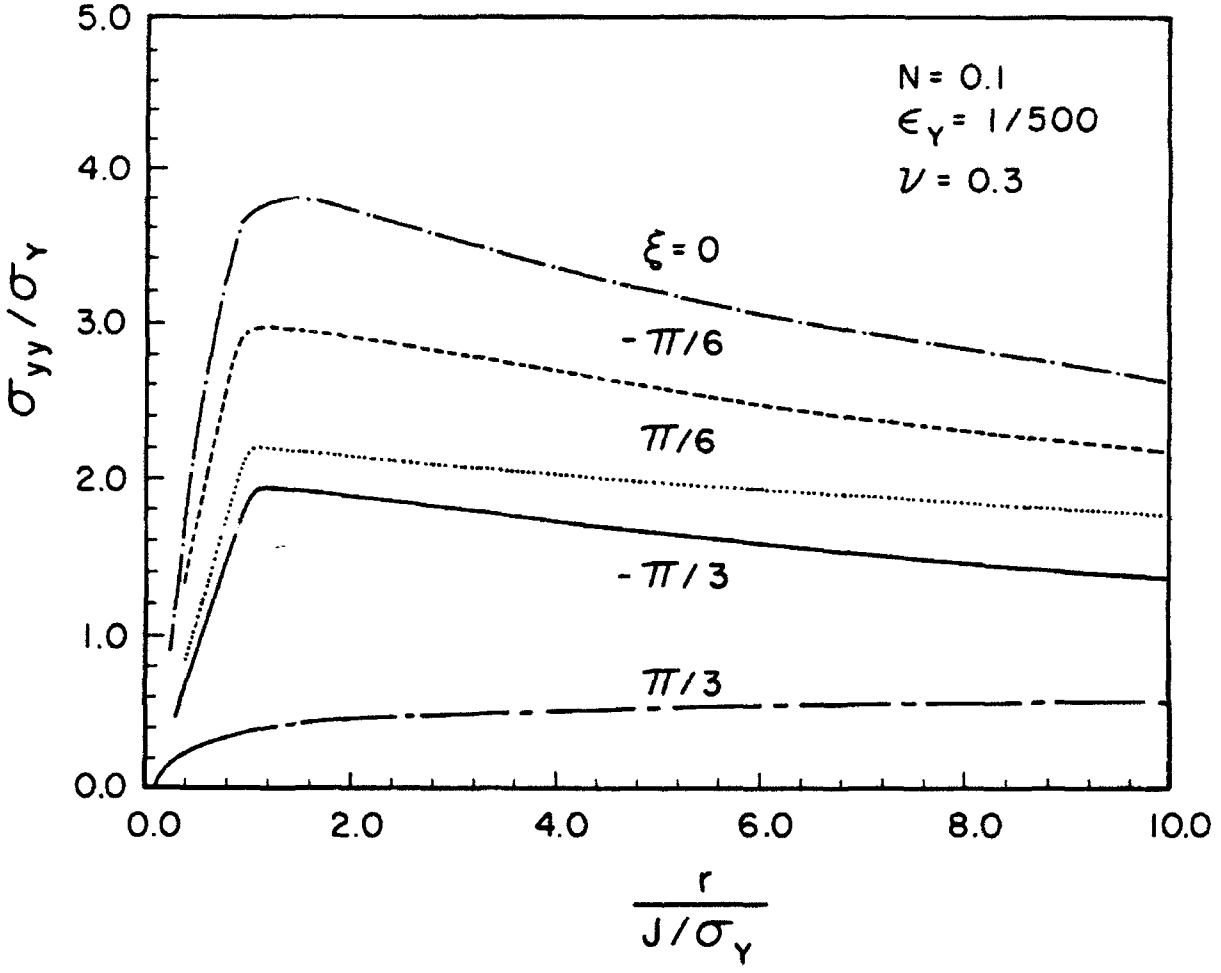
5.0
4.0
3.0
2.0
1.0
0.0
0.0
2.0
4.0
6.0
8.0
10.0
N = 0.1
ϵ_Y = 1/500
ν = 0.3
ξ = 0
-π/6
π/6
-π/3
π/3
σ_{yy}/σ_Y
$\frac{r}{J/\sigma_Y}$

Fig. 9

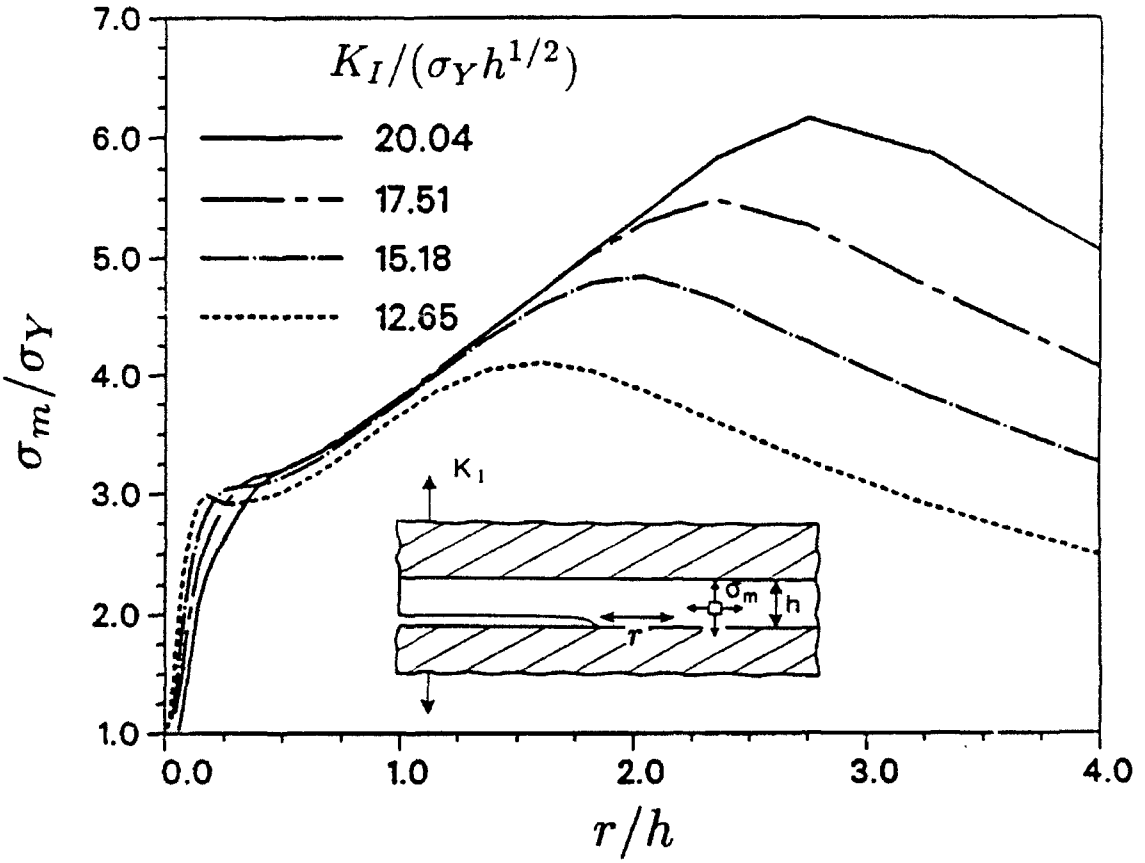
$K_I/(\sigma_Y h^{1/2})$
20.04
17.51
15.18
12.65
σ_m/σ_Y
r/h
7.0
6.0
5.0
4.0
3.0
2.0
1.0
0.0
1.0
2.0
3.0
4.0
K1
σm
h
r

Fig. 10

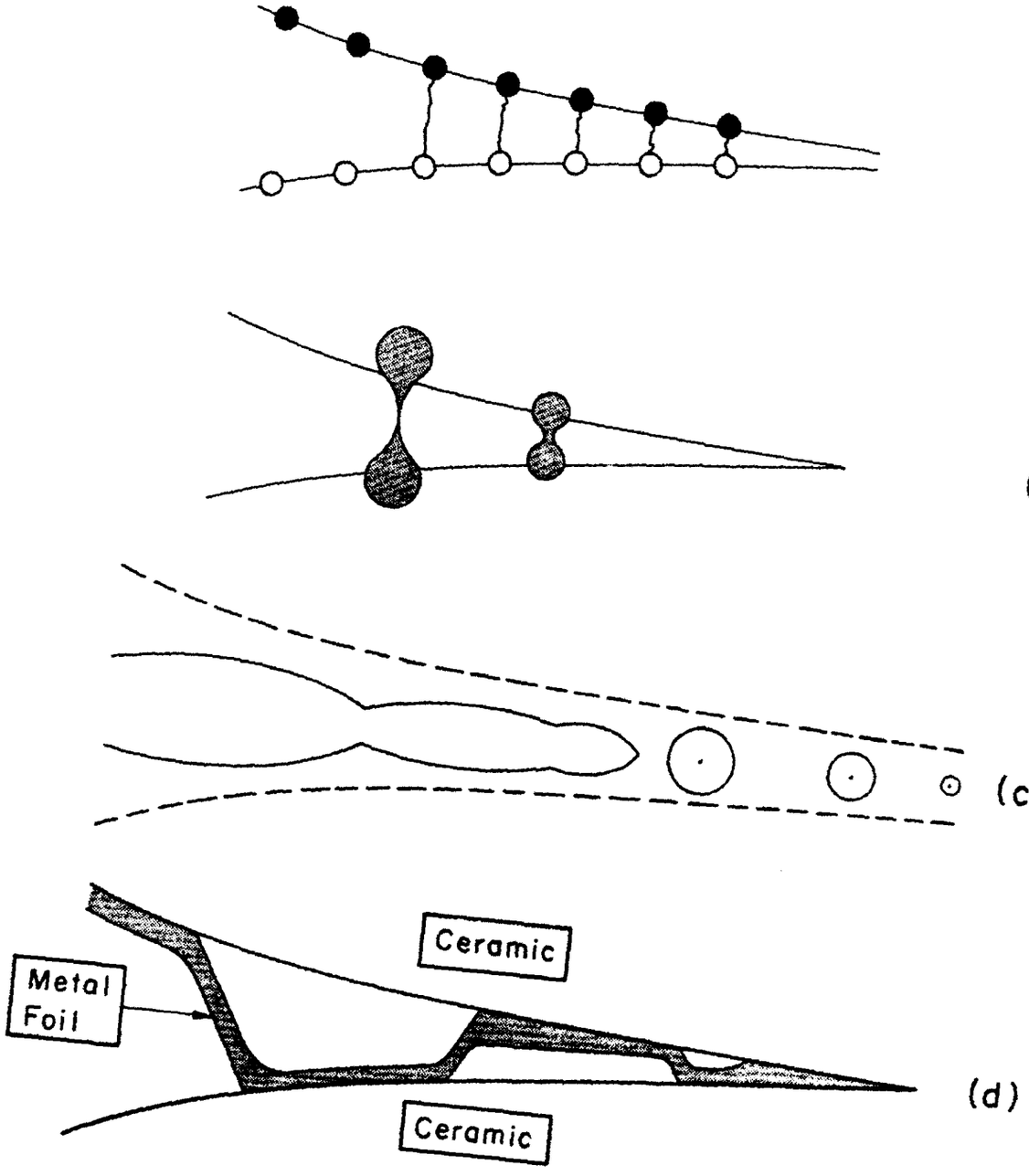

Fig. 11

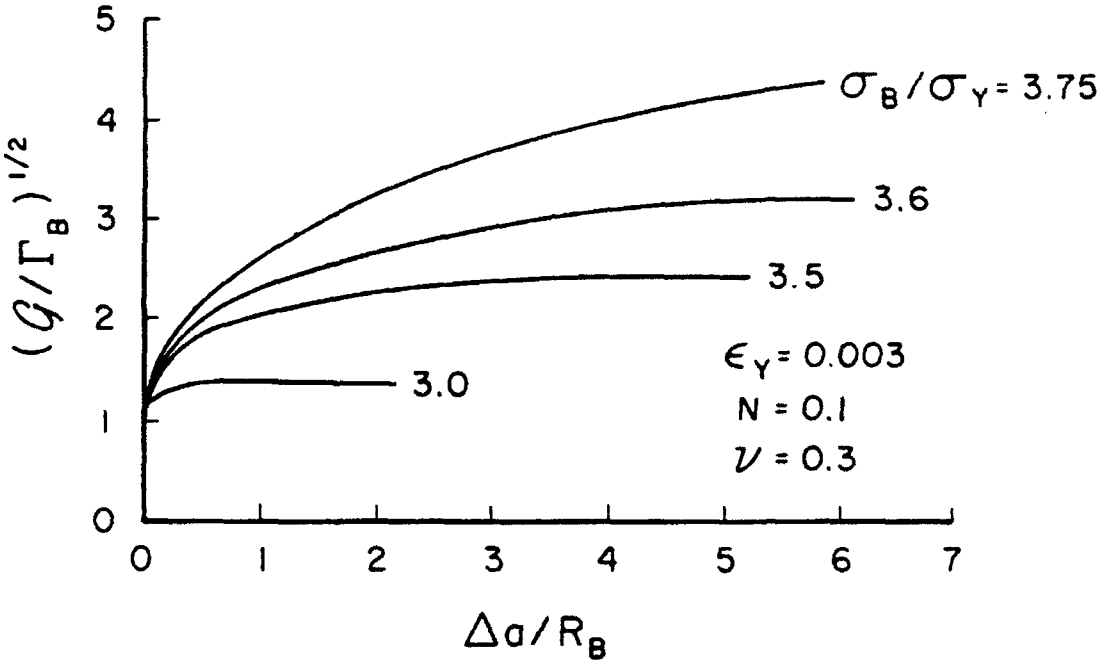
5
4
3
2
1
0
0
1
2
3
4
5
6
7
$(J/\Gamma_B)^{1/2}$
$\Delta a/R_B$
$\sigma_B/\sigma_Y = 3.75$
3.6
3.5
3.0
$\epsilon_Y = 0.003$
N = 0.1
$\nu = 0.3$

Fig. 12

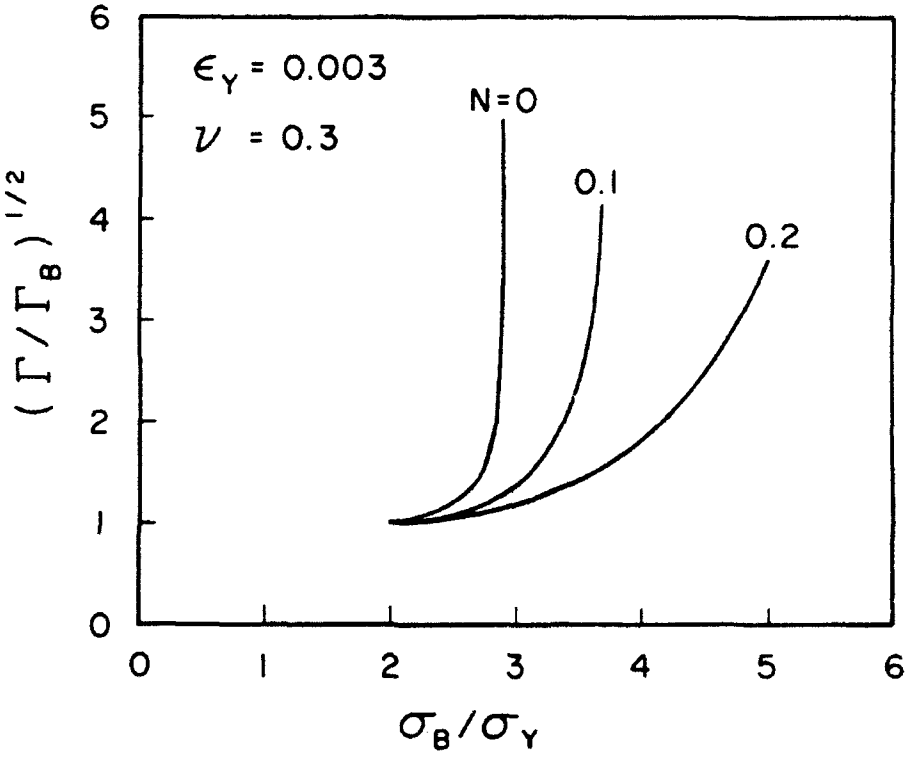
ϵ_Y = 0.003
ν = 0.3
N=0
0.1
0.2
$(\Gamma/\Gamma_B)^{1/2}$
σ_B/σ_Y
0
1
2
3
4
5
6

Fig. 13

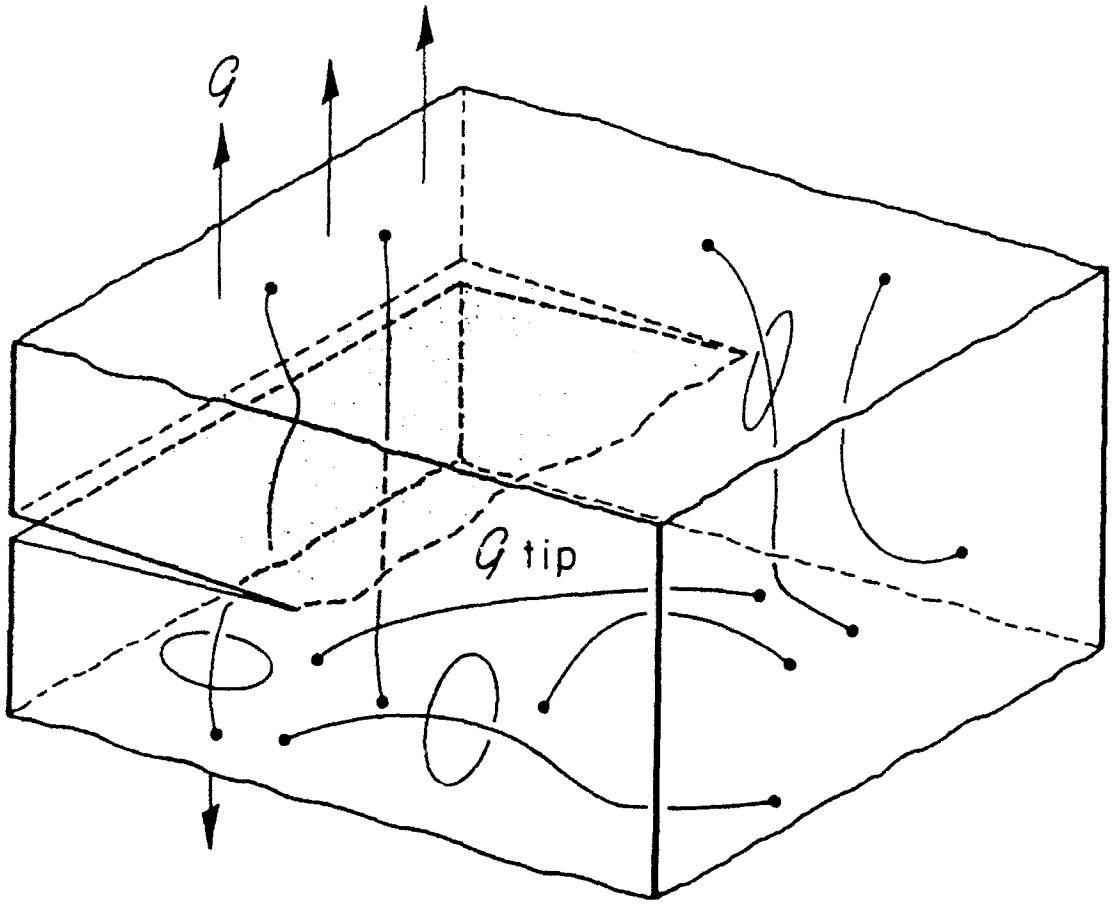

Fig. 14

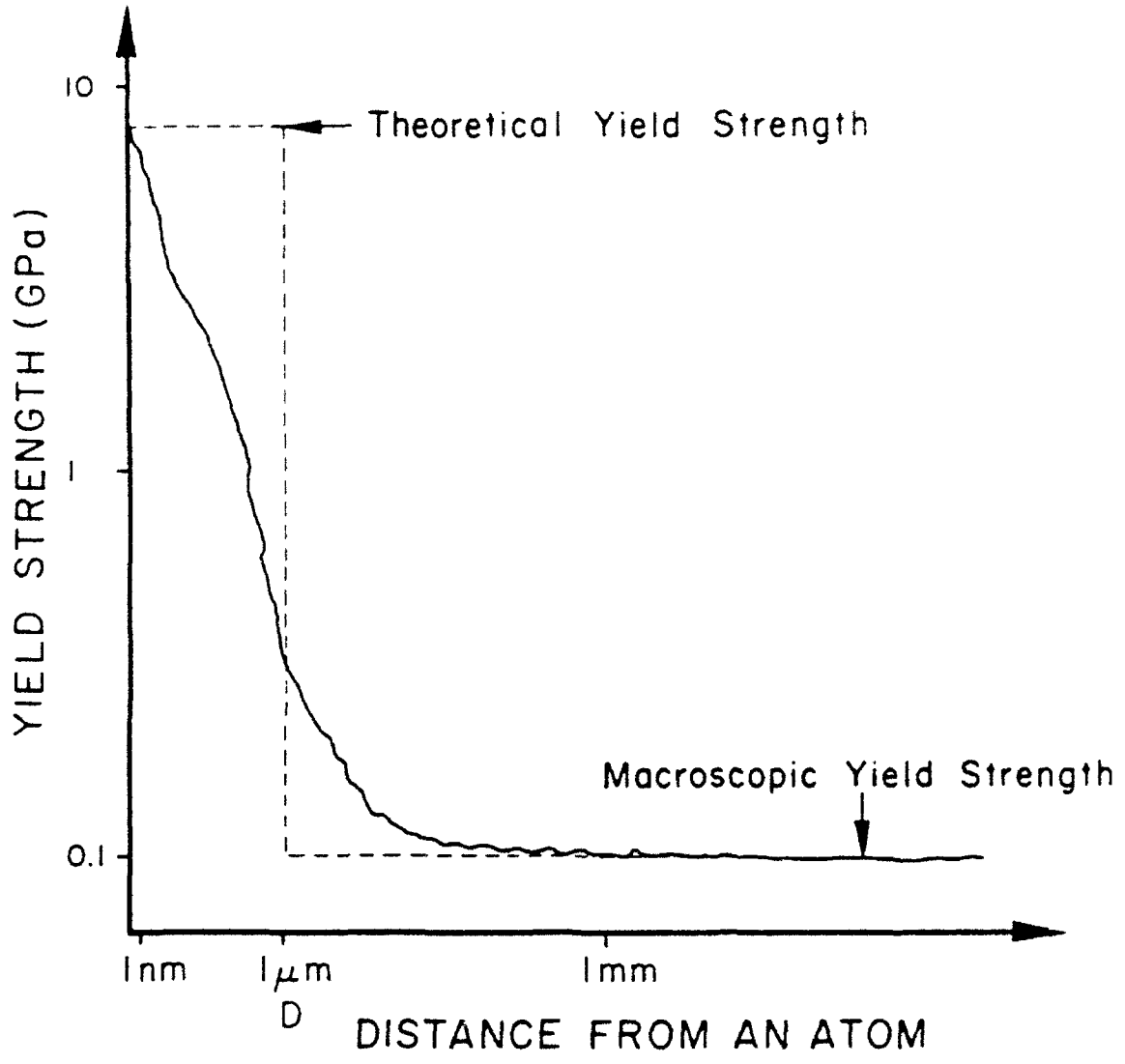
10
1
0.1
YIELD STRENGTH (GPa)
Theoretical Yield Strength
Macroscopic Yield Strength
1nm
1μm
D
1mm
DISTANCE FROM AN ATOM

Fig. 15

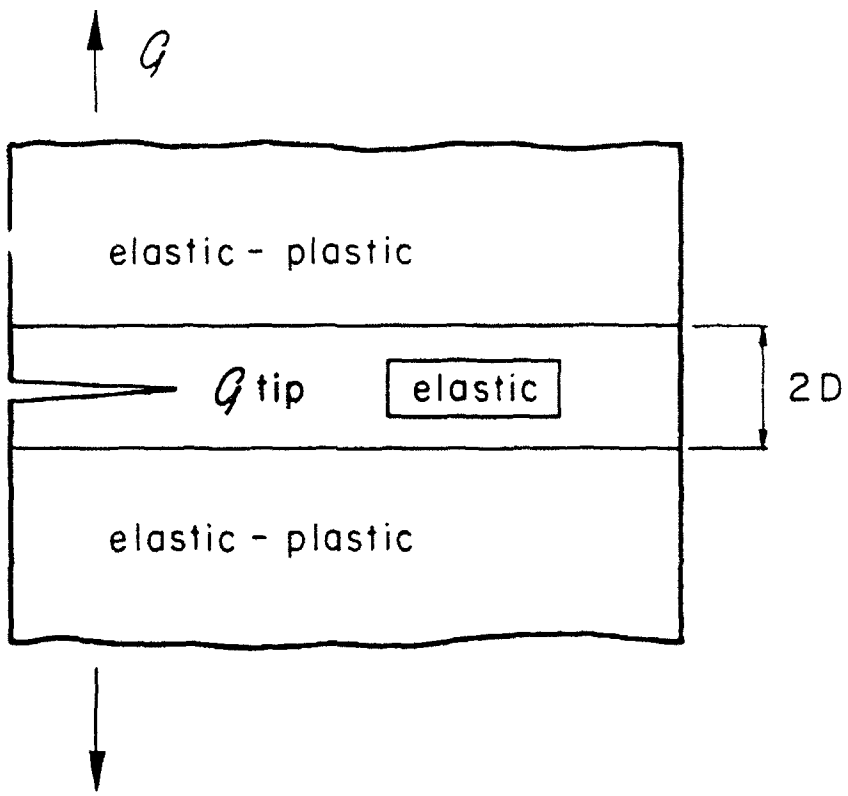

Fig. 16

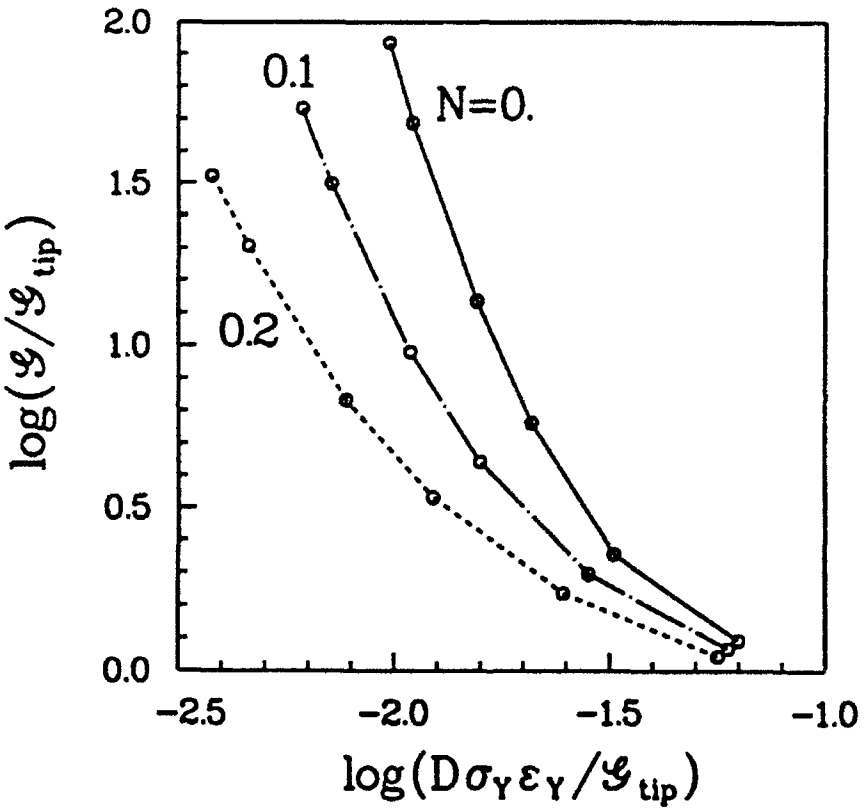

Fig. 17

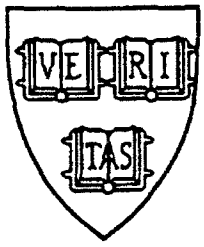

MECH-208

MODE II FRACTURE TOUGHNESS OF A BRITTLE ADHESIVE LAYER

Z. Cedric Xia and John W. Hutchinson

Division of Applied Sciences
HARVARD UNIVERSITY
Cambridge, Massachusetts 02138

March 1993

MODE II FRACTURE TOUGHNESS OF A BRITTLE ADHESIVE LAYER

Z. Cedric Xia and John W. Hutchinson

Division of Applied Sciences

Harvard University

Cambridge, Massachusetts, U.S.A.

ABSTRACT

This paper concerns the analytical estimation of the macroscopic mode II fracture toughness of a brittle adhesive layer sandwiched between and bonding together stiff substrates. The process of failure involves the propagation and coalescence of microscopic tensile cracks ahead of the macroscopic mode II crack tip. The basic problem at the heart of the analysis is the plane strain problem for a layer subject to shear and containing a periodic array of micro-cracks which grow and coalesce under the condition that their tips advance under pure mode I conditions. A numerical solution to this basic problem is obtained and is then used to make detailed predictions for conditions for tunneling of the micro-cracks and for the evolution of their shape and spacing. These predictions are used in turn to develop the shearing traction-displacement relation for the brittle adhesive layer. The work per unit length of layer needed to drive the microcracks to coalescence can be identified with the macroscopic work of fracture in mode II, Γ_{IIc}, as is discussed via a cohesive zone model. The macroscopic mode II toughness is predicted to be between 3 to 4 times the mode I fracture toughness, Γ_{Ic}, depending on constraints provided by substrates and very slightly on Poisson's ratio ν. The theoretical predictions are compared with experimental data reported in the literature. Also discussed are the consequences of the assumption underlying the analysis that there exists an ample population of initial flaws whose largest dimension is roughly comparable to the thickness of the layer.

1. INTRODUCTION

Once initiated, cracks in homogeneous, isotropic brittle materials tend to advance under mode I conditions, assuming continuously applied loads. Thus, for example, when a crack propagates under plane strain conditions it selects a trajectory such that its mode II stress intensity factor, K_{II}, vanishes. This so-called "local symmetry" condition dictates many crack patterns found in brittle thin films or substrates where cracking occurs. Recent studies have detailed a number of interesting crack paths governed by this condition. Examples include studies of the development of wing cracks under compressive loading by Ashby and Hallam (1986) and by Horii and Nemat-Nasser (1986), of spiral cracking around a strained cylindrical inclusion by Freund and Kim (1991), and of cracking behavior due to localized hot shock of a brittle substrate by Tvergaard *et al* (1993). The theoretical study most closely related to the present work is that of Fleck (1991) on the growth of periodic echelon cracks in an infinite substrate under combined shear and tensile loadings.

Macroscopic mode II crack growth is frequently observed in a very thin brittle adhesive layer which bonds together two substrates which confine the cracking process to the layer. If the crack does not follow one of the interfaces, one often observes scalloped fracture areas on the crack surface and many sigmoidal microcracks ahead of the main crack tip (see, for example, Hibbs and Bradley 1987, Smith and Grove 1987, Chai 1988, and Fleck 1992). Similar behavior takes in the matrix material between closely spaced parallel fibers in a composite. The fracture process seems to start with the initiation of sigmoidal tensile microcracks ahead of the crack tip and continue with the spreading of this damage leading to a distribution of microcracks such as that depicted in Fig.1a. Macroscopic shear crack growth is initiated by coalescence of the main tip with the tensile microcracks just ahead of it. The experimentally measured work of fracture needed to advance such a mode II crack is found to be greater than the mode I work of fracture, with Γ_{IIc}/Γ_{Ic} ranging from 3 to 10 for brittle or moderately brittle materials (Bradley 1989, Hibbs and Bradley 1987, and Fleck 1992).

The aim of this study is the analytical estimation of macroscopic mode II fracture toughness of a brittle adhesive layer, Γ_{IIc}, in terms of the mode I toughness of the adhesive, Γ_{Ic}. In mode I, the work of fracture of the sandwiched brittle layer *is* the mode I toughness of the adhesive, Γ_{Ic}, if the crack propagates in the interior of the layer and not along one of the interfaces between the adhesive and substrates (Fleck, Hutchinson and Suo, 1991). In developing the theoretical estimate of Γ_{IIc} it will be assumed that the spacing of the microcracks is small compared to the length of the zone of microcracking ahead of the macroscopic mode II crack. In effect, we work at two scales: the micro- and macroscales. On the microscale, we analyze the development of a periodic array of identical tensile microcracks, as shown in Fig.1b, and use these results to obtain a traction-displacement relation in shear, $\bar{\tau}(u)$, governing the macroscale behavior of the layer. A cohesive zone model of the mode II macrocrack is stipulated with $\bar{\tau}(u)$ as the shearing traction law in the cohesive zone ahead of the macrocrack. Well known arguments employing the J-integral give the desired connection

$$\Gamma_{IIc} = \int_0^{u_c} \bar{\tau}(u)du \tag{1}$$

where u_c is the shearing displacement at which the periodic microcracks coalesce and $\bar{\tau}$ drops to zero. The present study is the mode II counterpart to the modeling conducted by Ortiz (1988) of the effect of microcracks ahead of a mode I macrocrack.

The sections of the paper leading to explicit results from (1) are organized as follows. Section 2 provides the solution to the basic plane strain problem shown in Fig. 1b for a periodic array of curved cracks, in a layer subject to remote shear loading, growing and coalescing under the condition that the mode II stress intensity factors at each crack tip vanish. Three quantities from this solution are needed to carry out the computation of $\bar{\tau}(u)$ and the prediction of Γ_{IIc}: the energy release rate for the in-plane growth of the plane strain cracks, G_{ps}; the effective in-plane shear modulus $\bar{\mu}$ of the cracked layer; and the energy release rate, G_{ss}, for each of the cracks when they tunnel in a direction perpendicular to the trace plane shown in Fig. 1b. Complete results for these quantities are given in Section 2. The shearing traction-displacement relation, $\bar{\tau}(u)$, is derived in Section 3. This derivation has two steps. First, the evolution of the cracks' length and density as

a function of u is obtained using the basic results of Section 2. This step involves arguments as to when the microcracks will advance in their plane and when they will tunnel. It also involves the assumption that there exists a population of relatively large initial flaws in the adhesive from which the microcracks develop. Then, with the evolution of the length, shape and density of the cracks in hand, the traction-displacement law can be obtained from the results for $\bar{\mu}$. The final results for Γ_{IIc} are discussed in Section 4, along with a discussion of the implications of the assumption concerning the initial flaw population. Experimental observations which have been reported in the literature for mode II behavior of brittle adhesive layers are compared with the theory in this final section.

2. A PERIODIC ARRAY OF MODE I CRACKS IN A BRITTLE ADHESIVE LAYER SUBJECT TO SHEAR

2.1. The Plane Strain Problem

The plane strain problem is introduced in Fig. 1b. An adhesive layer of thickness 2H joins two substrates. It is often the case that the substrates are much stiffer than the adhesive. For the purpose of reducing the number of parameters in the problem and to simplify the analysis somewhat, we shall regard the substrates as two rigid grips perfectly bonded at each interface to the adhesive. The adhesive is taken to be isotropic, homogeneous and linearly elastic, with shear modulus μ and Poisson's ratio ν. The external loading is applied through prescribed relative translations, u and v, of the two rigid grips. Two limiting shear loading cases are analyzed corresponding to different constraints in the vertical direction. For a given prescribed tangential displacement u, either: (1) the grips are allowed to move freely in the vertical direction (*i.e.*, the average normal traction exerted on the grips is zero), or (2) the grips are totally clamped in the vertical direction (*i.e.*, v=0).

The spacing separating the periodically distributed cracks in Fig. 1b is taken as 2b, and the curvilinear length of each crack in the current state is denoted by 2a. The solution procedure adopted in this study is that of representing the cracks as superposition of continuously distributed

dislocations chosen to cancel the tractions on the crack surfaces via solution of coupled integral equations. The solution of a periodic array of dislocations in an elastic layer between rigid substrates is given in the Appendix. The outline of the setup of the integral equations and the numerical procedure for solving them can be found in Tvergaard *et al* (1993). The procedure for advancing the crack tips such that pure mode I conditions always prevail at the tips is the same as that employed by Fleck (1991). It is this part of the solution method which determines the shape of the evolving cracks, as is now further described.

The process is started with an array of very short straight cracks with spacing 2b and inclined at 45° to the x-axis such that they are normal to the maximum principal stress of the uncracked layer. Since the cracks are very small initially, they behave almost like isolated cracks subject to tension perpendicular to their plane, and thus can be regarded as pure mode I cracks. The method for generating the subsequent crack trajectories is as follows. With the crack at its current length having $K_{II}=0$, then the crack length is increased with the curvature of the next increment chosen such that the advanced tip is also in a state of pure mode I. More details of calculation procedure can be found in Fleck (1991). The plane strain energy release rate at the crack tips, G_{ps}, is related to the mode I stress intensity factor by the standard relation; the stress intensity factor is computed directly as the amplitude of the inverse square root singularity of the dislocation distribution at the ends of the crack.

When there are no cracks presented in the adhesive layer, the stress field is simply

$$\tau = \mu \frac{u}{2H} \tag{2}$$

and all other components are zero. After introduction of the periodic array of cracks, the average shear traction exerted at grips for a prescribed u is reduced below the value given by (2) and is denoted by $\bar{\tau}$. The effective shear modulus of the adhesive is denoted by $\bar{\mu}$ and is defined as

$$\bar{\mu} = \bar{\tau} \frac{2H}{u} \tag{3}$$

The effective shear modulus is an important property which indicates the damage to the shear strength of the adhesive layer when cracks are present. Its primary purpose in the present paper

will be to generate the traction-displacement relation $\bar{\tau}(u)$.

For a given crack shape, $\bar{\mu}$ is a function of the crack length/spacing ratio, a/b, the crack density ratio, H/b, and which of the two normal constraint conditions is imposed. This functional dependence can be determined from a direct computation of the average shear traction $\bar{\tau}$ when a value of u is prescribed, or it can be computed using a basic connection between compliance change and energy release rate derived as follows. Let s be the length of the evolving curved crack which started with length 0 and has grown to its current length 2a. The elastic strain energy U stored in the layer per crack (with spacing 2b) is

$$U = \frac{1}{2}\bar{\tau} u \, 2b = \frac{u^2 b}{2H}\bar{\mu} \tag{4}$$

The plane strain energy release rate G_{ps} at each tip at the current crack length 2a is given by

$$G_{ps}(a) = -\frac{1}{2}\frac{\partial U(a)}{\partial a} \tag{5}$$

The combination of (4) and (5) gives, together with the initial condition $\bar{\mu}=\mu$ when s=0,

$$\mu(a) = \mu - \frac{4H}{u^2 b}\int_0^a G_{ps}(s)\, ds \tag{6}$$

As the crack length 2a approaches the critical length $2a_c$ where the cracks coalesce, the effective modulus $\bar{\mu}$ must approach zero. This fact provides an additional consistency check on the accuracy of the numerical calculations.

The numerical results for G_{ps}, $\bar{\mu}$ and for the shapes of the crack trajectories are shown in Figs. 2-4 and will be explained in detail. The boundary value problems have displacement-type conditions along the grip interfaces, and therefore the solutions do depend on Poisson's ratio. The results shown in these figures were computed with $\nu=1/3$, but selected numerical checks indicated there is little dependence on ν for the normalized quantities employed. Recall that the solution process starts with a prescribed value of crack density H/b and with very short straight cracks oriented at 45^o to the centerline of the layer. The cracks are then advanced under pure mode I conditions. Two distinct behaviors are found, unlike the shapes discovered by Fleck (1991), who

considered an infinitely thick layer subject to combinations of shear and normal loading. In the case of the layer which has zero average normal traction, it is found that the cracks grow toward the interfaces of the adhesive and the rigid grips when the crack density, H/b, is less than about 0.81 with final shapes typical of those shown in the insert of Fig. 2a. For crack densities, H/b, greater than 0.81 the cracks do not impinge upon the rigid grips but instead turn toward their neighbors and coalesce, as shown in the inserts in Figs. 2b and 2c (here, again, the complete crack trajectories are shown). In the regime where the cracks coalesce, the shapes are relatively independent of H/b and the pattern scales with the spacing b. This limiting behavior would have been more evident had G_{ps} been normalized by b rather than H in the ordinate of Figs.2b and c (The choice of H rather than b for the normalization facilitates application of the results discussed later). When H/b is large, the present results agree with those of Fleck (1991) for echelon crack arrays in an infinitely thick slab. The transition in shapes in the second case, where the normal separation of the rigid grips is constrained to be zero, occurs at about H/b=2.6. The three parts of Fig. 2 display the dependence of the normalized G_{ps} on the crack length/spacing ratio, a/b, for the three values of the crack density parameter H/b, all for the case of no average normal traction. An important feature of this dependence is the existence of a local maximum in the normalized energy release rate which is attained when the cracks are still well away from coalescence. In the regime where the cracks coalesce, the normalized G_{ps} becomes unbounded as the tips approach the crack surface of their neighbor. It is again worth emphasizing, the trajectories shown are pure mode I trajectories, and at no point as the cracks are advanced do opposite points on the crack faces come into contact (*i.e.*, the cracks are fully open). Fig. 2 also contains results for the tunneling energy release rate, G_{ss}, which will be introduced in the next subsection.

The complete results for the normalized plane strain energy release rate are plotted in Fig. 3 for the entire range of H/b needed in the present study for each of the two limiting normal constraint cases. The companion curves for the normalized effective shear modulus of the layer, $\bar{\mu}/\mu$, are shown in Fig.4.

2.2. Steady-state Tunneling Cracks and Evaluation of G_{ss}

Crack nucleation and growth in an adhesive layer is a very complicated process. It is a full three dimensional problem in the sense that cracks will initiate from an existing population of flaws and propagate both in the plane (*i.e.*, in the (x,y) plane of Fig. 1) and out of the plane (*i.e.*, the z-direction in Fig.1) Extensive propagation out of the plane is referred to as tunnel cracking. This is a form of cracking which is very common in thin brittle films and layers (Beuth 1992, Ye *et al* 1992, Hutchinson and Suo 1991, and Ho and Suo 1993). It is the primary mechanism by which roughly equiaxed initial flaws become greatly extended cracks in the tunneling direction. This mechanism is clearly expected to play a dominant role in establishing cracks in the brittle shear layer which are very long in the out-of-plane direction compared to their in-plane length, *i.e.*, essentially plane strain cracks. In steady-state, the crack propagates in the out-of-plane direction at constant applied load with the tunnel front maintaining its shape as it advances. The steady-state energy release rate, G_{ss}, no longer depends on the tunneling length, nor on the initial flaw geometry.

The steady-state energy release rate G_{ss} along the tunneling front can be computed using quantities from the 2D plane strain crack solution without resorting to a 3D analysis. Since the energy released per unit length of tunneling in the z-direction equals the energy released to form the plane strain crack traversing the layer (on a per crack basis), it readily follows that (*e.g.*, Hutchinson and Suo, 1991)

$$G_{ss}(a) = \frac{1}{a}\int_0^a G_{ps}(s)ds \tag{7}$$

This is the relation which is used here to compute G_{ss}. An additional interesting relation between G_{ss} and G_{ps} noted by Beuth (1992), which will be of use later, is obtained by taking the derivative of (7) with respect to a

$$\frac{dG_{ss}}{da} = \frac{1}{a}(G_{ps} - G_{ss}) \tag{8}$$

Thus G_{ss}=G_{ps} defines a condition at which G_{ss} achieves a local maximum with respect to in-plane crack length.

Numerical results for G_{ss} can be generated using (7) and the results of Figs. 2 and 3. The three plots of Fig. 2 include curves of normalized G_{ss} illustrating the trends and the fact expressed by (8) that the maximum of G_{ss} at a prescribed u occurs where the two energy release rates are equal. Note that G_{ss} exceeds G_{ps} at crack lengths larger than those at the crossover point so that the crack driving force for tunneling will exceed that for in-plane extension in that regime. The results shown apply to a family of identical cracks spaced a distance 2b apart, all tunneling together as illustrated in Fig. 5a. We now take one further step and derive the steady-state energy release rate for a new set of tunnel cracks of identical cross-sectional shape which precisely bisect a pre-existing set of fully tunneled cracks, as depicted in Fig. 5b. The steady-state energy release rate for this new set of cracks is denoted by $\hat{G}_{ss}$.

2.3. $\hat{G}_{ss}$ for Sequential Tunnel Cracking

Consider now the derivation of the steady-state energy release rate for the sequential cracking process depicted in Fig. 5b, where a set of new cracks of spacing 2b tunnels, precisely bisecting a pre-existing set of spacing 2b. Let $G_{ss}(b)$ denote the result of §2.2 for tunnel cracks of spacing b and let $G_{ss}(2b)$ be the result for spacing 2b, both for the same prescribed value of u. Let $\hat{G}_{ss}$ be the energy release rate for the new set of tunneling cracks. Following the argument given by Hutchinson and Suo (1991), one has precisely

$$\hat{G}_{ss}(b) = 2G_{ss}(b) - G_{ss}(2b) \tag{9}$$

stating that the energy released by each new crack is the difference between the down-stream rate (for two cracks per new crack) and the up-stream rate. Thus, the steady-state energy release rate for the sequential process can also be obtained from the results for G_{ps} using (7) and (9). Curves of normalized $\hat{G}_{ss}$ as a function of a/b are plotted in Fig. 6 for various H/b for the two constraint

cases. Note that these results apply to a new set with spacing 2b tunneling between an existing set of spacing 2b, *i.e.* the situation depicted in Fig. 5b. In Section 3, results for $\hat{G}_{ss}$ and G_{ps} will be used in an approximate way to predict the evolution of both the spacing and lengths of the cracks in the layer as a function of u.

3. CRACK SPACING AND $\bar{\tau}(u)$

As a crack grows from an initial flaw in a brittle isotropic material comprising the layer, its crack front adjusts to a curved shape such that at every point it is in mode I with its energy release rate equal to the mode I toughness of the material, Γ_{Ic}. Once it has tunneled a distance of about two times its in-plane length the crack rapidly approaches the asymptotic steady-state condition analyzed for periodically spaced cracks in the previous section. Crack propagation is entirely in the out-of-plane direction, advancing under constant applied shear displacement u and leaving behind an in-plane crack of fixed shape and length. A rigorous analysis of this three dimensional process is extremely difficult and is not attempted for the present shear layer problem. (A three dimensional analysis has been carried out for a thin film cracking problem by Nakamura and Kamath (1992) demonstrating for that problem that steady-state conditions are essentially attained once the crack has grown to a length of about twice the film thickness.) As noted in the discussion of Fig. 2, except for very high crack densities, there is a range of a/b in which G_{ss} exceeds G_{ps}. This implies that the three dimensional process of growth from a roughly equiaxed initial crack-like flaw will involve both in-plane and out-of-plane growth until the crack reaches the point where out-of-plane tunneling is favored. Once steady-state is achieved, tunneling will be completed in the out-of-plane direction resulting in a set of plane strain cracks. Then, as u is further increased, these cracks will undergo further in-plane extension until conditions are met for a new set of cracks to begin tunneling between the present set. An approximate analysis of this sequential process is now given.

3.1. Evolution of Crack Density as a Function of u

Suppose a periodic array of fully tunneled plane strain cracks exists with spacing 2b. The condition for a new set to tunnel between the existing set as depicted in Fig. 5b is obtained as follows. When u reaches the level corresponding to $\hat{G}_{ss}(b) = \Gamma_{Ic}$, steady-state tunneling of the new set can occur with the outcome being a set of fully tunneled plane strain cracks of spacing b. Setting $\hat{G}_{ss}(b) = \Gamma_{Ic}$ and plotting the result in the form of $u\sqrt{\mu/(\Gamma_{Ic}H)}$ as a function of a/b for fixed values of H/b leads to curves such as those in Fig. 7. Note that for a given value of spacing 2b (*i.e.* a given value of H/b), there is a minimum value of u below which a set of new cracks cannot tunnel. If it is assumed that the *initial flaw population is sufficiently large and plentiful* such that the new set *will initiate and tunnel* when u reaches the minimum in Fig. 7 for the given H/b, then the crack spacing history lies along the trajectory of minima in Fig. 7. Given some initial spacing $2b_0$, say, then the subsequent spacings must be b_0, $b_0/2$, $b_0/4$, etc., for the sequential process envisioned, but a strict adherence to this sequence can be relaxed as described later. Fig. 8 displays the crack density parameter H/b determined as just outlined as a function of the normalized u for each of the two constraint cases. The threshold values correspond to the minimum values of normalized u where tunneling of isolated cracks can first occur. The crack density increases from zero to a very high density (*e.g.*, H/b=5 to 10) over a relatively small range of u, corresponding to roughly only a 75% increase above threshold. Each curve in Fig.8 is terminated with a horizontal dashed line at the crack density where the tunneling energy release rate no longer exceeds the plane strain release rate at any crack length a (cf. Fig. 2c). Exactly how new cracks develop in this regime is not clear, but tunneling is not expected. In any case, by the point where the crack density reaches these levels, all the important contributions to the macroscopic toughness have been made.

3.2 Traction-displacement Relation in Shear, $\bar{\tau}(u)$

With the relation between H/b and u in hand, it is possible to generate the desired relation $\bar{\tau}(u)$ in the following straightforward manner. For a prescribed value of u, obtain H/b from Fig. 8. This value characterizes the current spacing of the plane strain cracks. The in-plane length a of

these cracks is then obtained from the ratio a/b using the results in Fig. 7. Once a/b is known, use the curves of Fig. 4 to obtain $\bar{\mu}/\mu$. Then, by (3),

$$\bar{\tau}\sqrt{\frac{H}{\Gamma_{Ic}\mu}} = \frac{1}{2}\frac{\bar{\mu}}{\mu}u\sqrt{\frac{\mu}{\Gamma_{Ic}H}} \tag{10}$$

and it is this relation which is plotted for each of the constraint cases in Fig. 9. The peak values in Fig. 9 are associated with the onset of tunneling of widely spaced microcracks. The steep segments of the curves dropping from the peaks correspond to the range in which relatively widely spaced cracks tunnel with the sequential process of new sets tunneling and bisecting existing sets. The steep portion ends when the crack density reaches about H/b=2 for the case of zero average normal traction and at about H/b=3 for the case of zero normal displacement. At higher densities the interaction between the cracks becomes dominant and $\bar{\tau}$ falls gradually with increasing u. The curves are terminated at the points labeled by (u_c, $\bar{\tau}_c$) beyond which higher densities of tunneling cracks will not occur, *i.e.*, at the density cutoffs indicated in Fig. 8.

Strictly speaking, the construction of the relation between $\bar{\tau}$ and u described above should start with some initial wide spacing $2b_0$ and then faithfully bisect the spacing according to the discrete values b_0, $b_0/2$, etc., leading to curves in Fig. 9 which would be segmented. The curves in Fig. 9 are generated by applying the calculation described above continuously as a function of u, ignoring the discrete nature of the sequential bisection process. The difference between the curves thus obtained and any segmented curve generated using some initial wide spacing $2b_0$ is not appreciable. The procedure described above approximates the actual cracking process in another sense. The shape of the cracks in the (x,y) plane depends on the crack density H/b. Thus, in any actual process the shapes of cracks which tunnel at one value of u will differ from those tunneling at another value of u. The procedure used here takes the *shapes* of all the cracks to be the same and to be that shape associated with the current value of u.

4. MACROSCOPIC MODE II TOUGHNESS, Γ_{IIc}

The results in Fig. 9 for $\bar{\tau}(u)$ enable one to calculate Γ_{IIc} using (1). The final tail of $\bar{\tau}(u)$ has not been determined, and we neglect a small contribution to the integral in (1) by terminating the integration at u_c as taken in Fig. 9. The results of the integration are

$$\Gamma_{IIc} = 3.1\ \Gamma_{Ic} \quad \text{for zero average normal traction}$$

$$\Gamma_{IIc} = 4.2\ \Gamma_{Ic} \quad \text{for zero normal displacement}$$

The numerical results in this paper have all been calculated with a Poisson's ratio of 1/3, but, as mentioned earlier, the results are only weakly dependent on ν.

The present results are corroborated by Fleck's (1991) result, $\Gamma_{IIc}=2.7\ \Gamma_{Ic}$, obtained for a single array of periodically spaced, tensile plane strain microcracks in an infinite solid subject to pure shear at infinity. This result represents the work of fracture per unit area needed to drive the sigmoidal echelon cracks to coalescence. More work is absorbed in the process envisioned in the present paper because of the influence of the constraint of the substrates and the fact that new cracks initiate and tunnel between existing cracks as u is increased. Nevertheless, the fact that the two analyses give results which are not significantly different suggests that the sequential details of the microcracking process may play a secondary role.

The cohesive zone model on which the above results are based also can be used to calculate the length of the cohesive zone L (see Fig. 1a) in which the 'microscopic' traction-displacement relation $\bar{\tau}(u)$ holds. We have not computed L for the precise relation $\bar{\tau}(u)$ of Fig. 9, but a rough estimate indicates that it is on the order of H. Thus, the extent of the microcracking zone ahead of the macroscopic crack tip is only on the order of the most widely spaced cracks which make a significant contribution in the analysis leading to $\bar{\tau}(u)$, *i.e.* b≅H. This suggests that an analysis which accounts for the interaction between the macrocrack and the individual microcracks in a discrete manner may give somewhat different predictions. Further work along these lines may be

needed, especially if initiation from smaller flaws is considered important, as will be discussed below.

5. DISCUSSION

The results of present analysis are in general agreement with experimental data reported in the literature. In particular, Bradley (1989) presented his experimental results for the ratio of mode II delamination toughness to mode I delamination toughness for a variety of resin adhesives. The ratio Γ_{IIc}/Γ_{Ic} for the brittle resins varies from 3 to 11, with most data in the range from 3 to 6. It should be expected that the present theoretical results should tend to bound the experimental data from below for two reasons. Firstly, the response of the adhesive has been assumed to be purely elastic with no accounting for plasticity, and plasticity is expected to have more effect on the mode II toughness than the mode I toughness. Secondly, it has been assumed that there exists an ample population of initial flaws whose size is comparable to the thickness of the brittle adhesive layer. It is from these flaws that the tunnel cracks spread. If the population of initial flaws was of a size significantly smaller than the layer thickness (*e.g.*, on the order of H/5), then larger applied stresses would be necessary to initiate the tunnel cracks than is predicted by the steady-state tunneling analysis. The tunneling process would then involve the dynamic propagation of the microcracks and the dissipation of more energy than is predicted by the present quasi-static analysis. Assuming the microcracking process is brittle, we interpret the existence of experimentally measured ratios of Γ_{IIc}/Γ_{Ic} well in excess of 3 to be indirect evidence of the fact that those adhesives have initial flaws which are small compared to the layer thickness.

The present results for the mode II toughness are independent of the layer thickness 2H and do not depend explicitly on any details of the initial flaw population. In this sense the present results are similar to Fleck's result which is independent of the spacing of the periodically distributed echelon cracks. In the present modeling, this independence is a consequence of the assumption of an ample population of relatively large flaws. If, instead, there existed an ample population of small flaws, then one would expect the size of the flaws to enter into the dependence of Γ_{IIc},

primarily because an over-stress will be needed to initiate the tunnel cracking process. On the other hand, if the flaw population were sparse and widely spaced compared to the layer thickness, then one would expect the layer thickness as well as the spacing and, possibly, the size of the flaws to influence Γ_{IIc}. In either case, Γ_{IIc} is expected to exceed the 3 or 4 times Γ_{Ic} predicted by the present analysis.

Two constraint limiting constraint conditions have been considered leading to the two sets of predictions presented above. In addition, to simplify the analysis and to reduce the number of parameters in the problem, the compliance of the adjoining solids has been neglected compared to that of the adhesive. This is probably a reasonable approximation for many systems based on polymeric adhesives. For such systems, it would also seem that the second constraint assumption of zero normal displacement to the layer would be the more reasonable one, but that may depend on the details of the test specimen geometry. The main conclusion to be drawn from the results for the two limiting constraints is that there is not an unduly large difference in the resulting predictions.

ACKNOWLEDGMENTS

This work was supported in part by the DARPA University Research Initiative (Subagreement P.O.#KK3007 with the University of California, Santa Barbara, ONR Prime Contract N00014-92-J-1808), by the National Science Foundation Grant NSF-MSS-92-02141, and by the Division of Applied Sciences, Harvard University.

REFERENCES

Ashby, M.F. and Hallam, B.D. (1986). The failure of brittle solids containing small cracks under compressive stress states. *Act Met.* **34**, 497-510.

Beuth, J.L.(1992). Cracking of thin bonded films in residual tension. *Int. J. Solids Structures*, **29**, 1657-1675.

Bradley, W.L.(1989). Relationship of matrix toughness to interlaminar fracture toughness. in *Application of Fracture Mechanics to Composite Materials*, (Edited by K.Friedrich),

Elsevier Science Publishers B.V., 159-186.

Chai, H.(1988). Shear fracture. *Int. J. Fracture*, **37**, 137-159.

Fleck, N.A.(1991). Brittle fracture due to an array of microcracks. *Pro. R. Soc. Lond.A* **432**, 55-76.

Fleck, N.A.(1992). Private Communication.

Fleck, N.A., Hutchinson, J.W. and Suo, Z. (1991). Crack path selection in a brittle adhesive layer. *Int. J. Solids Structures* , **27**, 1683-1703.

Freund, L.B. and Kim, K.S.(1991). Spiral cracking around a strained cylindrical inclusion in a brittle material and implications for vias in integrated circuits. in *Mechanical Behavior of Materials and Structures in Microelectronics*, Eds. Z. Suhir, R. C. Cammarata and D. D. L. Chung, MRS Vol. 226, 1991, 291-302.

Hibbs, M.F. and Bradley, W.L.(1987). Correlations between micromechanical failure processes and the delamination toughness of Graphite/Epoxy systems. in *Fractography of Modern Engineering Materials* (Edited by J.E.Masters and J.Au), STP **948**, 68-97.

Ho, S. and Suo, Z. (1993). Tunneling cracks in constrained layers. *J. Appl. Mech.* (In press).

Horii, H. and Nemat-Nasser, S. (1986). Brittle failure in compression: splitting, faulting and brittle-ductile transition. *Phil. Trans. R. Soc. Lond.* A **319**, 337-374.

Hutchinson, J.W. and Suo, Z.(1991). Mixed mode cracking in layered materials. in *Advances in Applied Mechanics*, **28**, (Edited by J.W.Hutchinson and T.Y.Wu), Academic Press, New York, 63-191.

Nakamura, T. and Kamath, S.M. (1992). Three-dimensional effects in thin film fracture mechanics. *Mech. Mater.* **13**, 67-77.

Ortiz, M.(1988). Microcrack coalescence and macroscopic crack growth initiation in brittle solids. *Int. J. Solids Structures*, **24**, 231-250.

Rice, J.R.(1968). Mathematical analysis in the mechanics of fracture. Fracture, *An Advanced Treatise*, **II**, (Edited by H.Liebowitz), Academic Press, New York, 191-311.

Smith, B.W. and Grove, R.A.(1987). Determination of crack propagation directions in graphite/epoxy structures. in *Fractography of Modern Engineering Materials* (Edited by J.E.Masters and J.Au), STP **948**, 154-173.

Tvergaard, V., Xia, Z.C. and Hutchinson, J.W.(1993). Cracking due to localized hot shock. *J. Am. Ceram. Soc.*,**76** [3], 729-736.

Ye, T., Suo, Z. and Evans, A.G. (1992). Thin film cracking and the role of substrate and interface. *Int. J. Solids Structures* , **29**, 2639-2648.

APPENDIX. AN ARRAY OF DISLOCATIONS IN A BRITTLE ADHESIVE LAYER

The dislocation solution used to solve the plane strain problem is outlined here.

The plane strain elasticity problem is specified in Figure A1a. An array of edge dislocations with Burger's vector $\mathbf{b}=(b_x, b_y)$ lies along the x axis with uniform spacing π. The upper boundary lies along y=d and the lower boundary along y=-c. The elastic material has shear modulus μ and Poisson's ratio ν. The thickness of the layer is c+d=2H. The boundaries are considered to be rigid. The elastic solution to this problem is obtained by superimposing the solutions to the following two problems:

(a). An array of same dislocations lies in an infinite elastic body; and

(b). A dislocation-free strip of thickness 2H, with prescribed displacements along both upper and lower boundaries. The displacements are chosen to cancel that calculated from Problem a.

Problem a

The solution to this problem is given by the Muskhelishvili potentials

$$\phi(z) = A\ln(\mathrm{Sin}z), \qquad \Omega(z) = \overline{A}\ln(\mathrm{Sin}z) \tag{A1}$$

where

$$z \equiv x + iy, \qquad A = \frac{\mu(b_y - ib_x)}{4\pi(1-\nu)}$$

The stresses and displacements are given by

$$\sigma_x + \sigma_y = 2\,[\phi'(z) + \overline{\phi'(z)}\,] \tag{A2}$$

$$\sigma_y - \sigma_x + 2i\sigma_{xy} = 2\,[(\bar{z} - z)\phi''(z) + \Omega'(z) - \phi'(z)] \tag{A3}$$

and

$$2\mu(u_x + u_y) = (3 - 4\nu)\phi(z) + (\bar{z} - z)\overline{\phi'(z)} - \overline{\Omega(z)} \tag{A4}$$

The displacement along y=d and y=-c are periodic functions and thus can be expressed in term of Fourier Sine and Cosine series.

Problem b

Consider a dislocation-free strip with prescribed displacements along boundaries as shown in Figure A1c. Following Fleck *et al* (1991), we introduce two real potentials U(x,y) and X(x,y) satisfying

$$\nabla^4 U(x,y) = 0, \qquad \nabla^2 X(x,y) = 0, \qquad \frac{\partial^2 X(x,y)}{\partial x\,\partial y} = \frac{1}{4}\nabla^2 U(x,y) \tag{A5}$$

The stresses and displacements can be derived from

$$\sigma_x = \frac{\partial^2 U}{\partial y^2}, \qquad \sigma_y = \frac{\partial^2 U}{\partial x^2}, \qquad \sigma_{xy} = -\frac{\partial^2 U}{\partial x\,\partial y} \tag{A6}$$

$$2\mu u_x = -\frac{\partial U}{\partial x} + 4(1-\nu)\frac{\partial X}{\partial y}, \qquad 2\mu u_y = -\frac{\partial U}{\partial y} + 4(1-\nu)\frac{\partial X}{\partial x} \tag{A7}$$

The general procedure is to represent U(x,y), X(x,y) as Fourier series in x. Solutions of these two potentials can be derived by canceling the displacements u_x and u_y along boundaries y=a and y=-c obtained from (A4). The details of solution procedure are omitted here. Helpful hints can be found in Fleck *et al* (1991).

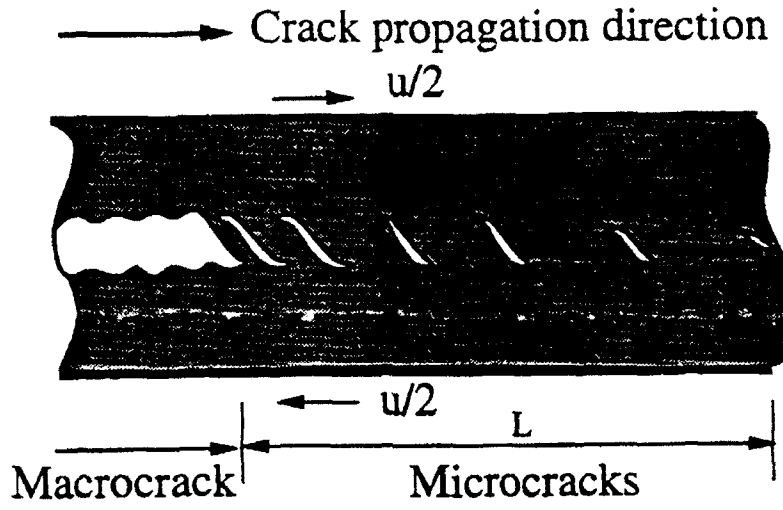

Fig. 1a. A schematic of the fracture process.

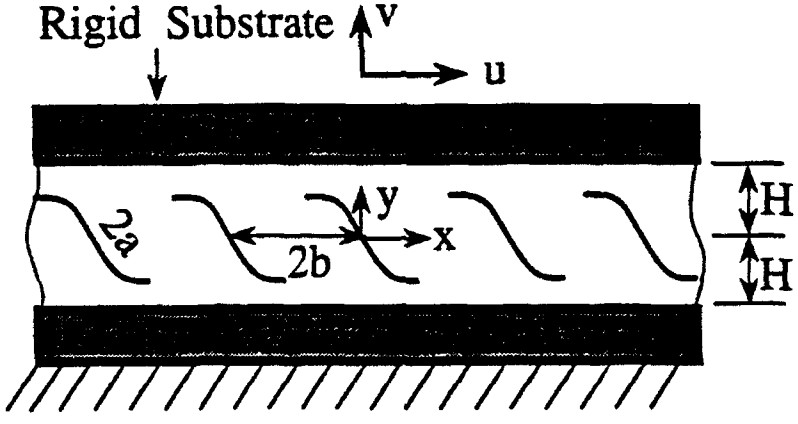

Fig. 1b. An array of curved tensile microcracks in the adhesive layer.

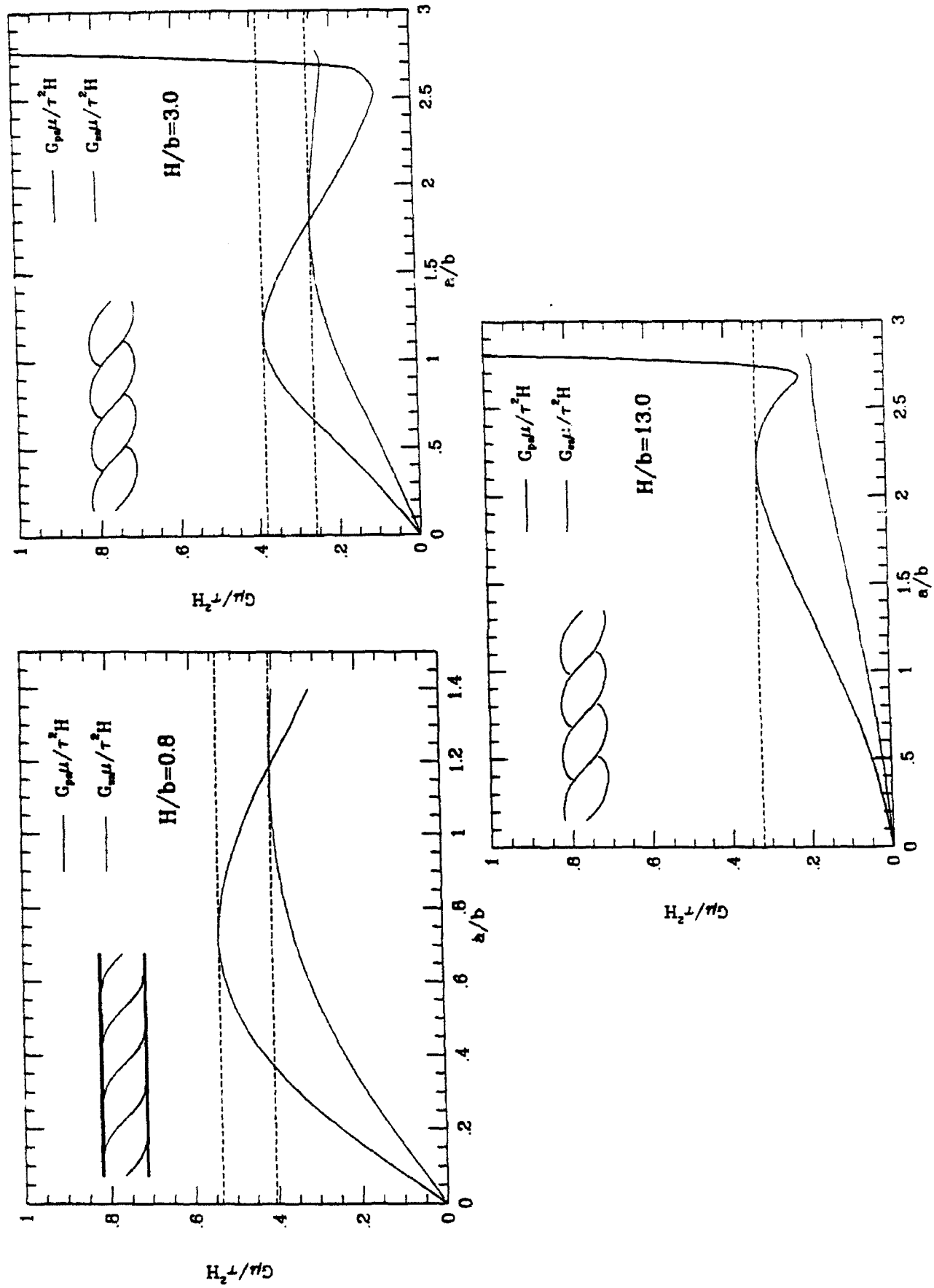

Fig. 2. Normalized G_{ps} and G_{ss} for three typical crack density parameter H/b and corresponding crack trajectories. (a) H/b=0.80, (b) H/b=3.0, (c) H/b=13.0.

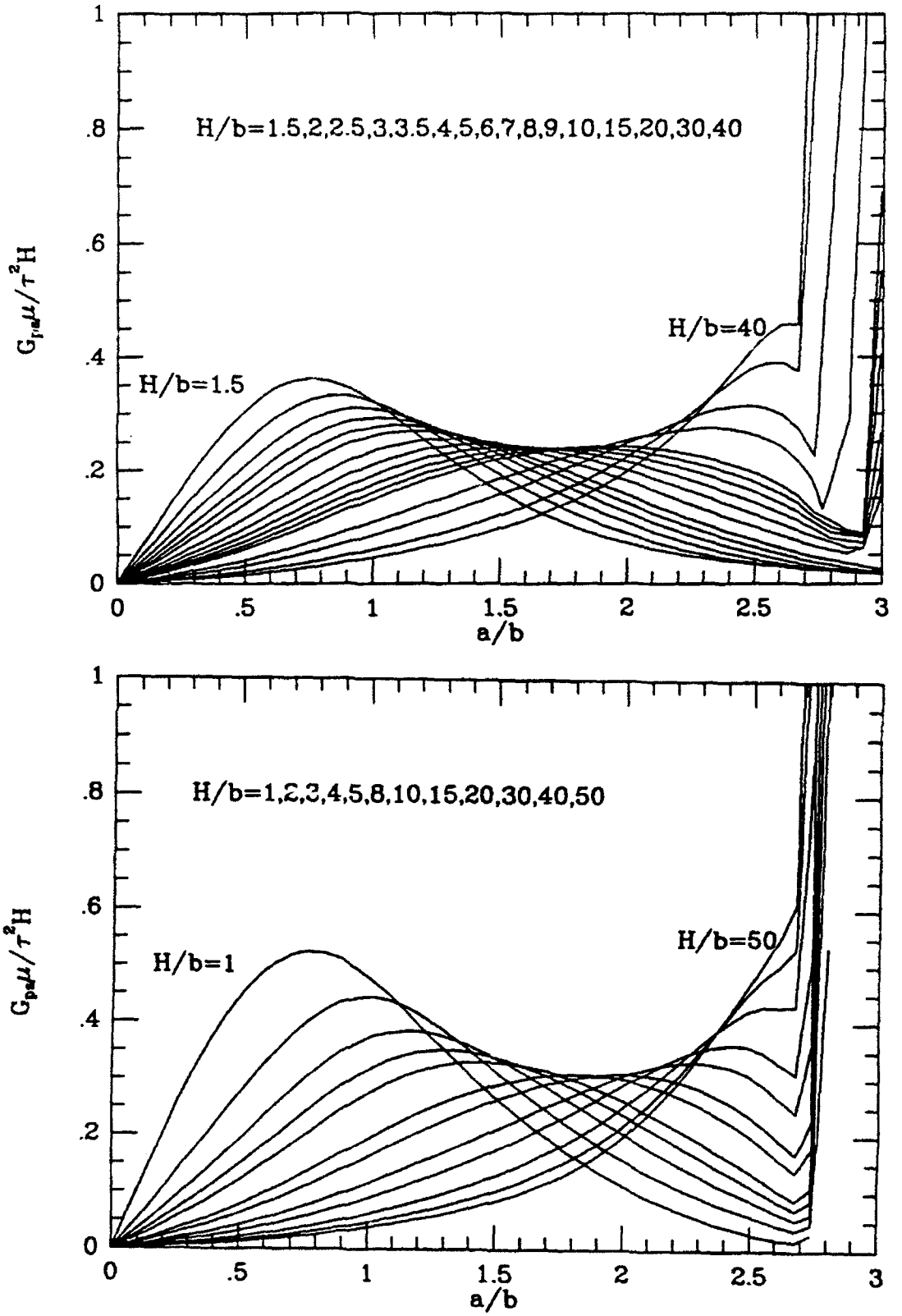

Fig. 3. Normalized G_{PS} for various crack density parameter H/b.
(a) For zero average normal traction constraint.
(b) For zero normal displacement constraint.

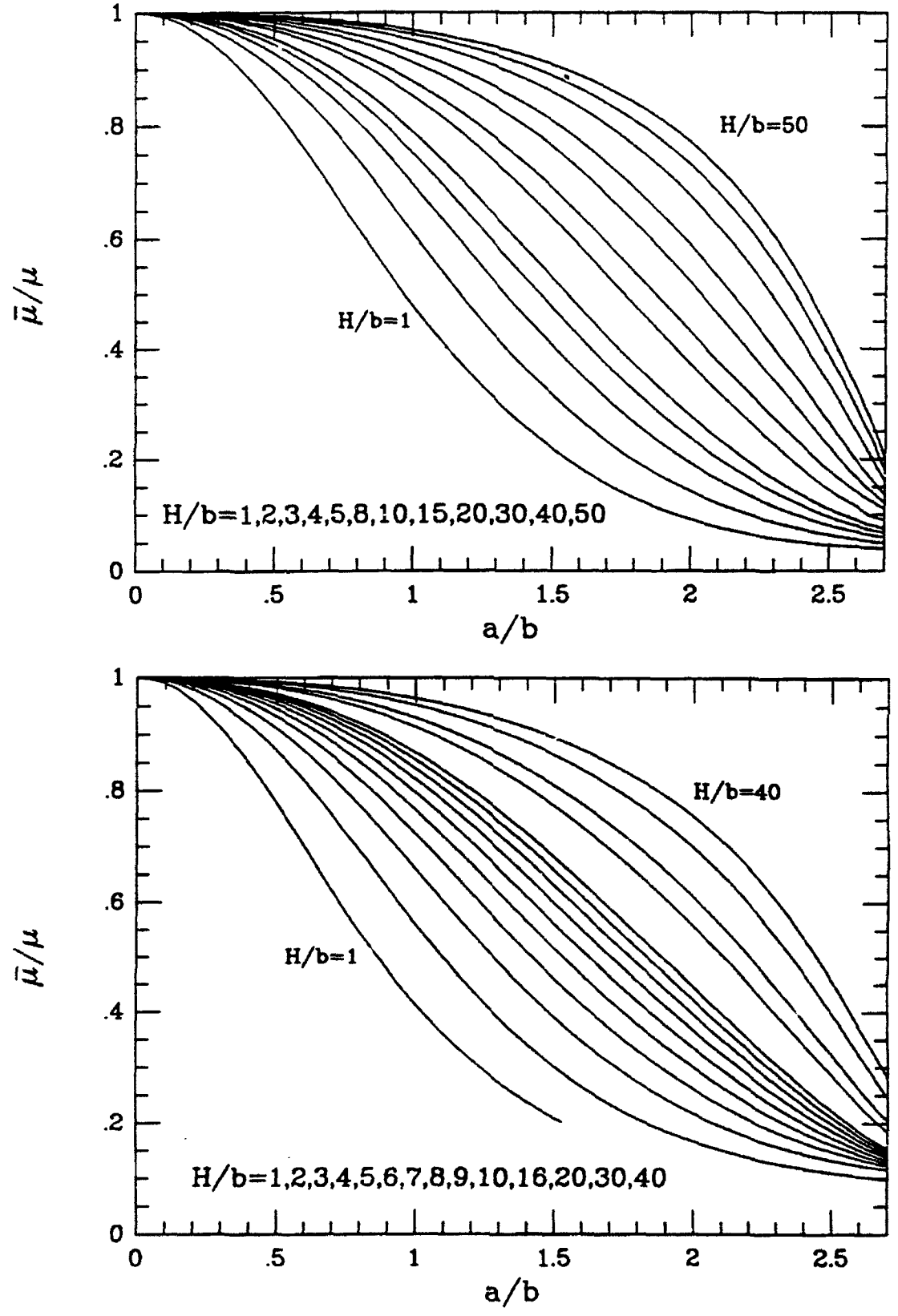

Fig. 4. Normalized effective shear modulus $\bar{\mu}$.
(a) For zero average normal traction constraint.
(b) For zero normal displacement constraint.

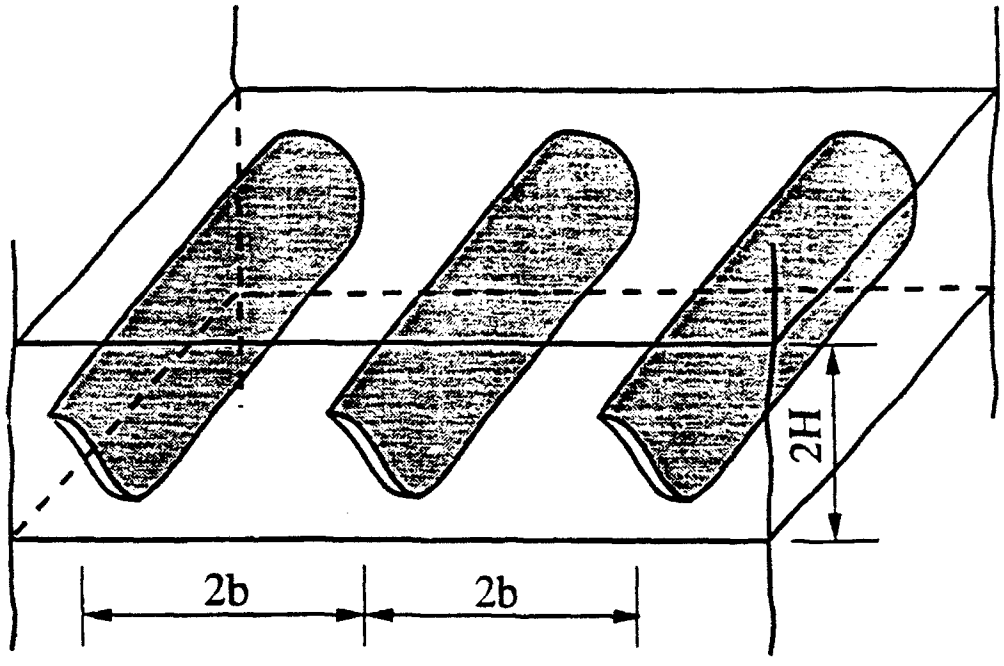

Fig. 5a. A set of tunneling cracks with spacing 2b in the adhesive layer.

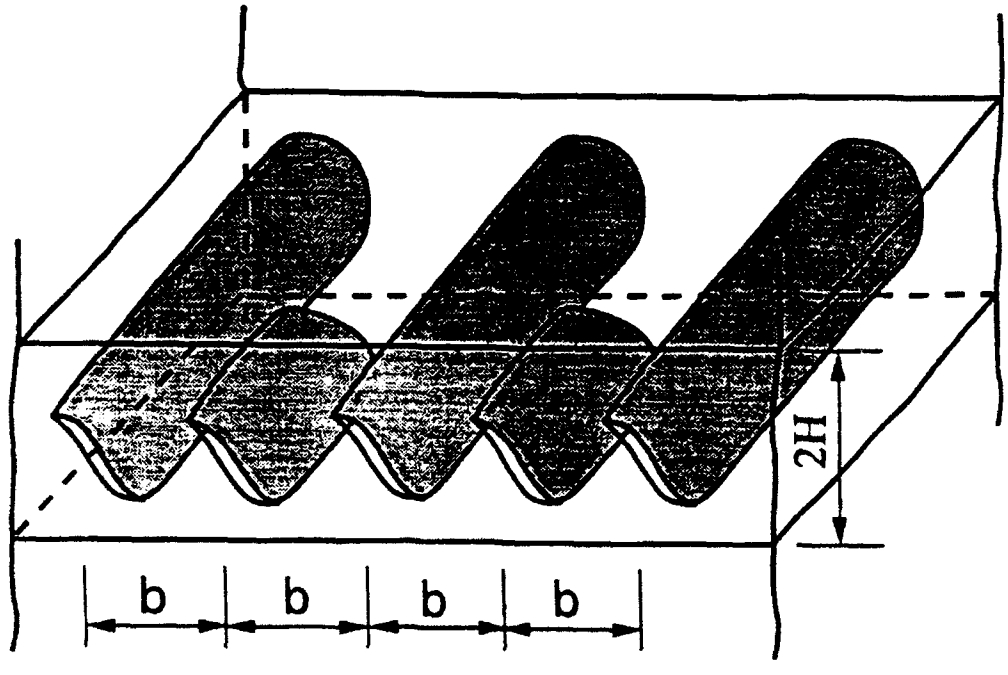

Fig. 5b. A new set of tunneling cracks bisecting a pre-existing set of fully tunneled cracks.

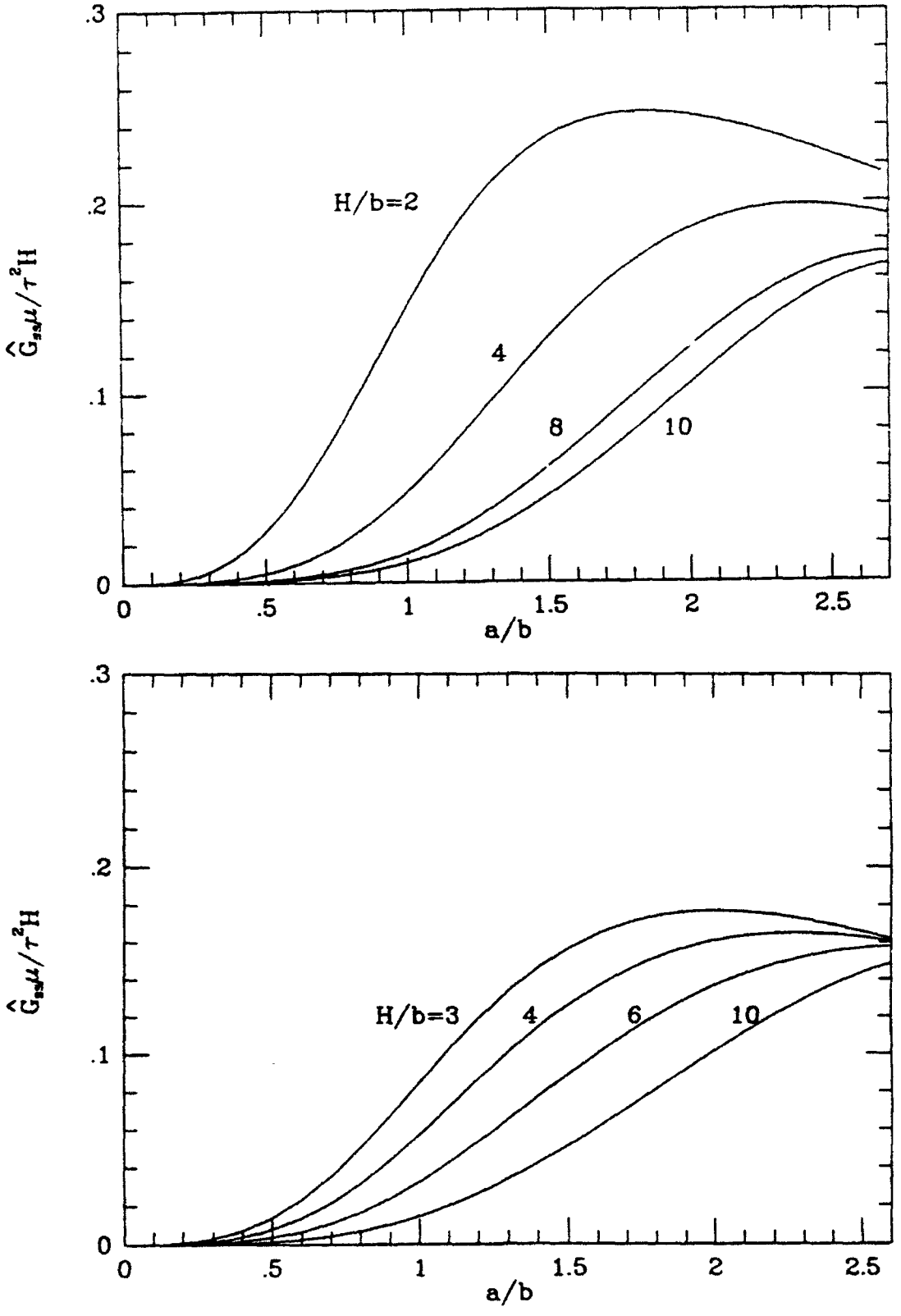

Fig. 6. Normalized $\hat{G}_{ss}$ as a function of a/b for various H/b (cf. Fig. 5b).
(a) For zero average normal traction constraint.
(b) For zero normal displacement constraint.

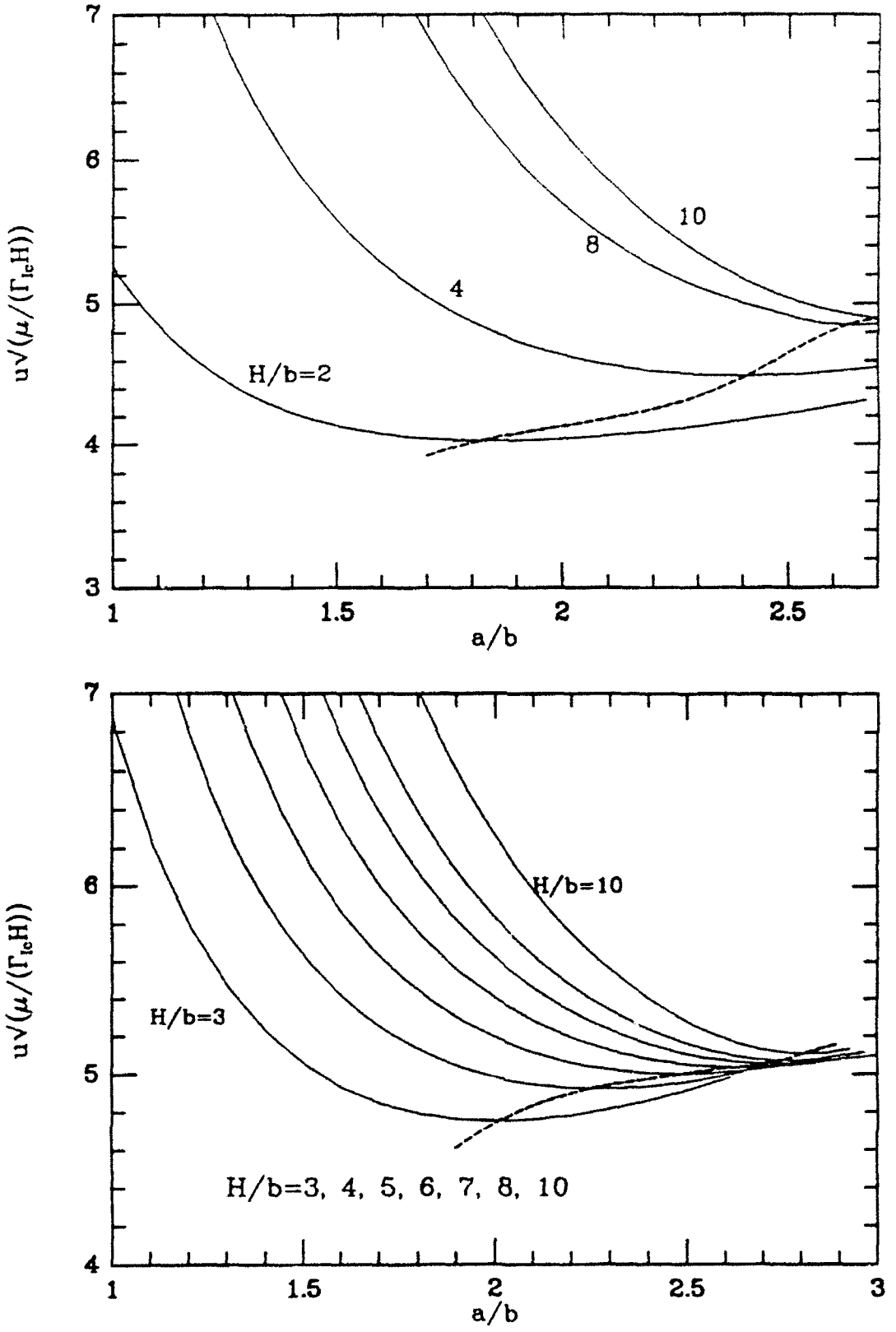

Fig. 7 Normalized u as a function of a/b with $\hat{G}_{ss}$ identified as Γ_{Ic}.
(a) For zero average normal traction constraint
(b) For zero normal displacement constraint.

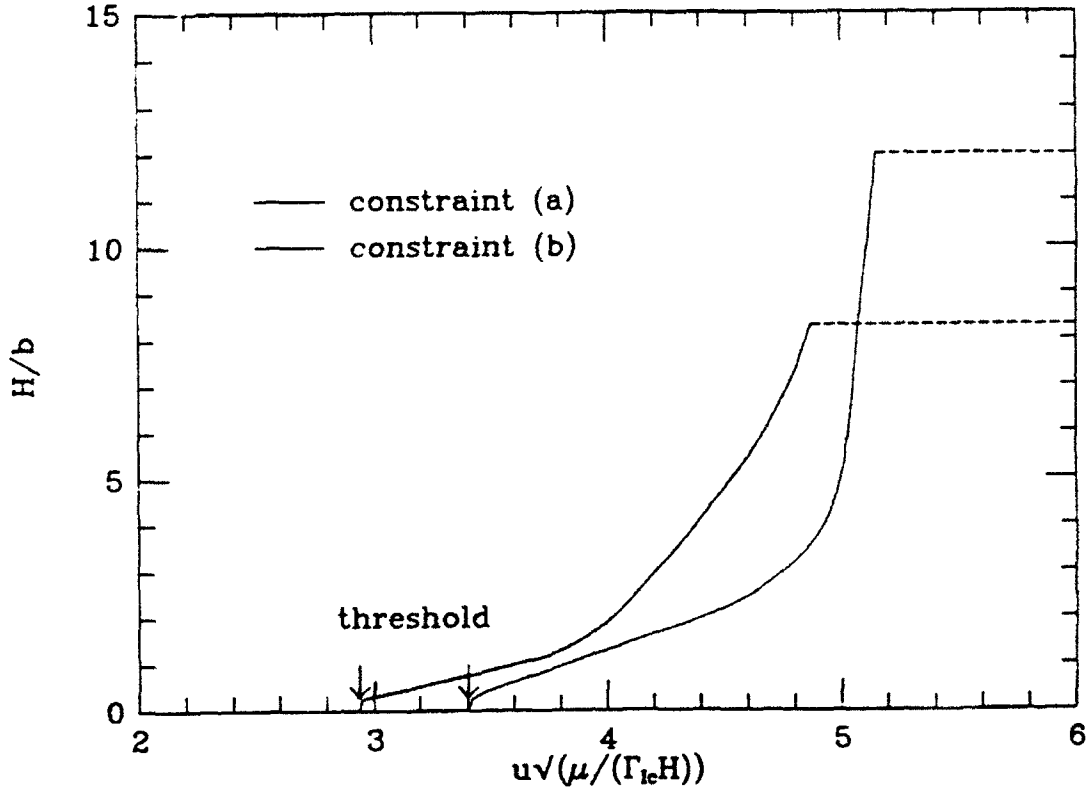

Fig. 8. Evolution of crack density H/b as a function of u.

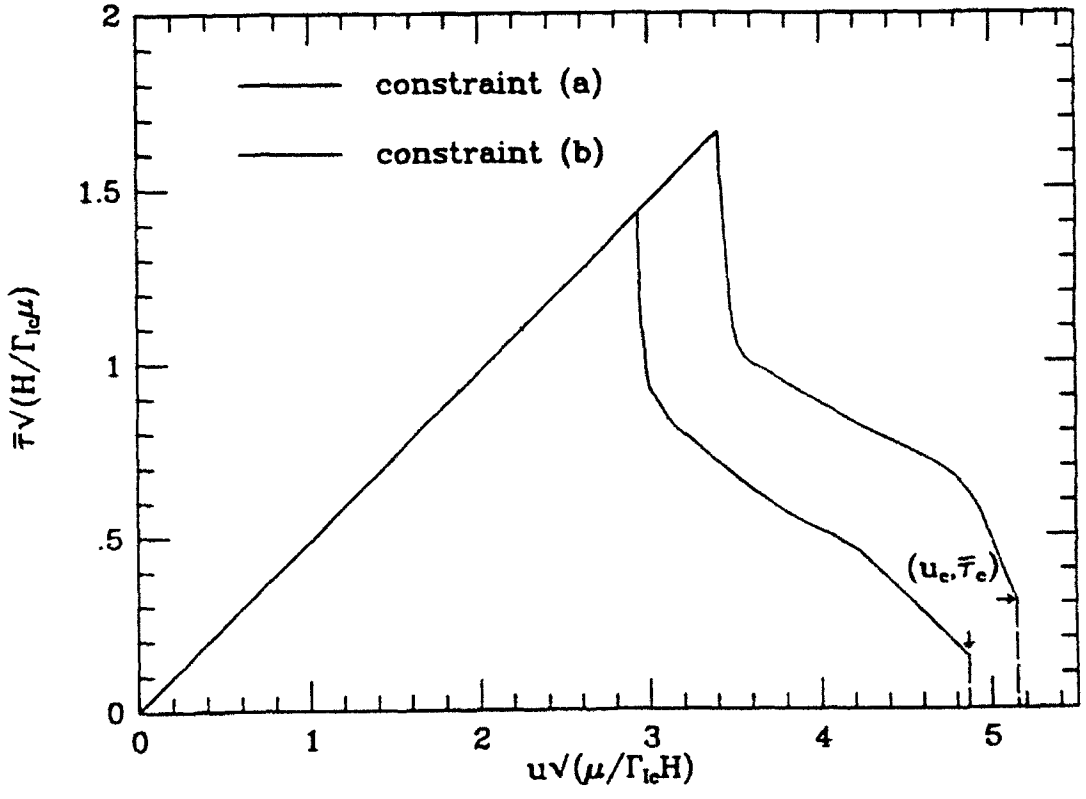

Fig. 9. The shearing traction-displacement relation $\bar{\tau}(u)$.

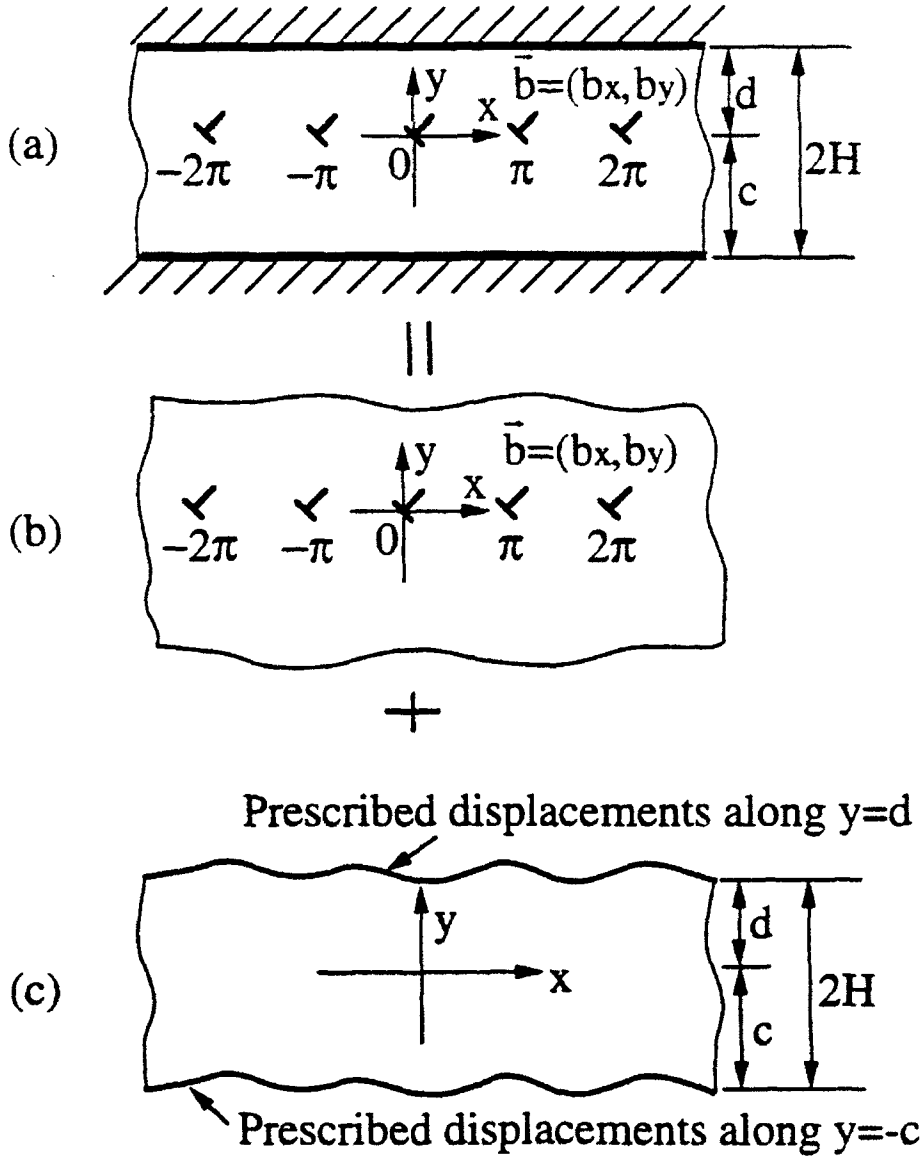

Fig. A1. Stress distribution solution by a superposition scheme.
(a) An array of dislocations in an elastic strip.
(b) An array of dislocations in an infinite elastic body.
(c) A dislocation-free strip with prescribed displacements along edges.

Int. J. Solids Structures Vol. 29, No. 13, pp. 1657–1676, 1992
Printed in Great Britain

0020-7683/92 $5.00+.00
© 1992 Pergamon Press plc

CRACKING OF THIN BONDED FILMS IN RESIDUAL TENSION

J. L. BEUTH, JR
Division of Applied Sciences, Harvard University, Cambridge, MA 02138, U.S.A.

(Received 2 March 1991; in revised form 5 November 1991)

Abstract—Solutions are obtained for two elastic plane strain problems relevant to the cracking of a thin film bonded to a dissimilar semi-infinite substrate material. The first problem is that of a crack in the film oriented perpendicular to the film substrate interface with the crack tip touching the interface. The second problem is that of a crack of the same geometry, but with length less than the film thickness, so that the crack tip is within the film. These problems are used to model several modes of crack extension in thin films bonded to thick substrate materials. Complete results from the solution of each problem are given over the full range of practical elastic mismatches. Dimensionless quantities important in describing the cracking of thin films are introduced and accurate approximate formulas based on the solution results are given for them. Applications are discussed, including criteria for avoiding thin film crack extension and a formula for the curvature change induced by the cracking of a thin film bonded to a substrate of finite thickness. The solution results, approximate formulas and information on their application provide the details necessary for the analysis of practical thin film cracking problems.

1. INTRODUCTION

The two problems solved here are shown in Fig. 1. Both of the elastic plane strain problems studied concern a single crack in an isotropic film (material 1) of thickness h, which is bonded to a semi-infinite isotropic substrate (material 2). In the fully cracked film problem (Fig. 1a), the crack is oriented perpendicular to the film substrate interface and has length h so that its tip touches the interface. The partially cracked film problem illustrated in Fig. 1b models a crack of identical geometry, but with length a, so that the crack tip is within the film (i.e. $a < h$). In both the fully cracked and partially cracked film problems, the crack faces are subject to uniform pressure loading, σ, which from a fracture mechanics standpoint is equivalent to a traction-free crack in a film supporting a uniform tensile stress σ prior to introduction of the crack. The tensile stress σ can be a residual stress in the film, such as a residual thermal stress, or an applied stress. Fracture mechanics quantities obtained from the solution of these two problems are used here to predict the cracking behavior of thin films bonded to thick substrate materials.

The work of Gecit (1979), Lu and Erdogan (1983a,b), Civilek (1985) and Suo and Hutchinson (1989, 1990), which represents only a portion of that done in the field, has served as the basis for obtaining the two problem solutions outlined in this study. Gecit (1979) outlines solution procedures for problems that include the two analysed in the current study, and presents solution results for some representative material combinations.

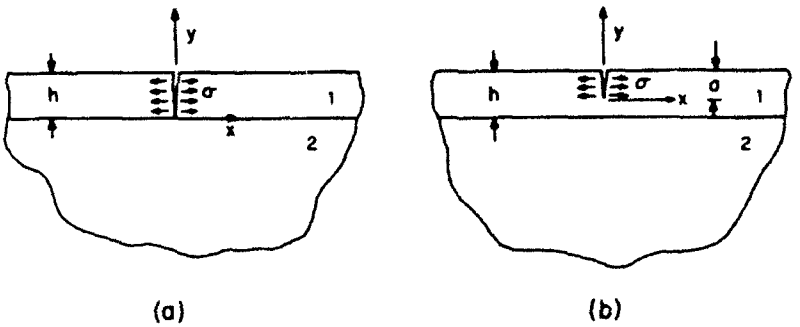

Fig. 1. (a) Fully cracked film. (b) Partially cracked film problems.

Lu and Erdogan (1983a,b) go further by presenting the theory and results for the solution of numerous problems of cracks in a bimaterial strip. As in the work of Geer (1979), their emphasis is placed on outlining the solution method and presenting results for select material combinations. In more recent work, Civelek (1985) provides the general solution procedure to the problem of one or more cracks in a finite strip of a single material. The solution and analysis of the problems of cracks lying on the interface and in the substrate of a bimaterial strip are detailed by Suo and Hutchinson (1989, 1990). The dislocation formulation and solution procedure applied to solve the bimaterial problems in this study closely follow those used by Civelek (1985) and Suo and Hutchinson (1989, 1990). To avoid a repetition of these earlier formulations, only a brief outline of the solution methods used here is provided in the Appendix.

Because there exists work in the literature offering special solutions to problems similar to those in this study, the main emphasis here is placed on application of the solution procedures to fully map out the dependence of the critical fracture mechanics quantities controlling thin film cracking behavior on the properties of the film substrate system. For the most part, numerical results existing in the literature are limited to a few special cases (e.g. specific elastic mismatches). Results which are sufficiently complete and general to be useful in applications are not available. To address the current need for such results, this paper presents solutions to the problems illustrated in Fig. 1 over the entire range of practical elastic mismatches. Fracture mechanics quantities extracted from the solutions are used to model not only 2-D in-plane cracking but also 3-D channelling of a crack across the film surface (look ahead to Fig. 3). Results for the fully cracked film problem are plotted and tabulated as a function of the material mismatch parameters. A simple approximate formula is introduced for the partially cracked film problem to make its results more usable. In Section 4, details are given concerning how the results from Sections 2 and 3 can be applied, first, to predict general film cracking behavior and, second, to specifically address the influence of cracking on the use of curvature methods for determining the residual stress in thin bonded films.

A substantial simplification in expressing the material dependence of both problems outlined in this study comes from the work of Dundurs (1969). His work shows that for any problem of a composite body made of two isotropic, elastic materials with prescribed tractions, the material dependence of the problem is reduced from three dimensionless parameters to the two "Dundurs parameters" α and β. For plane strain problems α and β are given by

$$\alpha = \frac{\bar{E}_1 - \bar{E}_2}{\bar{E}_1 + \bar{E}_2}, \quad \beta = \frac{\mu_1(1-2\nu_2) - \mu_2(1-2\nu_1)}{2\mu_1(1-\nu_2) + 2\mu_2(1-\nu_1)}, \tag{1}$$

where $\bar{E} = E/(1-\nu^2)$ is the material plane strain tensile modulus and μ is the material shear modulus. For material 1 having the same properties as material 2, $\alpha = \beta = 0$. For dissimilar materials, switching the 1-2 designation of the materials changes the sign of both α and β. It is clear from (1) that α can vary from -1 to $+1$. In addition, the physically admissible range of β with respect to α can be obtained by restricting μ to be positive and requiring $0 \leqslant \nu \leqslant \frac{1}{2}$ (Dundurs, 1969). This results in the restriction that $\alpha - 4\beta \leqslant 1$. Furthermore, the compilation by Suga *et al.* (1988) indicates that for most practical material combinations, values of β typically lie between $\beta = 0$ and $\beta = \alpha/4$. Although the β parameter *can* have significant influence, for most problems studied the role of α is more important than that of β. Because of this, the material dependence of the results presented in this paper is given in terms of α, with $\beta = 0$ and $\beta = \alpha/4$. For problems where a significant β dependence is evident, interpolation to the correct value of β between the practical limits of $\beta = 0$ and $\beta = \alpha/4$ is possible.

2. FULLY CRACKED FILM PROBLEM

Problem description and analysis

For the fully cracked film problem, with its crack tip at the interface (Fig. 1a), the tractions just ahead of the crack tip are of the form

Table 1. Crack tip singularity exponent, s, as a function of α for $\beta = 0$ and $\beta = \alpha/4$

α	−0.99	−0.80	−0.60	−0.40	−0.20	0.0
$\beta = 0$	0.4059	0.4173	0.4318	0.4496	0.4718	0.5000
$\beta = \alpha/4$	0.3121	0.3504	0.3882	0.4249	0.4616	0.5000
α	0.20	0.40	0.60	0.80	0.99	
$\beta = 0$	0.5364	0.5843	0.6495	0.7450	0.9417	
$\beta = \alpha/4$	0.5421	0.5912	0.6535	0.7438	0.9399	

$$\sigma_{xx}(0, y) = C_1 \frac{\sigma h^s}{(-y)^s}, \tag{2}$$

where C_1 is nondimensional and a function of α and β only. The stress singularity exponent, s, is a function of α and β and satisfies the following equation derived by Zak and Williams (1963):

$$\cos(s\pi) - 2\frac{\alpha-\beta}{1-\beta}(1-s)^2 + \frac{\alpha-\beta^2}{1-\beta^2} = 0, \tag{3}$$

where a value of $s = 1/2$ results for the case of identical film and substrate materials. Values of s as a function of α for $\beta = 0$ and $\beta = \alpha/4$ are given in Table 1 and plotted in Fig. 2. For the geometry illustrated in Fig. 1a, the mode I stress intensity factor is defined in this study as

$$K_I \equiv \lim_{y \to 0} [(-2\pi y)^s \sigma_{xx}(0, y)], \tag{4}$$

where K_I clearly has dimensions stress · (length)^s. In the case of no elastic mismatch, this generalized stress intensity factor simplifies to the conventional fracture mechanics definition for K_I with units stress · (length)$^{1/2}$.

The fully cracked film solution obtained in this study is used to analyse thin film cracking problems by introducing the following dimensionless quantities:

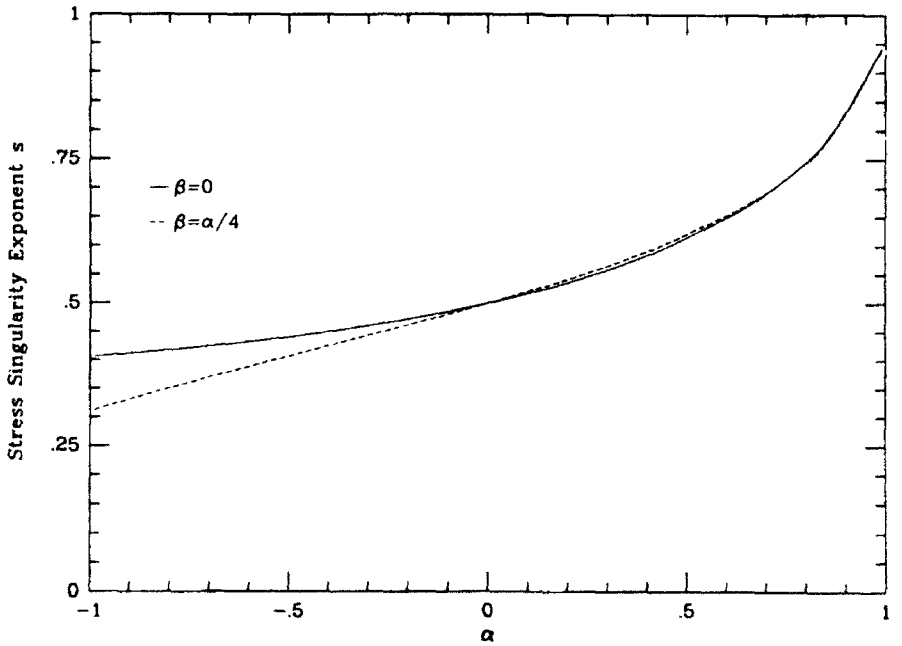

Fig. 2. Plot of crack tip singularity exponent, s, vs α for $\beta = 0$ and $\beta = \alpha/4$.

$$f(\alpha,\beta)=\frac{K_I}{\sigma\sqrt{\pi h}},\quad g(\alpha,\beta)=\frac{\int_0^h \delta(y)\,dy}{\frac{\sigma}{\bar{E}}h^2},\quad \delta^*(\alpha,\beta)=\frac{\delta(h)}{\frac{\sigma}{\bar{E}}h} \tag{5}$$

The first quantity, $f(\alpha,\beta)$, is a nondimensionalized stress intensity factor. For a film substrate combination having no elastic mismatch, $f(0,0) = 1.1215$, the value for an edge crack in a homogeneous half-plane (Tada *et al.*, 1985). The third quantity, $\delta^*(\alpha,\beta)$, is a nondimensionalized crack opening displacement evaluated at the top edge of the crack ($y = h$). For no elastic mismatch, $\delta^*(0,0) = 5.816$ (Tada *et al.*, 1985). The opening displacement of the crack faces at $y = h$ is a commonly measured experimental quantity. Values of δ^* are extracted from the analysis and presented here to allow correlation of the analysis with experiments.

The second quantity given in (5) is a nondimensionalized integral of the crack opening displacement. For the case of no elastic mismatch, $g(0,0) = (1.1215)^2$. This result can be obtained by noting that ΔE, the change in elastic energy per unit depth in the film substrate system due to the introduction of the crack, must be given by

$$\Delta E=\frac{\sigma}{2}\int_0^h \delta(y)\,dy. \tag{6}$$

Moreover, ΔE must satisfy the relation

$$\Delta E=\int_0^h \mathcal{G}\,da, \tag{7}$$

where $\mathcal{G}$ is the mode I energy release rate, which equals $K_I^2/\bar{E}$ for the case of no elastic mismatch. Substituting $K_I = 1.1215\sigma\sqrt{\pi a}$ into (7), equating with (6), and using the definition of $g(\alpha,\beta)$ in (5) gives $g(0,0) = (1.1215)^2$.

The dimensionless quantity g is introduced because of its relation to two physically significant quantities. In the section on applications, it is shown that $g(\alpha,\beta)$ can be related to the change in curvature of a film/substrate wafer due to the introduction of a film crack. The quantity to be discussed here is the steady-state energy release rate, $\mathcal{G}_{ss}$, of the 3-D crack as it channels across the film (Fig. 3). This mode of crack extension is described in detail by Hutchinson and Suo (1990). As the crack channels across the film, the crack front assumes a curved shape so that the energy release rate, $\mathcal{G}$, is the same at all points along it.

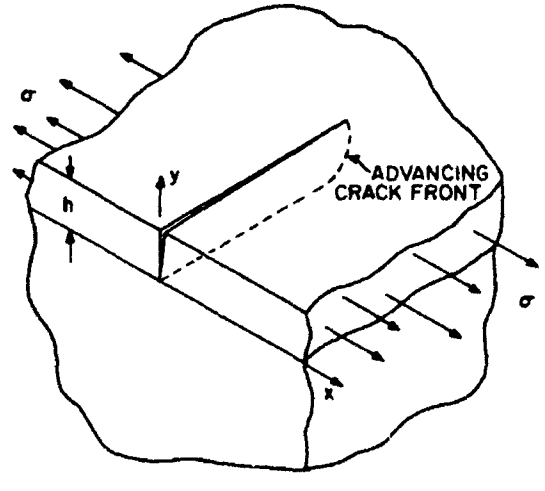

Fig. 3. Steady-state crack channelling across the film for the fully cracked film problem

For short channel lengths, the crack front shape and $\mathcal{G}$ change as the crack extends. However, for sufficiently long channelling cracks, a steady state is achieved so that the crack front shape and $\mathcal{G}$ remain constant. For such channelling cracks the steady-state energy release rate along the crack front, $\mathcal{G}_{ss}$, can be obtained without having to resort to a 3-D analysis and without having to account for crack front shape. Very recent work by Nakamura and Kamath (1991) indicates that steady-state conditions are quickly achieved by channelling cracks. They present a full 3-D analysis of crack channelling for the special case of a film bonded to a rigid substrate (i.e. $\alpha = -1$). Their results show that in this limiting case, steady-state conditions are achieved by channelling cracks having lengths about twice the film thickness.

For the steady-state condition, the total work release per unit length of crack propagation can be arrived at by subtracting the energy stored in a unit slice far behind the crack front from that of a unit slice far ahead of the crack front. This total work release per unit crack propagation is simply the quantity ΔE given in (6). The quantity $\Delta E\, h$ must therefore equal the energy release rate of the channelling crack, $\mathcal{G}_{ss}$. Using the definition of $g(\alpha, \beta)$ in (5), yields the following formula for the mode I steady-state energy release rate due to channelling:

$$\mathcal{G}_{ss} = \frac{1}{2}\frac{\sigma^2 h}{\bar{E}_1}\pi g(\alpha, \beta). \tag{8}$$

Numerical results

Table 2 gives values of $f(\alpha, \beta)$, $g(\alpha, \beta)$ and $\delta^*(\alpha, \beta)$ as a function of α for the fully cracked film problem. These values are also plotted in Figs 4, 5 and 6. As detailed in the Introduction, α can vary from -1 to $+1$ and in this paper β is restricted to the practical limits of $\beta = 0$ and $\beta = \alpha/4$. The definition of α given in (1) and the designation of the film as material 1 means that for a film that is stiff relative to the substrate, α is positive and for a compliant film α is negative.

The results plotted in Fig. 4 show that $f(\alpha, \beta)$ decreases as film stiffness increases. Values for f are approximately independent of β for positive α values (stiff film). There is a relatively strong β dependence for the negative α values, however. The results plotted in Fig. 5 show that $g(\alpha, \beta)$ (and thus the likelihood for channelling to occur) increases as film stiffness increases. The dependence of g on β is weak over the full range of α. In Fig. 6, the plot of $\delta^*(\alpha, \beta)$ as a function of α shows that δ^* exhibits characteristics that are essentially identical to those of g. Values for δ^* increase with the relative stiffness of the film and δ^* shows little dependence on β within the practical limits of $\beta = 0$ and $\beta = \alpha/4$.

3. PARTIALLY CRACKED FILM PROBLEM

Problem description and analysis

Because the crack tip is fully within the film, the partially cracked film problem exhibits the $r^{-1/2}$ stress singularity associated with classical fracture mechanics problems. Thus, the classical definition of stress intensity factor is used, with

$$K_1 \equiv \lim_{r \to 0}\left[\sqrt{2\pi r}\,\sigma_{yy}(0, r)\right]. \tag{9}$$

For the partially cracked film problem, the following two dimensionless quantities analogous to f and g for the fully cracked film problem are defined:

$$F\left(\alpha, \beta, \frac{a}{h}\right) = \frac{K_1}{\sigma(\pi h)^{1/2}}, \quad G\left(\alpha, \beta, \frac{a}{h}\right) = \frac{\int_0^a \delta(y)\,dy}{\pi\frac{\sigma}{\bar{E}_1}ah}. \tag{10}$$

Comparison with (5) shows that as a/h approaches 1, $G(\alpha, \beta, a/h)$ must approach $g(\alpha, \beta)$:

Table 2. f, g and δ^* as a function of α (fully cracked film problem) for $\beta = 0$ and $\beta = \pi/4$

					$f(\alpha, \beta)$ Compliant film						
α	−0.99	−0.95	−0.90	−0.80	−0.70	−0.60	−0.50	−0.40	−0.30	−0.20	−0.10
$\beta = 0$	1.780	1.760	1.734	1.680	1.623	1.563	1.500	1.432	1.364	1.285	1.205
$\beta = \pi/4$	3.206	3.047	2.866	2.549	2.280	2.050	1.849	1.672	1.513	1.371	1.241
					$f(\alpha, \beta)$ Stiff film						
α	0.10	0.20	0.30	0.40	0.50	0.60	0.70	0.80	0.90	0.95	0.99
$\beta = 0$	1.034	0.9427	0.8486	0.7522	0.6543	0.5557	0.4566	0.3562	0.2496	0.1874	0.1008
$\beta = \pi/4$	1.011	0.9067	0.8083	0.7142	0.6233	0.5343	0.4456	0.3546	0.2545	0.1935	0.1074
					$g(\alpha, \beta)$ Compliant film						
α	0.99	0.95	−0.90	−0.80	−0.70	−0.60	0.50	0.40	0.30	0.20	0.10
$\beta = 0$	0.8153	0.8257	0.8393	0.8684	0.9002	0.9352	0.9740	1.017	1.066	1.121	1.184
$\beta = \pi/4$	0.7117	0.7254	0.7431	0.7805	0.8212	0.8654	0.9140	0.9676	1.027	1.094	1.170
					$g(\alpha, \beta)$ Stiff film						
α	0.10	0.20	0.30	0.40	0.50	0.60	0.70	0.80	0.90	0.95	0.99
$\beta = 0$	1.344	1.448	1.576	1.737	1.949	2.245	2.692	3.479	5.400	8.430	22.68
$\beta = \pi/4$	1.360	1.481	1.628	1.813	2.052	2.382	2.876	3.730	5.775	8.940	23.83
					$\delta^*(\alpha, \beta)$ Compliant film						
α	0.99	0.95	0.90	0.80	0.70	0.60	0.50	0.40	0.30	0.20	0.10
$\beta = 0$	3.895	3.940	4.000	4.127	4.266	4.419	4.588	4.776	4.988	5.227	5.501
$\beta = \pi/4$	3.441	3.501	3.578	3.741	3.917	4.110	4.322	4.555	4.815	5.107	5.438
					$\delta^*(\alpha, \beta)$ Stiff film						
α	0.10	0.20	0.30	0.40	0.50	0.60	0.70	0.80	0.90	0.95	0.99
$\beta = 0$	6.190	6.636	7.182	7.870	8.770	10.01	11.89	15.13	22.89	34.71	87.48
$\beta = \pi/4$	6.261	6.786	7.423	8.218	9.249	10.66	12.75	16.34	24.75	37.32	93.14

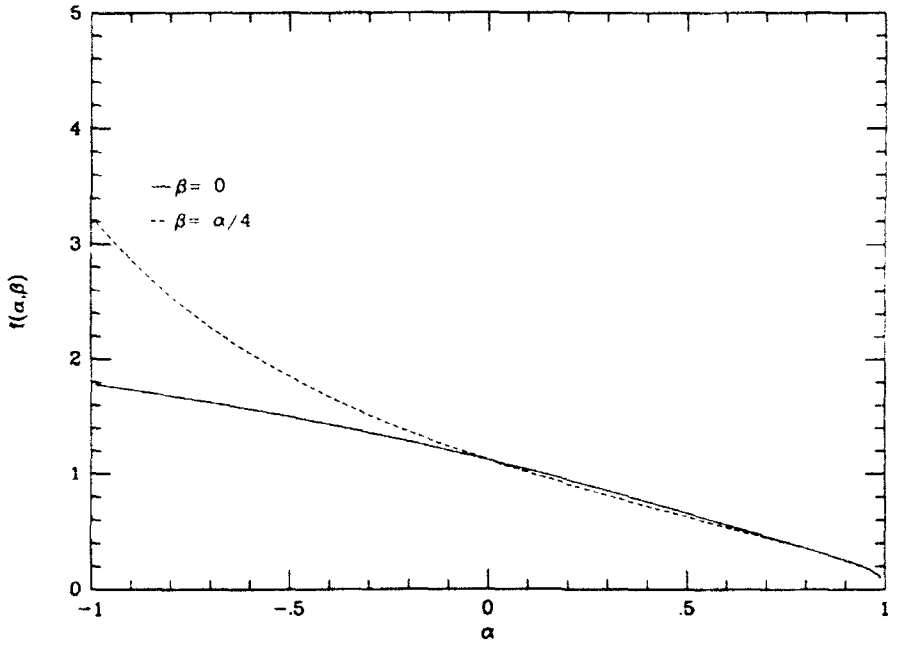

Fig. 4. Plot of $f(\alpha, \beta)$ vs α for $\beta = 0$ and $\beta = \alpha$ 4 for the fully cracked film problem.

however, due to the different stress singularities, $F(\alpha, \beta, a/h)$ does not in general approach $f(\alpha, \beta)$. In the absence of elastic mismatch, $F(0, 0, a/h) = 1.1215\sqrt{a/h}$ and $G(0, 0, a/h) = (1.1215)^2(a/h)$.

For a partially cracked film, two modes of crack extension are possible. The 2-D plane strain crack can extend toward the interface and the 3-D crack can channel across the film. For the channelling crack, a steady-state argument analogous to that made for the fully cracked problem gives that the total work release per unit crack extension must equal ΔE, where

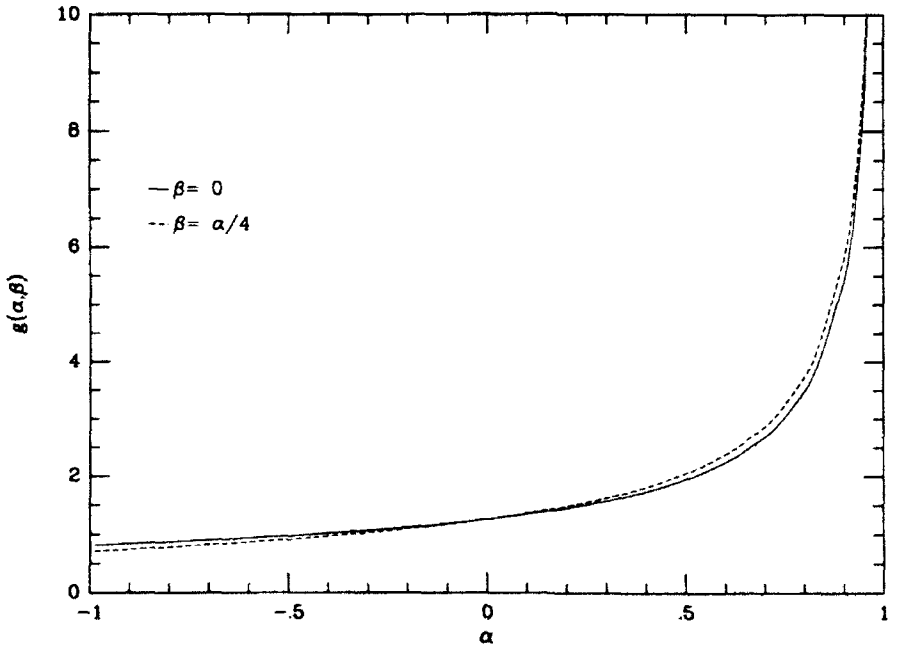

Fig. 5. Plot of $g(\alpha, \beta)$ vs α for $\beta = 0$ and $\beta = \alpha/4$ for the fully cracked film problem.

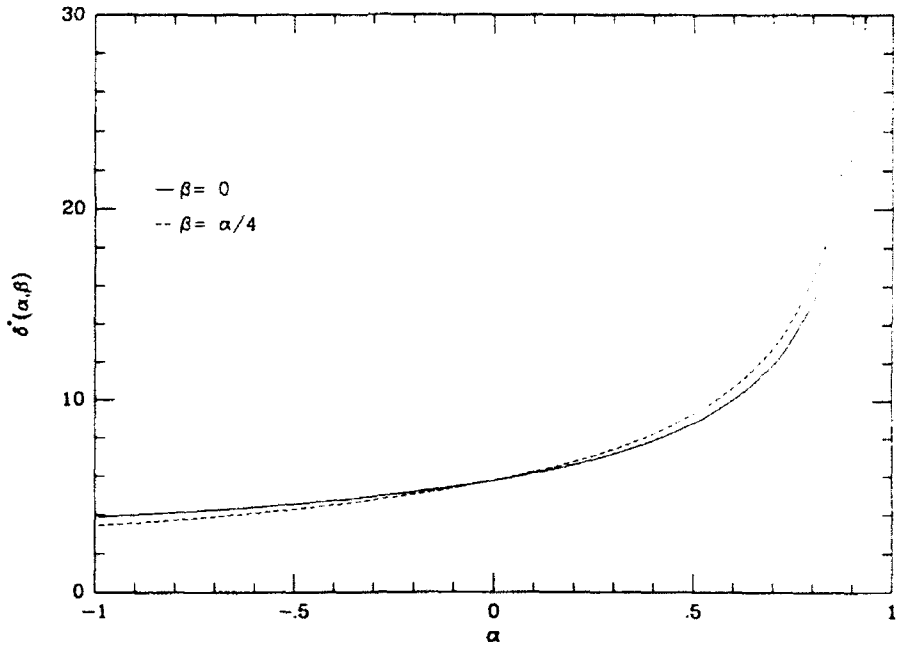

Fig. 6. Plot of $\delta^*(\alpha, \beta)$ vs α for $\beta = 0$ and $\beta = \alpha/4$ for the fully cracked film problem.

$$\Delta E = \frac{\sigma}{2}\int_0^a \delta(y)\,dy, \tag{11}$$

and now the extending crack front has a length a instead of h. The steady-state energy release rate of the channelling crack is thus given by $\mathcal{G}_{ss} = \Delta E/a$. Using the definition of $G(\alpha, \beta, a/h)$ yields the following equation for $\mathcal{G}_{ss}$:

$$\mathcal{G}_{ss} = \frac{1}{2}\frac{\sigma^2 h}{\bar{E}_1}\pi G\left(\alpha, \beta, \frac{a}{h}\right). \tag{12}$$

It is shown in the next section on numerical results that an existing flaw part-way through a film that is compliant with respect to the substrate will not propagate all the way to the film/substrate interface. In such cases, the 2-D plane strain crack will grow to a length, a, which is less than the film thickness, h, and (12) can be applied to predict whether 3-D channelling will occur.

Numerical results

Figures 7 and 8 provide plots of $F(a, \beta, a/h)$ as a function of a/h for select values of α and for $\beta = 0$ (Fig. 7) and $\beta = \alpha/4$ (Fig. 8). Although it is not obvious to the eye, there can, in general, be a β-dependence in the results which is significant. The trends in K_I (and thus F) as a function of a/h have been explored previously in the literature by Gecit (1979) and Lu and Erdogan (1983b). Regardless of the values of α and β, $F(\alpha, \beta, a/h)$ approaches the homogeneous half plane value of $1.1215\sqrt{a/h}$ as a/h approaches zero. For films that are compliant with respect to the substrate, a maximum in $F(\alpha, \beta, a/h)$ occurs within $0 < a/h < 1$ and F approaches zero as a/h approaches 1. Thus, given a flaw of a certain size in a compliant film, once the critical stress intensity factor is reached, the crack will grow toward the interface until $K_I = \sigma(\pi h)^{1/2}F$ becomes less than K_{Ic}, at a value of a/h close to, but less than, 1. In principle, then, an existing flaw in a film that is compliant with respect to the substrate will never propagate all the way to the interface. For films that are stiff relative to the substrate, F approaches infinity as a/h approaches 1. As a result, for a given flaw size in a

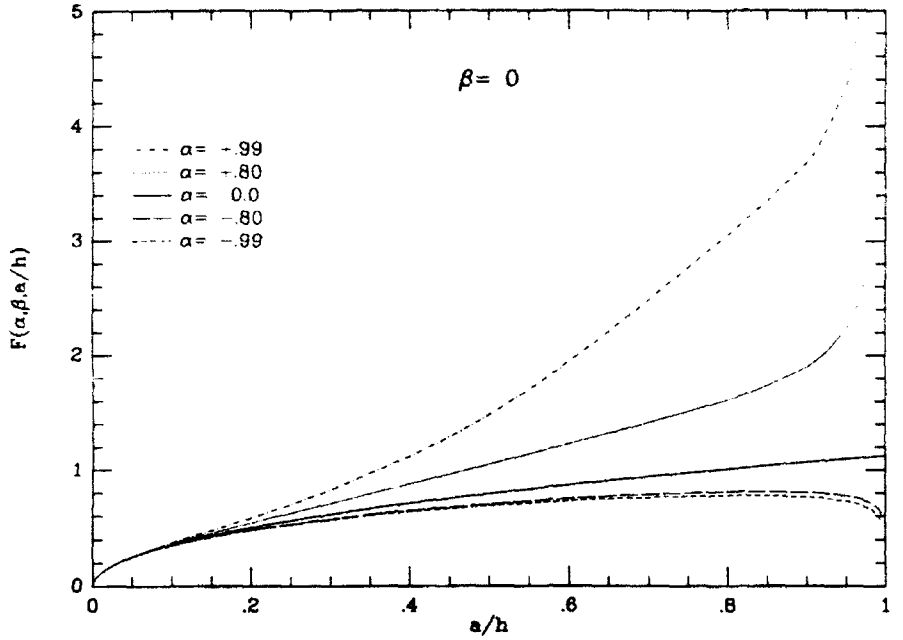

Fig. 7. Plot of $F(\alpha, \beta, a/h)$ vs a/h (partially cracked film problem) for $\beta = 0$.

stiff film, once K_{Ic} is reached the crack will propagate all the way to the interface, resulting in the fully cracked film problem.

Figures 9 and 10 offer plots of $G(\alpha, \beta, a/h)$ analogous to the plots of F in Figs 7 and 8. The values for G generally exhibit a weaker β-dependence than the F values. As a/h approaches zero, $G(\alpha, \beta, a/h)$ approaches the homogeneous half plane value of $(1.1215)^2(a/h)$ for all values of α and β. The plots show that compliant films exhibit a shallow maximum in G near $a/h = 1$. For stiff films, the maximum in G is at $a/h = 1$.

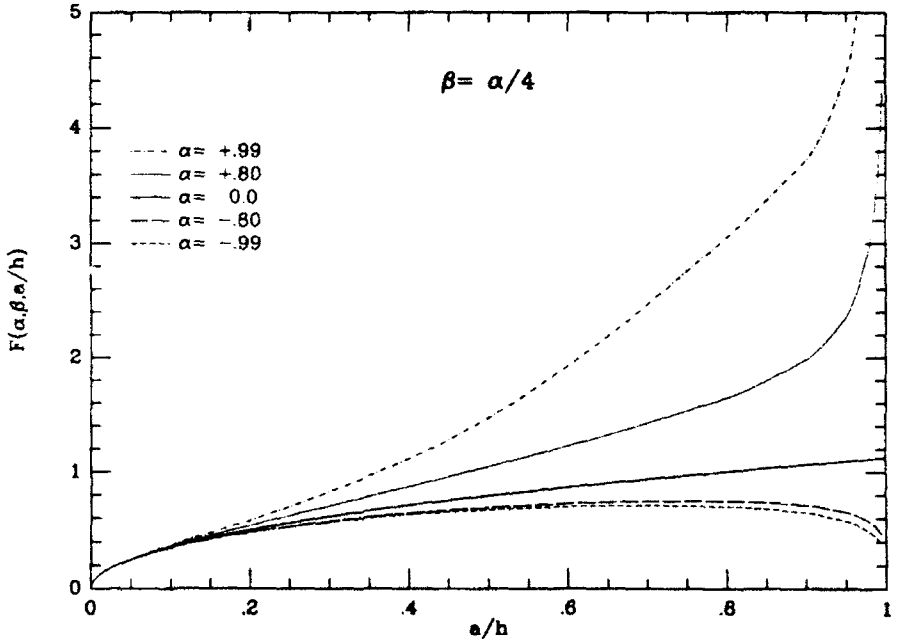

Fig. 8. Plot of $F(\alpha, \beta, a/h)$ vs a/h (partially cracked film problem) for $\beta = \alpha/4$.

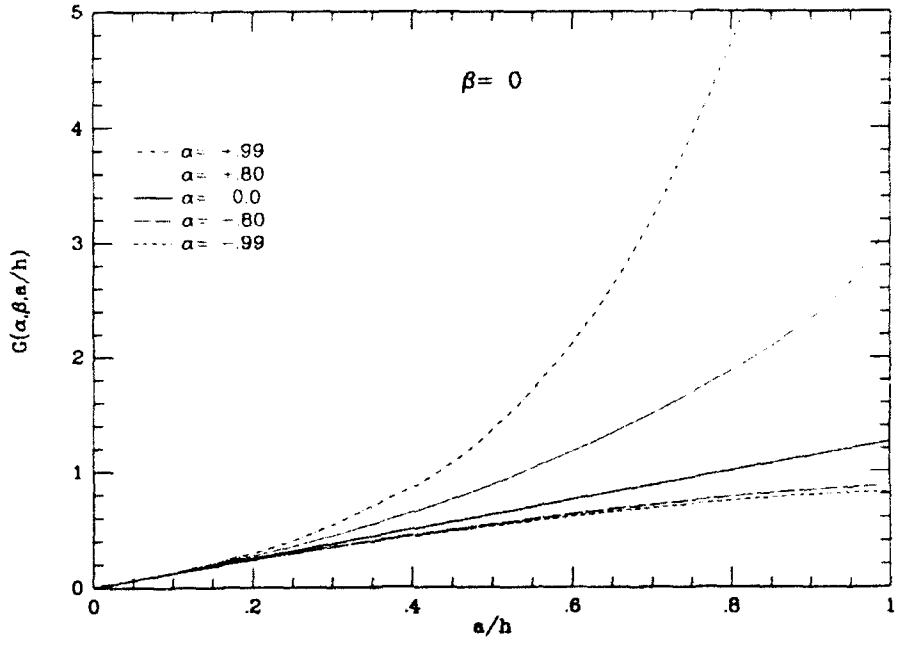

Fig. 9. Plot of $G(\alpha, \beta, a/h)$ vs a/h (partially cracked film problem) for $\beta = 0$.

Regardless of the stiffness of the film relative to the substrate, $G(\alpha, \beta, a/h)$ approaches $g(\alpha, \beta)$ as a/h approaches 1.

For a given compliant film/stiff substrate combination, the maximum values of F and G are of particular interest as design parameters. If K_{Ic} for the film is greater than $K_{I\max}$ calculated from $F_{\max}$, then no extension of the 2-D plane strain crack toward the interface is possible, irrespective of the initial flaw length. Similarly, if $\mathcal{G}_{Ic}$ for the film is greater than $\mathcal{G}_{ss(\max)}$ calculated from $G_{\max}$, then no channelling can occur. Approximate formulas for F

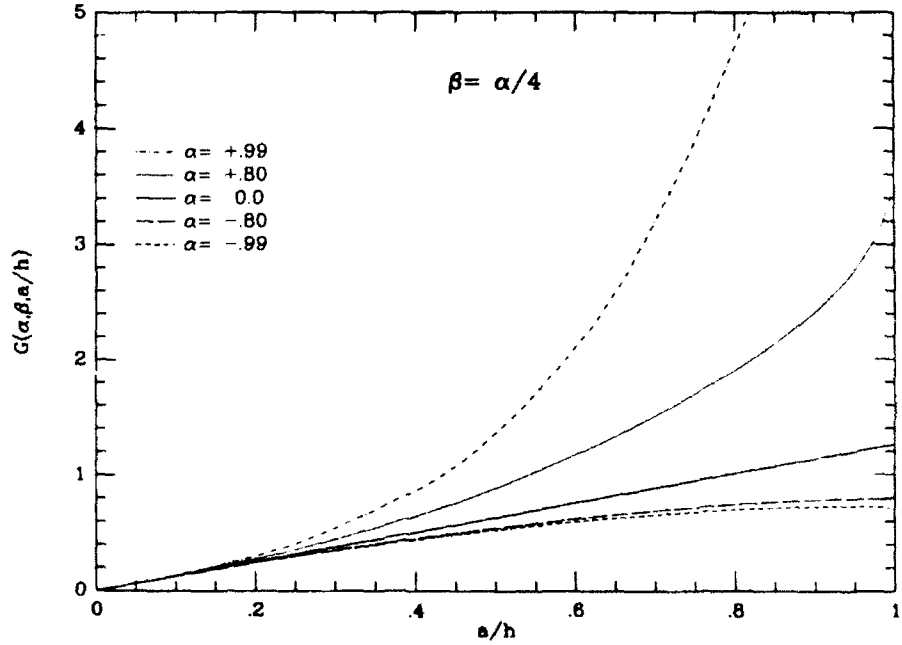

Fig. 10. Plot of $G(\alpha, \beta, a/h)$ vs a/h (partially cracked film problem) for $\beta = \alpha/4$.

and G are given in the next section. An important relation exists, however, coupling F and G at the location where G is a maximum.

Using the fact that $\mathcal{G}_{ss} = \Delta E\, a$ for the partially cracked film problem, and using a relation analogous to that given for the fully cracked problem in (7), yields the following relation for $\mathcal{G}_{ss}$:

$$\mathcal{G}_{ss} = \frac{1}{a}\int_0^a \mathcal{G}_{ps}\, da, \tag{13}$$

where the notation $\mathcal{G}_{ps}$ has been used in place of $\mathcal{G}$ to emphasize that it is the energy release rate of the 2-D plane strain crack. Taking the derivative of (13) with respect to a gives

$$\frac{d\mathcal{G}_{ss}}{da} = \frac{1}{a}\mathcal{G}_{ps} - \frac{1}{a^2}\int_0^a \mathcal{G}_{ps}\, da = \frac{1}{a}(\mathcal{G}_{ps} - \mathcal{G}_{ss}). \tag{14}$$

Thus, $d\mathcal{G}_{ss}\, da = 0$ for $\mathcal{G}_{ss}$ equal to $\mathcal{G}_{ps}$, which defines a condition for the location of the maximum of $\mathcal{G}_{ss}$ for the compliant film problem. Setting $\mathcal{G}_{ss}$ equal to $\mathcal{G}_{ps}$ and using the relation between $\mathcal{G}_{ss}$ and $G(\alpha, \beta, \alpha/h)$ in (12), the relation between K_I and $F(\alpha, \beta, a/h)$ in (10), and the fact that $\mathcal{G}_{ps} = K_I^2 \bar{E}_1$, gives that $F^2 = G/2$ at the value of a where $\mathcal{G}_{ss}$ is a maximum. Thus at the value of a/h where $F^2 = G/2$, it must be true that $G(\alpha, \beta, a/h)$ is maximized.

Figure 11 gives a typical plot of normalized values of $\mathcal{G}_{ps}$ calculated from K_I for the plane strain cracking problem and normalized values of $\mathcal{G}_{ss}$ for the channelling crack, both versus a/h. The figure delineates the role of the normalized film toughness, $\bar{E}_1\mathcal{G}_{1c}/\sigma^2 h$, on the likelihood for each type of film crack extension. Whether each type of cracking will actually occur is, in general, dependent on the length of initial flaws in the film. However, if $\bar{E}_1\mathcal{G}_{1c}/\sigma^2 h$ for the film is above the maximum of the normalized $\mathcal{G}_{ps}$ curve, no crack extension of either kind can occur for any initial flaw size. For a value of $\bar{E}_1\mathcal{G}_{1c}/\sigma^2 h$ for the film between the maximum of the $\mathcal{G}_{ps}$ curve and the maximum of the $\mathcal{G}_{ss}$ curve (located where the curves intersect and $F^2 = G/2$), extension of a plane strain crack toward the interface can occur, but channelling cannot. If the normalized $\mathcal{G}_{1c}$ of the film is below the maximum

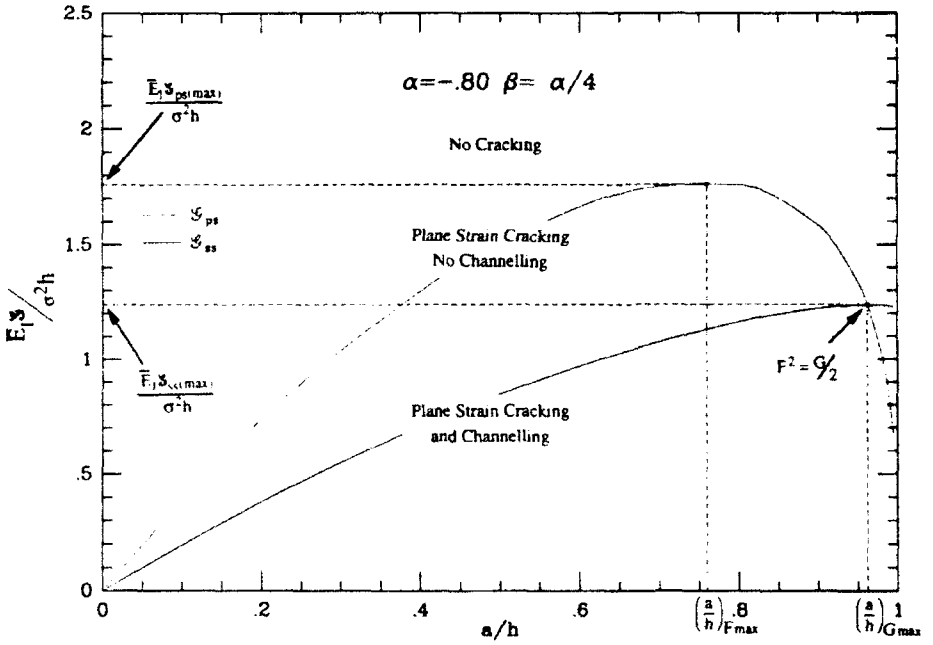

Fig. 11. Plot of regions of plane strain cracking and steady-state channelling vs a/h for $\alpha = -0.80$, $\beta = \alpha/4$.

of the ψ curve, then both types of cracking can occur. If plane strain crack extension is initiated, it will continue until ψ falls below ψ_{ss} at the value of a/h determined by the intersection of the normalized toughness with the right-hand portion of the ψ curve. Because $\psi_{max} > \psi_{ss}$ for $a/h_0 < a/h < 1$, if channeling is initiated it will proceed until the crack runs through the entire film or until a boundary is reached.

Approximate formulas

Presentation of the numerical results for I and G in a form that fully maps out their dependence on the three parameters γ, β and a/h is difficult. Thus approximate formulas are proposed here for the dimensionless quantities $I(\gamma, \beta, a/h)$ and $G(\gamma, \beta, a/h)$ to allow easier prediction of thin film cracking behavior based on the solution results. The approximation for $I(\gamma, \beta, a/h)$ elaborates upon a suggestion to this author by Z. Suo. It is

$$F\left(\gamma, \beta, \frac{a}{h}\right) = \frac{K_I}{\sigma\sqrt{\pi h}} = 1.1215\left(\frac{a}{h}\right)^{\lambda}\left(1 - \frac{a}{h}\right)^{-\lambda}\left(1 + z\frac{a}{h}\right) \tag{15}$$

where the γ and β dependence is through the Zak–Williams singularity λ and the fitting parameter z. The formula for F is defined so as to satisfy the following criteria:

(1) F must approach $1.1215(a/h)^{\lambda}$ for the case of no elastic mismatch ($\lambda = 1/2$).
(2) F must approach $1.1215(a/h)^{\lambda}$ as a/h approaches 0.
(3) F must have a $(1-a/h)^{-\lambda}$ singularity as a/h approaches 1.

Criterion 3 is arrived at by the following argument. First, the stress intensity factor for the fully cracked film problem is of the form $K_I^* = \sigma\sqrt{h}$. Second, the stress intensity factor for the partially cracked film problem must be of the form $K_I = \sigma(\text{length})^{-\lambda}$. For the case of the crack tip approaching the interface, with $(h-a) \ll h$, an asymptotic problem for K_I can be posed such that K_I must depend linearly on K_I^* and where the only length parameter is $(h-a)$. From the dimensionality of K_I^* and K_I it follows that K_I is proportional to $K_I^*(h-a)^{-\lambda}$ as a approaches h. Thus

$$\frac{K_I}{\sigma\sqrt{h}} \propto \left(1 - \frac{a}{h}\right)^{-\lambda}$$

as a/h approaches 1.

The parameter $z(\gamma, \beta)$ in (15) is a fitting parameter that is used to match the approximate formula to numerical values of F from the solution at $a/h = 0.98$. The idea behind using the parameter z is to increase the accuracy of the formula by matching the solution near $a/h = 1$, in a way similar to the way it is matched at $a/h = 0$. Criterion 1 requires that $z = 0$ for the case of no elastic mismatch. For compliant film problems, the approximation for I given in (15) exhibits a maximum at

$$2\left(\frac{a}{h}\right)_{I_{max}} = -b + \sqrt{b^2 + \frac{4}{4z - 2\lambda z}} \tag{16}$$

where

$$b = \frac{2 - 2\lambda - 3z}{4z - 2\lambda z}. \tag{17}$$

An approximate formula for $G(\gamma, \beta, a/h)$ is obtained by using the relation between ψ_{ss} and ψ_{ss} given in (13), along with the definition of F and the fact that $\psi_{ss} = K_I^2 I$. A change of variables produces a polynomial expression that can be integrated by hand to give the following formula

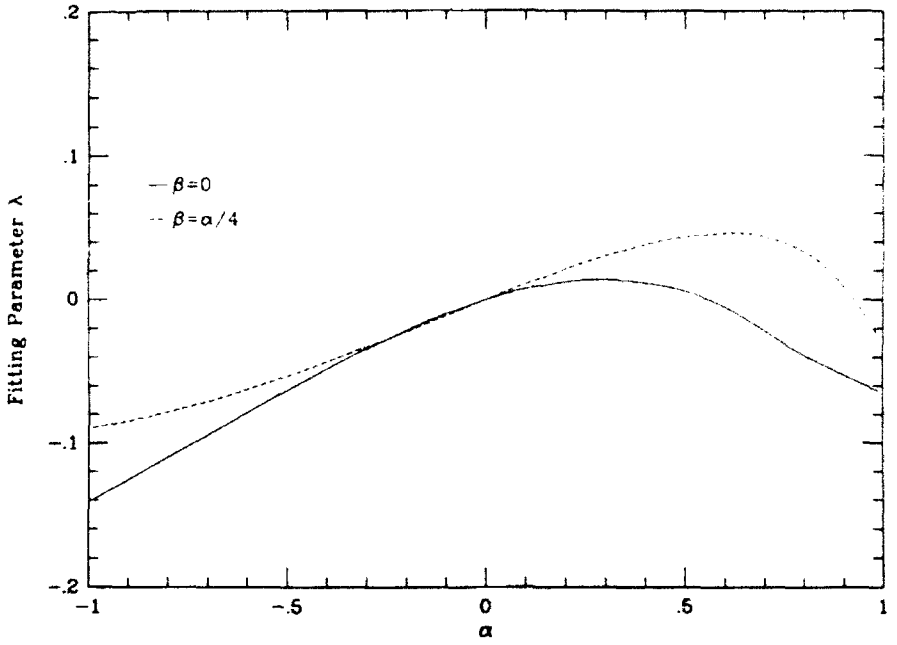

Fig. 12. Plot of approximate formula fitting parameter λ vs α for $\beta = 0$ and $\beta = \alpha/4$

$$G\left(\alpha, \beta, \frac{a}{h}\right) = -\frac{2h}{a}(1.1215)^2\left[b^{2-2s}\left(\frac{1+2\lambda+\lambda^2}{2-2s} - \frac{(1+4\lambda+3\lambda^2)b}{3-2s} + \frac{(2\lambda+3\lambda^2)b^2}{4-2s} - \frac{\lambda^2 b^3}{5-2s}\right)\right]_{b=1-(a/h)}^{b=1} \quad (18)$$

Figure 12 provides a plot of λ vs α for the two cases of $\beta = 0$ and $\beta = \alpha/4$. Numerical values are provided in Table 3. For the convenience of the reader, analogous data for s is provided in Table 1 and plotted in Fig. 2. These plots and tables can be used in conjunction with (15) and (18) to obtain approximate values of F and G for the partially cracked film problem. As indicated in Fig. 12, λ is typically small in magnitude and equal to zero for the case of identical film and substrate materials. Reasonable estimates can, in fact, be obtained for F and G by simply taking $\lambda = 0$.

Figures 13 and 14 provide comparisons of the approximate formulas for F and G with fully accurate numerical values which were plotted in Figs 8 and 10. In the figures, data points are from the solution and lines are generated from the approximate formulas for F and G. The plots clearly show that the approximate formulae are very accurate for the compliant film cases. For example, the maximum error in the formula for F for the case of $\alpha = -0.99$, $\beta = -0.2475$ (the bottom line in Fig. 13) is less than 2 percent. The formulae can thus serve as powerful, simple representations of the dependence of F and G on α, β, and a/h for compliant film problems. The formulae for F and G show some disagreement with the solution results for problems where the film is much stiffer than the substrate, however. Although the approximate formula for F gives good agreement with the actual

Table 3. Fitting parameter, λ, as a function of α for $\beta = 0$ and $\beta = \alpha/4$

α	−0.99	−0.80	−0.60	−0.40	−0.20	0.0
$\beta = 0$	−0.1399	−0.1103	−0.0790	−0.0488	−0.0215	0.0
$\beta = \alpha/4$	−0.0894	−0.0784	−0.0627	−0.0437	−0.0224	0.0

α	0.20	0.40	0.60	0.80	0.99
$\beta = 0$	0.0125	0.0119	−0.0049	−0.0383	−0.0638
$\beta = \alpha/4$	0.0215	0.0389	0.0465	0.0335	−0.0257

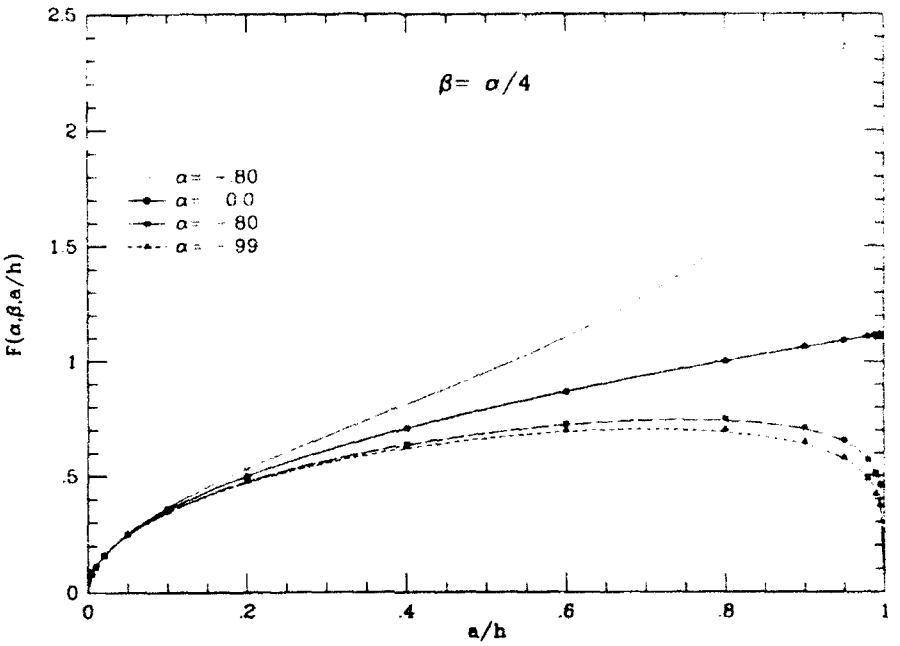

Fig. 13. Comparison of approximate formula for F and numerical solution data for $\beta = \alpha/4$

values of F near $a/h = 0$ and $a/h = 1$, the approximation underestimates F near $0.40 \leqslant a/h \leqslant 0.80$. Values of G are thus underestimated for $a/h \geqslant 0.40$. Care should thus be taken in using the formulas for F and G for stiff problems within these ranges of a/h.

4. APPLICATIONS OF THE RESULTS

Predicting thin film cracking behavior

The results for the partially cracked film problem show that a flaw of a given size in a film under residual tension will begin to propagate toward the interface when the stress

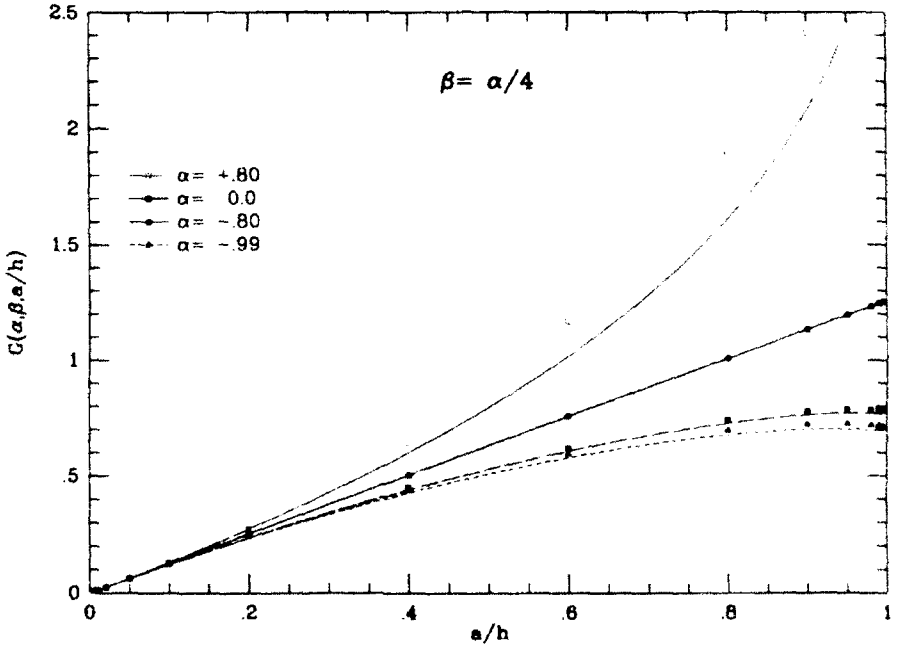

Fig. 14. Comparison of approximate formula for G and numerical solution data for $\beta = \alpha/4$

intensity factor, K_I, calculated from $F(\alpha, \beta, a/h)$ is greater than the K_{Ic} of the film. When this happens, the crack may or may not propagate all the way to the interface depending on whether the film is stiff or compliant with respect to the substrate. At the same time, for a given crack length there is a corresponding value of $G(\alpha, \beta, a/h)$ or $g(\alpha, \beta)$ that is related to the energy release rate of a steady-state crack channelling across the film, $\mathcal{G}_{ss}$. When $\mathcal{G}_{ss}$ is greater than the $\mathcal{G}_{Ic}$ of the film, crack channelling across the film will occur.

Hutchinson and Suo (1990) explore in detail these matters and others related to the cracking of thin films in tension. Figure 15 gives an illustration of how the results and approximate formulas presented in this study can be applied by a designer to determine what type of cracking can or cannot occur for a given film substrate combination, film thickness, h, and stress σ. Normalized values of $\mathcal{G}_{ps}$ and $\mathcal{G}_{ss}$ are plotted in Fig. 15 as a function of α, with $\beta = \alpha/4$, for comparison with normalized values of $\mathcal{G}_{Ic}$. An initial flaw size of $a/h = 0.80$ was used to calculate the plane strain energy release rate values. For stiff film cases, as long as initial flaws are smaller than $0.80h$, the plotted $\mathcal{G}_{ps}$ values represent upper bounds to the actual values. For compliant film cases, because the maximum of $\mathcal{G}_{ps}$ typically occurs near $a/h = 0.80$ (see Fig. 11), use of an initial flaw size of $a/h = 0.80$ to calculate $\mathcal{G}_{ps}$ values roughly corresponds to the most severe flaw possible. Similarly, $g(\alpha, \beta)$ for the fully cracked film problem was used to calculate the energy release rates for steady-state channelling. For a stiff film, the maximum value of $\mathcal{G}_{ss}$ occurs at $a/h = 1$. As illustrated in Fig. 11, for a compliant film the maximum in $\mathcal{G}_{ss}$ occurs very near $a/h = 1$. Because compliant film $\mathcal{G}_{ss}$ curves are very flat in the region near $a/h = 1$, use of $g(\alpha, \beta)$ to calculate $\mathcal{G}_{ss}$ yields a value that is very close to the maximum. In Fig. 15, for a value of normalized film toughness, $\bar{E}_f \mathcal{G}_{Ic}/\sigma^2 h$, which is above both curves, no crack extension can occur. For normalized toughnesses in the region between the curves, only plane strain crack extension toward the interface can occur. In the region below both curves, both plane strain extension and steady-state crack channelling can occur.

Curvature change due to cracking of a thin bonded film

The quantity $g(\alpha, \beta)$ for the fully cracked film problem is used here to calculate the change in curvature of a film/substrate wafer when cracking occurs in the film. The change in angular rotation of the wafer ends due to the introduction of a single plane strain crack

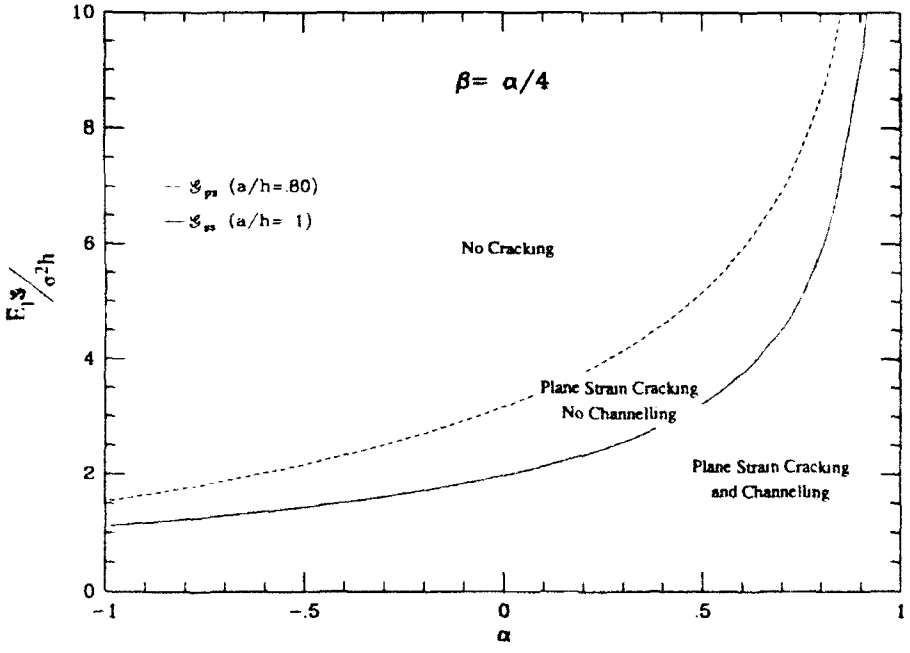

Fig. 15. Regions of plane strain cracking and steady-state channelling vs α for $\beta = \alpha/4$

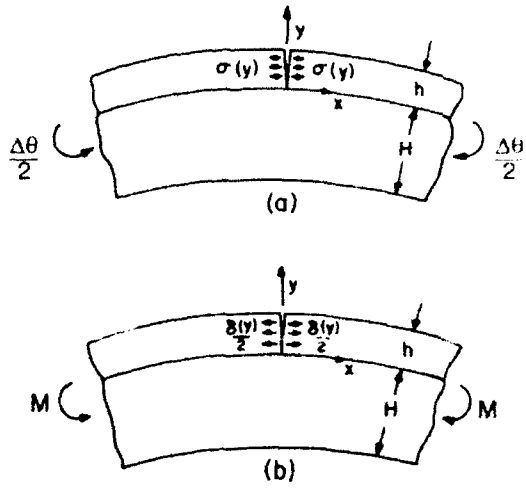

Fig. 16. Reciprocal theorem analysis used to calculate the angular rotation of the film substrate wafer ends due to cracking in the film.

of length h can be determined using the Reciprocal Theorem analysis illustrated in Fig. 16. The problem to be solved is that of a traction-free crack in a film supporting a tensile stress $\sigma(y)$ prior to introduction of the crack. The equivalent fracture mechanics problem is that of a cracked wafer with pressure $\sigma(y)$ applied to the crack faces (Fig. 16a). The unknown quantity to be solved for is $\Delta\theta$. The auxiliary problem, illustrated in Fig. 16b, is the same cracked wafer subject to a unit bending moment per unit depth, M, with crack opening displacements, $\delta(y)$. Reciprocity requires that

$$M^{(2)}\Delta\theta^{(1)} = \int_0^h \sigma(y)^{(1)}\delta(y)^{(2)}\,dy. \tag{19}$$

If the film is thin with respect to the substrate ($h \ll H$), the following assumptions are valid.

(1) The stress in the film, σ, is uniform. Thus σ for problem 1 is y-independent.

(2) For problem 2, the stress in the film prior to introduction of the crack is

$$\sigma^{(2)} = \frac{6M^{(2)}}{H^2}\frac{\bar{E}_1}{\bar{E}_2}. \tag{20}$$

(3) For problem 2, $\delta(y)$ is equal to the crack opening displacement for a film supporting a stress $\sigma^{(2)}$ and attached to an infinitely deep substrate (to lowest order in h/H).

For the second assumption to be true, the film must not contribute significantly to the bending stiffness of the film substrate wafer ($\bar{E}_1 h/\bar{E}_2 H \ll 1$). Substituting the above into (19) and using the definition of $g(\alpha, \beta)$ results in the following formula for $\Delta\theta$, the change in angular rotation of the film substrate ends due to the formation of a single crack:

$$\Delta\theta = 6\pi\frac{\sigma}{\bar{E}_2}\left(\frac{h}{H}\right)^2 g(\alpha, \beta). \tag{21}$$

This formula can also be used to estimate the change of curvature of the film substrate wafer due to the formation of multiple cracks, as long as the cracks are far enough apart to neglect interaction. Related calculations by Thouless (1990) which neglect elastic mismatch suggest that interaction only becomes significant when the crack spacing is less than 8 film thicknesses. If s_0 is designated as the average spacing between cracks in the film, then the change in curvature, $\Delta\kappa$, of the wafer due to the formation of multiple cracks is given by

$$\Delta K = 6\pi \frac{\sigma}{\bar{E}_{\text{sub}}} \left(\frac{h}{H}\right)^2 g(\alpha, \beta). \tag{22}$$

The formulae given in (21) and (22) have been derived assuming that an existing flaw or flaws in the film will propagate all the way to the film substrate interface, even though in theory this can only happen in a film which is stiff with respect to the substrate. However, the results for $F(\alpha, \beta, a/h)$ for the partially cracked film show that cracks in films which are compliant with respect to the substrate will *almost* extend to meet the interface. This fact and the fact that the plots of $G(\alpha, \beta, a/h)$ for compliant films are very flat near $a/h = 1$ indicate that no significant error is introduced by assuming all cracks in the film extend to the interface. The relation in (22) has been derived with a specific application in mind. An established experimental technique for estimating residual stresses in bonded thin films involves measuring the resulting change in curvature in the substrate due to application of the film. A concise description of the method, which assumes that no film cracking has occurred, is given by Nix (1989). Unfortunately, in many cases the thin bonded film does crack due to the residual stress. In such cases, (22) can be used to estimate the effect of film cracking on the measured curvature change. No other method of accounting for film cracking is currently available to experimenters using the curvature method to measure residual stress in thin films bonded dissimilar elastic substrates. In recent work, however, Thouless *et al.* (1991) have developed, on conjunction with the analysis presented here, relations for the curvature change for interacting cracks (i.e. spacing less than 8 film thicknesses) for the case of no elastic mismatch.

5. CONCLUSIONS

Solutions have been obtained for two elastic fracture mechanics problems that have been used to characterize the cracking of thin films bonded to thick substrate materials. A dimensionless plane strain stress intensity factor and a dimensionless integral of the crack opening displacement have been extracted from both solutions. The integral of the crack opening displacement has been related to the steady-state energy release rate for crack channelling across the film for both problems studied. To facilitate comparison of the analysis with experiments, a dimensionless crack opening displacement evaluated at the top of the crack has been extracted from the solution for the fully cracked film problem. Solution results have been presented for both problems and, for the partially cracked film problem, approximate formulae have been given for the dimensionless quantities as a function of the normalized crack length. The approximate formulae are most accurate when the film is compliant with respect to the substrate. Applications of the results and approximate formulae have been detailed. These include the roles of the nondimensional parameters in predicting the cracking of thin films. In addition, the integral of the crack opening displacement for the fully cracked film problem has been related to the change in curvature in a film/substrate wafer due to film cracking. The result is a complete set of solution results and approximate formulae for practical application in understanding the cracking behavior of thin films adhered to thick substrate materials.

Acknowledgements—This work was supported by the DARPA University Research Initiative (Subagreement P.O. # VB38639-0 with the University of California, Santa Barbara, ONR Prime Contract N00014-86-K0753), by NSF Grant MSM-88-12779 and by the Division of Applied Sciences, Harvard University. The author would like to thank John Hutchinson for his advice, input and inspiration throughout this effort and William Nix for motivating the work on calculating curvature changes due to film cracking. The author also gratefully acknowledges the efforts of Zhigang Suo in helping to formulate the approximate formulae presented.

REFERENCES

Civelek, M. B. (1985) Stress intensity factors for a system of cracks in an infinite strip. *Fracture Mechanics: Seventeenth Symposium* (Edited by M. F. Kanninen and A. T. Hopper), ASTM STP 868, 7–26.
Dundurs, J. (1969) Edge-bonded dissimilar orthogonal elastic wedges. *J. Appl. Mech.* **36**, 650–652.
Gecit, M. R. (1979) Fracture of a surface layer bonded to a half space. *Int. J. Engng Sci.* **17**, 287–295.

Hutchinson, J. W. and Suo, Z. (1991). Mixed mode cracking in layered materials. In *Advances in Applied Mechanics* (Edited by J. W. Hutchinson and T. Y. Wu) Vol. 29, pp. 63–191. Academic Press, New York.
Lu, M.-C. and Erdogan, F. (1983a). Stress intensity factors in two bonded elastic layers containing cracks perpendicular to and on the interface—I. Analysis. *Engng Fract. Mech.* **18**, 491–506.
Lu, M.-C. and Erdogan, F. (1983b). Stress intensity factors in two bonded elastic layers containing cracks perpendicular to and on the interface—II. Solution and results. *Engng Fract. Mech.* **18**, 507–524.
Nakamura, T. and Kamath, S. M. (1991). Three-dimensional effects in thin film fracture mechanics. To be published.
Nix, W. D. (1989). Mechanical properties of thin films. *Met. Trans. A* **20A**, 2217–2245.
Press, W. H., Flannery, B. P., Teukolsky, S. A. and Vetterling, W. T. (1986). *Numerical Recipes: The Art of Scientific Computing*. Cambridge University Press, 147–154.
Rice, J. R. (1968). Mathematical analysis in the mechanics of fracture. In *Fracture: An Advanced Treatise*, II (Edited by H. Liebowitz), pp. 191–311. Academic Press, New York.
Suga, T., Elssner, E. and Schmauder, S. (1988). Composite parameters and mechanical compatibility of material joints. *J. Comp. Mater.* **22**, 917–934.
Suo, Z. and Hutchinson, J. W. (1989). Steady-state cracking in brittle substrates beneath adherent films. *Int. J. Solids Structures* **25**, 1337–1353.
Suo, Z. and Hutchinson, J. W. (1990). Interface crack between two elastic layers. *Int. J. Fracture* **43**, 1–18.
Tada, H., Paris, P. and Irwin, G. (1985). *The Stress Analysis of Cracks Handbook* (2nd Edn). Paris Productions Inc., St. Louis, Mo.
Thouless, M. D. (1990). Crack spacing in brittle films on elastic substrates. *J. Am. Ceram. Soc.* **73**, 2144–2146.
Thouless, M. D., Olsson, E. and Gupta, A. (1991). Cracking of brittle films on elastic substrates. *Acta Metall. et Mater.* (to be published).
Zak, A. R. and Williams, M. L. (1963). Crack point singularities at a bimaterial interface. *J. Appl. Mech.* **30**, 142–143.

APPENDIX: PROBLEM SOLUTION

Solution procedure

Rice (1968) gives a general description of the dislocation formulation used by Civilek (1985) and Suo and Hutchinson (1989, 1990) and used in this study to solve the fully cracked and partially cracked film problems. Because of the similarity of the solution procedure used here with that detailed in previous work, the following is only a brief outline of the steps involved in solving the two cracked film problems. Figure 17 illustrates the superposition scheme used to solve the fully cracked film and partially cracked film problems. Figure 17c shows the fundamental problem that must be modelled, that of a semi-infinite bimaterial with a single edge dislocation at $(x = 0, y = \xi)$ with Burgers vector of magnitude b in the positive x direction. This problem is constructed by superimposing the problems of Figs 17a,b. Figure 17a shows an infinite bimaterial with a single dislocation in material 1 located at $(x = 0, y = \xi)$. The stresses in each material are a function of the material parameters α and β and the coordinates x, y and ξ. Methods of obtaining these stresses via complex variable analyses are outlined by Suo and Hutchinson (1989, 1990). A real variable analysis can also be applied, using methods similar to those of Civilek (1985). Figure 17b shows a semi-infinite bimaterial with no dislocation, but with tractions applied along its top boundary. The Fourier transform method for obtaining the solution for the problem in Fig. 17b is outlined by Civilek (1985) and Suo and Hutchinson (1989, 1990). If these tractions are set equal to the negative of the tractions along $y = h$ for the problem in Fig. 17a, then the result upon superposition is the problem in Fig. 17c, with a free surface along $y = h$.

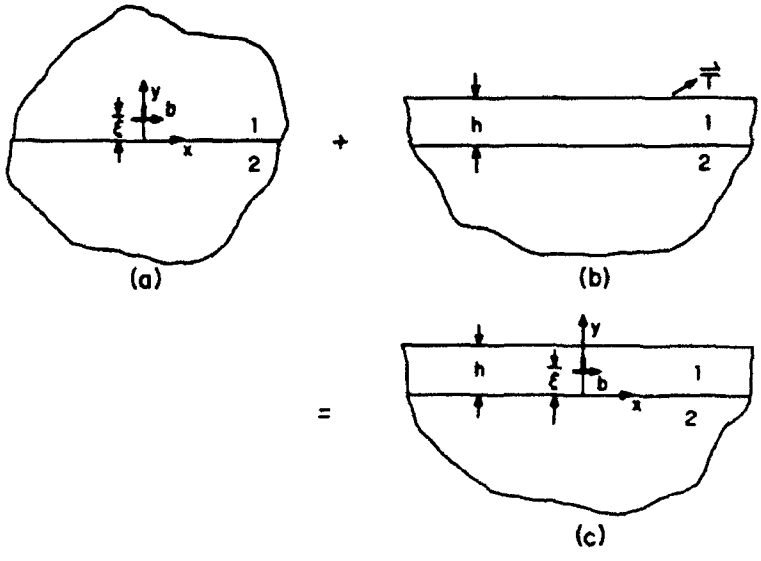

Fig. 17. Superposition scheme used to solve the cracked film problems.

Once the problem of a single dislocation in a semi-infinite bimaterial is constructed, the crack problem is modelled as a string of dislocations along the crack line, with a continuously variable Burgers vector magnitude $b(\xi)$. The crack face traction boundary condition for the particular problems at hand is that $\sigma_{yy}(x=0, y) = -\sigma$ where σ is a uniform pressure load applied to the crack faces. This loading configuration is, from a fracture mechanics standpoint, equivalent to a traction-free crack in a film supporting a uniform tensile stress σ prior to introduction of the crack. The crack face traction boundary condition is enforced by integration of the stresses along $x = 0$ with respect to the dislocation variable, ξ. The resulting integral equation takes the form

$$\sigma_{yy}(0, y) = -\sigma = \frac{-\mu_1}{2\pi(1-\nu_1)} \int_{a_0}^{h} b(\xi)\left[\frac{1}{(y-\xi)} + F_1(0, y, \xi) + F_2(0, y, \xi)\right] d\xi, \tag{A1}$$

where $a_0 = 0$ for the fully cracked film problem and $a_0 = (h-a)$ for the partially cracked film problem with crack length a. The first term, which is integrated in the Cauchy principal value sense, is from the dislocation solution for the problem in Fig. 17a. $F_1(x, y, \xi)$ and $F_2(x, y, \xi)$ are known kernel functions extracted from the solutions of the problems illustrated in Fig. 17a and Fig. 17b, respectively.

The unknown $b(\xi)$ is solved for by first introducing a change of variable

$$t = \frac{2(\xi - a_0)}{(h-a_0)} - 1, \tag{A2}$$

where t can vary from -1 to $+1$. Then $b(t)$ is expressed as a Chebyshev polynomial series with N unknown coefficients, C_i:

$$b(t) = \frac{1}{(t+1)^s} \sum_{i=1}^{N} C_i T_{i-1}(t), \tag{A3}$$

where s is the stress singularity exponent which satisfies (3) for the fully cracked film problem and which equals 1/2 for the partially cracked film problem. The $T_n(t)$ are the Chebyshev polynomial functions given by

$$T_n(t) = \cos(n \arccos(t)). \tag{A4}$$

An outline of Chebyshev approximation methods and numerical routines for their application are given by Press *et al.* (1986). The N values for the C_i are solved for by matching the traction boundary condition at N Gauss Legendre points along the crack faces. For the two problems solved in this study, a value of $N = 10$ gives satisfactory convergence of the results.

Quantities solved for

Once the solution is obtained for each problem by solving for the unknown $b(\xi)$, the fracture mechanics quantities

$$K_I = (2\pi)^s \frac{\mu_1}{2(1-\nu_1)} \lim_{\xi \to a_0} (b(\xi)(\xi - a_0)^s) \tag{A5}$$

and

$$\delta(y) = \int_{a_0}^{y} b(\xi)\, d\xi \tag{A6}$$

are extracted, where K_I is the mode I stress intensity factor and $\delta(y)$ is the crack opening displacement.

THE DIRECTIONALITY OF INTERFACIAL CRACKING IN BIMATERIALS

JIAN-SHENG WANG AND GLENN E. BELTZ
Division of Applied Sciences, Harvard University, Cambridge, MA 02138

ABSTRACT

Directionality of interfacial cracking resistance in bicrystals has been predicted by a modified Rice-Thomson model and supported by experimental results on $\Sigma 9$ [110]/($2\bar{2}1$) Cu bicrystals in Wang and Anderson's recent work. With the intention of extending this work to the behavior of interfacial cracks in dissimilar materials, Rice, Suo and Wang predicted that this directionality also occurs in bimaterials. Reported here are experimental results on Cu/sapphire specimens, which again support the prediction of the theory. A crack along the interface in a Cu/sapphire bimaterial is brittle and decohesion of the interface occurs when the crack propagates in the $[\bar{1}14]_{Cu}$ direction, whereas it is ductile and dislocation blunting operates if the crack is intended to propagate in the $[1\bar{1}4]_{Cu}$ direction. This finding is significant theoretical'y and is of helpful in understanding interfacial cracking in composites and film spalling in packaging materials.

INTRODUCTION

It has been well known that the cracking behavior of an interface between crystals depends strongly on its structure. It has been shown only recently, however, that for the same interface the cracking behavior depends also on the direction of the crack propagation. An interfacial crack that propagates in a ductile manner in one direction may undergo cleavage leading to a brittle decohesion in the opposite direction. Thus, the response of a stressed interfacial crack is not only interface structure dependent, but also growth direction dependent.

Intuitively, the cracking directionality is easy to understand. Any process which involves dislocation slip of Schmid type is dependent on the orientation of the active slip planes. For most interfaces, the configuration of the active slip systems at a crack tip is different when the direction of the crack propagation is reversed, leading to a directional dependence of the cracking behavior.

The directionality of cracking in bicrystals has been predicted by the Rice-Thomson model [1] and supported by experimental results on $\Sigma 9$ [110]/($2\bar{2}1$) Cu bicrystals in Wang and Anderson's recent work [2]. With the intention of extending this work to the behavior of interfacial cracks in dissimilar materials, Rice, Suo and Wang predicted that cracking directionality occurs also in bimaterials [3].

In the spirit of testing the idea that the competition between dislocation emission and cleavage decohesion controls the ductile versus brittle behavior of a metal/ceramic interface and that the cracking response is direction dependent, fracture behaviors of interfaces in bimaterials were investigated. Reported here are experimental results on Cu/sapphire specimens.

EXPERIMENTAL PROCEDURE AND RESULTS

Single crystals of copper used in the experiments were grown by a vertical Bridgman technique in an atmosphere of flowing argon gas. Rectangular pieces of 47.6x4.8x2.5 mm were cut via spark-cutting. After mechanically and chemically polishing and cleaning the ($2\bar{2}1$) surface of the Cu single crystal was bonded to the basal plane of a commercially-obtained sapphire slide (1 mm thick) by diffusion bonding. The diffusion bonding was carried out in an atmosphere of flowing forming gas (a gas mixture of 20% hydrogen + 80% argon) at 1313 K for 72 hours under a rigid graphite support clamp to maintain a compressive force during bonding. After

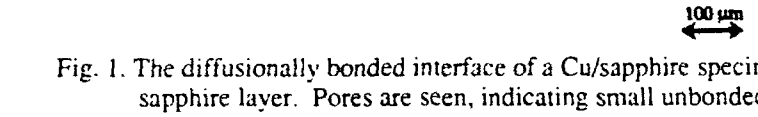

Fig. 1. The diffusionally bonded interface of a Cu/sapphire specimen viewed through the sapphire layer. Pores are seen, indicating small unbonded spots.

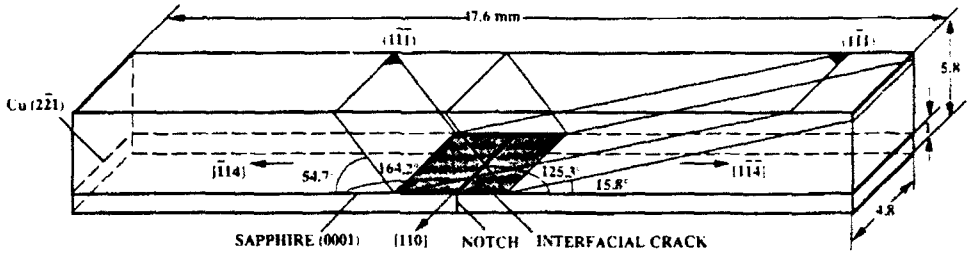

Fig.2. The geometry of the specimen and a schematic presentation of the slip plane configurations at the crack tips of the opposite directions.

bonding the specimen was cyclically annealed to reduce the interfacial stress and remove small grains which sometimes appeared near the interface during bonding. Observations through the optically transparent sapphire layer showed that the quality of the bonding was adequate; the interface was free of any potential reaction products and only a few pores were observed, indicating small unbonded spots (Fig. 1).

A pre-notch was created at the midpoint of the sapphire layer and then the specimen was subjected to a bend load so that an initial crack was produced and run to the Cu/sapphire interface, along which it branched a small amount in both directions, i. e. the $[\bar{1}14]_{Cu}$ and $[1\bar{1}\bar{4}]_{Cu}$ directions. The geometry of the specimen and the slip plane configurations at the crack fronts of the opposite directions are shown schematically in Fig. 2. The pre-cracked specimen was loaded under four-point bending with a screw-driven Instron mechanical testing machine until a nonlinear load versus deflection relation was noted, and then it was unloaded and reloaded several times to enable stable crack propagation. Debonding of the interface at the crack tip, whenever it occurred in either direction, was observed by an optical microscope through the sapphire layer. The energy release rate for debonding, G, was obtained from the load-deflection curve [3]. Slip traces, which indicate dislocation slip on active slip systems in the Cu single crystal, were observed on the polished (110) side surface of the crystal with SEM or optical microscopy.

Five identical specimens were tested in the same procedure. The average value of G was measured to be 5.5±0.5 J/m^2. Observations showed that in all specimens tested the interfacial crack propagated stably in the $[\bar{1}14]_{Cu}$ direction causing significant interfacial debonding; whereas in the $[1\bar{1}\bar{4}]_{Cu}$ direction plastic deformation occurred, causing crack tip blunting. An example which demonstrates this kind of asymmetrical cracking behavior is shown in Fig. 3. In one particular case the directional effect was profound: in the $[\bar{1}14]_{Cu}$ direction the crack propagated unstably all the way to the end of the specimen causing half of the sapphire layer to detach entirely from the specimen; whereas in the $[1\bar{1}\bar{4}]_{Cu}$ direction the crack propagated only a

Fig. 3. The side view of a Cu/sapphire specimen after mechanical testing which shows that the crack propagated only in the $[\bar{1}14]_{Cu}$ direction and crack tip blunting occurred in the $[1\bar{1}4]_{Cu}$ direction.

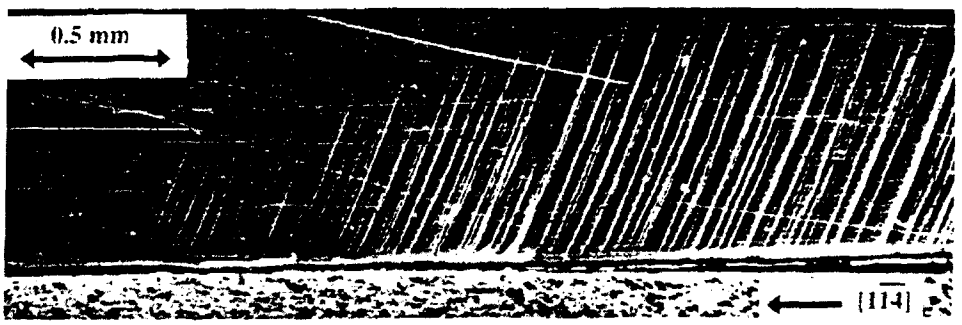

Fig. 4. The dark field optical photograph shows the dense slip lines in the vicinity of the crack which propagated in the $[1\bar{1}4]_{Cu}$ direction.

small amount. Dense slip lines on the polished $(110)_{Cu}$ side surface at the vicinity of the crack appeared (Fig. 4), indicating a large amount of plastic deformation. It was identified from the angle of the slip lines that in this case only the $(\bar{1}\bar{1}1)$ slip planes, which make an angle of 125.3° with the crack plane, were active. In the opposite direction the slip lines were much less dense, and again, only the $(1\bar{1}\bar{1})$ system was active which, in this direction, makes an angle of 54.7° with the crack plane.

As we will see in the next section of the paper, calculations by the modified Rice-Thomson model show that in the $[1\bar{1}4]_{Cu}$ direction, dislocations are easier to nucleate on $(1\bar{1}\bar{1})$ planes; in contrast, in the $[\bar{1}14]_{Cu}$ direction only $(1\bar{1}1)$ planes with the inclination angle of 164.2° may be activated and dislocation nucleation on $(1\bar{1}\bar{1})$ planes is very difficult. The slip lines observed in this direction is thus not produced by the crack tip emitted dislocations. Rather, they are induced by internal dislocations. The controlling process for the crack propagation in the $[\bar{1}14]_{Cu}$ direction is indeed interfacial debonding, while in the $[1\bar{1}4]_{Cu}$ direction the controlling process is dislocation slip: a strong directionality of interfacial cracking in the Copper/sapphire interface as that predicted by the modified Rice-Thomson model. Now, let us turn to the model.

DISCUSSION

The directionality of interfacial cracking might be partly understood in terms of the competition between dislocation emission from the crack tip and cleavage, a concept quantified initially by Rice and Thomson [4] to deal with ductile versus brittle response in crystals. An extended Rice-Thomson model was proposed by Rice, Suo and Wang [3] to treat the situation

involving a straight edge dislocation emanating from the tip of a crack lying on a metal/ceramic interface. In the model the energy release rate for dislocation emission from the crack tip, G_{disl}, and the energy release rate for debonding of the interface, G_{cleav}, were compared. If $G_{disl} < G_{cleav}$, dislocation emission was assumed to occur before interfacial decohesion, blunting the tip of the crack; the interface was predicted to be ductile. On the other hand, if $G_{disl} > G_{cleav}$, then decohesion was assumed to occur before dislocation emission and the interface was said to be intrinsically brittle. While G_{cleav} is relatively insensitive to the structure of the interface [2], G_{disl}, being mainly determined by the resolved shear stress on the slip plane, may change dramatically with the change of the inclination angle of the slip plane with respect to the crack plane. This occurs when changing the direction of crack growth in asymmetrical orientation like in Fig. 2, causing the directionality of interfacial cracking.

There are two levels of approaches in deriving the energy release rate for dislocation emission from a crack tip: an older approach following [1], which treats the dislocation as an elastic line singularity in a continuum solid; and a new approach [5], where the dislocation is treated in the Peierls-Nabarro sense. At present, both approaches can only treat the situation where the crack front lies in a slip plane. One advantage of the Peierls-type approach is that it avoids the use of a core cutoff parameter, a necessity in the singular dislocation line approach and the vaguest parameter in elastic dislocation theory.

In the extension of the theory to the metal/ceramic interface, both approaches regard the ceramic side of the interface as an elastic solid, in which no dislocation activity takes place; only in the metal side is dislocation activity assumed to be possible. With this assumption, a treatment similar to that for dislocation emission from a crack tip in single crystals may be adopted and the only modification needed is to introduce a new parameter: the atomic scale local phase angle, ψ', a measure of the ratio of local mode II to mode I conditions on a distance of atomic length scale from the crack tip, and is defined by

$$\psi' = \psi - \varepsilon \ln(h/b). \qquad (1)$$

Here ψ is the loading phase angle, depending on the loading conditions and also on the elastic combination of the bimaterial, ε is the oscillatory index characterizing the oscillatory stress field near the tip of an interfacial crack, h represents a characteristic length scale of the specimen and b, as usual, is the magnitude of the Burgers vector. Limited by the length of the paper, we are not going to the details of the model; only the major conclusions are given below. Readers who are interested in are referred to Rice, Suo and Wang [2] for the singular dislocation line approach and Rice [5] and Beltz and Rice [6] for the Peierls approach.

Considering joined isotropic solids under in-plane loadings, so that $K_{III}=0$ and the near tip field is fully characterized by a complex stress intensity factor K, Rice, Suo and Wang [2] derived the energy release rate needed for a straight edge dislocation emanating from the crack tip in a metal/ceramic interface as

$$G_{disl} = \frac{\mu_1 b^2}{(1-\nu_1)(1-\alpha)r_c}\left\{\frac{\cos\phi + (1-\nu_1)\sin\phi\tan\phi}{4\sqrt{\pi}\cosh(\pi\varepsilon)\,(\Sigma^{I}_{r\theta}(\theta)\cos\psi' + \Sigma^{II}_{r\theta}(\theta)\sin\psi')}\right\}^2. \qquad (2)$$

Here r_c is the dislocation core cutoff in the metal, μ_1 is the shear modulus and ν_1 the Poisson ratio of the metal, α is the Dundurs parameter which characterizes the elastic combination of the bimaterial, θ is the inclination angle of the slip plane with respect to the crack plane, ϕ is the angle between the Burgers vector and the normal to the crack front. $\Sigma^{I}_{r\theta}(\theta)$ and $\Sigma^{II}_{r\theta}(\theta)$ are the angular functions given in [3], which correspond to traction across the interface at $\theta=0$ of tensile and in-plane shear, respectively. Equation (2) reveals that G_{disl} is a strong function of the inclination angle θ and the local phase angle ψ'.

Unlike the typical situation when the local phase angle is defined based on a "laboratory" length scale, the distinction between ψ and ψ' in this context becomes important because the oscillatory stress field can give rise to a significant shift in the ratio of mode II to mode I type conditions when considering atomic-scale distances from the crack tip. For the Cu/sapphire

specimen shown in Fig. 2 under four-point bending conditions the loading phase angle ψ is about -52°, while the local phase angle ψ' is about -79°, indicating a significant mode II component of loading. Under these conditions, equation (2) gives the G_{disl} against θ as plotted in Fig. 5. The model predicts that G_{disl} is about 0.86 J/m^2 for cracking in the $[1\bar{1}4]_{Cu}$ direction and $(1\bar{1}\bar{1})$ planes with the inclination angle of 125.3° are potentially active; the $(1\bar{1}1)$ planes with the inclination angle of 54.7° are inactive because an extremely high value of G_{disl} is needed for dislocation nucleation on these planes. For the cracking direction of $[\bar{1}14]_{Cu}$, G_{disl} is predicted to be 4.9 J/m^2 and the potentially active slip planes are $(1\bar{1}1)$ which inclined at 164.2°; the $(1\bar{1}\bar{1})$ planes, in this case the inclination angle is 15.8°, are inactive. The parameter G_{cleav}, a measure of the coherence of the interface, is assumed to be independent of the cracking direction. As a reference, a lower bound of 0.475 J/m^2 might be quoted from a measurement of the adhesion of the Cu/Al_2O_3 interface [7]. Hence, dislocation emission is favored in the $[1\bar{1}4]_{Cu}$ direction and brittle crack growth should be favored in the $[\bar{1}14]_{Cu}$ direction, a prediction supported by our experimental results.

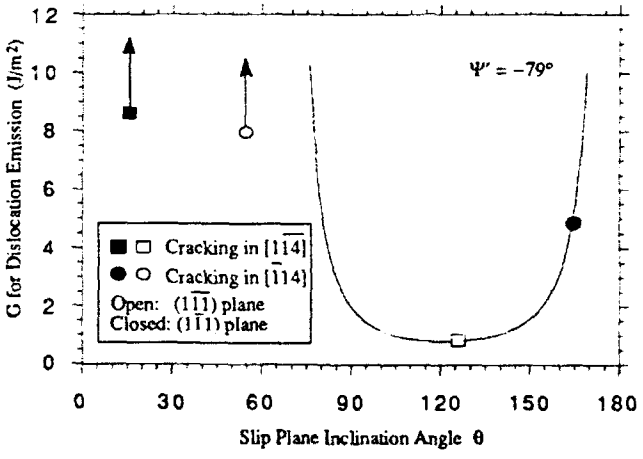

Fig. 5. The energy release rate for dislocation emission, G_{disl}, as a function of the inclination angle, θ, for the Cu/sapphire specimen under four-point bending conditions.

As a comparison, we quote here the calculations of the Peierls-approach by Beltz and Rice [5], which give G_{disl}=0.505 J/m^2 for the ductile direction and G_{disl}=2.76 J/m^2 for the brittle direction. There is a factor of 6 difference in G_{disl} for crack growth in the opposite directions and indeed, dislocation emission is preferred in the $[1\bar{1}4]_{Cu}$ direction and decohesion occurs in the $[\bar{1}14]_{Cu}$ direction as our experiments showed.

It is interesting to note that the ductile direction in Wang and Anderson's Cu bicrystals under tension conditions is the brittle direction in our Cu/sapphire specimens under bending conditions and vice versa, a result also predicted by Rice et.al [3]. This is attributable entirely to the phase angle effect and is discussed in more detail in [8].

CONCLUSIONS

The ductile versus brittle response of a stressed interfacial crack is not only interface structure dependent, but also direction dependent. An interfacial crack, which propagates in a brittle manner in one direction, might be ductile in the opposite direction. The different fracture behavior of bimaterial interfaces may be understood, at least qualitatively, by comparing the

crack tip energy release rate for dislocation emission from the crack tip against that for cleavage decohesion of the interface. The local phase angle exercises a strong influence upon the ductile versus brittle response of an interfacial crack.

Acknowledgements: We are grateful to J.R. Rice for helpful discussions. This work is supported by NSF through the MRL at Harvard University (grant DMR-89-20490) and a University Research Initiative, through an ONR/DARPA contract at UCSB (subcontract POAVB38639-0).

References

[1]. P.M. Anderson and J.R. Rice, Scripta Metall. 20, 1467 (1986) and P.M. Anderson, Ph.D. thesis, Harvard University, Cambridge, Mass. (1986).
[2]. J.-S. Wang and P.M. Anderson, Acta metall. mater. 39, 779 (1991).
[3]. J.R. Rice, Z. Suo and J.-S. Wang, in Metal-Ceramic Interfaces, Acta-Scripta Metallurgical Proceedings Series, Vol. 4, edited by M. Rühle, A.G. Evans, M. F. Ashby, and J.P. Hirth, pp. 269-294, Pergamon Press, Oxford (1990).
[4]. J. R. Rice and R. Thomson, Phil. Mag., 29, 73(1974).
[5]. J. R. Rice, "Dislocation Nucleation from a rack Tip: An Analysis Bases on the Peierls Concept", J. Mech. Phys. Solids, 1991, in press.
[6]. G.E. Beltz and J.R. Rice, "Dislocation Nucleation at Metal/Ceramic Interfaces", submitted to Acta metall. mater., 1991.
[7]. M. Nicholas, J. Mat. Sci., 3, 571(1968).
[8]. G.E. Beltz and J.-S. Wang, "Crack Direction Effects along Copper/Sapphire Interfaces", Submitted to Acta metall. mater., 1991.

Acta metall. mater. Vol. 40, No. 7, pp. 1675–1683, 1992
Printed in Great Britain. All rights reserved

0956-7151/92 $5.00 + 0.00
Copyright © 1992 Pergamon Press Ltd

CRACK DIRECTION EFFECTS ALONG COPPER SAPPHIRE INTERFACES

G. E. BELTZ and J.-S. WANG
Division of Applied Sciences, Harvard University, Cambridge, MA 02138, U.S.A.

(Received 4 November 1991)

Abstract—The Rice–Thomson model is used to predict the directional toughness of a copper–sapphire interface, consisting of a {221} face of a copper crystal bonded to a basal sapphire surface. Specimens of this type are subsequently tested, in the form of a layered beam (having two opposing cracking directions) subject to four-point bending and confirm the theoretical predictions. A general observation is that the ductile or brittle response of a crack on a metal–ceramic interface is strongly dependent on the relative orientation of available slip planes to the existing crack plane and growth direction. This conclusion is consistent with earlier results by Wang and Anderson on symmetric tilt grain boundaries in copper and explains, for example, why brittle cracking occurs in the [1$\bar{1}$3] direction along the {221} interface of a tensile-loaded copper bicrystal, but along the opposite [$\bar{1}$14] direction in bending-loaded copper–sapphire specimens with mixed mode conditions at the crack tips.

Résumé—On utilise le modèle de Rice et Thomson pour prévoir la ténacité directionnelle d'une interface cuivre–saphir, formée d'une face {221} d'un cristal de cuivre liée au plan basal du saphir. Des échantillons de ce type sont donc testés, ils ont la forme d'une poutre constituée de couches ayant deux directions de fissuration opposées) soumise à une flexion sur quatre points et les résultats confirment les prévisions théoriques. D'une manière générale, la réponse ductile ou fragile d'une fissure sur une interface métal–céramique dépend fortement de l'orientation relative des plans de glissement disponibles par rapport au plan de la fissure existante et à sa direction de croissance. Cette conclusion est en accord avec les précédents résultats de Wang et Anderson sur les joints de flexion symétriques dans le cuivre et explique, par exemple, pourquoi la fissuration fragile se produit dans la direction [1$\bar{1}$3] le long de l'interface {221} d'un bicristal de cuivre chargé en traction, et dans la direction opposée [$\bar{1}$14] dans des échantillons de cuivre–saphir chargés en flexion avec des conditions de mode mixte aux extrémités des fissures.

Zusammenfassung—Mit dem Rice–Thomson-Modell wird die Zähigkeit einer Kupfer–Saphir-Grenzfläche, die aus einer {221}-Kupferfläche und der Saphir-Basisebene besteht, vorausgesagt. Proben in der Form eines geschichteten Balkens, die zwei gegenüberliegende Rißrichtungen aufweisen, werden im Vierpunktbiegeversuch belastet, die Ergebnisse bestätigen die theoretischen Voraussagen. Eine allgemeine Beobachtung ist, daß das duktile oder spröde Verhalten eines Risses an einer Metall–Keramik-Grenzfläche sehr stark von der relativen Orientierung der verfügbaren Gleitsysteme bezüglich der bestehenden Rißebene und der Ausbreitungsrichtung des Risses abhängt. Diese Folgerung ist mit früheren Ergebnissen von Wang und Anderson zu symmetrischen Kippkorngrenzen in Kupfer verträglich und erklärt zum Beispiel, warum spröde Risse in der [1$\bar{1}$3]-Richtung entlang der {221}-Grenzfläche in einem zugbelasteten Kupfer-Bikristall auftreten, aber entlang der entgegengesetzten Richtung [$\bar{1}$14] in biegebelasteten Kupfer–Saphir-Proben unter Bedingungen einer gemischten Mode an den Rißspitzen.

INTRODUCTION

The behaviour of metal–ceramic bonds is of great *technological importance*, for example, in the field of electronic device packaging, and, needless to say, in metal–ceramic composites. In this paper, experimental results from fracture tests of single crystals of copper bonded on a {221} plane to the basal plane of sapphire are reported. At issue here is the ductile vs brittle response of the interfacial crack. If conditions are favorable for the nucleation and unstable propagation of a dislocation from an interfacial crack tip, is brittle crack propagation suppressed? An early attempt at answering this question was due to Rice and Thomson [1] in which the ductile versus brittle response of a material is assumed to be ultimately controlled by the completion between atomic decohesion and dislocation nucleation ahead of the crack tip. Later versions of this model [2–6] extended the Rice–Thomson model to treat the crack response along an interface by evaluating the competition in terms of the parameters G_{cleave}, the energy release rate for interfacial cleavage, and G_{disl}, the energy release rate associated with the emission of a single dislocation. The competition is shown schematically in Fig. 1, if $G_{cleave} < G_{disl}$, then the crack is said to propagate in a brittle manner, and the interface is said to be intrinsically brittle, conversely, if $G_{disl} < G_{cleave}$, then a dislocation moves away from the tip thus blunting and "shielding" the crack tip from further increases in applied loading, and the interface is said to be intrinsically ductile. The most dramatic

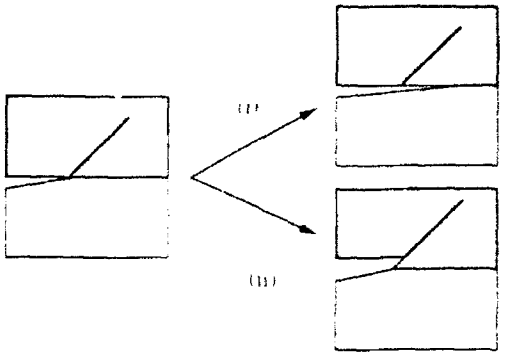

Fig. 1. Atomistically sharp interfacial crack on the left, showing the competition between cleavage decohesion (I) and dislocation emission (II).

effect related to this competition is the directional dependence of the interfacial crack response in symmetric tilt bicrystals as predicted by the model and experimentally observed [6].

The primary purpose of this paper is to test the idea that the competition between dislocation emission and cleavage decohesion controls the ductile versus brittle behaviour of a metal ceramic interface and that the crack response is direction-dependent, similar in spirit to the efforts of Wang and Anderson [6]. In their work, symmetric tilt bicrystals of copper with different bismuth segregation levels were tested. The most dramatic effect relating to the directionality occurred in a $\Sigma 9[110](2\bar{2}1)$ symmetric tilt copper bicrystal, in which two specimens were cut and notched *along the grain boundary so that a crack* would run in the opposite directions $[\bar{1}14]$ and $[1\bar{1}4]$, respectively. The specimens were fatigued under a mode I loading of increasing amplitude. The specimen with the $[\bar{1}14]$ cracking direction broke along the interface when the maximum bending stress reached 28.1 MPa, corresponding to $G \approx 2.5$ J m^{-2}. An intergranular fracture surface with cleavage "tongues" was observed. The other specimen, with a cracking direction of $[1\bar{1}4]$, was loaded under identical conditions and eventually fractured at a nominal stress of 76.7 MPa. The fracture surface contained large regions of ductile transgranular fatigue fracture and plastic tearing, and the G value, ≈ 21.0 J m^{-2}, was beyond the reliably measurable range for elastic fracture mechanics. The only difference between these two specimens was the cracking direction; hence it was concluded that the difference in ease with which dislocations could be nucleated at each crack tip was the cause of this behaviour.

ANALYSIS OF SPECIMEN

The specimens used in this work are the four-point bend specimens consisting of a metallic layer bonded to a thinner ceramic layer (see Fig. 2). This type of specimen was originally proposed by Charalambides *et al.* [7] and Suo and Hutchinson [8] for the testing of linear elastic interfacial fracture mechanics concepts. The usefulness of the specimen for a possible directional effect resulting from the use of an asymmetrically aligned metal single crystal was pointed out in the work of Rice *et al.* [5]. An advantage of this type of specimen is that when the crack is long compared with the thickness of the notched layer h, the complex stress intensity factor

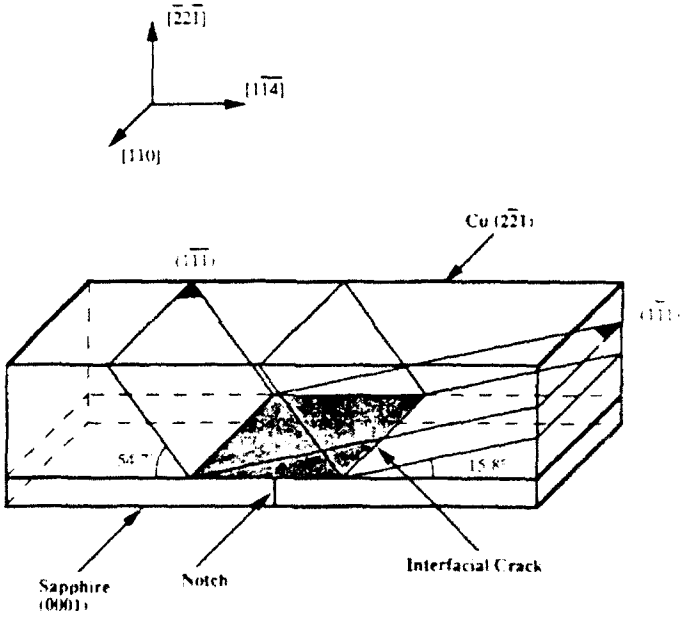

Fig. 2. Schematic of the specimen analyzed: a copper single crystal with its [221] face bonded to sapphire, loaded in bending with crack tips parallel to the [110] direction.

has the following form, which is independent of crack length

$$K = Y(\alpha, \beta, h)\, H(M\alpha)^{-\epsilon} e^{-\epsilon\Psi} \quad (1)$$

where M is the applied moment per unit width, and Y and Ψ are dimensionless functions of the thickness ratio and the Dundurs parameters α and β, which are given by

$$\alpha = \frac{(1-\nu_1)/\mu_1 - (1-\nu_2)/\mu_2}{(1-\nu_1)/\mu_1 + (1-\nu_2)/\mu_2},$$
$$\beta = \frac{1}{2}\,\frac{(1-2\nu_1)/\mu_1 - (1-2\nu_2)/\mu_2}{(1-\nu_1)/\mu_1 + (1-\nu_2)/\mu_2} \quad (2)$$

where μ and ν refer to the shear modulus and Poisson's ratio, respectively. Subscript 1 refers to the material on top, which is taken to be the metal, and subscript 2 refers to the ceramic phase. The functions Y and ψ may be found in [8] or [9]. By definition, ψ is the phase angle of the complex quantity $Kh^{i\epsilon}$, and the quantity $\tan\psi$ is a relative measure of the ratio of loading modes on length scales of order h from the tip. The parameter ϵ is known as the oscillation index, and is given by

$$\epsilon = \frac{1}{2\pi}\ln\left(\frac{1-\beta}{1+\beta}\right). \quad (3)$$

The stress intensity factor K reduces to the familiar $K_I + K_{II}$ when $\epsilon = 0$.

The intent of the four-point bend specimen is to compare crack growth in two opposing directions in the *same* specimen during the *same* mechanical test. *The orientation of the copper in these experiments* is the same as that in the Σ9 bicrystals tested by Wang and Anderson: the $(2\bar{2}1)$ face of the copper crystal is bonded to the sapphire surface, with the short dimension of the specimen parallel to the [110] direction in the copper. Once a crack runs through the sapphire and branches onto the interface in both directions, the crack fronts at both ends lie along the intersection of a pair of {111} slip planes of the copper crystal with the interface. The crack growth directions are hence $[\bar{1}14]_{Cu}$ and $[1\bar{1}4]_{Cu}$. Due to the asymmetry of the copper crystal, the crack oriented to run in the $[1\bar{1}4]_{Cu}$ direction encounters slip planes which are aligned at 15.8° and 125.3°, respectively, while the crack oriented to run in the $[\bar{1}14]_{Cu}$ direction encounters slip planes inclined at 54.7° and 164.2° (see Fig. 2).

For the study of dislocation emission from the tip of an interfacial crack, a parameter known as the *atomic scale phase angle*, ψ', has been introduced [5], which is the phase angle of the quantity $Kh^{i\epsilon}$, and thus is a measure of the ratio of local mode II to mode I conditions on atomic length scales from the crack tip. It is a simple exercise to show that the two angles are related by

$$\psi' = \psi - \epsilon\ln(h/b) \quad (4)$$

where b represents the magnitude of the Burgers vector. Unlike the typical situation when the local phase angle is defined based on a "laboratory" length scale, the distinction between ψ and ψ' in this context becomes important because the oscillatory stress field can give rise to a significant shift in the ratio of mode II to mode I type conditions when considering atomic-scale distances from the crack tip. The loading phase angle ψ is about −52°, while the local phase angle, ψ', is about −79° under four-point bending for the specimens analyzed in this work [5], indicating a significant mode II component of loading. Under these conditions, using a Rice Thomson model which had been specialized for bimaterial interfaces, Rice *et al.* [5] predicted that G_{ss} is about 0.86 J cm⁻² for cracking in the $[114]_{Cu}$ direction (dislocation emission is easiest on the slip plane inclined at 125.3°) and 4.9 J m⁻² for cracking in the $[\bar{1}14]_{Cu}$ direction (dislocation emission is easiest on the slip plane inclined at 164.2° in this case). The parameter $G_{ss(i)}$, a measure of the coherence of the interface, is assumed to be identical in either direction, hence brittle crack growth should be favored in the $[\bar{1}14]_{Cu}$ direction. It is interesting to point out that in the work of Wang and Anderson on bicrystals, the ductile cracking direction was $[\bar{1}14]$ and the brittle direction was $[1\bar{1}4]$, *the opposite to that predicted here for the bend specimen*. This is attributable entirely to the phase angle effect. Here, the atomic scale phase angle ψ' is −79°, while for a mode I loading of a symmetric tilt bicrystal it is 0°. Figure 3(a) which gives $G_{ss(i)}$ vs θ for copper sapphire interfaces loaded in such a manner as to give an atomic scale phase angle of −79°, highlights the effect of the slip plane inclination angle.

The phase angle effect is further illuminated by Fig. 3(b), which gives $G_{ss(i)}$ vs ψ' for the various slip plane inclination angles of interest. The dashed lines correspond to angles associated with the $[\bar{1}14]_{Cu}$ direction, and the solid lines correspond to angles associated with the $[1\bar{1}4]_{Cu}$ direction. Comparison of the curves at $\psi' = 0$ and $\psi' = -79°$ shows that the favored direction for dislocation emission reverses when the phase angle is altered.

DISLOCATION NUCLEATION BASED ON A PEIERLS MODEL

The methods for determining $G_{ss(i)}$ as discussed in the previous discussion were based on a modified Rice Thomson model [5], which treats a dislocation as an elastic singularity which exists ahead of the crack tip prior to loading. An unfortunate consequence of this usage is that a *core cutoff parameter* must be introduced into the analysis, which is usually assumed to be on the order of one atomic spacing. Argon [10] and, more recently, Schoeck [11] have recognized that a full dislocation is likely to emerge unstably from an incomplete, incipient dislocation at the tip, but a reasonably exact treatment has been given only recently by Rice [12]. That treatment, discussed in further detail by Beltz and Rice [13, 14], solves the elasticity problem of a traction free crack

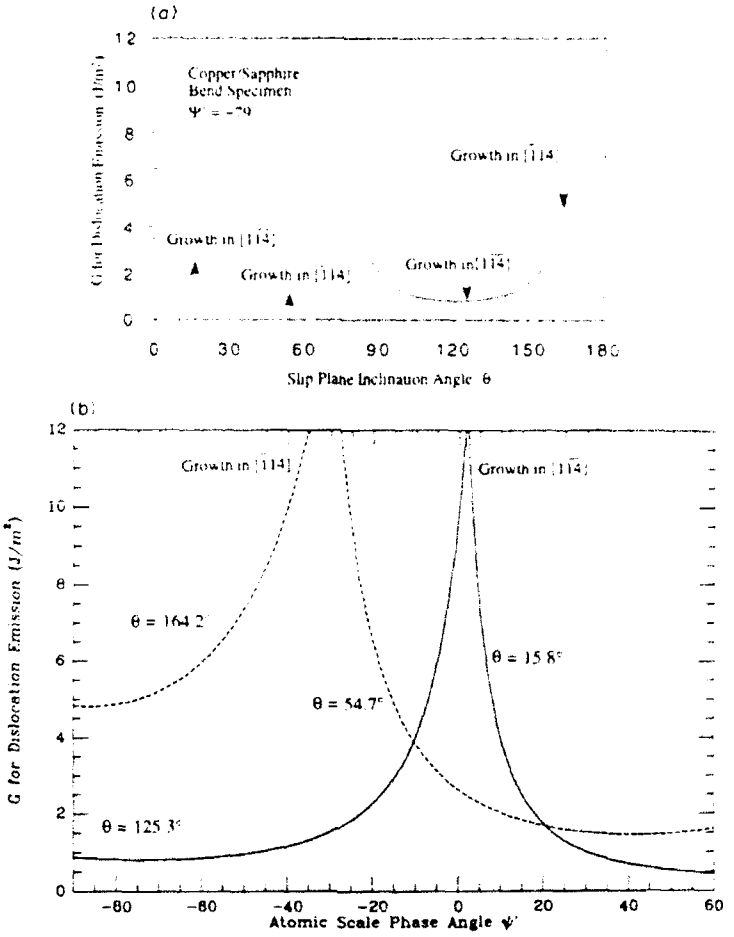

Fig. 3. (a) Plot of G_{disl} vs the slip plane inclination angle, as predicted by the Rice–Thomson model for a copper/sapphire interfacial crack; and (b) G_{disl} vs the atomic scale phase angle for various angles of interest. The solid lines give the relevant angles for crack propagation in the $[1\bar{1}4]_{Cu}$ direction, and the dashed lines represent angles relevant to propagation in the $[\bar{1}14]_{Cu}$ direction

with a Peierls-type stress versus displacement relation being satisfied as a boundary condition along a slip plane ahead of a crack tip. Once this problem is solved for a suitable constitutive relation for material sliding and perhaps opening along a slip plane, there is no need for the core cutoff parameters. The advantage of this method is that it allows for the existence of an extended dislocation core during nucleation, and eliminates uncertainty in choosing the core parameters. Numerical work by Beltz and Rice [14] agrees with the directional and phase angle effects given by the Rice–Thomson model [5] for the case of a metal/ceramic interface.

The directional effects observed here and in [16] are consistent with the fact that the ductile crack tip orientation involves slip planes which are more favored for dislocation motion (i.e. they have a higher resolved shear stress) than near the opposing crack tip. In light of the recent improvements in the modeling of dislocation nucleation, we feel it is appropriate to preview our experiments in terms of the newer theory. The approach requires a knowledge of the Peierls-type shear stress τ ($\equiv \sigma_{r\theta}$, on $\theta = 0$ in the case now discussed) vs relative atomic displacement (denoted Δ_1) relation such as the sinusoidal representation in Fig. 4(a); Δ_1 denotes the shift of one atomic plane relative to another at the slip surface. This curve gives the shear stress needed to locally shear atoms with respect to one another on a given slip plane, and is the fundamental input to the Peierls–Nabarro dislocation model [15, 16]. The initial slope of such a curve corresponds with an appropriate shear modulus. The parameter b is the magnitude of a Burgers vector and represents the periodicity of the stress–displacement relation. This type of data has been calculated through the use of pair potentials or the embedded atom method by several researchers [17–20]. The integral of such a curve from $\Delta_1 = 0$ to the unstable equilibrium at which the shear stress next vanishes (at $\Delta_1 = b/2$ in simple cases) has been called [12] the *unstable stacking energy*, denoted γ_{us}. An estimate of this solid

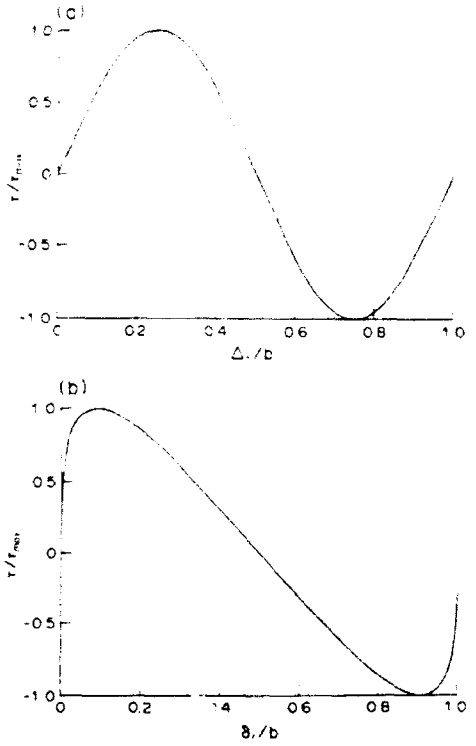

Fig. 4. Expected form of the shear stress τ vs: (a) relative atomic displacement Δ_r and (b) displacement discontinuity δ_r.

state parameter for copper, based on Frenkel theory (which models the τ vs Δ_r curve as a sine wave), gives a value of about 0.22 J/m^2.

Define δ_r as the displacement discontinuity on a mathematical cut coincident with the slip plane. We relate δ_r to the displacement Δ_r of the atomic planes at $\pm h/2$ from the cut by

$$\delta_r = u_r^{(+)} - u_r^{(-)} = \Delta_r - \frac{\tau h}{\mu} \tag{5}$$

where h is the interplanar spacing. This idealized cut represents the slip plane, and by adding to the displacement discontinuity δ_r across the cut (in what is otherwise considered a linear elastic continuum) the additional "elastic" displacement $h\tau/\mu$, we simulate approximately the relative displacement $\Delta_r = \delta_r + h\tau/\mu$ between atomic planes a distance h apart. If τ is now plotted versus δ_r, the curve becomes skewed so as to give an infinite slope at the origin [see Fig. 4(b)]. The integral of τ over half of a cycle remains equal to γ_{us}, however.

A J-integral calculation may be used to derive the following result for a mode II shear crack with a coplanar slip plane (see [21] for details)

$$G_{disl} = \frac{1-\nu}{2\mu}(K_{II}^{disl})^2 = \gamma_{us}. \tag{6}$$

With the exception of the nonlinear behavior along the slip plane, the material in this simple case is taken as an isotropic, linear elastic solid with shear modulus μ and Poisson's ratio ν. As discussed below, G_{disl} may be calculated for more realistic situations involving inclined slip planes, mixed mode loadings, and bimaterial crack tip fields; however, the above result illustrates a feature that pervades these complicated cases: the energy release rate for dislocation nucleation scales with the recently identified solid state parameter γ_{us}.

Further complexities arise when we include in the model the effects of normal tractions and dilatant openings across the slip plane. This situation occurs if a model I-type loading is added to the mode II situation just discussed, or in more realistic cases when the slip plane is inclined with respect to the crack plane. There are no reasons to assume that a given τ vs δ_r curve retains its shape if tension is superposed; hence the effect of superposed tension on the "effective" γ_{us} must be investigated. Argon [10] and Cheung *et al.* [22] have already noted the importance of softening in shear due to large tensile stresses across a slip plane. In recent analyses by Beltz and Rice [13, 14], more realistic configurations, including ones involving slip planes inclined at the angles 125.3° and 164.2° have been treated. The effect of tension/compression normal to the slip plane was treated by assuming a tensile stress vs normal component of separation relation consistent with the well-known fit, with energy proportional to $-(L+\Delta_\theta)\exp(-\Delta_\theta/L)$, to the universal bonding correlation of Ferrante *et al.* [23]. The parameter L is the characteristic length associated with the decohesion process (the tensile stress reaches a maximum, at $\Delta_r = 0$, when $\Delta_\theta = L$).

Results given in [14] for a simplified set of slip plane constitutive relations $\tau(\delta_r, \delta_\theta)$ and $\sigma(\delta_r, \delta_\theta)$ for copper are now summarized. In Fig. 5, the applied energy release rate G/γ_{us} is plotted as a function of the crack tip opening displacement δ_r^{tip}/b for the two angles of interest. Here b is the Burgers vector of the partial (i.e. $b_{total}/\sqrt{3}$). When $\theta = 125.3$ (i.e. crack growth in the $[1\bar{1}4]_{Cu}$ direction), unstable nucleation of a Shockley partial dislocation occurs at $G/\gamma_{us} = 1.839$. When $\theta = 164.2$ (crack growth in the

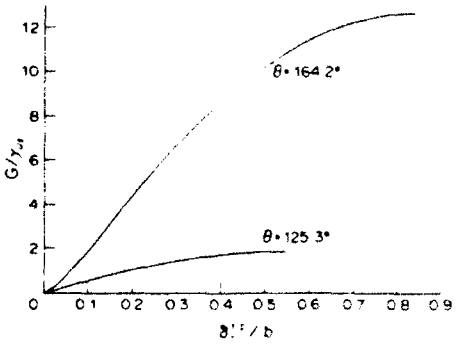

Fig. 5. The applied energy release rate versus the amount of slip at the crack tip for the two angles of interest, as predicted by the Peierls-type theory

$[\bar{1}14]_{Cu}$ direction), instability occurs at $G_{tip} = 12.55$. If we assume a value of 0.22 J m^{-2} for the unstable stacking energy, the relevant energy release rate values are $G_{duct} = 0.405$ J m^{-2} for the ductile direction and $G_{brit} = 2.76$ J m^{-2} in the brittle direction. There is more than a factor of 6 difference in G_{tip} for crack growth in the opposing directions; hence, it is concluded that dislocation nucleation is preferred in the $[1\bar{1}4]_{Cu}$ direction, and blunting should be favored in this growth direction.

EXPERIMENTAL

The single crystals of copper used in these experiments were grown by the vertical Bridgman technique in a graphite mold in an atmosphere of flowing argon gas. The crystal seeds were cut from pure copper crystals also grown by way of the Bridgman technique. The orientations of the seeds and the bicrystals were determined by the back-reflection Laue method with an accuracy of approximately $\pm 2^\circ$. The crystals used to make specimens were cut from the master ingot via spark-cutting, and were 47.6 mm by 2.5 mm by 4.8 mm. The copper pieces were diffusion bonded to 1 mm thick, commercially-obtained sapphire slides on the basal plane, at 1040°C, for 72 h, under a rigid graphite support clamp. The atmosphere consisted of a flowing hydrogen/80% argon (by volume) mixture. Several specimens were annealed after the bonding process in order to reduce the size and number of smaller grains which appeared near the copper/sapphire interface during diffusion bonding.

The surface of the sapphire layer in the specimens was "pre-notched," either by use of a diamond scribe or a diamond saw. The purpose of this was to insure that the initial crack through the sapphire would start at the midpoint of the specimen. The initial crack was induced by subjecting the specimen to either three- or four-point bending. After pre-cracking, the interfaces were observed through the sapphire layer to verify that the initial crack had branched onto the copper/sapphire interface in both directions. The specimens were then loaded under four-point bending until a nonlinear load versus time relation was noted. The specimens were unloaded and reloaded several times, and the interfaces of some specimens were observed after each unloading step. Five identical specimens were tested.

RESULTS AND DISCUSSION

The copper/sapphire interfaces appeared to be homogeneous, well-bonded, and free of any potential reaction products. This is consistent with the work of Heidt and Heimke [24] and Mulder and Klomp [25], which showed that the interdiffusion distance in the copper/sapphire system is negligible and that no additional chemical products are formed, when the interface is created under conditions similar to ours. When viewed via optical microscopy through the sapphire layer, pores were observed on the interface, as shown in Fig. 6; this is not uncommon in metal/ceramic interfaces involving a ductile metal and have been discussed in [26–28] and references therein. We note that the atomistic models for dislocation nucleation we utilize say nothing about the details of the bonding process or conditions at the interface in general, except that the interface be "atomically sharp." Effects relating to the interfacial strength enter the Rice–Thomson model through the parameter G_{cleave}, which we assume to be identical in the two crack growth directions. As an estimate of the order of magnitude of G_{cleave}, we quote the result of 0.475 J/m^2, for the work of adhesion of Cu/Al_2O_3, as measured by Nicholas [29] at a temperature near that of the melting temperature of copper. This value may be interpreted as a lower bound approximate value to the ideal work of fracture $2\gamma_{int}$ for the Cu/sapphire interface at room temperature.

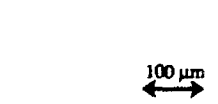

Fig. 6. View through the sapphire layer of the copper/sapphire interface, which shows the presence of pores after the diffusion bonding

After an initial crack was introduced on to the interface, crack growth occurred significantly in all specimens upon further loading in only *one* direction namely, the $[\bar{1}14]_{Cu}$ direction with respect to the copper crystal (see Fig. 7). In one case the effect was particularly dramatic: the crack propagating in the $[\bar{1}14]_{Cu}$ direction ran unstably all the way to the end of the specimen, causing half of the sapphire layer to become entirely detached. Figure 8(a) shows the notched area of the latter specimen after the bend-test; note that there was some crack growth in the ductile direction in this case. No future growth was observed, however, of the crack tips pointed in the $[1\bar{1}4]_{Cu}$ (ductile) direction. The crack fronts were typically rounded as schematically shown in Fig. 9, thus the crack tip pointed in the ductile direction is not visible from the side of most specimens (e.g. Fig. 7). Table 1 gives an estimate of the critical energy release rate for fracture of the brittle crack, as given by the bimaterial Irwin-type expression associated with equation (1) (as given, e.g. in [5]); the values hover in the range of 5–7 J m^{-2}.

Fig. 7. Side view of a copper sapphire specimen after mechanical testing, showing that the crack propagated only in the $[114]_{Al_2O_3}$ (brittle) direction.

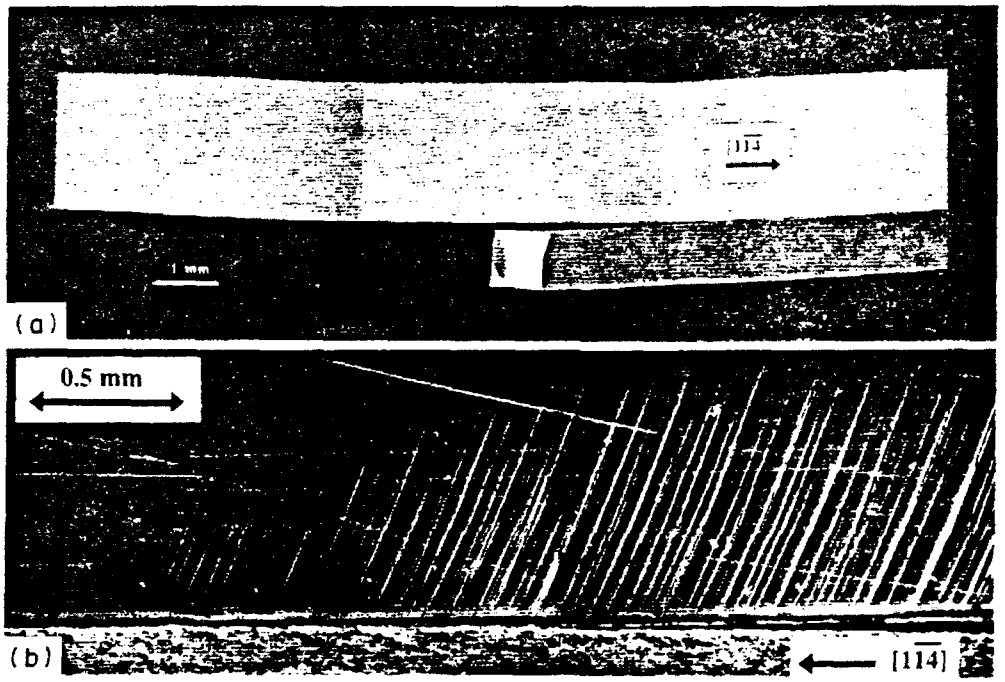

Fig. 8. Side view of a copper sapphire specimen after mechanical testing: (a) shows complete decohesion in the $[114]_{Al_2O_3}$ (brittle) direction accompanied by crack growth in the $[1\bar{1}4]_{Al_2O_3}$ (ductile) direction; and (b) shows the relatively high density of slip lines in the vicinity of the crack which propagated in the ductile direction.

Dense slip lines were present on the $(110)_{Al_2O_3}$ (side) surfaces in the vicinity of the crack tip oriented in the $[11\bar{4}]_{Al_2O_3}$ direction, indicating a large amount of dislocation activity. In contrast, interfacial debonding occurred along the $[\bar{1}14]_{Al_2O_3}$ (brittle) direction; slip lines were much less dense in this region of the specimen, indicating that a debonding process dominated. Figure 8(b) shows the slip traces observed in the vicinity of the ductile crack tip. These lines originally corresponded to the slip planes inclined at 125.3° with the crack plane, which is the predicted slip system (see Figs. 3 and 5), because the specimens were tested until

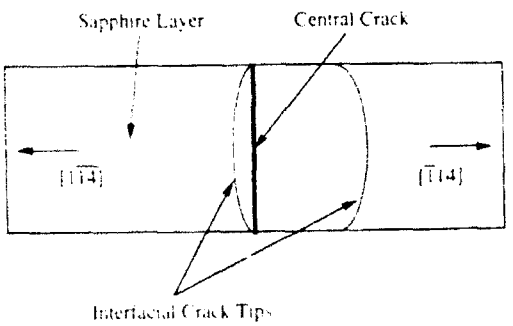

Fig. 9. Schematic showing the typical shape of the crack front as it propagated along the copper ceramic interface.

Table 1. Experimentally obtained values of G_{ss} for copper sapphire

Specimen number	G_{ss} (J/m^2)
1	[illegible]
2	[illegible]
3	[illegible]
4	[illegible]
5	[illegible]

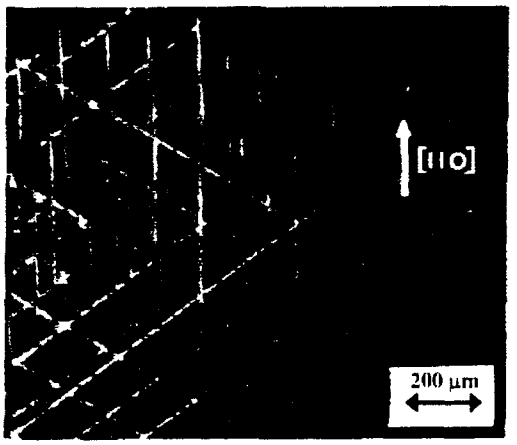

Fig. 10. Slip traces in the vicinity of the crack running the $[1\bar{1}4]_{Cu}$ (ductile) direction, as seen in this view of the interface. Note that slip lines are present for systems which do not intersect the crack front

macroscopic bending set in, these slip planes have been distorted somewhat within the plane, hence they are tilted slightly curved. Slip traces corresponding to the favored plane for dislocation emission from the brittle crack tip, at 164.2°, were not observed; in fact, the only system that appears to have been activated of the slip systems that contain a slip plane coplanar with the crack front is the system which contains a slip plane oriented at 125.3° with respect to the crack running in the $[1\bar{1}4]_{Cu}$ direction. It is evident from Fig. 10, however, that additional slip systems, having {111} type slip planes which are *not* coplanar with the crack front, were active, and provided further means for the accommodation of plastic flow and the dissipation of energy.

The results here have been explained in terms of theories which have only taken into account the emission of a single Shockley partial dislocation for the copper crystal orientation considered. Whereas the second partial dislocation to nucleate possesses a Burgers vector which is perpendicular to the crack front, the first does so at an angle which is 30° from the crack front. The numerical procedures associated with the Peierls-type nucleation model are not yet adequate to deal with the latter case, but a calculation presented in [12] suggests that the relevant values of G_{disl} will increase by a factor of $(4-3\nu) \approx 3$ to nucleate the first partial, thus retaining the factor of 6 difference between nucleation levels for the two cracking directions considered. The emission of partial dislocations within the earlier Rice–Thomson framework has been worked out in considerable detail by Anderson [30].

As alluded to in the experimental section, it was observed that crack growth proceeded initially in a symmetric fashion, i.e. crack growth occurred in both directions for a short time. The crack growing in the predicted ductile direction never grew longer than about 0.5 mm, however. This result can be rationalized by at least one explanation: the elasticity solution of equation (1) for this specimen assumes that the crack length is much longer than the thickness of the thin layer (i.e. the thickness of the sapphire). When the crack is short (i.e. of a comparable length scale to the sapphire thickness or shorter), the phase angle differs as given by an analysis by He and Hutchinson [31]. The local phase of the incipient cracks is less than the steady-state value of −79°, which leads to a condition where the values of G_{tip} at the two crack tips are more similar.

SUMMARY

Predictions of a modified Rice–Thomson model for the ductile versus brittle behaviour of cracks, which takes into account a bimaterial crack-tip field, are in general agreement with experimental observations of beam-type layered specimens consisting of copper bonded on a {221} face to sapphire. The agreement indicates that the different fracture behaviour of these bimaterial interfaces may be understood, at least qualitatively, by comparing the crack tip energy release rate for dislocation emission from the crack tip against that for cleavage decohesion of the boundary. The observations here are also in agreement with an improved method for calculating G_{disl} which takes into account the nonlinear core effects associated with extended dislocations.

Acknowledgements—This research is supported by a University Research Initiative (subcontract POAVB38639-0 from the University of California, Santa Barbara, based on ONR DARPA contract N00014-86-K-0753), and the NSF Materials Research Laboratory at Harvard (grant DMR-89-20490). We are grateful to James R. Rice for helpful discussion, and to H. Cao, A. G. Evans, I. Reimanis, and M. Rühle for their insights during the course of this work. The assistance of Joseph Bell in the laboratory is greatly appreciated.

REFERENCES

1. J. R. Rice and R. Thomson, *Phil. Mag.* **29**, 73 (1974).
2. D. Mason, *Phil. Mag.* **39**, 455 (1979).
3. P. M. Anderson and J. R. Rice, *Scripta metall.* **20**, 1467 (1986).
4. J. R. Rice, in *Chemistry and Physics of Fracture* (edited by R. M. Latanision and R. H. Jones), p. 22. Martinus Nijhoff, Dordrecht (1987).
5. J. R. Rice, Z. Suo and J. S. Wang, in *Metal–Ceramic Interfaces, Acta-Scripta Metallurgica Proc. Ser.* (edited by M. Rühle, A. G. Evans, M. F. Ashby and J. P. Hirth), Vol. 4, pp. 269–294. Pergamon Press, Oxford (1990).
6. J. S. Wang and P. M. Anderson, *Acta metall.* **39**, 779 (1991).
7. P. G. Charalambides, J. Lund, A. G. Evans and R. M. McMeeking, *J. appl. Mech.* **56**, 77 (1989).
8. Z. Suo and J. W. Hutchinson, *Int. J. Fract.* **43**, 1 (1990).
9. Z. Suo, Ph.D. thesis, Harvard Univ., Cambridge, Mass. (1989).
10. A. S. Argon, *Acta metall.* **35**, 185 (1987).
11. G. Schoeck, *Phil. Mag.* **A63**, 111 (1991).
12. J. R. Rice, *J. Mech. Phys. Solids* **40**, 239 (1992).

13. G. E. Beltz and J. R. Rice, in *Modeling the Deformation of Crystalline Solids: Physical Theory, Application, and Experimental Comparisons* (edited by Terry C. Lowe and Anthony Rollett) (1991). In press.
14. G. E. Beltz and J. R. Rice, *Acta metall. mater.*, in press.
15. R. E. Peierls, *Proc. Phys. Soc.* **52**, 23 (1940).
16. F. R. N. Nabarro, *Proc. Phys. Soc.* **59**, 59 (1947).
17. K. Cheung, Ph.D. thesis, M.I.T., Cambridge, Mass. (1990).
18. Y. Sun, J. R. Rice and L. Truskinovsky, in *High-Temperature Ordered Intermetallic Alloys* (Edited by L. A. Johnson, D. T. Pope and J. O. Stiegler), Vol. 213. MRS, Pittsburgh, Pa (1991).
19. M. Yamaguchi, V. Vitek and D. P. Pope, *Phil. Mag.* **43**, 1027 (1981).
20. Y. Sun, G. E. Beltz and J. R. Rice, manuscript in preparation.
21. J. R. Rice, *J. appl. Mech.* **35**, 379 (1968).
22. K. Cheung, A. S. Argon and S. Yip, *J. appl. Phys.* **69**, 2088 (1991).
23. J. Ferrante and J. R. Smith, *Phys. Rev. B* **31**, 3427 (1985).
24. G. Heidt and G. Heimke, *J. Mater. Sci.* **10**, 887 (1975).
25. C. A. M. Mulder and J. T. Klomp, *J. Physique* **46**, 111 (1985).
26. M. Ruhle and A. G. Evans, *Mater. Sci. Engng* **A107**, 187 (1989).
27. B. Derby and E. R. Wallach, *J. Mater. Sci.* **19**, 3140 (1984).
28. B. Derby, in *Metal Ceramic Interfaces, Acta-Scripta Metallurgica Proc. Ser.* (edited by M. Ruhle, A. G. Evans, M. F. Ashby and J. P. Hirth), Vol. 4, p. 161. Pergamon Press, Oxford (1990).
29. M. Nicholas, *J. Mater. Sci.* **3**, 571 (1968).
30. P. M. Anderson, Ph.D. thesis, Harvard Univ., Cambridge, Mass. (1986).
31. M.-Y. He and J. W. Hutchinson, *Int. J. Solids Struct.* **25**, 1053 (1989).

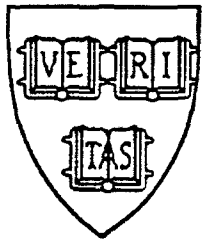

MECH-196

STEADY-STATE MATRIX CRACKING OF CERAMICS REINFORCED BY ALIGNED FIBERS AND TRANSFORMING PARTICLES

Yingqing Lawrence Cui and Bernard Budiansky

Division of Applied Sciences
HARVARD UNIVERSITY
Cambridge, Massachusetts 02138

July 1992

STEADY-STATE MATRIX CRACKING OF CERAMICS REINFORCED BY ALIGNED FIBERS AND TRANSFORMING PARTICLES

Yingqing Lawrence Cui and Bernard Budiansky
Division of Applied Sciences
Harvard University
Cambridge, MA 02138

ABSTRACT

Matrix fracture in ceramic composites is analysed for ceramics which are reinforced by both dilatantly transforming particles and fibers which are aligned in the direction perpendicular to the crack surfaces. Numerical results for the matrix cracking strength are given in terms of parameters associated with the individual reinforcing mechanisms, and coupling parameters that characterize their interaction. An energy balance relation governing the steady state matrix cracking is presented. The results suggest that transforming particles could increase the matrix cracking strength of aligned-fiber composites by up to about a factor of two.

INTRODUCTION

Multiple matrix cracking is a distinctive tensile damage mechanism that is often observed in brittle ceramics that are reinforced by unidirectionally aligned fibers. It plays a vital role in the performance of these materials. Tension applied to the composite in the direction of the fibers induces closely spaced matrix cracks normal to the fibers, and each crack completely traverses the material, but the applied load continues to be supported by unbroken fibers that bridge each matrix crack between its faces. The tensile stress required for the steady-state propagation of a single matrix crack, known as the *matrix cracking stress* , has been recognized as an important characterizing parameter of brittle-matrix fiber composites. The matrix cracking stress was first evaluated in the work of Aveston et al. (1971) for the limits of large and small frictional shear stresses at the fiber-matrix interfaces, and more recently by Budiansky et al. (1986) for intermediate shear values, via energy methods.

Brittle ceramics can also be reinforced by phase-transforming particles. It was discovered by Garvie et al (1975) that the apparent fracture toughness of ceramics may be increased by the introduction of tetragonal zirconia (ZrO_2) reinforcing particles. Experimental observations reveal that a tetragonal-to-monoclinic martensitic phase transformation takes place in the zirconia particles near a crack tip, and a permanently transformed region is left behind the edge of a growing crack. The *transformation toughening* of materials with very long initial cracks has

been studied theoretically (e.g. McMeeking and Evans, 1982; Budiansky et al 1983; Rose, 1986: Amazigo and Budiansky, 1988), and the transient growth of cracks in the presence of phase transformation has been analyzed by Stump and Budiansky (1989ab).

The aim of the present work is to see how phase transforming particles would affect the steady-state matrix cracking stress. The basic problem analyzed is illustrated in Fig. 1. A semi-infinite plane-strain matrix crack, driven by a uniform remote tension, is bridged by intact fibers and surrounded by a zone of transformed material. The main body of the paper begins with a concise review of the related results for each individual reinforcement, and then a novel analytical formulation of the governing non-linear integral equations of the problem is presented in terms of distributed dislocations and dilatations. An energy balance relation for the steady-state cracking is also presented and a numerical solution of the problem is obtained and discussed. The details of the numerical solution procedure, and the derivation of the energy relation, are presented in Appendices.

MATRIX CRACKING IN FIBER REINFORCED CERAMICS

Matrix cracking in unidirectionally reinforced ceramic composite is subject to resistance due to the effects of bridging fibers. For the limiting case of large scale matrix cracking with all fibers intact behind the crack tip, i.e. steady state matrix cracking, the critical tensile stress needed to keep the crack extending becomes independent of crack length. The studies by Aveston et al. (1971) and by Budiansky et al. (1986) contain the following result for the steady state matrix cracking stress σ_f^c. Under the assumptions that there is extensive interface slip between the matrix and bridging fibers and that there are no initial stresses, σ_f^c is given by

$$\sigma_f^c = \left[\frac{6c_f^2\left(1-\nu_m^2\right)K_m^2\tau E_f}{(1-c_f)RE}\right]^{\frac{1}{3}}\frac{E}{E_m} \tag{1}$$

where c_f is the volume concentration of fibers, R is the fiber radius, τ is the interface slipping shear resistance stress, and K_m is the critical Mode-I matrix stress intensity factor. The Young's moduli E, E_f and E_m are those of the composite, fiber, and matrix, respectively. A recent experimental study (Cao et al., 1990) reveals that Equation (1) correlates well with measured results for several materials.

TRANSFORMATION TOUGHENING

Transformation toughening, which results from the phase transformation of transforming particles (notably ZrO_2) that are embedded in a nontransforming ceramic matrix, was discovered by Garvie et al. (1975). The unconstrained, "stress-free" strain associated with such a phase transformation (i.e., the strain that would occur in the absence of surrounding material) consists of

a dilatation of about 4% and a shear strain of about 16%. Transformation toughening phenomena have usually been studied on the basis of a "supercritical" transformation model (see Budiansky et al 1983 for details) in which the transformation occurs completely within each particle when the mean stress $\sigma_m = \sigma_{kk}/3$ reaches the critical value σ_m^c. With the simplifying assumption of identical elastic moduli of particles and matrix, the composite may be modeled as an elastic continuum within which the stress-free transformation dilatation, where it occurs, has magnitude $c_t\theta^T$, where c_t is the volume concentration of transforming particles and θ^T is the stress-free particle dilatation. With some exceptions (e.g., Lambropoulos 1986; Sun et al 1991; Stump 1991), the effects of shear stress on triggering the transformation have usually not been considered, and the possible toughening effects of transformation shear strains have also generally been disregarded.

Growth of long cracks under a constant applied far-field K_T has been studied under these assumptions by McMeeking and Evans (1982) and Budiansky et al. (1983). In this work, the crack was assumed to be growing in a steady-state fashion, with cracking of the matrix at the crack tip at the critical matrix stress-intensity-factor K_m. A key transformation-toughening parameter that emerges from these studies is

$$\omega = \frac{1+\nu}{1-\nu}\frac{Ec_t\theta^T}{\sigma_m^c} \tag{2}$$

and results for the steady-state toughening ratio $\lambda_T = K_T/K_m$ were found for a limited range of ω. Amazigo and Budiansky (1988) extended this work and provided a complete solution for λ_T. The results shown in Fig. 2, a plot of $(\lambda_T)^{-1}$ versus the toughening parameter ω, confirmed the occurrence of "lock up" at $\omega=\omega_c \approx 30$, first predicted by Rose (1986). More recently, Stump and Budiansky (1989a) studied the transient growth of long cracks in ceramics. It was discovered that K/K_m reaches a peak value λ_T^{max} which exceeds the steady-state level λ_T at finite amounts of crack growth. The full results for $\left(\lambda_T^{max}\right)^{-1}$ as a function of the parameter ω are given by the lower curve of Fig. 2. It was found that the "lock-up" of the growing cracks occurs for the value $\omega \approx 20.2$. Stump and Budiansky (1989b) also studied the transient growth of finite cracks.

STEADY-STATE MATRIX CRACKING FOR COMBINED REINFORCEMENT

We now study the steady-state crack propagation of a fully bridged semi-infinite matrix crack in a ceramic reinforced by both aligned fibers and transforming particles. The supercritical transformation model introduced previously is used exclusively throughout this study. It is also assumed, for the sake of simplicity, that the fibers, transforming particles , and matrix all have the same Young's modulus E and Poisson's ratio ν, so that the composite is isotropic, and we continue to neglect initial stresses. It is further assumed that the critical shear resistance τ is not

affected by the presence of transforming particles. The critical matrix cracking stress σ_f^c of a ceramic reinforced only by aligned fibers and the steady-state toughening ratio λ_T of a ceramic reinforced only by transforming particles, which have been introduced in the previous sections, are considered to be known parameters, and a natural coupling parameter

$$s = (1+\nu)\sigma_f^c \Big/ \left[3\sigma_m^c\right] \tag{3}$$

which emerges from the analysis, is employed.

As the crack advances under steady-state conditions, "fresh" material undergoes phase transformation as it is crossed by a curve C in the vicinity of the crack tip (see Fig. 3), while previously transformed material remains in the wake of the tip, and new intact fibers bridge the crack faces. The coordinates of the leading portion of the steady-state transformation boundary, as shown in Fig. 3, are given by

$$z_0(\alpha) = x_0(\alpha) + iy_0(\alpha) = r_0(\alpha)[\cos\alpha + i\sin\alpha] \qquad (0 \le \alpha \le \hat{\alpha}) \tag{4}$$

where $\hat{\alpha}$ is the polar angle at which the phase boundary C makes a tangential connection to the horizontal wake boundary.

During the course of steady crack propagation the following conditions must be maintained:

(i) the mean stress must be equal to the critical transformation stress along the *exterior* of the leading edge of the transformed region, i.e.

$$\sigma_m(z) = \sigma_m^c \qquad \text{for } z \text{ on } C \tag{5}$$

(ii) the stress intensity factor at the crack tip should equal the critical value needed to propagate the crack, i.e.

$$K_{tip} = K_m\sqrt{1-c_f} \tag{6}$$

where the factor $\sqrt{1-c_f}$ comes from the fact that the critical crack-tip energy release rate in our problem has to be modified by the factor $(1-c_f)$ in order to simulate the reduction in the crack area associated with the presence of fibers.

(iii) the crack-face tensions are

$$\sigma_y(x,0) = p(x) \quad \text{for } -\infty \le x \le 0 \tag{7}$$

where p(x) is the smeared-out stress on the crack faces induced by bridging fibers, and p(x) must be connected appropriately to the crack-face displacements. Budiansky and Amazigo (1989) modeled the effects of bridging fibers by continuously distributed non-linear springs via an energy argument. Under the assumption that the fibers undergo large amounts of slipping inside the matrix, they provided a non-linear relation between the stress due to the bridging springs and crack opening displacement which governs the constitutive behaviour of the springs bridging the crack surfaces as follows:

$$p(x) = \beta\sqrt{v(x)} \tag{8}$$

where the spring constant β is

$$\beta = \left\{ \frac{4c_f^2 E_f E^2 \tau}{R(1-c_f)^2 (E_m)^2} \right\}^{\frac{1}{2}} \tag{9}$$

Under the present simplifying assumption $E_f = E_m = E$, Eq. (9) simplifies to

$$\beta = \left\{ \frac{4c_f^2 E \tau}{R(1-c_f)^2} \right\}^{\frac{1}{2}} \tag{10}$$

Now we proceed to satisfy the conditions (5),(6), and (8) by superposing three states of plane-strain elasticity produced as follows:

(a) apply the remote plane strain loading $\sigma_y = \sigma_{ft}^c$, $\sigma_z = \nu\sigma_{ft}^c$, where σ_{ft}^c is the critical matrix cracking stress in the presence of both fibers and transforming particles.

(b) subject the negative x-axis to the vertical displacement discontinuity gradient

$$\frac{\partial v(x,0^+)}{\partial x} - \frac{\partial v(x,0^-)}{\partial x} \equiv -\delta(x) \quad \text{for} -\infty \le x \le 0 \tag{11}$$

(c) impose the plane-strain transformation $\varepsilon_{\alpha\alpha}^T$ in the horizontal strip S (see Fig. 3), bounded on the right by the curve C. In plane strain, the connection between the *area* dilatation $\varepsilon_{\alpha\alpha}^T$ and the volumetric dilatation $c_t\theta^T$ is (Budiansky et al., 1983)

$$\varepsilon_{\alpha\alpha}^T = \frac{2}{3}(1+\nu)c_t\theta^T \tag{12}$$

For each problem, we shall calculate the mean-stress

$$\sigma_m = \tfrac{1}{3}\sigma_{kk} = \tfrac{1}{3}(1+\nu)(\sigma_x + \sigma_y) \tag{13}$$

and the crack-face tension $\sigma_y(x,0)$ for $x < 0$.

The trivial solution of problem (a) produces the mean stress

$$\sigma_m = \tfrac{1}{3}(1+\nu)\sigma_{ft}^c \tag{14}$$

everywhere, and gives the uniform crack-face stress

$$\sigma_y(x,0) = \sigma_{ft}^c \tag{15}$$

The solution of problem (b) can be written on the basis of the fundamental plane-strain solution for a single edge dislocation. Note that over the interval dx' the gradient jumps in Eq. (11) are equivalent to the vertical dislocation $-\delta(x')dx'$, which is equal to $2\frac{dv(x')}{dx'}dx'$ by symmetry. It follows that the normal stresses due to the dislocations in $(-\infty, 0)$ are

$$\sigma_y(x,y) = -D\int_{-\infty}^{0} \frac{(x-x')\left[3y^2 + (x-x')^2\right]}{\left[(x-x')^2 + y^2\right]^2} \frac{dv(x')}{dx'} dx' \tag{16}$$

$$\sigma_x(x,y) = D\int_{-\infty}^{0} \frac{(x-x')\left[y^2-(x-x')^2\right]}{\left[(x-x')^2+y^2\right]^2}\frac{dv(x')}{dx'}dx' \tag{17}$$

where
$$D = \frac{E}{2\pi(1-\nu^2)} \tag{18}$$

Accordingly, the mean stress (13) produced by the dislocations is

$$\frac{\sigma_{kk}(x,y)}{3} = -\frac{2D(1+\nu)}{3}\int_{-\infty}^{0} \frac{x-x'}{(x-x')^2+y^2}\frac{dv(x')}{dx'}dx' \tag{19}$$

and the crack-face tension produced by the dislocations is

$$\sigma_y(x,0) = -D\int_{-\infty}^{0} \frac{1}{x-x'}\frac{dv(x')}{dx'}dx' \qquad (-\infty < x < 0) \tag{20}$$

Problem (c) is readily handled by complex stress-potential methods (Muskhelishvili, 1963). We present only the final results for the potentials ϕ and ψ, in terms of which the stresses are given by

$$\sigma_x + \sigma_y = 2\left(\phi' + \overline{\phi'}\right) \tag{21}$$

$$\sigma_y - \sigma_x + 2i\tau_{xy} = 2\left(\bar{z}\phi'' + \psi'\right) \tag{22}$$

Let an arbitrary 2D region A with boundary Γ in an isotropically elastic body undergo a uniform volumetric strain $\varepsilon^T_{\alpha\alpha}$; then, for z=x+iy *outside* A,

$$\phi = \frac{iE\varepsilon^T_{\alpha\alpha}}{16\pi(1-2\nu)(1-\nu^2)}\oint_\Gamma \log(z-z_0)dz_0 \tag{23}$$

$$\psi = \frac{(3-4\nu)iE\varepsilon^T_{\alpha\alpha}}{16\pi(1-2\nu)(1-\nu^2)}\oint_\Gamma \log(z-z_0)d\bar{z}_0 - \frac{iE\varepsilon^T_{\alpha\alpha}}{16\pi(1-2\nu)(1-\nu^2)}\oint_\Gamma \frac{\bar{z}_0}{z-z_0}dz_0 \tag{24}$$

For z *inside* A, the extra term

$$-\frac{E\varepsilon^T_{\alpha\alpha}}{4(1-2\nu)(1+\nu)}z \tag{23}$$

must be added to ϕ in order to preserve the validity of the relation (19).

For z outside A

$$\phi'(z) = \frac{iE\varepsilon^T_{\alpha\alpha}}{16\pi(1-2\nu)(1-\nu^2)}\oint_\Gamma \frac{dz_0}{z-z_0} = 0 \tag{24}$$

which gives

$$\sigma_m = \frac{1}{3}(1+\nu)\left(\sigma_{xx}+\sigma_{yy}\right) = 0 \tag{25}$$

For the transformed region S of Fig. 3, the crack-face stress produced by the phase transformation

reduces to

$$\sigma_{yy}(x,0)=\frac{E\varepsilon_{aa}^{T}}{4\pi(1-\nu^2)}\mathrm{Re}\int_C\frac{dy_0}{x-z_0}\quad\text{for}\quad -\infty\le x\le 0 \tag{26}$$

where the integration along C proceeds from y_0=-H_T to y_0=+H_T.

Adding the contributions (14) and (19) gives the mean stress at points *outside* the transformed region, and then imposing the condition (5) on this mean stress requires that

$$\frac{(1+\nu)}{3}\sigma_{ft}^{c}-\frac{2D(1+\nu)}{3}\int_{-\infty}^{0}\frac{x_0-x'}{(x_0-x')^2+y_0^2}\frac{dv(x')}{dx'}dx'=\sigma_m^c\quad\text{for }(x_0,y_0)\text{ on C} \tag{27}$$

The sum of (15), (20), and (26) gives the crack-face stress p(x) to be substituted into the condition (8), which becomes

$$\sigma_{ft}^{c}-D\int_{-\infty}^{0}\frac{1}{x-x'}\frac{dv(x')}{dx'}dx'+\frac{Ec_t\theta^T}{6\pi(1-\nu)}\mathrm{Re}\int_C\frac{dy_0}{x-z_0}=\beta\sqrt{v(x)}\quad\text{for}-\infty\le x\le 0 \tag{28}$$

Finally, the crack-tip requirement (6) may be prescribed as

$$\lim_{x\to 0}\frac{E\sqrt{2\pi}}{4(1-\nu^2)}\frac{v(x)}{\sqrt{-x}}=K_m\sqrt{1-c_f} \tag{29}$$

The steady-state matrix cracking problem under combined reinforcement is governed by Eqs. (27-29), which may be nondimensionalized by introducing the reference length

$$L=D\sigma_f^c/\beta^2, \tag{30}$$

letting

$$\xi+i\eta=\rho(\cos\alpha+i\sin\alpha)=(x+iy)/L, \tag{31}$$

and writing

$$g=\left(\frac{\beta}{\sigma_f^c}\right)^2 v \tag{32}$$

$$\Sigma=\frac{\sigma_{fl}^c}{\sigma_f^c} \tag{32}$$

The resulting equations may be written as

$$\Sigma-2\int_{-\infty}^{0}\frac{\xi_0-\xi}{(\xi_0-\xi)^2+\eta_0^2}\frac{dg(\xi)}{d\xi}d\xi=\frac{1}{s} \tag{33}$$

$$\Sigma-\int_{-\infty}^{0}\frac{1}{\xi-\xi'}\frac{dg(\xi')}{d\xi'}d\xi'-\sqrt{g(\xi)}=\frac{\omega}{18\pi s}\int_C\frac{(\xi_0-\xi)d\eta_0}{(\xi_0-\xi)^2+\eta_0^2}\quad\text{for}\quad -\infty\le\xi\le 0 \tag{34}$$

$$\lim_{\xi \to 0} \frac{\sqrt{3}\pi}{2\sqrt{2}} \frac{g(\xi)}{\sqrt{-\xi}} = 1 \tag{35}$$

Here $\xi_0(\alpha)=\rho_0(\alpha)\cos\alpha$ and $\eta_0(\alpha)=\rho_0(\alpha)\sin\alpha$ define the shape of the leading phase boundary C; ω is the transformation-toughening parameter given by Eq. (2); and s is the coupling parameter defined in Eq. (3). Eqs. (33-35) constitute two integral equations and one scalar constraint for the unknowns functions $g(\xi)$, $\rho_0(\alpha)$, and the scalar *strengthening ratio* Σ, the combined-reinforcement cracking strength normalized by the cracking strength in the absence of transforming particles.

The numerical procedure used to solve these equations is described in Appendix A. Before presenting the solutions, however, we exhibit another scalar, energy-based relation, derived in Appendix B:

$$\Sigma^3 = 1 + \frac{\omega(1 - s\Sigma)\eta_0(\hat{\alpha})}{6\pi s^2} \tag{36}$$

where (see Fig. 3) $\eta_0(\hat{\alpha})$ is the non-dimensional height H_T/L of the transformed wake along each crack face. This relation provides a check on the numerical solution of the governing equations, but in addition it provides important restrictions on the values of the strengthening ratio Σ and the coupling parameter s. Note that for $\Sigma > 1$, (36) implies

$$\Sigma < 1/s \tag{37}$$

which therefore requires $s<1$. In other words, the steady-state matrix cracking stress can be increased by the addition of transforming particles only if

$$\sigma_f^c < \frac{1+\nu}{3}\sigma_m^c \tag{38}$$

and (37) says that the increased cracking stress σ_{ft}^c is also bounded by the right-hand side of (38). These inequalities are consistent with the fact that an applied stress equal to or greater than the upper bound would transform the entire space, and only if the phase-transformation dilatations are constrained by surrounding untransformed material will they reduce the crack-tip stress intensity.

The calculations described in Appendix A led to the curves shown in Fig. 4 for Σ vs. ω for various values of the coupling parameter s. The dotted lines show the bounds of Eq. (37). The calculations were terminated slightly below these bounds, because, consistent with the energy relation (36), it was found numerically that the size of the transformed region became very large as these bounds were approached, and accurate calculations became increasingly tedious. Curiously, the results for Σ become multiple-valued for Σ near 1/s; we suspect that only the lower branches may be physically significant. Furthermore, it is likely that values of ω greater than 30 -- the "lock-up" value for transformation toughening of long cracks--are not meaningful. For a given value of ω, the enhanced matrix cracking stress increases for decreasing values of s, but is fairly insensitive to s for $\omega<20$.

On the basis of the connection between the transformation-toughening ratio λ_T and ω (Fig. 2), results for Σ are also shown in Fig. 5 for Σ vs. λ_T. Up to what is probably the practical limit of λ_T=5, the results for Σ remain single-valued, and they suggest that the matrix cracking stress is susceptible to improvement via transformation toughening by only factors of about two or less.

The results can also be exhibited in terms of an alternative interaction parameter defined by $t = \omega / (3s)$, or

$$t = \frac{c_t \theta^T}{(1-\nu)\varepsilon_f^c} \tag{39}$$

where $\varepsilon_f^c \equiv \sigma_f^c / E$ is the critical matrix cracking strain in the absence of transforming particles.* Figs. 6 and 7, analogous to Figs. 4 and 5, show the matrix-cracking strength ratio for various values of t. In Fig. 6, the hyperbolic curve segments given by $\Sigma = 3t/\omega$ for each value of t correspond to the bound (37).

For a given ceramic composite system, the coupling parameter t can be more readily estimated than s. The measurements by Cao et al. (1990) of the cracking strains of several glass-ceramic/Nicalon- fiber composites indicate, for example, that in such systems, with $c_f = c_t = .3$, and $\theta^T = .04$, values of t in the range 10-15 would be appropriate.

An interesting question arises about the interpretation of the results in Fig. 7 if, for a given value of the coupling parameter t, the known value of λ_T lies beyond the end of the appropriate curve (e.g., t=10, λ_T=4). Presumably, the transformed region will have already become very large during the approach to steady state, the nearly unconstrained dilatations would no longer have a strengthening effect, and we would have Σ=1 *at* steady state cracking. But the peak stress during the transient stage of growth of an initially long matrix crack would attain a value close to the top of the curve. Similar remarks apply to the terminating curves in Figs. 4 and 6.

CONCLUDING REMARKS

The possibility of improving the matrix cracking resistance of aligned-fiber ceramic composites by the incorporation of phase-transforming particles has been demonstrated on the basis of simple models for the individual reinforcement mechanisms and their interaction. An energy balance equation for steady-state matrix cracking has been derived and the restrictions it imposes on matrix cracking in ceramic composites with combined reinforcement have been established. In particular, an upper bound was identified for the increase in the steady-state matrix cracking resistance provided by transforming particles. Numerical results for the matrix cracking

---

* This classical critical strain (Aveston et al 1971) is based on the assumption of pure tension at infinity, whereas, to simplify the formulation of the combined problem (for which plane strain near the crack tip is appropriately assumed) we postulated plane strain everywhere; the inconsistency is not important.

strength have been given in terms of parameters associated with the individual reinforcing mechanisms, and coupling parameters that characterize their interaction. These results suggest that transforming particles could increase the matrix cracking strength of aligned-fiber composites by up to about factor of two.

A companion study by Cui (1992) showed that transforming particles and aligned fibers could interact synergistically to increase the effective fracture toughness of a brittle ceramic containing a long, initially unbridged crack. The present demonstration that phase transformation can also increase the matrix cracking strength of fully bridged cracks provides an interesting contrast with the effects of fiber-matrix interface friction. Increasing the frictional resistance raises the matrix cracking strength, but lowers the small-scale bridging toughness; transforming particles increase both.

ACKNOWLEDGEMENT

This work was partially supported by the DARPA University Research Initiative (Subagreement P.O. # VB38639-0 with the University of California, Santa Barbara, ONR Prime Contract N00014-86-K-0753), the Office of Naval Research (Contract N00014-90-J-1377), and by the Division of Applied Sciences, Harvard University.

REFERENCES

Amazigo, J.C. and Budiansky, B (1988). "Interaction of particulate and transformation toughening", J. Mech Phys Solids **34**, pp 581-595

Amazigo, J.C. and Budiansky, B (1988). "Steady-state crack growth in supercritically transforming materials", Int. J. of Solids and Structures **24**, pp 751-755.

Aveston, J., Cooper, G.A. and Kelly, A. (1971) "The properties of fiber composites", pp . 15-26. Conference proceedings, National Physical Laboratory, Guildford. IPC Science and Technology Press Ltd.

Budiansky, B. and Amazigo, J.C. (1989). "Toughening by aligned, frictionally constrained fibers", J. Mech. Phys. Solids **37**, pp 93-109.

Cui, Y.L. (1992). "Interaction of fiber and transformation toughening", J. Mech. Phys. Solids, *in press*.

Budiansky, B., Hutchinson, J.W. and Lambropoulos, J.C. (1983)."Continuum theory of dilatant transformation toughening materials", Int. J. Solids Struc. **19**, pp 337-356.

Budiansky, B., Hutchinson, J.W. and Evans, A.G. (1986). "Matrix fracture in fiber-reinforced ceramics", J.Mech Phys Solids **34**, pp 167-189.

Cao, H.C., Bischoff, E., Sbaizero, O., Ruhle, M. and Evans, A.G. (1990). "Effect of interfaces on the properties of fiber-reinforced ceramics", J. Am. Ceram. Soc. **73**, pp 1691-1699.

Erdogan, F., and Gupta, G.D. (1972). "On the numerical solution of singular integral equations", Quart. Appl. Math. **29**, 525-534.

Evans, A.G. and Cannon, R.M. (1986). "Toughening of brittle solids by martensitic transformations", Acta. Met. **34**, pp 761-800.

Evans, A.G. and McMeeking, R.M. (1986). "On toughening of ceramics by strong reinforcements", Acta. Met. **34**, pp 2435-2440.

Garvie, R. C., Hannink, R.H. and Pascoe, R.T. (1975). "Ceramic steel", Nature **258**, pp 695-708.

Lambropoulos, J. C. (1986), "Shear, shape and orientation effects in transformation toughening", Int. J. Solids Struct. 22, pp 1083-1106.

Marshall, D.B., Cox, B.N. and Evans, A.G. (1985). "The mechanics of matrix cracking in brittle-matrix fiber composite", Acta. Met. **33**, pp 2013-2021.

McMeeking, R.M. and Evans, A.G. (1982). "Mechanics of transformation toughening in brittle materials", J. Am. Ceram. Soc. **65**, 242-246.

Rose, L.R.F. (1986). "The size of the transformed zone during steady-state cracking in transformation toughened materials", J. Mech. Phys. Solids **34**, pp 609-616

Sun, Q. P., Hwang, K.C. and Yu, S.W. (1991). " A micromechanics constitutive model of transformation plasticity with shear and dilatation effect ", J. Mech. Phys. Solids **39**, pp 507-524.

Stump, D.M. (1991). "The role of shear stresses and shear strains in transformation-toughening", Phil. Mag. A **64**, pp 879-902.

Stump, D.M. and Budiansky, B. (1989a). "Crack growth resistance in transformation toughened ceramics", Int. J. Solids Structure **25**, pp 635-646.

Stump, D.M. and Budiansky, B. (1989b). "Finite cracks in transformation-toughened ceramics", Acta. Met. **37**, pp 3297-3304.

APPENDIX A

NUMERICAL ANALYSIS

This Appendix describes the procedure used to solve Eqs. (33-35) for $g(\xi)$, $\rho_0(\alpha)$, and Σ. Let

$$\frac{dg(\xi)}{d\xi} = h(\xi) \tag{A1}$$

and introduce the coordinate transformation

$$\xi = \frac{w-1}{w+1} \qquad (-1 < w \le 1) \tag{A2}$$

The substitution

$$h\left(\frac{w-1}{w+1}\right) = \frac{(1+w)^2}{\sqrt{1-w^2}} f(w), \tag{A3}$$

will turn out to be useful. Eqs. (33-35) become

$$\Sigma - 4\int_{-1}^{1} \frac{\xi_0(1+w)+1-w}{\left\{[\xi_0(1+w)+1-w]^2+\eta_0{}^2(1+w)^2\right\}} \frac{(1+w)}{\sqrt{1-w^2}} f(w)\,dw = \frac{1}{s} \tag{A4}$$

$$\Sigma - (1+w)\int_{-1}^{1} \frac{1+w'}{w-w'} \frac{f(w')}{\sqrt{1-w'^2}}\,dw' - \sqrt{2\int_{-1}^{w} \frac{f(w')}{\sqrt{1-w'^2}}\,dw'}$$

$$= \frac{\omega(1+w)}{9\pi s}\int_{0}^{\hat{\alpha}} \frac{(1+w)\rho_0(\alpha)\cos\alpha+1-w}{[(1+w)\rho_0(\alpha)\cos\alpha+1-w]^2+[(1+w)\rho_0(\alpha)\sin\alpha]^2} \frac{d[\rho_0(\alpha)\sin\alpha]}{d\alpha}\,d\alpha \tag{A5}$$

$$-\pi\sqrt{6}\,f(w) = 1 \tag{A6}$$

Now write the finite-series approximations

$$\eta_0(\alpha) = \rho_0(\alpha)\sin(\alpha) = \sum_{n=1}^{N} a_n \sin\left[\frac{(2n-1)\pi}{2\hat{\alpha}}\alpha\right] \qquad 0 \le \alpha \le \hat{\alpha} \tag{A7}$$

and

$$f(w) = \sum_{k=1}^{M} b_k\, T_{k-1}(w) = \sum_{k=1}^{M} b_k \cos\left[(k-1)\cos^{-1} w\right] \tag{A8}$$

where $T_k(w)$ is the Chebyshev polynomial of the first kind of degree k. For given values of ω and s,the M+N coefficients a_n and b_k, together with the additional two unknowns Σ and $\hat{\alpha}$, were determined by collocation of Eqs. (A4) and (A5) at the M points

$$w_r = \cos\left(\frac{\pi r}{M+1}\right) \qquad (r = 1,2,\ldots M) \tag{A9}$$

and the N+1 points

$$\alpha_j = \frac{j\hat{\alpha}}{N} \qquad (j = 0,1,\ldots N) \tag{A10}$$

respectively, and enforcement of Eq. (A6). The definite integrals with respect to w in (A4) and (A5) were evaluated by means of the general Cauchy-Chebyshev formula (Erdogan and Gupta 1972)

$$\int_{-1}^{1} \frac{F(w)dw}{(w_r - w)\sqrt{1-w^2}} = \frac{\pi}{N+1}\sum_{p=1}^{M+1} \frac{F(w_p)}{w_r - w_p} \qquad (r = 1,2,\ldots M) \tag{A11}$$

and the standard Gaussian integration formula

$$\int_{-1}^{1}\frac{F(w)dw}{\sqrt{1-w^2}}=\frac{\pi}{M+1}\sum_{p=1}^{M+1}F(w_p) \tag{A12}$$

where

$$w_p=\cos\left[\frac{(2p-1)\pi}{2(M+1)}\right] \qquad (p=1,2,\ldots,M+1) \tag{A13}$$

The indefinite integral in (A5) is

$$\int_{-1}^{w}\frac{f(w')}{\sqrt{1-w'^2}}dw'=-b_1\cos^{-1}w-\sum_{k=2}^{M}\frac{b_k\sqrt{1-T_{k-1}^2(w)}}{k-1} \tag{A14}$$

Gaussian quadrature was used to evaluate the integrals with respect to α.

A Newton-Raphson iterative scheme was used to find solutions for the a_n's, b_k's, Σ, and $\hat{\alpha}$, with convergence specified by a relative change of less than .01% in the values of each of the unknowns in successive iterations. Solutions for Σ based on M=15 and N=5 were judged to be reasonably accurate, because they never differed by more than .15% from the values of Σ given by the energy relation (36), when the values of $\eta_0(\hat{\alpha})$ found from the numerical solutions were substituted therein.

APPENDIX B

We will write an energy equation associated with a unit advance of the semi-infinite, plane-strain crack in Fig. 3 during its steady-state propagation under the remote loading σ_{ft}^c. It will be assumed that the phase transformation is *critical*, but the results also hold for supercritical transformations (Budiansky et al 1983, denoted by BHL henceforth).

The equation is

$$(1-c_t)\mathcal{G}_m+\left[\sigma_m^c c_t\theta^T-\frac{E(c_t\theta^T)^2}{9(1-\nu)}\right]+\left[\pi_D-\pi_U\right]=0 \tag{B1}$$

where the first term, with $\mathcal{G}_m=K_m^2(1-\nu^2)/E$, is the energy released into the crack tip, and the first bracketed term, derived in BHL, represents the energy dissipated into the irreversible phase transformation. These two energy losses are balanced by the last bracketed term, which represents the difference between the potential energies of vertical strips of unit width far upstream (U) and downstream (D) of the crack tip. In our spring model, the upstream and downstream stresses σ_{ij}^U and σ_{ij}^D differ only in $|y|<H_T$, where the corresponding uniform strains are

$$\varepsilon_{ij}^U=\frac{1}{E}\left[(1+\nu)\sigma_{ij}^U-\nu\sigma_{kk}^U\delta_{ij}\right] \tag{B2}$$

and

$$\varepsilon_{ij}^D=\frac{1}{E}\left[(1+\nu)\sigma_{ij}^D-\nu\sigma_{kk}^D\delta_{ij}\right]+\tfrac{1}{3}c_t\theta^T\delta_{ij} \tag{B3}$$

with the usual (1,2,3) and (x,y,z) correspondence. The plane-strain conditions $\varepsilon_z^U = \varepsilon_z^D = 0$ give

$$\varepsilon_{\alpha\beta}^U = \frac{(1+\nu)}{E}\left[\sigma_{\alpha\beta}^U - \nu\sigma_{\gamma\gamma}^U\delta_{\alpha\beta}\right], \quad \sigma_z^U = \nu\sigma_{\gamma\gamma}^U \tag{B4}$$

$$\varepsilon_{\alpha\beta}^D = \frac{(1+\nu)}{E}\left[\sigma_{\alpha\beta}^D - \nu\sigma_{\gamma\gamma}^D\delta_{\alpha\beta}\right] + \tfrac{1}{3}(1+\nu)c_t\theta^T\delta_{\alpha\beta}, \quad \sigma_z^D = \nu\sigma_{\gamma\gamma}^D - \tfrac{1}{3}Ec_t\theta^T \tag{B5}$$

for Greek subscripts equal to 1,2.

The potential-energy difference $\pi_D - \pi_U$ may be written as

$$2H_T\left\{\tfrac{1}{2}\sigma_{ij}^D\left(\varepsilon_{ij}^D - \tfrac{1}{3}c_t\theta^T\right) - \tfrac{1}{2}\sigma_{ij}^U\varepsilon_{ij}^U\right\} - 2H_T\sigma_{ft}^c\left(\varepsilon_y^D - \varepsilon_y^U\right) + \int_0^{\delta^D} p(\delta)d\delta - \sigma_{ft}^c\delta^D \tag{B6}$$

The braced expression is the difference between the downstream and upstream *recoverable* strain energy densities, and the next term comes from the change in the potential of the applied loading σ_{ft}^c due to the extra vertical displacement that accumulates in $|y|<H_T$ because of the phase transformation. The integral is the strain energy in the springs at the downstream crack opening displacement δ^D corresponding to the spring loading $p=\sigma_{ft}^c$. (Here $p(\delta)$ represents the spring constitutive relation $p(\delta) = \beta\sqrt{\delta/2}$ consistent with Eq. (8)). The last term is the contribution of the crack opening displacement to the applied-load potential. The last two terms combine to give the complementary energy of the springs defined by

$$Q(\sigma_{ft}^c) = \int_0^{\sigma_{ft}^c}\delta(p)dp = \frac{2(\sigma_{ft}^c)^3}{3\beta^2} \tag{B7}$$

The evaluation of the strain-energy terms is simplified by introducing $\tilde{\sigma}_{ij} = \sigma_{ij}^D - \sigma_{ij}^U$. Then, with

$$\tilde{\varepsilon}_{ij} = \frac{1}{E}\left[(1+\nu)\tilde{\sigma}_{ij} - \nu\tilde{\sigma}_{kk}\delta_{ij}\right] \tag{B8}$$

the braced term in (B6) may be written as

$$\Delta\mathcal{E} = \tfrac{1}{2}\tilde{\sigma}_{ij}\tilde{\varepsilon}_{ij} + \tilde{\sigma}_{ij}\varepsilon_{ij}^U \tag{B9}$$

Equilibrium gives $\sigma_y^U = \sigma_y^D = \sigma_{ft}^c$, so $\tilde{\sigma}_y = 0$, and since $\varepsilon_z^U = 0$, (B8) is just

$$\Delta\mathcal{E} = \tfrac{1}{2}(\tilde{\sigma}_x\tilde{\varepsilon}_x + \tilde{\sigma}_z\tilde{\varepsilon}_z) + \tilde{\sigma}_x\varepsilon_x^U \tag{B10}$$

Compatibility of strain at $y=\pm H_T$ requires $\varepsilon_x^D = \varepsilon_x^U$. With $\sigma_x^U = 0$, Eqs. (B4-B5, B8) then imply that

$$\sigma_x^D = \tilde{\sigma}_x = \tilde{\sigma}_z = -\frac{Ec_t\theta^T}{3(1-\nu)}, \quad \varepsilon_x^U = -\frac{\nu(1+\nu)}{E}\sigma_{ft}^c, \quad \tilde{\varepsilon}_x = \tilde{\varepsilon}_z = -\frac{c_t\theta^T}{3} \tag{B11}$$

and we get

$$\Delta\mathcal{E} = \frac{E(c_t\theta^T)^2}{9(1-\nu)} + \frac{\nu(1+\nu)c_t\theta^T}{3(1-\nu)} \tag{B12}$$

Eqs. (B4-B5) also give

$$\varepsilon_y^D - \varepsilon_y^U = \frac{(1+\nu)c_t\theta^T}{3(1-\nu)} \tag{B13}$$

and assembling the contributions of (B7), (B12), and (B13) to (B6) produces

$$\pi_D - \pi_U = 2H_T\left[\frac{E(c_t\theta^T)^2}{9(1-\nu)} - \frac{(1+\nu)\sigma_{ft}^c c_t\theta^T}{3}\right] - Q(\sigma_{ft}^c) \tag{B14}$$

Substitution into (B1) gives

$$Q(\sigma_{ft}^c) = (1-c)\mathcal{G}_m + 2H_T c_t\theta^T\left[\sigma_m^c - \frac{(1+\nu)\sigma_{ft}^c}{3}\right] \tag{B15}$$

Now note that for matrix cracking with only fiber reinforcement, this reduces to the result (Budiansky and Amazigo 1989)

$$Q(\sigma_f^c) = (1-c)\mathcal{G}_m = \frac{2(\sigma_f^c)^3}{3\beta^2} \tag{B16}$$

and therefore

$$\frac{Q(\sigma_{ft}^c)}{Q(\sigma_f^c)} = 1 + \frac{3\beta^2 H_T\sigma_m^c c_t\theta^T}{(\sigma_f^c)^3}\left[1 - \left(\frac{1+\nu}{3}\right)\frac{\sigma_{ft}^c}{\sigma_m^c}\right] \tag{B17}$$

Finally, introduction of the normalizing length L defined by Eq. (30), together with the parameters ω and s (Eqs. (2,3)), gives

$$\Sigma^3 = 1 + \left(\frac{\omega}{6\pi s^2}\right)\left(\frac{H_T}{L}\right)(1 - s\Sigma) \tag{B18}$$

in terms of the strengthening ratio $\Sigma = \sigma_{ft}^c/\sigma_f^c$. This is the result (36) in the text.

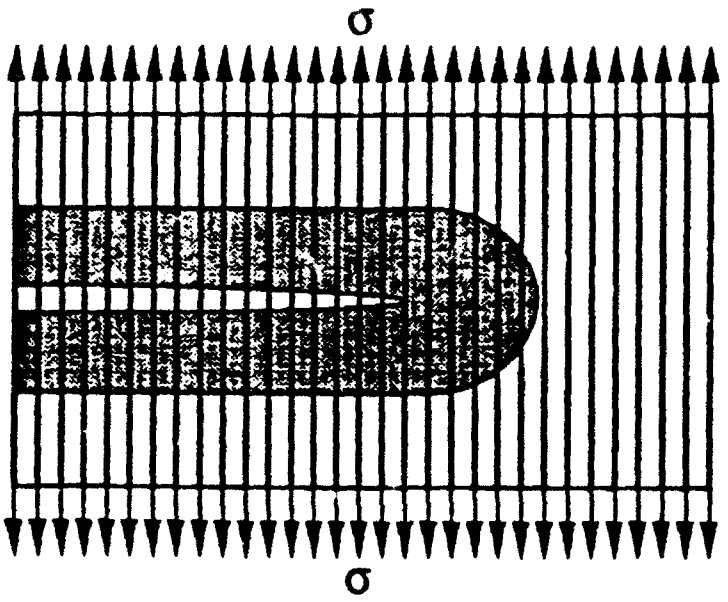

Fig. 1 Steady – state matrix cracking; combined reinforcements.

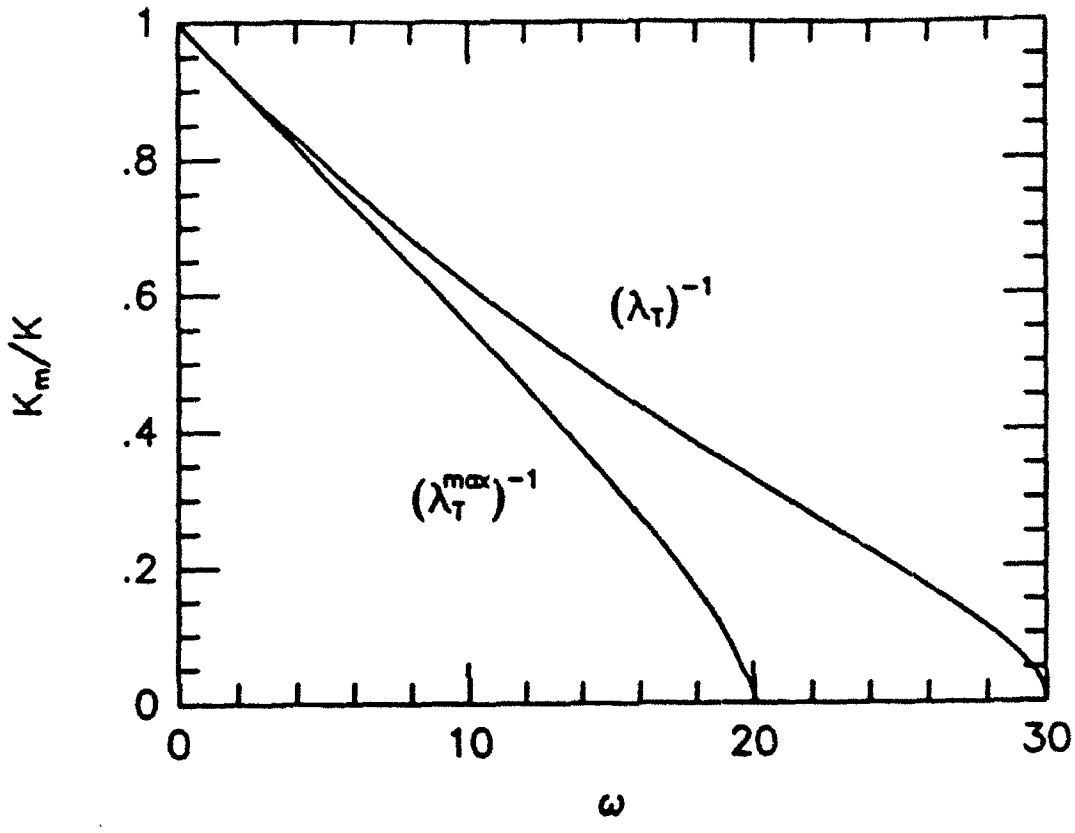

Fig. 2. Reciprocal toughness ratios versus the toughening parameter ω.

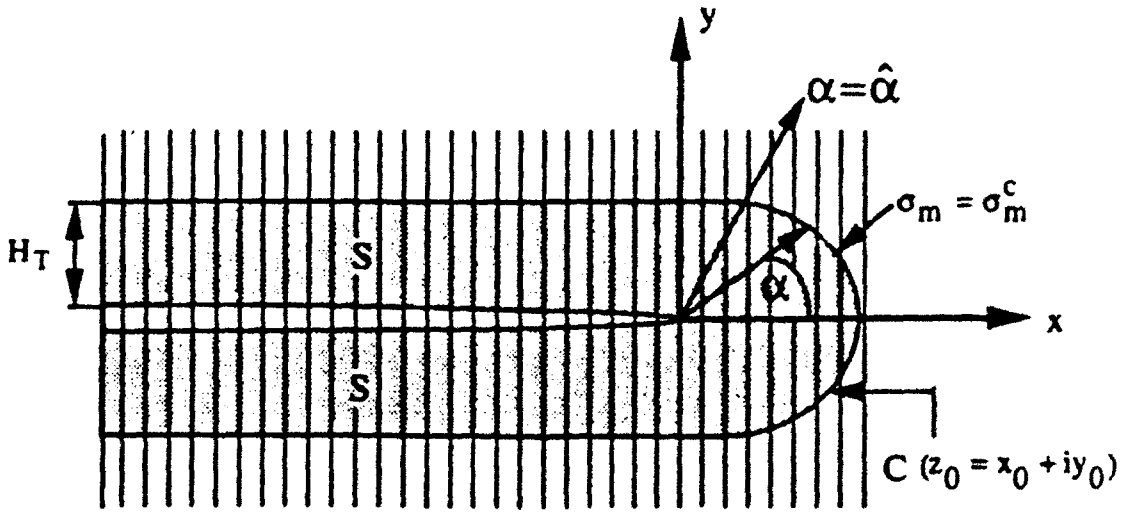

Fig. 3 Zone of phase – transformed particles and fibers bridging the crack faces

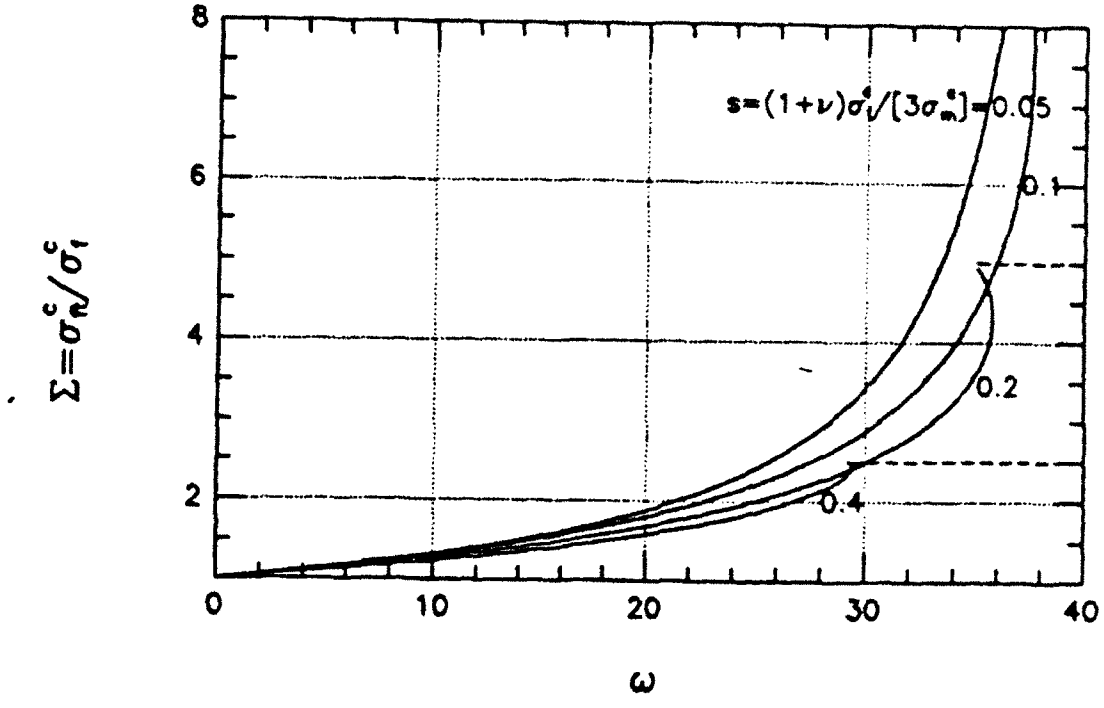

Fig. 4. Strengthening ratio $\Sigma = \dfrac{\sigma_{fl}^c}{\sigma_f^c}$ vs. ω, various s.

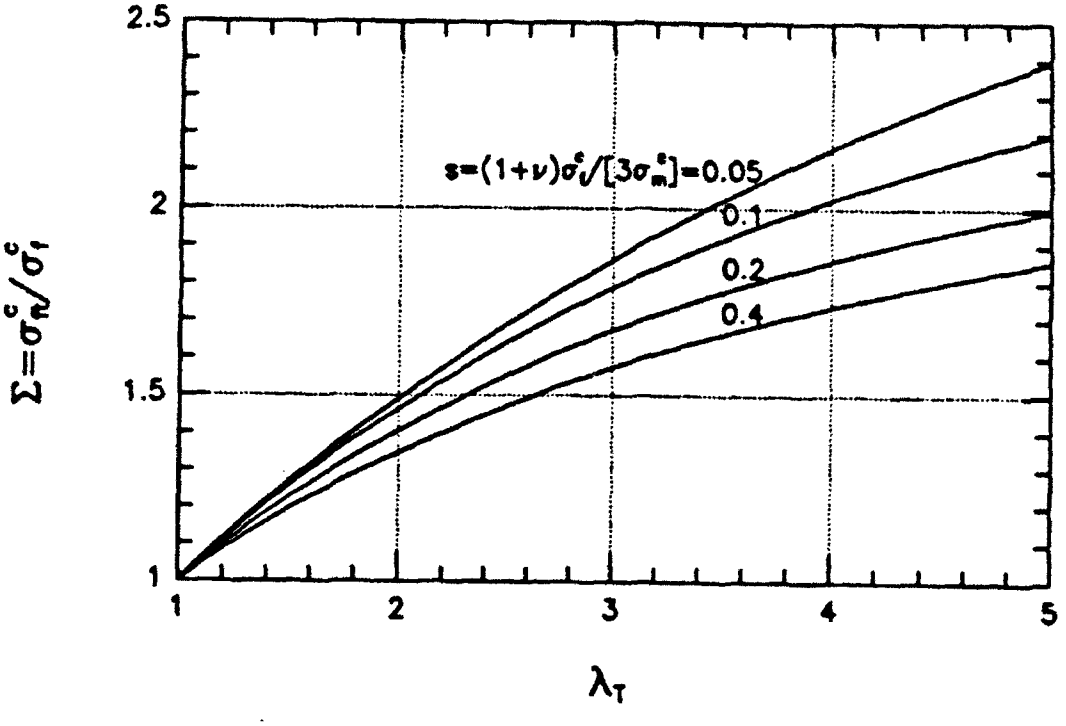

Fig. 5. Strengthening ratio $\Sigma = \dfrac{\sigma_{fl}^c}{\sigma_f^c}$ vs. λ_T, various s.

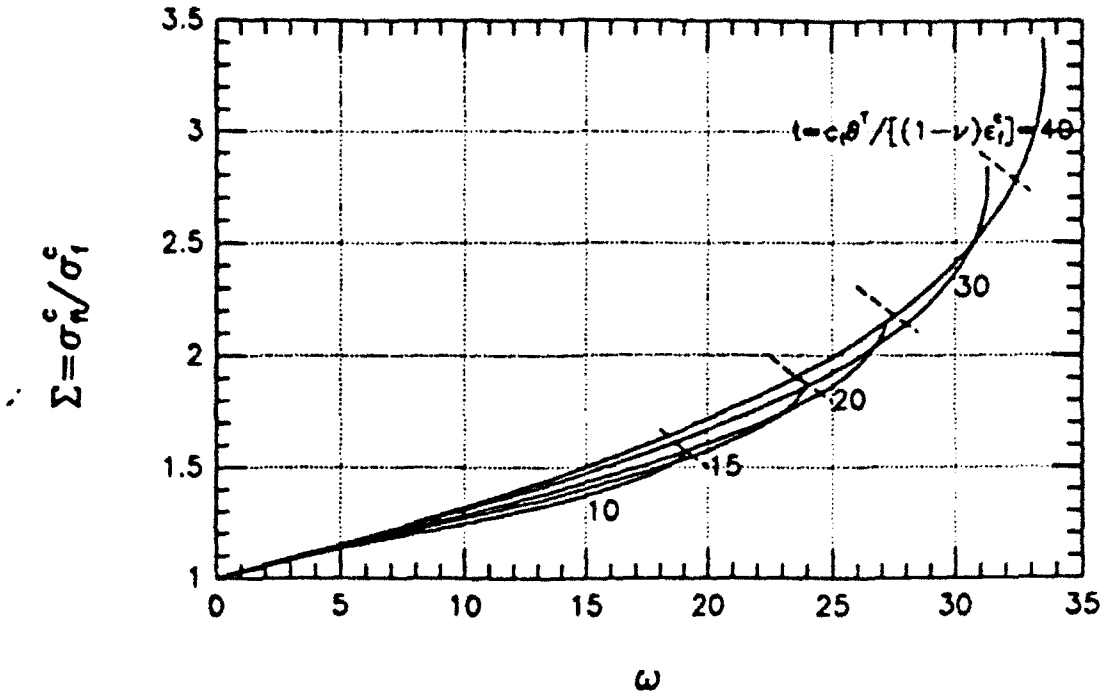

Fig. 6. Strengthening ratio $\Sigma = \dfrac{\sigma_{fl}^c}{\sigma_f^c}$ vs. ω, various t.

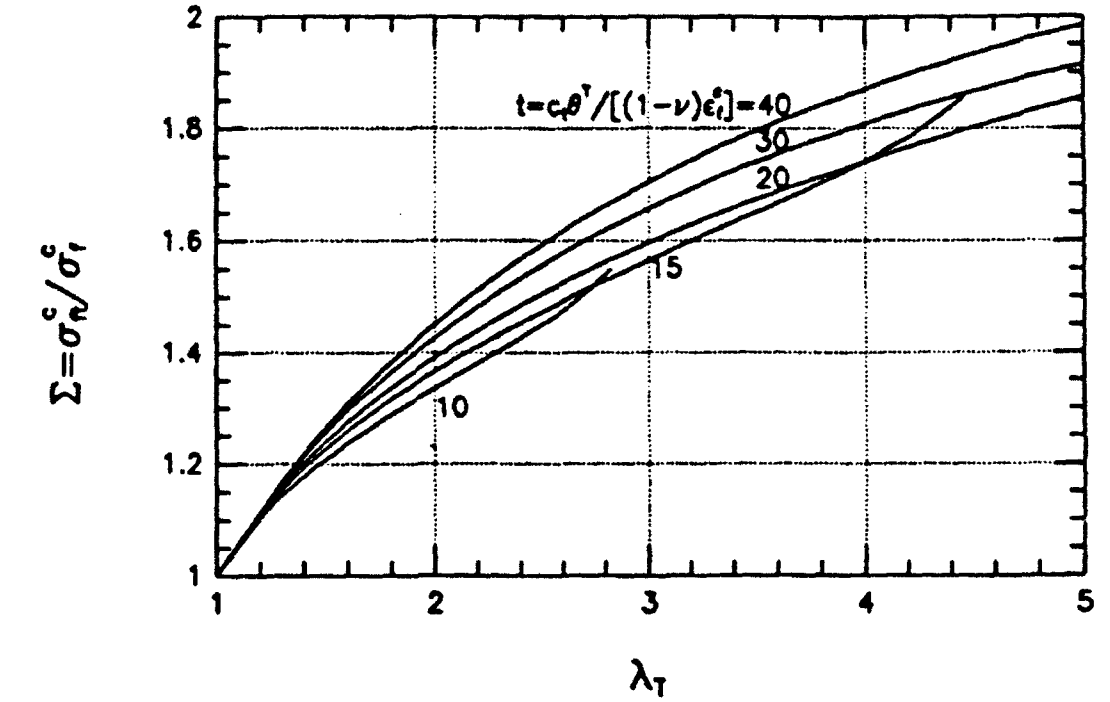

Fig. 7. Strengthening ratio $\Sigma = \dfrac{\sigma_{fl}^c}{\sigma_f^c}$ vs. λ_T, various t.

Acta metall. mater. Vol. 40, No. 6, pp. 1259–1265, 1992
Printed in Great Britain. All rights reserved

0956-7151/92 $5.00 + 0.00
Copyright © 1992 Pergamon Press Ltd

A HIGH-TOUGHNESS γ-TITANIUM ALUMINIDE

H. E. DÈVE[1,*], A.G. EVANS[2] and D. S. SHIH[3,‡]

[1]3M, Metal Matrix Composite Group, 3M Center, St Paul, MN 55144-1000, [2]Materials Department, College of Engineering, University of California, Santa Barbara, CA 93106 and [3]McDonnell Douglas Co., Research Laboratories, P.O. Box 516, MC 1111041, St Louis, MO 63166-0516, U.S.A.

(Received 7 October 1991)

Abstract—A high-toughness γ-TiAl with a lath microstructure has been characterized. The presence of a laminated structure that consists of α_2 plates between γ laths has been shown to govern the toughness. The lath microstructure promotes dissipation through a combination of process zone and crack bridging mechanisms. Mechanical twinning in the γ-phase contributes to the toughness through the formation of a twin process zone, while regions consisting of intact lath colonies act as bridging ligaments in the crack wake. The measured steady-state toughness of $\sim 25\ \mathrm{MPa}\sqrt{\mathrm{m}}$ is consistent with preliminary estimates of dissipation: which indicate that similar contributions arise from deformation within the bridging ligaments and from twinning in the process zone.

Résumé—On a caractérisé un alliage TiAl/γ à haute ténacité à microstructure en lattes. On montre que la présence d'une structure en lamelles qui consiste en plaquettes de phase α_2 situées entre des lattes de phase γ gouverne la ténacité. La microstructure en lattes provoque une dissipation par une combinaison de zones de transformation et de mécanismes de pontage de fissures. Le maclage mécanique dans la phase γ contribue à la ténacité par la formation de zones de maclage, tandis que les régions formées de colonies de lattes intactes agissent comme des liens de pontage dans l'ouverture de la fissure. La ténacité mesurée en régime permanent ($\sim 25\ \mathrm{MPa}\sqrt{\mathrm{m}}$) est en accord avec des estimations préliminaires de la dissipation: ceci indique que des contributions semblables proviennent de la déformation à l'intérieur des ligaments de pontage et du maclage dans la zone de transformation.

Zusammenfassung—Hochzähes γ-TiAl mit Latten-Mikrostruktur wird charakterisiert. Die vorliegende laminierte Struktur, bestehend aus α_2-Platten zwischen γ-Latten, bestimmt die Zähigkeit. Die Latten-Mikrostruktur fördert die Dissipation über eine Kombination von Prozeßzonen- und Rißüberbrückungsmechanismen. Mechanische Zwillingsbildung in der γ-Phase trägt zur Zähigkeit über die Bildung einer Zwillings-Prozeßzone bei; dagegen wirken Bereiche, die aus intakten Lattenkolonien bestehen, als überbrückende Fasern in der Rißöffnung. Die gemessene stationäre Zähigkeit von $\sim 25\ \mathrm{MPa}\sqrt{\mathrm{m}}$ ist mit vorläufigen Abschätzungen der Dissipation verträglich. Das weist darauf hin, daß ähnliche Beiträge von der Verformung innerhalb der überbrückenden Fasern und von der Zwillingsbildung in der Prozeßzone herrühren.

1. INTRODUCTION

The application of γ-TiAl for high-temperature structural components is limited by its relatively low toughness. Most measurements indicate an initiation toughness of about $8\ \mathrm{MPa}\sqrt{\mathrm{m}}$, with minimal increase in resistance with crack extension [1]. Various approaches for improving toughness have been demonstrated, through process zone and bridging zone mechanisms [3–6]. Compositions and microstructures that encourage mechanical *twinning* within a *process zone* have been shown to produce a material with a steady-state toughness of $\sim 16\ \mathrm{MPa}\sqrt{\mathrm{m}}$ (Fig. 1) [2], but the strength of such materials is relatively low. Ductile phase reinforcement with Nb and Nb alloys has provided major improvements in toughness, through plastic dissipation in the reinforcing phase within a *bridging zone* [1, 3–7] (Fig. 1). In this case, the fracture resistance increases with crack extension and depends on such variables as the flow strength and ductility of the reinforcement, the extent of interface debonding, the friction at the interface, as well as the volume fraction, the size and morphology of the reinforcement. The highest toughness (Fig. 1) has been achieved with laminates that exhibit appreciable interface debonding [4]. Such materials are anisotropic, with relatively poor through-thickness properties and, consequently, are most appropriate for composites subject to biaxial loading. Ductile reinforcement toughening concepts have also been used to develop tough isotropic intermetallics. One approach is to choose a material system that has a eutectic between the intermetallic of interest and a refractory metal, leading to a two-phase intermetallic/metallic microstructure. This concept has been demonstrated for the system Nb_5Si_3/Nb [7]. Another approach is addressed in this article, based on toughening mechanisms promoted in laminate microstructures between γ-TiAl and α_2-Ti_3Al [8–10]. The responsible mechanisms are not explicitly known, but it has been demonstrated that the γ-phase is susceptible to

†Formerly with: Materials Department, University of California, Santa Barbara, CA 93106, U.S.A.
‡Formerly with: General Electric Aircraft Engines, 1 Neuman Way, Cincinnati, OH 45215, U.S.A.

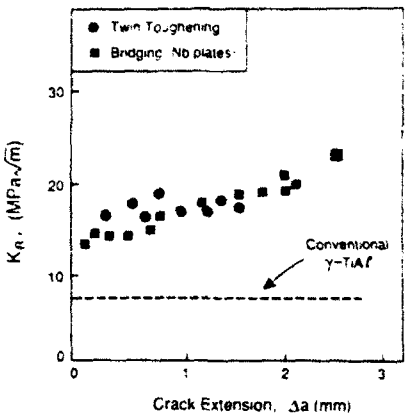

Fig. 1. The effects of twinning and of Nb laminate layers on the resistance curves for γ-TiAl.

twinning and dislocation activity [8], whereas the α_2 is essentially dislocation free.

2. MATERIALS AND MICROSTRUCTURES

Three different materials have been investigated [8]. Material A is a single phase γ-TiAl having composition Ti–52Al. This material has an equiaxed grain structure with a grain size of $\sim 100\,\mu$m. The other two materials both have composition Ti–48Al–2Cr–2Nb, but heat treated to produce different microstructures. Material B has an equiaxed duplex, microstructure consisting of primary γ-TiAl grains of size $15\,\mu$m and lamellar grains, $25\,\mu$m in diameter, that consist of γ-TiAl and α_2-Ti_3Al laths. Material C has a fully transformed lath microstructure (Fig. 2) with a prior-α grain size ≈ 1 mm. Transmission electron microscopy of this material [Fig. 2(b)] has revealed that the laths consist, on average, of thin ($\sim 0.1\,\mu$m) layers of α_2 between γ layers $\sim 1\,\mu$m in thickness. The γ layers also contain annealing twins, γ^T. The laminates may thus be regarded as colonies of γ, γ^T and α_2 laths. The orientation relationships between α_2 and γ are

$$\{0001\}\alpha_2 // \{111\}\gamma_T$$

$$\langle 1\bar{2}01\rangle\alpha_2 // \langle 110\rangle\gamma_T$$

The standard crystallographic elements characterizing the annealing and mechanical twin systems in $L1_0$ structure are [2]

$$K_1, K_2, \eta_1, \eta_2 \equiv (111), (11\bar{1}), \tfrac{1}{2}[11\bar{2}], \tfrac{1}{2}[11\bar{2}].$$

The primary laminate colonies inside the prior-α grains are often intersected by secondary colonies located in the center of the grains [Fig. 2(a)]. The secondary colonies often have an important role as bridging ligaments (or crack nucleation sites), as elaborated later.

3. MEASUREMENTS AND OBSERVATIONS

3.1. Test procedures

The fracture resistance of these materials has been obtained using a notched, three-point bending specimen. Precracking has been conducted in monotonic loading in a servohydraulic machine subject to control from the displacement on the compressed face opposite the notch. Subsequent loading was conducted *in situ* in the scanning electron microscope (SEM), as needed to monitor the sequence of events that accompany crack extension. For this purpose, prior to testing, the side faces of the specimen were given an optical quality metallographic polish followed by electropolishing. Prior to and following crack propagation, the surfaces were characterized in the scanning electron microscope using backscattered electron imaging in order to obtain a strong compositional contrast that reveals the lath structure.

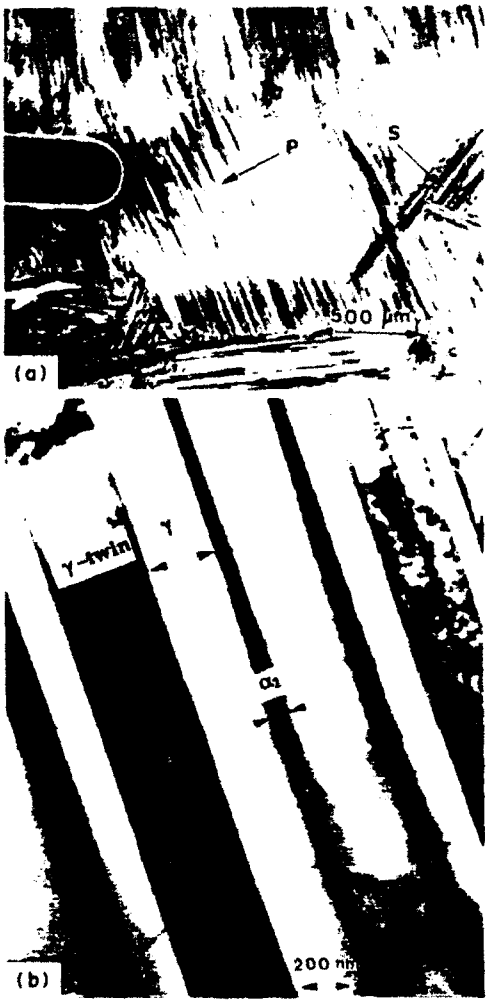

Fig. 2. The transformed lath microstructure in material C. (a) SEM of polished and etched surface. Note the presence of primary and secondary laminate colonies. (b) TEM showing the α_2 and twinned γ layers.

Unfortunately, this imaging technique does not distinguish the strong compositional contrast of the lath structure from the weak topographic contrast produced by shear events such as mechanical twinning. Therefore, complementary observation of slip and shear features was done using Nomarski imaging in an optical microscope. Additional information characterizing the non-linear behavior of the materials was obtained by measuring the compressive stress-strain curves, $\sigma(\epsilon)$, using standard specimens.

3.2. Results

The fracture resistance information obtained on the three materials is summarized in Fig. 3. The equiaxed duplex microstructure of Ti–48Al–2Cr–2Nb gave a fracture resistance comparable to single phase γ-TiAl (10 MPa$\sqrt{m}$ or 500 Jm^{-2}). The materials with transformed lath microstructure exhibited initial crack pop-in at a similar resistance. However, further crack occurred at a substantially higher resistance, which increased to ~25 MPa$\sqrt{m}$ (or ~3 kJm^{-2}) after crack extensions of ~1 mm, consistent with previous measurements [9, 10]. The increase in toughness over that of single-phase γ-TiAl is thus ~2.5 kJm^{-2}.

The compressive stress–strain behavior of materials B and C (Fig. 4) indicates a yield strength, $\sigma_0 \approx 400$ MPa, followed by extensive strain hardening. Comparison with a single-phase γ-TiAl (Fig. 4) that deforms by mechanical twinning suggests that the presence of the non-deformable α_2 laths strengthens the material. This phenomenon is qualitatively consistent with the influence of high-aspect ratio elastic discs on the flow strength [11].

In the tough, laminated material, several key observations have been made in the scanning electron and optical microscopes. Those colonies having laminate planes within about 45° to the mode I crack plane initially exhibit low resistance to crack propagation, comparable to that for γ-TiAl [Fig. 5(a)]. Crack extension is associated with the formation of slip events, presumably mechanical twins, in the γ-layers parallel to the laminate planes [Fig. 5(b)]. The density

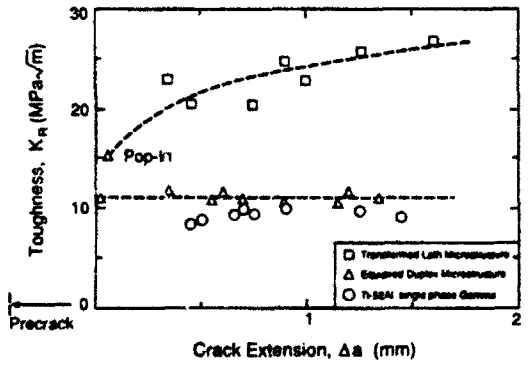

Fig. 3. Resistance curves measured for the three materials, A, B and C.

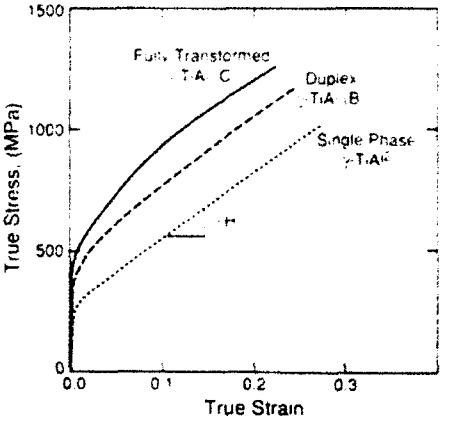

Fig. 4. Compressive stress-strain response of materials B and C compared to the stress-strain response of a similar single phase γ-TiAl that exhibits twinning [2].

of mechanical twins in the process zone varies as a function of the distance from the crack plane. Within the resolution limit of the optical microscope, there is a high twin density in a 10 μm zone around the crack and a much weaker twin activity in a zone up to 200 μm wide, [Fig. 5(b)]. Continued crack extension occurs with a relatively complex three-dimensional

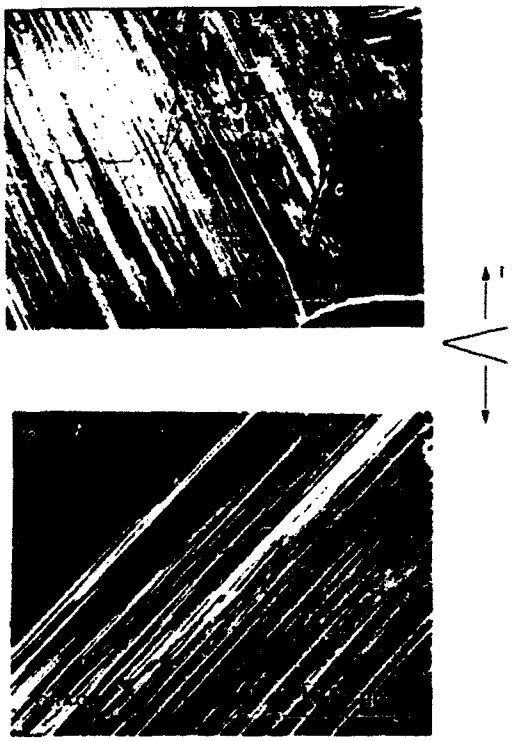

Fig. 5. (a) Scanning electron microscope of a crack propagating parallel to the lath structure. Note the presence of bridging ligaments, at B. (b) Nomarski imaging of stress induced shearing events that form in a process zone around the crack. Note that the main crack arrested at point A in an intense twin process zone. A secondary crack, C, has formed parallel to the primary crack.

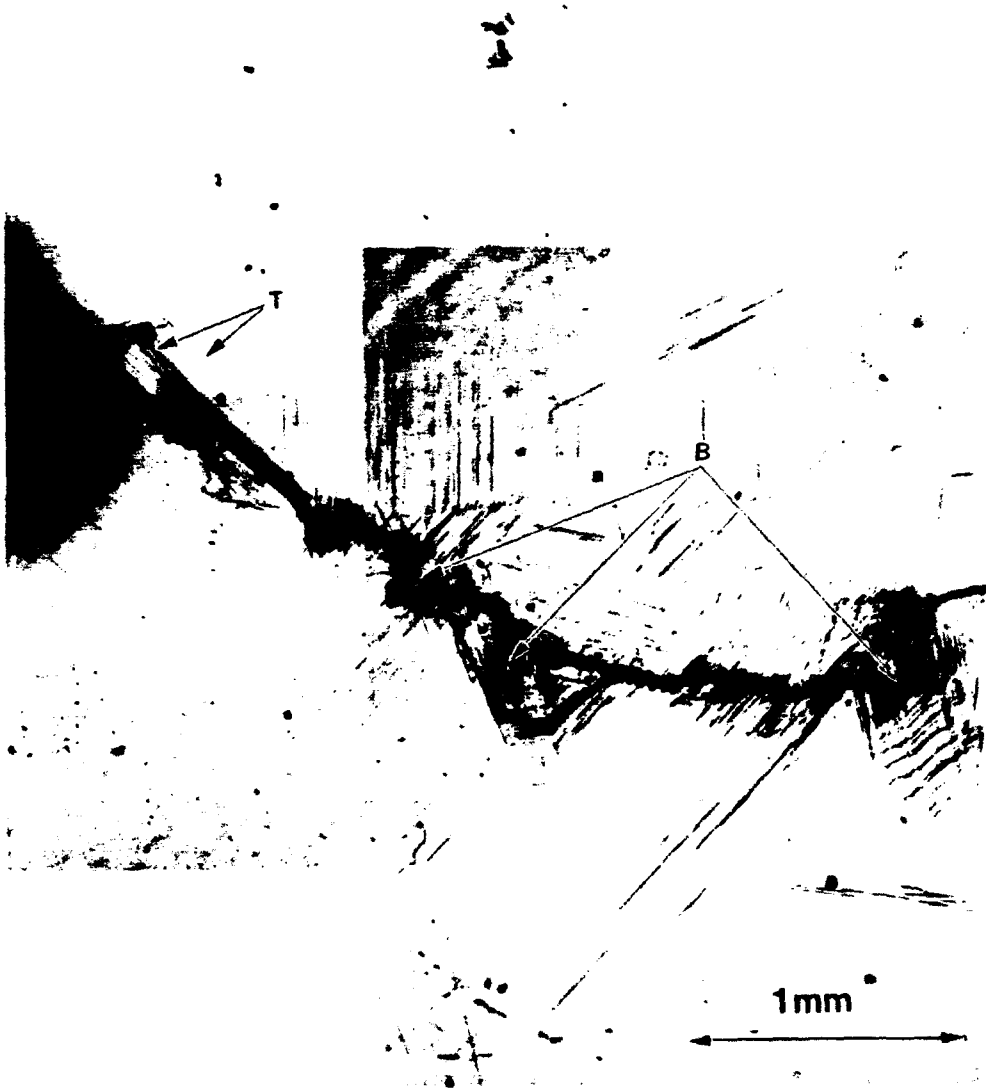

Fig. 6. Optical micrograph of a two phase TiAl intermetallic that exhibits a combination of process zone and bridging mechanisms. The shear traces associated with mechanical twinning in a process zone are exemplified by the trace marked T, while bridging ligaments are marked B.

morphology, involving a twin process zone (Fig. 6), coupled with bridging (Fig. 7), with a mix of multiple cracking along laminate planes, and shearing of bridging ligaments (Fig. 7). The basic elements of the fracture process are summarized in the schematic presented in Fig. 8. The crack front proceeds by brittle fracture, seeking those colonies having planes oriented close to the mode I path through the material. Such crack advance is accompanied by the formation of a process zone around the crack faces, as witnessed by the formation of shear traces, presumably twins, parallel to the lathes. The cracks seemingly renucleate ahead of the main crack, preferentially in regions containing mechanical twins,† at the intersections of primary and secondary lath colonies. This process generates intact ligaments bridging the main crack. Upon further crack opening, the bridging ligaments deform by shearing mechanisms, presumably by twinning in the γ-TiAl phase, and eventually fail by debonding parallel to the laminate plates, leading to a bridging zone length, $L \approx 200\ \mu m$.

This general view of the fracture process is consistent with SEM observations of the fracture surface (Fig. 10). These reveal an essentially continuous cleavage path with colony-sized islands subject to distortions in the form of deformed ligaments [9, 10].

†Mechanical twins in the $L1_0$ structure produce a shear strain, 0.749. It is conceivable that this strain could induce microcracking due to incompatibility of deformation at twin boundaries.

The associated area fraction of bridging ligaments on the fracture surface is, $f \approx 0.2$.

Measurements of the shear strain of conjugate traces *within the ligaments* [Fig. 8(b)] provide additional information of interest. The conjugate traces reveal that the shear strain in bridging ligaments is about 0.7, similar to the twinning strain for γ-TiAl (0.749). The average ligament thickness, $d \approx 50\ \mu$m. Ligament deformation is governed by the angle θ, between the shear planes and the mode I crack plane (Fig. 9) and the debond length, l. The angle θ is found to be in the range, $60 < \theta < 30$ and the debond length $l \approx d$.

4. ANALYSIS

The model of the fracture process in the lath microstructure [Fig. 8(b)] allows a rationalization of the improvement in fracture resistance, with the following basic features. Crack extension initiates at an energy release rate governed by the fracture resistance of the brittle constituent. As the crack

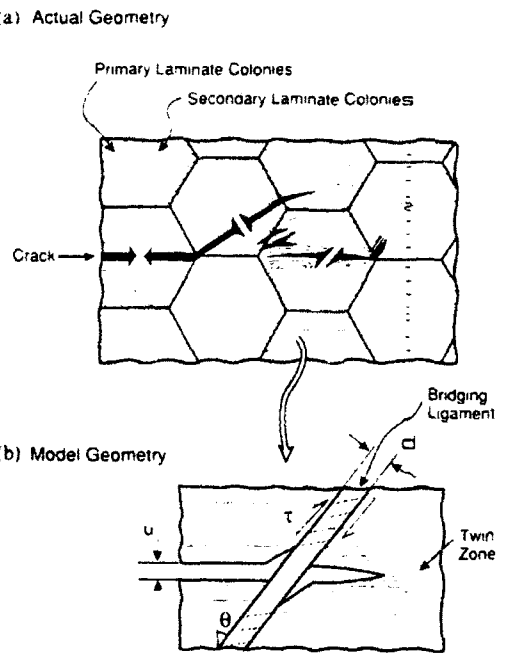

Fig. 8. Schematic indicating the dominant features of the cracking process.

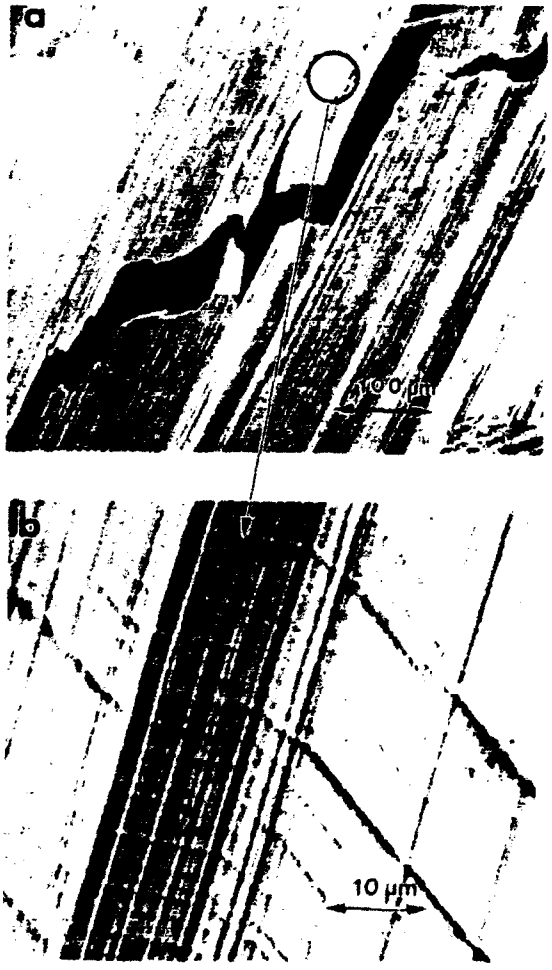

Fig. 7. (a) Example of a bridging ligaments. (b) SEM image of the shear traces within the ligament.

extends, dissipation occurs, governed by the nonlinear deformation associated with the shearing events along the laminate planes through process zone and bridging mechanisms. A comparison of the measured steady-state toughening $\Gamma_{ss} \approx 3\ \mathrm{kJm}^{-2}$ with predictions for each mechanism provides a preliminary assessment of their relative importance in accordance with

$$\Gamma_{ss} = \Gamma_0 + \Gamma_b + \Gamma_p \qquad (1)$$

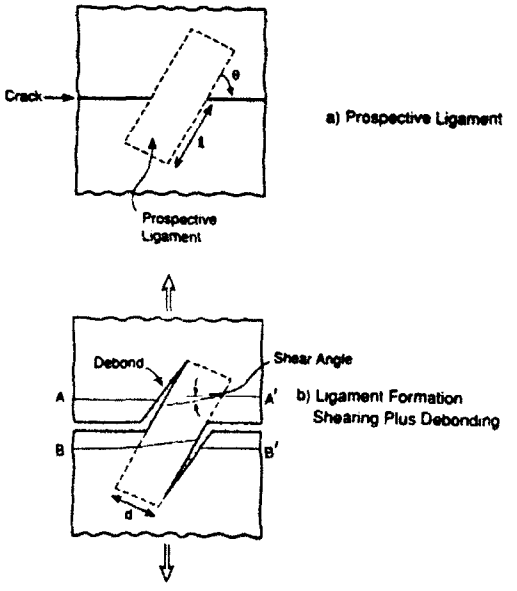

Fig. 9. Schematic of the bridging and debonding mechanisms.

Fig. 10. SEM micrograph showing the fracture surface of a bridging ligament.

where Γ_0 is the brittle fracture resistance of the twin planes that govern the crack path. Γ_b is the dissipation in the bridging ligaments and Γ_p the dissipation in the twin process zone.

Before proceeding, a consistency check is made based on the width, h, of the the twin process zone. In steady-state, this zone is predicted to be [12, 13]

$$h = (\sqrt{3}/12\pi)(E\Gamma_{ss}/\sigma_0^2). \quad (2)$$

Based on the measured values of Γ_{ss} and σ_0 (Table 1), h is predicted to be $\sim 200\,\mu$m, consistent with experimental observations (Fig. 6). This zone is similar in width to that found in a γ-TiAl that exhibits twin toughening [2], for which $\Gamma_p \approx 1\,\text{kJm}^{-2}$. Also, the ratio of the hardening H to the modulus E is similar (Fig. 4). Since h and H/E appear to be the important quantities affecting the twin toughening [2], it seems reasonable to suppose that the process zone toughening in the present material is also $\Gamma_p \approx 1\,\text{kJm}^{-2}$.

The bridging zone dissipation is usually dominated by plastic deformation within the ligaments† which can occur in accordance with the schematic indicated on Fig. 11, wherein debonding in conjunction with a twinning shear allows the crack to open, as the ligament deforms. The plastic dissipation per unit area of crack is approximately

$$\Gamma_b \approx f l \tau_0 \gamma_0 f_T \quad (3)$$

where τ_0 and γ_0 are, respectively, the shear stress needed for twinning and the twinning shear strain and f_T in the volume fraction of the γ-phase *within the ligaments* that undergo twinning. Based on the information given in Table 1, equation (3) gives $\Gamma_b \approx 1\,\text{kJm}^{-2}$.

The additive contribution of each mechanism provides an increase in toughness of $\sim 2\,\text{kJm}^{-2}$ comparable to the measured value of $\sim 2.5\,\text{kJm}^{-2}$. Dissipation within both the process zone and bridging ligaments thus appears to adequately rationalize the measured toughening. However, *prediction* of trends in toughness with microstructure requires additional analysis and insight.

†The debond energy being relatively small.

Table 1. A summary of laminate characteristics

Average width of bridging ligaments, $d \approx 50\,\mu$m
Area fraction of bridging colonies, $f \approx 0.2$
Twin shear strain, $\gamma_0 \approx 0.74$
Twin shear stress, $\tau_0 \approx 200$ MPa
Volume fraction of twins in the bridging colonies, $f_T \approx 0.4$
Fracture energy of γ-TiAl twin interfaces, $\Gamma_0 \approx 300$–$500\,\text{Jm}^{-2}$
Young's modulus, $E \cong 200$ GPa
Process zone width, $h \approx 200\,\mu$m
Yield strength, $\sigma_0 \approx 400$ MPa

5. CONCLUDING REMARKS

The relatively high toughness provided by the laminate microstructure is consistent with dissipation governed by twinning of the γ-phase. The twinning occurs within a process zone, as well as within crack bridging ligaments, with about equal contributions arising from the process and bridging zones. Process zone twin toughening has been identified with other, predominantly γ-TiAl, microstructures [2]. The laminate microstructures appear to provide an *additional* contribution to the toughness by allowing the formation of bridging ligaments, which experience extensive deformation between the crack faces as the crack extends. The ability of the laminates to locally deflect cracks appear to be central to the incidence of appreciable bridging, leading to the large local strains and the dissipation that occurs by twinning within the bridging ligaments, once formed.

Further research of a basic nature on shear deformation by twinning (and associated dislocation mechanisms) in laminated structures is needed to address the above features of the toughening process and to provide a *predictive model*. Specifically, a rigorous model that incorporates the constitutive behavior of the twinning material is required to relate the toughening to aspects of the twin process zone, comparable to that for transformation toughening [12, 13]. A basic mechanics of the microstructural features that govern the formation and the response of bridging ligaments also needs to be developed, along the lines established for debonding and dissipation in fiber composites [14].

REFERENCES

1. C. K. Elliott, G. R. Odette, G. E. Lucas and J. W. Sheckard, *MRS Proc.* **120**, 695 (1988).
2. H. E. Dève and A. G. Evans, *Acta metall. mater.* **6**, 171 (1991).
3. H. C. Cao, B. J. Dalgleish, H. E. Dève, C. Elliott, A. G. Evans, R. Mehrabian and G. R. Odette, *Acta metall.* **37**, 2969 (1989).
4. H. E. Dève, A. G. Evans, G. R. Odette, R. Mehrabian, M. L. Emiliani and R. J. Hecht, *Acta metall. mater.* **38**, 1491 (1990).
5. G. R. Odette, W. Sheckard and G. E. Lucas, *Acta metall. mater.* In press.
6. H. E. Dève and M. Maloney, *Acta metall. mater.* **39**, 2275 (1991).

7. S. Mazdiyasni and D. B Miracle. *MRS Proc.* **194**, 155 (1990).
8. D. S. Shih, S. C. Huang, G. K. Scarr, H. Jang and J. C. Chesnutt. *Microstructure Property Relationship in Titanium Aluminides and Alloys* (edited by Y. M. Kim and R. R. Boyer) p. 135. The Metall. Soc., Warrendale, Pa (1991).
9. D. E. Larsen, M. L. Adams, S. L. Kampe, L. Christodolou and J. D. Bryant. *Scripta metall. mater.* **24**, 851 (1990).
10. S. L. Kampe, J. A. Clarke and L. Christodolou. *Mater. Res. Soc. Symp.* **194**, 225 (1990).
11. G. Bao, J. W. Hutchinson, and R. M. McMeeking. *Acta metall. mater.* **39**, 1871 (1991).
12. R. M. McMeeking and A. G. Evans. *J. Am. Ceram. Soc.* **65**, 242 (1982).
13. B. Budiansky, J. W. Hutchinson and J. C. Lambropoulos. *Int. J. Solids Struct.* **19**, 337 (1983).
14. M. Y. He and J. W. Hutchinson. *J. appl. Mech.* **56**, 270 (1989).

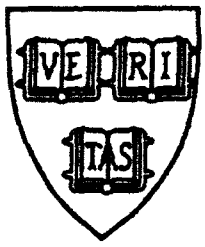

MECH-204

ON THE MECHANICS OF STRESS-INDUCED PHASE TRANSFORMATION IN ZIRCONIA

Bernard Budiansky and Lev Truskinovsky

Division of Applied Sciences
HARVARD UNIVERSITY
Cambridge, Massachusetts 02138

February 1993

ON THE MECHANICS OF STRESS-INDUCED PHASE TRANSFORMATION IN ZIRCONIA

Bernard Budiansky

Division of Applied Sciences, Harvard University, Cambridge, MA 02138, U.S.A.

and

Lev Truskinovsky

Department of Aerospace Engineering and Mechanics, University of Minnesota, Minneapolis, MN 55455, U.S.A.

ABSTRACT

Some consequences of a simple theoretical model for the stress-induced, isothermal phase transformation of an isolated tetragonal zirconia crystal are studied. The transformation to a monoclinic state is viewed as mechanical buckling from one homogeneous geometrical configuration to another. The model is used to predict the manner in which an applied shear stress should interact with hydrostatic stress in causing the transformation, and also the reverse monoclinic-to-tetragonal phase change. An isolated tetragonal inclusion in an elastic matrix is also considered, and its response to a far-field combination of shear and hydrostatic stress is analyzed.

INTRODUCTION

The discovery by Garvie et al (1975) of the transformation-toughening effects of zirconia (ZrO_2) particles embedded in a brittle matrix has spawned a large literature on the subject (see Evans and Heuer 1980, Evans and Cannon 1986, Green et al 1989, Rühle and Evans 1989 for reviews), and research continues apace. Early theoretical analyses of transformation toughening were based on the assumption that a tetragonal-to-monoclinic phase transformation of zirconia inclusions is provoked by a critical hydrostatic tension (McMeeking and Evans 1982, Budiansky et al 1983), and the same basis was used in several later studies (e.g. Rose 1986, Amazigo and Budiansky 1988, Stump and Budiansky 1989ab). But in several theoretical studies (e.g., Evans and Cannon 1986; Lambropoulos 1986; Chen and Reyes Morel 1987; Sun et al 1990; Stump 1991) shear-stress effects on transformation toughening have been explored, and found to be substantial (and in Stump's work, startling). Furthermore, experiments on composites (Chen and Reyes Morel 1986) have shown that shear and hydrostatic stress may interact significantly in triggering the m→t transformation.

In this paper we explore some consequences of a simple theoretical model for the stress-induced, isothermal phase transformation of an isolated tetragonal zirconia crystal. The

transformation is viewed as mechanical buckling from one homogeneous geometrical configuration to another. The analytical formulation is based on the most elementary polynomial strain-energy functional that is sufficiently rich to imply the t→m transformation at a critical pressure. A similar functional has been written for zirconia by Chan (1988), but we explore its implications in rather different directions here. The model is used to predict the manner in which an applied shear stress should interact with hydrostatic stress in causing the transformation, and also the reverse m→t transformation. The theory also implies constraints on the signs and ratios of some of the elastic constants in the monoclinic phase. These results will be confronted with those of recent acoustic experiments by Nevitt et al (1988) and atomic *ab initio* calculations by Cohen et al (1988).

On the basis of an idealized, approximate version of the model, we also look briefly at an isolated tetragonal inclusion in an elastic matrix, and study its response to a far-field combination of shear and hydrostatic stress vis-a-vis that of an unconstrained crystal.

MODELING GOALS

Guided by various experimental observations (particularly those of Block et al 1985), we shall postulate several basic phenomenological features of the phase transformations of zirconia, and attempt to build a mathematical mechanical model that is consistent with these characteristics and permits the prediction of others. We will assume that (i) at a fixed temperature a single crystal of zirconia is stable in a tetragonal configuration for sufficiently high pressures*; (ii) under *decreasing* pressure, the zirconia suddenly snaps into a homogeneous monoclinic phase (see Fig. 1) at a critical pressure $p=p_c$; and (iii) under subsequent reapplication of *increasing* pressure, a sudden reverse transformation back to the tetragonal phase occurs at $p=p_c'>p_c$. The data of Block et al show room-temperature values of $p_c \approx 2.8$ GPa and $p_c' = p_c + \Delta p_c \approx 3.4$ GPa during such pressure cycles, and also indicate that for increasing temperature both critical pressures decrease linearly, with Δp_c remaining constant. This hysteretic behavior is illustrated schematically by the phase diagram in pressure-temperature space sketched in Fig. 2, wherein the solid line represents the tetragonal-to-monoclinic (t→m) transformation under decreasing pressure at constant temperature *or* decreasing temperature at fixed pressure, and the dashed line is the m→t boundary for increasing pressure or increasing temperature. The obvious analogous interpretations of these boundaries are presumed to apply for curved paths in pressure-temperature space, but in the rest of this paper we will restrict ourselves to consideration of isothermal phase changes.

---

* At room temperature, the high-pressure phase may really be slightly orthorhombic rather than tetragonal (Arashi et al 1988; Chiao and Chen 1990), but our elementary analysis remains applicable.

The current lore of zirconia has it that at room temperature, and under purely hydrostatic loading, a dilatational strain θ_T of about .04 should occur during the tetragonal-to-monoclinic phase transformation. The magnitude of the accompanying shear strain γ_T with respect to *one* of the two original pairs of a-c axes (see Fig. 1) is believed to be about .16, while the a-a axes, as well as the other a-c pair, remain orthogonal as they transform into the a-b and b-c axes in the monoclinic phase. Clearly, the transformation shear strain may be positive or negative (corresponding to symmetry related variants of the monoclinic configuration) and so the sudden martensitic t-to-m phase change induced by decreasing pressure has the earmarks of a symmetry-breaking, mechanical instability akin to the buckling of an imperfection-sensitive structure. (The general theory of buckling and post-buckling behavior of elastic structures is due to Koiter 1945; see Budiansky 1974 for a review.) Following up on this point of view, we propose to regard the t-to-m phase change under hydrostatic pressure as the result of a buckling instability at a critical pressure p_c that follows from an appropriately invented strain-energy functional of the dilatation θ and the shear strain γ in the a-c axes. The formulation should also be consistent with the hysteresis in critical pressure associated with the reverse transformation. The main goal of the exercise will then be to see -- *without further assumptions or the introduction of additional adjustable parameters* -- what the model would predict about the simultaneous effects of applied shear stress and pressure in provoking the t-to-m phase change and its reversal. Other implications of the model will also be deduced and assessed.

While this program contemplates an unconstrained zirconia single crystal, it can also be imagined applicable to a *partially stabilized* zirconia crystal containing a dopant (e.g., CaO, MgO, CeO_2, Y_2O_3) by adjustment of the magnitudes of p_c, p_c', and if necessary, θ_T and γ_T. However, stabilization of a zirconia inclusion by surrounding elastic material is another matter, and we will use the Eshelby (1958) equations to make a preliminary study of the phase change of an isolated spherical zirconia inclusion in an elastic medium subjected to combined hydrostatic stress and shear. Here *twinning* becomes important, and we will make a few remarks about this.

MODEL ASSUMPTIONS AND CALCULATIONS

Strain-energy, potential energy, and equilibrium

We contemplate a tetragonal crystal subjected to an applied stress, but restrict ourselves to external loading that consists only of hydrostatic stress $\sigma=-p$ and shear stress τ in a pair of a-c axes (Fig. 3), and assume that the isothermal elastic strain energy density at room temperature may be written as a smooth function $F(\theta,\gamma)$ of the associated dilatation and shear strain. Thus we suppress the possibility that a shear strain with respect to the other pair of a-c tetragonal axes will occur. Also, for convenience, we assume that $F(0,0)=0$, and that θ is measured from the

tetragonal state corresponding to $\gamma=\sigma=\tau=0$. The following polynomial choice for $F(\theta,\gamma)$ is the simplest one that will have the modeling consequences that we seek:

$$F(\theta,\gamma)=\tfrac{1}{2}K\theta^2+\tfrac{1}{2}G\gamma^2-C\theta\gamma^2+\tfrac{1}{4}B\gamma^4+\tfrac{1}{6}D\gamma^6 \tag{1}$$

In the conventional small-strain approximation, the specific potential energy (i.e., the Gibbs free energy) of the loaded system is then defined by

$$\Phi=F(\theta,\gamma)-\sigma\theta-\tau\gamma \tag{2}$$

and equilibrium states (θ,γ) are governed by the conditions

$$\frac{\partial\Phi}{\partial\theta}=\frac{\partial\Phi}{\partial\gamma}=0 \tag{3}$$

of stationary potential energy. These equilibrium states need not, of course, be stable.

Hydrostatic loading ($\tau=0$)

With τ dropped, we get the equilibrium equations

$$K\theta-C\gamma^2=\sigma \tag{4a}$$

$$(G-2C\theta)\gamma+B\gamma^3+D\gamma^5=0 \tag{4b}$$

The *fundamental* solution is

$$\theta_0=\sigma/K,\ \gamma_0=0 \tag{5}$$

which identifies K as the tetragonal bulk modulus, *which we assume to be positive*. But we require that for increasing σ (i.e., decreasing p) this solution change from stable to unstable at some critical value of σ. Since $\partial^2\Phi/\partial\gamma^2=G-2C\sigma/K$ is positive when the fundamental state is stable, we must have $C>0$, and so the tetragonal configuration becomes unstable for $\sigma>\sigma_c$ where

$$\sigma_c=-p_c=\frac{KG}{2C} \tag{6}$$

is the critical hydrostatic stress for phase transformation. Note the parameter G will be negative if the tetragonal phase is unstable in the stress-free state.

An alternative solution of (4) with $\gamma\neq0$ is specified by

$$\theta=\frac{\sigma}{K}+\frac{C}{K}\gamma^2 \tag{7a}$$

$$\sigma-\sigma_c=\left[\frac{BK}{2C}-C\right]\gamma^2+\left[\frac{DK}{2C}\right]\gamma^4 \tag{7b}$$

which provide σ and θ explicitly in terms of γ^2. This solution bifurcates from the fundamental one (5) at $\sigma=\sigma_c$. These equations can be put into an illuminating nondimensional form. For $\gamma>0$, we demand that the relation between σ and γ implied by Eq. (7b) have the form sketched in Fig. 4, with a minimum at $\sigma_c'=\sigma-\Delta\sigma$; and Eqs. (7) should have the solutions $\theta=\sigma/K+\theta_T$ and $\gamma=\gamma_T$ at $\sigma=\sigma_c$, corresponding to the monoclinic-phase strains . (There is, of course, a symmetrical solution with $\gamma<0$.) If we eliminate the constants in Eqs. (7) in favor of K, θ_T,γ_T, and $\Delta\sigma$, we get

$$\begin{cases} B = 2K\left(\dfrac{\theta_T^2}{\gamma_T^4}\right) - \dfrac{8\Delta\sigma\theta_T}{\gamma_T^4} \\ C = K\left(\dfrac{\theta_T}{\gamma_T^2}\right) \\ D = \dfrac{8\Delta\sigma\theta_T}{\gamma_T^6} \end{cases} \tag{8}$$

and we can write Eqs. (7) as

$$\frac{\theta - \theta_0}{\theta_T} = \left(\frac{\gamma}{\gamma_T}\right)^2 \tag{9a}$$

$$\frac{\sigma - \sigma_c}{\Delta\sigma} = 4\left[-\left(\frac{\gamma}{\gamma_T}\right)^2 + \left(\frac{\gamma}{\gamma_T}\right)^4\right] \tag{9b}$$

where θ_0 is the linear function of σ given in (5). These equations provide the nondimensional relations between load and distortion shown by the solid curves in Figs. 5ab. We review the behavior these curves reflect. Starting out from the tetragonal phase (γ=0) with $\sigma<\sigma_c$, increasing σ simply induces elastic dilatation changes until the martensitic phase transformation into the monoclinic state occurs as a consequence of the buckling instability at $\sigma=\sigma_c$. Then γ jumps to γ_T and θ increases suddenly by the amount θ_T. Under subsequent stress reversal, the material snaps back to the tetragonal shape when σ reaches $\sigma_c - \Delta\sigma$.

An immediate consequence of our simple model is that the instantaneous strain *reductions* γ_T^r and θ_T^r during the reverse m→t transformation are given by $\gamma_T^r = \gamma_T/\sqrt{2}$ and $\theta_T^r = \theta_T/2$, substantially smaller than the jumps of the t→m phase change. Clearly, such special relations can not have any basic significance, and are not to be regarded as predictions. Rather, they emphasize the likely need for more elaborate energy functionals in order to achieve consistency with the details of actual relations between direct and reverse transformation strains. Such experimental data for pressure cycling are not known to us.

Combined loading: hydrostatic stress and shear

It is convenient to work with the reduced energy functional $\Phi-\Phi_0$, where Φ_0, defined as the potential energy of the fundamental tetragonal state (5) under pure hydrostatic stress, is given by

$$\Phi_0 = \tfrac{1}{2}K\theta_0^2 - \sigma\theta_0 \tag{10}$$

Then Eqs. (1), (2), (6) and (8) provide a nondimensional reduced energy Ψ that may be written as

$$\Psi(\theta,\gamma) \equiv \frac{\Phi-\Phi_0}{\Delta\sigma\theta_T} = \frac{\omega}{2}\left[\frac{\theta-\theta_0}{\theta_T} - \left(\frac{\gamma}{\gamma_T}\right)^2\right]^2 - \left(\frac{\sigma-\sigma_c}{\Delta\sigma}\right)\left(\frac{\gamma}{\gamma_T}\right)^2 - 2\left(\frac{\gamma}{\gamma_T}\right)^4 + \frac{4}{3}\left(\frac{\gamma}{\gamma_T}\right)^6 - \left(\frac{\tau\gamma_T}{\Delta\sigma\theta_T}\right)\frac{\gamma}{\gamma_T} \tag{11}$$

where

$$\omega = \frac{K\theta_T}{\Delta\sigma} \tag{12}$$

The equilibrium equations $\frac{\partial\Psi}{\partial\theta} = \frac{\partial\Psi}{\partial\gamma} = 0$ give

$$\frac{\theta-\theta_0}{\theta_T} = \left(\frac{\gamma}{\gamma_T}\right)^2 \tag{13a}$$

$$\left[\frac{\sigma-\sigma_c}{\Delta\sigma}\right]\frac{\gamma}{\gamma_T} = 4\left[-\left(\frac{\gamma}{\gamma_T}\right)^2 + \left(\frac{\gamma}{\gamma_T}\right)^4\right]\frac{\gamma}{\gamma_T} - \frac{z}{2} \tag{13b}$$

where we have introduced the nondimensional shear stress parameter

$$z \equiv \left(\frac{\tau}{\Delta\sigma}\right)\left(\frac{\gamma_T}{\theta_T}\right) \tag{13c}$$

(The θ-γ relation (13a) is the same as it was for τ=0.) Eqs. (13) provide the dashed curves in Figs. 5ab, which show how the application of a constant shear stress, represented by several values of z, affects the relations between hydrostatic stress and strain. The important thing to note is that in the presence of shear the t→m phase transformation under increasing σ is no longer associated with a *bifurcation* instability, as it was for τ=0. Instead, for a range of non-zero τ's, the phase change reflects *limit-point* buckling at the local maximum in the σ-γ (or σ-θ) relation, and the critical stress σ_{max} for the t→m jump may be reduced substantially below σ_c by the presence of shear. For small values of τ, the snapping stress σ_{max} implied by Eq. (13) is given asymptotically by

$$\sigma_{max} \approx \sigma_c - 3(\Delta\sigma)^{1/3}\left(\frac{\tau\gamma_T}{2\theta_T}\right)^{2/3} \tag{14}$$

The reverse m→t transformation stress σ_{min} is also lowered by shear stress (linearly for small τ), and the hysteresis $[\sigma_{max}$-$\sigma_{min}]$ is less than the original $\Delta\sigma$. Further, for sufficiently large values of shear stress, namely

$$\tau > \frac{48}{25}\sqrt{\frac{3}{10}}\frac{\theta_T\Delta\sigma}{\gamma_T} \tag{15}$$

the tetragonal-to-monoclinic transition under increasing σ becomes gradual, losing its buckling character, and under reverse loading the trip back follows the same continuous path. All of this is

qualitatively consistent with the buckling behavior of imperfection-sensitive structures, in which small initial displacements lead to catastrophic collapse at loads significantly lower than the critical bifurcation load.

Stress-space phase diagram

Eq. (13b) implies that for $\sigma=\sigma_{max}$ *or* $\sigma=\sigma_{min}$, the variables γ, σ, and τ must satisfy the relations

$$z \equiv \frac{\tau\gamma_T}{\Delta\sigma\theta_T} = 2\left(\frac{\gamma}{\gamma_T}\right)\left[-\frac{\sigma-\sigma_c}{\Delta\sigma} - 4\left(\frac{\gamma}{\gamma_T}\right)^2 + 4\left(\frac{\gamma}{\gamma_T}\right)^4\right] \tag{16a}$$

$$\frac{\sigma-\sigma_c}{\Delta\sigma} = -4\left[3\left(\frac{\gamma}{\gamma_T}\right)^2 - 5\left(\frac{\gamma}{\gamma_T}\right)^4\right] \tag{16b}$$

where Eq. (16b) follows from the condition, for fixed τ, $(\partial\sigma/\partial\gamma)_\tau = 0$ applied to (16a). Hence Eqs. (16) provide a parametric representation, via γ/γ_T, for the t→m and m→t phase boundaries shown in Fig. 6. The range $0 \le \gamma/\gamma_T \le \sqrt{3/10}$ gives σ_{max} and the lower boundary, for σ_{min}, corresponds to $\sqrt{3/10} \le \gamma/\gamma_T \le \sqrt{1/2}$. These curves intersect tangentially at the *critical point* $z=(48/25)\sqrt{3/10}$, $(\sigma-\sigma_c)/\Delta\sigma=-1.8$, corresponding to $\left(\partial^2\sigma/\partial\gamma^2\right)_\tau = 0$. Note the vertical slope at $\tau=0$ of the t→m boundary, consistent with Eq. (15). (The reflection of these curves about the σ-axis provides the stress-space phase boundaries for $\tau<0$.) The long arrows in Fig. 6 emphasize the directions of stress change that provoke t→m and m→t phase changes, and the distance between the two curves represents the hysteresis. But the phase diagram is also valid for arbitrary stress paths in σ-τ stress space that cross the boundaries from the inside to the outside of the region they bound. Finally, we note that stress paths that remain outside this region induce only continuous strain changes, like those shown by the bottom curves of Fig. 5.

The t→m curve can be imagined analogous to a "yield" locus of plasticity theory, and then the associated jumps in θ and γ are like plastic strains. But in conventional plasticity theory a "normality" rule constrains the plastic strain ratios. In our problem, the condition of normality means that at each point on the t→m phase boundary, the t→m jumps $\delta\theta$ and $\delta\gamma$, and increments $d\sigma$ and $d\tau$ *along* the curve, would have to satisfy the relation $\delta\theta d\sigma+\delta\gamma d\tau=0$. This is clearly not so; indeed, at $\tau=o$, normality would imply $\delta\theta=0$!

It may be of interest to note that normality *would* hold if the phase jumps were arbitrarily required to occur (reversibly) on a phase boundary in σ-τ space corresponding to the Maxwell condition of equal Gibbs energy in the two phases, rather than at the states of limit-point instability. Since the energy is

$$F = \int_{(0,0)}^{(\theta,\gamma)} (\sigma d\theta + \tau d\gamma) - \sigma\theta - \tau\gamma = \int_{(0,0)}^{(\sigma,\tau)} (\theta d\sigma + \gamma d\tau) \tag{17}$$

we have $dF=\theta d\sigma+\gamma d\tau$ along any curve in σ-τ space. The energy jump $\delta F=0$ therefore implies $\delta[dF] = \delta\theta d\sigma+\delta\gamma d\tau=0$ along the Maxwell locus. (This kind of argument was used by Rice (1971) to make normality plausible in plasticity.) But we emphasize that there is no apparent reason to impose the Maxwell condition on martensitic phase changes that display stress hysteresis.

Monoclinic elastic moduli

A credibility check on our model can be made by calculating the predicted cross-compliance $d\gamma/d\sigma \equiv (\partial\gamma/\partial\sigma)_\tau$ of the stable monoclinic phase at zero pressure and shear, and comparing with available experimental data (Nevitt et al 1988) and atomic-theory estimates (Cohen et al 1988).

From Eq.(9b), the shear strain γ_0 at $\sigma=\tau=0$ (and room temperature) is given by

$$\frac{\gamma_0}{\gamma_T} = \sqrt{\frac{1+\sqrt{1-\sigma_c/\Delta\sigma}}{2}} \tag{18}$$

and the *cross-compliance* $d\gamma/d\sigma$ follows from (9b) by differentiation. The reciprocal of this compliance is the monoclinic cross-modulus given by

$$\left(\frac{d\gamma}{d\sigma}\right)^{-1} = 8\left(\frac{\Delta\sigma}{\gamma_0}\right)\left(\frac{\gamma_0}{\gamma_T}\right)^2\left[-1+2\left(\frac{\gamma_0}{\gamma_T}\right)^2\right] \tag{19a}$$

$$= 8\left(\frac{\Delta\sigma}{\gamma_0}\right)\left(\frac{\gamma_0}{\gamma_T}\right)^2\sqrt{1-\frac{\sigma_c}{\Delta\sigma}} \tag{19b}$$

This is the slope of the σ-γ curve (Fig. 4) at $\sigma=0$, $\gamma=\gamma_0$. Similarly, by differentiation of Eq. (13), we get the monoclinic shear modulus at $\sigma=\tau=0$ as

$$\left(\frac{d\gamma}{d\tau}\right)^{-1} = 16\left(\frac{\Delta\sigma}{\gamma_0}\right)\left(\frac{\theta_T}{\gamma_T}\right)\left(\frac{\gamma_0}{\gamma_T}\right)^3\sqrt{1-\frac{\sigma_c}{\Delta\sigma}} \tag{20}$$

The *sign* of the predicted value of $(d\gamma/d\sigma)^{-1}$ is of particular interest. Our model says it is positive, which means that incremental hydrostatic tension applied to room-temperature, monoclinic zirconia should *increase* the shear angle γ defined in Figs. (1) and (2). Careful attention to sign convention is clearly crucial in the assessment of this prediction vis-a-vis the measurements of Nevitt at al and the atomic calculations of Cohen et al. Telephone communication with both Nevitt and Cohen has confirmed that they used conventional monoclinic axes (Nye 1957), for which the β-angle between the a and c axes (Fig. 1) is *greater* than 90°, whereas we adopted the twinned configuration having an acute angle between the a and c axes. This means that we have to change the signs of their reported tension-shear cross-compliances when we use them to make comparisons with the predictions of Eq. (19). (More precisely, in terms of the standard crystallographic compliances S_{ij}, our $d\gamma/d\sigma$ is equal to $[-S_{15}-S_{25}-S_{35}]$.)

Guided by the measurements of Block et al (1985) for room-temperature zirconia we assume $\sigma_c=-2.8$ GPa and $\Delta\sigma=.6$ GPa in Eq. (18) to get $\gamma_0/\gamma_T=1.30$. Although the

transformation strain γ_T has usually been presumed equal to about .16 , this is evidently based on the value of $(\beta-\pi/2)$, where $\beta\approx 99°$ is the reported magnitude of the angular lattice parameter of monoclinic zirconia at zero pressure and room temperature (Green et al 1989). Hence it is more appropriate to use .16 as the value of γ_0, rather than γ_T, in (19) and (20). A room-temperature value of θ_T is not well established, but we will evaluate Eq. (20) using the assumption $\gamma_T/\theta_T = 4$. This is consistent with lattice-parameter data quoted by Green et al (1989, p.220) for monoclinic ZrO_2 at 956°C and tetragonal ZrO_2 at 1152°C, which indicate $\theta_T \approx .03$, rather than the usually assumed value .04.

Table I shows the magnitudes of $(d\gamma/d\sigma)^{-1}$ and $(d\gamma/d\tau)^{-1}$ thereby given by (19) and (20), together with the values (for our coordinate system) derived from the measurements of Nevitt et al and the atomic estimates of Cohen et al.

TABLE I

Monoclinic Moduli (GPa)

(σ_c=−2.8 GPa, $\Delta\sigma$=.6 GPa, γ_0=.16, $\gamma_T/\theta_T = 4$)

modulus	Eqs. (18-20)	Nevitt et al	Cohen et al
$(d\gamma/d\sigma)^{-1}$	121	− 680	400, 260
$(d\gamma/d\tau)^{-1}$	78	65	90, 64

The two sets of numbers in the last column correspond to two different atomic structures that were assumed by Cohen et al for monoclinic zirconia.

Not too much significance should be attached to the absolute magnitudes of our numbers, because our model is so primitive. But the difference in sign between our result for the cross-modulus and Nevitt's experimental value is disappointing, because it is hard to see how our model could easily be modified to change the sign of $d\gamma/d\sigma$. Of course, the same sign difference between the Nevitt and Cohen results do suggest that final judgement may be premature. In this connection, we have scrutinized the elastic constants tabulated by Simmons and Wang (1971) for 21 different monoclinic materials, and we find that $d\gamma/d\sigma$ is positive for 12 of these, and negative for the rest. Perhaps our model and variants thereof could make sense only for some kinds of monoclinic materials and not others. (Also, we remain uneasy about the consistency of the sign conventions for monoclinic crystals used by various authors.)

Although our zirconia model has failed to pass the experimental credibility check we sought, we will stay with it a little longer, and explore some of its consequences concerning phase changes of *inclusions* from tetragonal to monoclinic, and back.

Elastically constrained crystals

We contemplate next an isolated, single tetragonal crystal embedded in an infinite matrix of non-transforming, isotropic, linearly elastic material, and seek to determine critical combinations of

stress at infinity that will cause its transformation to a monoclinic phase. We restrict ourselves to the application of just two stress types at infinity, namely hydrostatic stress σ^{∞} and a single shear stress τ^{∞}, the latter aligned with the a-c axes (Fig. 3) of the tetragonal inclusion. In this exploratory study, we will make some simplifying assumptions, as follows:

(i) the inclusion will be assumed to be spherical;

(ii) strains will be assumed homogenous in the inclusion; specifically, twinning will be presumed not to occur;

(iii) we will continue to apply the single crystal relations (9a) and (13) connecting σ, τ, θ, and γ to the inclusion, with σ reinterpreted as the *mean* normal stress. This represents an extra simplifying assumption, because the constrained crystal will suffer stress states that are more complex than the combination of pure hydrostatic loading and simple shear which we contemplated in our study of the unconstrained crystal;

(iv) the bulk modulus of the matrix will be set equal to the tetragonal bulk modulus K of the inclusion.

Assumption (ii) is drastic. Constrained tetragonal zirconia inclusions generally *do* display multiple twinned monoclinic bands when they transform. It seems nevertheless worthwhile to pursue the idealized constrained-crystal model we have set, to see how the calculations go, in preparation for the considerably more sophisticated analysis that would be needed to take twinning *into account*; and to gain some insight into the magnitudes of stresses and strains that would be involved in a hypothetical twin-free transformation.

The exact Eshelby-Hill relations (Eshelby 1959; Hill 1965) for a homogeneous spherical inclusion can be written as

$$\begin{cases} \sigma^{\infty} - \sigma = K\left(\alpha^{-1} - 1\right)(\theta - \theta^{\infty}) \\ \tau^{\infty} - \tau = G_M\left(\beta^{-1} - 1\right)(\gamma - \gamma^{\infty}) \end{cases} \tag{21}$$

in terms of the bulk modulus K and shear modulus G_M of the matrix, and the Eshelby parameters

$$\alpha = \frac{1+\nu}{3(1-\nu)}, \quad \beta = \frac{2(4-5\nu)}{15(1-\nu)} \tag{22}$$

The strains at infinity are $\theta^{\infty} = \sigma^{\infty}/K$ and $\gamma^{\infty} = \tau^{\infty}/K$. With $G_M = K[3(1-2\nu)]/[2(1-\nu)]$, Eqs. (21) together with the inclusion relations (13) may be used to eliminate σ and τ, and get the connections

$$\frac{\theta - \theta^{\infty}}{\theta_T} = \alpha\left(\frac{\gamma}{\gamma_T}\right)^2 \tag{22a}$$

$$\left[\frac{\sigma^{\infty} - \sigma_c}{\Delta\sigma} - \lambda\omega(\gamma_T/\theta_T)^2\right]\frac{\gamma}{\gamma_T} = 4\left[-c\left(\frac{\gamma}{\gamma_T}\right)^2 + \left(\frac{\gamma}{\gamma_T}\right)^4\right]\frac{\gamma}{\gamma_T} - \frac{(\tau^{\infty}/\Delta\sigma)(\gamma_T/\theta_T)}{2\beta} \tag{22b}$$

where

$$\lambda = \frac{3(1-2\nu)(7-5\nu)}{4(1+\nu)(4-5\nu)} \tag{23}$$

and $$c = 1 - \omega(1-\alpha)/4 \tag{24}$$

It now follows from (22b) that for $\tau^{\infty}=0$, the tetragonal inclusion strains remain equal to $\theta = \theta^{\infty}$ and $\gamma = 0$ until σ^{∞} reaches the bifurcation stress

$$\begin{aligned}\sigma_c^{\infty} &= \sigma_c + \lambda\omega\Delta\sigma(\gamma_T/\theta_T)^2 \\ &= \sigma_c + \lambda K\gamma_T^2/\theta_T\end{aligned} \tag{25}$$

The inclusion strains will then have finite jumps *only* if c>0, with magnitudes

$$\bar{\gamma}_T = \sqrt{c}\gamma_T, \quad \bar{\theta}_T = \alpha c\theta_T \tag{26}$$

During reverse loading the jump back to the tetragonal state will occur at $\sigma^{\infty} = \sigma_c^{\infty} - \Delta\sigma^{\infty}$, where

$$\Delta\sigma^{\infty} = c^2(\Delta\sigma) \tag{27}$$

is the hysteresis in σ^{∞}. The relations (22) may now be rewritten to look very much like those in (13) for the unconstrained crystal, as follows:

$$\frac{\theta - \theta^{\infty}}{\bar{\theta}_T} = \left(\frac{\gamma}{\bar{\gamma}_T}\right)^2 \tag{28a}$$

$$\left[\frac{\sigma^{\infty} - \sigma_c^{\infty}}{\Delta\sigma^{\infty}}\right]\frac{\gamma}{\bar{\gamma}_T} = 4\left[-\left(\frac{\gamma}{\bar{\gamma}_T}\right)^2 + \left(\frac{\gamma}{\bar{\gamma}_T}\right)^4\right]\frac{\gamma}{\gamma_T} - \frac{\bar{z}}{2} \tag{28b}$$

where $$\bar{z} \equiv \frac{\alpha}{\beta}\left(\frac{\tau^{\infty}}{\Delta\sigma^{\infty}}\right)\left(\frac{\bar{\gamma}_T}{\bar{\theta}_T}\right) \tag{29}$$

Accordingly, for c>0, all of the results plotted in Figs. 5-6 become applicable to the constrained crystal, simply by substituting σ^{∞}, σ_c^{∞}, $\Delta\sigma^{\infty}$ for σ, σ_c, and $\Delta\sigma$, respectively, and replacing γ_T, θ_T, and z by $\bar{\gamma}_T$, $\bar{\theta}_T$, and $\bar{z}$. For the special case ν=.2, Eqs. (22) give $\alpha=\beta$=.5, and the analogy between Eqs. (13-14) and Eqs. (28-29) becomes perfect. For this choice of ν, we get λ=3/8 and c=1-ω/8.

For c<0, Eqs. (22) show that even with τ^{∞}=0 the inclusion would undergo a smooth transition to a monoclinic-like state as the remote hydrostatic tension is increased beyond its critical value. This corresponds to the case called "subcritical" by Budiansky et al (1983); their "supercritical" case, in which the constrained inclusion transforms abruptly at a critical stress, corresponds to c>0.

A rough estimate of σ_c^{∞} via Eq. (25), with λ=3/8, K=150 GPa, σ_c=−3 GPa, γ_T=.12, and θ_T=.03, gives σ_c^{∞}=24 Gpa. This seems much too high; working backwards from measured toughnesses of transformation-toughened materials suggests values of σ_c^{∞} around 1/2 GPa. Some reduction of the elastic constraint on inclusions can be attributed to inclusion interaction, but the chief culprit invalidating the calculation of σ_c^{∞} must be twinning. Finally, we note that for ν=.2, the supercritical transformation criterion c>0 requires $\omega = K\theta_T/\Delta\sigma < 8$; with $\Delta\sigma$=.6, we get the estimate ω=10 -- too high for supercriticality.

Twin bands and twinning

There are at least two distinct ways in which twinned configurations could occur in transforming crystals (Chen and Chiao 1983), thereby invalidating our calculations. First of all, even an unconstrained tetragonal crystal can be expected to suffer twinning as it transforms to the monoclinic state, as a consequence of habit-plane compatibility requirements when a phase-change interface sweeps across the crystal (Wayman 1964). Second, minimum-energy requirements associated with the phase change of an elastically constrained embedded single crystal may induce bands of monoclinic variants, as has generally been observed in all but very small inclusions. At least qualitatively, this kind of twin-band development, and the dependence of the number of twin bands on crystal size, may be understood (e. g., Evans et al, 1981) on the basis of a trade-off between the reduced elastic strain energy provoked by multiply twinned configurations of transforming embedded inclusions and the band interface surface energies. A quantitative mechanical analysis of these twinning issues and their interactions, in the spirit of the present approach, remains to be executed. Not least of the difficulties in such a task is the stipulation of the required twin-band interface energies, the magnitudes of which are not known.

CONCLUDING REMARKS

Subject to the admittedly drastic simplification of permitting only homogeneous states in both constrained and unconstrained crystals, we have presented a model for tetragonal-to-monoclinic transformation in zirconia, and the reverse phase change, under a simple state of combined hydrostatic tension σ and shear τ. The nature of the combined σ-τ stress conditions for phase change has been explored, albeit speculatively, as have several other implications of the model. Similar studies involving more complex stress states of loading can be undertaken, and the more challenging problem of incorporating twinning effects remains to be met.

ACKNOWLEDGEMENTS

We are grateful for instructive comments by Professor Arthur Heuer concerning the essential role of twinning in zirconia phase transformation. This work was supported in part by the National Science Foundation under a Materials Research Laboratory grant (DMR-89-20490), in part by a DARPA University Research Initiative grant (Subagreement P.O. No.VB38639-0 with the University of California, Santa Barbara, ONR Prime Contract 00014-86-K-0753), by the Division of Applied Sciences, Harvard University, and by the Department of Aerospace Engineering and Mechanics, University of Minnesota.

REFERENCES

Amazigo, J.C. and Budiansky, B. (1988). "Steady-state crack growth in supercritically transforming materials", Int. J. of Solids and Structures **24**, 751-755.

Arashi, H., Skimomura, O., Yagi, T., Akimoto, S., and Kudok. Y. (1988). "P-T Phase diagram of ZrO_2 determined by in situ X-ray diffraction, Measurements at high pressures and high temperatures", in Advances in Ceramics, v. 24, Science and Technology of Zirconia III, Am. Ceram. Soc., Westerville, OH, 493-500 .

Garvie, R. C., Hannink, R.H. and Pascoe, R.T. (1975). "Ceramic steel", Nature **258**, 695-708.

Block, S., Da Jornada, J.A.H., and Piermarini, G.J. (1985). "Pressure-temperature phase diagrams of Zirconia", J. Am. Ceram. Soc. 68, 497-99

Budiansky, B. (1974). "Theory of Buckling and Post-Buckling Behavior of Elastic Structures", Advances in Applied Mechanics, Vol. 14, Academic Press, Inc., 1-65.

Budiansky, B., Hutchinson, J.W. and Lambropoulos, J.C. (1983)."Continuum theory of dilatant transformation toughening materials", Int. J. Solids Struc. **19**, 337-356.

Chan, S.K. (1988). "The polymorphic transformations of Zirconia", Physica **B 150**, 212-222.

Chen, I-W. and Chiao, Y-H. (1983). "Martensitic nucleation in ZrO_2", Acta metall., **31**, 1627-1638.

Chiao, Y-H and Chen, I-W. (1990). "Martensitic growth in ZrO_2", Acta metall. mater., **38**, 1163-1174.

Cohen, R.E., Mehl, M.J. and Boyer, L.L. (1988). "Phase transitions and elasticity in Zirconia", Physica **B 150**, 1-9.

Eshelby, J. D. (1957). "The Determination of the Elastic Field of an Ellipsoidal Inclusion , and Related problems", Pro. Roy. Soc. **A241**, 376-396.

Evans, A.G., Burlingame, N., Rory, M. and Kriven, W.M. (1981). "Martensitic transformations in zirconia – particle size effects and toughening", Acta Metall. **29**, 447-456.

Evans, A.G. and Cannon, R.M. (1986). "Toughening of brittle solids by martensitic transformations", Acta Metall. **34**, 761-800.

Evans, A.G., and Heuer, A.H. (1980). "Review: Transformation toughening in ceramics: Martensitic transformations in crack-tip stress fields", J. Am. Ceram. Soc. 63, 241-248.

Garvie, R.C., Hannink, R.H.J. and Pascoe, R.T. (1975). "Ceramic steel", Nature **258**, 695-708.

Green, D. J., Hannink, R.H.J., and Swain, M. V. (1989). *Transformation Toughening of Ceramics*, CRC Press.

Hill, R. (1965). "Continuous Micro-mechanics of Elastoplastic Polycrystals", J. Mech. Phys. Solids **13**, 89-101.

Koiter, W. T. (1945). "On the Stability of Elastic Equilibrium" (in Dutch). Thesis, Delft Univ., H. J. Paris, Amsterdam; English Transl. (a) NASA TT-F10, 833 (1967), (b) AFFDL-TR-70-25 (1970).

Lambropoulos, J. C. (1986). "Shear, shape and orientation effects in transformation toughening", Int. J. Solids Struct. **22**, 1083-1106.

McMeeking, R.M. and Evans, A.G. (1982). "Mechanics of transformation toughening in brittle materials", J. Am. Ceram. Soc. **65**, 242-246.

Nevitt, M.V., Chan, S.K., Liu, J.Z., Grimsditch, H.H. and Fang, Y. (1988). "The elastic properties of monoclinic ZrO_2", Physica **B 150**, 230-233.

Nye, J. F. (1957). *Physical Properties of Crystals*, Oxford Univ. Press, London.

Rice, J. R. (1971). "Inelastic Constitutive Relations for Solids: An Internal Variable Theory and Its Application to Metal Plasticity", J. Mech. Phys. Solids, **19**, 433-455.

Rose, L.R.F. (1986). "The size of the transformed zone during steady-state cracking in transformation toughened materials", J. Mech. Phys. Solids **34**,. 609-616.

Rühle, M. and Evans, A.G. (1989). "High toughness ceramics and ceramic composites", Progress in Materials Science **33**, 85-167.

Simmons, G. and Wang, H. (1971). *Single Crystal Elastic Constants and Calculated Aggregate Properties: A Handbook*, MIT Press, Cambridge, MA.

Stump, D.M. (1991). "The role of shear stresses and shear strains in transformation-toughening", Phil. Mag. **A 64**, 879-902.

Stump, D.M. and Budiansky, B. (1989a). "Crack growth resistance in transformation toughened ceramics", Int. J. Solids Structure **25**, 635-646.

Stump, D.M. and Budiansky, B. (1989b). "Finite cracks in transformation-toughened ceramics", Acta. Met. **37**, 3297-3304.

Sun, Q.P., Huang, Y., Yu, S.P. and Hwang, K.C. (1990). "Toughening analysis of Mode I and Mode III cracks in PSZ and TPZ ceramics", preprint.

Wayman, C.M. (1964). *Introduction to the Crystallography of Martensitic Transformations*, Macmillan, New York.

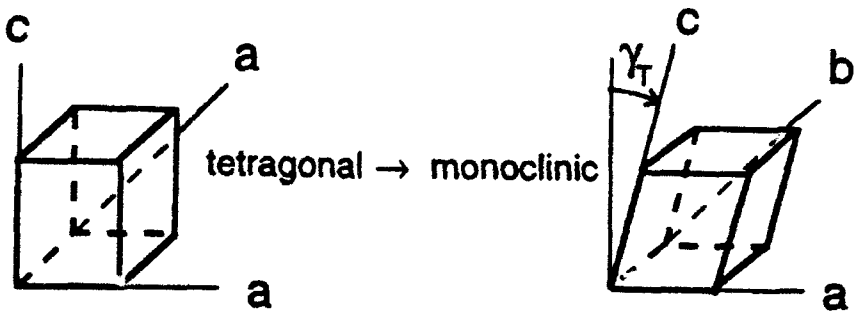

Fig. 1. Tetragonal and monoclinic axes.

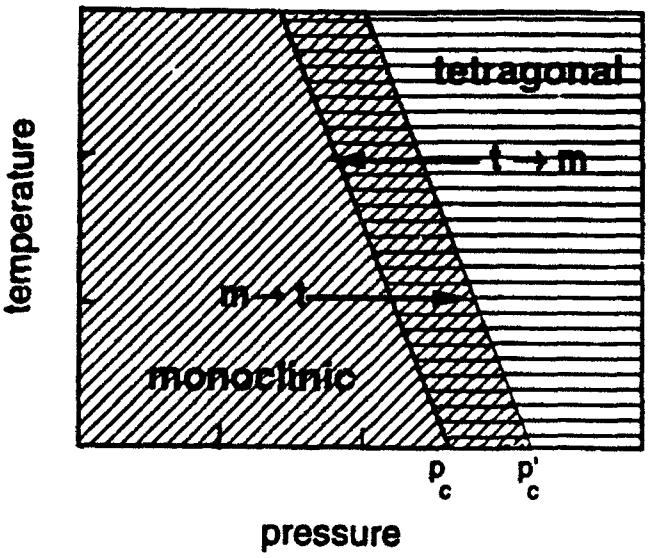

Fig. 2. Schematic pressure-temperature phase diagram.

Fig. 3. Hydrostatic stress σ and shear stress τ applied to the tetragonal crystal produces dilatation θ and shear strain γ.

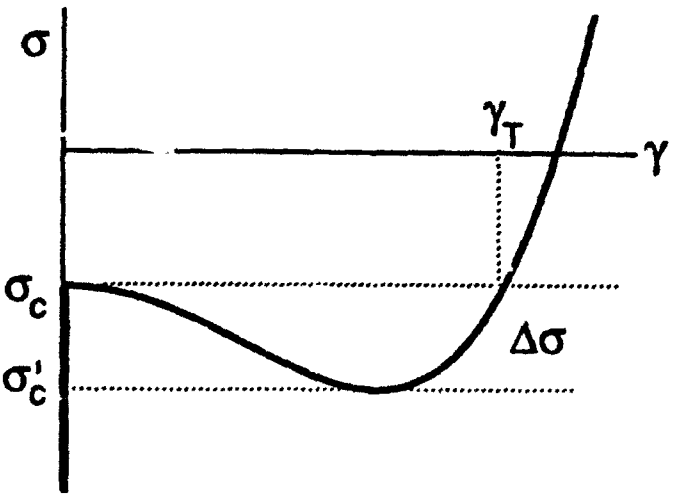

Fig. 4. Schematic relation between hydrostatic stress σ and shear strain γ>0.

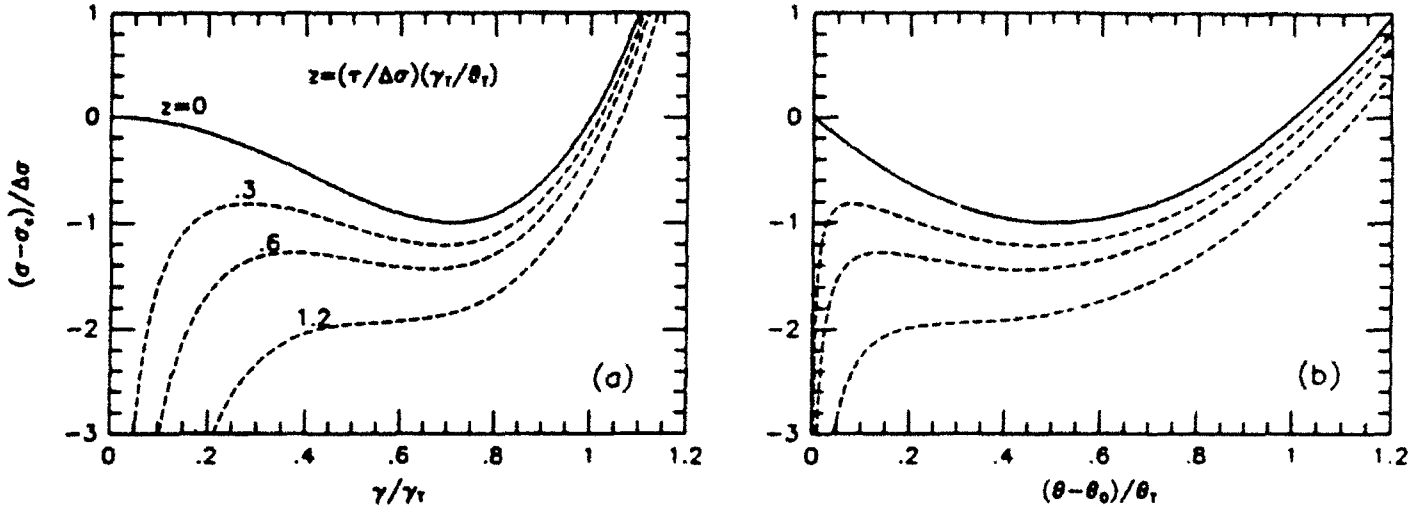

Fig. 5. Non-dimensional hydrostatic-stress change vs. (a) normalized shear strain and (b) normalized dilatation change, for various values of the non-dimensional shear stress parameter z.

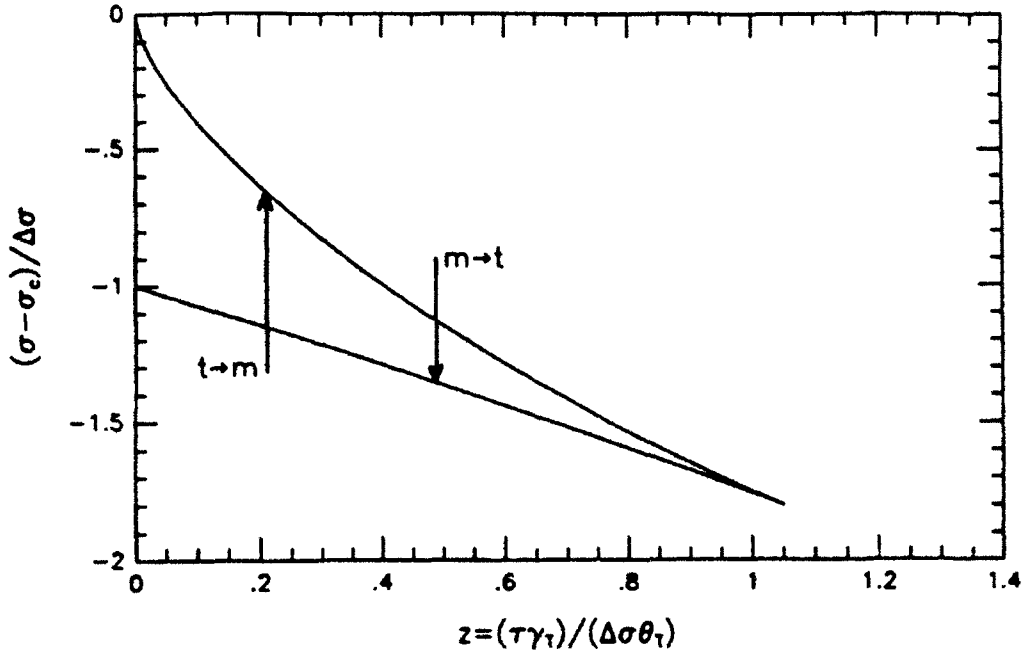

Fig. 6. Non-dimensional, isothermal phase diagram, showing combinations of hydrostatic stress σ and $\tau>0$ for phase change; the arrows show directions of loading in stress-space for the tetragonal-to- monoclinic transformation and its reverse.

Scripta METALLURGICA et MATERIALIA
Vol. 26, pp. 1675-1680, 1992
Printed in the U.S.A.
Pergamon Press Ltd.
All rights reserved

Deformation of Nanoscale Cermets

by
A.G. Evans
Materials Department, University of California
Santa Barbara, CA 93106-5050

and
J.P. Hirth
Mechanical and Materials Engineering Department
Washington State University
Pullman, WA 99164-2920

(Received March 23, 1992)

Introduction

Cobalt-tungsten carbide cermets are prototypical dual-phase composites wherein the metal is the minor phase (volume fraction, $f_m = 0.1\text{-}0.2$), but is continuous, because of capillarity effects at the interphase interfaces during sintering. The refinement of such composites into the nanometer size scale regime is of interest and indeed, has been achieved [1], with the expectation that nanoscale refinement will enhance such properties as hardness and tensile strength. The role of plastic flow in the metal phase on the stress/strain curve of these composites is addressed in this article. The emphasis of most previous analyses of dual-phase metal/ceramic composites has been on the flow strength of systems with dispersed particles, in the $f_m > 0.5$ range. The results have been interpreted either by using a dislocation pile-up approach [2] or (for $f_m > 0.8$) by considering dislocation loops bowing around particles [3]. Here, we suggest that neither of these models is appropriate for cermets with small metal fraction ($f_m < 0.2$) at size scales in the nanometer regime. Instead, flow in the metal is related to single dislocations moving in the metal channels, controlled by an Orowan-type relation. Furthermore, the constraint of the less deformable WC is shown to provide strong flow strength elevation. The latter effect has previously been evaluated for structures in the micrometer (or greater) regime in terms of a continuum approach [4].

The flow properties are expected to be sensitive to microstructural details, especially the morphology of the metal phase. Two bounds are analyzed (Fig. 1): i) both phases are continuous, with the metal as a cylindrical network along the three-grain interface of the ceramic, ii) only the metal is continuous and thus serves as a "matrix" with embedded ceramic particles. In all cases, it is assumed that the stress is below that at which cracks form in the ceramic, that the interfaces are "strong" (do not debond) and that the ceramic is elastic. Analysis of the latter morphology is approached from two perspectives: one based strictly on continuum plasticity, wherein there are no size effects, and the other using dislocation models. Comparison of these two approaches provides important insight about nanoscale issues.

0036-9748/92 $5.00 + .00
Copyright (c) 1992 Pergamon Press Ltd.

Analysis

Both Phases Continuous

When both the metal and ceramic are continuous, the stress/strain behavior without cracking should be bilinear (Fig. 2a) and essentially the same as that found for *either a metal matrix composite with continuous* ceramic fibers [5] or a ceramic with a dispersed metal phase [6]. The initial modulus, E_o, is governed by that for the composite E, and the slope, E_t, beyond the "knee" is related to modulus of the composite with *all* of the stress borne by the ceramic. The intermediate behavior around the "knee" is governed by the flow properties of the metal, through the evolution of load shedding to the ceramic. The magnitude of E_t depends on the precise morphology of the metal, analogous to the strong effects of pore shape on the modulus of porous bodies. Two extremes are of interest. When the metal has the morphology of rods aligned along the loading axis, the "rule-of-mixtures" applies, such that

$$E_t/E = (1-f_m) \tag{1a}$$

Conversely, when the metal occurs as an isolated spherical phase

$$E/E_t = 1+[10/(7-5\nu_c)]f_m/(1-f_m) \tag{1b}$$

where ν_c is Poisson's ratio for the ceramic. The corresponding composite Poisson's ratio is

$$\nu_t = (1/2)-E_t(1-2\nu_c)/2E \tag{1c}$$

The location of the "knee" and the behavior in its vicinity are strongly influenced by the highly constrained nature of the plastic flow in the metal. Consequently, there are major effects of morphology and of residual stress caused by thermal expansion misfit. The details are not addressed in this article.

Continuous Metal Phase

Continuum Approach

Some basic continuum results [7,8] are reviewed first. The stress/strain curve for a thin metal layer between elastic plates (Fig. 2b), in the absence of work hardening in the metal, exhibits a non-linear transient with high apparent work hardening of the composite, followed by a limit stress, σ_t, given by;

$$\sigma_t/\sigma_o = (3/4)+(1/4)d/h \tag{2}$$

where σ_o is the uniaxial yield strength of the metal, h is the metal thickness and d the plate width. This limit stress develops after strains in the metal layer of order ϵ_o, where ϵ_o is the uniaxial yield strain. If the metal layer in the composite has uniform width *everywhere*, the initial value of d/h in Eqn. (2) is related to the metal volume fraction, in approximate accordance with

$$f_m = 3h/d. \tag{3a}$$

More generally,

$$f_m = 3\chi h/d \tag{3b}$$

where χ is dependent on the excess metal phase at three- and four-grain interfaces. The simplistic results obtained by inserting Eqn. (3c) into Eqn. (2) have several obvious limitations. The most important problems are concerned with i) the metal phase *morphology*, ii) metal phase *redistribution* and iii) *work hardening* in the metal. Even when the metal is perfectly plastic, σ_t is sensitive to χ, which dictates the metal concentration at which the ceramic phase becomes connected, f_m^*. This effect is illustrated in Fig. 2 for the case of a ceramic phase having nominal "equiaxed" morphology. As expected, $\sigma_t/\sigma_o \to \infty$ as $f_m \to f_m^*$. Hence the definition of f_m^* in terms of the metal phase morphology is *critical*. In addition, *conservation of volume* in the metal (assuming no debonding and no cavitation) requires metal redistribution, such that the metal phase thickness h along the transverse interfaces diminishes as the composite deforms. In the limit, h can reach zero, leading to contact of

ceramic grains and a decrease in the effective value of the area fraction f_m in some regions. This effect further elevates the flow strength as the composite deforms and obviates the existence of a limit load. Finally, work hardening in the metal increases the flow strength. Some typical effects for power law hardening with equiaxed particles (when $f_m \approx 0.8$) are illustrated in Fig. 3.

In summary, the dramatic effects of morphology and of work hardening in the metal on the stress/strain curve establish that predictions are only meaningful when complete experimental information is available concerning these factors. Without this information, the utility of the continuum description cannot be evaluated. However, it is emphasized that the continuum approach does not give a particle size effect in the absence of cracking, debonding and cavitation, at least when the morphology is size independent. Clear experimental information that particle size is important, in some cases, indicates the need for a dislocation-based approach to address certain aspects of the flow behavior.

Dislocation Approach

In the nanometer size regime, two issues are important. Dislocations can neither bow around the ceramic particles, because of geometric constraints, nor can they be sustained in a pileup array, because the stress to sustain two dislocations (the minimum size pileup) exceeds that to move a single loop. Instead, loops nucleate and deposit at the interface, as shown in Fig. 4a. The segment of these loops remaining in the metal phase can then move in the z direction as represented in Fig. 4b. In the case depicted, the dislocations in the interface are considered to be edge dislocations and the moving segments screw dislocations. The structure is analogous to that within i) persistent slip bands in fatigued metals [9]; ii) heavily deformed pearlite [10]; and iii) strained multilayer structures (strained superlattices) [11]. When the modulus of the ceramic exceeds that of the metal, the dislocations encounter an image repulsion and stand off a distance y_o from the interface [12,13]. For an extreme case of Al_2O_3/Nb, with a shear modulus ratio of 6, the stand-off distance is $y_o = 0.09h$. Hence, for most cases, this image effect can be neglected.[‡]

The resolved effective shear stress to move the dislocation segment is

$$\tau = \mu b \cos\phi / h \tag{4}$$

where μ is the shear modulus, b is the Burgers length and ϕ is defined in Fig. 4c. The angle ϕ is dictated by the line energy of the moving (screw) segment,

$$(W_s/L) = (\mu b^2/4\pi)\ln(h/b) \tag{5a}$$

relative to that of the edge segment deposited at the interface

$$W_e/L = [\mu b^2/4\pi(1-\nu)]\ln(\lambda/b) \tag{5b}$$

Here, λ is the mean dislocation spacing in the interface. Usually, as soon as microstrain is imposed on the system, λ decreases with strain to a limiting value , 2-3b [14]. The relation among the above quantities is: $\cos\phi = W_e/W_s$. Consequently, since W_s depends weakly on h, the power dependence of τ on h deviates only slightly from -1 [*] [15].

The resolved effective shear stress must equal the resolved flow strength, such that,

$$\sigma_{yy} - \sigma_{xx} = \tau/m = \mu b \cos\phi / mh \tag{6}$$

where m is the Schmid factor for the active glide plane. The relationship between σ_{yy} and σ_{xx} depends on the constraint that develops in the thin metal layers. This, in turn, depends on the plastic flow that occurs around the corners of the ceramic particulate, between the transverse and normal layers. If such flow in inhibited, the system behaves in a strictly elastic manner. Conversely, if this process occurs readily, the composite flow strength

[‡] If it is significant, the effective Orowan segment length becomes $h-2y_o$ instead of h.

[*] Usually, scatter in data is such that it is difficult to discern deviations from -1 power.

is dictated by a constraint factor, analogous to that for the continuum phenomenon, Eqn. (1). Furthermore, composite flow is controlled by the *transverse layer thickness*, which *decreases* as the composite deforms, leading to geometric hardening. Specifically, since the plastic strain is limited to the metal phase, the transverse plastic strain is

$$\epsilon^p_{xx} \equiv \epsilon^p_{yy}/2 = -\Delta h/2d \tag{7a}$$

whereupon the transverse layer thickness reduces to

$$h/d = (h_o/d)+\epsilon^p_{xx} \tag{7b}$$

where h_o is the initial metal layer thickness. The ratio h_o/d is, in turn, related to the metal volume fraction, subject to the metal phase morphology parameter χ, Eqn. (3b). The plated dislocations in Fig. 4a provide load shedding to the ceramic phase just as in the continuum analysis. Hence, Eqn. (2) applies to this case with $\sigma_0=\tau/m$, Eqn. (6). The limit flow strength for nanoscale structure thus becomes,

$$\sigma_f = \frac{9\cos\phi\chi^2(b/d)\mu}{4m[f_m-(3\chi/2)\epsilon^p_{yy}]^2}\left\{1+\frac{f_m}{\chi}\left[1-\frac{3\chi\epsilon^p_{yy}}{2f_m}\right]\right\} \tag{8a}$$

$$= [9\cos\phi\chi^2(b/d)\mu/4mf_m]\ [1+3\chi\epsilon^p_{yy}/f_m] \tag{8b}$$

Consequently, when f_m is small and the metal phase morphology dictates that $\chi > 1$, *constraint becomes a dominant factor*, leading to linear hardening. Furthermore, there is a nanoscale size effect, associated with the term b/d. Note that the linearity in the hardening is qualitatively similar to the flow behavior expected when the ceramic phase is continuous.

Acknowledgement

The research was supported by the DARPA University Research Initiative at the University of California, Santa Barbara, under ONR contract No. 00014-86-K-0753.

References

1. B.E. Kear, Rutgers University, research in progress.
2. N.P. Louat and M.A. Imam, *Scripta Metall.*, **23**, 721, (1989).
3. J.C. Williams and J.P. Hirth, in *Rapid Solidification Processing Principles and Technologies, III*, Ed. R. Mehrabian, National Bureau of Standards, Gaithersburg, MD, 1983, p. 135.
4. T. Christman, A. Needleman and S. Suresh, *Acta Metall. Mater.*, **37**, 3029, (1989).
5. G.J. Dvorak and Y.N. Bahei-El-Din, *J. Appl. Mech.* **49**, 327, (1982).
6. B. Budiansky, Appendix in L.S. Sigl, P.A. Mataga, R.J. Dalgleish, R.M. McMeeking and A.G. Evans, *Acta Metall.*, **36**, 945, (1988).
7. G. Bao, J.W. Hutchinson and R.M. McMeeking, *Acta. Metall. Mater.*, **39**, 1871, (1991).
8. R. Hill, Mathematical Theory of Plasticity, Oxford Univ. Press (1961).
9. D. Kuhlmann-Wilsdorf and C. Laird, *Mat. Sci. Eng.*, **27**, 137, (1977); **37**, 11, (1979).
10. M. Dollar, I.M. Bernstein and A. Thompson, *Acta Metall.*, **36**, 311, (1988).
11. R. Hull and J.C. Bean, *J. Vac. Sci. Tech.*, **A7**, 2580, (1989).
12. J.S. Koehler, *Phys. Rev.*, **B2**, 547, (1970).
13. S.V. Kamat, J.P. Hirth and B. Carnahan, *Mater. Res. Soc. Symp. Proc.*, **103**, 55, (1988).
14. J.P. Hirth and J. Lothe, *Theory of Dislocations*, 2nd edition, Wiley, New York, 1982.
15. M.F. Ashby, *Acta Metall.*, **14**, 679, (1966).

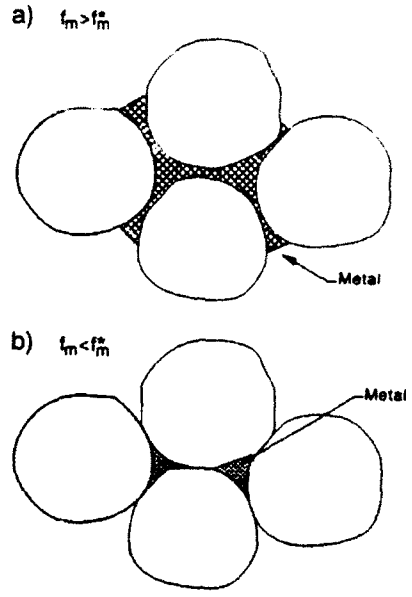

Fig.1. Ceramic-metal composites with (a), the metallic phase continuous and (b), both phases continuous.

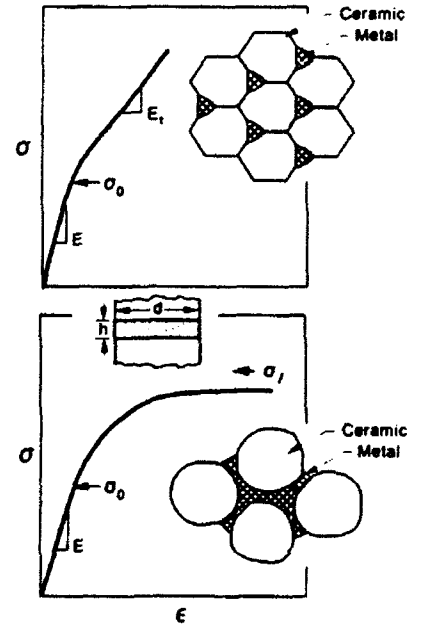

Fig. 2. Typical stress-strain curves for ceramic-metal composites with (a), both phases continuous and (b), the metallic phase continuous

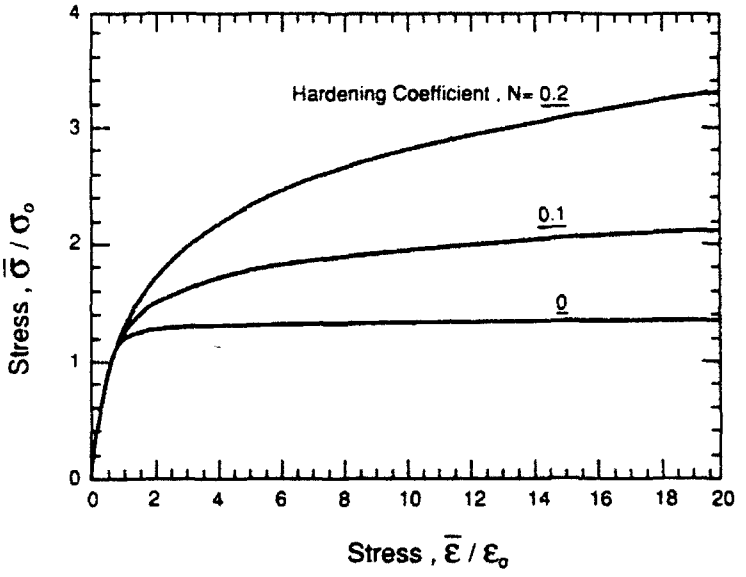

Fig. 3. Effect of power law hardening exponent N on the stress-strain behavior of a metal matrix-equiaxed ceramic particulate composite with f_m = 0.8 [7].

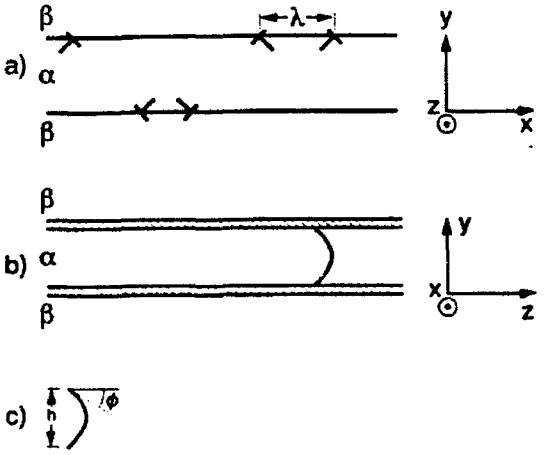

Fig. 4. Dislocations formed in α phase and (a), deposited at or near interface (view along dislocation line), (b), bowing out and moving (view perpendicular to (a). (c) shows the geometry of the bowed segment.